Advances in Experimental Medicine and Biology 1093

Guoyan Zheng · Wei Tian · Xiahai Zhuang
Editors

Intelligent Orthopaedics

Artificial Intelligence and Smart Image-guided Technology for Orthopaedics

Springer

Advances in Experimental Medicine and Biology

Volume 1093

More information about this series at http://www.springer.com/series/5584

Guoyan Zheng • Wei Tian • Xiahai Zhuang
Editors

Intelligent Orthopaedics

Artificial Intelligence and Smart Image-guided Technology for Orthopaedics

Springer

Editor
Guoyan Zheng
University of Bern
Bern, Switzerland

Xiahai Zhuang
Fudan University
Shanghai, China

Wei Tian
Beijing Jishuitan Hospital
Peking University
Beijing, Beijing, China

ISSN 0065-2598 ISSN 2214-8019 (electronic)
Advances in Experimental Medicine and Biology
ISBN 978-981-13-1395-0 ISBN 978-981-13-1396-7 (eBook)
https://doi.org/10.1007/978-981-13-1396-7

Library of Congress Control Number: 2018958708

This Springer imprint is published by the registered company Springer Nature Singapore Pte Ltd.
The registered company address is: 152 Beach Road, #21-01/04 Gateway East, Singapore 189721, Singapore

Contents

1 Computer-Aided Orthopaedic Surgery: State-of-the-Art and Future Perspectives

Guoyan Zheng and Lutz-P. Nolte

Abstract

Introduced more than two decades ago, computer-aided orthopaedic surgery (CAOS) has emerged as a new and independent area, due to the importance of treatment of musculoskeletal diseases in orthopaedics and traumatology, increasing availability of different imaging modalities and advances in analytics and navigation tools. The aim of this chapter is to present the basic elements of CAOS devices and to review state-of-the-art examples of different imaging modalities used to create the virtual representations, of different position tracking devices for navigation systems, of different surgical robots, of different methods for registration and referencing, and of CAOS modules that have been realized for different surgical procedures. Future perspectives will be outlined. It is expected that the recent advancement on smart instrumentation, medical robotics, artificial intelligence, machine learning, and deep learning techniques, in combination with big data analytics, may lead to smart CAOS systems and intelligent orthopaedics in the near future.

G. Zheng (✉) · L.-P. Nolte
Institute for Surgical Technology and Biomechanics, University of Bern, Bern, Switzerland
e-mail: guoyan.zheng@istb.unibe.ch

Keywords

Computer-aided orthopaedic surgery (CAOS) · Smart instrumentation · Medical robotics · Artificial intelligence · Machine learning · Deep learning · Big data analytics · Intelligent orthopaedics

1.1 Introduction

The human musculoskeletal system is an organ system that includes the bones of the skeleton and the cartilages, ligaments, and other connective tissues that bind tissues and organs together. The main functions of this system are to provide form, support, stability, and movement to the body. Bones, besides supporting the weight of the body, work together with muscles to maintain body position and to produce controlled, precise movements. Musculoskeletal disease is among the most common causes of severe long-term disability and practical pain in industrialized societies [1]. The impact and importance of musculoskeletal diseases are critical not only for individual health and mobility but also for social functioning and productivity and economic growth on a larger scale, reflected by the proclamation of the Bone and Joint Decade 2000–2010 [1].

G. Zheng et al. (eds.), *Intelligent Orthopaedics*, Advances in Experimental Medicine and Biology 1093, https://doi.org/10.1007/978-981-13-1396-7_1

Both traumatology and orthopaedic surgery aim at the treatment of musculoskeletal tissues. Surgical steps such as the placement of an implant component, the reduction and fixation of a fracture, ligament reconstruction, osteotomy, tumour resection, and the cutting or drilling of bone should ideally be carried out as precisely as possible. Not only will optimal precision improve the post-operative outcome of the treatment, but it will also minimize the risk factors for intra- and post-operative complications. To this end, a large number of pure mechanical guides have been developed for various clinical applications. The pure mechanical guides, though easy to use and easy to handle, do not respect the individual patient's morphology. Thus, their general benefit has been questioned (see for example [2]). Additionally, surgeons often encounter the challenge of limited visibility of the surgical situs, which makes it difficult to achieve the intended procedure as accurately as desired. Moreover, the recent trend towards increased minimally invasive surgery makes it more and more important to gain feedback about surgical actions that take place subcutaneously. Just as a Global Positioning System (GPS)-based car navigation provides visual instruction to a driver by displaying the location of the car on a map, a computer-aided orthopaedic surgery (CAOS) module allows the surgeon to get real-time feedback about the performed surgical actions using information conveyed through a virtual scene of the situs presented on a display device [3, 4]. Parallel to the CAOS module to potentially improve surgical outcome is the employment of surgical robots that actively or semi-actively participate in the surgery [5].

Introduced more than two decades ago [3–5], CAOS has emerged as a new and independent area and stands for approaches that use computer-enabled tracking systems or robotic devices to improve visibility to the surgical field and increase application accuracy in a variety of surgical procedures. Although CAOS modules use numerous technical methods to realize individual aspects of a procedure, their basic conceptual design is very similar. They all involve three major components: a therapeutic object (TO in abbreviation, which is the target of the treatment), a virtual object (VO in abbreviation, which is the virtual representation in the planning and navigation computer), and a so-called navigator that links both objects. For reasons of simplicity, the term "CAOS system" will be used within this article to refer to both navigation systems and robotic devices.

The central element of each CAOS system is the navigator. It is a device that establishes a global, three-dimensional (3-D) coordinate system (COS) in which the target is to be treated and the current location and orientation of the utilized end effectors (EE) are mathematically described. End effectors are usually passive surgical instruments but can also be semi-active or active devices. One of the main functions of the navigator is to enable the transmission of positional information between the end effectors, the TO and the VO. For robotic devices, the robot itself plays the role of the navigator, while for surgical navigation a position tracking device is used.

For the purpose of establishment of a CAOS system through coactions of these three entities, three key procedural requirements have to be fulfilled. The first is the calibration of the end effectors, which means to describe the end effectors' geometry and shape in the coordinate system of the navigator. For this purpose, it is required to establish physically a local coordinate system at the end effectors. When an optical tracker is used, this is done via rigid attachment of three or more optical markers onto each end effector. The second is registration, which aims to provide a geometrical transformation between the TO and the VO in order to display the end effect's localization with respect to the virtual representation, just like the display of the location of a car in a map in a GPS-based navigation system. The geometrical transformation could be rigid or non-rigid. In literature, a wide variety of registration concepts and associated algorithms exist (see the next section for more details). The third key ingredient to a CAOS system is referencing, which is necessary to compensate for possible motion of the navigator and/or the TO during the surgical actions to be controlled. This is done by either attaching a so-called dynamic reference bases (DRB) holding three or more optical markers to the TO or immobilizing the TO with respect to the navigator.

The rest of the chapter is organized as follows. Section 1.2 will review the state-of-the-art examples of basic elements of CAOS systems. Section 1.3 will present clinical fields of applications. In Sect. 1.4, future perspectives will be outlined, followed by conclusion in Sect. 1.5.

1.2 Basic Elements of CAOS Systems

1.2.1 Virtual Object

The VO in each CAOS system is defined as a sufficiently realistic representation of the musculoskeletal structures that allows the surgeon to plan the intended intervention, as exemplified in Fig. 1.1a Intra-operatively, it also serves as the "background" into which the measured position of a surgical instrument can be visualized (see Fig. 1.1b for an example). Though most of the time VO is derived from image data of the patient, it can also be created directly from intra-operative digitization without using anymedical image data. Below detailed examples of different forms of VOs will be reviewed.

When the VO is derived from medical image data, these data may be acquired at two points in time: either pre-operatively or intra-operatively. Two decades ago, the VOs of majority CAOS systems were derived from pre-operatively acquired CT scans, and a few groups also tried to use magnetic resonance imaging (MRI) [6, 7]. In comparison with MRI, CT has clear advantages of excellent bone-soft tissue contrast and no geometrical distortion despite its acquisition inducing radiation exposure to the patient. Soon after the introduction of the first CAOS systems, the limitations of pre-operative VOs were observed, which led to the introduction of intra-operative imaging modalities. More specifically, the bony morphology may have changed between the time of image acquisition and the actual surgical procedure. As a consequence, the VO may not necessarily correspond to the TO any more leading to unpredictable inaccuracies during navigation or robotic procedures. This effect can be particularly adverse for traumatology in the presence of unstable fractures. To overcome this problem in the field of surgical navigation, the use of intra-operative CT scanning has been proposed [8], but the infrastructural changes that are required for the realization of this approach are tremendous,

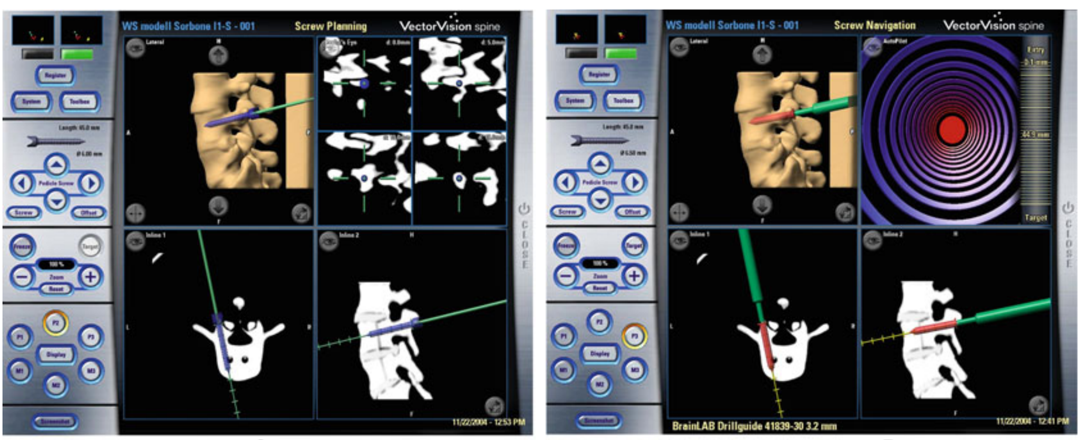

A B

Fig. 1.1 Example of CT-based navigational feedback. These screenshots show a CT-based CAOS system during pre-operative planning (**a**) and intra-operative navigation (**b**) of pedicle screw placement. (Courtesy of Brainlab AG, Munich, Germany)

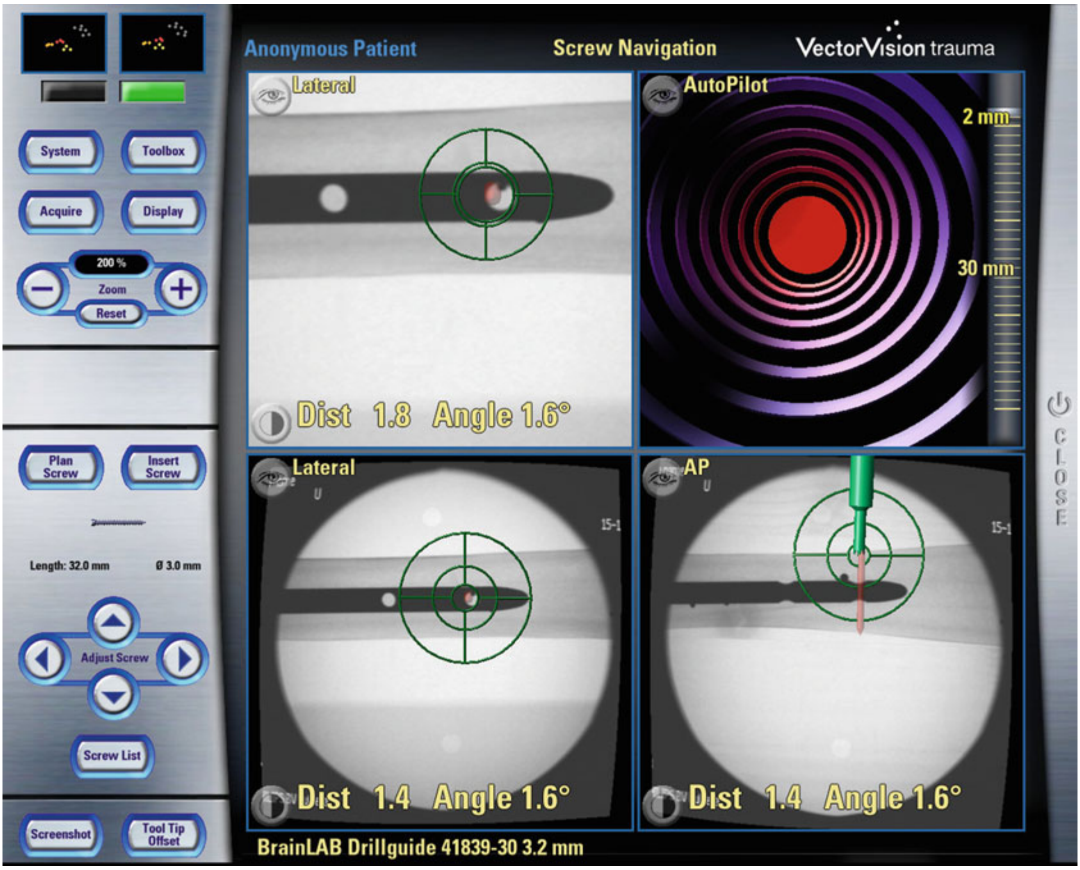

Fig. 1.2 Example of fluoroscopy-based navigation. This screenshot shows the fluoroscopy-based navigation for distal locking of an intramedullary nail. (Courtesy of Brainlab AG, Munich, Germany)

often requiring considerable reconstruction of a hospital's facilities. This has motivated the development of navigation systems based on fluoroscopic images [9–11]. The image intensifier is a well-established device during orthopaedic and trauma procedures but has the limitations that the images generated with a fluoroscope are usually distorted and that one-dimensional information gets lost due to image projection. To use these images as VOs therefore requires the calibration of the fluoroscope which aims to compute the image projection model and to compensate for the image distortion [9–11]. The resultant systems are therefore known as "fluoroscopy-based navigation systems" in literature [9–11]. Additional feature offered by a fluoroscopy-based navigation system is that multiple images acquired from different positions are co-registered to a common coordinate system established on the target structure via the DRB technique. Such a system can thus provide visual feedback just like the use of multiple fluoroscopes placed at different positions in constant mode but without the associated radiation exposure, which is a clear advantage (see Fig. 1.2 for an example). This technique is therefore also known as "virtual fluoroscopy" [11]. Despite the fact that in such a system, only two-dimensional (2-D) projected images with low contrast are available, the advantages offered by a fluoroscopy-based navigation system preponderate for a number of clinical applications in orthopaedics and traumatology.

In order to address the 2-D projection limitation of a fluoroscopy-based navigation system, a new imaging device was introduced [12] that enables the intra-operative generation of 3-D flu-

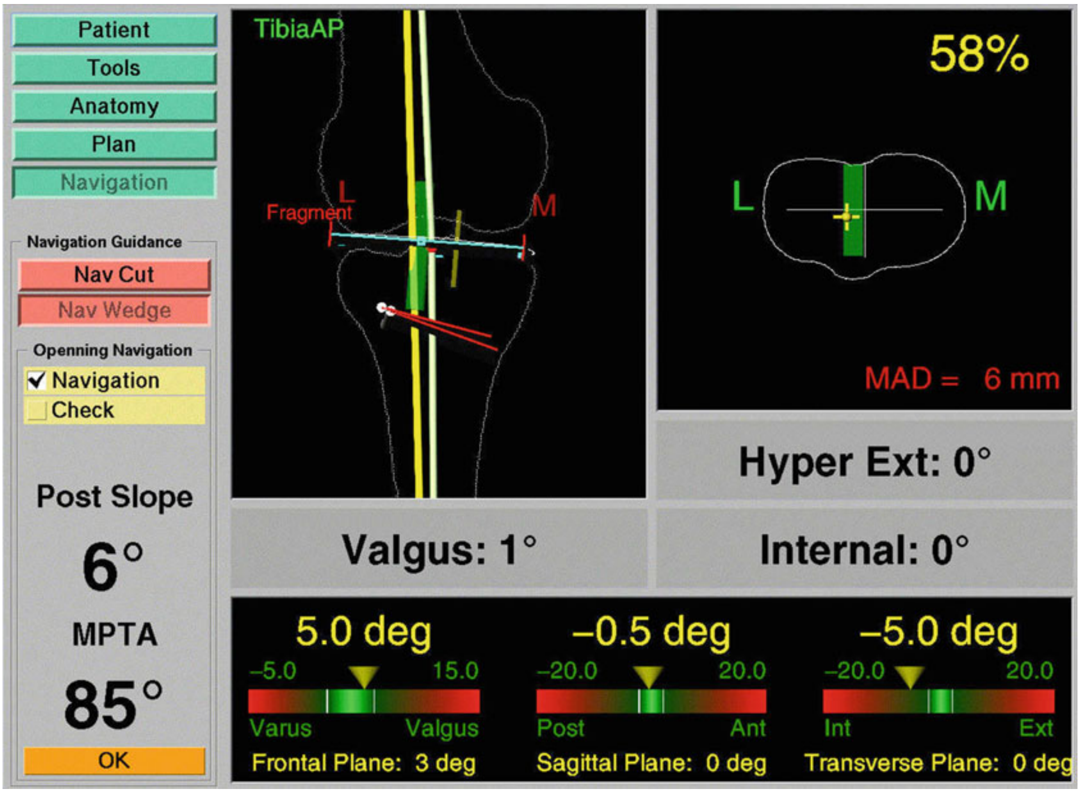

Fig. 1.3 Navigation using surgeon-defined anatomy approach. This virtual model of a patient's knee is generated intra-operatively by digitizing relevant structures. Although a very abstract representation, it provides sufficient information to enable navigated high tibial osteotomy

oroscopic image data. It consists of a motorized, isocentric C-arm that acquires series of 50–100 2-D projections and reconstructs from them $13 \times 13 \times 13$ cm^3 volumetric datasets which are comparable to CT scans. Being initially advocated primarily for surgery at the extremities, this "fluoro-CT" has been adopted for usage with a navigation system and has been applied to several anatomical areas already [13, 14]. As a major advantage, the device combines the availability of 3-D imaging with the intra-operative data acquisition. "Fluoro-CT" technology is under continuous development involving smaller and non-isocentric C-arms, "closed" C-arm, i.e. O-arm™ design [15, 16], faster acquisition speeds, larger field of view, and also flat panel technology.

A last category of navigation systems functions without any radiological images as VOs. Instead, the tracking capabilities of the system are used to acquire a graphical representation of the patient's anatomy by intra-operative digitization. By sliding the tip of a tracked instrument on the surface of a surgical object, the spatial location of points on the surface can be recorded. Surfaces can then be generated from the recorded sparse point clouds and used as the virtual representation of the surgical object. Because this model is generated by the operator, the technique is therefore known as "surgeon-defined anatomy" (SDA) (Fig. 1.3). It is particularly useful when soft tissue structures such as ligaments or cartilage boundaries are to be considered that are difficult to identify on CTs or fluoroscopic images [17]. Moreover, with SDA-based systems, some landmarks can be acquired even without the direct access to the anatomy. For instance, the centre of the femoral head, which is an important landmark during total hip and knee replacement, can be

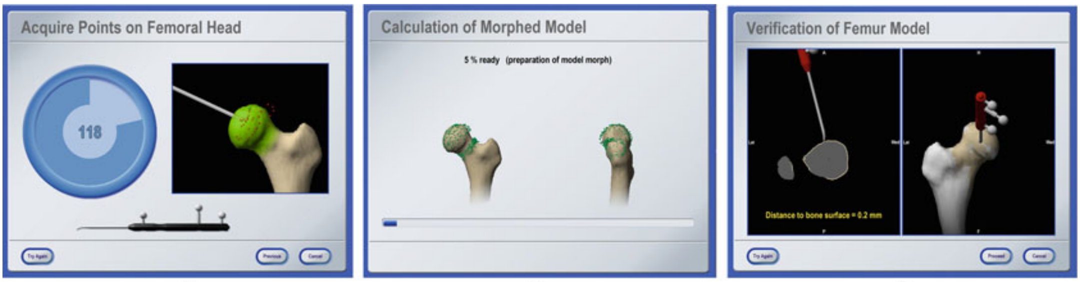

A B C

Fig. 1.4 An example of bone morphing. Screenshots of different stages of an intra-operative bone morphing process. (**a**) Point acquisition; (**b**) calculation of morphed model; and (**c**) verification of final result. (Courtesy of Brainlab AG, Munich, Germany)

calculated from a recorded passive rotation of the leg about the acetabulum. It should be noted that the generated representations are often rather abstract and not easy to interpret as exemplified in Fig. 1.3. This has motivated the development of the so-called “bone morphing” techniques [18, 19], which aim to derive a patient-specific model from a generic statistical forms of the target anatomical structure and a set of sparse points that are acquired with the SDA technique [20]. As the result, a realistic virtual model of the target structure can be presented and used as a VO without any conventional image acquisition (Fig. 1.4).

1.2.2 Registration

Position data that is used intra-operatively to display the current tool location (navigation system) or to perform automated actions according to a pre-operative plan (robot) are expressed in the local coordinate system of the VO. In general, this coordinate system differs from the one in which the navigator operates intra-operatively. In order to bridge this gap, the mathematical relationships between both coordinate spaces need to be determined. When pre-operative images are used as VOs, this step is performed interactively by the surgeon during the registration, also known as matching. A wide variety of different approaches have been developed and realized following numerous methodologies [21].

Early CAOS systems implemented paired-point matching and surface matching [22]. The operational procedure for paired-point matching is simple. Pairs of distinct points are defined pre-operatively in the VO and intra-operatively in the TO. The points on the VO are usually identified pre-operatively using the computer mouse, while the corresponding points on the TO are usually done intra-operatively with a tracked probe. In the case of a navigation system, the probe is tracked by the navigator, and for a robotic surgery, it is mounted onto the robot’s actuator [23]. Although paired-point matching is easy to solve mathematically, the accuracy of the resultant registration is low. This is due to the fact that the accuracy of paired-point matching depends on an optimal selection of the registration points and the exact identification of the associated pairs which is error prone. One obvious solution to this problem is to implant artificial objects to create easily and exactly identifiable fiducials for an accurate paired-point matching [23]. However, the requirement of implanting these objects before the intervention causes extra operation as well as associated discomfort and infection risk for the patient [24]. Consequently, none of these methods have gained wide clinical acceptance. The other alternative that has been widely adopted in early CAOS systems is to complement the paired-point matching with surface matching [25, 26], which does not require implanting any artificial object and only uses the surfaces of the VO as a basis for registration.

Other methods to compute the registration transformation without the need for extensive pre-operative preparation utilize intra-operative imaging such as calibrated fluoroscopic images or calibrated ultrasound images. As described above, a limited number of fluoroscopic images (e.g. two) acquired at different positions are calibrated and co-registered to a common coordinate system established on the target structure. A so-called "2-D-3-D registration" procedure can then be used to find the geometrical transformation between the common coordinate system and a pre-operatively acquired 3-D CT dataset by maximizing a similarity measurement between the 2-D projective representations and the associated digitally reconstructed radiographs (DRRs) that are created by simulating X-ray projections (see Fig. 1.5 for an example). Intensity-based as well as feature-based approaches have been proposed before. For a comprehensive review of different 2-D-3-D registration techniques, we refer to [21].

Another alternative is the employment of intra-operative ultrasonography. If an ultrasound probe is tracked by a navigator and its measurements are calibrated, it may serve as a spatial digitizer with which points or landmarks on the surfaces of certain subcutaneous bony structures may be acquired. This is different from the touch-based digitization done with a conventional probe which usually requires an invasive exposure of the surfaces of the target structures. Two different tracked mode ultrasound probes are available. A (amplitude)-mode ultrasound probes can measure the depth along the acoustic axis of the device. Placed on the patient's skin, they can measure percutaneously the distance to tissue borders, and the resulting point coordinates can be used as inputs to any feature-based registration algorithm. The applicability of this technique has been demonstrated previously but with certain limitations which prevent its wide usage [27, 28]. More specifically, the accuracy of the A-mode ultrasound probe-based digitization depends on how well the probe can be placed perpendicularly to the surfaces of the target bony structures, which is not an easy task when the subcutaneous soft tissues are thick. Moreover, the velocity of sound during the probe calibration is usually different from the velocity of sound when the probe is used for digitization as the latter depends on the properties of the traversed tissues. Such a velocity difference will lead to unpredictable inaccuracies when the probe is used to digitize deeply located structures. As a consequence, the successful application of this technique remains limited to a narrow field of application. In contrast to an A-mode probe, a B (brightness)-mode ultrasound probe scans a fan-shaped area.

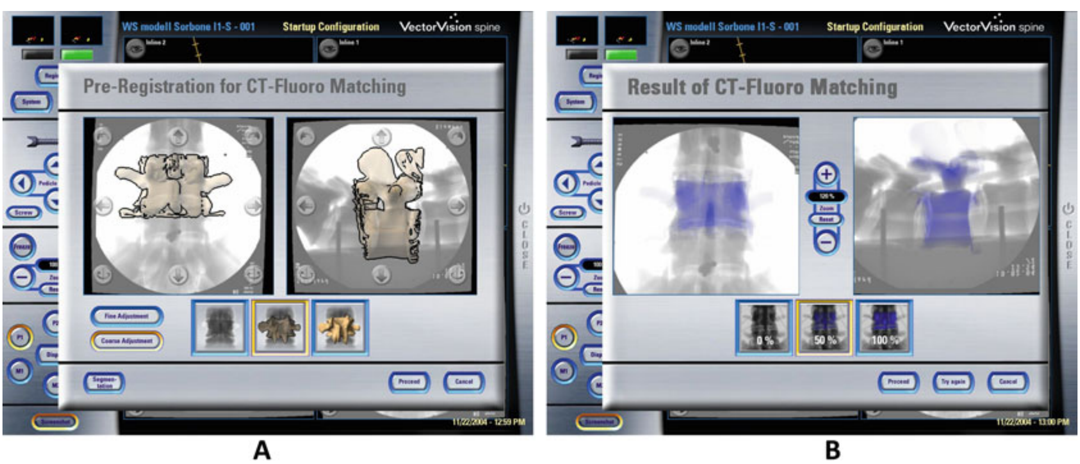

Fig. 1.5 An example of CT-fluoro matching. Screenshots of different stages of a CT-fluoro matching process. (**a**) Preregistration for CT-fluoro matching and (**b**) results of CT-fluoro matching. (Courtesy of Brainlab AG, Munich, Germany)

It is therefore able to detect also surfaces that are examined from an oblique direction, though the errors caused by the velocity difference still persist. In order to extract the relevant information for the registration of pre-operative CT scans, the resulting, usually noisy images need to be processed [29]. As for the intra-operative processing of fluoroscopic images, the use of B-mode ultrasound for registration is not reliable in every case and consequently remains the subject of CAOS research [30, 31].

It is worth to point out that if the VO is generated intra-operatively, registration is an inherent process [21]. This is due to the fact that since the imaging device is tracked during data acquisition, the position of any acquired image is recorded with respect to the local coordinate system established on the TO. The recorded device position, together with the additional image calibration process, automatically establishes the spatial relationship between the VO and the TO during image acquisition, which is a clear advantage over the interactive registration in the case of pre-operative images serving as VOs. Therefore, registration is not an issue when using intra-operative CT, 2-D, 3-D fluoroscopy or O-arm, or the SDA concept.

Radermacher et al. [32] introduced an alternative way to match pre-operative planning with the intra-operative situation using individual templates. The principle of individualized templates is to create customized templates based on patient-specific 3-D bone models that are normally segmented from pre-operative 3-D data such as CT or MRI scan. One feature about the individual templates is that small reference areas of the bone structures are integrated into the templates as the contact faces. By this means, the planned position and orientation of the template in spatial relation to the bone are stored in a structural way and can be reproduced intra-operatively by adjusting the contact faces of the templates until an exact fit to the bone is achieved. By integrating holes and/or slots, individualized templates function as tool guides, e.g. for the preparation of pedicle screw holes [32] or as cutting jigs used in total knee and hip replacement surgery [33–35].

1.2.3 Navigator

Registration closes the gap between VO and TO. The navigator enables this connection by providing a global coordinate space. In addition, it links the surgical end effectors, with which a procedure is carried out, to the TO that they act upon. From a theoretical standpoint, it is the only element in which surgical navigation systems and surgical robotic systems differ.

1.2.3.1 Robots

For this type of CAOS technology, the robot itself is the navigator. Intra-operatively, it has to be registered to the VO in order to realize the plan that is defined in the pre-operative image dataset. The end effectors of a robot are usually designed to carry out specific tasks as part of the therapeutic treatment. Depending on how the end effectors of a robot act on the patient, two different types of robots can be found in literature. The so-called active robots conduct a specific task autonomously without additional support by the surgeon. Such a system has been applied for total joint replacement [5], but their clinical benefit has been strongly questioned [36]. For traumatology applications, the use of active robots has only been explored in the laboratory setting [37, 38]. One possible explanation is that the nature of fracture treatment is an individualized process that does not include many steps that an active robot can repetitively carry out.

In contrast to active robotic devices, passive or semi-active robots do not carry out a part of the intervention autonomously but rather guide or assist the surgeon in positioning the surgical tools. At present there are two representatives of this class, both for bone resection during total knee arthroplasty (TKA). The Navio system (Blue Belt Technologies Inc. Pittsburgh, PA, USA) [39] is a hand-held semi-active robotic technology for bone shaping that allows a surgeon to move freely in order to resect the bone as long as this motion stays within a pre-operatively defined safety volume. The Mako system [40] is a passive robotic arm system providing oriental and tactile guidance. Both the Navio and the Mako systems require additional tracking technology as described in the next sub-section. During the surgical procedure, the system is under the direct surgeon control and gives real-time tactile feedback to the surgeon. Other semi-active robots such as SpineAssist (Mazor Robotics Ltd., Israel) can be seen as intelligent gauges that place, for example, cutting jigs or drilling guides automatically [41, 42].

1.2.3.2 Tracker

The navigator of a surgical navigation system is a spatial position tracking device. It determines the location and orientation of objects and provides these data as 3-D coordinates or 3-D rigid transformations. Although a number of tracking methods based on various physical media, e.g. acoustic, magnetic, optical, and mechanical methods, have been used in the early surgical navigation systems, most of today's products rely upon optical tracking of objects using operating room (OR) compatible infrared light that is either actively emitted or passively reflected from the tracked objects. To track surgical end effectors with this technology then requires the tools to be adapted with reference bases holding either light-emitting diodes (LED, active) or light-reflecting spheres or plates (passive). Tracking patterns with known geometry by means of video images has been suggested [43, 44] as an inexpensive alternative to an infrared-light optical tracker.

Optical tracking of surgical end effectors requires a direct line of sight between the tracker and the observed objects. This can be a critical issue in the OR setting. The use of electromagnetic tracking systems has been proposed to overcome this problem. This technology involves a homogeneous magnetic field generator that is usually placed near to the surgical situs and the attachment of receiver coils to each of the instruments allowing measuring their position and orientation within the magnetic field. This technique senses positions even if objects such as the surgeon's hand are in between the emitter coil and the tracked instrument. However, the homogeneity of the magnetic field can be easily disturbed by the presence of certain metallic objects causing measurement artefacts that may decrease the achievable accuracyconsiderably [45, 46]. Therefore, magnetic tracking has been employed only in very few commercial navigation systems and with limited success.

Recently inertial measurement unit (IMU)-based navigation devices have attracted more and more interests [47–51]. These devices attempt to combine the accuracy of large-console CAOS systems with the familiarity of conventional alignment methods and have been successfully applied to applications including TKA [47, 48], pedicle screw placement [49], and periacetabular osteotomy (PAO) surgery [50, 51]. With such devices, the line-of-sight issues in the optical surgical navigation systems can be completely eliminated. Technical limitations of such devices include (a) relatively lower accuracy in comparison with optical tracking technique and (b) difficulty in measuring translations.

1.2.4 Referencing

Intra-operatively, it is unavoidable that there will be relative motions between the TO and the navigator due to surgical actions. Such motions need to be detected and compensated to secure surgical precision. For this purpose, the operated anatomy is linked to the navigator. For robotic surgery this connection is established as a physical linkage. Large active robots, such as the early machines used for total joint replacement, come with a bone clamp that tightly grips the treated structure or involve an additional multi-link arm, while smaller active and semi-active devices are mounted directly onto the bone. For all other tracker types, bone motion is determined by the attachment of a DRB to the TO [52], which is designed to house infrared LEDs, reflecting markers, acoustic sensors, or electromagnetic coils, depending on the employed tracking technology. Figure 1.6 shows an example of a DRB for an active optical tracking system that is attached to the spinous process of a lumbar vertebra. Since the DRB is used as an indicator to inform the tracker precisely about movements of the operated bone, a stable fixation throughout the entire duration of the procedure is essential.

Fig. 1.6 Dynamic reference base. A dynamic reference base allows a navigation system to track the anatomical structure that the surgeon is operating on. In the case of spinal surgery, this DRB is usually attached to the processus spinosus with the help of a clamping mechanism. It is essential that it remains rigidly affixed during the entire usage of the navigation system on that vertebra

1.3 Clinical Fields of Applications

Since the mid-1990s when first CAOS systems were successfully utilized for the insertion of pedicle screws at the lumbar and thoracic spine and total hip replacement procedures [3, 4], a large number of modules covering a wide range of traumatological and orthopaedic applications have been developed, validated in the laboratory and in clinical trials. Some of them needed to be abandoned, because the anticipated benefit failed to be achieved or the technology proved to be unreliable or too complex to be used intra-operatively. Discussing all these applications would go beyond the focus of this article. Thus, here we focus on a review of the most important applications with the most original technological approaches.

While there was clearly one pioneering example of robot-assisted orthopaedic surgery – ROBODOC [5] – the first spinal navigation systems were realized independently by several research groups, almost in parallel [3, 4, 52–56]. These systems used pre-operative CT scans as the VO, relied upon paired-point and surface matching techniques for registration, and were based on optical or electromagnetic trackers. Their initial clinical success [57–59] boosted the development of new CAOS systems and modules. While some groups tried to use the existing pedicle screw placement systems for other clinical applications, others aimed to apply the underlying technical principle to new clinical challenges by developing highly specialized navigation systems [60, 61]. With the advent of alternative imaging methods for the generation of VOs, the indication for the use of one or the other method was evaluated more critically. For instance, it became evident that lumbar pedicle screw insertion in the standard degenerative case could be carried out with fluoroscopy-based navigation sufficiently accurate, thus avoiding the need for a pre-operative CT.

A similar development took place for total knee replacement. Initially, this procedure was supported by active [36, 62] and semi-active or passive [39, 40] robots, as well as navigation systems using pre-operative CTs [63], but with a few exceptions, the SDA approach [64] is today's method of choice.

Fluoroscopy-based navigation still seems to have a large potential to explore new fields of application. The technology has been mainly used in spinal surgery [65]. Efforts to apply it to total hip arthroplasty (THA) [66] and the treatment of long-bone fractures [67] have been commercially less successful. The intra-operative 3-D fluoroscopy or O-arm has been explored intensively [13–16]. It is expected that with the advent of the flat panel technology, the use of fluoro-CT as a virtual object generator will significantly grow [16].

Recently, computer-assisted surgery using individual templates has gained increasing attention. Initially developed for pedicle screw fixation [32], such a technique has been successfully

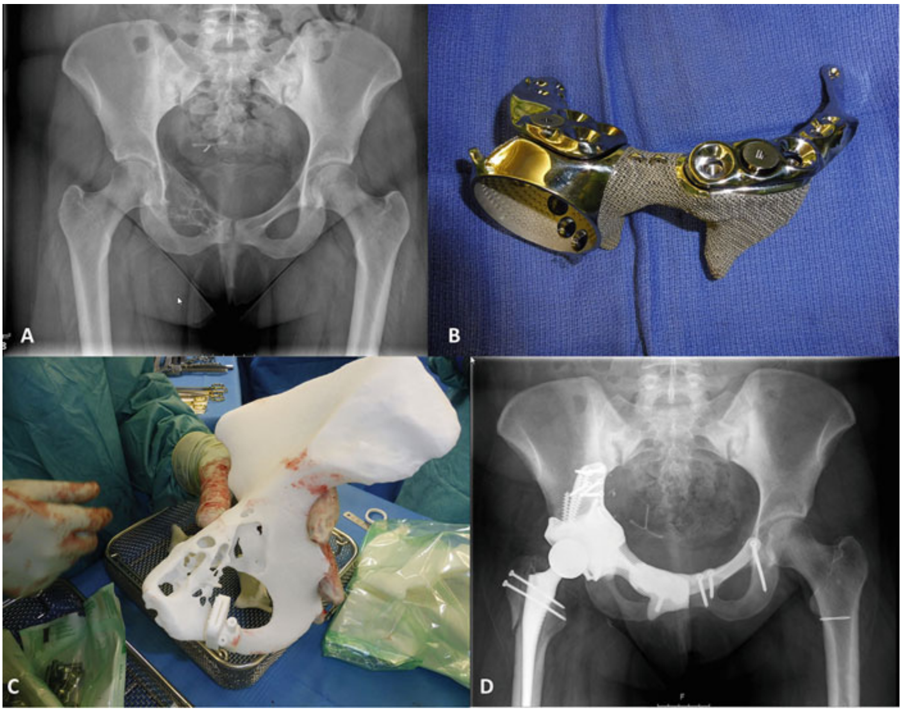

Fig. 1.7 Patient-specific instrumentation for pelvic tumour resection surgery. These images show the application of patient-specific instrumentation for pelvic tumour treatment. Implant and template manufactured by Mobelife NV, Leuven, Belgium. (**a**) A pre-operative X-ray radiograph, (**b**) the implant; (**c**) the patient-specific guide; (**d**) a post-operative X-ray radiograph. (Courtesy of Prof. Dr. K Siebenrock, Inselspital, University of Bern, Switzerland)

reintroduced to the market for total knee arthroplasty [33, 68, 69], hip resurfacing [34, 70], total hip arthroplasty [35], and pelvic tumour resection [71, 72] (see Fig. 1.7 for an example). It should be noted that most of the individual templates are produced using additive manufacturing techniques, while most of the associated implants are produced conventionally.

1.4 Future Perspectives

Despite its touted advantages, such as decreased radiation exposure to the patient and the surgical team for certain surgical procedures and increased accuracy in most situations, surgical navigation has yet to gain general acceptance among orthopaedic surgeons. Although issues related to training, technical difficulty, and learning curve are commonly presumed to be major barriers to the acceptance of surgical navigation, a recent study [73] suggested that surgeons did not select them as major weaknesses. It has been indicated that barriers to adoption of surgical navigation are neither due to a difficult learning curve nor to a lack of training opportunities. The barriers to adoption of navigation are more intrinsic to the technology itself, including intra-operative glitches, unreliable accuracy, frustration with intra-operative registration, and line-of-sight issues. These findings suggest that significant improvements in the technology will be required to improve the adoption rate of surgical navigation. Addressing these issues from the following perspectives may provide solutions in the continuing effort to implement surgical navigation in everyday clinical practice.

- *2-D or 3-D image stitching*. Long-bone fracture reduction and spinal deformity correction are two typical clinical applications that frequently use the C-arm in its operation.

Such a surgery usually involves corrective manoeuvers to improve the sagittal or coronal profile. However, intra-operative estimation of the amount of correction is difficult, especially in longer instrumentation. Mostly, anteroposterior (AP) and lateral fluoroscopic images are used but have the disadvantage to depict only a small portion of the target structure in a single C-arm image due to the limited field of view of a C-arm machine. As such, orthopaedic surgeons nowadays are missing an effective tool to image the entire anatomical structure such as the spine or long bones during surgery for assessing the extent of correction. Although radiographs obtained either by using a large field detector or by image stitching can be used to image the entire structure, they are usually not available for intra-operative interventions. One alternative is to develop methods to stitch multiple intra-operatively acquired small fluoroscopic images to be able to display the entire structure at once [74, 75]. Figure 1.8 shows an image stitching example for spinal intervention. The same idea can be extended to 3-D imaging to create a panoramic cone beam computed tomography [76]. At this moment, fast and easy-to-use 2-D or 3-D image stitching systems are still under development, and as the technology evolves, surgical benefits and improved clinical outcomes are expected.

- *Image fusion*. Fusion of multimodality pre-operative image such as various MRI or CT datasets with intra-operative images would allow for visualization of critical structures such as nerve roots or vascular structures during surgical navigation. Different imaging modalities provide complementary information regarding both anatomy and physiology. The evidence supporting this complementarity has been gained over the last few years with increased interest in the development of platform hardware for multimodality imaging. Because multimodality images by definition contain information obtained using different imaging methods, they introduce new degrees of freedom, raising questions beyond those related to exploiting each single modality separately. Processing multimodality images is then all about enabling modalities to fully interact and inform each other. It is important to choose an analytical model that faithfully represents the link between the modalities without imposing phantom connections or suppressing existing ones. Hence it is important to be as data driven as possible. In practice, this means making the fewest assumptions and using the simplest model, both within and across modalities. Example models include linear relationships between underlying latent variables; use of model-independent priors such as sparsity,

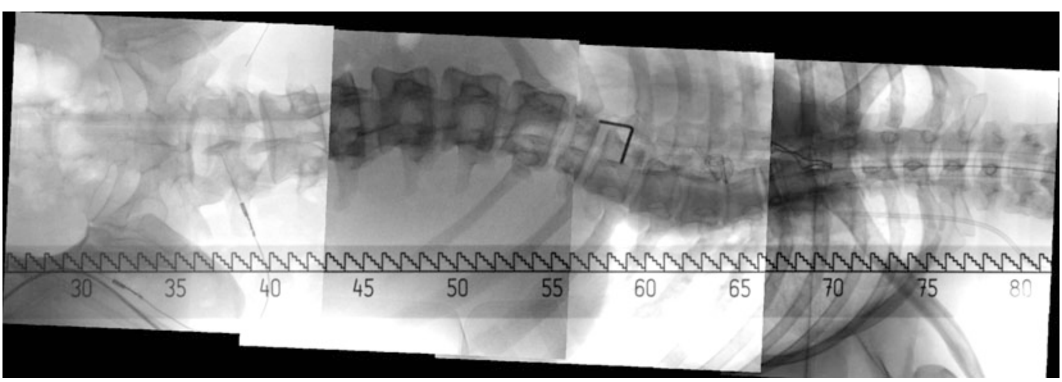

Fig. 1.8 Image stitching for spinal interventions. Several small field-of-view C-arm images are stitched into one big image to depict the entire spine

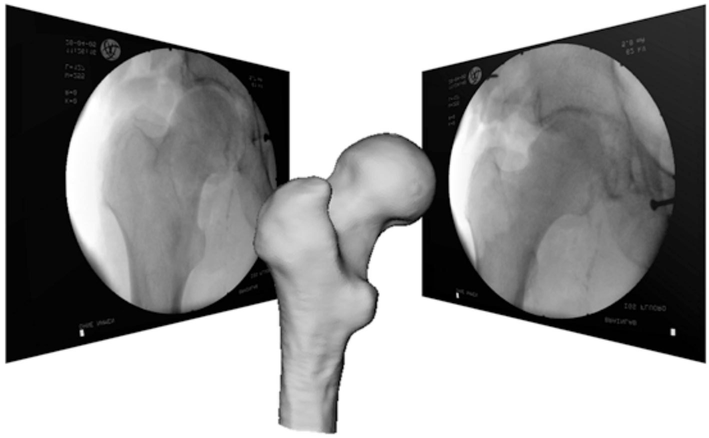

Fig. 1.9 An example of statistical shape model-based 2-D-3-D reconstruction. Reconstruction of bone surface from two calibrated fluoroscopic images and a statistical shape model using deformable registration

non-negativity, statistical independence, low rank, and smoothness; or both. Such a principle has been successfully applied to solving challenging problems in a variety of applications [77]. Despite the evident potential benefit, the knowledge of how to actually exploit the additional diversity that multimodality images offer is currently at its preliminary stage and remains open for exploration.

- *Statistical shape and deformation analysis*. Statistical shape and deformation analysis [78] has been shown to be useful for predicting 3-D anatomical shape and structures from sparse point sets that are acquired with the SDA technique. Such a technique is heavily employed in so-called "image-free" navigation systems that are commercially available in the market, mainly for knee and hip surgery. However, with the availability of statistical shape models of other anatomical regions, the technique could be applied to any part of the skeleton. Such approaches bear significant potential for future development of computer navigation technology since they are not at all bound to the classical pointer-based acquisition of bony features. In principle, the reconstruction algorithms can be tuned to any type of patient-specific input, e.g. intra-operatively acquired fluoroscopic images [79] or tracked ultrasound [30], thereby potentially enabling new minimally invasive procedures. Figure 1.9 shows an example of bone surface reconstruction from calibrated fluoroscopic images and a statistical shape model. Moreover, prediction from statistical shape models is possible not only for the geometric shape of an object. Given statistical shape and intensity models, "synthetic CT scans" could be predicted from intra-operatively recorded data after a time-consuming computation. With more and more computations shifted from CPUs to graphics processing units (GPUs), it is expected that statistical shape and deformation analysis-based techniques will be used in more and more CAOS systems [80].
- *Biomechanical modelling*. Numerical models of human anatomical structures may help the surgeon during the planning, simulation, and intra-operative phases with the final goal to optimize the outcome of orthopaedic surgical interventions. The terms "physical" or "biomechanical" are often used. While most of existing biomechanical models serve for the basic understanding of physical phenomena, only a few have been validated for the general prediction of consequences of surgical interventions.

  The situation for patient-specific models is even more complex. To be used in clinical practice, ideally the exact knowledge of the underlying geometrical tissue configuration and associated mechanical properties as well as the loading regime is required as input for appropriate mathematical frameworks.

In addition these models will not only be used pre-operatively but need to function also in near real time in the operating theatre.

First attempts have been made to incorporate biomechanical simulation and modelling into the surgical decision-making process for orthopaedic interventions. For example, a large spectrum of medical devices exists for correcting deformities associated with spinal disorders. Driscoll et al. [81] developed a detailed volumetric finite element model of the spine to simulate surgical correction of spinal deformities and to assess, compare, and optimize spinal devices. Another example was presented in [82] where the authors showed that with biomechanical modelling the instrumentation configuration can be optimized based on clinical objectives. Murphy et al. [83] presented the development of a biomechanical guidance system (BGS) for periacetabular osteotomy. The BGS aims to provide not only real-time feedback of the joint repositioning but also the simulated joint contact pressures.

Another approach is the combined use of intra-operative sensing devices with simplified biomechanical models. Crottet et al. [84] introduced a device that intra-operatively measures knee joint forces and moments and evaluated its performance and surgical advantages on cadaveric specimens using a knee joint loading apparatus. Large variation among specimens reflected the difficulty of ligament release and the need for intra-operative force monitoring. A commercial version of such a device (e-LIBRA Dynamic Knee Balancing System, Synvasive Technology, El Dorado Hills, CA, USA) became available in recent years and is clinically used (see, e.g. [85]). It is expected that incorporation of patient-specific biomechanical modelling into CAOS systems with or without the use of intra-operative sensing devices may eventually increase the quality of surgical outcomes [86]. Research activities must focus on existing technology limitations and models of the musculoskeletal apparatus that are not only anatomically but also functionally correct and accurate.

- *Musculoskeletal imaging.* Musculoskeletal imaging is defined as the imaging of bones, joints, and connected soft tissues with an extensive array of modalities such as X-ray radiography, CT, ultrasonography, and MRI. For the past two decades, rapid but cumulative advances can be observed in this field, not only for improving diagnostic capabilities with the recent advancement on low-dose X-ray imaging, cartilage imaging, diffusion tensor imaging, MR arthrography, and high-resolution ultrasound but also for enabling image-guided interventions with the introduction of real-time MRI or CT fluoroscopy, molecular imaging with PET/CT, and optical imaging into operating room [87].

One recent advancement that has found a lot of clinical applications is the EOS 2-D/3-D image system (EOS imaging, Paris, France), which was introduced to the market in 2007. The EOS 2-D/3-D imaging system [88] is based on the Nobel Prize-winning work of French physicist Georges Charpak on multiwire proportional chamber, which is placed between the X-rays emerging from the radiographed object and the distal detectors. Each of the emerging X-rays generates a secondary flow of photons within the chamber, which in turn stimulate the distal detectors that give rise to the digital image. This electronic avalanche effect explains why a low dose of primary X-ray beam is sufficient to generate a high-quality 2-D digital radiograph, making it possible to cover a field of view of 175 cm by 45 cm in a single acquisition of about 20s duration [89]. With an orthogonally co-linked, vertically movable, slot-scanning X-ray tube/detector pairs, EOS has the benefit that it can take a pair of calibrated posteroanterior (PA) and lateral (LAT) images simultaneously [90]. EOS allows the acquisition of images while the patient is in an upright, weight-bearing (standing, seated, or squatting) position and can image the full length of the body, removing the need for digital stitching/manual joining of multiple images [91]. The quality and nature of the image generated by EOS system are comparable or even better than computed radiography (CR) and digital radiography (DR) but with much lower radiation dosage [90]. It was reported by Illés et al. [90] that absorbed radiation dose by various organs during a full-body EOS 2-D/3-D examination required to perform a surface 3-D reconstruction was 800–1000 times less than the amount of radiation during a typical CT scan required for a volumetric 3-D reconstruction. When compared with conventional or digitalized radiographs [92], EOS system allows a reduction of the X-ray dose of an order 80–90%. The unique feature of simultaneously capturing a pair of calibrated PA and LAT images of the patient allows a full 3-D reconstruction of the subject's skeleton [90, 93, 94]. This in turn provides over 100 clinical parameters for pre- and post-operative surgical planning [90]. With a phantom study, Glaser et al. [95] assessed the accuracy of EOS 3-D reconstruction by comparing it with 3-D CT. They reported a mean shape reconstruction accuracy of 1.1±0.2 mm (maximum 4.7 mm) with 95% confidence interval of 1.7 mm. They also found that there was no significant difference in each of their analysed parameters ($p > 0.05$) when the phantom was placed in different orientations in the EOS machine. The reconstruction of 3-D bone models allows analysis of subject-specific morphology in a weight-bearing situation for different applications to a level of accuracy which was not previously possible. For example, Lazennec et al. [96] used the EOS system to measure pelvis and acetabular component orientations in sitting and standing positions. Further applications of EOS system in planning total hip arthroplasty include accurate evaluation of femoral offset [97] and rotational alignment [98]. The low dose and biplanar information of the EOS 2-D/3-D imaging system introduce key benefits in contemporary radiologyand open numerous and important perspectives in CAOS research.

Another novel technology on 2-D/3-D imaging was introduced in [99], which had the advantage of being integrated with any conventional X-ray machine. A mean reconstruction parameter of 1.06±0.20 mm was reported. This technology has been used for conducting 3-D pre-operative planning and post-operative treatment evaluation of TKA based on only 2-D long leg standing X-ray radiographs [100].

- *Artificial intelligence, machine learning, and deep learning*. Recently artificial intelligence and machine learning-based methods have gained increasing interest in many different fields including musculoskeletal imaging and surgical navigation. Most of these methods are based on ensemble learning principles that can aggregate predictions of multiple classifiers and demonstrate superior performance in various challenging problems [77, 101, 102]. A crucial step in the design of such systems is the extraction of discriminant features from the images [103]. In contrast, many deep learning algorithms that have been proposed recently, which are based on models (networks) composed of many layers that transform input data (e.g. images) to outputs (e.g. segmentation), let computers learn the features that optimally represent the data for the problem at hand. The most successful type of models for image analysis to date are convolutional neural networks (CNN) [104], which contain many layers that transform their input with convolution filters of a small extent. Deep learning-based methods have been successfully used to solve many challenging problems in computer-aided orthopaedic surgery [105–108]. Figure 1.10 shows an example of the application of cascaded fully convolutional networks (FCN) for automatic segmentation of lumbar vertebrae from CT images [108]. It is expected that more and more solutions will be developed based on different types of deep learning techniques.

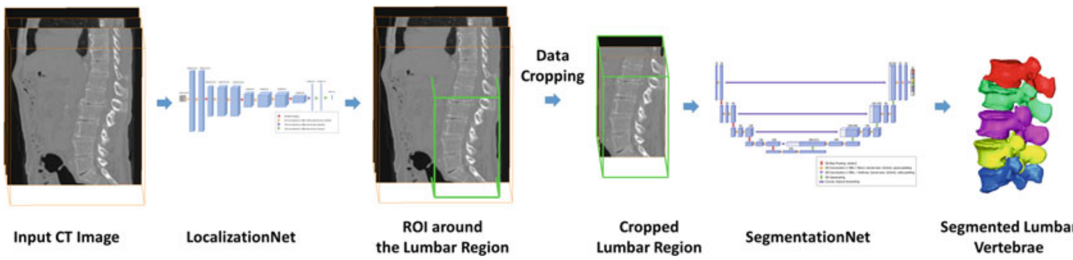

Fig. 1.10 A schematic view of using cascaded fully convolutional networks (FCN), which consists of a localization net and a segmentation net for automatic segmentation of lumbar vertebrae from CT images

1.5 Conclusions

More than two decades have passed since the first robot and navigation systems for CAOS were introduced. Today this technology has emerged from the laboratory and is being routinely used in the operating theatre and might be about to become state of the art for certain orthopaedic procedures.

Still we are at the beginning of a rapid process of evolution. Existing techniques are being systematically optimized, and new techniques will constantly be integrated into existing systems. Hybrid CAOS systems are under development, which will allow the surgeon to use any combinations of the above-described concepts to establish virtual object information. New generations of mobile imaging systems, inherently registered, will soon be available. However research focus should particularly be on alternative tracking technologies, which remove drawbacks of the currently available optical tracking and magnetic devices. This in turn will stimulate the development of less or even non-invasive registration methods and referencing tools. Force-sensing devices and real-time computational models may allow establishing a new generation of CAOS systems by going beyond pure kinematic control of the surgical actions. For keyhole procedures there is distinct need for smart end effectors to complement the surgeon in its ability to perform a surgical action. The recent advancement on smart instrumentation, medical robotics, artificial intelligence, machine learning, and deep learning techniques, in combination with big data analytics, may lead to smart CAOS systems and intelligent orthopaedics in the near future.

Acknowledgements This chapter was modified from the paper published by our group in *Frontiers in Surgery* (Zheng and Nolte 2016; 2:66). The related contents were reused with the permission.

References

1. WHO (2003) The burden of musculoskeletal conditions at the start of the new millennium. Report of a WHO Scientific Group. WHO Technical Report Series, 919, Geneva, 2003, pp 218. ISBN: 92-4-120919-4
2. Digioia AM 3rd, Jaramaz B, Plakseychuk AY, Moody JE Jr, Nikou C, Labarca RS, Levison TJ, Picard F (2002) Comparison of a mechanical acetabular alignment guide with computer placement of the socket. J Arthroplast 17:359–364
3. Amiot LP, Labelle H, DeGuise JA, Sati M, Brodeur P, Rivard CH (1995) Image-guided pedicle screw fixation – a feasibility study. Spine 20(10): 1208–1212
4. Nolte LP, Zamorano LJ, Jiang Z, Wang Q, Langlotz F, Berlemann U (1995) Image-guided insertion of transpedicular screws. A laboratory set-up. Spine (Phila Pa 1976) 20(4):497–500
5. Mittelstadt B, Kazanzides P, Zuhars J, Williamson B, Cain P, Smith F, Bargar WL (1996) The evolution of a surgical robot from prototype to human clinical use. In: Taylor RH, Lavallée S, Burdea GC, Mösges R (eds) Computer integrated surgery. The MIT Press, Cambridge, pp 397–407
6. Martel AL, Heid O, Slomczykowski M, Kerslake R, Nolte LP (1998) Assessment of 3-dimensional magnetic resonance imaging fast low angle shot images for computer assisted spinal surgery. Comput Aided Surg 3:40–44
7. Cho HS, Park IH, Jeon IH, Kim YG, Han I, Kim HS (2011) Direct application of MR images to computer-assisted bone tumor surgery. J Orthop Sci 16:190–195
8. Jacob AL, Messmer P, Kaim A, Suhm N, Regazzoni P, Baumann B (2000) A whole-body registration-free navigation system for image-guided surgery and interventional radiology. Invest Radiol 35: 279–288

9. Hofstetter R, Slomczykowski M, Bourquin Y, Nolte LP (1997) Fluoroscopy based surgical navigation: concept and clinical applications. In: Lemke HU, Vannier MW, Inamura K (eds) Computer assisted radiology and surgery. Elsevier Science, Amsterdam, pp 956–960
10. Joskowicz L, Milgrom C, Simkin A, Tockus L, Yaniv Z (1998) FRACAS: a system for computer-aided image-guided long bone fracture surgery. Comput Aided Surg 36:271–288
11. Foley KT, Simon DA, Rampersaud YR (2001) Virtual fluoroscopy: image-guided fluoroscopic navigation. Spine 26:347–351
12. Ritter D, Mitschke M, Graumann R (2002) Markerless navigation with the intra-operative imaging modality SIREMOBIL Iso-C3D. Electromedica 70:47–52
13. Grützner PA, Waelti H, Vock B, Hebecker A, Nolte L-P, Wentzensen A (2004) Navigation using fluoro-CT technology. Eur J Trauma 30:161–170
14. Rajasekaran S, Karthik K, Chandra VR, Rajkumar N, Dheenadhayalan J (2010) Role of intraoperative 3D C-arm-based navigation in percutaneous excision of osteoid osteoma of lone bones in children. J Pediatr Orthop 19:195–200
15. Lin EL, Park DK, Whang PG, An HS, Phillips FM (2008) O-Arm surgical imaging system. Semin Spine Surg 20:209–213
16. Qureshi S, Lu Y, McAnany S, Baird E (2014) Three-dimensional intraoperative imaging modalities in orthopaedic surgery: a narrative review. J Am Acad Orthop Surg 22(12):800–809
17. Sati M, Stäubli HU, Bourquin Y, Kunz M, Nolte LP (2002) Real-time computerized in situ guidance system for ACL graft placement. Comput Aided Surg 7:25–40
18. Fleute M, Lavallée S, Julliard R (1999) Incorporating a statistically based shape model into a system for computer assisted anterior cruciate ligament surgery. Med Image Anal 3:209–222
19. Stindel E, Briard JL, Merloz P, Plaweski S, Dubrana F, Lefevre C, Troccaz J (2002) Bone morphing: 3D morphological data for total knee arthroplasty. Comput Aided Surg 7:156–168
20. Zheng G, Dong X, Rajamani KT, Zhang X, Styner M, Thoranaghatte RU, Nolte L-P, Ballester MA (2007) Accurate and robust reconstruction of a surface model of the proximal femur from sparse-point data and a dense-point distribution model for surgical navigation. IEEE Trans Biomed Eng 54:2109–2122
21. Zheng G, Kowal J, Gonzalez Ballester MA, Caversaccio M, Nolte L-P (2007) Registration technique for computer navigation. Curr Orthop 21:170–179
22. Lavallée S (1996) Registration for computer-integrated surgery: methodology, start of the art. In: Taylor RH, Lavallée S, Burdea GC, Mösges R (eds) Computer integrated surgery. The MIT Press, Cambridge, pp 77–97
23. Bargar WL, Bauer A, Börner M (1998) Primary and revision total hip replacement using the Robodoc system. Clin Orthop 354:82–91
24. Nogler M, Maurer H, Wimmer C, Gegenhuber C, Bach C, Krismer M (2001) Knee pain caused by a fiducial marker in the medial femoral condyle: a clinical and anatomic study of 20 cases. Acta Orthop Scand 72:477–480
25. Besl PJ, McKay ND (1992) A method for registration of 3-D shapes. IEEE Trans Pattern Anal 14(2):239–256
26. Baechler R, Bunke H, Nolte L-P (2001) Restricted surface matching – numerical optimization and technical evaluation. Comput Aid Surg 6: 143–152
27. Maurer CR, Gaston RP, Hill DLG, Gleeson MJ, Taylor MG, Fenlon MR, Edwards PJ, Hawkes DJ (1999) AcouStick: a tracked A-mode ultrasonography system for registration in image-guided surgery. In: Taylor C, Colchester A (eds) Medical image computing and image-guided intervention – MICCAI'99. Springer, Berlin, pp 953–962
28. Oszwald M, Citak M, Kendoff D, Kowal J, Amstutz C, Kirchhoff T, Nolte L-P, Krettek C, Hüfner T (2008) Accuracy of navigated surgery of the pelvis after surface matching with an a-mode ultrasound proble. J Orthop Res 26:860–864
29. Kowal J, Amstutz C, Langlotz F, Talib H, Gonzalez Ballester MA (2007) Automated bone contour detection in ultrasound B-mode images for minimally invasive registration in image-guided surgery – an in vitro evaluation. Int J Med Rob Comput Assisted Surg 3:341–348
30. Schumann S, Nolte L-P, Zheng G (2012) Compensation of sound speed deviations in 3D B-mode ultrasound for intraoperative determination of the anterior pelvic plane. IEEE Trans Inf Technol Biomed 16(1):88–97
31. Wein W, Karamalis A, Baumgarthner A, Navab N (2015) Automatic bone detection and soft tissue aware ultrasound-CT registration for computer-aided orthopedic surgery. Int J Comput Assist Radiol Surg 10(6):971–979
32. Radermacher K, Portheine F, Anton M et al (1998) Computer assisted orthopaedic surgery with image based individual templates. Clin Orthop Relat Res 354:28–38
33. Hafez MA, Chelule KL, Seedhom BB, Sherman KP (2006) Computer-assisted total knee arthroplasty using patient-specific templating. Clin Orthop Relat Res 444:184–192
34. Kunz M, Rudan JF, Xenoyannis GL, Ellis RE (2010) Computer-assisted hip resurfacing using individualized drill templates. J Arthroplast 25:600–606
35. Shandiz MA, MacKenzie JR, Hunt S, Anglin C (2014 Sept) Accuracy of an adjustable patient-specific guide for acetabular alignment in hip replacement surgery (Optihip). Proc Inst Mech Eng H 228(9):876–889

36. Honl M, Dierk O, Gauck C, Carrero V, Lampe F, Dries S, Quante M, Schwieger K, Hille E, Morlock MM (2003) Comparison of robotic-assisted and manual implantation of a primary total hip replacement. A prospective study. J Bone Joint Surg 85A8:1470–1478
37. Oszwald M, Ruan Z, Westphal R, O'Loughlin PF, Kendoff D, Hüfner T, Wahl F, Krettek C, Gosling T (2008) A rat model for evaluating physiological responses to femoral shaft fracture reduction using a surgical robot. J Orthop Res 26: 1656–1659
38. Oszwald M, Westphal R, Bredow J, Calafi A, Hüfner T, Wahl F, Krettek C, Gosling T (2010) Robot-assisted fracture reduction using three-dimensional intraoperative fracture visualization: an experimental study on human cadaver femora. J Orthop Res 28:1240–1244
39. Jaramaz B, Nikou C (2012) Precision freehand sculpting for unicondylar knee replacement: design and experimental validation. Biomed Tech 57(4):293–299
40. Conditt MA, Roche MW (2009) Minimally invasive robotic-arm-guided unicompartmental knee arthroplasty. J Bone Joint Surg 91(Suppl 1):63–68
41. Ritschl P, Machacek F, Fuiko R (2003) Computer assisted ligament balancing in TKR using the Galileo system. In: Langlotz F, Davies BL, Bauer A (eds) Computer assisted orthopaedic surgery – 3rd annual meeting of CAOS-International (Proceedings). Steinkopff, Darmstadt, pp 304–305
42. Shoham M, Burman M, Zehavi E, Joskowicz L, Batkilin E, Kunicher Y (2003) Bone-mounted miniature robot for surgical procedures: concept and clinical applications. IEEE Trans Rob Autom 19:893–901
43. de Siebenthal J, Gruetzner PA, Zimolong A, Rohrer U, Langlotz F (2004) Assessment of video tracking usability for training simulators. Comput Aided Surg 9:59–69
44. Clarke JV, Deakin AH, Nicol AC, Picard F (2010) Measuring the positional accuracy of computer assisted surgical tracking systems. Comput Aided Surg 15:13–18
45. Meskers CG, Fraterman H, van der Helm FC, Vermeulen HM, Rozing PM (1999) Calibration of the "Flock of Birds" electromagnetic tracking device and its application in shoulder motion studies. J Biomech 32:629–633
46. Wagner A, Schicho K, Birkfellner W, Figl M, Seemann R, Konig F, Kainberger F, Ewers R (2002) Quantitative analysis of factors affecting intraoperative precision and stability of optoelectronic and electromagnetic tracking systems. Med Phys 29:905–912
47. Nam D, Cody EA, Nguyen JT, Figgie MP, Mayman DJ (2014) Extramedullary guides versus portable, accelerometer-based navigation for tibial alignment in total knee arthroplasty: a randomized, controlled trial: winner of the 2013 Hap Paul Award. J Arthroplast 29(2):288–294
48. Huang EH, Copp SN, Bugbee WD (2015) Accuracy of a handheld accelerometer-based navigation system for femoral and tibial resection in total knee arthroplasty. J Arthroplast 30(11):1906–1910
49. Walti J, Jost GF, Cattin PC (2014) A new cost-effective approach to pedicular screw placement. In: AE-CAI 2014, LNCS 8678. Springer, Heidelberg, pp 90–97
50. Pflugi S, Liu L, Ecker TM, Schumann S, Cullmann JL, Siebenrock K, Zheng G (2016) A cost-effective surgical navigation solution for periacetabular osteotomy (PAO) surgery. Int J Comput Assist Radiol Surg 11(2):271–280
51. Pflugi S, Vasireddy R, Lerch T, Ecker TM, Tannast T, Boemake N, Siebenrock K, Zheng G (2018) A cost-effective surgical navigation solution for periacetabular osteotomy (PAO) surgery. Int J Comput Assist Radiol Surg 13(2):291–304
52. Nolte LP, Visarius H, Arm E, Langlotz F, Schwarzenbach O, Zamorano L (1995) Computer-aided fixation of spinal implants. J Imag Guid Surg 1:88–93
53. Foley KT, Smith MM (1996) Image-guided spine surgery. Neurosurg Clin N Am 7:171–186
54. Glossop ND, Hu RW, Randle JA (1996) Computer-aided pedicle screw placement using frameless stereotaxis. Spine 21:2026–2034
55. Kalfas IH, Kormos DW, Murphy MA, McKenzie RL, Barnett GH, Bell GR, Steiner CP, Trimble MB, Weisenberger JP (1995) Application of frameless stereotaxy to pedicle screw fixation of the spine. J Neurosurg 83:641–647
56. Merloz P, Tonetti J, Pittet L, Coulomb M, Lavallée S, Sautot P (1998) Pedicle screw placement using image guided techniques. Clin Orthop 354:39–48
57. Amiot LP, Lang K, Putzier M, Zippel H, Labelle H (2000) Comparative results between conventional and image-guided pedicle screw installation in the thoracic, lumbar, and sacral spine. Spine 25: 606–614
58. Laine T, Lund T, Ylikoski M, Lohikoski J, Schlenzka D (2000) Accuracy of pedicle screw insertion with and without computer assistance: a randomised controlled clinical study in 100 consecutive patients. Eur Spine J 9:235–240
59. Schwarzenbach O, Berlemann U, Jost B, Visarius H, Arm E, Langlotz F, Nolte LP, Ozdoba C (1997) Accuracy of image-guided pedicle screw placement. An in vivo computed tomography analysis. Spine 22:452–458
60. Digioia AM 3rd, Simon DA, Jaramaz B et al (1999) HipNav: pre-operative planning and intra-operative navigational guidance for acetabular implant placement in total hip replacement surgery. In: Nolte LP, Ganz E (eds) Computer Assisted Orthopaedic Surgery (CAOS). Hogrefe & Huber, Seattle, pp 134–140
61. Croitoru H, Ellis RE, Prihar R, Small CF, Pichora DR (2001) Fixation based surgery: a new technique for distal radius osteotomy. Comput Aided Surg 6:160–169

62. Siebert W, Mai S, Kober R, Heeckt PF (2002) Technique and first clinical results of robot-assisted total knee replacement. Knee 9:173–180
63. Delp SL, Stulberg SD, Davies B, Picard F, Leitner F (1998) Computer assisted knee replacement. Clin Orthop 354:49–56
64. Dessenne V, Lavallée S, Julliard R, Orti R, Martelli S, Cinquin P (1995) Computer assisted knee anterior cruciate ligament reconstruction: first clinical tests. J Image Guid Surg 1:59–64
65. Nolte LP, Slomczykowski MA, Berlemann U, Strauss MJ, Hofstetter R, Schlenzka D, Laine T, Lund T (2000) A new approach to computer-aided spine surgery: fluoroscopy-based surgical navigation. Eur Spine J 9:S78–S88
66. Zheng G, Marx A, Langlotz U, Widmer KH, Buttaro M, Nolte LP (2002) A hybrid CT-free navigation system for total hip arthroplasty. Comput Aided Surg 7:129–145
67. Suhm N, Jacob AL, Nolte LP, Regazzoni P, Messmer P (2000) Surgical navigation based on fluoroscopy – clinical application for image-guided distal locking of intramedullary implants. Comput Aided Surg 5:391–400
68. Sadoghi P (2015) Current concepts in total knee arthroplasty: patient specific instrumentation. World J Orthop 6(6):446–448
69. Camarda L, D'Arienzo A, Morello S, Peri G, Valentino B, D'Arienzo M (2015 Apr) Patient-specific instrumentation for total knee arthroplasty: a literaturereview. Musculoskelet Surg 99(1):11–18
70. Olsen M, Naudie DD, Edwards MR, Sellan ME, McCalden RW, Schemitsch EH (2014 Mar) Evaluation of a patient specific femoral alignment guide for hip resurfacing. J Arthroplasty 29(3):590–595
71. Cartiaux O, Paul L, Francq BG, Banse X, Docquier PL (2014) Improved accuracy with 3D planning and patient-specific instruments during simulated pelvic bone tumor study. Ann Biomed Eng 42(1):205–213
72. Personal communication with Prof. Dr. K. Siebenrock, Inselspital, University of Bern
73. Rahmathulla G, Nottmeier E, Pirris S, Deen H, Pichelmann M (2014) Intraoperative image-guided spinal navigation: technical pitfalls and their avoidance. Neurosurg Focus 36(3):E3
74. Wang L, Traub J, Weidert S, Heining SM, Euler E, Navab N (2010) Parallax-free intra-operative x-ray image stitching. Med Image Anal 14(5):674–686
75. Chen C, Kojcev R, Haschtmann D, Fekete T, Nolte L, Zheng G (2015) Ruler based automatic C-arm image stitching without overlapping constraint. J Digit Imaging 28(4):474–480
76. Chang J, Zhou L, Wang S, Clifford Chao KS (2012) Panoramic cone beam computed tomography. Med Phys 39(5):2930–2946
77. Chen C, Belavy D, Yu W, Chu C, Armbrecht G, Bansmann M, Felsenberg D (2015 Aug) G Zheng. Localization and segmentation of Localization and Segmentation of 3D Intervertebral Discs in MR Images by Data Driven Estimation. IEEE Trans Med Imaging 34(8):1719–1729
78. Zheng G, Li S, Székely G (2017) Statistical shape and deformation analysis: methods, implementation and applications. Elesvier, London
79. Zheng G, Gollmer S, Schumann S, Dong X, Feilkas T, González Ballester MA (2009 Dec) A 2D/3D correspondence building method for reconstruction of a patient-specific 3D bone surface model using point distribution models and calibrated X-ray images. Med Image Anal 13(6):883–899
80. Yu W, Tannast M, Zheng G (2017) Non-rigid free-form 2D-3D registration using b-spline-based statistical deformation model. Pattern Recongn 63: 689–699
81. Driscoll M, Mac-Thiong JM, Labelle H, Parent S (2013) Development of a detailed volumetric finite element model of the spine to simulate surgical correction of spinal deformities. Biomed Res Int 2013:931741
82. Majdouline Y, Aubin CE, Wang X, Sangole A, Labelle H (2012 Nov 26) Preoperative assessment and evaluation of instrumentation strategies for the treatment of adolescent idiopathic scoliosis: computer simulation and optimization. Scoliosis 7(1):21
83. Murphy RJ, Armiger RS, Lepistö J, Mears SC, Taylor RH, Armand M (2015 Apr) Development of a biomechanical guidance system for periacetabular osteotomy. Int J Comput Assist Radiol Surg 10(4):497–508
84. Crottet D, Kowal J, Sarfert SA, Maeder T, Bleuler H, Nolte LP, Dürselen L (2007) Ligament balancing in TKA: Evaluation of a force-sensing device and the influence of patellar eversion and ligament release. J Biomech 40(8):1709–1715
85. De Keyser W, Beckers L (2010 Dec) Influence of patellar subluxation on ligament balancing in total knee arthroplasty through a subvastus approach. An in vivo study. Acta Orthop Belg 76(6):799–805
86. de Steiger RN, Liu YL, Graves SE (2015 Apr 15) Computer navigation for total knee arthroplasty reduces revision rate for patients less than sixty-five years of age. J Bone Joint Surg Am 97(8):635–642
87. Jolesz FA (2014) Introduction. In: Jolesz FA (ed) Intraoperative imaging and image-guided therapy. Springer, London, pp 1–23
88. Dubousset J, Charpak G, Skalli W, Deguise J, Kalifa G (2010) EOS: A new imaging system with low dose radiation in standing position for spine and bone & joint disorders. J Musculoskeleta Res 13: 1–12
89. Wybier M, Bossard P (2013 May) Musculoskeletal imaging in progress: the EOS imaging system. Joint Bone Spine 80(3):238–243
90. Illés T, Somoskeöy S (2012) The EOS imaging system and its use in daily orthopaedic practice. Int Orthop 36:1325–1331

91. Wade R, Yang H, McKenna C et al (2013) A systematic review of the clinical effectivenss of EOS 2D/3D x-ray imaging system. Eur Spine J 22: 296–304
92. Deschenes S, Charron G, Beaudoin G et al (2010) Diagnostic imaging of spinal deformities – Reducing patients radiation dose with a new slot-scanning x-ray imager. Spine 35:989–994
93. Langlois K, Pillet H, Lavaste F, Rochcongar G, Rouch P, Thoreux P, Skalli W (2015 Oct) Assessing the accuracy and precision of manual registration of both femur and tibia using EOS imaging system with multiple views. Comput Methods Biomech Biomed Eng 18(Suppl 1):1972–1973
94. Ferrero E, Lafage R, Challier V, Diebo B, Guigui P, Mazda K, Schwab F, Skalli W, Lafage V (2015 Sept) Clinical and stereoradiographic analysis of adult spinal deformity with and without rotatory subluxation. Orthop Traumatol Surg Res 101(5): 613–618
95. Glaser DA, Doan J, Newton PO (2012) Comparison of 3-Dimensional spinal reconstruction accuracy. Spine 37:1391–1397
96. Lazennec JY, Rousseau MA, Rangel A, Gorin M, Belicourt C, Brusson A, Catonne Y (2011) Pelvis and total hip arthroplasty acetabular component orientation in sitting and standing positions: measurements reproductibility with EOS imaging system versus conventional radiographies. Orthop Traumatol Surg Res 97:373–380
97. Lazennec JY, Brusson A, Dominique F, Rousseau MA, Pour AE (2015) Offset and anteversion reconstruction after cemented and uncemented total hip arthroplasty: an evaluation with the low-dose EOS system comaring two- and three-dimensional imaging. Int Orthop. 39(7):1259–1267
98. Folinais D, Thelen P, Delin C, Radier C, Catonne Y, Lazennec JY (2011) Measuring femoral and rotational alignment: EOS system versus computed tomography. Orthop Traumatol Surg Res 99: 509–516
99. Zheng G, Schumann S, Alcoltekin A, Jaramaz B, Nolte L-P (2016) Patient-specific 3D reconstruction of a complete lower extremity from 2D X-rays.In: Proceedings of MIAR 2016, LNCS 9805. Springer, Heidelberg, pp 404–414
100. Hommel H, Alcoltekin A, Thelen B, Stifter J, Schwägli T, Zheng G (2017) 3X-Plan: A novel technology for 3D prosthesis planning using 2D X-ray radiographs. Proc CAOS 2017:93–95
101. Glocker B, Feulner J, Criminisi A, Haynor DR, Konukoglu E (2012) Automatic localization and identification of vertebrae in arbitrary field-of-view CT scans. In: Proceedings of MICCAI 2012; 15(Pt3). Springer, Heidelberg, pp 590–598
102. Liu Q, Wang Q, Zhang L, Gao Y, Sheng D (2015) Multi-atlas context forests for knee MR image segmentation. MLMI@MICCAI 2015:186–193
103. Litjens G, Kooi T, Bejnordi BE, Setio AAA, Ciompi F, Ghafoorian M, van der Laak JAWM, van Ginneken B, Sánchez CI (2017) A survey on deep learning in medical image analysis. Med Image Anal 42:60–88
104. Krizhevsky A, Sutskever I, Hinton GE (2012) ImageNet classification with deep convolutional neural networks. Advances in Neural Information Processing Systems 25, Curran Associates, Inc., 2012, 1097–1105
105. Prasoon A, Petersen K, Igel C, Lauze F, Dam E, Nielsen M (2013) Deep feature learning for knee cartilage segmentation using a triplanar convolutional neural network. MICCAI 2013 16(Pt2): 246–253
106. Zeng G, Yang X, Li J, Yu L, Heng P-A, Zheng G (2017) 3D U-net with multi-level deep supervision: fully automatic segmentation of proximal femur in 3D MR images. MLMI@MICCAI 2017: 274–282
107. Li X, Dou Q, Chen H, Fu CW, Qi X, Belavý DL, Armbrecht G, Felsenberg D, Zheng G, Heng PA (2018) 3D multi-scale FCN with random modality voxel dropout learning for intervertebral disc localization and segmentation from multi-modality MR images. Med Image Anal 45:41–54
108. Janssens R, Zeng G, Zheng G (2017) Fully automatic segmentation of lumbar vertebrae from CT images using cascaded 3D fully convolutional networks. arXiv:1712.01509

Computer-Aided Orthopedic Surgery: Incremental Shift or Paradigm Change?

2

Leo Joskowicz and Eric J. Hazan

Abstract

Computer-aided orthopedic surgery (CAOS) is now about 25 years old. Unlike neurosurgery, computer-aided surgery has not become the standard of care in orthopedic surgery. In this paper, we provide the technical and clinical context raised by this observation in an attempt to elucidate the reasons for this state of affairs. We start with a brief outline of the history of CAOS, review the main CAOS technologies, and describe how they are evaluated. We then identify some of the current publications in the field and present the opposing views on their clinical impact and their acceptance by the orthopedic community worldwide. We focus on total knee replacement surgery as a case study and present current clinical results and contrasting opinions on CAOS technologies. We then discuss the challenges and opportunities for research in medical image analysis in CAOS and in musculoskeletal radiology. We conclude with a suggestion that while CAOS acceptance may be more moderate than that of other fields in surgery, it still has a place in the arsenal of useful tools available to orthopedic surgeons.

L. Joskowicz (✉)
School of Computer Science and Engineering, The Hebrew University of Jerusalem, Jerusalem, ISRAEL
e-mail: josko@cs.huji.ac.il

E. J. Hazan
Traumatology and Emergency Departments, Instituto Nacional de Rehabilitacion, Mexico City, MEXICO

Keywords

Computer-aided orthopedic surgery · Image-guided surgery · Medical robotics

2.1 Introduction

Computer-based technologies, including both software and hardware, are playing an increasingly larger and more important role in defining how surgery is performed today. Orthopedic surgery was, together with neurosurgery, the first clinical specialty for which image-guided navigation and robotic systems were developed. Computer-aided orthopedic surgery (CAOS) is now about 25 years old. During this time, a wide variety of novel and ingenious systems have been proposed, prototyped, and commercialized for most of the main orthopedic surgery procedures, including knee and hip joint replacement, cruciate ligament surgery,

G. Zheng et al. (eds.), *Intelligent Orthopaedics*, Advances in Experimental Medicine and Biology 1093, https://doi.org/10.1007/978-981-13-1396-7_2

spine surgery, corrective osteotomy, bone tumor surgery, and trauma surgery, among others.

While CAOS technologies are nowadays visible and known to many orthopedic surgeons worldwide, their adoption has been relatively slow, especially when compared to other technologies such as robotic minimally invasive surgery (daVinci Surgical System, Intuitive Surgical). This raises a number of questions, e.g., What are the known clinical benefits of CAOS technologies? Why has CAOS been a progressive technology and not a disruptive one? Has CAOS led to a paradigm change in some of the orthopedic surgery procedures? What is the future of CAOS? What role has medical image analysis played in CAOS and what is its future?

In this paper, we present a personal perspective on the key aspects of CAOS in an attempt to answer these questions. We start with a brief history of CAOS from its beginnings, emergence, expansion, and steady progress phases. We then outline the main CAOS technologies and describe how they are evaluated. Next, we summarize the current views on their clinical impact and their acceptance by the orthopedic community worldwide. We focus on total knee replacement surgery as a case study and present the clinical results and contrasting opinions on CAOS technologies. We then discuss the challenges and opportunities for research in medical image analysis in CAOS and in musculoskeletal radiology and conclude with an observation: while CAOS acceptance may be more moderate than that of other fields in surgery, it still has a place in the arsenal of useful tools available to orthopedic surgeons.

2.2 A Brief History of CAOS

CAOS started over 25 years ago, with the introduction of four key technologies: 3D bone surface modeling from CT scans, surgical robotics, real-time surgical navigation, and, later, patient-specific templates. The main CAOS concepts and technical elements emerged in the mid- to late 1990s; the first clinical results started to appear in the clinical literature in the late 1990s. The International Society for Computer Assisted Orthopaedic Surgery was established in 2000 and has held yearly meetings since. The early and mid-2000s witnessed a rise in the introduction of commercial systems and the publication of small- and medium-sized clinical studies. The late 2000s to date featured a slow consolidation period, with larger and more specific comparative clinical studies, multicenter studies, and meta-studies. It also featured mature image processing and surgical planning software, image-based navigation systems, robotic systems, and routine patient-specific guide design and related production services.

Bone modeling from CT scans stemmed from 3D segmentation and surface mesh construction methods such as the Marching Cubes algorithm introduced by Lorensen and Cline [1] in the late 1980s. A variety of segmentation methods and mesh smoothing and simplification methods were developed in the early 1990s. These patient-specific anatomical models are essential for preoperative planning, intraoperative registration, visualization, navigation, and postoperative evaluation.

The first robotic system in orthopedics was ROBODOC, a customized industrial active robot designed for total hip replacement (THR) to optimize the bone/implant interphase by machining the implant cavity [2]. ROBODOC development started in the late 1980s at the IBM T.J. Watson Research Center and at the University of California at Davis; it was first used for human surgery in 1992 and became a commercial product in 1995 (developed by Integrated Surgical Systems and owned since 2008 by Curexo Technology Corp.). The system includes a preoperative planning module that allows surgeons to select the size and position of the acetabular cup and femoral stem based on automatically built 3D surface models of the pelvis and hip joint bone from a preoperative CT scan. Based on this plan, it automatically generates a specific machining plan for the femoral stem cavity, which is then executed during surgery after pin-based contact registration between the patient and the plan. The system was later extended to total knee replacement (TKR) surgery to perform the femoral and tibial cuts; the first human surgery was performed in the year 2000. To date, over 28,000 ROBODOC surgeries have been performed worldwide. Other robotic systems, such as Acrobot for TKR and Ortho Marquet for THR, were also developed in the late 1990s.

Computer-aided navigation concepts for various orthopedic procedures were developed in the early 1990s. The first CAOS navigation systems for pedicle screw insertion in spine surgery were presented in Lavallee et al. [3] and Nolte et al. [4]. They were based, as many others that followed, on accurate off-the-shelf real-time optical tracking technology (Northern Digital Inc., NDI). Preoperative planning and intraoperative visualization are based on 3D surface models of the vertebrae obtained from a CT scan. These systems were shown to greatly improve the accuracy and safety of pedicle screw insertion, particularly in deformed vertebrae and spine scoliosis. Fluoroscopy-based and imageless navigation systems were later developed for total hip and total knee replacement, for bone fracture surgery (FRACAS, [5]), and for anterior cruciate ligament (ACL) reconstruction. Commercial systems for these procedures were launched in the early 2000s by companies such as Medtronic, BrainLab, Stryker, Aesculap, and Praxim.

Individual templates, also called patient-specific jigs, were introduced in the late 1990s by Radermacher et al. [6]. The idea is to create a disposable custom-made cutting and/or drilling jig that is then stably and uniquely mounted on the patient bone anatomy to guide the surgeon's surgical actions. The advantages of individual templates are that they uniquely fit the patient, that they do not require adjustment, and that they are closest to the conventional surgical approach. Initially, the custom jigs were manufactured by computer numerical control (CNC) machining. The first human intervention was performed in 1993 for periacetabular repositioning osteotomy and in 1997 for TKR. Their clinical adoption was relatively slow until the late 2000s. With the popularization of 3D additive printing and related cloud-based design and manufacturing systems, their use has considerably expanded.

From 2000 to 2008, CAOS witnessed rapid technology transfer and the introduction of new commercial systems by both established and new companies. This trend included about a dozen navigation systems for hip, knee, and spine surgery and the advent of several robotic systems such as patient-mounted miniature system for pedicle screw insertion in spine surgery (Mazor Robotics) [7] and unicompartmental knee arthroplasty (UKA) (Mako Surgical Corporation, Fig. 2.1). Also, larger and midterm clinical studies appeared for navigated TKR, THR, and spine surgery.

The 2008–2014 period was a relatively slow consolidation period. CAOS technologies did not achieve the expected across-the-board clinical acceptance and associated market penetration. Specific adoption rates varied by procedure and by country: CAOS navigation technologies were found to have better acceptance in France, Europe, and certain Asian countries, while robotic UKA fared much better in the USA. An interesting development was the introduction of smart tools such as the Hip Sextant (HipXpert, Surgical Associates Ltd.) and the Navio handheld drill for knee surgery (Blue Belt Technologies). In parallel, a series of critical meta-studies showed that while the radiological outcomes of CAOS surgeries were superior to those of conventional surgery, there was no proven clinical/functional benefit to the use of CAOS, in particular for TKR.

Since 2014, CAOS technologies appear to be progressing steadily, with a ramp-up in their clinical use and acceptance for specific procedures and locations worldwide. A major event was the acquisition of Mako Surgical Corporation by Stryker, a large and established medical device and medical equipment manufacturer. While CAOS did not cause the disruption and revolution some expected it to be, it is carving its own space in the orthopedic surgeon portfolio.

a

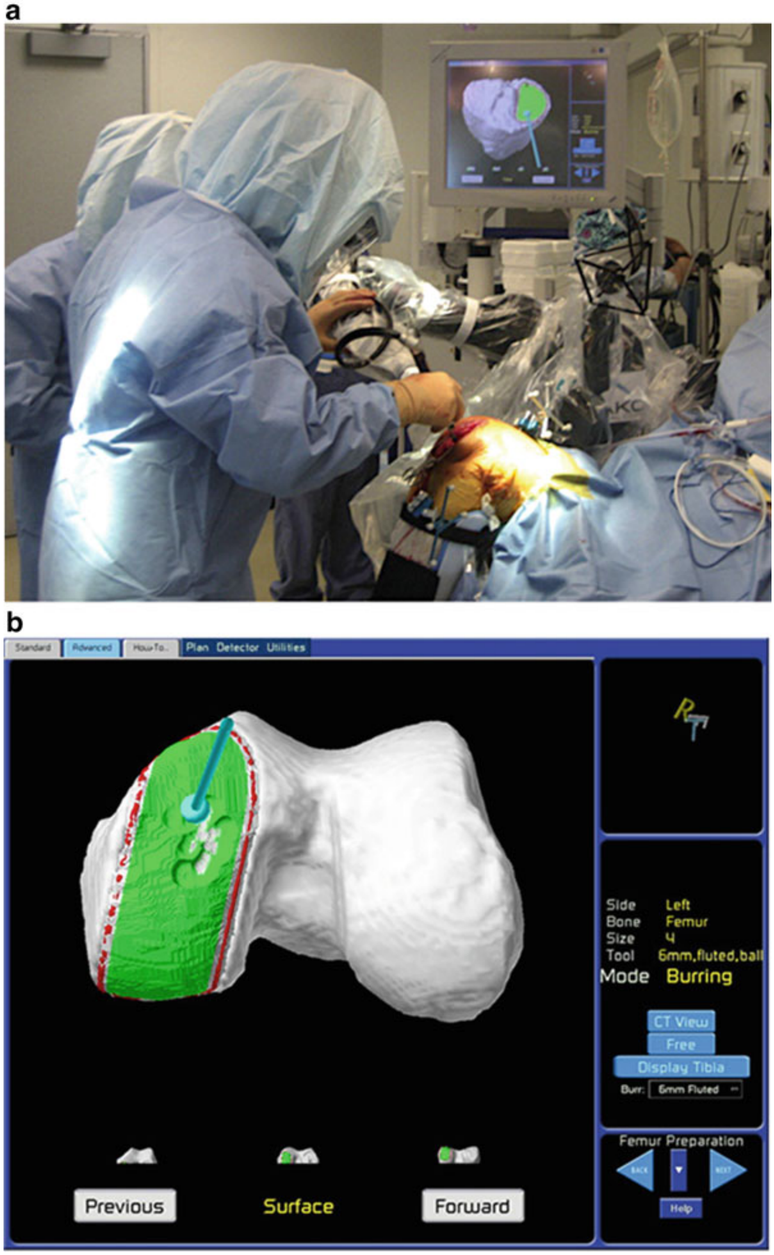

Fig. 2.1 Illustration of the intraoperative setting for a unicompartmental knee replacement robotic surgery: (**a**) view from behind the surgeon (center) showing him machining the condyle with support from the semi-active robot arm based on the screen plan; (**b**) computer screen showing the bone upper tibial bone model (white), the contour of the condylar implant cavity to be machined (red), and the machining progress (green); (**c**) surgeons evaluating the intraoperative situation (part of the optical tracker can be seen on the upper left corner); (**d**) view of the surgeon hand holding the optically tracked drill (Photos courtesy of Dr. Andrew Pearle, Hospital for Special Surgery, New York, USA, while performing a surgery with the Mako robotic-arm-assisted surgery, Stryker)

Fig. 2.1 (continued)

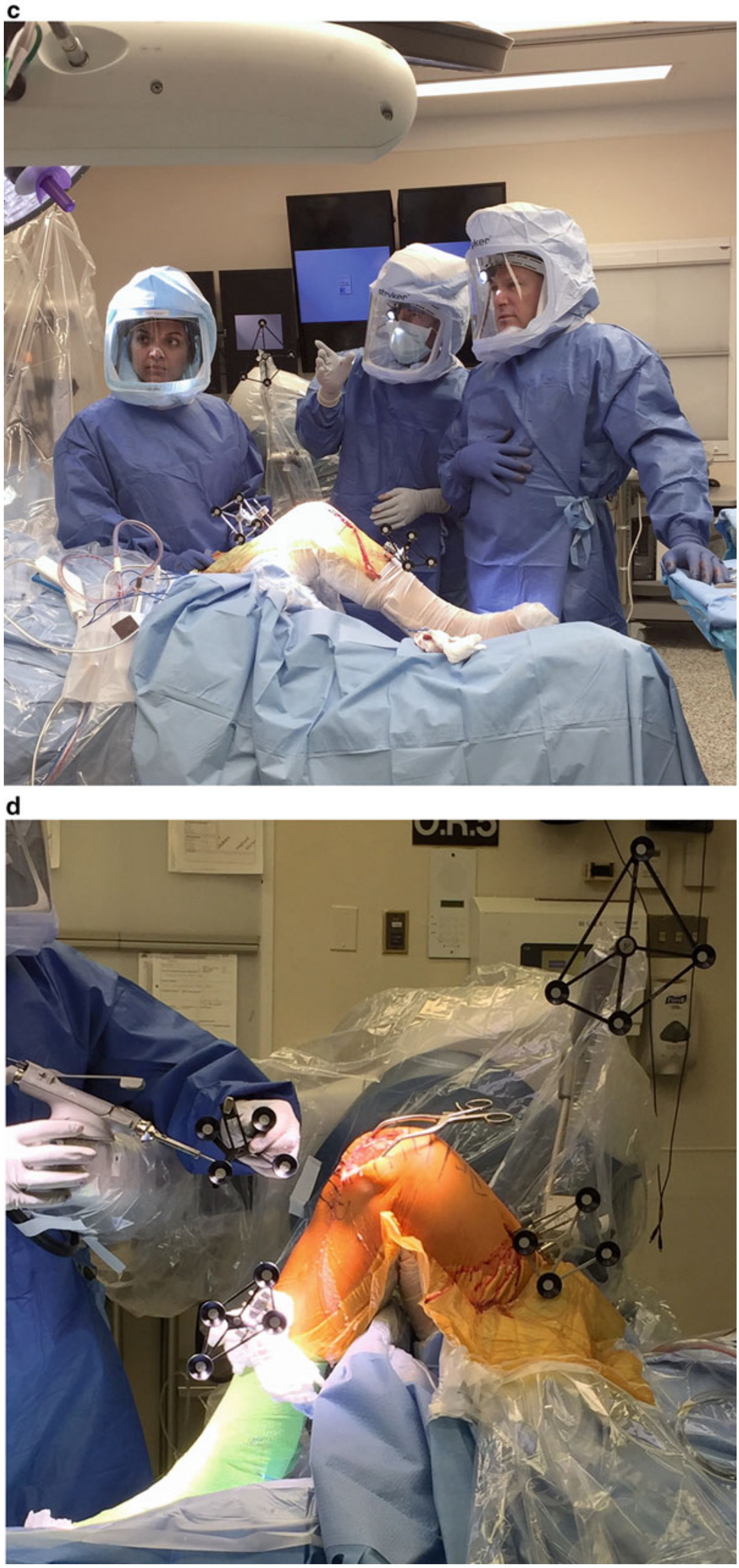

2.3 CAOS Technologies

CAOS relies on a number of mature technologies. These include a variety of imaging modalities (X-ray, MRI, CT, US, video), real-time tracking (optical, electromagnetic, mechanical), 3D additive printing, and various robotics technologies, including smart instruments. From the medical image analysis perspective, the key technologies include bone segmentation in X-ray and CT images and rigid 2D/3D and 3D/3D registration.

CAOS is about integration, so most commercial systems combine mature technologies with new ones. Existing CAOS systems can be broadly categorized into either image-guided (CT-based, X-ray fluoroscopy-based, and imageless) navigation systems, positioning systems (patient-specific jigs, bone- and table-mounted self-positioning robots), assistive (semi-active) robotic systems, or active robotic systems. Nearly all include a preoperative planning system, which constitutes an orthopedic CAD station. Careful attention is paid to two key aspects: the surgical workflow and the surgeon ergonomy. For a detailed description of the principles of CAOS technologies and clinical applications, see Liebergall et al. [8] and Zheng and Li [9].

2.4 Evaluation of CAOS Technologies

The clinical and technical evaluation of CAOS technologies is essential to establish indications and counter-indications of the technologies, to establish risk and cost/benefit assessments, to objectively compare between commercial systems, and to evaluate emerging technologies.

Clinical evaluation consists of radiological and functional studies based on preoperative and short-, mid-, and long-term postoperative data. Radiological studies are mostly X-ray based – they report common quantitative measures such as leg length, abduction angles, implant alignment, and implant wear. Functional studies report standardized orthopedics measures, such as Hip and Knee Society scores. The studies evaluate the outcome of an approach and/or technology on a cohort of patients or can be comparative, usually conventional surgery vs. CAOS. Some studies target specific populations and/or conditions, e.g., young patients, obese patients, and patients with severe deformities and/or revision surgery. Comprehensive meta-studies for THR [10], TKR [11], and spine surgery [12] have been recently published.

Technical evaluations analyze the characteristics of the CAOS system, such as precision, accuracy, repeatability, and related issues. The technical evaluation measures are provided with respect to one or more clinical targets, e.g., angle, leg-length discrepancy, and include in vitro and cadaver studies. In 2010, a standard for assessing the accuracy performance of surgical assistance technologies, jointly developed by the International Society for Computer Assisted Orthopaedic Surgery and the American Society for Testing of Materials, was introduced [13]. However, it is not relevant for directly measuring the accuracy of an actual surgical gesture, so its actual impact on surgical procedures is difficult to evaluate.

CAOS technologies have obviated the need to revise and extend existing clinical and technical evaluation procedures. Currently, there is no consensus on how to evaluate the accuracy of surgical procedures [14]. The three basic questions are: (1) How is accuracy defined? (2) How can accuracy be measured experimentally? and (3) How should accuracy be analyzed from a clinical perspective? Clearly, surgical accuracy is multifactorial – the lack of a standardized evaluation protocol affects the ability to compare clinical results from different hospitals using different surgical protocols, tools, and technologies. Moreover, the definition of a patient-specific surgical accuracy target – e.g., axis alignment, varus/valgus angles – has an intrinsic uncertainty that also needs to be quantified. Improving the accuracy of a surgical procedure whose main technical target measure has a large uncertainty is unlikely to yield a clinical benefit and/or be cost-effective.

The lack of agreed-upon standards also affects how clinical studies are conducted. For example, many studies compare the performance of conventional vs. CAOS technology. Some studies report that CAOS technologies help, while others report no benefit. However, without a clear understanding of what the target value and its uncertainty are, the interpretation may be partial and inconclusive. For example, common misconceptions fail to distinguish between measurement error and measurement uncertainty and between accuracy and precision. Another misconception is that improved accuracy yields improved outcomes. Moreover, the accuracy and precision of the execution of a surgical procedure (or part of it) can easily be overshadowed by other factors such as patient demographics and comorbidities, pre- and postoperative care protocols, individual adherence to these protocols, and variations in the surgical technique. Indeed, this is most likely the reason that many computer-aided techniques have not been able to show clinical benefit as measured by validated patient-assessed outcome measures.

An important task for the CAOS community is to improve and extend clinical and technical standards to allow objective quantitative comparison.

2.5 Clinical Impact and Acceptance

The clinical impact and acceptance of CAOS systems have been slow when compared to other surgical technologies. Considering that orthopedic surgery is one of the specialties with the largest patient volumes worldwide, it is, on average, infrequently used. While a few centers report a use of CAOS technologies for nearly all their joint and spine procedures, CAOS technologies are not used broadly, even in developed countries. A conservative estimate places CAOS surgeries to less than 5% of all orthopedic surgeries in the USA, Europe, and Asia. There are several reasons for this state of affairs, which we will examine next.

CAOS technology is currently mostly used for primary TKR and THR surgery. Next come anterior cruciate ligament (ACL) reconstruction, spine surgery (pedicle screw insertion), UKA, osteotomies (high tibial and hip), and trauma surgery (long bones and pelvic fractures). Emerging procedures include hip resurfacing, bone tumor resection, reverse shoulder arthroplasty, and elbow, hand, and ankle surgery.

It is recognized that the main technical advantages of CAOS technologies over conventional surgery include improved implant positioning accuracy and the homogenization of positioning results (smaller variation and fewer outliers) as compared to conventional techniques. The benefits are greater for difficult cases and for revisions. It is commonly inferred that greater accuracy translates in lower rates of implant failure and therefore into better long-term outcomes.

To illustrate the clinical effects and acceptance of CAOS technologies, consider next the case of knee surgery. Computer-assisted TKR is today the most successful and widespread application of CAOS technology, with nearly 500,000 surgeries documented in various registries around the world. CAOS assistance consists mostly of support for the accurate positioning of the bone cutting tools to shape the ends of the femur and tibia to match the implant interface. It is mainly performed with imageless navigation and patient-specific templates. Soft tissue balancing tools and software are also available and are important for optimal joint stability and outcome.

While navigated TKR has become the standard of care in some centers in Germany, its penetration in North America has been nearly inexistent. For example, over 30% of surgeons in Germany use TKR CAOS technology, while in France 6% and in the UK less than 3% [15]. Some of the reasons are stated in a variety of studies; they include good results and high satisfaction of existing conventional procedures, additional operative time, extra cost, lack of insurance coverage, poor ergonomics, surgeon age, lack of quantitative results, and lack of evaluation standards.

Indeed, there is an ongoing debate about the benefits of CAOS in TKR. A recent study of the Australian Orthopaedic Association National Joint Replacement Registry (2003–2012, 44,573 patients) that examines the effect of computer navigation on the rate of revision of primary TKR shows that computer navigation reduced both the overall revision rate of TKR and specifically the revision rate due to loosening/lysis, which is the most common reason for revision. In patients less than 65 years of age at 9 years from surgery, the rate was reduced from 7.8% for conventional TKR to 6.3% for navigated TKR.

The study by Picard et al. [15] reports that in 29 studies of CAOS versus conventional TKR, 3 main measures – mechanical axis misalignment >3°, frontal plane femoral component misalignment, and tibial component misalignment – occurred in 9.0% of CAOS vs. 31.8% of conventional TKR patients. They note that while navigation has indisputably demonstrated an improvement in alignment of TKR components, the question concerning the tolerable limits of acceptable alignment that guarantees functionality without compromising the function and longevity of the prosthesis remains debatable.

Very recently, van der List et al. [11] conducted a meta-analysis of 40 comparative studies and 3 registries on computer navigation with a total of 474,197 patients and 21 basic science and clinical studies on robotic-assisted TKR. Twenty-eight of these comparative computer navigation studies reported Knee Society total scores in 3504 patients. Stratifying by type of surgical variables, no significant differences were noted in outcomes between surgery with computer-navigated TKR controlling for alignment and component positioning versus conventional TKR. However, significantly better outcomes were noted following computer-navigated TKR that also controlled for soft tissue balancing versus conventional TKR. The literature review on robotic systems showed that these systems can, similarly to computer navigation, reliably improve lower leg alignment, component positioning, and soft tissue balancing. Furthermore, two studies comparing robotic-assisted with computer-navigated surgery reported the superiority of robotic-assisted surgery in controlling these factors. They observe that even though most clinical studies, meta-analysis, and systematic reviews of TKR favor a higher accuracy and consistency of optimal implant alignment and soft tissue balancing with navigation or robotic assistance over conventional surgery, no clear improvement in functional outcome could be demonstrated as of today. They recognize that larger randomized control trials as well as a longer follow-up are needed to elicit significant differences in the future to justly evaluate these technologies.

Overall, we observe that CAOS technologies have neither become the standard of care of any orthopedic procedure nor has it led to a paradigm shift. This is in contrast with stereotactic neurosurgery, in which navigation is the standard of care, or various laparoscopic surgeries with a robotic system. Unlike neurosurgery, most orthopedic procedures are not life-threatening, have a larger margin of tolerance for inaccuracies, and require longer evaluation times to determine their mid- to long-term benefits.

In terms of surgeon acceptance, CAOS is facing challenges similar to those faced by laparoscopic surgery when it was introduced. Picard et al. [15] point out that the main factors limiting TKR navigation spreading among orthopedic surgeons are most likely ergonomics and economics. They conclude that the main reasons for which there is opposition to CAOS technologies are based on inaccurate and/or misleading observations and the lack of data to support the cost-effectiveness of using navigation [16]. On the other hand, certain procedures, such as UKA, are recently experiencing an upward trend in the USA for younger patients with severe wear of one knee compartment thanks to the introduction of the Mako RIO system (Stryker) – over 50,000 UKA surgeries have been reported to date since its inception in 2010 (Fig. 2.1). We believe that while CAOS TKR is not yet mainstream, it will still prove to be a useful tool for surgeons, especially for surgeons that do only a few surgeries per year (“low volume surgeons”) and for difficult and unusual cases.

2.6 Medical Image Analysis in Orthopedics and CAOS

Medical image analysis (MEDIA) research is at the core of CAOS technologies and has made significant contributions to orthopedics in general. We expect this to be increasingly so in the future.

We identify next what are, in our opinion, the challenges and opportunities of medical image analysis research in CAOS and orthopedics at large. These include musculoskeletal radiology [9], surgical planning and execution and outcome evaluation [17, 18], and surgical training and surgeon skill evaluation.

Musculoskeletal radiology presents a vast field of untapped opportunities. It covers a wide spectrum of imaging modalities used in orthopedics, mostly X-ray, CT, and MRI. The opportunities include computerized support for image interpretation and diagnosis of various orthopedic conditions – dislocation, occult fractures, spine instability, and various injuries – the automatic detection of missed conditions, and the identification of diagnostic misclassifications. It also includes automatic and systematic incidental finding discovery and early warning for clinical conditions, e.g., osteoporosis and scoliosis.

In parallel, the continuous development of new and improved imaging protocols and devices, such as the EOS® full-body standing low-dose X-ray orthopedic imaging system, intraoperative X-ray fluoroscopy and cone-beam CT scans (O-arm, Medtronic), and robotized patient positioning and imaging system (Artis zeego, Siemens), all includes image processing and modeling capabilities. Additional image processing opportunities include image stitching for panoramas, statistical model creation, image fusion, and multimodal registration, to name a few.

An emerging field with great potential is big data radiology. The increasing amount medical imaging scan acquired in clinical practice constitutes a vast database of untapped diagnostically relevant information. Radiologists and clinicians are increasingly struggling under the burden of diagnosis and follow-up of such an immense amount of data. The vast amount of information in this valuable, unstructured clinical data represents an untapped gold mine to support a wide variety of clinical tasks, such as the retrieval of patient cases with similar radiological images, image-based retrospective incidental findings, large-scale radiological population and epidemiologic studies, and preventive medicine by early radiological detection. In the context of CAOS and musculoskeletal radiology, these tasks include optimization of patient-specific surgery planning, population-based postoperative radiological assessment, and treatment and condition assessment, e.g., osteoporosis assessment and sacroiliac joint pain.

Finally, surgeon teaching, training, accreditation, and evaluation is another developing area in which the generation of patient-specific 3D anatomical models plays a key role in the development of simulators, case studies, and examination platforms.

2.7 Closing Remarks

In conclusion, we believe that there has never been a better time for the development of CAOS technologies and for related medical image analysis research. According to BCC Research [19], the global market for medical robotics and computer-assisted surgical (MRCAS) technologies is expected to grow to $4.6 billion by 2019, with a 5-year compound annual growth rate of 7%. Factors such as steadily aging global population and increasing demand for minimally invasive surgical procedures such as heart and orthopedic surgery are spurring significant opportunities in this market worldwide. In particular, CAOS applications are expected to more than triple their market share between 2013 and 2019.

We expect CAOS systems to become that standard of care in many orthopedic applications and to continue to provide challenging applied research topics. We suggest that while CAOS acceptance may be more moderate than that of laparoscopic surgery, whose adoption was met with initial resistance and took many years to lead to a paradigm change and may not be disruptive, it still has a place in the arsenal of useful tools available to orthopedic surgeons, in the benefit of the patient.

Acknowledgment This chapter was modified from the paper published by our group in *Medical Image Analysis* (Joskowicz and Hazan 2016; 33:84–90). The related contents are reused with permission.

References

1. Lorensen WE, Cline HE (1987) Marching cubes: a high resolution 3D surface construction algorithm. ACM SIGGRAPH Comput Graph 21(4):163–169
2. Taylor RH, Mittelstadt BD, Paul HA, Hanson W, Kazanzides P, Zuhars JF, Williamson B, Musits BL, Glassman E, Bargar WL (1994) An image-directed robotic system for precise orthopaedic surgery. IEEE Trans Robot Automat 10(3):261–275
3. Lavallee S, Sautot P, Troccaz J, Cinquin P, Merloz P (1995) Computer-assisted spine surgery: a technique for accurate transpedicular screw fixation using CT data and a 3D optical localizer. Comput Aided Surg 1:65–73
4. Nolte LP, Visarius H, Arm E, Langlotz F (1995) Computer-aided fixation of spinal implants. J Image Guid Surg 1(2):88–93
5. Joskowicz L, Milgrom C, Simkin A, Tockus L, Yaniv Z (1999) FRACAS: a system for computer-aided image-guided long bone fracture surgery. Comput Aided Surg 3(6):271–288
6. Radermacher K, Portheine F, Anton M, Zimolong A, Kaspers G, Rau G, Staudte H-W (1998) Computer assisted orthopaedic surgery with image-based individual templates. Clin Ortho Relat Res 54: 28–38
7. Shoham M, Lieberman IH, Benzel EC, Zehavi E, Zilberstein B, Roffman M, Bruskin A, Fridlander A, Joskowicz L, Brink-Danan S, Knoller N (2007) Robotic assisted spinal surgery: from concept to clinical practice. Comput Aided Surg 12(2): 105–115
8. Liebergall M, Joskowicz L, Mosheiff R (2015) Computer-aided orthopaedic surgery in skeletal trauma. In: Bucholz R, Heckman J (eds) Rockwood and green's fractures in adults, 8th edn. Lippincott Williams and Wilkins, Philadelphia, pp 575–607
9. Zheng G, Li S (2016) Computational radiology for orthopaedic interventions. Springer, New York
10. Gandhi R, Marchie A, Farrokhyar F, Mahomed N (2009) Computer navigation in total hip replacement: a meta-analysis. Int Orthop 33(3):593–597
11. van der List JP, Chawla H, Joskowicz L, Pearle AD (2016) Current state of computer navigation and robotics in unicompartmental and total knee arthroplasty: a systematic review with meta-analysis. Knee Surg Sports Traumatol Arthrosc 24(11): 3482–3495
12. Aoude AA, Fortin M, Figueiredo F, Jarzem P, Ouellet J, Weber MH (2015) Methods to determine pedicle screw placement accuracy in spine surgery: a systematic review. Eur Spine J 24:990–1004
13. ASTM International (2010) ASTM standard F2554-10: standard practice for measurement of positional accuracy of computer assisted surgical systems. ASTM International, West Conshohocken www.astm.org
14. Cartiaux O, Jenny J-Y, Joskowicz L (2016) Accuracy in orthopaedic surgery assisted by navigation systems, robots and 3D printers: how is it defined, how could It be measured experimentally, and how should it be analyzed from a clinical perspective? J Bone Bone Surg 99(e39):1–8
15. Picard F, Clarke J, Deep K, Gregory A (2014) Computer assisted knee replacement surgery: is the movement mainstream? Ortho Muscular Syst 3(2):1000153
16. Walker R, Monda M, Chauhan S (2010) Focus on: navigation for TKR. J Bone Joint Surg
17. Kovler I, Joskowicz L, Kronman A, Weill Y, Salavarrieta J (2015) Haptic computer-assisted patient specific preoperative planning for orthopaedic fracture surgery. Int J Comput Aided Radiol Surg 10(10):1535–1546
18. Ritacco LE, Milano FE, Chao E (2016) Computer-assisted musculoskeletal surgery: thinking and executing in 3D. ISBN: 978-3-319-12942-6, Print, 978-3-319-12943-3, Online Book, Springer.
19. BCC Research (2015) Medical robotics and computer aided surgery report, http://www.bccresearch.com

3 CAMISS Concept and Its Clinical Application

Wei Tian, Yajun Liu, Mingxing Fan, Jingwei Zhao, Peihao Jin, and Cheng Zeng

Abstract

This chapter intends to provide an overview of computer-assisted minimally invasive spine surgery (CAMISS) and its clinical application. Since minimally invasive spine surgery was first brought out, the concept of decreasing the damage to patient was soon become popular. However, without the proper surgical field, the spine surgery can be very dangerous. The minimally invasive concept was restricted in promotion until the computer-assisted navigation system break down the obstacles. The CAMISS technique achieves better clinical outcomes with the advantages of smaller invasion, less injury, and better recovery and also became the gold standard for spine surgery. The spatial distribution concept and the respiration-induced motion concept help in promoting the accuracy and safety of the CAMISS concept. The CAMISS concept also facilitated the developing of robotic techniques, which was considered as the future of orthopedic surgery.

W. Tian (✉) · Y. Liu · M. Fan · J. Zhao · P. Jin · C. Zeng
Spine Department, Beijing Jishuitan Hospital, Beijing, China
e-mail: tianweijst@vip.163.com

Keywords

Computer-assisted minimally invasive spine surgery (CAMISS) · Clinical applications · Computer-assisted navigation · Medical robotics · Intelligent orthopedics

3.1 MISS

In 1968, Wiltse et al. found that there was an operative space between the multifidus and longissimus muscles [1], which is called the classic Wiltse approach. Compared with the traditional approaches, the Wiltse approach does not need to dissect paravertebral muscles, which could reduce the amount of bleeding and the damage to soft tissue [2]. In addition, the traditional incision is prone to damage the medial branch of the spinal nerve and cause the innervation of the muscle by retracting the multifidus during the operation. However, the Wiltse approach splits multifidus from the lateral part and retains the intact structure and the innervation of the muscle. It also avoids the muscle atrophy caused by denervation and is helpful for the recovery of postoperative spinal function [3]. The MISS method uses a special minimally invasive device

G. Zheng et al. (eds.), *Intelligent Orthopaedics*, Advances in Experimental Medicine and Biology 1093, https://doi.org/10.1007/978-981-13-1396-7_3

to achieve the best surgical effect by minimal surgical injury and less dissection. Since Foley first completed lumbar posterior fusion by MISS technique [4], many experts have tried this method and achieved positive results. Compared with the traditional incision operation, MISS method has the advantages of smaller injury, less bleeding, faster postoperative recovery, and less postoperative pain [5, 6]. As MISS method chooses the physiological space between the multifidus and longissimus muscles as the incision entry, it does not need to peel the muscle ligament and will not damage the blood vessel, avoiding postoperative anemia and transfusion-related complications [7]. In addition, the MISS method also preserves the tendon origin of multifidus, which makes the function of muscle relatively intact after operation; as a result, the postoperative recovery is fast and the incidence of complications such as lumbosacral pain and lumbar instability is quite low [8]. In addition, the minimally invasive instruments have more uniform and lower pressure on the muscles. Stevens found that the average maximum pressure caused by minimally invasive retractor is about 1/3 of that by open retractor [9]. The postoperative MRI also showed that muscle edema was significantly less in minimally invasive operation group than that in open surgery group.

However, in order to achieve minimally invasive surgery, MISS sacrifices the wide and clear operation field. Therefore, the narrow operation field is the key problem in MISS method. In traditional posterior spinal surgery, the surgeon usually operates under the naked eyes. The surgeon needs to identify the location and direction of pedicle screw implantation through specific structures such as bony markers. The range of decompression and location of fusion should also be determined by intraoperative situations. The basis of these operations is to fully expose the operation field. However, because of its narrow incision, MISS method cannot get as clear and complete field as traditional surgery. Therefore, many problems have been caused.

- The displacement rate of pedicle screw was higher. Since Boucher reported in 1959 [10], the pedicle screw system has been improved and become a major method of fixation for posterior spinal surgery. The accuracy of pedicle screw placement determines the fixed strength of the built-in body. If a pedicle screw is displaced, the surrounding structure may be injured, and surgical complications may occur. Therefore, before pedicle screw placement, the surgeon needs to go through the patient's imaging information carefully and determine the entry point according to the specific bone markers, such as the crista lambdoidalis method. It is the entry point that the intersection of the lumbar vertebral lamina epitaxy and the accessory crista converge. Roy Camile et al. put forward the straight comparison method [11], which is based on converge point of the extension line of the facet joint and the horizontal axis of the transverse process axis as the entry point. All of the above methods need to be fully exposed to articular process, accessory process, or transverse process, which is difficult to achieve in minimally invasive surgery. The severe misplacement rate of MISS pedicle screw studied by Schwender is up to 4.1% [12]. These severely misplaced screws may cause neurological complications and other surgical complications.
- The decompression is not enough. Under the premise of fully exposed operation field, traditional method can carefully identify the anatomical structure. However, the operation field of MISS method is small and deep, which make it difficult to identify the area of decompression in the operation.
- Higher exposure to radiation. Radiation exposure is one of the most important topics in recent years. The short-term, medium-term, and long-term hazards caused by radiation have been paid more and more attention. In the traditional open operation, the screw implantation point can be determined according to the anatomical markers identified by the naked eyes. However, in MISS the operator needs to increase the frequency of radiation to guide and confirm the position. Tian et al. suggested that the radiation dose of the MISS operation is higher than that of the traditional operation by meta-analysis [13].

- The learning curve is steep. Before starting the MISS method, a surgeon needs to practice more and gain enough experience in open operation. Besides, the operation of MISS needs to be assisted by perspective and other methods. However, research shows that the error rate by two-dimensional X-ray to determine the accuracy of pedicle screw implantation is less than 50% [14]. Therefore, except for the perspective guide, the operator's experience and judgment is also important. In addition, the learning curve of the MISS operation is also increased as the indistinct anatomical markers and the inaccurate position of decompression [15].

3.2 Navigation Technique

Navigation-assisted orthopedic surgery technique has been widely applied since the late twentieth century. Compared with traditional methods, navigation-guided surgery has advantages, especially with respect to accuracy. The nominate accuracy of a navigation system, which is measured in lab environment, can be within 0.5 mm. However, in clinical practice, the desired accuracy cannot be easily obtained and sustained. To analyze the accuracy of a navigation system in clinical environment, we developed a novel method to measure the clinical accuracy [16], finding out that many clinical factors can affect the clinical accuracy, including the spatial distribution of equipment, light from shadowless lamp, movement of the camera and bed, etc.

3.2.1 The Spatial Distribution of the Equipment

The ideal accuracy of the navigation system relies on the spatial distribution of the equipment (Fig. 3.1). Before we decide where the navigation equipment, especially the camera, should be placed, we should know the accuracy at different distance between the camera and the surgical field and the visual scope of the camera.

The first factor we should consider when we decide the distance is the accuracy. We measured the clinical accuracy of different distance between the camera and the patient tracker on the active infrared navigation system using point-

Fig. 3.1 Operative setup of an intraoperative 3D fluoroscopy-based navigation system. The distance between the camera and the surgical field and the orientation of the camera should be decided carefully to get ideal accuracy

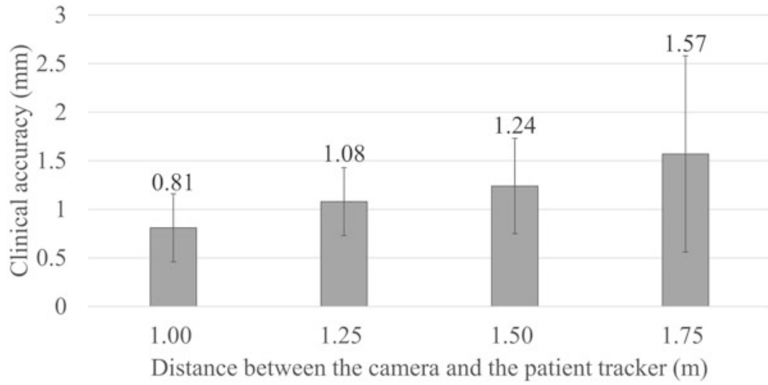

Fig. 3.2 Clinical accuracy of an active infrared navigation system using point-to-point registration without surface matching based on preoperative CT under different distances. For each column N=90. The registration and measurement procedures used a same vertebra adjacently caudal to the vertebra with the patient tracker

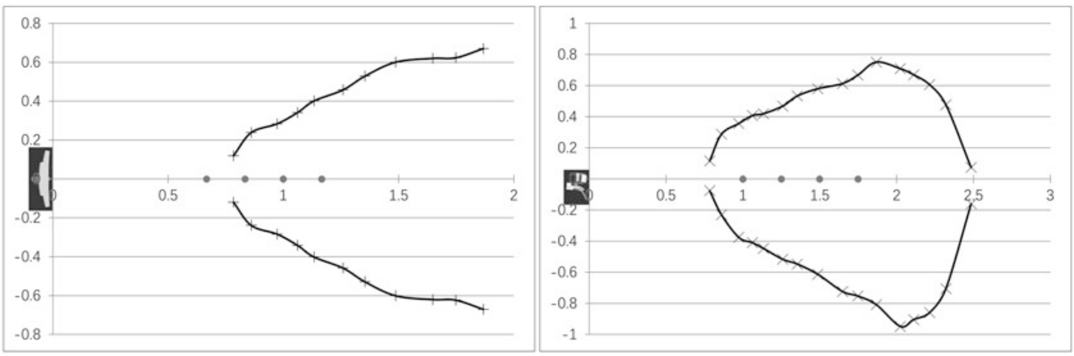

Fig. 3.3 Visual scope of an active infrared navigation system in top view (left) and side view (right). The units are in meters. Axis X is the distance between the camera and a registered stylus tool. Markers + and × represent the max visible positions away from the midline measured on the horizontal or vertical plane. Markers • shows the positions of the patient tracker under different distances

to-point registration based on preoperative CT, finding out that the clinical accuracy varies on different distances. The nearer the distance between the camera and the patient tracker, the better the clinical accuracy (Fig. 3.2).

Another key factor to decide the distribution of the equipment is the visual scope of a camera. The visual scope varies among different navigation brands. However, the visual scopes of two receiver cameras are similar in shape, because they have similar architectures and algorithms. A typical visual scope is as shown in Fig. 3.3.

The visual scope of the navigation system varies at different distance and has a maximum scope vertically and horizontally at about 2 meters. Larger visual scope can facilitate the placing of other equipment, among which the ISO-C 3D C-arm is the most important one because the tracker of the C-arm is far from the center of the visual scope during the scanning.

The clinical accuracy of different distances was measured at the centers of the visual scope as shown in Fig. 3.3. However, in clinical practice, we noticed that the accuracy deteriorates when away from the central area. After detailed measurement, we got an iso-accuracy line. If all procedures were taken inside the area surrounded by the line, the clinical accuracy would not exceed a certain value (Fig. 3.4).

For point-to-point registration, inside the area surrounded by the iso-accuracy line of 1.2 mm, it would be accurate enough for lumbar and lower-thoracic surgeries. However, the maximum permissible error of a pedicle screw at the cervical and mid-thoracic spine is less than 1 mm. To meet the requirement, we should take advantage of auto-registration based on intraoperative CBCT. Using this registration method, the clinical accuracy of the same system is 0.74 (SD 0.30) mm at the camera-tracker distance of 1.5 meters.

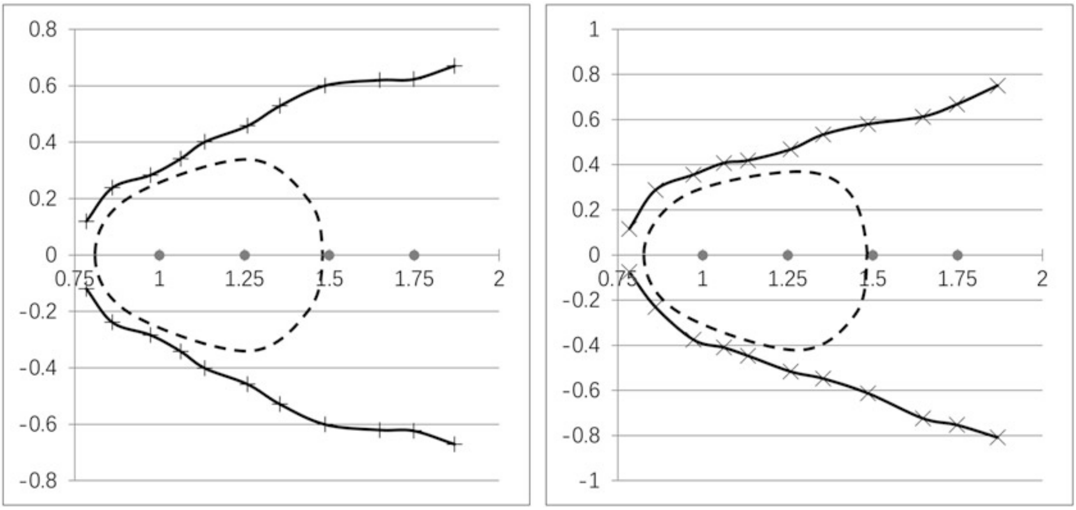

Fig. 3.4 Illustration of an iso-accuracy line in vertical and horizontal plane using point-to-point registration. Inside the area of the dashed line, the clinical accuracy should not exceed 1.2 mm. The solid lines indicate the visual borders of the camera. The units are in meters

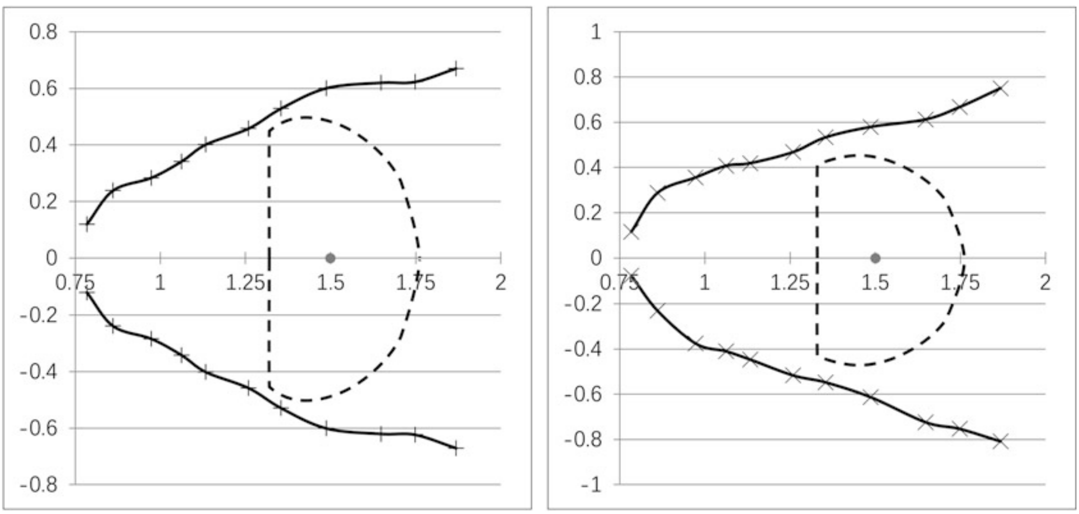

Fig. 3.5 Illustration of an iso-accuracy line in vertical and horizontal plane using auto-registration. Inside the area of the dashed line, the clinical accuracy should not exceed 1.0 mm. Note the sharp edge at the distance of 1.35 meters which is the nearest distance for the intraoperative CBCT scan. The solid lines indicate the visual borders of the camera. Marker • shows the positions of the patient tracker at which the clinical accuracy is 0.74 mm. The units are in meters

The iso-accuracy line of 1.0 mm using auto-registration is shown in Fig. 3.5

In conclusion, the recommended spatial distribution of the equipment is different for the point-to-point registration and the auto-registration. To get stable clinical accuracy, the trackers of the patient and the tools should stay near the central visual ray at a limited distance as illustrated in Fig. 3.4 and Fig. 3.5 It is important to get ideal anticipated clinical accuracy by refining the spatial distribution before MIS surgeries since it is barely possible to check the accuracy empirically by identifying the bony landmarks in MISS. The areas shown in the figures are only precisely suitable for the navigation system model used in this analysis. However, other navigation system models, which use the same basic technique, should have similar results.

3.2.2 The Clinical Accuracy of Different Types of Registration

The clinical accuracy of a navigation system is important in spinal surgery. Study shows that the maximum permissible translational error of a pedicle screw at the cervical spine, the mid-thoracic spine, and the thoracolumbar junction is less than 1 mm [17].

The clinical accuracy of the point-to-point registration varies significantly among different vertebral segments. On the camera-tracker distance of 1.25 meters (shown as the second solid dot from left in Fig. 3.3), which is a balance between clinical accuracy and surgical range, the clinical accuracy of the most accurate segment, which is used as the registration vertebra, is 1.08 mm in average as shown in Fig. 3.2 In the vertebrae next to the registration segment, the clinical accuracy becomes 1.37 to 1.50 mm. One vertebra further, the clinical accuracy is over 2.40 mm, which is unacceptable for most spinal surgeries (Fig. 3.6).

For the auto-registration, the clinical accuracy shows no significant difference among the segments in the CBCT scan area. On the camera-tracker distance of 1.5 meters (shown as the solid dot in Fig. 3.5), the average of all segments was 0.74 (SD 0.30) mm, which is significantly better than in the registration segment of point-to-point registration.

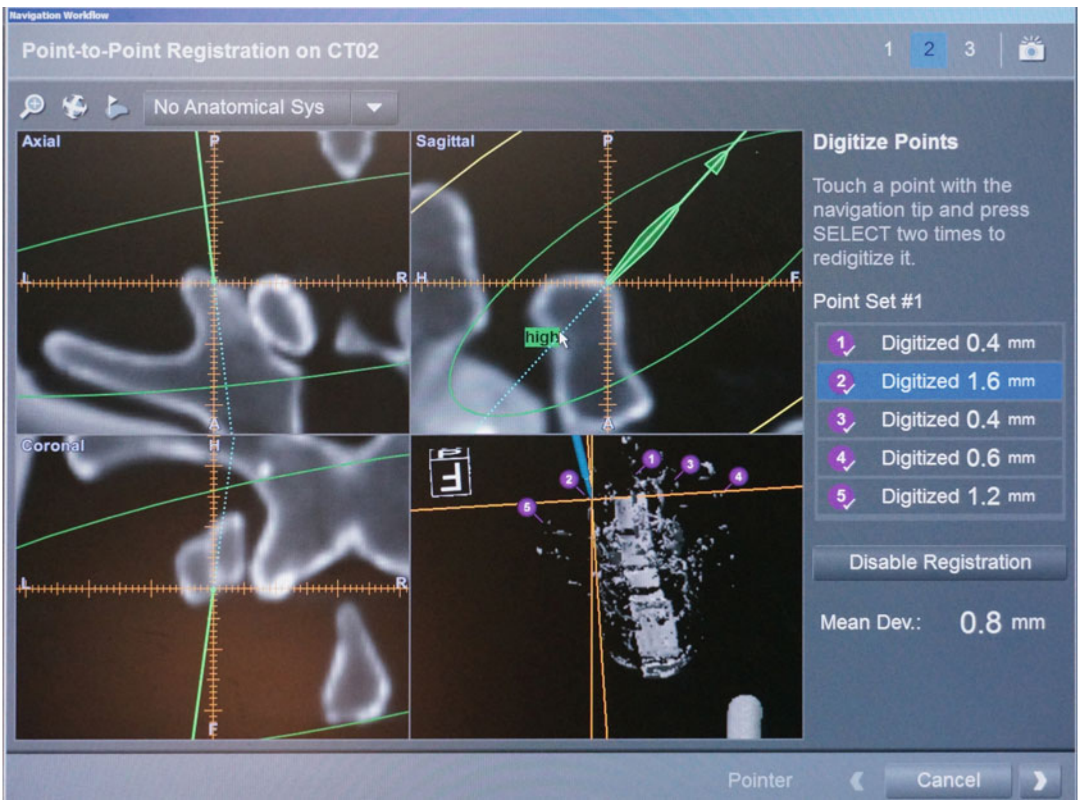

Fig. 3.6 Point-to-point registration on a sawbone model with titanium beads on surface used as markers of registration and accuracy measuring. Note that the "mean dev" is numerically related to, however, much lower than, the actual clinical accuracy of the registration. The best average clinical accuracy of the system using point-to-point registration is 1.08 mm

The recommended registration method is the auto-registration based on intraoperative CBCT. It can achieve higher clinical accuracy, which meets the need of surgeries in cervical spine, the mid-thoracic spine, and the thoracolumbar junction and provide larger operative area for the surgical tools because it can maintain high accuracy on larger distance compared with the point-to-point registration. In addition, all the vertebrae in a single CBCT scan can be operated, which reduces rescan times.

For point-to-point registration, the registration vertebra and the two vertebrae next to it can be accurate enough in lumbar surgeries. However, only on the registration vertebra, the clinical accuracy can barely meet the criteria of accuracy in the 1 mm parts such as cervical spine. Putting the camera nearer to the patient tracker may improve the accuracy. Re-registration when target vertebra changes is essential for surgeries in the 1 mm parts.

Newly made navigation devices may be better in accuracy and visual scope for both point-to-point and auto-registration. However, accuracy checking, re-registration, and rescanning are always the key to achieve high accuracy.

3.2.3 Clinical Factors Affecting the Clinical Accuracy

Different equipment acts differently to clinical factors such as movement of the camera or the surgical bed after registration. The clinical accuracy of a navigation system that was made in the early 2000s deteriorates significantly when the camera or the surgical bed changes position or angle. The accuracy of the system is also unstable when the shadowless lamps are turned on. However, the newer system that was made in the late 2000s is not affected by the factors [16].

For any new navigation system, it is recommended not to change the position of the camera as well as the surgical bed after the registration procedure during operation until the system is proved able to maintain the accuracy under those factors. One way to test the device is to use anatomical bone markers; however, the result will be not very convincing since the anatomical markers are not easily located accurately. Another fast way is to connect the patient tracker firmly to a stylus and check the relative coordinate of the stylus under the clinical factors. If the coordinate hardly changes, the system is not affected by the factors.

3.2.4 Clinical Criteria for Navigation

Computer-assisted navigation technique has been set up as a nationwide industry guideline in China, which is published in the Chinese *Journal of Orthopaedics* in 2016, which is led and organized by Beijing Jishuitan Hospital. Since the beginning of 2009, the Chinese Medical Association orthopedics society organized more than 50 orthopedics experts in investigating the accuracy, safety, and influence factors and 14 other subjects. Besides, the evidence-based medical research on this subject was also set. In 2010, the People's Republic of China National Health and Family Planning Commission (formerly the Ministry of Health of People's Republic of China) set up the national medical service standard committee and formulated the standard of computer navigation-assisted spine surgery. From 2009 to 2012, a large multicenter clinical study was carried out to further optimize the operating standards. In 2014, the Chinese Orthopaedic Association and the Chinese Journal of Orthopaedics launched the "computer navigation assisted spinal surgery guide" project and invited nationwide experts to discuss and finally form the existing version.

3.2.4.1 Applicable People

The application of this guide is to the doctors, technicians, and nurses involved in computer navigation and spinal surgery.

3.2.4.2 Epidemiology of Navigation Standards

The accuracy of computer navigation-assisted spinal surgery is obviously better than that of traditional surgery [18]. The results of the study show that computer navigation-assistedspinal surgery can significantly reduce the radiation exposure of doctors and patients during the operation and improve the accuracy and safety of minimally invasive surgery for spinal surgery.

3.2.4.3 Indication of Computer Navigation-Assisted Spinal Surgery

Computer-assisted navigation technique is suitable for most spinal surgery, including spinal traumatic diseases, degenerative diseases, spinal deformities, spinal tumors, and spinal infections. The computer navigation-assisted system is mainly designed to improve the accuracy of internal fixation and to localize the area of lesions, especially in the situation such as unclear of bony anatomical landmarks, osteopathic variation and deformity. It is especially suitable for minimally invasive spinal surgery and spinal revision surgery [1, 2].

1. Spinal traumatic diseases

   Fracture of odontoid process, unstable Hangman's fracture, lower cervical spine fracture, and thoracolumbar fracture
2. Spinal degenerative diseases

   Cervical disc herniation, cervical spinal stenosis, cervical posterior longitudinal ligament ossification, thoracic ligamentum flavum ossification, lumbar disc herniation, lumbar spinal stenosis, and lumbar spondylolisthesis
3. Spinal deformities

   The deformity of the upper cervical spine, the congenital severe spondylolisthesis, the scoliosis and the kyphosis
4. Spinal tumors

   Spinal vertebral tumors and intraspinal tumors
5. Spinal infections

   Spinal tuberculosis

3.2.4.4 Contraindication of Computer Navigation-Assisted Spinal Surgery

1. The patient has systemic diseases include: severe hemorrhagic disease, severe heart disease, severe respiratory disease, and other diseases intolerant of anesthesia or surgery.
2. The patient is unable to accept the position requirements of spinal surgery, such as posterior spinal surgery, and the patient cannot accept the prone position.
3. The patient is unable to receive radiographic radiation during the operation.
4. The placement of the tracer cannot meet the requirements of the operation.
5. The image quality could not be obtained to meet the requirements of the operation.

3.2.4.5 Learning Curve

Computer navigation is an auxiliary technique for surgery. The technique needs to be trained by a certain amount of training and mastery of its essentials. In the early stage of computer navigation, the operation time and the accuracy of screw implantation will be affected by the learning curve. After a period of accumulation, the operation time will be shortened, and the accuracy of implantation is increased [3].

3.3 Robotic Technique

The world's first medical robot was introduced by Y.S. Kwoh in 1988 [19]; he used a PUMA 200 series to do the CT-guided stereotactic brain surgery, and the absolute positioning accuracy was significantly improved by his results. However, the surgery time is long, and the robot arm based on the industrial platform was not safe enough. His try promoted the innovation of surgical robot based on image navigation.

Santos-Munné JJ introduced an intraoperative image fusion method into a robot system which was used for pedicle crew placement; the robot was based on the PUMA 560 series [20]. This fusion technique will fuse the intraoperative X-ray image with preoperative planned trajectory and then guide the surgeon's drilling using the hole in the end effector of the robot arm. This fusion method realized the dream of putting surgical plan into the real surgery and pushing forward the preoperative planning method.

The booming of orthopedic robot was in joint placement. In 1992, ISS (Integrated Surgical Systems, USA) introduced RoboDoc, the first orthopedic robotic system for joint replacement applications [21]. It is a fully autonomous operation robotic system which approved by FDA certification. RoboDoc completed more than 20,000 cases of joint replacement, and clinical studies have found that it can effectively improve the accuracy of joint prosthesis implantation and reduce the incidence of intraoperative fractures, but at the same time, its shortcomings such as prolonged operation time, system failure, and higher incidence of sciatic nerve injury prevent its widespread application.

For the safety issues, surgeons as the executor of the surgery have begun to intervene in the robot-assisted surgery, that is, human-robot collaborative surgery. Imperial College London introduced Acrobot Precision Surgical Systems in 2001 [22]; this system is a synergistic, semi-autonomous robotic system, and most of all, this robot has the "Active Constrained Control" design, which means when the robot arm is working according to the predefined path, the surgeon can pull the robot arm at any time to terminate the activity or adjust. After releasing the robot arm, it can continue to act according to the original path. This breakthrough innovation greatly improves the safety. Acrobot Precision Surgical Systems was also designed for joint replacement surgery and also approved by FDA certification. The RIO (Robotic Arm Interactive Orthopedic) System was similar to Acrobot, designed mainly for total knee or unicondylar knee replacement. Previous studies have found that such robotic-assisted arthroplasty with less surgical incision and shorter recovery time can shorten the study curve of young doctors. The tibiofemoral angle, the short-term knee mobility, and the function score are all better than the traditional surgery group [23]. The orthopedic robot enables orthopedic surgeons to treat patient-specific, early- to mid-stage osteoarthritic knee disease with consistent, reproducible precision.

In spinal surgery, Mazor Surgical Technologies Inc. developed a 6-DOF parallel robot system called Renaissance system in 2001. The Renaissance has a diameter of 50mm and a height of 80mm and a weight of only 250g. The "Hover-T" technology allows it to be directly attached to the patient's vertebral. This system is a passive robot system that guides the surgeon to do internal fixation of the spine and has received FDA and CE certification.

3.3.1 Combination of Navigation and Robotic Technology

Though booming in medical robot field, the medical robot still has shortcomings, such as complicated manipulation methods, limited working area, and can only do specific surgery but cannot be used universally. And most of all, nearly all commercial medical robots were based on pre-operation X-ray or pre-operation CT scans, but not real-time tracking, which means the navigation used in medical robot now were "faked navigation." The "faked navigation" only reflects the hidden structures at the time the patient takes the pre-operation X-ray or the pre-operation CT; if the patient moved during the surgery, the positon of the hidden structures changed, and the pre-operation images will not tell the surgeon the changed information, which will lead to serious consequences to the patient.

To solve this question and facilitate CAMISS, Tian Wei introduced the "real-time navigation" into the medical robot. The commercial product TianJi robot® was a robot-assisted surgical navigation device based on 3D fluoroscopy [24]. This system consists of a robotic system, optical tracking system and surgical planning, and navigation system.

3.3.1.1 Robotic System

The robotic system mainly consists of a robotic arm and its controller, which were built on a mobile platform. The 6 DOF robotic arm has a maximum reach radius of 850 mm, and each of the joint is free to move between -360 and +360 degrees. It contains a universal tool base mounted at the end of the robot arm. The reference frames, localizer plates, guide holder, and surgical instruments can be mounted onto the base. The mobile platform is equipped with four castors and the self-balancing docking system. These allow for easy docking and removal of the robotic system from the side of the patient table.

3.3.1.2 Optical Tracking System

The optical tracking system consists of an infrared stereo camera and two reference frames. One reference frame is attached to the robot tool base, and the other is attached to a spinous process. The camera projects and detects reflected infrared light from reflecting spheres on the reference frames. In this way, the optical tracking system can capture the robot and vertebra movements in real-time as well as calculate their three-dimensional vector displacements such that the robot can compensate for displacement.

3.3.1.3 Surgical Planning and Navigation System

Implant targeting and trajectory planning are performed based on the intraoperative 3D fluoroscopy images acquired from ARCADIS Orbic 3D C-arm (Siemens Medical Solution, Erlangen, Germany). The automatic patient registration will be performed based on fiducial markers. After registration, surgeons can plan the trajectory on the aligned images. Once confirmed, the plan is sent to the robotic system for execution. For safety reasons, the software enables trajectory simulation and emergency stopping to avoid an accident. The surgical planning and navigation system also can automatically calculate the distance and angle between the real path and planned path, which could guide the robot system's micro-movement. In this way, the robot system can always maintain accurately positioning using the predefined surgical trajectory.

The high accuracy of real-time navigation combined with medical robot makes it perform not only lumbar vertebral surgery but also the cervical surgery. This system has already finished the robot-assisted anterior odontoid screw fixation in 2015 and even the posterior c1-2 transarticular screw fixation for atlantoaxial instability in 2015 [24, 25]. It is also a universal medical robot which can perform not only spine surgery but also the traumatic surgery. It has been applied in many hospitals in different provinces or city around the country to promote the application of patients benefiting 12 million people. The death rate of severe multiple traumas has decreased from 25% to 9%, and the surgical accuracy has increased to 98%. These results demonstrate that our system has achieved the goal of "high-risk surgery safely, complex surgery precisely, and key operation procedure intelligently".

3.3.1.4 Accuracy of Navigation-Based Robot-Assisted Spinal CAMISS

Safety and accuracy are two vital aspects for judging a medical robot: the lower the incidence of error and misplacement, the more accurate would be robotic insertion of a pedicle screw. Countless details of robot designs have been enhanced to satisfy the demands for safety and accuracy, but it is still not enough.

Posterior pedicle screw fixation is one of the commonest spine surgical techniques. The indications include vertebral fracture, degenerative disease, deformity, and spine tumors. Although there are many advantages of pedicle screw fixation, some severe complications can happen due to misplacement of screws, such as injury of surrounded dura, spinal cord, nerve root, vessel, and screw loosening caused by repeated screw insertion. Plus, fusion in the thoracic spine is more risky than lumbar spine, because the width of pedicle is narrower in the thoracic spine and spinal cord exists in thoracic spinal canal. Although the accuracy of screw placement is so important for spine surgery, the misplacement rate of pedicle screw is around 10∼40% as reported. Inaccuracy of spine robot may cause unexpected damage during robot-assisted spine surgery. For pedicle screw placement surgery, the malposition rate of pedicle screws using traditional free-hand methods was reported to range from 9.7% to 15.0%. Even minor cortex or pedicle violation could lead to severe complications such as neurological or vascular injury. Limits of precision and safety for screw placement always exist because of the limits of surgeons their own.

In order to break those limits in spine surgery, many scientists are working on the study of surgical robot. One representative instance is the SpineAssist (Mazor Surgical Technologies [HQ] Ltd., Cesarea, Israel), which has been the only commercially used robot in the spine surgery. This surgical robot was formed with a steward parallel robot and a guiding rod fixed on the moving platform. During the operation, the robot fixed on the patient can adjust position and orientation of the guiding rod, through which the surgeon can manually drill the screw paths. Although this robot system has been proven to be accurate in pedicle screw fixation, the working area is not proper for patients with severe deformity because of the limit of its platform. And this system is based on preoperative CT images and intraoperative two-dimensional fluoroscopy images. So basically, it cannot provide accurate intraoperative real-time tracking when patient's position changes during a surgery.

TianJi Robot® system is a new surgical robot system that is designed by Beijing Jishuitan Hospital. Surgeons use the system to make preoperative planning based on intraoperative three-dimensional fluoroscopy images. It has a serial-structured mechanical arm to guide the surgeon finding a proper entry point and trajectory as planned. It provides a trajectory and allows surgeons drill a K-wire into the marked point on pedicle. The drilling and screw insertion are still performed by the surgeon manually. One of the advantages of this robot system is it can be applied in upper and lower cervical surgeries.

According to previous studies, the accuracy of pedicle screw placement assisted by TianJi Robot® system was tested. The overall mean deviation of pedicle screws was 1.34±0.66mm, with 90% evaluated as grade A according to the Gertzbein and Robbins criteria and 10% evaluated as grade B. And no intra- or postoperative complications were found. There is no study that compares the accuracy of TianJi Robot® system with other spine surgical robot systems. One previous study showed the results of a cadaveric study using SpineAssist for 36 pedicle screws insertion with an overall deviation of 0.87±0.63 mm. A retrospective study of SpineAssist system showed that 98.3% of 646 pedicle screws were class A or B according to the Gertzbein and Robbins criteria with mean deviations of 1.2±1.49 and 1.1±1.15 mm on the axial and sagittal planes. According to previous studies, the mean diameter of the pedicle in adults ranged between 4.6 and 6.5 mm in the cervical spine and was significantly smaller in C4 (5.1 mm). Although the diameter of the lumbar pedicle is much wider than those of other spinal segments, the mean pedicle diameter of the widest segment (L5) was still only 14.54 mm. The pedicle diameter would be much smaller in children.

3.3.1.5 Influence of Respiration-Induced Vertebral Motion and Drilling Slippery Problem

There are basically two types of surgical robots used in spine surgery. One type of the robot can provide a working path for surgical instruments and guarantees instruments' steadiness. It thus acts as a guidance system. An example is the TianJi robot®. The other type of robot provides a working path for its own instrument and performs the drilling automatically. An example is the Robotic Spinal Surgery System (RSSS). For both types of robot, the purpose of the system is to reach the target pedicle and insert screws without displacement. There are many important structures around the vertebrae, including the dura, nerves, and vessels. For both types of robot, the movement of the target pedicle during the operation could lead to unexpected damage. Thus, unnecessary movement of the patient and slippery instruments during the operation must be avoided. Respiration-induced physical movement of the patient's body, however, is difficult to eliminate.

Respiratory movements induce movement of the whole body, including spinal vertebral bodies, thereby decreasing the accuracy of robot-guided pedicle screw placement. Previous study showed that a great amount of motion occurs in spinal segments during the normal course of general anesthesia. Respiration-induced body movement during the operation is inevitable. Body movement, however, is a predictable random motion. A prone-positioned patient under general anesthesia has a specific predictable pattern of respiration-induced body movement. In previous study, the position displacement was significantly less in the left-right (LR) direction than in the superior-inferior (SI) or anterior-posterior (AP) direction. It may because the human being body is almost symmetrical in the LR direction.

Thus, the body movement could be an equivalent offset in the LR direction during respiration. There is no such an equivalent force for the SI and AP directions during lung expansion. Thus, body movement is more significant in those directions.

Respiration-induced motion in vertebral segments is not even. Displacement was greater in the lower thoracic and lumbar spine and had more regional activity than the rest of the spinal segments. The respiration-induced deviation is more than 1 mm in both the SI and AP directions, with more than 2 mm total displacement. The magnitude of the displacement caused by respiration was thus large in the thoracic and lumbar regions. The mean total displacement of thoracic regions was more than 2 mm between the peaks of inspiration and expiration. Although the breathing pattern was repeatable, these magnitudes of displacement are not tolerable for elaborate spinal pedicle screw fixation surgery. For robot-assisted surgery, a displacement of more than 2 mm could lead to perforation of a pedicle screw, causing injury to nearby tissues including the dura, nerves, or vessels leading to serious consequences. With respiratory motion of this magnitude, the traditional registration process of correlating virtual computer images with the patient is nullified, and targeting of pedicle screw placement would be inaccurate. Therefore, respiration-induced body movement is a key issue in robot-assisted spine surgery.

Drilling slippery is another common incident that may significantly decrease the accuracy of pedicle screw placement. The anatomy feature of facet joint is the main cause of slippery. Thus, using a bur to make a groove before drilling is a useful tip to avoid slippery.

One option for solving respiratory problem is to make the robot move along with the vertebral movement caused by respiration. If the robot is small enough, it can be fitted with additional hardware that is fixed on the related spine, such as the Hover-T used in SpineAssist (MAZOR Robotics, Orlando, FL, USA). The Hover-T fixed to the patient's spine through a spinous process clamp achieved rigid and steady connection with the bone, which means it was able to move along with the vertebral movement and lower the relative movement between the vertebrae and the robot. However, it is impossible to fix a large spinal robot to the patient.

One solution to diminishing this deviation caused by respiration is to redesign the software of the robot to correct the position of the robot's arm by adapting it to the patient's respiration. The software should be able to analyze the respiratory motion pattern of the patient and thus adjust the robot's arm movement to synchronize with the respiration-induced vertebral movement. Also, it may be possible to guide a robotic arm to insert a pedicle screw only during the period of peak inspiration when the position of the vertebral body is almost constant (to within 0.1–0.2 mm for nearly 3s). This window should be able to be extended by modifying the respiration rate during the general anesthesia.

3.4 CAMISS

MISS technique is used to reduce the second injury of patients after surgery. However, it has many problems. One of the key point of MISS techniques is to pursuit the minimally invasive surgery, which sacrificed the operating fields. Most of the time, the surgery has to be carried out under the condition of the "invisible" field, which increases the difficulty and complications of the surgery and leads to a prolonged learning curve. It takes time and effort for young surgeon to manage and carry out this minimally invasive surgery to benefit patients. Therefore, this technique is restricted in promotion. Recently, the introduction of Computer-Assisted Navigation System (CANS) overcomes the difficulties. The CANS method can assist the operation procedure by converting the visual image to nonvisual image. Then with the help of the computer-assisted navigation system, the operator can identify the pathway of pedicle screws and decompression area exactly, which greatly make up for the shortcomings of narrow vision field arising from MISS technique. Therefore, the combination of CANS and MISS technique, with the name of computer-assisted minimally invasive spine surgery (CAMISS), makes the spine surgery more secure and accurate.

3.4.1 The Definition of CAMISS Technique

The CAMISS technique, which is first introduced by Professor Tian from Beijing Jishuitan Hospital, is a new method to combine the CANS and MISS technique together in order to give full play of each advantage and make up for the insufficiency [26]. Meanwhile, by using the computer-assisted navigation system, the operator can locate the anatomical position more precisely, which makes up for the shortcomings of insufficient operative field by MISS technique. Besides, the computer-assisted navigation system also improves the accuracy of screw placement and decompression area, which will benefit for reducing the surgical complications (Fig. 3.7).

3.4.2 The Composition of CAMISS

3.4.2.1 Intraoperative Real-Time Navigation System

The same as the other navigation system, intraoperative real-time navigation system includes image acquisition module, data processing module, and signal tracing module. The image acquisition module is a high-precision C-arm, which can perform intraoperative high-speed scanning and capture three-dimensional images as the same resolution as a CT scan. Data processing module contains the mainframe of navigation computer and a rapid imaging system. The data processing module can obtain the data collected from the C-arm quickly and present it in the display screen of the mainframe computer. The main purpose of the tracing signal module is to trace the signal by infrared positioning method, which includes the infrared receiver and some navigation surgical instruments, such as tracer, guiding device, sharp instrument, pedicle opener, registry, calibrator, and spine clamps.

3.4.2.2 Minimally Invasive Devices

The minimally invasive devices mainly include minimally invasive retractor (such as the tubular retractor), minimally invasive internal fixation system (such as long-tail hollow pedicle screw), etc.

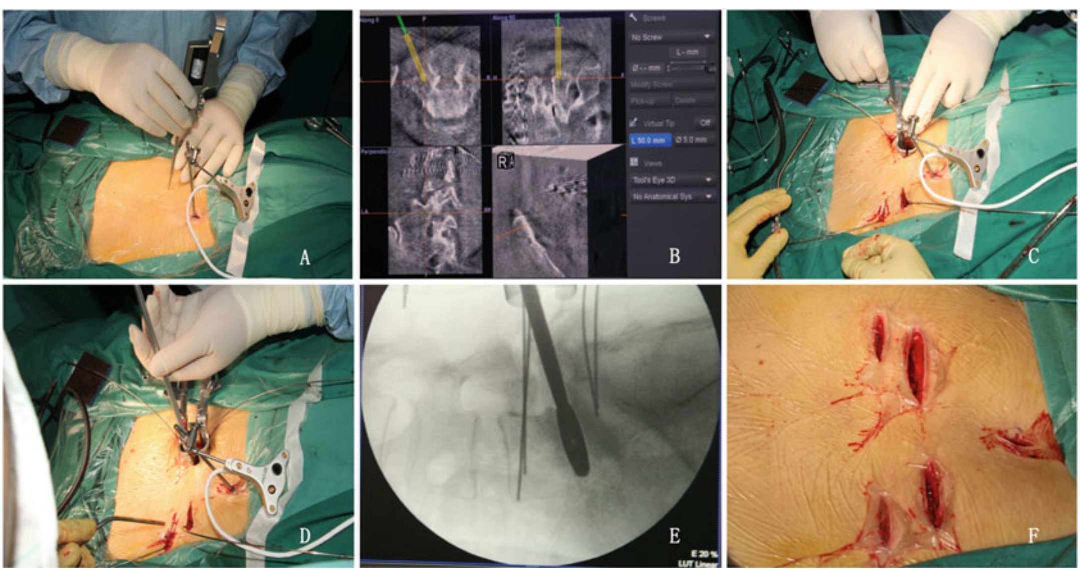

Fig. 3.7 The procedure of CAMISS operation. A-B. Using the navigation system to determine the place, depth, and screw type. C. Decompressing under the minimally invasive channel. D. Implanting the intervertebral fusion cage through the minimally invasive channel. E. X-ray scan. F. The minimal invasion of operation

3.4.2.3 The Advantages of CAMISS Technique

The CAMISS technique is a combination of navigation and minimally invasive technique, which is aiming at drawing on each other's comparative advantages. A global survey on the application of navigation technique revealed that more than three-quarters of the surgeons agreed that when applied in spine surgery, navigation technique has obvious advantages. CAMISS technique has many benefits. It is good at reducing the paraspinal muscle injury, accelerating the postoperative recovery, as well as increasing the effectiveness of the operation. Besides, CAMISS technique can also improve the operation accuracy, reduce intraoperative complications, and improve the safety of operation. During the CAMISS operation, the surgeons hardly need to operate under the perspective. Besides, the study by Mendelsohn et al. showed that operation under the help of navigation system can reduce the radiation exposure to both the operators and the patients. In addition, the National Standards Committee of Health Planning Commission has approved the guideline of spine surgery navigation, which is led by Beijing Jishuitan Hospital. The industry standard has established a detailed navigation application process, which makes the operation of navigational devices easier and feasible. Thanks to this standard guideline, the surgeon's learning curve for CAMISS technique is also shortened.

3.4.2.4 Clinical Indications

The CAMISS technique is suitable for the surgical treatment of most degenerative diseases of the spine. The key points for the treatment of spinal degenerative diseases include both nerve decompression and spinal fusion. In the field of nerve decompression, the navigation system can accurately determine the range of decompression and complete the decompression with minimally invasive and accurate decompression. In the field of spinal fusion, the use of intraoperative real-time three-dimensional navigation technique can automatically register the real-time intraoperative data and complete percutaneous implantation of pedicle screw implants, which reduced the paraspinal muscle ligament injury caused by the exposure of anatomical operation field. Besides, the CAMISS method can also achieve a more precise minimally invasive pedicle screw implantation. Meanwhile, CAMISS can significantly reduce the radiation exposure of surgeons. Nowadays, CAMISS technique has been widely used in lumbar disc herniation, lumbar spinal stenosis, lumbar spondylolisthesis, and other spinal degenerative diseases. The surgical procedures include MIS-PLIF, percutaneous endoscopic lumbar discectomy, and radiofrequency ablation.

CAMISS technique is highly recommended in the below situations in order to improve the accuracy and safety of surgery.

- Accurate lumbar decompression
- Percutaneous minimally invasive screw implantation
- Difficulties in screw implantation caused by deformity of the lumbar spine, lumbar refurbishment, etc.
- High-precision operation, such as prefilled cement-reinforced screws

3.4.3 Future of CAMISS

The concept of minimally invasive surgery is one of the most popular opinions in the field of medicine, especially in the field of surgery. It is a central issue on how to reduce the injury caused by operation and accelerate the postoperative recovery. In the field of spinal surgery, accurate implantation, precise decompression, and minimally invasion are the hot spots in recent years.

However, only pursuing minimally invasive surgery, at the cost of inadequate operation field, will bring various problems. In order to achieve minimally invasive surgery, MISS method sacrifices the clear operation field as a result of which many problems were caused. Besides, it is also necessary to determine the range of decompression and fusion position through intraoperative condition with the help of a fully exposed surgical field.

The concept of CAMISS is based on the combination of MISS and intraoperative real-time three-dimensional navigation. With the help of navigation, the screw insertion and decompression area can be determined directly by image. The navigation technique also ensures the accuracy of pedicle screw implantation and overcomes the shortcomings by MISS method. Therefore, the CAMISS technique is the innovation and progress on the basis of MISS.

On the one hand, this CAMISS can achieve the minimally invasive surgical operation, reduce the damage to the muscles, and maximally retain the soft tissue. Nowadays, this technique is consistent with the popular concept of enhanced recovery after surgery (ERAS). ERAS was first introduced by Professor Kehlet from the University of Copenhagen in 2001. Recently, the perioperative rehabilitation has become one of the important measurements of surgical treatment. ERAS refers to the use of some evidence-based medicine methods to optimize perioperative management in order to reduce surgical stress response, reduce postoperative complications, accelerate recovery, shorten hospitalization time, and reduce hospitalization expenses [27]. In the field of spinal surgery, CAMISS technique is a promising example. CAMISS is good at minimizing operative injury, reducing intraoperative bleeding and postoperative drainage, accelerating perioperative recovery, and reducing all kinds of intraoperative and postoperative complications.

On the other hand, CAMISS technique uses the three-dimensional real-time image navigation to guarantee the safety of operation and reduce the serious operative complications due to incorrect placement of internal fixation. In the field of spinal surgery, the complexity of the spine structure as well as various influence factors leads to the difficulty of operation and arises a high demand for operational skills. Thanks to the navigation system, the operators can place the pedicle screws more precisely and safely. Besides, the operative efficiency is greatly improved. In addition, young surgeons can also benefit from this technique as the learning curve is greatly shortened.

In conclusion, CAMISS technique integrates the minimally invasive concept of MISS and the advantage of navigation system, which make the combination of precise treatment and the minimally injury come true. After more than 10 years of practice, CAMISS has been widely recognized and applied in China and around the world. Based on this concept, the "spine surgery minimally invasive navigation technology guide" has now entered the second round of deliberations and will soon become a national industry guide to be promoted and applied. The intelligent department of orthopedics based on this concept has been established and great achievement has been made in Beijing Jishuitan Hospital, especially in the field of orthopedics robot system. With the continuous improvement of the navigation technique and the development of minimally invasive concept, it is believed that CAMISS technique will be applied more widely in the field of spinal surgery and benefit both the patients and surgeons more in the future.

References

1. Wiltse LL, Bateman JG, Hutchinson RH, Nelson WE (1968) The paraspinal sacrospinalis-splitting approach to the lumbar spine. J Bone Joint Surg Am 50:919–926
2. Olivier E, Beldame J, Ould Slimane M, Defives T, Duparc F (2006) Comparison between one midline cutaneous incision and two lateral incisions in the lumbar paraspinal approach by Wiltse: a cadaver study. Surg Radiol Anat 28:494–497
3. Hansen L, de Zee M, Rasmussen J, Andersen TB, Wong C, Simonsen EB (2006) Anatomy and biomechanics of the back muscles in the lumbar spine with reference to biomechanical modeling. Spine 31:1888–1899
4. Foley KT, Lefkowitz MA (2002) Advances in minimally invasive spine surgery. Clin Neuro-Surg 49:499–517
5. Kim CW, Siemionow K, Anderson DG, Phillips FM (2011) The current state of minimally invasive spine surgery. J Bone Joint Surg Am 93:582–596
6. Lee KH, Yue WM, Yeo W, Soeharno H, Tan SB (2012) Clinical and radiological outcomes of open versus minimally invasive transforaminal lumbar interbody fusion. Eur Spine J 21:2265–2270
7. Shunwu F, Xing Z, Fengdong Z, Xiangqian F (2010) Minimally invasive transforaminal lumbar interbody fusion for the treatment of degenerative lumbar diseases. Spine 35:1615–1620
8. Park Y, Ha JW (2007) Comparison of one-level posterior lumbar interbody fusion performed with a minimally invasive approach or a traditional open approach. Spine 32:537–543
9. Stevens KJ, Spenciner DB, Griffiths KL et al (2006) Comparison of minimally invasive and conventional open posterolateral lumbar fusion using magnetic

resonance imaging and retraction pressure studies. J Spinal Disord Tech 19:77–86
10. Boucher HH (1959) A method of spinal fusion. J Bone Joint Surg Br 41-B:248–259
11. Roy-Camille R, Saillant G, Mazel C (1986) Internal fixation of the lumbar spine with pedi-cle screw plating. Clin Orthop Relat Res:7–17
12. Schwender JD, Holly LT, Rouben DP, Foley KT (2005) Minimally invasive transforaminal lumbar interbody fusion (TLIF): technical feasibility and initial results. J Spinal Disord Tech 18(Suppl):S1–S6
13. Tian NF, Wu YS, Zhang XL, Xu HZ, Chi YL, Mao FM (2013) Minimally invasive versus open transforaminal lumbar interbody fusion: a meta-analysis based on the current evidence. Eur Spine J 22: 1741–1749
14. Ferrick MR, Kowalski JM, Simmons ED Jr (1997) Reliability of roentgenogram evaluation of pedicle screw position. Spine 22:1249–1252; discussion 53
15. Lee JC, Jang HD, Shin BJ (2012) Learning curve and clinical outcomes of minimally invasive transforaminal lumbar interbody fusion: our experience in 86 consecutive cases. Spine 37:1548–1557
16. Liu Y, Zhao J, Fan M, Lv Y, Liu W, Tian W (2016) Clinical factors affecting the accuracy of a CT-based active infrared navigation system. Int J Med Robot 12:568–571
17. Rampersaud YR, Simon DA, Foley KT (2001) Accuracy requirements for image-guided spinal pedicle screw placement. Spine 26:352–359
18. Sengupta DK, Herkowitz HN (2005) Degenerative spondylolisthesis: review of current trends and controversies. Spine 30:S71–S81
19. Kwoh YS, Hou J, Jonckheere EA, Hayati S (1988) A robot with improved absolute positioning accuracy for CT guided stereotactic brain surgery. IEEE Trans Bio-med Eng 35:153–160
20. Santos-Munné JJPM, Stulberg SD et al (1995) A stereotactic/ robotic system for pedicle screw placement. In: Morgan K, Satava R, Sieburg H et al (eds) Proceedings of the medicine meets virtual reality III conference. IOS Press/Ohmsha, San Diego, pp 326–333
21. Karthik K, Colegate-Stone T, Dasgupta P, Tavakkolizadeh A, Sinha J (2015) Robotic surgery in trauma and orthopaedics: a systematic review. Bone Joint J 97-B:292–299
22. Jakopec M, Harris SJ, Rodriguezy Baena F, Gomes P, Cobb J, Davies BL (2001) The first clinical application of a “hands-on” robotic knee surgery system. Comput Aided Surg 6: 329–339
23. Lonner JH (2009) Introduction: robotic arm-assisted unicompartmental knee arthroplasty. Am J Orthop 38:2
24. Tian W (2016) Robot-assisted posterior c1-2 transarticular screw fixation for atlantoaxial instability: a case report. Spine 41(Suppl 19):B2–B5
25. Tian W, Wang H, Liu YJ (2016) Robot-assisted anterior odontoid screw fixation: a case report. Orthop Surg 8:400–404
26. Lang Z, Tian W, Liu Y, Liu B, Yuan Q, Sun Y (2016) Minimally invasive pedicle screw fixation using intraoperative 3-dimensional fluoroscopy-based navigation (CAMISS technique) for hangman fracture. Spine 41:39–45
27. Kehlet H (2011) Fast-track surgery-an update on physiological care principles to enhance recovery. Langenbecks Arch Surg 396: 585–590

4 Surgical Navigation in Orthopedics: Workflow and System Review

Chidozie H. Ewurum, Yingying Guo, Seang Pagnha, Zhao Feng, and Xiongbiao Luo

Abstract

Orthopedic surgery is a widely performed clinical procedure that deals with problems in relation to the bones, joints, and ligaments of the human body, such as musculoskeletal trauma, spine diseases, sports injuries, degenerative diseases, infections, tumors, and congenital disorders. Surgical navigation is generally recognized as the next generation technology of orthopedic surgery. The development of orthopedic navigation systems aims to analyze pre-, intra- and/or postoperative data in multiple modalities and provide an augmented reality 3-D visualization environment to improve clinical outcomes of surgical orthopedic procedures. This chapter investigates surgical navigation techniques and systems that are currently available in orthopedic procedures. In particular, optical tracking, electromagnetic localizers and stereoscopic vision, as well as commercialized orthopedic navigation systems are thoroughly discussed. Moreover, advances and development trends in orthopedic navigation are also discussed in this chapter. While current orthopedic navigation systems enable surgeons to make precise decisions in the operating room by integrating surgical planning, instrument tracking, and intraoperative imaging, it still remains an active research field which provides orthopedists with various technical disciplines, e.g., medical imaging, computer science, sensor technology, and robotics, to further develop current orthopedic navigation methods and systems.

Keywords

Surgical navigation · Intelligent orthopedics · Workflow and system · Review

4.1 Introduction

The human body consists of muscular and skeletal systems that compose of bones, cartilages, ligaments, and other tissues to connect all anatomical structures together [14]. These structures are responsible for support, balance, and stamina. The human body relies on the skeleton and muscles for the maintenance of shape, posture, movement, rigidity, and others [19]. Several deficiencies possibly result in the ineffective ability of the skeletal and muscular system to function in the provision of the requirements of the human body. This is known to be one of the leading causes

C. H. Ewurum · Y. Gu · S. Pagnha · Z. Feng · X. Luo (✉)
Department of Computer Science, Xiamen University, Xiamen, China
e-mail: xluo@xmu.edu.cn

G. Zheng et al. (eds.), *Intelligent Orthopaedics*, Advances in Experimental Medicine and Biology 1093, https://doi.org/10.1007/978-981-13-1396-7_4

of several types of disabilities including both the long-term and short-term ones.

Orthopedic surgery is a field of surgery which is essentially devoted to the appendicular and axial skeletons also with the anatomical structures that are related to. This surgical field contains several subfields or subspecialties ranging from arthritis, tumors, metabolic conditions, inherited conditions, congenital conditions, soft tissue process, fractures, and others [28]. More specifically, orthopedic surgery is to treat several conditions arising from the malfunctioning of the muscular and skeletal tissues. These treatments usually contain implant placements, reduction of fractures, reconstruction of torn ligaments, resection of tumors, osteotomy, drilling of bones (amputations), and others [22]. Unfortunately, these treatment procedures with surgical risks can lead to permanent conditions such as loss of the body parts or even loss of lives if proper precautions are not taken to avoid certain errors that arise truly from human errors. During the two decades, to reduce or avoid surgical risks, various medical instruments and surgery methods have been developed to assist surgeons to obtain successful orthopedic surgery, especially to provide surgeons with real-time and 3-D visualization and monitoring of the surgical procedure [10].

Computer-assisted orthopedic surgery is generally a new clinical procedure that is associated with various computer technologies such as computer vision and computer graphics. Such a surgical procedure is employed for surgical planning and simulation, navigation or guidance, monitoring, and visualization [12]. More specifically, surgical navigation is the core element of computer-assisted orthopedic surgery systems. When surgeons manipulate surgical instruments during orthopedic intervention, surgical navigation can accurately track and intuitively visualize these instruments in real time related to anatomical targets. Furthermore, such navigation provides surgeons with useful information such as the location of the anatomical structures, identification of regions of interest, real-time feedback, and monitoring of the surgical instrument's position and orientation in six degrees of freedom (6DoF).

This chapter reviews various aspects of surgical navigation in orthopedics. First, the concept of navigation in surgery is defined. Next, we thoroughly discuss the surgical workflow of orthopedic navigation, followed by showing currently available systems. Finally, the future development of orthopedic navigation is described.

4.2 Navigation in Surgery

The initial idea of effective and precise location of surgical instruments associated with anatomical structures in the human body during surgery can be traced back to the late nineteenth century [8]. With a large amount of technological advances in the past three decades, this initial idea has been evolved to *navigation in surgery*. Such evolution has been heavily helped with the exponential growth of the processing power of computers coupled with the availability of specialized and dedicated systems capable of providing real-time processing and feedback during surgical procedures. Additionally, clinical technicians have constantly pushed for the development of new technologies to solve the challenges faced in surgical procedures.

Navigation in surgery is generally a new concept to improve and boost various surgical and therapeutic procedures, e.g., neurosurgery [9], endoscopic interventions [17], and image-guided radiation therapy [3]. This concept can be decomposed into two major problems arisen from various surgical procedures [18]: (1) Where are the anatomical structures in the body? (2) How do surgeons safely and quickly get to and locate them? Surgical navigation can solve the two problems by precisely and simultaneously localizing the internal structures, organs, and surgical tools in a safe and minimally invasive way. Nowadays surgical navigation is widely used in orthopedic surgery to locate the anatomical targets and to empower surgeons to recognize where they are and how they manipulate surgical instruments to accurately reach the targets.

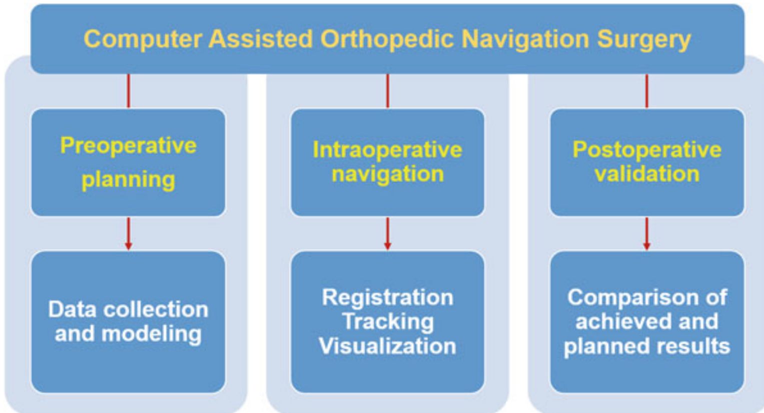

Fig. 4.1 The surgical workflow and steps of computer assisted orthopedic navigation surgery

4.3 Orthopedic Navigation: Methodology and Systems

According to a report from Datamonitor Healthcare,[1] approximately 5.3 million orthopedic surgeries were implemented in 2010, and those numbers are estimated to be 6.6 millions in 2020. To meet with this large increase, innovative medical approaches and systems are steadily required worldwide in the field of orthopedics. On the other hand, surgeons expect precise and efficient placement and alignment during orthopedic surgery such as knee or hip implantation. Moreover, several main technical problems, such as length restoration, offset of bones, or accurate implant positioning, remain challenging in the scientific community. All those aspects requires novel approaches and medical devices to improve orthopedic surgery.

Orthopedic navigation is generally recognized as the new generation of orthopedic surgery. The new generation can provide surgeons with preoperative planning and accurate positioning of operational implants during intraoperative intervention [32]. Furthermore, surgical navigation in orthopedics enables to collect data in specific structural replacements (e.g., knee joint). These collected data, such as measurable values mostly in a discrete representation form and the laxity of the knee joint when it is being moved over a range of positions, are vital information to assist surgeons in reacting soft tissues and balancing in real time during surgery.

This section discusses the surgical workflow of orthopedic navigation and reviews currently available orthopedic navigation systems.

4.3.1 Surgical Workflow

Orthopedic navigation surgery generally involves several essential steps (Fig. 4.1): (1) preoperative data collection and processing, (2) patient-to-model registration, (3) intraoperative tracking, and (4) direct visualization. In addition, postoperative validation is also very important. All these steps are discussed in the following.

4.3.1.1 Multimodal Modeling

Orthopedic navigation surgery usually involves multiple information modalities including preoperative and intraoperative data. Computed tomography (CT) scans or magnetic resonance (MR) images are most commonly preoperative data used to analyze orthopedic abnormalities before surgery. Intraoperative data such as fluoroscopic images and external tracking data are very important for surgical navigation.

While CT provides much good bony details, MR shows very useful tissue information. Both CT and MR images are segmented to obtain regions of interest. Based on the segmented results, surface models of orthopedic structures such as bones and knee can be reconstructed in 3-D [31]. These models are not only used for preoperative

[1] https://pharmaintelligence.informa.com/

planning but also used as 3-D maps during orthopedic navigation.

4.3.1.2 Spatial Registration

Spatial registration refers to as an conversion or transformation of coordinates within one space and those within another space so as to achieve correspondence between the two coordinates in two different spaces, i.e., it estimates the transformation relationship between the physical spaces of preoperative and intraoperative data and maps two spaces of virtual and real coordinate systems such that anatomical structures in the virtual space correspond to the same structures in the real space.

In particular, this procedure aims to associate preoperative 3-D model representation of the internal anatomy with intraoperative imaging that usually uses fluoroscopy to directly visualize the operative sites in the patient. The registration step is quite important for orthopedic navigation. Before 3-D CT or MR images acquired preoperatively can be used for surgical guidance, these images or prebuilt 3-D anatomical models must be registered to a patient's anatomical system defined on the surgical field. In this respect, it is also called image-to-patient registration. Spatial registration is usually performed with the aid of geometric features such as landmarks, frames, surfaces, and others. Two main approaches have been reported in the literature: (1) fiducial-based registration and (2) fiducial-free registration.

(1) Fiducial-Based Registration. As the most commonly used approach, it exactly performs a surface-matching procedure. This requires to reconstruct sufficient bone surface from preoperative images and predefine fiducials or markers.

There are two kinds of fiducials that can be used for the registration. Anatomical or natural markers are manually determined. Surgeons usually select 4–5 points or markers from preoperative images or the 3-D surface model and align these points to their corresponding points on the patient during intervention. The point-pair matching accuracy ranges from 0.3 to 0.8 mm as reported in [16, 29]. CT-fluoroscopy matching was also proposed. Two intraoperative fluoroscopic images were automatically aligned to CT slices after a manual adjustment [25]. On the other hand, artificial markers can be placed before CT scan. Cho et al. [4] proposed to place more than three K-wires around the bones and then perform CT scanning. These K-wires also can be easily visualized on fluoroscopic images. Subsequently, Cho et al. [5] also used resorbable pins as artificial markers, while they employed a MR scanner to avoid radiation. The registration error was reported from 0.3 to 1.7 mm.

(2) Fiducial-Free Registration. Intraoperative 3-D imaging can directly generate 3-D shape or surface of the bony structure. This provides another alternative that performs 3-D surface matching between intraoperatively generated and preoperatively reconstructed surfaces without using any anatomical or artificial fiducials. Intraoperative 3-D surface generation commonly uses tracked and calibrated fluoroscopic and ultrasound images. However, the low quality of fluoroscopic or ultrasound images potentially limits the accuracy of the generated 3-D surface.

Additionally, multimodal image registration also plays an important role in orthopedic navigation surgery. As mentioned above CT and MR images provide various useful information, respectively. It is natural to fuse CT and MR images to improve the visualization of target regions during orthopedic surgery. Figure 4.2 illustrates a software interface that performs CT-MR fusion for navigation.

In general, spatial registration is a prerequisite to various image-guided navigation systems and definitely a very important step to realize orthopedic navigation. The acceptable registration accuracy required from clinical applications is not defined yet and also different from various orthopedic navigation systems. The currently reported registration accuracy is generally less than 2.0 mm.

4.3.1.3 Real-Time Tracking

Orthopedic navigation systems must track surgical tools in real time during surgery. Such tracking aims to temporarily and continuously orient the surgical instrument to target regions in the patient. Based on real-time tracking, surgeons can visualize and synchronize the surgical instru-

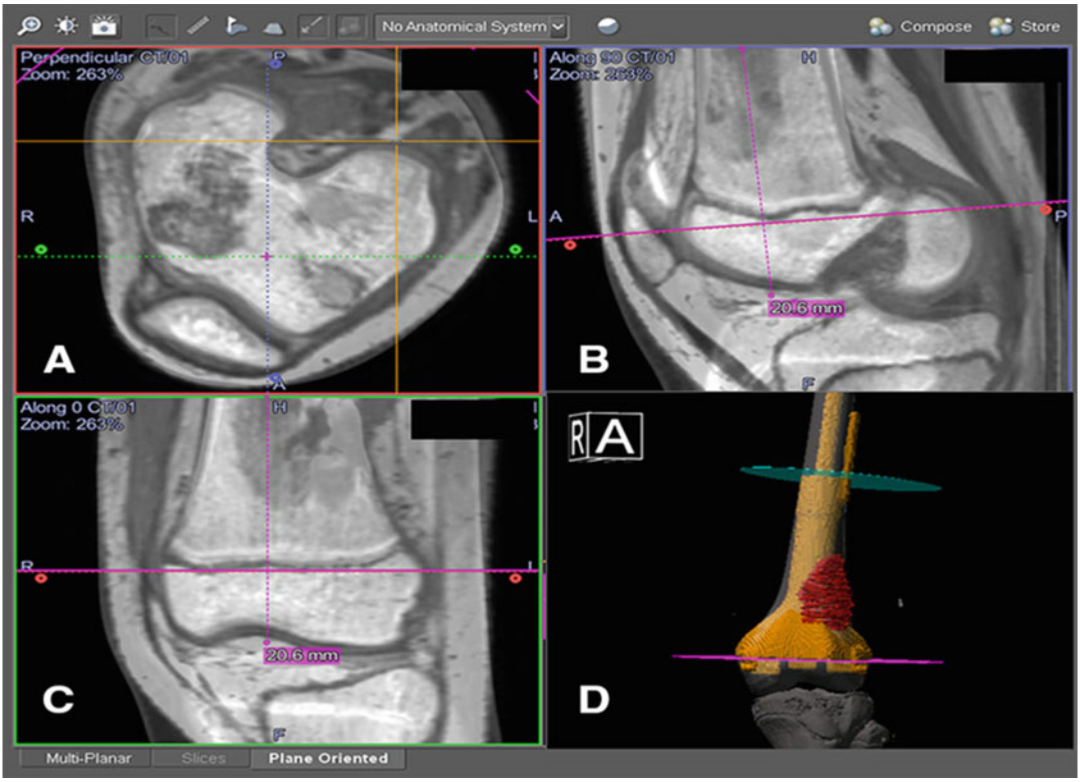

Fig. 4.2 OrthoMap 3-D module version 2.0 can show CT-MR image registration to assist the navigation. (Image courtesy of Stryker, Mahwah, NJ, USA)

ment in 3-D surface models reconstructed from preoperative data. To this end, various external trackers have been developed [18].

External tracking devices usually consist of control units, sensing volume generator, and sensors (e.g., coils or reflective marker spheres). The sensor is usually fixed at the surgical instruments. The control unit and sensing volume generator work together to estimate the position of the senor. After a calibration between the sensor and surgical tool, the surgeon can successfully and automatically navigate the surgical tool on the basis of the continuous measurements of the sensor.

Currently, commonly used external trackers include optical tracking and electromagnetic tracking (Fig. 4.3). The former senses infrared-emitting or retroreflective markers affixed to a surgical tool or object and only can be used for rigid surgical instruments outside the body. The latter uses embedded sensor coils to perceive the location of the surgical instrument and can be employed to track flexible instruments inside the body. More recently, a stereovision tracking device has been commercialized. This technology perceives depth information and 3-D structure derived from video information from two or more video cameras (Fig. 4.4).

Additionally, motion analysis cameras can be introduced for tracking. These cameras provide kinematic measurements to mathematically calculate rotation centers through the movement of opposite skeletal structures usually attached with fixed markers, and marker information in the anatomy of the bone structures also can be collected by mobile marker pointers using the method of triangulation.

Real-time tracking is a vital component that synchronizes various information in orthopedic navigation. It generally uses external tracking

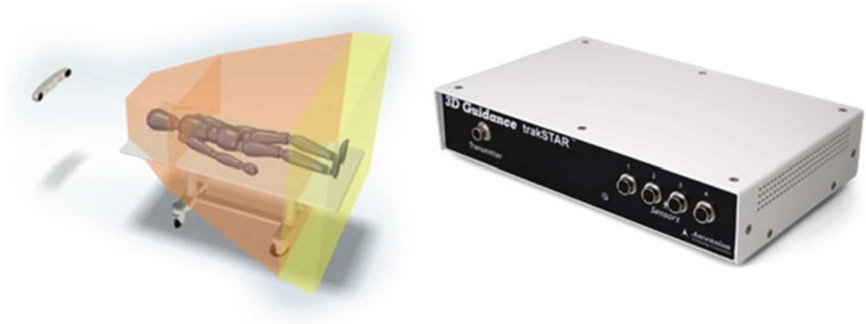

Fig. 4.3 Optical tracking and EM trackers (Polaris, Aurora, and 3-D Guidance trakSTAR) with EM sensors. (Image courtesy of Northern Digital Inc., Waterloo, Canada)

Fig. 4.4 Available MicronTracker models and the ClaroNav tool (an ergonomic probe handle with two permanent targets). (Image courtesy of ClaroNav, Toronto, Canada)

devices including sensors that are integrated with the surgical tools and navigate them associated with the skeletal structures. The tracking devices discussed above have their own advantages and disadvantages. How to select a proper tracking device is an open issue but partially relies on a typical application.

4.3.1.4 Direct Visualization

Preoperative and intraoperative data should be represented properly to surgeons during orthopedic intervention. Multimodal data representation approaches in orthopedic navigation require to provide surgeons with critical structural information in real time and minimally interrupt the surgical workflow. Particularly, volumetric data (e.g., CT and MR) must be presented to the surgeon in an intuitive manner that shows important and understandable anatomical structures in the patient.

Currently, there are generally three ways to visualize 3-D volumetric data: (1) planar visualization, (2) surface rendering, and (3) volume rendering. Planar visualization approaches basically display orthogonal slices in three directions of axial, sagittal, and coronal axes. Volume rendering is a visualization technique that employs a transfer function to allocate an opacity or color associated with the voxel intensity to each voxel in volumetric data [20], while surface rendering depends on preoperatively segmented 3-D data that are further processed by an intermediate step (e.g., using the marching cubes algorithm) to generate anatomical 3-D models [21].

All the data used in orthopedic navigation and represented by any one of three approaches mentioned above are eventually shown on screens or monitors. This empowers surgeons with intuitively monitoring the movement of the surgical tools related to preoperatively reconstructed 3-

D models and the anatomical structures in the patient in the operating room. In addition, direct visualization allows the orthopedic navigation system to efficiently calculate initial superlative implant or repairable position, resulting in effective preparation for bones making use of navigated tools, while analyzing soft tissues for proper ligament balancing over a range of rotation based on physical or simulated kinematic curves.

4.3.1.5 Postoperative Validation

Postoperative validation is necessary to evaluate the surgical outcome of orthopedic navigation. Successful orthopedic guidance should properly recover orthopedic structure function of patients, especially replace or resect the bones, knee, or joint in a high precision. Unsuccessful procedures possibly bring physical suffering or even disability to patients and increase economic burden and hospital stay time.

Although no gold standard has been reported in the literature, postoperative assessment of orthopedic navigation usually includes several aspects: (1) surgical (e.g., replacement or resection) accuracy, (2) recovery of orthopedic function, and (3) surgical complication. After surgery, CT or MR images may be acquired for orthopedic patients for postoperative validation purpose. Therefore, surgeons can visualize these images to inspect the surgical outcome. On the other hand, postoperative and preoperative image registration is also an effective way to evaluate the replacement or resection accuracy after orthopedic navigation surgery. Moreover, the recovery of the physical functions of the orthopedic structures on the patient is the most important outcome of orthopedic surgery. After recovering the bones, muscles, and joints in the musculoskeletal system, orthopedic patients are expected to do everyday physical activities exactly as normal or healthy peoples can act. Additionally, orthopedic surgery possibly generates complication after a surgery. These unanticipated problems should be minimized to avoid additional therapy.

4.3.2 Available Systems

Orthopedic navigation systems are surgical areas that are widely developed in the scientific community. Many commercialized systems are available to navigate orthopedic procedures. Various approaches and systems are used in orthopedic navigation for preoperative, intraoperative, and postoperative procedures. All of them aim to maximize the surgical outcome while minimizing the surgical risk.

Technically, these approaches are categorized into two main types: (1) fluoroscopy-based navigation and (2) dynamic CT-based navigation.

4.3.2.1 Fluoroscopy-Based Navigation

In this navigation, preoperative CT or MR images must be acquired. These images are processed and reconstructed to be 3-D models that are associated with localization of surgical tools and implants during surgery (Fig. 4.5). While external trackers are placed on specific anatomical reference points on the skeletal structure of interest, these points are indicated by a small series of fluoroscopic images.

A C-arm fluoroscopy-based navigation system usually contains a workstation and a monitor, external tracking systems, fluoroscopy, a clamp with dynamic reference frame, and several optically marked instruments. Devices used for calibration are usually two parallel plates that consist of radiopaque metal spheres. Optical tracking are most commonly used to determine the position and orientation of surgical instruments in real time; hence, it provides real-time navigation.

Fluoroscopy-based navigation has several specific features. First, it boasts in its virtual fluoroscopy which provides surgeons with virtual images in real time and determination of the most appropriate location from the gallery of these images. Next, this navigation does not rely on real-time changes on the patient since the navigation depends totally on the chosen images from the virtual image gallery. Furthermore, it has evolved to 3-D fluoroscopy-based navigation

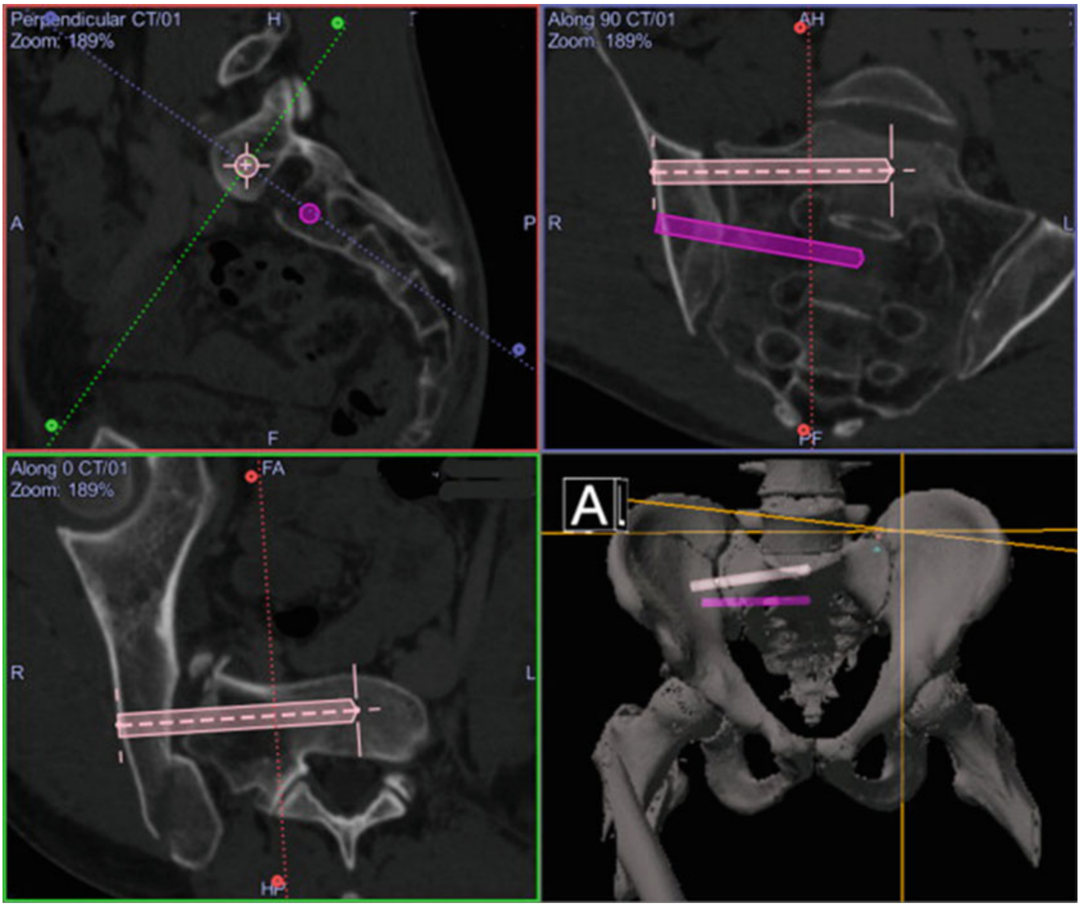

Fig. 4.5 Fluoroscopy-based navigation: CT-based three orthogonal reconstructions along the planned screw axis were illustrated. (Image courtesy of Takao et al. [26])

which provides additional benefits such as axial plane visualization that acts as a real-time CT scanner. Figure 4.6 shows a real-time view of CT and 3-D fluoroscopy matching.

Fluoroscopy-based navigation still has some limitation. 3-D virtual images are generated from specific 2-D X-ray projection rather than from optimized 3-D images. This implies that reconstructing 3-D virtual fluoroscopic images depends heavily on interpreting 2-D projected information, in turn, which relies critically on knowledge and skills of surgeons. Furthermore, fluoroscopic images are rather difficult to obtain in specific patients such as obese patients. This requires to reduce parallax effects by aligning the irrespective of size and the surgical field of interest to the fluoroscopic image viewing. Additionally, radiation is unavoidable in surgery.

4.3.2.2 Dynamic CT-Based Navigation

Cone-beam CT (CBCT) or O-arm is an intraoperative imaging technique that is introduced for dynamic and real-time visualization of anatomical structures on the patient in the operating room. Hence, it also can be used for navigation. While CBCT images are used to reconstruct 3-D models of regions of interest, they also can directly visualize the structures, implants, and surgical tools in a dynamic state during surgical navigation. Two primary methods or modes can be employed to collect and use 3-D CBCT images. Supervision mode requires to plan several steps that will

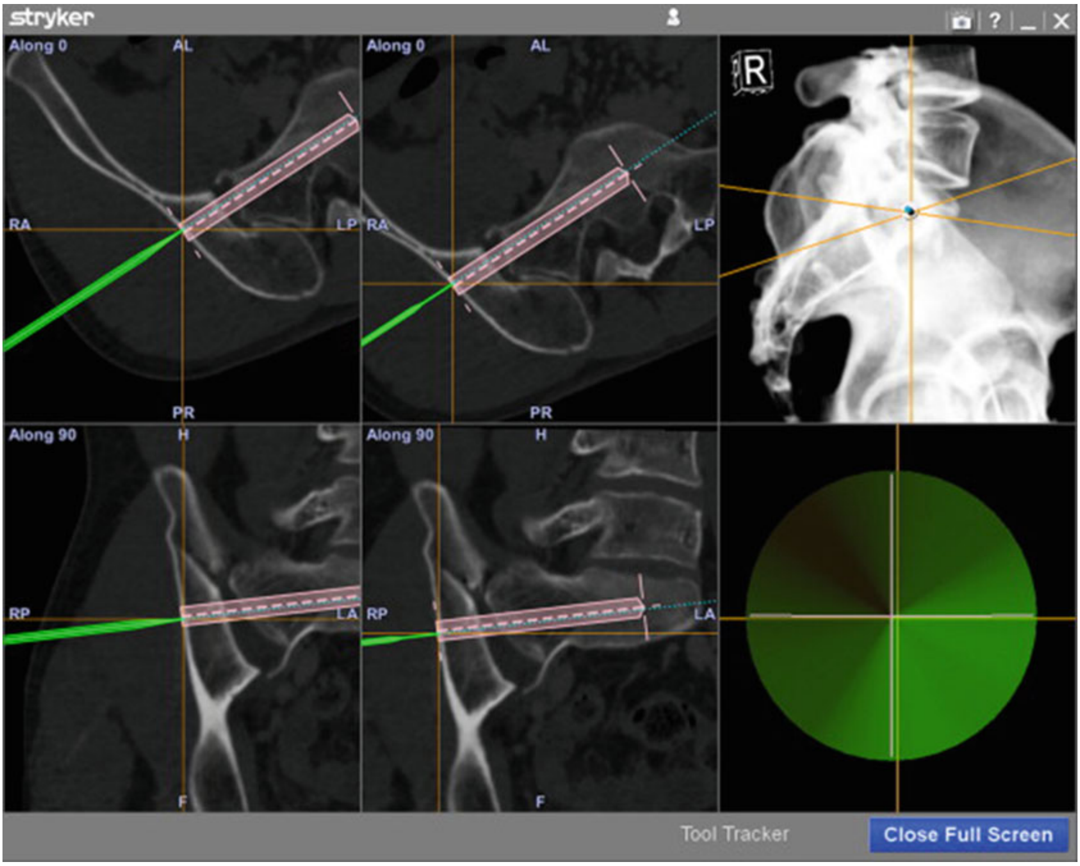

Fig. 4.6 Fluoroscopy-based navigation: CT-fluoroscopy matching displays the preoperatively planned screw position on CT images. (Image courtesy of Takao et al. [26])

be performed in the surgical procedure, and it guides surgeons by matching each of surgical steps with initially planned and simulated steps on a monitor during surgery. Real-time mode monitors the surgical tools and skeletal structures of interest (implants or repairable) that are directly moved to the surgical places.

CBCT or O-arm-driven navigation systems (Figs. 4.7 and 4.8) empower surgeons with accurate representation of the anatomical structures and effective administration of orthopedic surgical procedures such as implantations and bracing without requirement of surgical planning before surgery. While C-arm-based fluoroscopy provides orthopedic navigation with continuous static 2-D images in real time, it gives only a planar and 2-D image at a time untilrepositioned and does not permit simultaneous 3-D imaging. Compared to radiographs or C-arm fluoroscopy alone, 3-D O-arm mode provides enhanced imaging information and accurate intraoperative visualization of the position of bones and/or navigation implants. Therefore, dynamic CT-based navigation is a promising way to reduce intraoperative complications and simultaneously improve surgical outcomes.

In general, no matter what types are used in orthopedic navigation, CT or MR images are preoperatively acquired for surgical planning. The major difference between the fluoroscopy-based and dynamic CT-based navigation approaches is that the former offers 2-D planar images, while the latter can provide 3-D volumetric imaging data like a CT system. Currently, thesetypes are

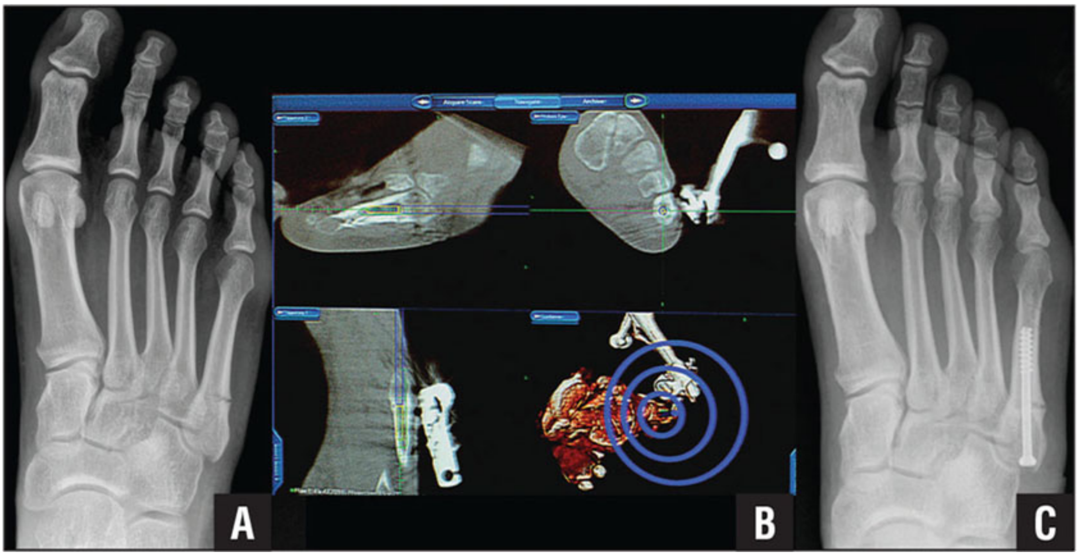

Fig. 4.7 Intraoperative CBCT-based navigation for percutaneous fixation: (**a**) the non-union fracture observed on a MR image of the right foot before surgery, (**b**) the target trajectory and screw implantation across the fracture part during surgery, and (**c**) the satisfactory fixation and healing of the fracture observed on a MR image after surgery. (Image courtesy of Chowdhary et al. [6])

widely used by medical device companies such as BrainLAB and Stryker, discussed in the following.

4.3.2.3 BrainLAB System

BrainLAB produces orthopedic navigation to meet with currently active patients who demand good structures (e.g., hip and knee) and require precise alignment and individual soft tissue balancing essential in total various arthroplasty surgeries.

BrainLAB's HIP 6 allows precise hip arthroplasty based on navigation that can reduce outliers and improve acetabular placement, as well as obtain more consistent leg length restoration. With five easy steps, HIP 6 can efficiently calculate cup or stem position and determine leg length and offset without repositioning the patient. KNEE3 from BrainLAB is a smart image-free navigation software that visualizes and summarizes the complex interaction between 3-D kinematics, joint stability, and implant alignment. Compared to conventional surgical techniques, BrainLAB's spinal navigation empowers accurate screw placement and reduction of fluoroscopy exposure, as well as enhanced visualization of instruments, skin incisions, and trajectories. Figure 4.9 shows various BrainLAB's orthopedic navigation systems.

4.3.2.4 Stryker System

As one of leading companies in orthopedic navigation, Stryker also provides hip and knee navigation software for precise orthopedic surgery with unparalleled accuracy and control in total hip and knee replacements. Figure 4.10 displays Stryker's Navigation System II that is equipped with OrthoMap software systems.

The Navigation System II has some specific features. First, dual articulating arms provide surgeons and staffs with maximum flexibility for positioning during surgery. More importantly, it employs Stryker's own highly accurate and reliable digital cameras as the tracking devices with large working volume and virtually no jitter. Moreover, the Navigation System II provides the ability to import multimodal information such as fluoroscopic, microscopic, and endoscopic images, enabling surgeons to compare unaffected and affected anatomy with automatic symmetrical visualization as a preoperative and intraop-

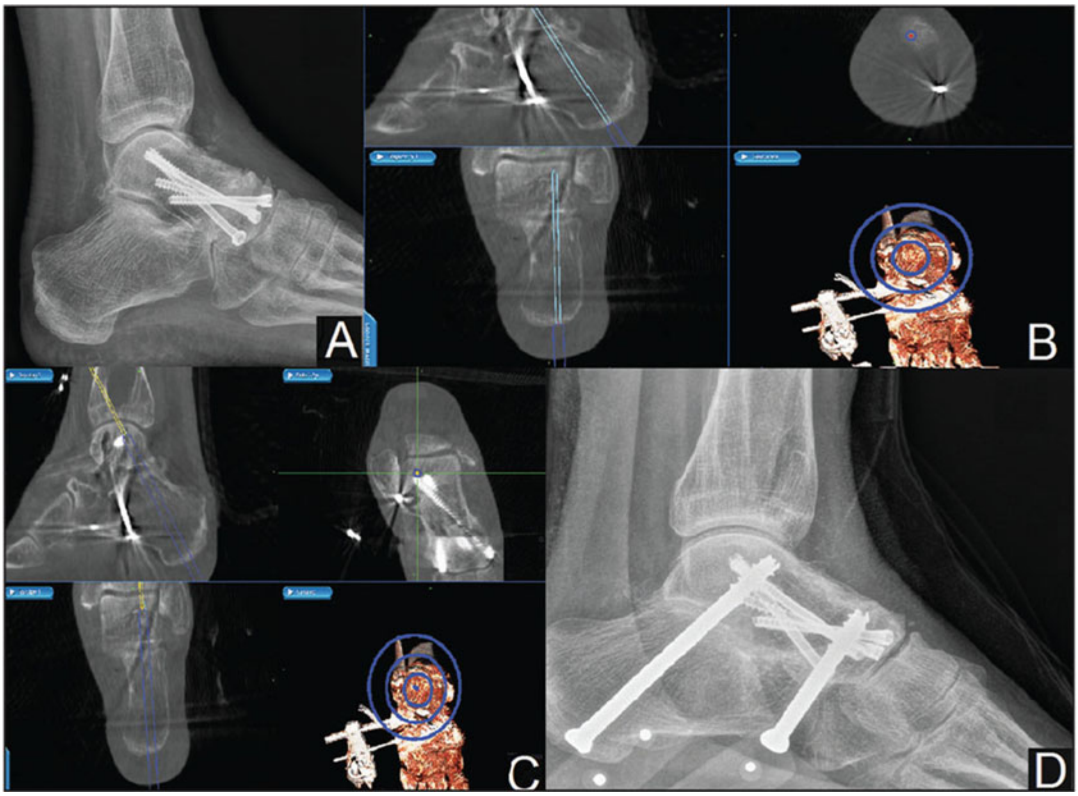

Fig. 4.8 Intraoperative CBCT-based navigation for percutaneous arthrodesis of the subtalar joint: (**b**) and (**c**) display the target trajectory and screw implantation across the subtalar joint. (Image courtesy of Chowdhary et al. [6])

erative guidance. Additionally, it contains three OrthoMap software systems including Precision Knee Navigation Software, Express Knee Navigation Software, and Versatile Hip Navigation Software.

More recently, Stryker has developed Mako that is a robotic arm-assisted system (Fig. 4.11). Mako can be used for total hip or knee surgery. It provides patients with a personalized surgical experience. Moreover, Mako provides patients with a more predictable surgical experience during joint replacement surgery.

4.3.2.5 NAVIO System

Smith & Nephew PLC is an international producer of advanced wound management, arthroscopy, and orthopedic reconstruction products and has successfully developed the NAVIO surgical system that is widely used for orthopedic surgery including knee replacement, joint replacement, and bone resection (Fig. 4.12).

The NAVIO surgical system is generally designed to provide surgeons with component positioning, ligament balancing, and bone preparation. Most interestingly, NAVIO performs an image-free navigation workflow, which is totally different from BrainLAB and Stryker's systems. While an image-based navigation workflow usually includes diagnosis, preoperative data acquisition (e.g., CT or MR scans), preoperative data analysis and planning, intraoperative planning, and surgery, the image-free workflow contains only diagnosis, intraoperative planning, and surgery.

Image-free navigation strategy brings NAVIO with several specific advantages. First, intraoperative real-time imaging and computing eliminates time and costs associated with preoperative imaging and planning, which not only simplifies the surgical procedure but also reduces radiation exposure for patients. Moreover, NAVIO implements navigation without collecting a CT or MR

Fig. 4.9 BrainLAB's hip, knee, and spine navigation surgery systems. (Image courtesy of Brainlab AG, Munich, Germany)

Fig. 4.10 Stryker's Navigation System II provides hip, knee, and spine navigation surgery. (Image courtesy of Stryker Corporation, Kalamazoo, USA)

Fig. 4.11 Stryker's robotic arm-assisted Mako system. (Image courtesy of Stryker Corporation, Kalamazoo, USA)

scan and provides surgical personnel and patients with a patient-specific plan without additional procedures related to other image-based workflows that can increase cost or delay surgery. In this respect, virtual representation of patient anatomy is generated by using direct anatomic mapping and kinematic registration. More interestingly, NAVIO employs a handheld instrument to precisely resect bone approved by the surgeon within the patient-specific plan, which offers a unique and flexible method to arthroplasty. Additionally, the NAVIO surgical system allows a cost-effective method that gives a cutting-edge surgical practice and achieves outcomes predictable to the plan.

4.4 Future Development

Orthopedic navigation techniques are widely developed, and many commercial systems are available to clinical applications. However, as a matter of fact, different orthopedic patients have various and unique physical external and internal structures. Such patient variation results in various limitations in current orthopedic navigation. The future development of orthopedic navigation includes multimodal fusion, shape sensing, robotics, oncology, and academic collaboration, discussed in the following.

4.4.1 Multimodal Fusion

Various imaging multimodalities such as CT, MR, PET, and fluoroscopic images provide surgeons with different structural and functional information. While these information are obtained in different imaging spaces, multimodal information synchronization is essential to boost orthopedic navigation [2]. Unfortunately, seamless fusion of these information remains challenging for surgical navigation in various clinical procedures including orthopedic surgery. A future direction is the development of accurate and robust fusion of preoperative and intraoperative information.

Fig. 4.12 NAVIO surgical system. (Image courtesy of Smith & Nephew PLC, London, UK)

4.4.2 Shape Sensing

The unique shape of the bone is used to register the preoperative plan with the position of the patient in the operating room. On the other hand, intraoperatively located surgical tools are very important for orthopedic navigation. The use of shape sensing for tracking anatomical structures and surgical instruments is a novel idea to improve accuracy and precision of orthopedic navigation [11]. More recently, shape sensing techniques were thoroughly reviewed for minimally invasive surgery [24]. In addition, orthopedic navigation system with sensorized devices is a promising way to report anatomical alignment and feedback in real time during surgery [23].

4.4.3 Orthopedic Robotics

Orthopedic surgery has been incorporated with robotic ethnology for the planning and performance of total hip replacement in 1992 [15]. Subsequently, robotic-assisted surgery has been most popular in unicompartmental arthroplasty, which results in greater accuracy of surgical implantation compared with conventional techniques. Although robotic-assisted orthopedic surgery has been demonstrated superior accuracy in most short-term studies, it still suffers from various limitations [15]. Robotic-assisted orthopedic surgery warrants further research and development.

4.4.4 Orthopedic Oncology

Surgical navigation in orthopedic oncology is a relatively new research area [29]. It is an extension of computer-assisted orthopedic navigation. While orthopedic navigation offers real-time direct visualization and accurate tracking of anatomical and pathologic structures and surgical instruments, it limits bulky navigation facilities, a long time of settings, and a lack of stable cut instruments [30]. Further development is to address these limitations and improve its efficiency and robustness.

4.4.5 Simulation and Validation

Although current orthopedic navigation systems combine preoperative images for resection planning, they have no support for simulation such as virtual bone resection and assessment of the resection defect and bone allograft selection from a 3-D virtual bone bank. It still remain unique and largely unexplored engineering challenges to build training simulators for orthopedic surgery, e.g., it is difficult to simulate both the large forces and subtle haptic feedback [27]. On the other hand, the navigation system (hardware and software) generated error has been generally disregarded [13]. Unbiased validation of accuracy and precision of orthopedic navigation requires to investigate the impact of extra-articular deformity on the system-level errors generated during intraoperative resection measurement [1].

4.4.6 Academic Collaboration

Recently, Conway et al. [7] proposed a model for academic collaboration in orthopedic surgery. Such a collaboration aims to solve major problems in orthopedic surgery worldwide. Although this model specified much methodological aspects, it still remains many challenges, e.g., the relative lack of objective, measurable outcomes regarding its interventions, and the financial sustainability [7]. Future recommendation is to extend this model that demands for new partnerships and efforts.

4.5 Closing Remarks

This chapter discusses surgical navigation in orthopedics. Computer-assisted orthopedic navigation surgery is generally considered as the new generation of orthopedic surgery. To realize orthopedic navigation, various techniques have been reviewed, such as multimodal modeling, spatial registration, real-time tracking, and direct visualization. In particular, several available orthopedic navigation systems were reviewed in this chapter. Although orthopedic navigation is a relatively mature field, it still requires further development including multimodal fusion, shape sensing, robotics, oncology, simulation and validation, and academic collaboration. These developments will definitely progress current orthopedic navigation and surgery approaches and systems to a completely new stage of intelligent orthopedics.

References

1. Angibaud LD, Dai Y, Liebelt RA, Gao B, Gulbransen SW, Silver XS (2015) Evaluation of the accuracy and precision of a next generation computer-assisted surgical system. Clin Orthop Surg 7(2):225–233
2. Aponte-Tinao LA, Ritacco LE, Milano FE, Ayerza MA, Farfalli GF (2015) Techniques in surgical navigation of extremity tumors: state of the art. Curr Rev Muscoskelet Med 8(4):319–323
3. Bostel T, Nicolay NH, Grossmann JG, Mohr A, Delorme S, Echner G, Haring P, Debus J, Sterzing, F (2014) Mr-guidance – a clinical study to evaluate a shuttle-based MR-linac connection to provide MR-guided radiotherapy. Radiat Oncol 9:12
4. Cho HS, Oh JH, Han I, Kim HS (2009) Joint-preserving limb salvage surgery under navigation guidance. Eur J Surg Oncol 100(3):227–232
5. Cho HS, Park IH, Jeon IH, Kim YG, Han I, Kim HS (2011) Direct application of MR images to computer-assisted bone tumor surgery. J Orthop Sci 16(2):190–195
6. Chowdhary A, Drittenbass L, Dubois-Ferrière V, Stern R, Assal M (2016) Intraoperative 3-dimensional computed tomography and navigation in foot and ankle surgery. Orthopedics 39(5): e1005–e1010
7. Conway DJ, Coughlin R, Caldwell A, Shearer D (2017) The institute for global orthopedics and traumatology a model for academic collaboration in orthopedic surgery. Front Public Health 5:Article 146

8. Enchev Y (2009) Neuronavigation: geneology, reality, and prospects. Neurosurg Focus 27(3):E11
9. Golby AJ (2015) Image-guided neurosurgery. Elsevier, Amsterdam
10. Harijan A, Halvorson EG (2011) Eponymous instruments in plastic surgery. Plast Reconstr Surg 127(1):456–465
11. He X, Popovic A, Flexman ML, Thienpharapa P, Noonan DP, Kroon R, Reinstein AL (2017) Shape sensing for orthopedic navigation. US Patent US20170281281A1, 5 Oct 2017
12. Hernandez D, Garimella R, Eltorai AEM, Daniels AH (2017) Computer-assisted orthopaedic surgery. Orthop Surg 9(2):152–158
13. Hsu HM, Chang IC, Lai TW (2016) Physicians perspectives of adopting computer-assisted navigation in orthopedic surgery. Int J Med Inform 94(10):207–214
14. Hutchinson M (2006) A brief atlas of the human body. Benjamin Cumming, San Francisco
15. Lang JE, Mannava S, Floyd AJ, Goddard MS, Smith BP, Mofidi A, Seyler TM, Jinnah RH (2011) Robotic systems in orthopaedic surgery. Bone Jt J 93(10):1296–1299
16. Li J, Wang Z, Guo Z, Chen GJ, Yang M, Pei GX (2014) Precise resection and biological reconstruction under navigation guidance for young patients with juxta-articular bone sarcoma in lower extremity: preliminary report. J Pediatr Orthop 34(1):101–108
17. Luo X, Wan Y, He X, Mori K (2015) Observation-driven adaptive differential evolution and its application to accurate and smooth bronchoscope three-dimensional motion tracking. Med Image Anal 24(1):282–296
18. Luo X, Mori K, Peters T (2018, in press) Advanced endoscopic navigation: surgical big data, methodology, and applications. Annu Rev Biomed Eng 20:221–251
19. Marieb EN, Hoehn KN (2015) Human anatomy & physiology. Pearson, Harlow
20. Moreland K (2013) A survey of visualization pipelines. IEEE Trans Vis Comput Graph 19(3):367–378
21. Nielson G (2003) On marching cubes. IEEE Trans Vis Comput Graph 9(3):283–297
22. Resnick D, Kransdorf M (2004) Bone and joint imaging. Elsevier-Saunders, Philadelphia
23. Roche M, Boillot M, McIntosh J (2015) Orthopedic navigation system with sensorized devices. US Patent US9011448, 21 Apr 2015
24. Shi C, Luo X, Qi P, Li T, Song S, Najdovski Z, Fukuda T, Ren H (2017) Shape sensing techniques for continuum robots in minimally invasive surgery: a survey. IEEE Trans Biomed Eng 64(8):1665–1678
25. So TY, Lam YL, Mak KL (2010) Computer-assisted navigation in bone tumor surgery: seamless workflow model and evolution of technique. J Pediatr Orthop 468(11):2985–2991
26. Takao M, Nishii T, Sakai T, Yoshikawa H, Sugano N (2014) Iliosacral screw insertion using CT-3D-fluoroscopy matching navigation. Injury 45(6):988–994
27. Thomas GW, Johns BD, Kho JY, Anderson DD (2015) The validity and reliability of a hybrid reality simulator for wire navigation in orthopedic surgery. IEEE Trans Hum Mach Sys 45(1):119–125
28. Wiesel SW, Delahay JN (2011) Essentials of orthopedic surgery. Springer, New York
29. Wong KC, Kumta SM (2013) Computer-assisted tumor surgery in malignant bone tumors. Clin Orthop Relat Res 471(3):750–61
30. Wong KC, Kumta SM (2014) Use of computer navigation in orthopedic oncology. Curr Surg Rep 2(4):47
31. Zheng G, Dong X, Rajamani KT, Zhang X, Styner M, Thoranaghatte RU, Nolte LP, Ballester MAG (2007) Accurate and robust reconstruction of a surface model of the proximal femur from sparse-point data and a dense-point distribution model for surgical navigation. IEEE Trans Biomed Eng 54(12):2109–2122
32. Zheng G, Nolte LP (2015) Computer-assisted orthopedic surgery: current state and future perspective. Front Surg 2:66

Check for updates

5 Multi-object Model-Based Multi-atlas Segmentation Constrained Grid Cut for Automatic Segmentation of Lumbar Vertebrae from CT Images

Weimin Yu, Wenyong Liu, Liwen Tan, Shaoxiang Zhang, and Guoyan Zheng

Abstract

In this chapter, we present a multi-object model-based multi-atlas segmentation constrained grid cut method for automatic segmentation of lumbar vertebrae from a given lumbar spinal CT image. More specifically, our automatic lumbar vertebrae segmentation method consists of two steps: affine atlas-target registration-based label fusion and bone-sheetness assisted multi-label grid cut which has the inherent advantage of automatic separation of the five lumbar vertebrae from each other. We evaluate our method on 21 clinical lumbar spinal CT images with the associated manual segmentation and conduct a leave-one-out study. Our method achieved an average Dice coefficient of $93.9 \pm 1.0\%$ and an average symmetric surface distance of 0.41 ± 0.08 mm.

Keywords

Multi-object model-based multi-atlas segmentation · Grid cut · CT · Lumbar vertebrae · Affine registration · Label fusion · Image-guided spinal surgery

5.1 Introduction

The field of medical image computing and computer-assisted interventions has been playing an increasingly important role in diagnosis and treatment of spinal diseases during the past 20 years. An accurate segmentation of individual vertebrae from CT images are important for many clinical applications. After segmentation, it is possible to determine the shape and condition of individual vertebrae. Segmentation can also assist early diagnosis, surgical planning, and locating spinal pathologies like degenerative disorders, deformations, trauma, tumors, and fractures. Most computer-assisted diagnosis and planning systems are based on manual

Weimin Yu and Wenyong Liu contributed equally to this paper

W. Yu · G. Zheng (✉)
Institute for Surgical Technology and Biomechanics, University of Bern, Bern, Switzerland
e-mail: guoyan.zheng@istb.unibe.ch

W. Liu
School of Biological Science and Medical Engineering, Beihang University, Beijing, China

Beihang Advanced Innovation Centre for Biomedical Engineering, Beihang University, Beijing, China

L. Tan · S. Zhang
The Institute of Digital Medicine, Third Military Medical University, Chongqing, China

G. Zheng et al. (eds.), *Intelligent Orthopaedics*, Advances in Experimental Medicine and Biology 1093, https://doi.org/10.1007/978-981-13-1396-7_5

segmentation performed by physicians. The disadvantage of manual segmentation is that it is time-consuming and the results are not really reproducible because the image interpretations by humans may vary significantly across interpreters.

Vertebra segmentation is challenging because the overall morphology of the vertebral column. Although the shape of the individual vertebrae changes significantly along the spine, most neighboring vertebrae look very similar and are difficult to distinguish. In recent years, a number of spine segmentation algorithms for CT images have been proposed. The proposed methods range from unsupervised image processing approaches, such as level set [14] and graph cut methods [1], to geometrical model-based methods such as statistical anatomical models or probabilistic atlas-based methods [8, 10, 12, 16, 17] and to more recently machine learning and deep learning-based methods [4, 5, 15].

In this chapter, we proposed a two-stage method which consists of the localization stage and the segmentation stage. The localization stage aims to identify each lumbar vertebra, while the segmentation stage handles the problem of labeling each lumbar vertebra from a given 3D image. Previously, we have developed a method to fully automatically localize landmarks for each lumbar vertebra in CT images with context features and reported a mean localization error of 3.2 mm [6]. In this paper, we focus on the segmentation stage where the detected landmarks in the localization stage are used to initialize our segmentation method.

To this end, we propose to use affinely registered multi-object model-based multi-atlases as shape prior for grid cut segmentation of lumbar vertebrae from a given target CT image. More specifically, our segmentation method consists of two steps: affine atlas-target registration-based label fusion and bone-sheetness assisted multi-label grid cut. The initial segmentation obtained from the first step will be used as the shape prior for the second step.

The chapter is organized as follows. In the next section, we will describe the method. Section 5.3 will present the experimental results, followed by discussions and conclusions in Sect. 5.4.

5.2 Method

Figure 5.1 presents a schematic overview of the complete workflow of our proposed approach. Without loss of generality, we assume that for the lth ($l \in \{1, 2, 3, 4, 5\}$) lumbar vertebra, there exists a set of N_l atlases with manually labeled segmentation and manually extracted landmarks. In the following, details of each step will be presented.

5.2.1 Affine Atlas-Target Registration-Based Label Fusion

Given the unseen lumbar spinal CT image, we assume that a set of landmarks have been already detected for each lumbar vertebra. The following steps are conducted separately for each lumbar vertebra.

Using the detected anatomical landmarks, paired-point scaled rigid registration are performed to align all N_l atlases of the lth lumbar vertebra to the target image space. We then select $N_{l,s} \ll N_l$ atlases with the least paired-point registration errors for the atlas affine registration step as described below.

Each selected atlas consists of a CT volume and a manual segmentation of the corresponding lumbar vertebra. For every selected atlas, we perform a pair-wise atlas-target affine registration using the intensity-based registration toolbox “Elastix” [11]. Using the obtained 3D affine transformation, we can align the associated manual segmentation of the selected atlas to the target image space. Then the probability of labeling a voxel x in the target image space as part of the lth lumbar vertebra is computed with average voting:

$$p_{l,x} = \frac{1}{N_{l,s}} \sum_{i=1}^{N_{l,s}} A_i(x) \qquad (5.1)$$

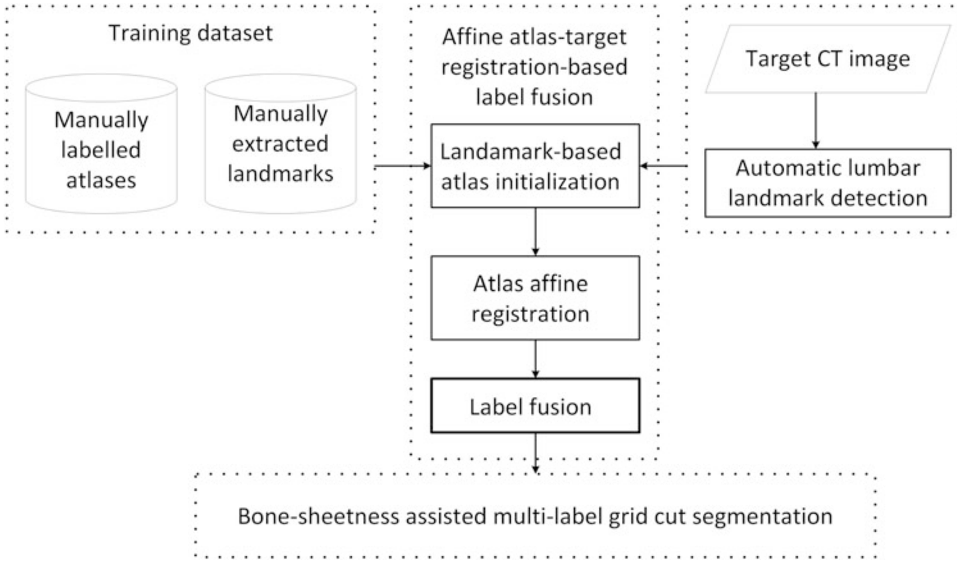

Fig. 5.1 The flowchart of our proposed segmentation method. See text for details

where $A_i(x) \in \{0, 1\}$ is the label of the ith atlas at voxel x after aligned to the target image space.

A simple thresholding is then conducted to get an initial binary segmentation of the lth lumbar vertebra:

$$L_l(x) = \begin{cases} 0; & p_{l,x} < T \\ 1; & p_{l,x} \geqslant T \end{cases} \tag{5.2}$$

where T is the threshold and is empirically selected as 0.35.

Above steps are conducted for all five lumbar vertebrae.

5.2.2 Bone-Sheetness Assisted Grid Cut

The initial segmentation obtained in the last step is usually not accurate enough as only affine atlas-target registrations are used. To further improve the segmentation accuracy, we proposed to use bone-sheetness assisted multi-label grid cut taking the initial segmentation as the shape prior.

Grid cut is a fast multi-core max-flowmin-cut solver optimized for grid-like graphs [9]. The task of multi-label grid cut is to assign an appropriate label $L(x)$ to every voxel x in the image space Ω of the target image I. In our case, labels $L(x) \in \{0, 1, 2, 3, 4, 5\}$ are employed for the purpose of labeling the target image into six different regions including background region (BK, $L(x) = 0$) and the five lumbar vertebral regions (for the lth lumbar vertebra L_l, $L(x) = l$). After segmentation, the target image will be partitioned into six sub-image regions, i.e., $\Omega = \{\Omega_{BK} \cup \Omega_{l_1} \cup \Omega_{l_2} \cup \Omega_{l_3} \cup \Omega_{l_4} \cup \Omega_{l_5}\}$.

Grid cut, similar to graph cut [3], is an energy minimization segmentation framework based on combinatorial graph theory. The typical energy function of a multi-label grid cut $E(L)$ is defined as

$$\begin{aligned} E(L) \;=\; & \sum_{x\in\Omega} R_x(L(x)) \\ & + \lambda \sum_{(x,y)\in\mathcal{N}} B_{x,y}(L(x), L(y)) \end{aligned} \tag{5.3}$$

where $R_x(L(x))$ is the pixel-wised term which gives the cost of assigning label $L(x) \in \{0, 1, 2, 3, 4, 5\}$ to voxel x, $B_{x,y}(L(x), L(y))$ is the pair-wised term which gives the cost of assigning labels to voxel x and y in a user-defined neighborhood system $\mathcal{N}$, and λ adjusts the balance between the pixel-wised term and pair-wised term.

In general, grid cut methods define the energy based on intensity information. However, weak bone boundaries, narrow inter-bone space, and low intensities in the trabecular bone make image intensity alone a relatively poor feature to discriminate adjacent joint structures [13]. This can be addressed by applying image enhancement using sheetness filter to generate a new feature image (sheetness score map) [7]. For each voxel in the target image space Ω, a sheetness score BS is computed from the eigenvalues $|\lambda_1| \leq |\lambda_2| \leq |\lambda_3|$ of local Hessian matrix with scale σ as

$$BS_x(\sigma) = \left(\exp\left(\frac{-R^2_{\text{sheet}}}{2\alpha^2}\right)\right)\left(1 - \exp\left(\frac{-R^2_{\text{blob}}}{2\gamma^2}\right)\right)\left(1 - \exp\left(\frac{-R^2_{\text{noise}}}{2\xi^2}\right)\right) \tag{5.4}$$

where α, γ, ξ are the parameters [7]. $R_{\text{sheet}} = \frac{|\lambda_2|}{|\lambda_3|}$, $R_{\text{blob}} = \frac{|2\lambda_3 - \lambda_2 - \lambda_1|}{|\lambda_3|}$, $R_{\text{noise}} = \sqrt{\lambda_1^2 + \lambda_2^2 + \lambda_3^2}$.

For every pixel x, we have the computed sheetness score $BS_x \in [0, 1]$, where larger score associates with higher possibility that this pixel belongs to a bone region. With the computed sheetness score map and the initial segmentation, we define each term of the energy function as described below:

Pixel-wised term Based on the initial segmentation obtained in the last step, the target image space Ω can be separated into six sub-image regions, i.e., $\Omega = \{\Omega'_{BK} \cup \Omega'_{l_1} \cup \Omega'_{l_2} \cup \Omega'_{l_3} \cup \Omega'_{l_4} \cup \Omega'_{l_5}\}$, where each sub-image region is obtained from the corresponding initial segmentation. By further employing the computed sheetness score map and the Hounsfield units (HU) of different tissues, the exclusion regions for each structure can be defined as

$$\begin{cases} E_{\neg L_1} & = \{v \notin \Omega'_{L_1} \text{and} \mathcal{I}(x) \leq -50\text{HU}\} \\ E_{\neg L_2} & = \{v \notin \Omega'_{L_2} \text{and} \mathcal{I}(x) \leq -50\text{HU}\} \\ E_{\neg L_3} & = \{v \notin \Omega'_{L_3} \text{and} \mathcal{I}(x) \leq -50\text{HU}\} \\ E_{\neg L_4} & = \{v \notin \Omega'_{L_4} \text{and} \mathcal{I}(x) \leq -50\text{HU}\} \\ E_{\neg L_5} & = \{v \notin \Omega'_{L_5} \text{and} \mathcal{I}(x) \leq -50\text{HU}\} \\ E_{\neg BK} & = \{v \notin \Omega'_{BK} \text{and} \mathcal{I}(x) \geq 200\text{HU} \wedge BS_v > 0\} \end{cases} \tag{5.5}$$

where -50HU and 200HU are selected following [13]. The $R_x(L(x))$ is then defined as

$$R_x(L(x)) = \begin{cases} 1 & \text{if} L(x) = 0 \text{and} x \in E_{\neg BK} \\ 1 & \text{if} L(x) = 1 \text{and} v \in E_{\neg L_1} \\ 1 & \text{if} L(x) = 2 \text{and} v \in E_{\neg L_2} \\ 1 & \text{if} L(x) = 3 \text{and} v \in E_{\neg L_3} \\ 1 & \text{if} L(x) = 4 \text{and} v \in E_{\neg L_4} \\ 1 & \text{if} L(x) = 5 \text{and} v \in E_{\neg L_5} \\ 0 & \text{otherwise} \end{cases} \tag{5.6}$$

Pair-wised term As the sheetness filter enhances the bone boundaries, we employ the computed sheetness score map to define the pair-wised term:

$$B_{x,y}(L(x), L(y)) \propto \exp\{-\frac{|BS_x - BS_y|}{\sigma_s}\} \cdot \delta(L(x), L(y)) \tag{5.7}$$

where σ_s is a constant scaling parameter and

$$\delta(L(x), L(y)) = \begin{cases} 1 & \text{if} L(x) \neq L(y) \\ 0 & \text{otherwise} \end{cases} \tag{5.8}$$

5.3 Experimental Results

We evaluated our method on 21 clinical lumbar spinal CT data with the associated manual segmentation. The size of the data ranges from 512 × 512 × 318 voxels to 512 × 512 × 433 voxels. The voxel spacing of the data ranges from 0.43 × 0.43 × 0.7 mm^3 to 0.29 × 0.29 × 0.7 mm^3. In this paper, we conducted a leave-one-out (LOO) cross-validation study to evaluate the performance of the present method. More specifically, each time we took 1 out of the 21 CT data as the test data and the remaining 20 CT data as the atlases, and we chose $N_{l,s}$ to be 5. The process was repeated for 21 times, with each CT data used exactly once as the test data. In each time, the segmented results of the test data were compared with the associated ground truth manual segmentation. For each vertebra in a test CT data, we evaluate the average symmetric surface distance (ASSD), the Dice coefficient (DC), precision, and recall.

Table 5.1 presents the segmentation results of the cross-validation study, where the results on each individual vertebra as well as on the entire lumbar region are presented. Our approach achieves a mean DC of 93.9 ± 1.0% and a mean ASSD of 0.41 ± 0.08 mm on the entire lumbar region. In each fold, it took about 12 min to finish segmentation of all five lumbar vertebrae of one test image. Figure 5.2 shows a segmentation example.

Table 5.1 Segmentation results of the leave-one-out cross validation on 21 clinical spinal CT data

	DC (%)	ASSD (mm)	Precision (%)	Recall (%)
L1	94.2 ± 0.8	0.39 ± 0.06	91.9 ± 1.7	96.7 ± 1.6
L2	94.1 ± 0.8	0.39 ± 0.05	91.6 ± 1.9	96.7 ± 1.6
L3	93.8 ± 1.0	0.42 ± 0.07	91.0 ± 2.3	96.8 ± 1.7
L4	94.0 ± 0.9	0.40 ± 0.06	91.4 ± 2.0	96.9 ± 1.6
L5	93.7 ± 1.1	0.45 ± 0.11	91.2 ± 2.6	96.3 ± 2.1
Lumbar	93.9 ± 1.0	0.41 ± 0.08	91.4 ± 2.1	96.7 ± 1.8

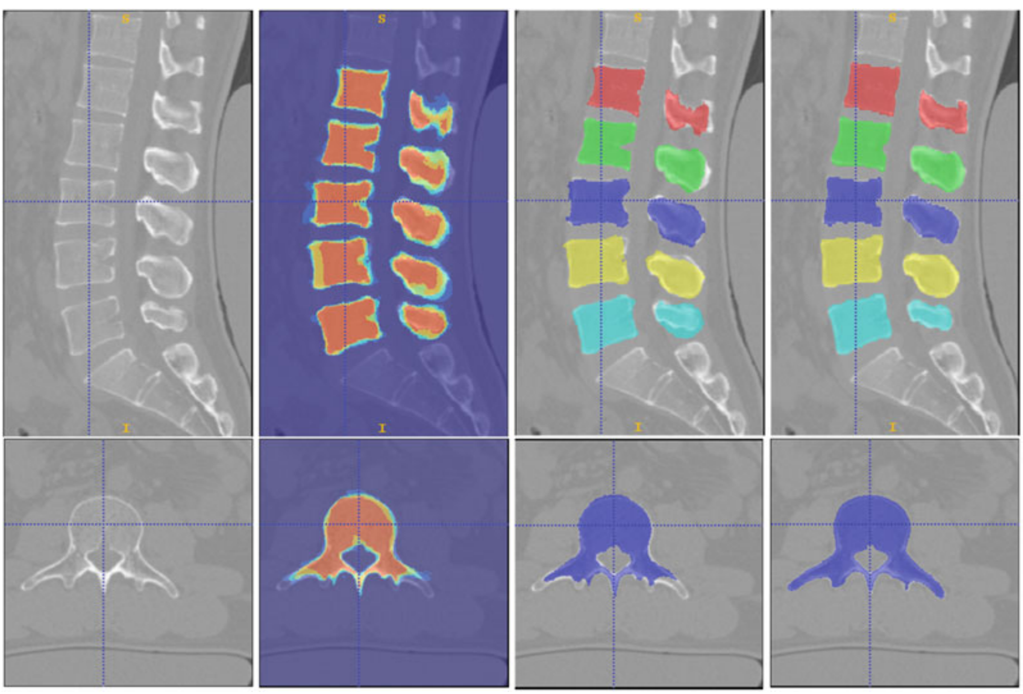

Fig. 5.2 A lumbar vertebrae segmentation example. Top row: sagittal view. Bottom row: axial view. For both rows, from left to right: the input image, the probability map, the initial segmentation obtained from the affine atlas-target registration-based label fusion, and the final results

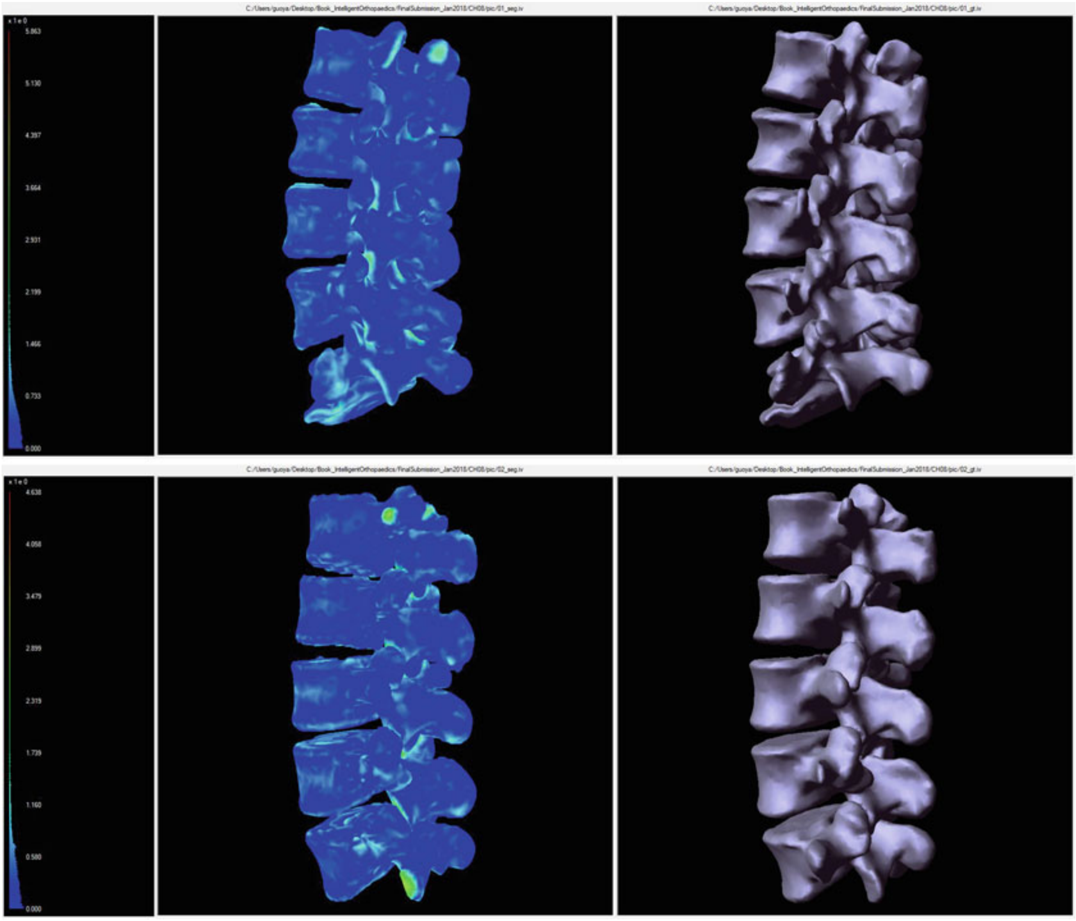

Fig. 5.3 Color-coded error distributions of two segmented lumbar vertebral segments in comparison to the corresponding ground truth. In each row, the left column shows the error bar; the middle column shows the segmented lumbar vertebral segment with color-coded error distributions; and the right column shows the ground truth model

Figure 5.3 shows color-coded error distributions of two cases. Our automatic segmentation when applied to the case shown in the top row achieved a mean error of 0.47 mm and a 95 percentile error of 1.25 mm. For the case shown in the bottom row, the achieved mean segmentation error was found to be 0.42 mm and the 95 percentile error was 1.13 mm.

5.4 Discussions and Conclusions

Previous atlas-based methods [17] where nonrigid registration between atlases and the target image is required, may not work here considering the weak bone boundaries and narrow inter-bone space of neighboring vertebrae. In this paper, we only need to affinely register atlases with the target image, and the accurate segmentation is then obtained by the bone-sheetness-assisted multi-label grid cut which has additional advantage of automatic separation of the five lumbar vertebrae from each other.

In conclusion, we proposed a method for automatic segmentation of lumbar vertebrae from clinical CT images. The results obtained from the LOO experiment demonstrated the efficacy of the proposed approach.

References

1. Aslan M, Ali A, Chen D, Arnold B, Farag A, Xiang P (2010) 3D vertebrae segmentation using graph cuts with shape prior constraints. In: Proceedings of the ICIP 2010, pp 2193–2196, Hong Kong, China
2. Balmain Sports Medicine (2014) Common lumbar spine injuries. https://www.balmainsportsmed.com.au/injury-library/injury-information/lumber-and-spine.html. [Online; Accessed 09 Oct 2017]
3. Boykov Y, Kolmogorov V (2004) An experimental comparison of min-cut/max-flow algorithms for energy minimization in vision. IEEE Trans Pattern Anal Mach Intell 26(9):1124–1137
4. Chen H, Shen C, Qin J et al (2015) Automatic localization and identification of vertebrae in spine ct via a joint learning model with deep neural network. In: Proceedings of the MICCAI 2015, pp 515–522, Munich, Germany
5. Chu C, Belavy D et al (2015) Fully automatic localization and segmentation of 3D vertebral bodies from CT/MR images via a learning-based method. PLoS One 10(11):e0143327
6. Damopoulos D, Glocker B, Zheng G (2017) Automatic localization of the lumbar vertebral landmarks in CT images with context features. In: Proceedings of the 2017 MICCAI-MSKI workshop, pp 56–68, Quebec City, Canada
7. Descoteaux M, Audette M, Chinzei K, Siddiqi K (2005) Bone enhancement filtering: application to sinus bone segmentation and simulation of pituitary surgery. In: Proceedings of the MICCAI 2005, pp 9–16, Palm Springs, USA
8. Ibragimov B, Likar B, Pernus F, Vrtovec T (2014) Shape representation for efficient landmark-based segmentation in 3-D. IEEE Trans Med Imaging 33(4):861–874S. https://doi.org/10.1109/TMI.2013.2296976
9. Jamriška O, Sýkora D, Hornung A (2012) Cache-efficient graph cuts on structured grids. In: Proceedings of the CVPR 2012, pp 3673–3680, Rhode Island, USA
10. Kadoury S, Labelle H, Paragios N (2013) Spine segmentation in medical images using manifold embeddings and higher-order MRFs. IEEE Trans Med Imaging 32(7):1227–1238. https://doi.org/10.1109/TMI.2013.2244903
11. Klein S, Staring M, Murphy K, Viergever M, Pluim J (2010) Elastix: a toolbox for intensity-based medical image registration. IEEE Trans Med Imaging 29(1):196–205
12. Korez R, Ibragimov B, Likar B, Pernus F, Vrtovec T (2015) A framework for automated spine and vertebrae interpolation-based detection and model-based segmentation. IEEE Trans Med Imaging 34:1649–1662
13. Krčah M, Székely G, Blanc R (2011) Fully automatic and fast segmentation of the femur bone from 3D-CT images with no shape prior. In: Proceedings of the ISBI 2011, pp 2087–2090, Chicago, USA
14. Lim P, Bagci U, Bai L (2013) Introducing willmore flow into level set segmentation of spinal vertebrae. IEEE Trans Biomed Eng 60(1):115–122
15. Sekuboyina A, Kukacka J, Kirschke J, Menze B, Valentinitsch A (2017) Attention-driven deep learning for pathological spine segmentation. In: Proceedfing of 2017 MICCAI-MSKI workshop, pp 104–115, Quebec City, Canada
16. Štern D, Likar B, Pernus F, Vrtovec T (2011) Parametric modelling and segmentation of vertebral bodies in 3D CT and MR spine images. Phys Med Biol 56:7505–7522. https://doi.org/doi:10.1088/0031-9155/56/23/011
17. Yao J, Burns J, Forsberg D et al (2016) A multi-center milestone study of clinical vertebral CT segmentation. Comput Med Imaging Graph 49:16–28

Deep Learning-Based Automatic Segmentation of the Proximal Femur from MR Images

6

Guodong Zeng and Guoyan Zheng

Abstract

This chapter addresses the problem of segmentation of proximal femur in 3D MR images. We propose a deeply supervised 3D U-net-like fully convolutional network for segmentation of proximal femur in 3D MR images. After training, our network can directly map a whole volumetric data to its volume-wise labels. Inspired by previous work, multi-level deep supervision is designed to alleviate the potential gradient vanishing problem during training. It is also used together with partial transfer learning to boost the training efficiency when only small set of labeled training data are available. The present method was validated on 20 3D MR images of femoroacetabular impingement patients. The experimental results demonstrate the efficacy of the present method.

Keywords

MRI · Segmentation · Femoroacetabular impingement (FAI) · Proximal femur · Deep learning · Fully Convolutional Network (FCN) · Deep supervision

G. Zeng · G. Zheng (✉)
Institute for Surgical Technology and Biomechanics, University of Bern, Bern, Switzerland
e-mail: guoyan.zheng@istb.unibe.ch

6.1 Introduction

Femoroacetabular Impingement (FAI) is a cause of hip pain in adults and has been recognized recently as one of the key risk factors that may lead to the development of early cartilage and labral damage [1] and a possible precursor of hip osteoarthritis [2]. Several studies [2, 3] have shown that the prevalence of FAI in young populations with hip complaints is high. Although there exist a number of imaging modalities that can be used to diagnose and assess FAI, MR imaging does not induce any dosage of radiation at all and is regarded as the standard tool for FAI diagnosis [4]. While manual analysis of a series of 2D MR images is feasible, automated segmentation of proximal femur in MR images will greatly facilitate the applications of MR images for FAI surgical planning and simulation.

The topic of automated MR image segmentation of the hip joint has been addressed by a few studies which relied on atlas-based segmentation [5], graph cut [6], active model [7,8], or statistical shape models [9]. While these methods reported encouraging results for bone segmentation, further improvements are needed. For example, Arezoomand et al. [8] recently developed a 3D active model framework for segmentation of proximal femur in MR images, and they reported an average recall of 0.88.

G. Zheng et al. (eds.), *Intelligent Orthopaedics*, Advances in Experimental Medicine and Biology 1093, https://doi.org/10.1007/978-981-13-1396-7_6

Recently, machine learning-based methods, especially those based on convolutional neural networks (CNNs), have witnessed successful applications in natural image processing [10, 11] as well as in medical image analysis [12–15]. For example, Prasoon et al. [12] developed a method to use a triplanar CNN that can autonomously learn features from images for knee cartilage segmentation. More recently, 3D volume-to-volume segmentation networks were introduced, including 3D U-Net [13], 3D V-Net [14], and a 3D deeply supervised network [15].

In this chapter, we propose a deeply supervised 3D U-net-like fully convolutional network (FCN) for segmentation of proximal femur in 3D MR images. After training, our network can directly map a whole volumetric data to its volume-wise label. Inspired by previous work [13, 15], multi-level deep supervision is designed to alleviate the potential gradient vanishing problem during training. It is also used together with partial transfer learning to boost the training efficiency when only small set of labeled training data are available.

6.2 Method

Figure 6.1 illustrates the architecture of our proposed deeply supervised 3D U-net-like network. Our proposed neural network is inspired by the 3D U-net [13]. Similar to 3D U-net, our network also consists of two parts, i.e., the encoder part (contracting path) and the decoder part (expansive path). The encoder part focuses on analysis and feature representation learning from the input data, while the decoder part generates segmentation results, relying on the learned features from the encoder part. Shortcut connections are established between layers of equal resolution in the encoder and decoder paths. The difference between our network and the 3D U-net is the introduction of multi-level deep supervision, which gives more feedback to help training during back propagation process.

Previous studies show small convolutional kernels are more beneficial for training and performance. In our deeply supervised network, all convolutional layers use kernel size of $3 \times 3 \times 3$ and strides of 1, and all max pooling layers use

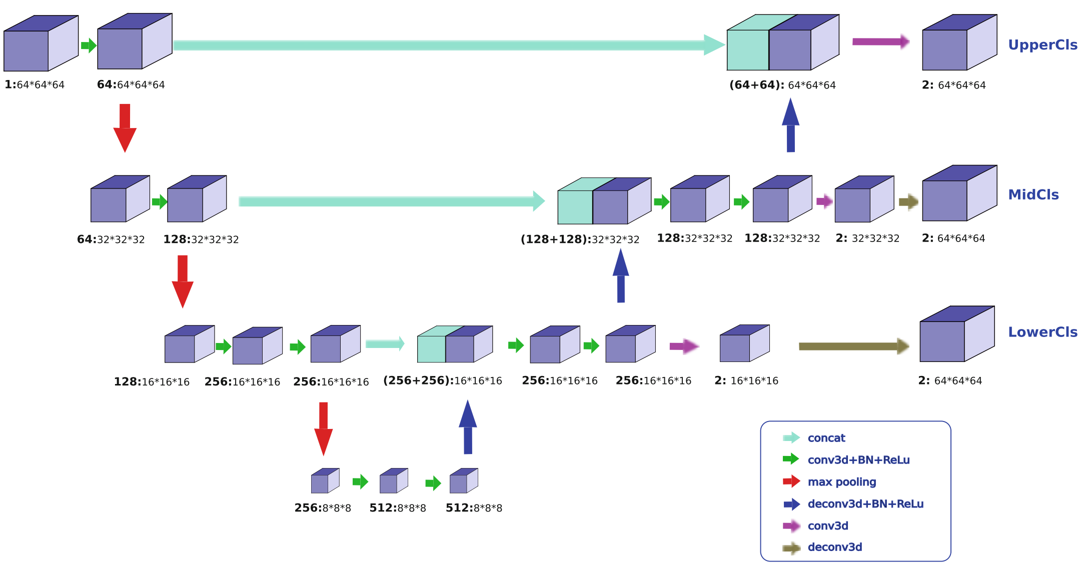

Fig. 6.1 Illustration of our proposed network architecture

kernel size of $2 \times 2 \times 2$ and strides of 2. In the convolutional and deconvolutional blocks of our network, batch normalization (BN) [16] and rectified linear unit (ReLU) are adopted to speed up the training and to enhance the gradient back propagation.

6.2.1 Multi-level Deep Supervision

Training a deep neural network is challenging. As the matter of gradient vanishing, final loss cannot be efficiently back propagated to shallow layers, which is more difficult for 3D cases when only a small set of annotated data is available. To address this issue, we inject two branch classifiers into network in addition to the classifier of the main network. Specifically, we divide the decoder path of our network into three different levels: lower layers, middle layers, and upper layers. Deconvolutional blocks are injected into lower and middle layers such that the low-level and middle-level features are upscaled to generate segmentation predictions with the same resolution as the input data. As a result, besides the classifier from the upper final layer ("UpperCls" in Fig. 6.1), we also have two branch classifiers in lower and middle layers ("LowerCls" and "MidCls" in Fig. 6.1, respectively). With the losses calculated by the predictions from classifiers of different layers, more effective gradient back propagation can be achieved by direct supervision on the hidden layers.

Let W be the weights of main network and w^l, w^m, w^u be the weights of the three classifiers "LowerCls," "MidCls," and "UpperCls," respectively. Then the cross-entropy loss function of a classifier is:

$$\mathscr{L}_c(\chi; W, w^c) = \sum_{x_i \in \chi} -\log p(y_i = t(x_i)|x_i; W, w^c)) \tag{6.1}$$

where $c \in \{l, m, u\}$ represents the index of the classifiers; χ represents the training samples; and $p(y_i = t(x_i)|x_i; W, w^c)$ is the probability of target class label $t(x_i)$ corresponding to sample $x_i \in \chi$.

The total loss function of our deep-supervised 3D network is:

$$\mathscr{L}(\chi; W, w^l, w^m, w^u) = \sum_{c \in \{l,m,u\}} \alpha_c \mathscr{L}_c(\chi; W, w^c) + \lambda(\psi(W) + \sum_{c \in \{l,m,u\}} \psi(w^c)) \tag{6.2}$$

where $\psi()$ is the regularization term (L_2 norm in our experiment) with hyper-parameter λ; $\alpha_l, \alpha_m, \alpha_u$ are the weights of the associated classifiers.

By doing this, classifiers in different layers can also take advantages of multi-scale context, which has been demonstrated in previous work on segmentation of 3D liver CT and 3D heart MR images [15]. This is based on the observation that lower layers have smaller receptive fields, while upper layers have larger receptive fields. As a result, multi-scale context information can be learned by our network which will then facilitate the target segmentation in the test stage.

6.2.2 Partial Transfer Learning

It is difficult to train a deep neural network from scratch because of limited annotated data. Training deep neural network requires large amount of annotated data, which are not always available, although data augmentation can partially address the problem. Furthermore, randomly initialized parameters make it more difficult to search for an optimal solution in high-dimensional space. Transfer learning from an existing network, which has been trained on a large set of data, is a common way to alleviate the difficulty. Usually the new dataset should be similar or related to the dataset and tasks used in the pre-training stage. But for medical image applications, it is difficult to find an off-the-shelf 3D model trained on a large set of related data of related tasks.

Previous studies [17] demonstrated that weights of lower layers in deep neural network are generic, while higher layers are more related to specific tasks. Thus, the encoder path of our neural network can be transferred from models pre-trained on a totally different dataset. In the field of computer vision, lots of models are trained on very large dataset, e.g., ImageNet [18], VGG16 [19], GoogleNet [20], etc. Unfortunately, most of these models were trained on 2D images. 3D pre-trained models that can be freely accessed are rare in both computer vision and medical image analysis fields.

C3D [21] is one of the few 3D models that has been trained on a very large dataset in the field of computer vision. More specifically, C3D is trained on the Sports-1M dataset to learn spatiotemporal features for action recognition. The Sports-1M dataset consists of 1.1 million sports videos, and each video belongs to one of 487 sports categories.

In our experiment, C3D pre-trained model was adopted as the pre-trained model for the encoder part of our neural network. For the decoder parts of our neural network, they were randomly initialized.

6.2.3 Implementation Details

The proposed network was implemented in Python using TensorFlow framework and trained on a desktop with a 3.6 GHz Intel(R) i7 CPU and a GTX 1080 Ti graphics card with 11GB GPU memory.

6.3 Experiments and Results

6.3.1 Dataset and Preprocessing

We evaluated our method on a set of unilateral hip joint data containing 20 T1-weighted MR images of FAI patients. We randomly split the dataset into two parts, ten images are for training and the other ten images are for testing. Data augmentation was used to enlarge the training samples by rotating each image (90, 180, 270) degrees around the z-axis of the image and flipped horizontally (y-axis). After that, we got in total 80 images for training.

6.3.2 Training Patches Preparation

All sub-volume patches to our neural network are in the size of $64 \times 64 \times 64$. We randomly cropped sub-volume patches from training samples whose size are about $300 \times 200 \times 100$. In the phase of training, during every epoch, 80 training volumetric images were randomly shuffled. We then randomly sampled patches with batch size 2 from each volumetric image for n times ($n = 5$). Each sampled patch was normalized as zero mean and unit variance before fed into network.

6.3.3 Training

We trained two different models, one with partial transfer learning and the other without. More specifically, to train the model with partial transfer learning, we initialized the weights of the encoder part of the network from the pre-trained C3D [21] model and the weights of other parts from a Gaussian distribution($\mu = 0, \sigma = 0.01$). In contrast, for the model without partial transfer learning, all weights were initialized from Gaussian distribution($\mu = 0, \sigma = 0.01$).

Each time, the model was trained for 14,000 iterations, and the weights were updated by the stochastic gradient descent (SGD) algorithm (momentum = 0.9, weight decay = 0.005). The initial learning rate was 1×10^{-3} and halved by 3000 every training iterations. The hyperparameters were chosen as follows: $\lambda = 0.005$, $\alpha_l = 0.33$, $\alpha_m = 0.67$, and $\alpha_u = 1.0$.

6.3.4 Test and Evaluation

Our trained models can estimate labels of an arbitrary-sized volumetric image. Given a test

Table 6.1 Quantitative evaluation results on testing datasets

	Surface distance (mm)			Volume overlap measurement			
ID	Mean	STD	Hausdorff distance	DICE	Jaccard	Precision	Recall
Pat01	0.17	0.31	3.8	0.989	0.978	0.992	0.985
Pat02	0.27	0.46	5.3	0.986	0.973	0.985	0.987
Pat03	0.19	0.35	4.1	0.987	0.975	0.995	0.979
Pat04	0.23	0.67	13.0	0.987	0.974	0.992	0.982
Pat05	0.12	0.21	4.3	0.989	0.979	0.991	0.988
Pat06	0.14	0.26	4.5	0.990	0.980	0.995	0.985
Pat07	0.41	0.95	7.0	0.978	0.958	0.984	0.973
Pat08	0.39	0.93	5.2	0.981	0.963	0.994	0.968
Pat09	0.12	0.17	11.0	0.990	0.981	0.990	0.990
Pat10	0.15	0.28	5.3	0.988	0.976	0.991	0.984
Average	0.22	–	6.4	0.987	0.974	0.991	0.982

volumetric image, we extracted overlapped subvolume patches with the size of $64 \times 64 \times 64$ and fed them to the trained network to get prediction probability maps. For the overlapped voxels, the final probability maps would be the average of the probability maps of the overlapped patches, which were then used to derive the final segmentation results. After that, we conducted morphological operations to remove isolated small volumes and internal holes as there is only one femur in each test data. When implemented with Python using TensorFlow framework, our network took about 2 min to process one volume with size of $300 \times 200 \times 100$.

The segmented results were compared with the associated ground truth segmentation which was obtained via a semiautomatic segmentation using the commercial software package called Amira.[1] Amira was also used to extract surface models from the automatic segmentation results and the ground truth segmentation. For each test image, we then evaluated the distance between the surface models extracted from different segmentation as well as the volume overlap measurements including Dice overlap coefficient [22], Jaccard coefficient [22], precision, and recall.

6.3.5 Results

Table 6.1 shows the segmentation results using the model trained with partial transfer learning. In comparison with manually annotated ground truth data, our model achieved an average surface distance of 0.22 mm, an average Dice coefficient of 0.987, an average Jaccard index of 0.974, an average precision of 0.991, and an average recall of 0.982. Figure 6.2 shows a segmentation example and the color-coded error distribution of the segmented surface model.

We also compared the results achieved by using the model with partial transfer learning with the one without partial transfer learning. The results are presented in Table 6.2, which clearly demonstrate the effectiveness of the partial transfer learning.

6.4 Conclusion

We have introduced a 3D U-net-like fully convolutional network with multi-level deep supervision and successfully applied it to the challenging task of automatic segmentation of proximal femur in MR images. Multi-level deep supervision

[1] http://www.amira.com/

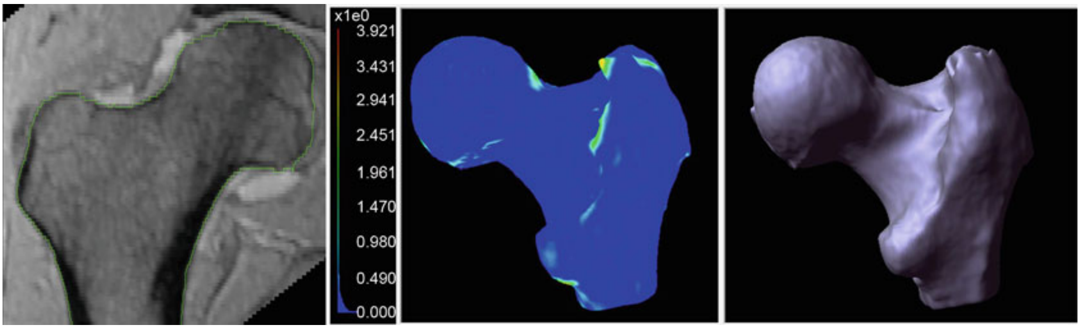

Fig. 6.2 A segmentation example (left) and the color-coded error distribution of the surface errors (right)

Table 6.2 Comparison of the average results of the proposed network on the same test dataset when trained with and without transfer learning

	Surface distance (mm)			Volume overlap measurement			
Learning method	Mean	STD	Hausdorff distance	DICE	Jaccard	Precision	Recall
Without transfer learning	0.67	–	12.4	0.975	0.950	0.985	0.964
With transfer learning	0.22	–	6.4	0.987	0.974	0.991	0.982

and partial transfer learning were used in our network to boost the training efficiency when only small set of labeled 3D training data were available. The experimental results demonstrated the efficacy of the proposed network.

Acknowledgements This chapter was modified from the paper published by our group in *the MICCAI 2017 Workshop on Machine Learning in Medical Imaging* (Zeng and Zheng, MLMI@MICCAI 2017: 274-282). The related contents were reused with the permission. This study was partially supported by the Swiss National Science Foundation via project 205321_163224/1.

Ethics

The medical research ethics committee of Inselspital, University of Bern, Switzerland, approved the human protocol for this investigation. Informed consent for participation in the study was obtained.

References

1. Laborie L, Lehmann T, Engester I et al (2011) Prevalence of radiographic findings thought to be associated with femoroacetabular impingement in a population-based cohort of 2081 healthy young adults. Radiology 260:494–502
2. Leunig M, Beaulé P, Ganz R (2009) The concept of femoroacetabular impingement: current status and future perspectives. Clin Orthop Relat Res 467: 616–622
3. Clohisy J, Knaus E, Hunt DM et al (2009) Clinical presentation of patients with symptomatic anterior hip impingement. Clin Orthop Relat Res 467: 638–644
4. Perdikakis E, Karachalios T, Katonis P, Karantanas A (2011) Comparison of MR-arthrography and MDCT-arthrography for detection of labral and articular cartilage hip pathology. Skeletal Radiol 40:1441–1447
5. Xia Y, Fripp J, Chandra S, Schwarz R, Engstrom C, Crozier S (2013) Automated bone segmentation from large field of view 3D MR images of the hip joint. Phys Med Biol 21:7375–7390
6. Xia Y, Chandra S, Engstrom C, Strudwick M, Crozier S, Fripp J (2014) Automatic hip cartilage segmentation from 3D MR images using arc-weighted graph searching. Phys Med Biol 59:7245–66
7. Gilles B, Magnenat-Thalmann N (2010) Musculoskeletal MRI segmentation using multi-resolution simplex meshes with medial representations. Med Image Anal 14:291–302
8. Arezoomand S, Lee WS, Rakhra K, Beaule P (2015) A 3D active model framework for segmentation of proximal femur in MR images. Int J CARS 10:55–66
9. Chandra S, Xia Y, Engstrom C et al (2014) Focused shape models for hip joint segmentation in 3D magnetic resonance images. Med Image Anal 18: 567–578
10. Krizhevsky A, ISutskever, Hinton G (2012) Imagenet classification with deep convolutional neural networks. In: Pereira F, Burges CJC, Bottou L, Weinberger KQ (eds) Advances in neural information

processing systems, vol 25. Curran Associates, Inc., Red Hook, pp 1097–1105
11. Long J, Shelhamer E, Darrell T (2015) Fully convolutional networks for semantic segmentation. In: Proceedings of the IEEE conference on computer vision and pattern recognition (CVPR 2015), pp 3431–3440, Boston
12. Prasson A, Igel C, Petersen K et al (2013) Deep feature learning for knee cartilage segmentation using a triplanar convolutional neural network. In: Proceedings of the 16th international conference on medical image computing and computer assisted intervention (MICCAI 2013), vol 16(Pt 2), pp 246–53, Nagoya
13. Cicek O, Abdulkadir A, Lienkamp S, Brox T, Ronneberger O (2016) 3D u-net: learning dense volumetric segmentation from sparse annotation. In: Proceedings of the 16th international conference on medical image computing and computer assisted intervention (MICCAI 2016). LNCS, vol 9901, pp 424–432, Athens
14. Milletari F, Navab N, Ahmadi SA (2016) V-net: fully convolutional neural networks for volumetric medical image segmentation. In: Proceedings of the 2016 international conference on 3D vision (3DV). IEEE, pp 565–571, Stanford
15. Dou Q, Yu L, Chen H, Jin Y, Yang X, Qin J, Heng PA (2017) 3D deeply supervised network for automated segmentation of volumetric medical images. Med Image Anal 41:40–54
16. Ioffe S, Szegedy C (2015) Batch normalization: accelerating deep network training by reducing internal covariate shift. In: Proceedings of international conference on machine learning (ICML 2015), Lille
17. Yosinski J, Clune J, Bengio Y, Lipson H (2014) How transferable are features in deep neural networks? In: Advances in neural information processing systems, pp 3320–3328, Curran Associates, Inc.
18. Deng J, Dong W, Socher R, Li LJ, Li K, Fei-Fei L (2009) ImageNet: a large-scale hierarchical image database. In: Proceedings of the IEEE conference on computer vision and pattern recognition (CVPR 2009), Miami Beach
19. Simonyan K, Zisserman A (2014) Very deep convolutional networks for large-scale image recognition. arXiv:1409.1556
20. Szegedy C, Liu W, Jia Y et al (2015) Going deeper with convolutions. In: Proceedings of the IEEE conference on computer vision and pattern recognition (CVPR 2015), Boston. IEEE, pp 1–9
21. Tran D, Bourdev L, Fergus R, Torresani L, Paluri M (2015) Learning spatiotemporal features with 3D convolutional networks. In: Proceedings of the IEEE international conference on computer vision (CVPR 2015), pp 4489–4497, Boston
22. Karasawa K, Oda M, Kitasakab T et al (2017) Multi-atlas pancreas segmentation: atlas selection based on vessel structure. Med Image Anal 39:18–28

7 Muscle Segmentation for Orthopedic Interventions

Naoki Kamiya

Abstract
Skeletal muscle segmentation techniques can help orthopedic interventions in various scenes. In this chapter, we describe two methods of skeletal muscle segmentation on 3D CT images. The first method is based on a computational anatomical model, and the second method is a deep learning-based method. The computational anatomy-based methods are modeling the muscle shape with its running and use it for segmentation. In the deep learning-based methods, the muscle regions are directly acquired automatically. Both approaches can obtain muscle regions including shape, area, volume, and some other image texture features. And it is desirable that the method be selected by the required orthopedic intervention. Here, we show each design philosophy and features of a representative method. We discuss the various examples of site-specific segmentation of skeletal muscle in non-contrast images using torso CT and whole-body CT including in cervical, thoracoabdominal, surface and deep muscles. And we also mention the possibility of application to orthopedic intervention.

N. Kamiya (✉)
Aichi Prefectural University, Nagakute, Japan
e-mail: n-kamiya@ist.aichi-pu.ac.jp

Keywords
CT · Skeletal muscle segmentation · Orthopedic interventions · Computational anatomy · Deep learning · Fully Convolutional Network (FCN)

7.1 Introduction

Segmentation of skeletal muscle is an important theme for orthopedic intervention. Because orthopedic surgery is targeted to locomotor apparatus disease, skeletal systems such as bones and joints and skeletal muscles surrounding it and the nervous system that controls them are the main treatment target. Given that this motor organ relates to physical exercise and works in cooperation with each other, even if just one of the motor organs fails, problems arise in physical exercise. Of course, multiple exercise organs may be disrupted at the same time. Therefore, orthopedic surgery consists of a number of specialized fields, such as site, disease, and sports medicine, and it covers a wide range of patients, including those with trauma, congenital disease, and age-related diseases. Exercise organs may be disturbed at the same time. Therefore, in orthopedic surgery, it consists of a number of specialized fields such as site, disease, and sports medicine, and it covers

G. Zheng et al. (eds.), *Intelligent Orthopaedics*, Advances in Experimental Medicine and Biology 1093, https://doi.org/10.1007/978-981-13-1396-7_7

a wide range of patients including traumatology, congenital disease, and age-related diseases.

The skeletal muscle targeted in this chapter is histologically a striated muscle, which contrasts with the smooth muscle of visceral organs. Therefore, the segmentation problem on medical images is often difficult to resolve whether using automatic, semiautomatic, or manual methods. Specifically, each tissue is imaged because of the difference in the absorption amount of X-rays in computed tomography (CT) and magnetic resonance difference in MRI, so there is no extreme difference in gray value between skeletal muscle and visceral organ. Furthermore, skeletal muscle exists in the whole body; its shape varies from spindle muscle, feathered muscle, half-winged muscle, and saw muscle, and at the same time, individual differences are significant. Therefore, the automatic segmentation of skeletal muscle in medical images is an extremely difficult task. As described above, the automatic segmentation of skeletal muscle on medical images is a difficult task, but it is very important. It is an aid to surgical interventions.

Because skeletal muscles are distributed throughout the whole body, it goes beyond orthopedic interventions and is of interest in general surgical interventions. In other words, it is necessary to accurately understand the position and amount of the muscle region before the intervention. Recognition of the muscle region is also required for the understanding, prevention, and treatment of pathological conditions during bone and muscle diseases. Furthermore, in sports medicine, it is necessary to recognize not only diseases but also the muscles of different parts to understand posture-holding ability and developmental characteristics. Thus, in clinical practice, the site-specific segmentation of the muscle to be observed is necessary as the most basic technology. However, in the current clinical situation, the segmentation of the site-specific skeletal muscle is performed manually or semiautomatically by a doctor.

The following section introduces our two types of attempts at muscle segmentation applicable to orthopedic interventions.

7.1.1 Computational Anatomy-Based Skeletal Muscle Segmentation

This section describes skeletal muscle segmentation based on computational anatomy. In the computational anatomical project [1], we constructed a CT image database with quality and quantity that can cover the diversity of the human body, and we constructed a computational anatomy model according to the target organ and application purpose. In particular, automatic recognition of anatomical structures from trunk CT images based on a computed anatomical model attempted an automatic recognition of various human organs, and many achievements were published [2]. For the skeletal muscle described in this chapter, many site-specific models were constructed and used for muscle segmentation [3].

As mentioned above, the skeletal muscle of the human body is greatly different among individuals as with organs. For example, it includes a variety of diseases such as atrophy due to disease, decreases due to age, increases by exercise and training, and recovery due to rehabilitation. Therefore, skeletal muscle modeling requires mathematical representation of skeletal muscle position, shape, and gray value distribution.

We achieved skeletal muscle segmentation based on computational anatomy modeling of skeletal muscle with the following steps. Figure 7.1 shows the outline of the construction of the computational anatomy model of skeletal muscle and the skeletal muscle segmentation method using this model.

As shown in Fig. 7.1, in generating the skeletal muscle model, various information on the skeletal muscle is acquired using the training data set. Here, the anatomical specialist manually accumulates the origin and insertion coordinates which are the anatomical attachment positions of the skeletal muscle on the skeleton and at the same time acquires the region information of the skeletal muscle manually or semiautomatically and uses it for model construction. Based on the information regarding the positions, shapes, and

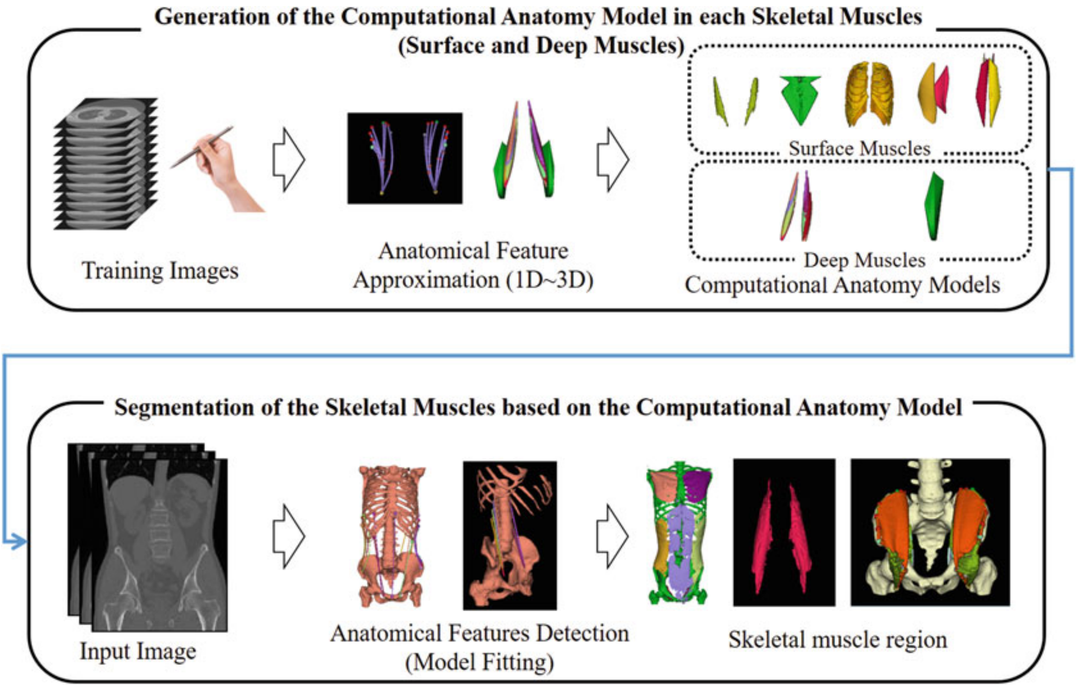

Fig. 7.1 Outline of the computational anatomy model of the skeletal muscles and its application for the skeletal muscle segmentation

gray value of the skeletal muscles in each part, characteristic modeling unique to each muscle is realized.

In the computational anatomy model project, nine regions (surface muscle, sternocleidomastoid muscle, trapezius muscle, supraspinous muscle, large pectoral muscle, intercostal muscle, oblique abdominal muscle, and rectus abdominis muscle; deep muscle, psoas major muscle, iliac muscle) of skeletal muscle modeling-based segmentation were realized [3–6]. In the skeletal muscle segmentation process based on the computational anatomy model, it is important to apply the calculated anatomy model of the skeletal muscle to test cases. In other words, it is necessary to arrange the skeletal muscle model in a test image, absorb the individual difference as a difference from the model, and segment the skeletal muscle region correctly. In the test case to be recognized, as in skeletal muscle modeling, we recognize the location of the origin and insertion, which are features of skeletal muscle, as landmarks (LMs), and we get the running of skeletal muscle by connecting between landmarks. Then a skeletal muscle model is placed on the running of the obtained muscle. Since the skeletal muscle model only expresses general features of muscles, fitting is performed according to personal characteristics after being placed. In the fitting process, the gray value and the maximum diameter of the objective muscle are acquired from the test image and used for recognition as a fitting parameter.

The important point here is that in modeling skeletal muscles and segmentation using models, we treat the anatomical features of skeletal muscle with three parameters: origin/insertion, direction, and shape. Then, on the computer, these parameters correspond to the feature point (LM), the centerline, and the shape model, respectively. Table 7.1 shows the correspondence between anatomical features and computer expression on skeletal muscle modeling. From Table 7.1, each feature expresses one- to three-dimensional information on skeletal muscle features.

Table 7.1 Correspondence between anatomical features and expression on computer in skeletal muscle modeling

	Anatomical feature	On the computer
Dot (1-D)	Origin, insertion	Landmarks (LMs)
Line (2-D)	Muscle direction	Centerline
Surface (3-D)	Shape	Shape model

The following shows a typical outcome of the skeletal muscle segmentation based on our skeletal muscle modeling. First, the segmentation of the iliopsoas muscle [7, 8], which is a deep muscle, is shown in Fig. 7.2. The iliopsoas muscle consists of the psoas major muscle and the iliac muscle, modeling is performed for each muscle part, and site-specific skeletal muscle information is obtained. Since each muscle can be anatomically treated as an iliac muscle, a model combining two individual models is taken as an iliopsoas model. By applying this lumbar muscle complex model to the test case, the iliopsoas region is segmented. In this modeling, this is the key to how to automatically acquire the landmark and how to model the muscle running and the muscle shape shown in Table 7.1 as the anatomical features. We approximate the outline of the skeletal muscle using a quadratic function and preliminarily define the gradient, which is one of the parameters of the quadratic function, as the muscle-specific shape parameter. Then the value of the intercept, which is a parameter of the remaining quadratic function, is dynamically calculated in the segmentation process as a parameter of individual difference, and a shape model reflecting the individual difference is obtained. Finally, it is placed on the centerline connecting the origin and insertion LMs, which is the anatomical definition, and the segmentation result of the muscle is obtained from the gray value.

The iliopsoas is a muscle involved in gait function and posture maintenance. Its relationship to decreasing age and lumbago has been clarified, and it is also an important line in orthopedic intervention.

Next, the outline of surface muscle segmentation is shown in Fig. 7.3. As shown in Fig. 7.3, we constructed a site-specific skeletal muscle model for various surface muscles [2–6]. Surface muscles have different distribution as well as shape for each part. Furthermore, it has various shapes as compared with the organ area. Therefore, it is difficult to create an outer shape model, and what is expressed as a model is the key feature of the muscle features. We used the position of the origin and insertion of the muscle and the centerline connecting them to model the surface muscle. Modeling is achieved with the sternocleidomastoid muscle, trapezius muscle, supraspinous muscle, intercostal muscle, rectus abdominis muscle, oblique abdominal muscle, and erector spinae muscle, acquisition of landmarks based on anatomical definition, and connection between landmarks. We simulated the running of the muscle fibers with the centerline. As a result, segmentation of skeletal muscle was realized even in a region with a large number of surrounding organ tissues and an abdominal region lacking skeletal information which is important information of skeletal muscle.

Surface muscles, including body cavity areas, the surface muscles present in the body surface area, are the subjects to access bones and tendons by orthopedic surgical procedures. Therefore, we believe that performing skeletal muscle segmentation helps orthopedic intervention.

We outlined the method of segmentation of surface and deep muscles based on skeletal muscle modeling using torso CT images that we realized. Although this is a result using the torso CT image, we believe that the same idea can be applied to the MRI image. We also believe that realization and advancement (accuracy, versatility, and processing speed) of automatic skeletal muscle segmentation by these computational anatomy model will be the basic technology for the advancement and efficiency improvement of accumulation, analysis, and use of human anatomical structure in the future. In fact, since the skeletal muscle is present in the entire human body to surround the organ and skeleton area, it can also be used as preprocessing in computer-aided diagnosis (CAD) and computer-assisted surgery (CAS) system.

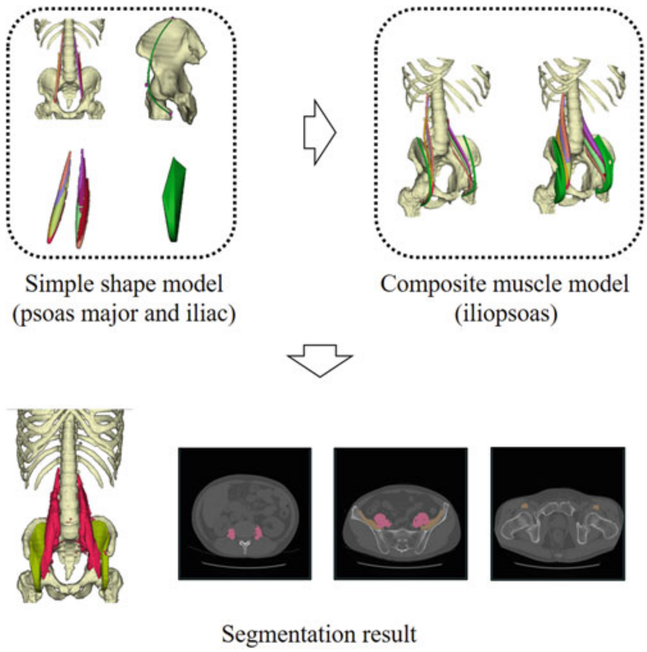

Fig. 7.2 Segmentation of deep muscle (iliopsoas) based on computational anatomy model

7.1.2 Deep Learning-Based Skeletal Muscle Segmentation

Here we describe skeletal muscle segmentation using machine learning. Segmentation using machine learning has been realized in the organ region [9], but its method has not been sufficiently verified in skeletal muscles, and it is also necessary to study it in skeletal muscles having complicated shape variations. We have experimented on the erector spinae muscle [6], which is a large muscle and which was difficult to construct a conventional shape model. Figure 7.4 shows the architecture of FCN-8s we used for testing. Here, in learning of three epochs, ten cases were used for learning, and ten cases were taken as test cases. As a result, the average agreement value was 82.8% (78.5% in the conventional modeling-based method [10]), and it is suggested that muscle segmentation by deep learning may improve the recognition rate at the region where it is difficult to generate a shape model.

Figure 7.5 shows the recognition result of the spinal column erector (coincidence ratio with the ground truth image is 80.3%). In this figure (right), the green region is a region coinciding with the ground truth image. Similarly, the red region is extracted excessively, and the blue color is not extracted region. From these results, it is possible to recognize a wide range of superficial muscles with high accuracy, but it is understood that the segmentation accuracy of the boundary with the trapezius muscle overlapping with the stratification is a future task.

Currently, various architectures are proposed for segmentation task based on machine learning in medical images. Especially, U-net has been well known for its efficacy in the field of medical image segmentation, where the decoder employs a similar corresponding architecture of the encoder. Our group achieved automatic segmentation of multiple organs from torso CT images using segmentation based on FCN and voting principle [11]. In comparison of segmentation methods based on FCN versus U-net, we obtained results that FCN and voting-based methods are realistic methods for segmenting CT images [12].

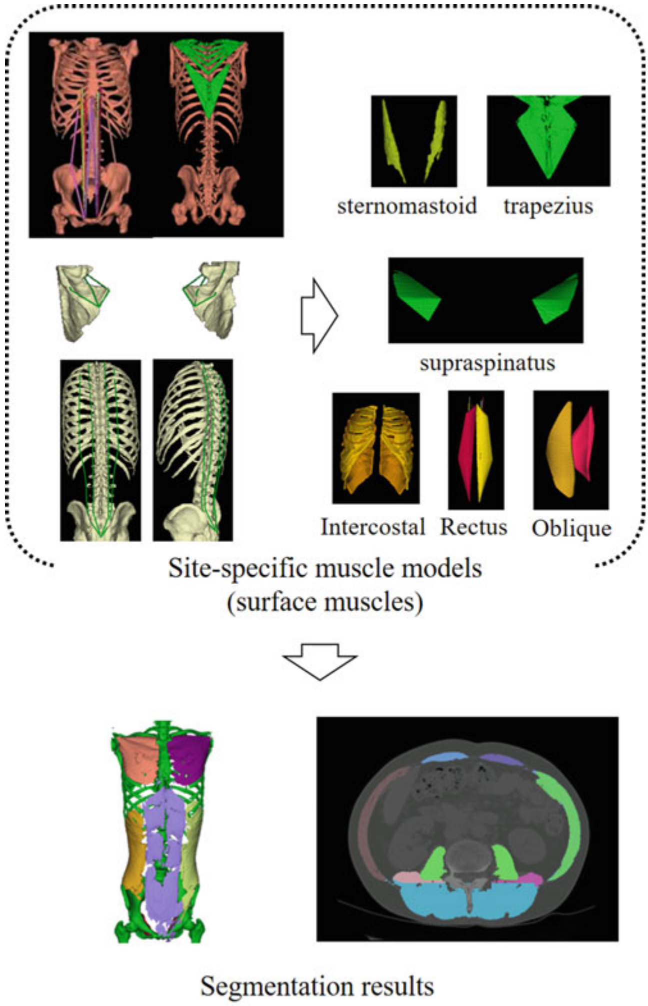

Fig. 7.3 Segmentation of surface muscles based on computational anatomy model

Thus, skeletal muscle segmentation using a deep learning, despite ten cases and very little training images, the streak across difficult extensive creation of a conventional shape model, and a high matching rate without special tuning it, was obtained. For example, Fig. 7.6 shows a very noisy case, showing a small difference in contrast between skeletal muscle and other tissues. Blue is the correct region, yellow is the over-extracted, and red is the unextracted region. Although skeletal muscle segmentation by deep learning has just begun, it can be thought of as a powerful method of muscle segmentation. In the next section, we will also refer to the future development of skeletal muscle segmentation using deep learning.

7.1.3 Futures on the Skeletal Muscle Segmentation

Finally, we describe our recent skeletal muscle segmentation approach. Of course, as already mentioned, it goes without saying that the method using machine learning will be further adopted in the future. However, considering a clinical application, segmentation of skeletal muscle needs to be considered from two aspects.

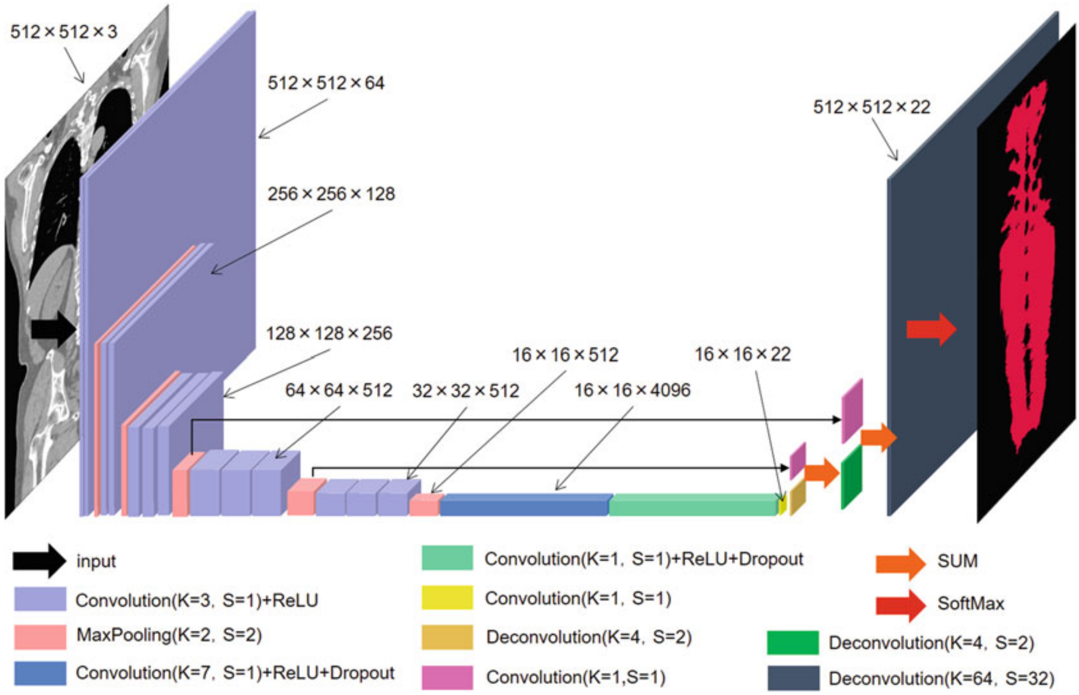

Fig. 7.4 Architecture of erector spinae muscles segmentation based on deep CNN (K, kernel size; S, stride)

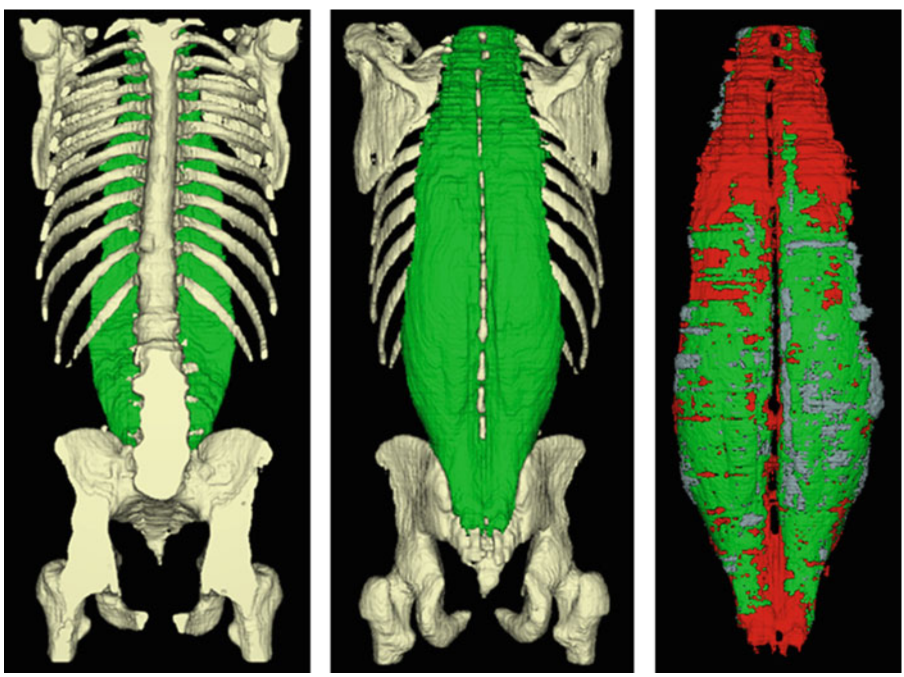

Fig. 7.5 Segmentation result of the erector spinae muscles using deep CNN (left, anterior side; center, dorsal side; right, evaluation result (red, over-extracted; blue, unextracted; green, matched))

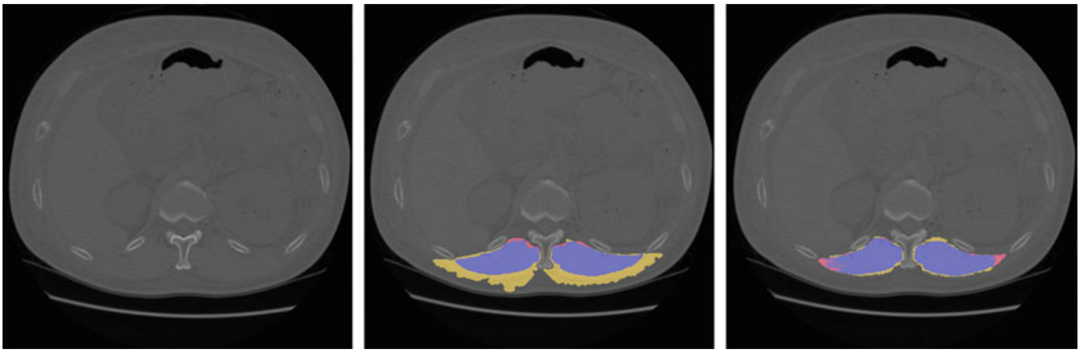

Fig. 7.6 Skeletal muscle recognition using deep learning in cases where skeletal muscle boundary is unclear (left, original CT; center, model-based method; right, deep CNN-based method (blue, matched; red, unextracted; yellow, over-extracted))

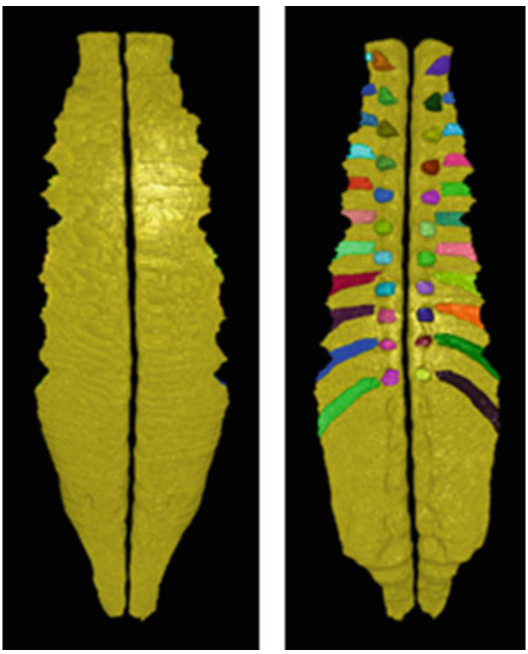

Fig. 7.7 Origin and insertion on the erector spinae muscle

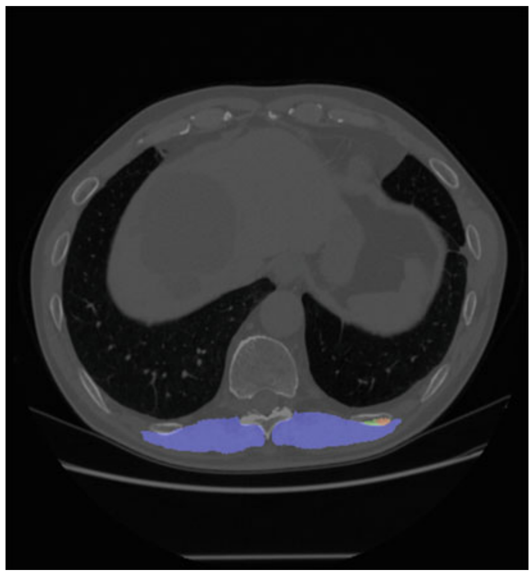

Fig. 7.8 Recognition results with origin and insertion on the erector spinae muscle

One is when skeletal muscle segmentation itself has to mean. In other words, to perform surgical assistance or mechanical intervention, it is sufficiently valuable to accurately obtain the segmentation area. Secondly, in the rehabilitation area and sports medicine, it must be able to express and explain exactly the relationship between the origin and insertion of skeletal muscle and bone and skeletal muscle. Therefore, we worked on a method to simultaneously present muscle region and origin/insertion information to segmentation result by learning not only segmentation result of skeletal muscle but also the anatomical correlation of skeletal muscle and bone in deep learning. Figure 7.7 shows the origin and insertion positions attached to the erector spinae muscles. Figure 7.8 shows a cross section of the result of learning on only the right side of Fig. 7.7. Compared to the contralateral side, it can be

Fig. 7.9 Segmentation results in whole-body CT images

confirmed that, in addition to the muscle recognition result, information on skeletal muscle and bone attachment part is also shown. As a result, in the segmentation of skeletal muscle in deep learning, there is the possibility that origin and insertion information important to the anatomy of skeletal muscle, which is information that cannot be obtained by the conventional model-based method, can be recognized at once. This result can be applied to the rehabilitation of skeletal muscle segmentation using deep learning and is applicable to sports medicine.

We also performed skeletal muscle segmentation using whole-body CT images [6, 13] to measure the muscle volume of the skeletal muscle region of the whole body excluding the body cavity region. Figure 7.9 shows the results of automatic recognition of skeletal muscle in whole-body CT images.

Whole-body CT images are used as part of the diagnosis of amyotrophic lateral sclerosis, which is an intractable disease. Therefore, we use the segmentation result of skeletal muscle to analyze the difference of skeletal muscle features in amyotrophic lateral sclerosis cases and diseases accompanied by other muscular atrophy cases [14]. At present, we analyze the left and right difference of recognized muscle and texture analysis. Figure 7.10 shows an example of segmental analysis of skeletal muscle on the whole-body CT image recognized in Fig. 7.9. We segmented the whole body into 22 areas and analyzed whether there is a difference in texture features between ALS cases and other muscle disease groups with atrophy. Using 36 cases, the initial result that there are differences between ALS and other atrophic myopathies in five texture features (information measures of correlation 2, contrast, inverse difference moment,

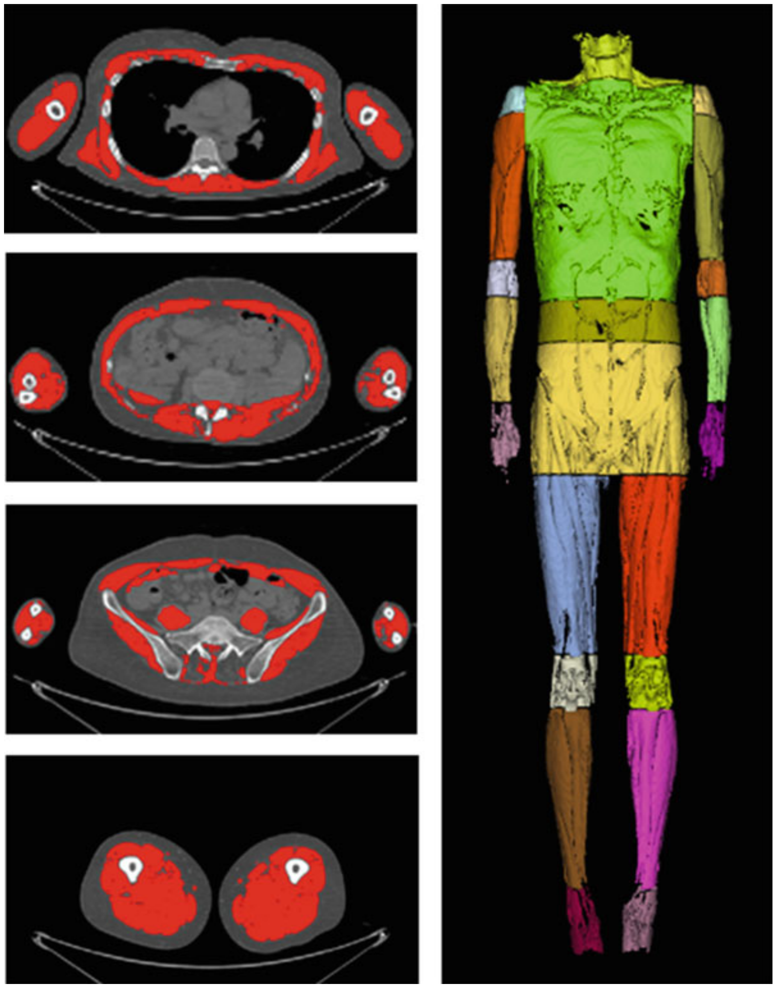

Fig. 7.10 Segmental analysis of the skeletal muscle in whole-body CT images

correlation, difference variance) was obtained. Figure 7.11 shows the difference between the feature quantities of the ALS group and the muscle atrophy group of the texture feature quantity IMC2 in the upper arm. The result is that the number of cases is still small and it is necessary to further analyze the disease group such as neurogenic diseases and myogenic diseases. However, it is suggested that image feature analysis using skeletal muscle segmentation results may be one candidate for discrimination of diseases between atrophic myopathies.

7.1.4 Conclusion

As described above, here we show our research on surface muscle and deep muscle for skeletal muscle segmentation for orthopedic intervention. The features based on the computational anatomy model and the deep learning-based method are shown, and selection of each method is required depending on the target muscle at orthopedic intervention. From now on, it is expected that it will be advanced from both the computational anatomical model and the deep learning, and at the same time, it will be expected to add a differentiation of intractable diseases as one of the clinical applications of the skeletal muscle segmentation.

Acknowledgments This work was supported in part by a JSPS Grant-in-Aid for Scientific Research on Innovative Areas (Multidisciplinary Computational Anatomy, #26108005 and # 17H05301) and a JSPS Grant-in-Aid for Young Scientists (B) (#15K21588) and for Challenging Exploratory Research (#16K15346), JAPAN.

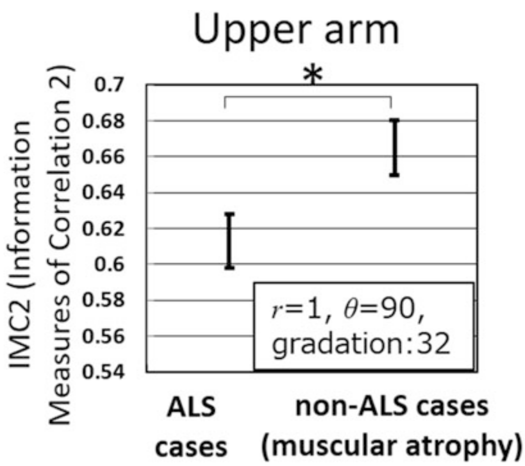

Fig. 7.11 Result of texture feature analysis in upper limb using segmented muscle regions

References

1. Kobatake H, Masutani Y et al (2017) Computational anatomy based on whole body imaging: basic principles of computer-assisted diagnosis and therapy, Springer. https://www.springer.com/us/book/9784431559740
2. Fujita H, Hara T, Zhou X et al (2014) Model construction for computational anatomy: progress overview FY2009-FY2013. In: Proceeding of the fifth international symposium on the project "Computational Anatomy", pp 25–35. http://www.fjt.info.gifu-u.ac.jp/publication/803.pdf
3. Hanaoka S, Kamiya N, Sato Y et al (2017) Skeletal muscle, understanding medical images based on computational anatomy models, pp 165–171, Springer. https://link.springer.com/chapter/10.1007/978-4-431-55976-4_3
4. Fujita H, Hara T, Zhou X et al (2015) Function integrated diagnostic assistance based on multidisciplinary computational anatomy – plan of five years and progress overview FY2014 -. In: Proceeding of the first international symposium on the project "Multidisciplinary Computational Anatomy", pp 45–51
5. Fujita H, Hara T, Zhou X et al (2016) Function integrated diagnostic assistance based on multidisciplinary computational anatomy models -Progress overview FY 2015-. In: Proceeding of the second international symposium on the project "Multidisciplinary Computational Anatomy", pp 91–101
6. Fujita H, Hara T, Zhou X et al (2017) Function integrated diagnostic assistance based on multidisciplinary computational anatomy models. In: Proceeding of the third international symposium on the project "Multidisciplinary Computational Anatomy", pp 95–105
7. Kamiya N, Zhou X, Chen H et al (2012) Automated segmentation of psoas major muscle in X-ray CT images by use of a shape model: preliminary study. Radiol Phys Technol 5(1):5–14
8. Kamiya N, Zhou X, Azuma K et al (2016) Automated recognition of the iliac muscle and modeling of muscle fiber direction in torso CT images. In: Proceeding of SPIE medical imaging 2016, Computer-Aided Diagnosis, 9785, 97853K-97853K-4, https://doi.org/10.1117/12.2214613
9. Zhou X, Takayama R, Wang S et al (2017) Deep learning of the sectional appearances of 3D CT images for anatomical structure segmentation based on an FCN voting method. Med Phys 44(10): 5221–5233
10. Kume M, Kamiya N, Zhou X et al (2017) Automatic recognition of erector spinae muscle in torso CT image and its possibility as prognostic predictor of COPD. In: Proceeding of the 9th annual meeting of Japanese Society of Pulmonary Functional Imaging, 47
11. Zhou X, Ito T, Takayama R et al (2016) Three-dimensional CT image segmentation by combining 2D fully convolutional network with 3D majority voting, proceeding of workshop on the 2nd Deep Learning in Medical Image Analysis (DLMIA) in MICCAI 2016. LNCS 10008: 111–120
12. Zhou X, Takayama R, Wang S et al (2017) Deep learning of the sectional appearances of 3D CT images for anatomical structure segmentation based on an FCN voting method. Med Phys 44(10): 5221–5233
13. Kamiya N, Ieda K, Zhou X et al (2017) Automated analysis of whole skeletal muscle for muscular atrophy detection of ALS in whole-body CT images: preliminary study, Proc. of SPIE Medical Imaging 2017, Computer-Aided Diagnosis, 10134, 1013442-1-1013442-6. https://doi.org/10.1117/12.2251584
14. Kamiya N, Asano E, Zhou X et al (2017) Segmental recognition of skeletal muscle in whole-body CT images and its texture analysis using skeletal muscle models. Int J Comput Assist Radiol Surg 12(1): S275

8 3X-Knee: A Novel Technology for 3D Preoperative Planning and Postoperative Evaluation of TKA Based on 2D X-Rays

Guoyan Zheng, Alper Alcoltekin, Benedikt Thelen, and Lutz-P. Nolte

Abstract

This chapter introduces a solution called ”3X-knee” that can robustly derive 3D models of the lower extremity from 2D long leg standing X-ray radiographs for preoperative planning and postoperative treatment evaluation of total knee arthroplasty (TKA). There are three core components in 3X-knee technology: (1) a knee joint immobilization apparatus, (2) an X-ray image calibration phantom, and (3) a statistical shape model-based 2D-3D reconstruction algorithm. These three components are integrated in a systematic way in 3X-knee to derive 3D models of the complete lower extremity from 2D long leg standing X-ray radiographs acquired in weight-bearing position. More specifically, the knee joint immobilization apparatus will be used to rigidly fix the X-ray calibration phantom with respect to the underlying anatomy during the image acquisition. The calibration phantom then serves two purposes. For one side, the phantom will allow one to calibrate the projection parameters of any acquired X-ray image. For the other side, the phantom also allows one to track positions of multiple X-ray images of the underlying anatomy without using any additional positional tracker, which is a prerequisite condition for the third component to compute patient-specific 3D models from 2D X-ray images and the associated statistical shape models. Validation studies conducted on both simulated X-ray images and on patients' X-ray data demonstrate the efficacy of the present solution.

G. Zheng (✉) · A. Alcoltekin · B. Thelen · L.-P. Nolte
Institute for Surgical Technology and Biomechanics, University of Bern, Bern, Switzerland
e-mail: guoyan.zheng@istb.unibe.ch

Keywords

Total knee arthroplasty (TKA) · Planning · Treatment evaluation · 2D-3D reconstruction · X-ray image calibration · Statistical shape model

8.1 Introduction

Total knee arthroplasty (TKA) is regarded as one of the most successful orthopedic procedures [1, 2]. TKA can relieve pain and improve knee function. The reported survival rates are greater than 90% after 15 years [1,2]. Although there are many factors influencing the success of TKA, it is generally agreed that it is important to choose appropriate sizes of the femoral and tibial components and to position them accurately. Thus, it is important to develop new technologies to

G. Zheng et al. (eds.), *Intelligent Orthopaedics*, Advances in Experimental Medicine and Biology 1093, https://doi.org/10.1007/978-981-13-1396-7_8

plan TKA precisely and to measure the outcome accurately.

The importance of preoperative planning should not be underestimated. Successful preoperative planning can prevent the use of undersized and oversized knee implants, while inadequate preoperative planning may lead to various complications including aseptic loosening, instability, polyethylene wear, and dislocation of the patella [3]. Radiographs are usually used for preoperative planning in TKA. More specifically, a full-length anteroposterior (AP) radiograph is used to determine the mechanical and anatomical axes, and lateral radiographs are used to define component sizes and the anatomical axis. In order to measure the rational alignment, 2D CT slice-based approaches were developed [4], where the rotational alignment of the femoral component is determined by measuring the angle between the transepicondylar axis and the posterior condylar line. These 2D approaches have the advantages that they are useful and do not require much time or special techniques. Additionally, preoperative planning also provides the surgeon with a tool to ascertain that the correct prosthetic component sizes are available and can be of assistance in logistic and stock management for the operating theaters.

In the past, both digital and analogue radiography-based preoperative planning systems have been introduced into the market. However, the reported accuracy for these systems varies. Kobayashi et al. [5] conducted a study to compare the accuracy of preoperative templating in TKA using conventional 2D and CT-based 3D procedures. They found that the 3D procedure was more accurate (59%) than the 2D procedure (56%) in predicting implant size, but the difference was not statistically significant. Trickett et al. [6] investigated the reliability and accuracy of digital templating in THA and reported an accuracy of 48% for predicting the size of femoral component and an accuracy of 55% in predicting the size of tibial component. Recently, Ettinger et al. [7] conducted another study to compare 2D versus 3D templating in TKA of 94 patients. They reported that the femoral and tibial 2D digital templating in predicting the correct implant size varied from 43.6% to 59.5% and 52.1% to 68% of the cases when three examiners with different experiences conducted the digital templating. Apart from the implant size, malrotation of femoral and/or tibial component is another important factors leading to revision of TKA. Okamoto et al. [8] reported that 2D planning could result in internal rotation of the femoral component in TKA. The significant differences between 2D and 3D techniques are attributed to the following factors: (1) measurement using radiographs are affected by limb position and deformities as well as radiograph magnification and (b) 2D CT slices are affected by the orientation of the patient's legs during the scan.

In comparison with 2D planning, CT-based 3D planning of TKA offers several advantages [5, 7–9] such as avoiding errors resulting from magnification and incorrect patient positioning, providing true 3D depiction of the underlying anatomy, and offering accurate information on bone quality. Several studies have demonstrated that 3D CT-based preoperative planning of TKA are more accurate than 2D radiograph-based preoperative planning [7–9].

The situation for the postoperative measurements remains the same. AP and lateral-medial (LM) weight-bearing long leg standing radiographs are frequently used to measure prosthesis alignment after TKA. AP long leg standing radiograph are usually used to assess the valgus/varus alignment in the coronal plane while the assessment of flexion/extension alignment is conducted in the LM long leg standing radiograph, though the measured values are subject to rotation and magnification errors [10]. Thus, the spatial positioning of a TKA component can only be precisely described with use of a 3D CT, where evaluating the position of the femoral component in reference to the femur (from the hip to the knee center) is separately done from the evaluation of the position of the tibial component in reference to the tibia (from the knee to the ankle center). For this purpose, special CT imaging protocols were developed [11, 12], which usually involve the acquisition of 3D CT volumes around hip, knee, and angle joints.

CT-/MRI-based approaches to derive three-dimensional (3D) models for preoperative planning and postoperative treatment evaluation of TKA, however, suffer from the disadvantages that they are expensive and/or induce high-radiation doses to the patient. An alternative is to reconstruct surface models from two-dimensional (2D) X-ray or C-arm images. Although single X-ray or C-arm image-based solutions have been presented before for certain specific applications [13, 14], it is generally agreed that in order to achieve an accurate surface model reconstruction, two or more images are needed. For this purpose, one has to solve three related problems, i.e., patient tracking/immobilization, image calibration, and 2D-3D reconstruction. Depending on the applications, different solutions have been presented before, which will be reviewed below.

Patient tracking/immobilization means to establish a coordinate system on the underlying anatomy and to co-register the acquired multiple images with respect to this common coordinate system. In the literature, both external positional tracker-based solutions and calibration phantom-based solutions have been introduced [15–20]. The methods in the former categories usually require a rigid fixation of the so-called dynamic reference base (DRB) onto the underlying anatomy, whose position can be tracked in real time by using an external positional tracker [15–17]. In contrast, the methods in the latter categories eliminate the requirement of using an external positional tracker [18–20]. In such a method, the calibration phantom itself acts as a positional tracker, which requires the maintenance of a rigid relationship between the calibration phantom and the underlying anatomy during image acquisition. Although not mentioned in the context of 2D-3D reconstruction, immobilization solutions [21, 22] have been developed before to maintain such a rigid fixation.

The second related problem is image calibration, which means to determine the intrinsic and extrinsic parameters of an acquired image. The image is usually calibrated with respect to the common coordinate system established on the underlying anatomy. When an external positional tracker is used, this means the coordinate system established on the DRB [15–17]. When a calibration phantom acts as a positional tracker, this usually means a coordinate system established on the phantom itself [18, 20]. Another issue is how to model the X-ray projection, which determines the way how the imaging parameters are calculated. No matter what kind of model is used, a prerequisite condition before the imaging parameters can be calculated is to establish correspondences between the 3D fiducials on the calibration phantom and their associated 2D projections.

The third problem is related with the methods used to compute 3D models from 2D-calibrated X-ray images. The available techniques can be divided into two categories: those based on one generic model [23, 24] and those based on statistical shape and/or appearance models (SSM) [25–28]. The methods in the former categories derive a patient-specific 3D model by deforming a generic model while the SSM-based methods use a SSM to produce only the statistically likely types of models and to reduce the number of parameters to optimize. Hybrid methods, which combine the SSM-based methods with the generic model-based methods, have also been introduced. For example, Zheng et al. [29] presented a method that combines SSM-based instantiation with thin-plate spline-based deformation.

The contribution of this chapter is a novel technology called ”3X-knee” that can robustly derive 3D models of the lower extremity from 2D long leg standing X-ray radiographs. We are aiming to develop a solution that will address all three problems as we mentioned above. 3X-knee, as an integrated solution, consists of three core components: (1) a knee joint immobilization apparatus, (2) an X-ray image calibration phantom, and (3) a statistical shape model-based 2D-3D reconstruction algorithm. These three components are integrated in a systematic way in 3X-knee to derive 3D models of the complete lower extremity from 2D long leg standing X-ray radiographs acquired in weight-bearing position. More specifically, the knee joint immobilization apparatus will be used to rigidly fix the X-ray calibration phantom with respect to the underlying anatomy during the image acquisition. The calibration phantom then serves for two purposes. For one side, the phantom will allow one to calibrate the projection parameters of any acquired X-ray image. For the other side, the phantom also allows one to track positions of multiple X-ray images of the underlying anatomy without using any additional positional tracker, which is a prerequisite condition for the third component to compute patient-specific 3D models from 2D X-ray images and the associated statistical shape models.

The chapter is organized as follows. Section 8.2 presents the materials and methods. Section 8.3 describes the experimental results, followed by discussions and conclusions in Sect. 8.4.

8.2 Material and Methods

A schematic view of the complete pipeline of the present method is shown in Fig. 8.1. It starts with the immobilization of the image calibration phantom with respect to the underlying anatomy (both femur and tibia), followed by patient tracking and calibration of each acquired image, and ended by computing patient-specific 3D models from the calibration X-ray images. Below a detailed description about each component will be given.

8.2.1 Immobilization

It is important to maintain the rigid relationship between the calibration phantom and the underlying anatomy. Without such a fixed relationship, the relative movement between the calibration phantom and the underlying anatomy will lead to inconsistent correspondences between the projections of the same anatomical features in different images such that a reconstruction of the 3D models of the underlying anatomy will not be able to achieve. When multiple anatomical structures around a joint are involved, such as the situation when one would like to derive 3D models of the complete extremity, all the involved

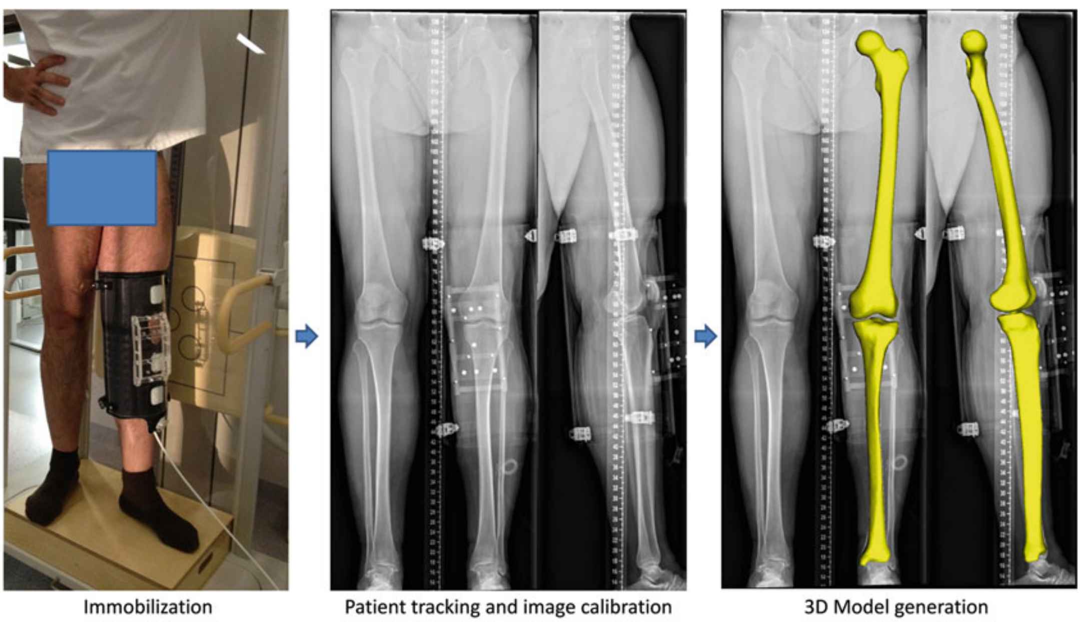

Fig. 8.1 A schematic view of the present invention. From left to right: immobilization, patient tracking and image calibration, and 3D model generation

Fig. 8.2 The immobilization device when applied to the knee joint. It is a two-layer construction with force enhancement mechanism

anatomical structures around a joint have to be maintained rigidly with respect to the image calibration phantom throughout the complete image acquisition procedure. Thus, due to the mobility of a joint, the conventional way of using a belt or a jacket to fix the calibration phantom to a patient cannot guarantee no relative movement between the calibration jacket and the underlying anatomy during the image acquisition.

In this paper we developed a new way of immobilizing all the involved anatomical structures as well as the calibration phantom. Our immobilization device is a two-layer construction. See Fig. 8.2 for a prototype. The inner layer comprises a bag filled with a granular material with an encapsulated shell to which the bag is mounted. Furthermore, between the encapsulated shell and the bag, a hollow space is formed for receiving pressured air in order to produce a force on the bag to immobilize a knee joint. The inner layer is then further enhanced with the introduction of an outer layer of hard shell which can add further force to the inner layer fixation with four force enhancement clips, a mechanism that has been widely used in designing ski boots. A second purpose of the outer layer of hard shell is to rigidly carry the image calibration phantom such that all the involved underlying anatomical structures can be maintained rigidly with respect to the calibration phantom.

8.2.2 Patient Tracking and Image Calibration

The aim of the X-ray image calibration is to compute both the intrinsic and the extrinsic parameters of an acquired image. This is achieved by developing a mobile phantom as shown in Fig. 8.3. There is a total of 16 sphere-shaped fiducials embedded in this phantom: 7 big fiducials with diameter of 8.0 mm and 9 small fiducials with diameter of 5.0 mm. The 16 fiducials are arranged in three different planes: all 7 big fiducials are placed in one plane and the rest 9 small fiducials distributed in other two planes. Furthermore, the seven big fiducials are arranged to form three line patterns as shown in Fig. 8.3,

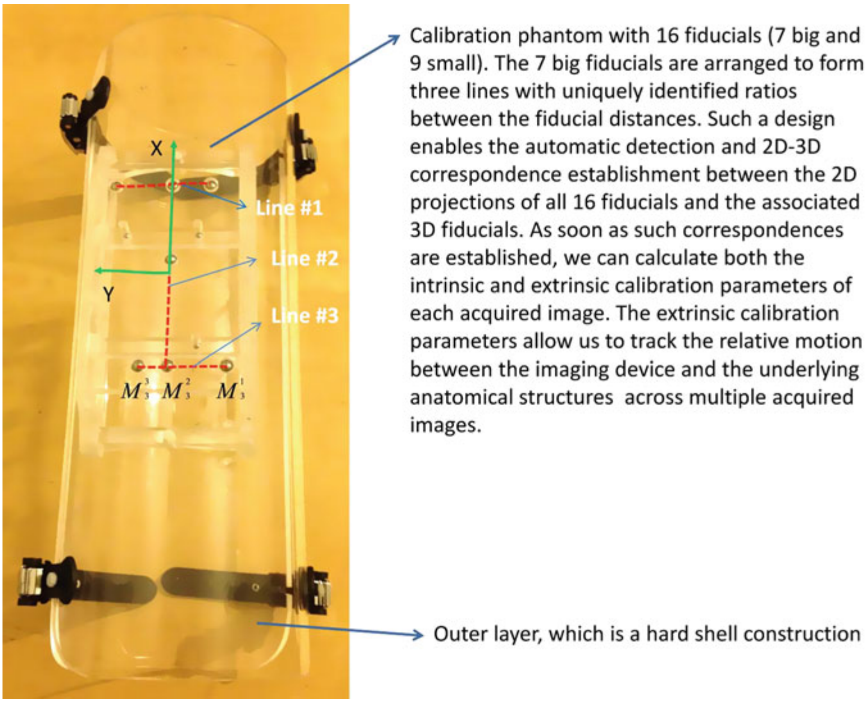

Fig. 8.3 The calibration phantom attached on the outer layer of our immobilization device. The calibration phantom is designed for both patient tracking and image calibration

left. Every line pattern consists of three fiducials $\{M_i^1, M_i^2, M_i^3\}, i = 1, 2, 3$ with different ratios $\{r_i = |M_i^1 M_i^2|/|M_i^2 M_i^3|\}$. The exact ratio for each line is used below to identify which line pattern has been successfully detected.

After an X-ray image is acquired, we first extract the subregion containing the phantom projection. We then apply a sequence of image processing operations to the image. As those fiducials are made from steel, a simple threshold-based method is first used to segment the image. Connected component labeling is then applied to the binary image to extract a set of separated regions. Morphology analysis is further applied to each label connected component to extract two types of regions: candidate regions from big fiducial projections and candidate regions from small fiducial projections. The centers of these candidate regions are regarded as projections of the center of a potential fiducial. Due to background clutter, it is possible that some of the candidate projections are outliers and that we may miss some of the true fiducial projections. Furthermore, to calculate both the intrinsic and the extrinsic parameters, we have to detect the phantom in the image. Here phantom detection means to establish the correspondences between the detected 2D fiducial projection centers and their associated 3D coordinates in the local coordinate system of the phantom. For this purpose, a robust simulation-based method as follows is proposed. The precondition to use this method to build the correspondences is that one of the three line patterns has been successfully detected. Due to the fact that these line patterns are defined by big fiducials, chance of missing all three line patterns is rare.

We model the X-ray projection using a pinhole camera.

$$\alpha[I_x, I_y, 1]^T = \mathbf{K}(\mathbf{R}[x, y, z]^T + \mathbf{T}) = \mathbf{P}[x, y, z, 1]^T \tag{8.1}$$

where α is the scaling factor, $\mathbf{K}$ is the intrinsic calibration matrix, and $\mathbf{R}$ and $\mathbf{T}$ are the extrinsic rotation matrix and translational vector, respectively. Both the intrinsic and the extrinsic projection parameters can be combined into a 3-by-4 projection matrix $\mathbf{P}$ in the local coordinate system established on the mobile phantom.

The idea behind the simulation-based method is to do a pre-calibration to compute both the intrinsic matrix $\mathbf{K}$ and the extrinsic parameters $\mathbf{R}_0$ and $\mathbf{T}_0$ of the X-ray image acquired in a reference position. Then, assuming that the intrinsic matrix $\mathbf{K}$ is not changed from one image to another (we only use this assumption for building the correspondences), the projection of an X-ray image acquired at any other position with respect to the phantom can be expressed as

$$\alpha[I_x, I_y, 1]^T = \mathbf{K}(\mathbf{R}_0(\mathbf{R}^x\mathbf{R}^y\mathbf{R}^z[x, y, z]^T + \mathbf{T}) + \mathbf{T}_0) \tag{8.2}$$

where $\mathbf{R}^x$, $\mathbf{R}^y$, $\mathbf{R}^z$, and $\mathbf{T}$ are the rotation matrices around three axes (assuming the z-axis is in parallel with the view direction of the calibration phantom at the reference position, see the middle column of Fig. 8.3 for details) and the translation vector from an arbitrary acquisition position to the reference position, respectively, expressed in the local coordinate of the mobile phantom. To detect the phantom projection when an image is acquired in a new position, the simulation-based method consists of two steps.

Image normalization The purpose of this step is to remove the influence of the parameters $\mathbf{R}^z$, α, and $\mathbf{T}$ on the phantom detection by normalizing the image acquired at the new position as follows. Assuming that we know the correspondences of fiducials on one line pattern, which is defined by three landmarks M_1, M_2, and M_3 with their correspondent projections at IM_1, IM_2, and IM_3, we can define a 2D coordinate system based on IM_1, IM_2, and IM_3, whose origin O is located at $(IM_1 + IM_2)/2$ and the x-axis is defined along the direction $O \rightarrow IM_3$. Accordingly a 2D affine transformation $T_{\text{normalize}}$ can be computed to transform this line pattern-based coordinate system to a standard 2D coordinate system with its origin at (0, 0) and x-axis along direction (1, 0) and at the same time to normalize the length of the vector $IM_1 \rightarrow IM_3$ to 1. By applying $T_{\text{normalize}}$ to all the fiducial projections, it can be observed that for a pair of fixed $\mathbf{R}^x$ and $\mathbf{R}^y$, we can get the same normalized image no matter how the other parameters $\mathbf{R}^z$, α, and $\mathbf{T}$ are changed because the influence of these parameters is just to translate, rotate, and scale the fiducial projections, which can be compensated by the normalization operation. Therefore, the fiducial projections after the normalization will only depend on the rotational matrices $\mathbf{R}^x$ and $\mathbf{R}^y$.

Normalized image-based correspondence establishment Since the distribution of the fiducial projections in the normalized image only depends on the rotation matrices $\mathbf{R}^x$ and $\mathbf{R}^y$, it is natural to build a look-up table which up to a certain precision (e.g., 1°) contains all the normalized fiducial projections with different combination of $\mathbf{R}^x$ and $\mathbf{R}^y$. This is done off-line by simulating the projection operation using Eq. (8.1) based on the pre-calibrated projection model of the X-ray machine at the reference position. For an image acquired at position other than the reference, we apply the normalization operation as described above to all the detected candidate fiducial projections. The normalized candidate fiducial projections are then compared to those in the look-up table to find the best match. Since the items in the look-up table are generated by a simulation procedure, we know exactly the correspondence between the 2D fiducial projections and their corresponding 3D coordinates. Therefore, we can establish the correspondences between the candidate fiducial projections and the fiducials embedded in the phantom.

Once the correspondences are established, we can further fine-tune the fiducial projection location by applying a cross-correlation-based template matching. After that, the direct linear transformation algorithm [30] is used to compute the projection matrix $\mathbf{P}$.

8.2.3 2D-3D Reconstruction

After image calibration, we independently match the femoral and the tibial SSMs with the input X-ray images. The 2D-3D reconstruction algorithm as introduced in [29] is used for reconstructing both femoral and tibial models.

8.3 Experimental Setup

After local institution review board (IRB) approval, we conducted two studies to validate the efficacy of the present method, with one based on simulated X-ray images and the other based on clinical X-ray images.

CT data of 12 cadavers (24 legs) were used in the first study. For each leg, two digitally reconstructed radiographs (DRRs), one from the anteroposterior (AP) direction and the other from the later-medial (LM) direction, were generated and used as the input to the iLeg software. In generating the DRRs, we set the distance from the focal point to film as 2000 mm and the pixel resolution in the range of 0.20 to 0.25 mm. The purpose of the first study was designed to validate the accuracy of the 2D-3D reconstruction algorithm when applied to reconstruction of 3D models of the complete lower extremity. Thus, for each leg, the two DRRs were used as the input to the 2D-3D reconstruction algorithm to derive patient-specific 3D models of the leg. In order to evaluate the 2D-3D reconstruction accuracy, we conducted a semiautomatic segmentation of all CT data using the commercial software Amira (Amira 5.2, FEI Corporate, Oregon, USA). The reconstructed surface models of each leg were then compared with the surface models segmented from the associated CT data. Since the DRRs were generated from the associated CT data, the surface models were reconstructed in the local coordinate system of the CT data. Thus, we can directly compare the reconstructed surface models with the surface models segmented from the associated CT data, which we took as the ground truth. Again, we used the software Amira to compute distances from each vertex on the reconstructed surface models to the associated ground truth models.

The full leg 2D-3D reconstruction validation results of 24 legs are shown in Table 8.1. When the reconstructed models were compared with the surface models segmented from the associated CT data, a mean reconstruction accuracy of 1.07 ± 0.19, 1.05 ± 0.23, 1.07 ± 0.21, and 1.07 ± 0.19 mm was found for left femur, right femur, left tibia, and right tibia, respectively. When looking into the reconstruction of each subject, we found an average reconstruction accuracy in the range of 0.8 to 1.3 mm. Overall, the reconstruction accuracy was found to be 1.06 ± 0.20 mm. Figure 8.4 shows an example of comparison of reconstructed surface models (gray solid) with the surface models segmented from the associated CT data (red transparent).

The second study was evaluated on 23 patients for preoperative planning. All the patients under-

Table 8.1 Full leg 2D-3D reconstruction accuracy (mm)

	Femur		Tibia		
Subject	Left	Right	Left	Right	Average
#1	1.5	1.2	1.1	1.1	1.2
#2	1.0	1.0	1.0	0.9	1.0
#3	0.9	0.8	1.1	0.8	0.9
#4	1.2	1.3	1.1	1.2	1.2
#5	1.2	1.4	0.7	0.9	1.1
#6	1.0	1.1	1.4	1.2	1.2
#7	1.0	1.3	0.9	0.9	1.0
#8	1.0	0.9	0.8	1.0	0.9
#9	1.2	1.2	1.3	1.4	1.3
#10	1.1	0.9	1.3	1.3	1.2
#11	0.8	0.7	0.9	0.9	0.8
#12	0.9	0.8	1.2	1.2	1.0
Overall	1.1	1.1	1.1	1.1	1.06 ± 0.20

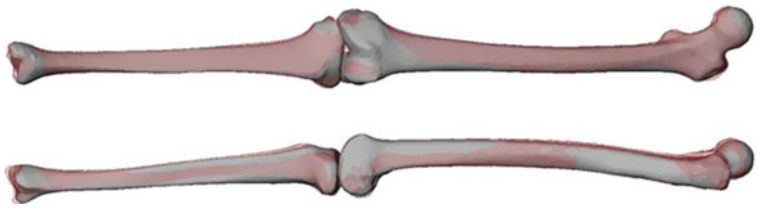

Fig. 8.4 Comparison of reconstructed surface models (gray solid) with the surface models segmented from the associated CT data (red transparent). Top, AP view; bottom, LM view

Table 8.2 Absolute differences between preoperative planning parameters measured from 3D CT-based method and 3X technique

Femoral parameters	3D CT	3X	Differences
AMA (°)	5.73 (3.65–7.72)	5.84 (3.66–8.30)	0.24 ± 0.19
NSA (°)	123.98 (113.38–135.05)	125.41 (118.4–136.3)	1.98 ± 1.85
mLDFA (°)	93.19 (85.54–99.87)	92.84 (83.13–98.99)	0.91 ± 0.89
Tibial parameters	3D CT	3X	Differences
MPTA (°)	89.01 (84.49–92.22)	87.82 (84.91–94.81)	2.62 ± 1.68
Slope (°)	91.52 (84.13–98.46)	92.80 (87.91–96.79)	2.86 ± 2.08

went a CT scan according to a standard protocol [31]. Image acquisition consisted of three separate short spiral axial scans: (1) ipsilateral hip joint, (2) affected knee joint, and (3) ipsilateral ankle joint. Additionally, two long leg standing X-ray images were acquired for each affected leg and were used as the input to 3X technology to derive patient-specific models of the leg. Corresponding morphological parameters measured from 3D CT data were regarded as the ground truth in order to evaluate the accuracy of 3X technology. The following morphological parameters which are important for planning femoral component are measured: (a) anatomical-mechanical angle (AMA), which is defined as the angle between the anatomic and mechanical axis; (b) neck-shaft angle (NSA), which is defined as the medial angle between the shaft axis and the neck axis; and (c) mechanical lateral distal femoral angle (mLDFA), which is defined as the lateral angle between the anatomical axis and the distal femoral knee joint orientation line. Similarly, we measured the following morphological parameters for planning tibial components:

(a) Medial proximal tibial angle (MPTA), which is defined as the medial angle between the mechanical axis and the proximal tibial knee orientation line. The mechanical axis is created with tibial plateau center and the distal tibia center while the proximal tibial knee orientation line is the line which intersects medical and lateral tibial plateau.
(b) Posterior tibial slope, which is defined as the posterior angle between the mechanical axis and the medial plateau axis. Table 8.2 shows the differences between preoperative planning angular parameters measured from 3D CT-based method and 3X technique. Absolute differences for all angular parameters are smaller than 3°, which is regarded accurate enough for clinical applications [32].

It was found that the immobilization device mounting time ranged from 1 to 5 min and there was no device loosing. All 2D-3D reconstructions were successful. Figure 8.5 shows a reconstruction example.

8.4 Discussions and Conclusions

In this paper, we presented a novel technology called 3X-knee to address three challenges in deriving 3D patient-specific models of the lower extremity from 2D long leg standing X-ray radiographs, i.e., patient tracking/immobilization, image calibration, and 2D-3D reconstruction.

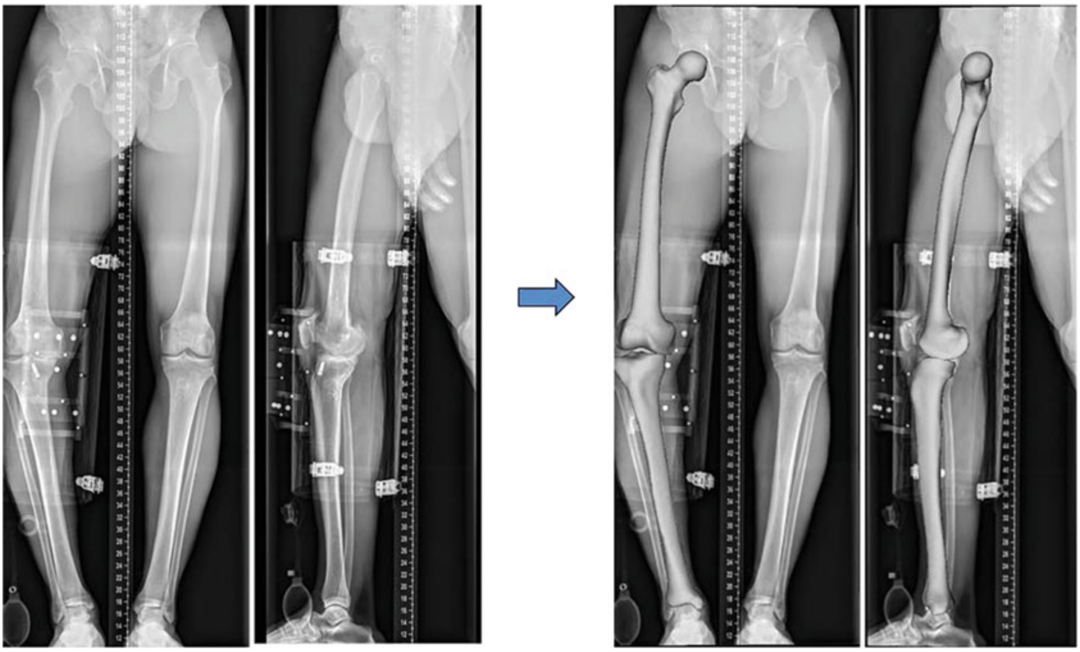

Fig. 8.5 An example of reconstructing patient-specific 3D models of the lower extremity from 2D X-ray images

Although there exist a large number of work addressing either one of the three problems, there is only few work targeting for solving all three problems. Chriet et al. [19] proposed to use a calibration jacket-based solution for the 3D reconstruction of the human spine and rib cage from biplanar X-ray images. However, only using a calibration jacket is hard to prevent the relative movement between the calibration jacket and the underlying anatomy during image acquisition. An alternative solution is to develop a specialized X-ray imaging device, as exemplified by the development of the EOS imaging system [33], where two images are simultaneously acquired, thus eliminating the requirement of patient tracking. However, due to the relative high acquisition and maintenance costs, the EOS imaging system at this moment is only available in a few big clinical centers and is not widely available.

Acknowledgements This chapter was modified from the paper published by our group in *the 7th International conference on Medical Imaging and Augmented Reality (MIAR 2016)* (Zheng et al., MIAR2016: 404–414). The related contents were reused with the permission.

References

1. Rodricks D, Patil S, Pulido P, Colwell C (2007) Press-fit condylar design total knee arthroplasty. fourteen to seventeen-year follow-up. J Bone Joint Surg Am 89:89–95
2. Vessely M, Whaley A, Harmsen W, Schleck C, Berry D (2006) The Chitranjan Ranawat award: long-term survivorship and failure modes of 1000 cemented condylar total knee arthroplasties. Clin Orthop Relat Res 452:28–34
3. Kim Y, Park J, Kim J, Park S (2014) The relationship between the survival of total knee arthroplasty and postoperative coronal, sagittal and rotational alignment of knee prosthesis. Int Ortho 38:379–385
4. Hirschmann M, Konala P, Amsler F, Iranpour F, Friederich N, Cobb J (2011) The position and orientation of total knee replacement components: a comparison of conventional radiographs, transverse 2D-CT slices and 3D-CT reconstruction. J Bone Joint Surg Br 93:629–633
5. Kobayashi A, Ishii Y, Takeda M, Noguchi H, Higuchi H, Toyabe S (2012) Comparison of analog 2D and digital 3D preoperative templating for predicting implant size in total knee arthroplasty. Comput Aided Surg 17:96–101
6. Trickett R, Hodgson P, Forster M, Robertson A (2009) The reliability and accuracy of digital templating in total knee replacement. J Bone Joint Surg Br 91(8):903–906

7. Ettinger M, Claassen L, Paes P, Calliess T (2016) 2D versus 3D templating in total knee arthroplasty. Knee 23:149–151
8. Okamoto S, Mizu-uchi H, Okazaki K, Hamai S, Tashiro Y, Nakahara H, Iwamoto Y (2016) Two-dimensional planning can result in internal rotation of the femoral component in total knee arthroplasty. Knee Surg Sports Traumatol Arthrosc 24:229–235
9. De Valk E, Noorduyn J, Mutsaerts E (2016) How to assess femoral and tibial component rotation after total knee arthroplasty with computed tomography: a systematic review. Knee Surg Sports Traumatol Arthrosc 24:3517–3528
10. Bäthis H, Perlick L, Tingart M, Lü ring C, Zurakowski D, Grifka J (2004) Alignment in total knee arthroplasty: a comparison of computer-assisted surgery with the conventional technique. J Bone Joint Surg Br 86:682–687
11. Henckel J, Richards R, Lozhkin K, Harris S, Rodriguez y Baena F, Barrett A, Cobb J (2006) Very low-dose computed tomography for planning and outcome measurement in knee replacement. The imperial knee protocol. J Bone Joint Surg Br 88:1513–1518
12. Matziolis G, Krocker D, Weiss U, Tohtz S, Perka C (2007) A prospective, randomized study of computer-assisted and conventional total knee arthroplasty. three-dimensional evaluation of implant alignment and rotation. J Bone Joint Surg Am 89:236–243
13. Novosad J, Cheriet F, Petit Y, Labelle H (2004) Three-dimensional 3-D reconstruction of the spine from a single x-ray image and prior vertebra models. IEEE Trans Biomed Eng 51(9):1628–1639
14. Zheng G (2000) Statistically deformable 2D/3D registration for estimating post-operative cup orientation from a single standard AP X-ray radiograph. Ann Biomed Eng 38(9):2910–2927
15. Yaniv Z, Joskowicz L, Simkin A, Garza-Jinich M, Milgrom C (1998) Fluoroscopic image processing for computer-aided orthopaedic surgery. In: Proceedings of the MICCAI 1998, pp 325–334
16. Hofstetter R, Slomczykowski M, Sati M, Nolte LP (1999) Fluoroscopy as an imaging means for computer-assisted surgical navigation. Comput Aided Surg 4(2):65–76
17. Livyatan H, YanivL Z, Joskowicz L (2002) Robust automatic C-Arm calibration for fluoroscopy-based navigation: a practical approach. In: Proceedings of the MICCAI 2002, pp 60–68
18. Jain A, Fichtinger G (2006) C-arm tracking and reconstruction without an external tracker. In: Proceedings of the MICCAI 2006, pp 494–502
19. Cheriet F, Laporte C, Kadoury S, Labelle H, Dansereau J (2007) A novel system for the 3-D reconstruction of the human spine and rib cage from biplanar X-ray images. IEEE Trans Biomed Eng 54(7):1356–1358
20. Schumann S, Dong X, Puls M, Nolte LP, Zheng G (2012) Calibration of C-arm for orthopedic interventions via statistical model-based distortion correction and robust phantom detection. In: Proceedings of the ISBI 2012, pp 1204–1207
21. Carter CR, Hicken GJ (2005) Device for immobilizing a patient and compressing a patient's skeleton, joints and spine during diagnostic procedures using an MRI unit, CT scan unit or x-ray unit. US Patent 6,860,272
22. Schmit BP, Keeton M, Babusis B (2005) Restraining apparatus and method for use in imaging procedures. US Patent 6,882,878
23. Mitton D, Landry C, Véron S, Skalli W, Lavaste F, De Guise JA (2000) 3D reconstruction method from biplanar radiography using non-stereocorresponding points and elastic deformable meshes. Med Biol Eng Comput 38(2):133–139
24. Yu W, Zheng G (2014) Personalized x-ray reconstruction of the proximal femur via a new control point-based 2D-3D registration and residual complexity minimization. VCBM 2014:155–162
25. Sadowsky O, Chintalapani G, Taylor RH (2007) Deformable 2D-3D registration of the pelvis with a limited field of view, using shape statistics. In: Proceedings of the MICCAI'07, pp 519–526
26. Ahmad O, Ramamurthi K, Wilson KE, Engelke K, Prince RL, Taylor RH (2010) Volumetric DXA (VXA) – a new method to extract 3D information from multiple in vivo DXA images. J Bone Miner Res 25:2468–2475
27. Baka N, Kaptein BL, de Bruijne M, van Walsum T, Giphart JE, Niessen WJ, Lelieveldt BP (2011) 2D-3D reconstruction of the distal femur from stereo X-ray imaging using statistical shape models. Med Image Anal 15:840–850
28. Zheng G (2011) Personalized X-ray reconstruction of the proximal femur via intensity-based non-rigid 2D-3D registration. MICCAI 2011, Part II. LNCS, vol 6982, pp 598–606
29. Zheng G, Gollmer S, Schumann S, Dong X, Feilkas T, González Ballester MA (2009) A 2D/3D correspondence building method for reconstruction of a patient-specific 3D bone surface model using point distribution models and calibrated X-ray images. Med Image Anal 13:883–899
30. Hartley R, Zisserman A (2004) Multiple view geometry in computer vision, 2nd edn. Cambridge University Press, Cambridge
31. Matziolis G, Krocker D, Weiss U, Tohtz S, Perka C (2007) A prospective, randomized study of computer-assisted and conventional total knee arthroplasty. Three-dimensional evaluation of implant alignment and rotation. J Bone Joint Surg Am 89: 236–243
32. Ettinger M, Claassen L, Paes P, Calliess T (2016) 2D versus 3D templating in total knee arthroplasty. Knee 23:149–151
33. Wybier M, Bossard P (2013) Musculoskeletal imaging in progress: the EOS imaging system. Joint Bone Spine 80(3):238–243

9 Atlas-Based 3D Intensity Volume Reconstruction from 2D Long Leg Standing X-Rays: Application to Hard and Soft Tissues in Lower Extremity

Weimin Yu and Guoyan Zheng

Abstract

In this chapter, the reconstruction of 3D intensity volumes of femur, tibia, and three muscles around the thigh region from a pair of calibrated X-ray images is addressed. We present an atlas-based 2D-3D intensity volume reconstruction approach by combining a 2D-2D nonrigid registration-based 3D landmark reconstruction procedure with an adaptive regularization step. More specifically, an atlas derived from the CT acquisition of a healthy lower extremity, together with the input calibrated X-ray images, is used to reconstruct those musculoskeletal structures. To avoid the potential penetration of the reconstructed femoral and tibial volumes that might be caused by reconstruction error, we come up with an articulated 2D-3D reconstruction strategy, which can effectively preserve knee joint structure. Another contribution from our work is the application of the proposed 2D-3D reconstruction pipeline to derive the patient-specific volumes of three thigh muscles around the thigh region.

W. Yu · G. Zheng (✉)
Institute for Surgical Technology and Biomechanics, University of Bern, Bern, Switzerland
e-mail: guoyan.zheng@istb.unibe.ch

Keywords

Atlas · Intensity volume · 2D-3D reconstruction · X-ray · Lower extremity · Soft tissue

9.1 Introduction

In order to reduce radiation exposure to patients, 2D-3D reconstruction, which can reconstruct 3D patient-specific models from 2D X-ray images, is proposed as an alternative to CT scan for certain applications. Depending on the output, those 2D-3D reconstruction methods can be generally classified into two categories [1]: 3D surface model reconstruction [2, 3] and 3D intensity volume reconstruction [4–7]. The methods in the former category compute 3D patient-specific surface models from one or multiple 2D X-ray images. No intensity information or information about cortical bone is available. The methods in the second category generate 3D patient-specific volumes from a limited number of X-ray images. Most of the previous work tried to solve the ill-posed problem of 2D-3D volume reconstruction by introducing different statistical prior models, while Yu et al. [7] firstly explored the potential of atlas-based 2D-3D intensity volume

G. Zheng et al. (eds.), *Intelligent Orthopaedics*, Advances in Experimental Medicine and Biology 1093, https://doi.org/10.1007/978-981-13-1396-7_9

reconstruction. To our knowledge, none of the above mentioned methods have been applied to reconstruct the intensity volumes of a complete lower extremity.

In this chapter we present an atlas-based 2D-3D intensity volume reconstruction approach which is an extension of the previous work [7], and we apply it to reconstruct 3D intensity volumes of femur, tibia, and three muscles around the thigh region from a pair of 2D X-ray images.

The remainder of the chapter is arranged as follows: the techniques of the proposed atlas-based 2D-3D reconstruction method will be described in Sect. 9.2. Section 9.3 will present the results of our validation experiments on several datasets, followed by the discussions and conclusions in Sect. 9.4.

9.2 Materials and Methods

9.2.1 Atlas Preparation

The atlas consists of the template volumes of femur and tibia as well as the template volumes of rectus femoris muscle, vastus lateralis and intermedius muscle, and vastus medialis muscle (if reconstructing these thigh muscles) which are segmented from the CT data of a healthy lower extremity. In addition, the atlas includes two sets of sparse 3D landmarks $\left(\left\{L_{\text{femur},n}\right\}_{n=1}^{N_1}\right.$ and $\left.\left\{L_{\text{tibia},n}\right\}_{n=1}^{N_2}\right)$ extracted from the outer surfaces and the intramedullary canal surfaces of the template volumes.

9.2.2 The 2D-3D Reconstruction Pipeline

The 2D-3D reconstruction process is aiming to fit the atlas to a pair of X-ray images, one acquired from the anterior-posterior (AP) direction and the other from an oblique view (not necessary the lateral-medial (LM) direction). Both images are calibrated and co-registered to a common coordinate system called **c**. A template volume $I(x)$ is aligned to the reference space **c** via a forward mapping: $I\left(x_c\left(T_g, T_d\right)\right) = I\left(T_g \circ T_d \circ x_f\right)$, where x_f is a point in the template space. Here, a global scaled-rigid transformation T_g and a local deformation T_d are to be determined via a 2D-3D scaled-rigid registration stage and a 2D-3D intensity volume reconstruction stage. Both stages are based on the procedure of 2D-2D nonrigid registration-based 3D landmark reconstruction.

The 2D-2D nonrigid registration-based 3D landmark reconstruction follows the previous work [7] which is organized in a hierarchical style: (1) DRR generation and 3D landmark projection, (2) nonrigid 2D-2D intensity-based registration, and (3) triangulation-based landmark reconstruction. Inspired by the work [2], 3D sparse landmarks instead of the B-spline control points used in the previous work are adapted.

Given the initial transformation of the template volumes to the common coordinate system **c** via landmark-based alignment, we can generate virtual 2D radiographic images and also project those 3D sparse landmarks. The nonrigid 2D deformation fields obtained from the registration module based on the registration library "elastix" [8] enable us to look for the dimensional correspondences represented by the paired 2D projected landmarks, and then new 3D sparse landmarks are reconstructed via triangulation.

9.2.2.1 2D-3D Scaled-Rigid Alignment

2D-3D scaled-rigid alignment is conducted via the paired-point matching between the reconstructed 3D landmarks and the original 3D landmarks in the atlas (see Fig. 9.1, left), and we iteratively compute $\left\{T_g^t\right\}_{t=1,2,3,...}$ in order to handle those complicated pose differences. The 2D-3D similarity alignment is applied to femur and tibia individually, and finally we can obtain two scaled-rigid transformations T_g^{femur} and T_g^{tibia}. Figure 9.1, right, shows an example of the 2D-3D scaled-rigid alignment which can handle large pose difference.

9.2.2.2 2D-3D Intensity Volume Reconstruction

2D-3D intensity volume reconstruction starts with the reconstructed 3D sparse landmarks

$\left(\left\{L'_{\text{femur},n}\right\}_{n=1}^{N_1}\text{ or }\left\{L'_{\text{tibia},n}\right\}_{n=1}^{N_2}\right)$ and the original 3D landmarks in the atlas $\left(\left\{L_{\text{femur},n}\right\}_{n=1}^{N_1}\text{ or }\left\{L_{\text{tibia},n}\right\}_{n=1}^{N_2}\right)$. Firstly, we transform these reconstructed landmarks back to thespace of the atlas with $T_g^{-1,\text{femur}}$ and $T_g^{-1,\text{tibia}}$, and then two local deformations T_l^{femur} and T_l^{tibia} can be computed using 3D thin-plate-spline transformation as follows:

$$\begin{cases} T_l^{\text{femur}} \leftarrow T_{TPS}\left(\left\{L_{\text{femur},n}\right\}_{n=1}^{N_1}, \left\{T_g^{-1,\text{femur}} \circ L'_{\text{femur},n}\right\}_{n=1}^{N_1}\right) \\ T_l^{\text{tibia}} \leftarrow T_{TPS}\left(\left\{L_{\text{tibia},n}\right\}_{n=1}^{N_2}, \left\{T_g^{-1,\text{tibia}} \circ L'_{\text{tibia},n}\right\}_{n=1}^{N_2}\right) \end{cases} \tag{9.1}$$

Notice that the obtained transformations T_l^{femur} and T_l^{tibia} are usually ill-posed since there is no restriction on the behaviors of 3D deformation fields, which may lead to poor reconstruction results (see Fig. 9.2). Therefore, we apply an adaptive regularization on the B-spline grid(s) sampled from T_l^{femur} and T_l^{tibia} in order to derive the anatomically correct results.

The adaptive regularization strategy begins with the layout of a combined B-spline grid or two individual B-spline grids in terms of the articulated or individual 2D-3D reconstruction methods by interpolating the displacements at the control points from T_l^{femur} and T_l^{tibia}. Following the previous work [9], the displacement vectors $\mathbf{d}_{ijk}$ at the control points are regularized based on the Neumann boundary condition on the control points [10]. Figure 9.3 illustratesthe 3D deformations computed from each step of the regularization.

In order to prevent the reconstructed femur and tibia from penetrating each other, we investigated two strategies to reconstruct the associated structures:

I. Individual 2D-3D reconstruction. The reconstruction of femur and tibia is completely individual, and each time just one anatomy will be reconstructed. As indicated, there is no consideration over the articulation of the knee joint.
II. Articulated 2D-3D reconstruction. A combined B-spline grid is placed over the space of the template volumes, and the displacement $\mathbf{d}_{ijk}$ at a control point $\mathbf{C}_{ijk}$ is computed either by T_l^{femur} or by T_l^{tibia}, dependingon

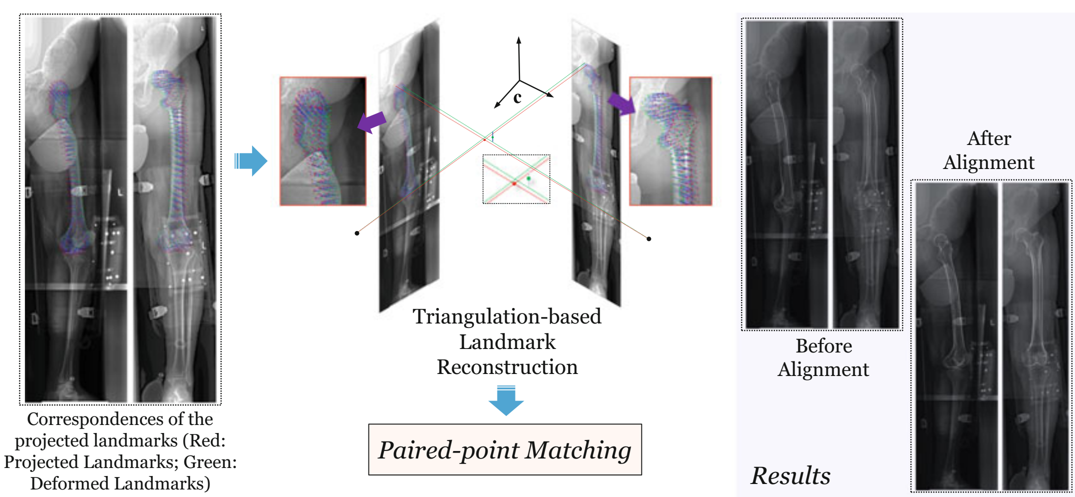

Fig. 9.1 An illustration of 2D-3D scaled-rigid alignment

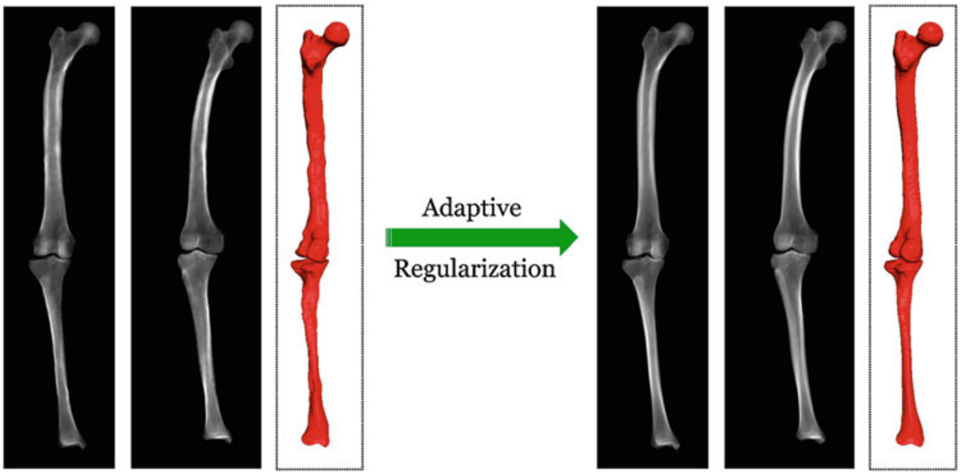

Fig. 9.2 A comparison of the reconstruction of femur and tibia without the adaptive regularization strategy

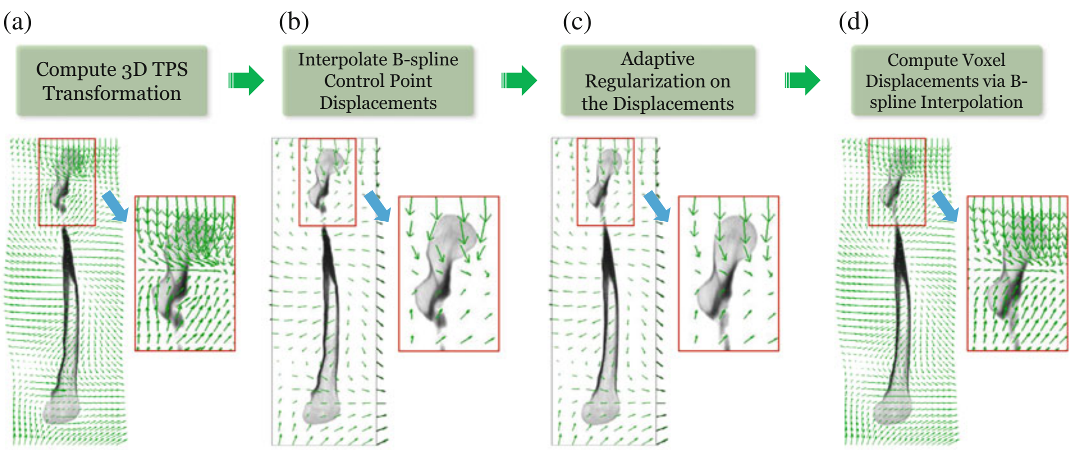

Fig. 9.3 A comparison of the deformation fields derived from a TPS transformation and from the regularized B-spline transformation. (**a**) Voxel-wise 3D deformation field computed from the TPS transformation. (**b**) Displacements of the B-spline control points interpolated from the TPS transformation. (**c**) Adaptive regularization on the displacements of these B-spline control points. (**d**) Voxel-wise 3D deformation field interpolated from the regularized B-spline transformation

the relative position between a predefined axis-aligned plane ζ (see Fig. 9.4, left) and $\mathbf{C}_{ijk}$:

$$\begin{cases} if\ \mathbf{C}_{ijk}\ is\ \text{above}\ \zeta,\ \mathbf{d}_{ijk} \leftarrow T_l^{\text{femur}}\left(\mathbf{C}_{ijk}\right) \\ if\ \mathbf{C}_{ijk}\ is\ \text{below}\ \zeta,\ \mathbf{d}_{ijk} \leftarrow T_l^{\text{tibia}}\left(\mathbf{C}_{ijk}\right) \end{cases} \tag{9.2}$$

We found that the reconstruction accuracy is basically the same for both strategies, while the qualitative comparison of reconstructing knee joint structure demonstrates the superiority of the articulated 2D-3D reconstruction method over the individual one (see Fig. 9.4, right).

9.2.2.3 The Reconstruction of Three Muscles Around the Thigh Region

The obtained 3D deformation fields from the reconstruction pipeline provide the potential of reconstructing the muscles in the thigh region. Currently, we just focus on the reconstruction of (1) rectus femoris muscle, (2) vastus lateralis and intermedius muscle, and (3) vastus medialis muscle.

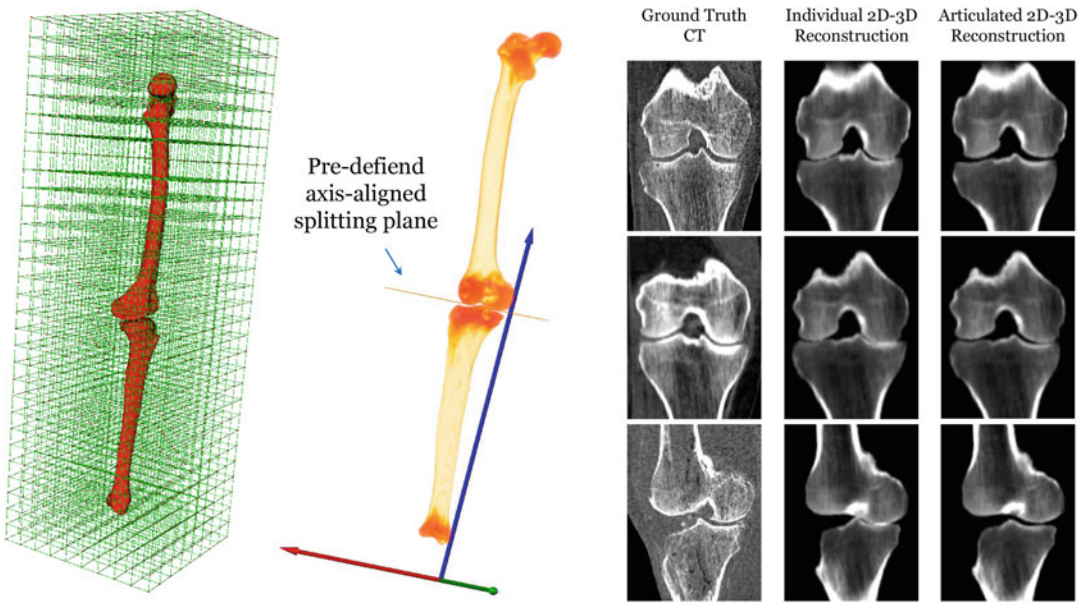

Fig. 9.4 The schematic view of the articulated 2D-3D reconstruction method (left) and the qualitative comparison with the individual 2D-3D reconstruction method (right)

9.3 Experiments and Results

Approved by a local institution review board (IRB), we conducted three experiments to validate the proposed reconstruction pipeline in regard to different motivations.

9.3.1 Experiment on CT Dataset of 11 Cadaveric Legs

Each CT data has a voxel spacing of $0.78 \times 0.78 \times 1$ mm, and we chose a healthy CT data from them to create the atlas for all experiments. For the atlas, we segmented the binary labels of the femoral and tibial structures as well as their cortical bone regions, and 641 landmarks for femur and 872 landmarks for tibia were extracted from these binary labels.

In this experiment, we would like to evaluate the overall reconstruction accuracy of femur and tibia as well as the reconstruction accuracy of their intramedullary canal regions. Therefore, for the left 10 sets of CT volumes, we segmented the binary labels of the femoral and tibial structures as well as their cortical bone regions for each CT data as the ground truth, and also we generated a pair of virtual 2D radiographic images (DRRs) as the reference images (see Fig. 9.5, top).

We assessed both the individual and the articulated 2D-3D reconstruction strategies, and the results are shown in Fig. 9.5, left. Here, the average surface distance (ASD) and the dice coefficient (DC) for the overall reconstruction and the reconstruction of cortical bone region (i.e., CBRASD and CBRDC) were measured. From the results, there is no statistically significant difference in accuracy, but it is distinct in the preservation of knee joint structure from the two strategies (see Fig. 9.4). Figure 9.5, right, shows a qualitative comparison of the reconstructed volumes with the associated ground truth volumes for both femur and tibia.

9.3.2 Experiment on X-Ray Images from Patients

Ten pairs of X-ray images were collected for this experiment, which is more challenging due to the image quality. Since only the CT data around three local regions (hip, knee, and ankle

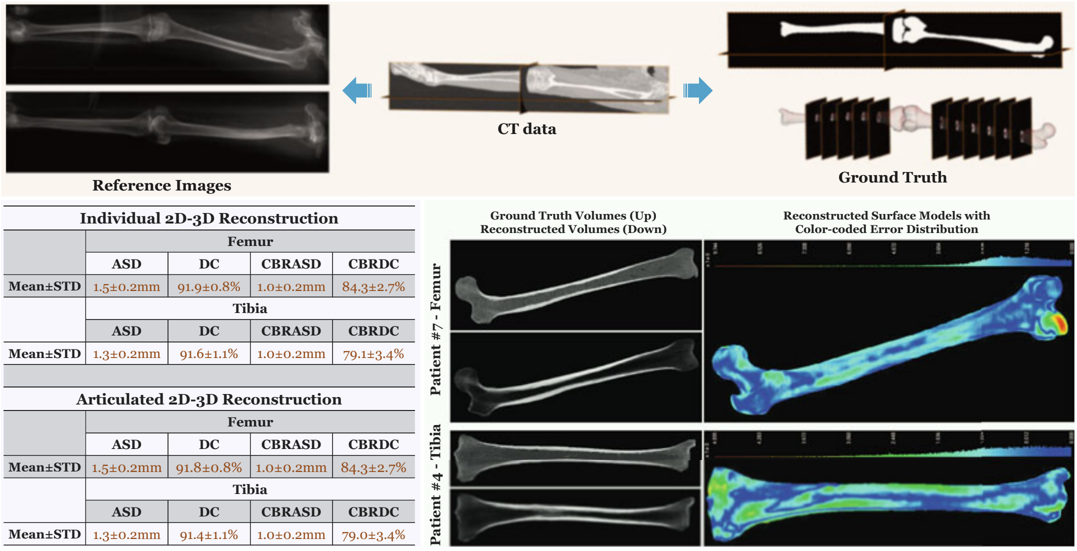

Individual 2D-3D Reconstruction

	ASD	DC	CBRASD	CBRDC
Femur				
Mean±STD	1.5±0.2mm	91.9±0.8%	1.0±0.2mm	84.3±2.7%
Tibia				
Mean±STD	1.3±0.2mm	91.6±1.1%	1.0±0.2mm	79.1±3.4%

Articulated 2D-3D Reconstruction

	ASD	DC	CBRASD	CBRDC
Femur				
Mean±STD	1.5±0.2mm	91.8±0.8%	1.0±0.2mm	84.3±2.7%
Tibia				
Mean±STD	1.3±0.2mm	91.4±1.1%	1.0±0.2mm	79.0±3.4%

Fig. 9.5 The reference images and the ground truth from each CT data (top) and the quantitative (bottom, left) and qualitative (bottom, right) results of the experiment conducted on ten cadaveric legs

	#01	#02	#03	#04	#05	#06	#07	#08	#09	#10	Mean±STD
PF-ASD [mm]	1.2	1.2	0.8	0.9	1.3	1.2	1.5	2.2	1.4	0.9	1.3±0.4
DF-ASD [mm]	1.5	1.4	1.5	1.3	1.6	1.9	1.8	1.5	1.4	1.2	1.5±0.2
PT-ASD [mm]	1.1	1.1	1.4	1.2	1.4	1.4	2.2	1.6	1.8	1.4	1.5±0.3
DT-ASD [mm]	1	1.3	1.5	1.5	1.2	1.4	1.5	0.9	1.2	1.5	1.3±0.2

Fig. 9.6 The average surface distances measured between the reconstructed surface models and the ground truth surface models

joint) were available, the reconstruction accuracy was evaluated by comparing the surface models extracted from the ground truth CT data with those extracted from the reconstructed volumes after rigidly aligning them together.

The average surface distance for the local regions including proximal femur (PF-ASD), distal femur (DF-ASD), proximal tibia (PT-ASD), and distal tibia (DT-ASD) were measured. The quantitative results are shown in Fig. 9.6, left, where an overall reconstruction accuracy of 1.4 mm was found, and Fig. 9.6, right, shows a reconstruction case.

9.3.3 Experiment on Reconstructing Three Thigh Muscles

We also evaluated the accuracy of reconstructing three thigh muscles on a set of 12 one-side CT data with the associated ground truth segmentations around the thigh region [11]. One CT volume was randomly chosen to create the atlas, and we conducted the experiment on the left 11 cases. We measured the dice coefficient (DC) to evaluate the reconstruction accuracy of the three thigh muscles, and the results are shown in Fig. 9.7, ranging from 78% to 85%.

Case	Musculoskeletal Structure Reconstruction – DICE [%]			
	Femur	Rectus Femoris Muscle	Vastus Lateralis & Intermedius Muscle	Vastus Medialis Muscle
#01	93.4	84.6	86.3	74.5
#02	94	85.5	85.8	78.2
#03	90.7	76.2	86.3	80.3
#04	92.8	81.9	82.2	79
#05	90.8	83.4	77.7	74.2
#06	90	71.3	85.5	81.9
#07	89.7	81.3	86	75.3
#08	91.8	77.3	86.1	79.2
#09	92	74	80.1	73.2
#10	90.8	84.6	88.6	79.9
#11	92.4	84.5	88.3	79.8
Overall	91.7±2.4	80.4±4.9	84.8±3.4	77.8±2.9

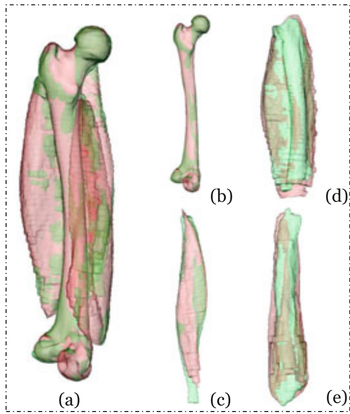

Fig. 9.7 (**a**) The femur and thigh muscle reconstruction accuracy: red (ground truth surface) and green (reconstructed surface); (**b**) femur; (**c**) rectus femoris muscle; (**d**) vastus lateralis and intermedius muscle; (**e**) vastus medialis muscle

9.4 Discussion and Conclusion

We presented an atlas-based 2D-3D intensity volume reconstruction approach, which to our knowledge is probably the first attempt to derive patient-specific musculoskeletal structures in the lower extremity. Our method has the advantage of combining the robustness of 2D-3D landmark reconstruction with the smoothness properties inherent to B-spline-based 3D regularization. In order to preserve knee joint structure, we proposed an articulated 2D-3D reconstruction strategy which can derive the anatomically correct reconstruction results, and we also investigated the reconstruction of three thigh muscles via the proposed reconstruction pipeline, which holds the potential to be used in the clinical routine in future. The comprehensive results from a set of experiments demonstrated the efficacy of this 2D-3D reconstruction method.

Acknowledgements This chapter was modified from the paper published by our group in *the MICCAI 2017 International Workshop on Imaging for Patient-Customized Simulation and Systems for Point-of-Care Ultrasound* (Yu and Zheng, BIVPCS/POCUS@MICCAI2017: 35-43). The related contents were reused with their permission.

References

1. Markelj P, Tomaževič D, Likar B, Pernuš F (2012) A review of 3D/2D registration methods for image-guided interventions. Med Image Anal 16:642–661
2. Zheng G, Gollmer S, Schumann S, Dong X, Feilkas T, González Ballester MA (2009) A 2D/3D correspondence building method for reconstruction of a patient-specific 3D bone surface model using point distribution models and calibrated X-ray images. Med Image Anal 13:883–899
3. Baka N, Kaptein BL, de Bruijne M, van Walsum T, Giphart JE, Niessen WJ, Lelieveldt BP (2011) 2D-3D reconstruction of the distal femur from stereo X-ray imaging using statistical shape models. Med Image Anal 15:840–850
4. Yao J, Taylor RH (2003) Assessing accuracy factors in deformable 2D/3D medical image registration using a statistical pelvis model. In: ICCV 2003, pp 1329–1334
5. Ahmad O, Ramamurthi K, Wilson KE, Engelke K, Prince RL, Taylor RH (2010) Volumetric DXA (VXA) – a new method to extract 3D information from multiple in vivo DXA images. J Bone Miner Res 25: 2468–2475
6. Zheng G (2011) Personalized X-ray reconstruction of the proximal femur via intensity-based non-rigid 2D-3D registration. In: MICCAI 2011, pp 598–606
7. Yu W, Chu C, Tannast M, Zheng G (2016) Fully automatic reconstruction of personalized 3D volumes of the proximal femur from 2D X-ray images. Int J Comput Assist Radiol Surg 11(9):1673–1685

8. Klein S, Staring M, Murphy K, Viergever MA, Pluim JP (2010) Elastix: a toolbox for intensity-based medical image registration. IEEE Trans Med Imag 29(1):196–205
9. Myronenko A, Song X (2009) Adaptive regularization of ill-posed problems: application to non-rigid image registration. arXiv:0906.3323
10. Strang G (1999) The discrete cosine transform. SIAM Rev 41(1):135–147
11. Chu C, Takao M, Ogawa T, Yokota F, Sato Y, Zheng G (2016) Statistical shape modeling of compound musculoskeletal structures around the thigh region. In: ISBI 2016, pp 885–888

10 3D Ultrasound for Orthopedic Interventions

Ilker Hacihaliloglu

Abstract

Ultrasound is a real-time, non-radiation-based imaging modality with an ability to acquire two-dimensional (2D) and three-dimensional (3D) data. Due to these capabilities, research has been carried out in order to incorporate it as an intraoperative imaging modality for various orthopedic surgery procedures. However, high levels of noise, different imaging artifacts, and bone surfaces appearing blurred with several mm in thickness have prohibited the widespread use of ultrasound as a standard of care imaging modality in orthopedics. In this chapter, we provided a detailed overview of numerous applications of 3D ultrasound in the domain of orthopedic surgery. Specifically, we discuss the advantages and disadvantages of methods proposed for segmentation and enhancement of bone ultrasound data and the successful application of these methods in clinical domain. Finally, a number of challenges are identified which need to be overcome in order for ultrasound to become a preferred imaging modality in orthopedics.

Keywords

3D ultrasound · Orthopedic interventions · Segmentation · Enhancement · Machine learning · Validation

10.1 Introduction

The three phases of a computer-assisted orthopedic surgery (CAOS) system are preoperative planning, intraoperative execution, and postoperative evaluation (Fig. 10.1). A modification of this loop can also be extended to nonsurgical orthopedic procedures. Since the discovery of X-ray in 1895 and its first use in 1895 for a presurgical needle imaging procedure and in 1896 for surgical removal of a bullet, imaging has played an important role in interventional guidance. Investigating the closed loop shown in Fig. 10.1, we can see that imaging is one of the major building blocks of all the three phases. Currently many imaging modalities are employed for various image-guided interventions [82]; however, not all of them are suitable for CAOS procedures.

The most common imaging modalities currently employed in orthopedic procedures are 2D plain X-ray, computed tomography (CT), magnetic resonance imaging (MRI), and 2D/3D

I. Hacihaliloglu (✉)
Department of Biomedical Engineering, Rutgers University, Piscataway, NJ, USA

Department of Radiology, Rutgers Robert Wood Johnson Medical School, New Brunswick, NJ, USA
e-mail: ilker.hac@soe.rutgers.edu

G. Zheng et al. (eds.), *Intelligent Orthopaedics*, Advances in Experimental Medicine and Biology 1093, https://doi.org/10.1007/978-981-13-1396-7_10

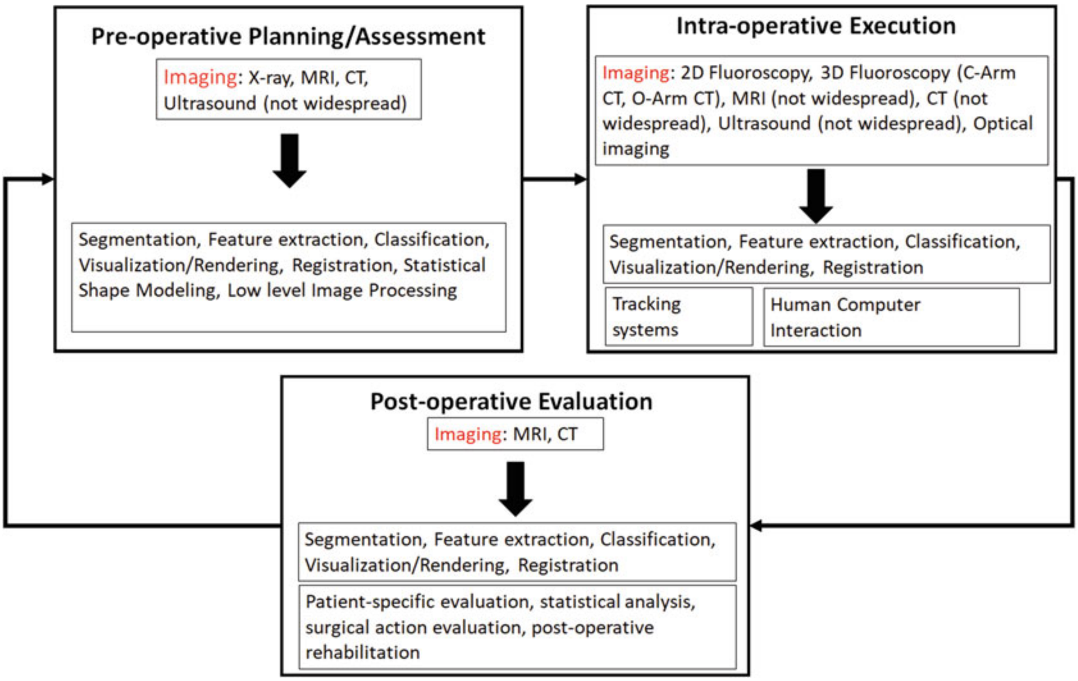

Fig. 10.1 Three phases of orthopedic surgery. Preoperative planning/assessment, intraoperative execution, and postoperative evaluation are connected with a closed loop representing a full CAOS system

fluoroscopy [2,9,19,24,45,61,65,66,70]. Among these imaging modalities, 2D fluoroscopy is the most commonly used modality for intraoperative visualization and guidance [41, 68]. Since the beginning of 2000, 3D fluoroscopy imaging has also been used for various CAOS procedures for intraoperative guidance. Studies have shown improved surgical outcome using 3D fluoroscopy compared to 2D fluoroscopy [36, 46, 81]. However, high costs associated with this imaging modality have prohibited the widespread employment. Except MRI, all of these imaging modalities expose surgical team and patients to harmful ionizing radiation [34]. A study investigating the exposure of the orthopedic surgeons' hands to radiation, during the surgery, found an exposure of 20 mrem/case which is reported to be 187 times greater than the amount predicted by the manufacturer [34]. For comparison, a chest X-ray exposes the patient to about 20 mrem. Both the National Council on Radiation Protection and the International Commission of Radiological Protection recommend a maximum exposure of the hands of 50,000 mrem, which allows up to 2500 cases per year. Though 20 mrem/case is below this limit, however, receiving nearly the equivalent of a chest X-ray per case indicates special care must be taken especially if we think the amount of surgeries a surgeon has to perform. It is reasonable to keep the radiation exposure as low as possible, regardless of safety regulations.

In order to eliminate or reduce the considerable exposure of ionizing radiation, to both patients and surgical teams, inherent to fluoroscopic imaging, focus has been given to design ultrasound-based CAOS systems [1, 8, 10, 14, 16, 17, 23, 44, 74, 76]. Ultrasound has traditionally been used to image muscle interfaces, organs, and blood flow in real-time. Since there is no clinically reported risk of using ultrasound, it is still regarded as the only safe method to image a fetus. Real-time scanning, lack of radiation, low cost, and being portable makes this imaging modality a suitable alternative to fluoroscopy for intraoperative imaging. Various studies, investigating the potential of ultrasound-based CAOS procedures, have reported improved surgical accuracy, decreased invasiveness of the procedure, and decreased overall radiation exposure time [10, 74]. Nevertheless, imaging bone using ultrasound still continues to be challenging due to high levels of speckle and imaging artifacts complicating the interpretation of the collected data. Furthermore, due to the beam width in elevation direction, bone surfaces appear several millimeters (mm) in thickness, and the surface response profile is affected by the direction of the ultrasound transducer with respect to the imaged bone anatomy. Finally, having a limited field of view, and manual operation of the ultrasound transducer causes additional difficulties during the collection of high quality ultrasound data further limiting the widespread applicability of this imaging modality in CAOS procedures. Due to these difficulties, initial investigations of ultrasound have focused on using this modality as a digitization tool, rather than an imaging modality, to collect intraoperative patient data which was later registered to a preoperative plan developed from CT or MRI images. Main focus was given to develop accurate, automatic, and real-time registration methods. A detailed review of ultrasound-based registration approaches can be found in [67].

Due to widespread availability and ease of data collection, earlier work in ultrasound-based CAOS procedures focused on the use of 2D ultrasound. With the recent advancements made in the design of 3D transducers, volumetric ultrasound imaging is now extensively used in various clinical procedures and becoming more investigated for orthopedic procedures as well. In this chapter our focus will be on approaches developed for segmentation and enhancement of bone surfaces. Furthermore, we provided a detailed overview of numerous applications of 3D ultrasound in the domain of orthopedic surgery. Specifically, we discuss the advantages and disadvantages of methods proposed for improving the quality of ultrasound data and the successful application of these methods in clinical domain. Finally, a number of challenges are identified which need to be overcome in order for ultrasound to become a preferred imaging modality in orthopedics.

10.2 Bone Surface Response Profile in Ultrasound Data

Ultrasound images are acquired using pulse-echo imaging technique and displayed in brightness mode (B-mode). Small pulses of sound waves are created using piezoelectric crystals which are interconnected electronically inside the ultrasound transducer. Piezoelectric crystals grow and shrink in response to an electrical current and produce ultrasound pulses. The summation of all pulses generated by the piezoelectric crystals forms the ultrasound beam. The generated sound waves are described in terms of their wavelength, frequency, and amplitude. The direction of ultrasound pulse propagation along the beam line is referred to as the axial direction, the direction in the image plane perpendicular to axial is called the lateral direction, and the direction perpendicular to the image plane is called elevational direction. Ultrasound image resolution in axial direction is related to the duration of the transmitted pulse and increases with increasing ultrasound frequency. However, since wavelength and frequency are inversely related, increasing the ultrasound wave frequency limits the depth of imaging. Lateral and elevational resolution is related to the width of the ultrasound beam. Lateral resolution can be improved by increasing bandwidth and the central frequency of the transmitted pulse [71].

An ultrasound image is formed when the generated sound waves are transmitted into the body, reflected off the tissue interface, and returned to the transducer. The strength of the reflected sound wave, intensity of the displayed structures in the ultrasound image, depends on the difference in acoustic impedance between adjacent structures. Acoustic impedance (Z) is calculated as:

$$Z = \rho \times c. \tag{10.1}$$

Here ρ is the density of the tissue and c is speed of the sound in that specific tissue. Table 10.1 displays various values for ρ, c, and Z values. The fraction of the incident intensity that is reflected is given by the equation:

Table 10.1 Sound wave speed and impedances of different tissues [71]

Tissue	Speed(c) [m/s]	Density(ρ) [kg/m^3]	Impedance(Z) [$10^6 \times$ kg/m^{2}s]
Air (25°C)	346	1.15	0.0004
Fat	1450	951	1.38
Water (25°C)	1493	991	1.48
Soft tissue	1540	1058	1.63
Liver	1550	1058	1.64
Blood (37°C)	1570	1064	1.67
Bone	4000	950–1850	3.8–7.4

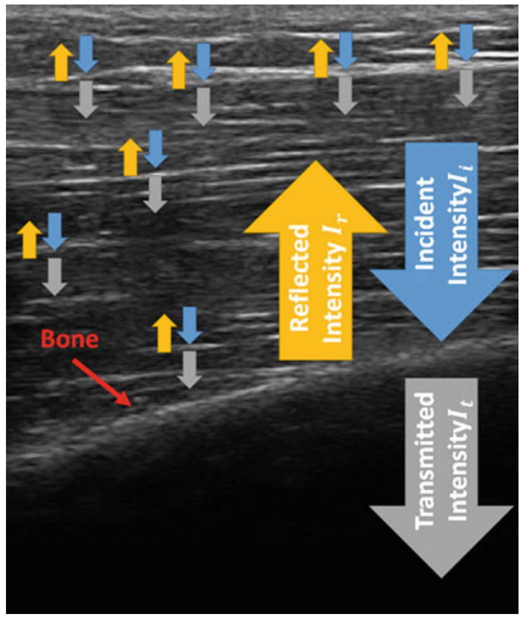

Fig. 10.2 Sound wave propagation in tissue. Incident, reflected, and transmitted waves are represented as blue, orange, and gray arrows, respectively. Red arrows point to a small section of the bone surface. The image is obtained from radius bone in vivo

$$\frac{I_r}{I_i} = \left(\frac{Z_2 - Z_1}{Z_2 + Z_1}\right)^2. \tag{10.2}$$

In the above equation, Z_1 and Z_2 represent acoustic impedance of two different mediums. Incident and reflected intensity wave values are denoted with I_i and I_r, respectively. As the acoustic impedance difference between two adjacent tissue increases, the more ultrasound energy will be reflected back to the transducer at that specific boundary location. This process is depicted in Fig. 10.2 as an example.

Investigating Table 10.1 we can see that bone tissue has the highest acoustic impedance value among all the tissue types. Therefore at the tissue bone boundary, most of the sound wave will be reflected back to the transducer, and the I_r value at that specific interface will be very high. This is the main reason why bone boundaries are depicted with high-intensity value in the B-mode ultrasound data. Since most of the signal is reflected back at the bone boundary, the energy of the transmitted wave (I_t) interior to the bone surface will be very low and will not propagate back to the transducer. This results in the generation of a low-intensity region, denoted as the shadow region, in the collected ultrasound data and is one of the typical US imaging artifacts denoting that interior bone surfaces cannot be imaged with ultrasound (Fig. 10.3).

Compared to appearance of bone in CT, MRI, or fluoroscopy data, the bone surface response profile in ultrasound is not a sharp edge and has a thickness denoted as bone response thickness

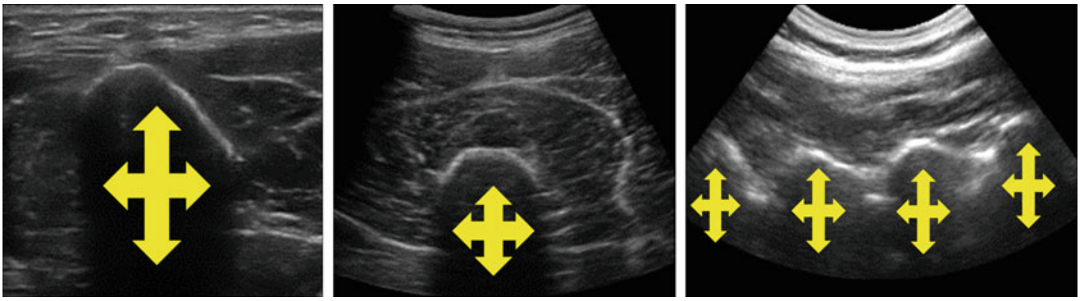

Fig. 10.3 In vivo ultrasound images of various bone surfaces. Left: distal radius. Middle: femur. Right: spine. Yellow arrows point to the shadow regions present in all the ultrasound images

(Fig. 10.3). The two main reasons why the bone surface produces a thick response are: (1) 3D geometry of the imaged bone surface and (2) finite beam width in the elevation direction. When imaging complex anatomy (such as spine), each imaging array (piezoelectric crystal) will receive reflections from bone surfaces outside its direct lie of sight and produce a thicker response [39]. Imaging tilted surfaces, or tilting the ultrasound transducer while imaging, will also increase the surface response thickness since the reflected waves will no longer reach all the imaging arrays. Figure 10.4 shows two different ultrasound images of the distal radius bone. The two images are obtained from the same anatomical region without changing the location of the ultrasound transducer during the scanning. During the collection of the right image shown in Fig. 10.4, the transducer was tilted with respect to the imaged bone surface (schematic plot of the process is provided in bottom row in Fig. 10.4). Investigating the two B-mode ultrasound images, we can see how a simple tilting of the transducer affects the bone surface response profile. This qualitative investigation also shows one of the most important drawbacks of ultrasound imaging, namely, being a user-operated imaging modality causing additional difficulties during data collection since a single-degree deviation angle by the operator can reduce the signal strength by 50% [63]. For more details about the physics of ultrasound image formation, the reader is referred to the following publications [5, 63, 71, 72].

10.3 Basic Principles of 3D Ultrasound Data Acquisition

One of the main advantages of 2D ultrasound for intraoperative applicability is that it can provide real-time imaging of the scanned anatomy. With the technological advancement made in the transducer design, real-time volumetric ultrasound acquisition is possible. Consequently, 3D ultrasound-based surgical procedures are becoming widely available. In this section we will provide information on how volumetric ultrasound data is collected in order to provide a general understanding of how this data can be employed in orthopedic procedures.

Techniques which are currently used to acquire 3D ultrasound data can be classified into three groups: (1) mechanical scanning, (2) 2D array scanning, and (3) freehand scanning.

10.3.1 Mechanical Scanning

In conventional 2D transducers, piezoelectric crystals are arranged linearly. Mechanical transducers move the linearly arranged crystals in a predefined spatial or angular intervals using a motorized mechanical assembly. Using the accurate knowledge of the relative positions and orientations of the acquired multiple 2D scans, a 3D volume can be reconstructed with high accuracy. The most common mechanical scanning modes are translation, rotation, and

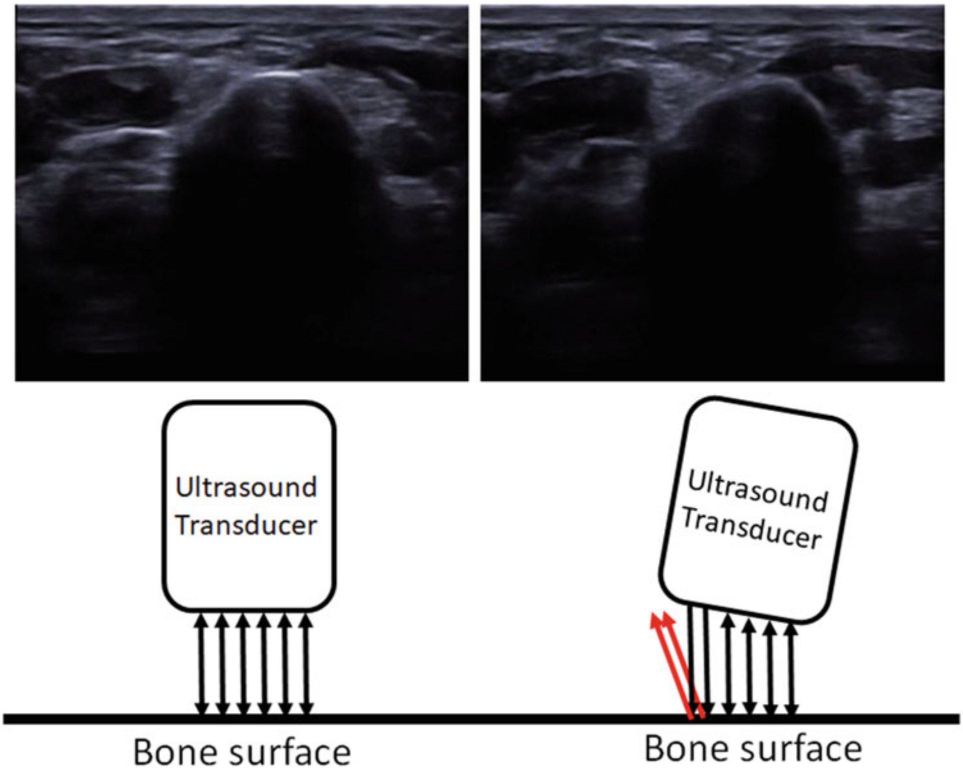

Fig. 10.4 In vivo ultrasound images of distal radius. Top row: left image is obtained when the transducer is aligned with respect to the bone surface, while the image shown on the right is obtained tilting the ultrasound transducer with respect to the bone surface. Bottom row: schematic plot of the transducer orientation with respect to the imaged bone surface. Red arrows indicate ultrasound waves reflecting away from the transducer surface

oscillation [21]. Figure 10.5 displays an example of a mechanical transducer with linear scanning.

10.3.2 2D Array Scanning

Two problems associated with mechanical scanning are: (1) low resolution in elevation direction and (2) long time for image acquisition, and volume reconstruction limiting the applicability of these transducers for real-time guidance. In order to provide solutions to these problems, research has focused on the design of 2D array transducers (Fig. 10.5b). In 2D array scanning, beam focusing can be achieved in elevation and lateral directions providing an improvement over mechanical scanning. These transducers generate a diverging beam in a pyramidal shape, and the reflected sound wave echoes are processed to integrate 3D US images in real time. The main disadvantage of 2D array transducers is related to the difficulties faced during the design of these transducers. Since the electrical impedance of each crystal in 2D array is much greater than that of 1D array impedance, matching becomes a challenging procedure [75]. In order to reduce the difficulties in fabrication, the size of the array cannot be arbitrarily large, leading to small field of view problem. Finally, the cost associated with these transducers is much higher compared to mechanical scanning due to the increased number of crystals.

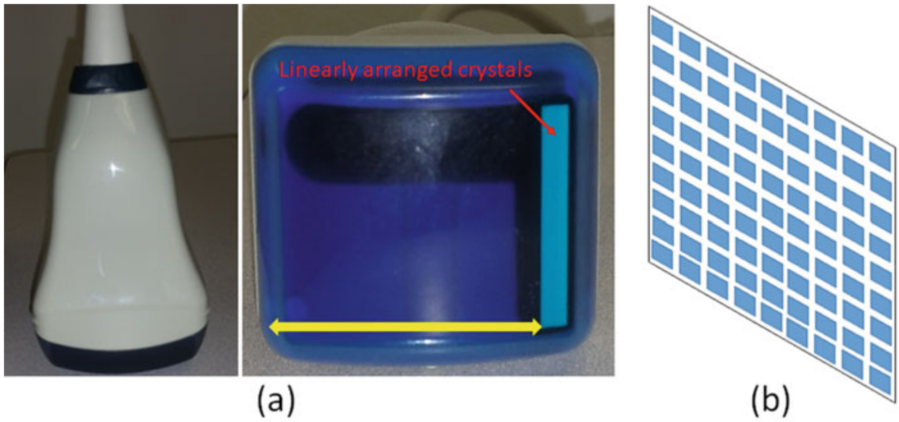

Fig. 10.5 (**a**) Mechanical scanning. Left: motorized 3D ultrasound transducer side view. Right: motorized 3D ultrasound transducer scanning surface view. Linearly arranged piezoelectric crystals are moved with the motorized setup in a predefined direction denoted with yellow arrow. (**b**) Schematic plot of 2D matrix array transducer imaging surface. Each blue region represents a single crystal

10.3.3 Freehand Scanning

Freehand scanning is performed by acquiring a series of 2D ultrasound images, using conventional 2D transducer, over a region of interest. Freehand scanning is a two-step process. First, in order to record the relative location of each scan, a position sensor must be attached to the transducer. The second step involves reconstruction of the 3D volume using the position and image information [69]. The most common method for obtaining position information is by using tracking technologies such as electromagnetic, optical, or mechanical. In ultrasound-based CAOS applications, most research has focused on the use of electromagnetic and optical tracking due to the widespread applicability of these technologies in orthopedic procedures. Optical tracking systems are more accurate than the electromagnetic tracking systems [43]. However, a direct line of sight between the tracking device and the optical markers needs to be established at all times. On the other hand, electromagnetic tracking systems are not as accurate as the optical systems, but they do not require direct line of sight between the tracked instrument and the magnetic field generator. For a detailed review of currently employed tracking technologies, the reader is referred to [43, 57]. This first step also involves ultrasound transducer calibration. Calibration is required in order to relate the 2D image information to the tracker 3D coordinate system. With this process each pixel in the ultrasound image is converted to a 3D coordinate measured in millimeters. For a detailed review of various calibration methods, the reader is referred to [49].

Based on the technique used, the reconstruction algorithms can be divided into three different groups: pixel-based methods (PBM), voxel-based methods (VBM), and function-based methods (FBM) [69]. VBM travel all the image voxels in a target volume, and the corresponding pixels are inserted from the input images. PBM traverse the input pixels and insert them into the corresponding target volume. In FBM, particular functions (such as a polynomial) are fitted to the input pixels and are used for creating the voxel grid [69].

10.4 Segmentation of Bone Surfaces from Ultrasound Data

In the early reported work, bone surfaces were manually segmented from the collected ultrasound data [16, 74]. However, manual bone segmentation is time-consuming, complicated, and prone to significant inter- and intra-user error. In order to render the problem more tractable, several research groups have tried to automate the segmentation process [27]. Accurate, robust, and real-time segmentation still continues to be an open research question in orthopedic procedures. Since the initial applications of ultrasound-based CAOS systems incorporated tracked 2D ultrasound, most previous research has focused on developing automated 2D segmentation methods. Volumetric data was processed by applying the developed 2D segmentation methods on each individual slice. Some researchers have focused on the development of 3D segmentation methods in order to take advantage of the surface continuity in the elevation direction [31]. However, until to date the main focus still remains on the development of 2D segmentation methods. The validation of the proposed segmentation methods is usually performed by comparing the automatically extracted surfaces against manual expert segmentation. We provide more information about the specific metrics used for validation in Sect. 10.5 of this chapter. The proposed automatic methods can be classified into four main categories: (1) methods based on image intensity and gradient information, (2) methods based on image phase information, (3) joint methods which use image phase and intensity information, and (4) methods based on machine learning. Below we will provide more information on each of these categories.

10.4.1 Bone Segmentation Based on Image Intensity and Gradient Information

Initial work on the segmentation of bone surfaces used image intensity and gradient information. Amin et al. [1] used the fact that bone surfaces appear as a high-intensity feature followed by a low-intensity region representing the shadow region. A directional edge detection and Gaussian blurring function was applied to the collected ultrasound data. The extracted surfaces were refined during the registration step. The developed system was validated on a single subject schedule for a hip replacement surgery. This initial study did not report the segmentation accuracy, but the reported ultrasound-CT registration mean error for translation and rotation was 1.27 mm and 0.59°. In a separate work, Kowal et al. [44] proposed a framework which consisted of depth initialized intensity thresholding, image morphology, adaptive thresholding, and contour connecting operations. Validation results performed on ex vivo bovine and porcine femur bone achieved a segmentation accuracy of 0.42 mm. The reported processing time was 0.8 s per slice. This work was later used on a phantom study in order to evaluate a new ultrasound registration method [73]. A multistage framework was proposed by Daanen et al. [18] for segmentation of in vivo and cadaver ultrasound scans obtained from sacrum bone. A fuzzy intensity image (FII) was calculated using Otsu thresholding and intensity transformation operation. The obtained FII was masked with a gradient image and used as an input to a ray casting method which resulted in the segmented bone surfaces. Validation studies performed on three different cadavers and in vivo patients resulted in a minimum segmentation accuracy of 0.45 mm. The reported average processing time was 3.4 s. Foroughi et al. [22] proposed a dynamic programming approach where the image shadow information was incorporated into the proposed algorithm to guide the segmentation. The reported segmentation accuracy on cadaver scans, obtained from femur and pelvis bone surfaces, was less than 0.3 mm. In a different study, the same approach was used for localization of pelvic anatomical coordinate system where the extracted bone surfaces were registered to a statistical atlas of the pelvis [23]. Rasoulian et al. [59] extended the method of [23] for the segmentation of vertebrae bone surfaces and subsequent registration to a statistical shape model. In a more recent publication [15], a parallel implementation (using Intel Math Kernel Library), of the proposed method [22], was performed and validated for registering a spine statistical shape model to 3D ultrasound volumes obtained from a mechanical transducer. The reported processing time for segmenting a single volume was 0.6 s [15]. In a different work, the segmentation approach proposed in [59] was used for processing volumetric ultrasound data obtained using freehand scanning with electromagnetic tracking [60]. This study is also one of the initial ones where a complete ultrasound-guided spinal injection system was validated on in vivo scans. In [48], a three-step process was proposed for segmentation of bone surfaces from 2D ultrasound data with a specific clinical focus on locking of the intramedullary nail in tibia fracture reduction procedures. The three steps include vertical gradient filtering, shortest path calculation, and contour closing using polynomial interpolation. In vivo validation results obtained from nine volunteer scans achieved a mean maximum root mean square error (RMSE) value of 0.8 mm with a processing time of 10–15 images per second. A feature descriptor, bone confidence localizer (BCL), was proposed in [79]. BCL feature descriptor was calculated by combining orientation filtered ultrasound data and confidence map [42] image. The confidence map is obtained using a graph-based method to represent the ultrasound signal attenuation inside the tissue. The final bone surface was extracted thresholding the calculated BCL image. For validation freehand ultrasound volumes, using electromagnetic tracking, were collected from a single human cadaver leg. Scanned regions were femur, tibia, and fibula bones. The reported segmentation accuracy was 1.47 mm for the femur bone and 3.63 mm for the tibia/fibula bones. The developed segmentation method was operating in real time. However, the reported success rates (percentage of correctly segmented bones) were 82% for femur and 72% for tibia/fibula bones [79].

Incorporation of CT bone information, obtained during registration, was also proposed by different groups in order to improve the robustness of the segmentation. Ionescu et al. [38] proposed a two-stage segmentation process. During the first stage, denoised ultrasound data were segmented using watershed algorithm. The segmentation result was updated during the US-CT registration process. Validation results on in vivo vertebra bone scans achieved a max registration accuracy of 1.9 mm and 0.87°. In [11], where various image analysis methods (such as image thresholding, morphology operations, connected component labeling, and cubic B-spline smoothing) were used to design a segmentation framework. The segmented surfaces were modified during the CT-ultrasound registration process. Validation was performed on freehand ultrasound volumes obtained from single human femur cadaver using electromagnetic tracking. The authors report a segmentation accuracy of 0.38 mm with a processing time of 20–30 ms per slice. In [56], bone ultrasound data was converted to a probability image using the physics of ultrasound bone imaging, thresholding, and a training framework. Training images were obtained using manual segmentation. The enhanced images were registered to a CT scan. 3D freehand ultrasound scans were collected using optical tracking from three female cadavers. Specific attention was given to femur and pelvis bones. The reported RMSE for target registration error was 1.6 mm.

10.4.2 Bone Segmentation Based on Image Phase Information

The use of local phase information for processing ultrasound data has been previously investigated by various groups for non-orthopedic applications [52]. Several groups have suggested that image phase information is a more robust feature for acoustic boundary detection. In the context of processing bone ultrasound data Hacihaliloglu et al. [29] proposed, for the first time, the use of local phase image features for enhancement of bone ultrasound data. In their successive work, this method was also extended to 3D for processing volumetric ultrasound data with a specific clinical focus on distal radius and pelvic bone surface imaging [30–32].

Image phase information can be extracted using band-pass quadrature filters. For a more extensive review of various quadrature filter types, the reader is referred to [13]. The most commonly applied band-pass quadrature filter for processing ultrasound data is the Log-Gabor filter [25, 30, 51]. Some research has also focused on the use of monogenic filter based on monogenic signal theory [20]. Accurate and robust enhancement requires the optimization of the filter parameters. In [31, 32], an optimization framework was proposed where filter parameters were optimized using the information obtained from the bone image features. In [3,4], frequency domain information was used to optimize 2D and 3D filter parameters. Validation on cadaver studies obtained from scaphoid bones achieved an average mean surface and Hausdorff distance errors of 0.7 and 1.8 mm, respectively. Most of the methods based on the use of local phase image information enhance the appearance of bone surfaces in the ultrasound data while suppressing the typical imaging artifacts. Therefore, a post-processing method is usually required to segment the enhanced bone features. This can be performed using a bottom-up ray casting method and selecting the pixel in each vertical column belonging to the highest gradient or highest intensity value. A segmentation approach similar to [22] can also be used. Enhanced local phase bone features can also be used as an input to a registration method without the need for segmentation. In the context of epidural anesthesia procedures where ultrasound is used for real-time guidance, Hacihaliloglu et al. [33] enhanced spine bone surfaces using local phase tensor filter. Enhanced bone surfaces were registered to statistical shape model of the spine. The reported target registration error was 2 mm. Recently, our group has also proposed a method for the enhancement of bone shadow regions using image phase information [26]. Investigating Fig. 10.6 we can see that the proposed method classifies the ultrasound data into distinct regions corresponding to soft tissue interface, bone region, and the shadow region. In [28], we have incorporated the enhanced bone shadow and phase features into a dynamic programming-based segmentation method. Validation, performed in 150 in vivo ultrasound scans obtained from seven volunteers, achieved a mean surface localization error of 0.26 mm. Currently, our group is trying to extend these features for processing 3D ultrasound.

10.4.3 Bone Segmentation Based on Image Intensity and Phase Information

Approaches belonging to this group generally combine image intensity and phase features for improving the robustness of the segmentation. Jia et al. [40] incorporated image intensity and phase features into a dynamic programming approach which was proposed in [22]. Validation was performed on six healthy volunteers by collecting 2D ultrasound scans from greater trochanter bone. The average euclidean distance error, of the proposed method, was 0.12 mm with a processing time of 4.1 s. In [12], ultrasound was proposed as an imaging modality for scoliosis monitoring. A classification method, where image intensity and phase features were used during training, was proposed for segmenting the ultra-

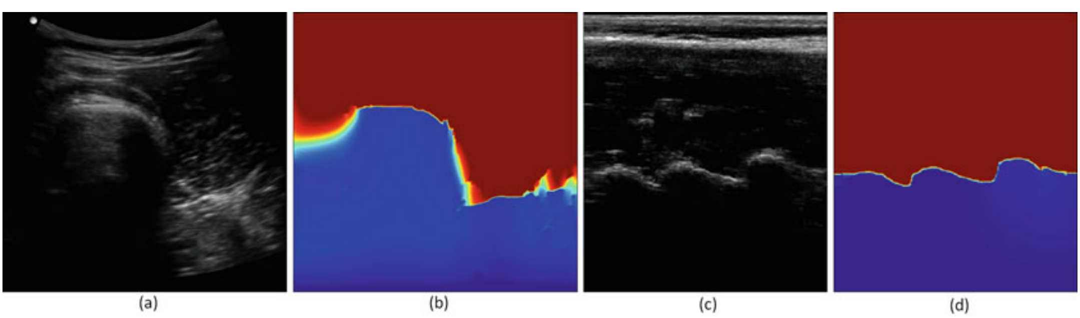

Fig. 10.6 (**a**) B-mode in vivo femur ultrasound image. (**b**) Shadow enhancement result of (**a**). (**c**) B-mode in vivo spine ultrasound image. (**d**) Shadow enhancement result of (**c**). In all the shadow-enhanced images, the shadow region is denoted with dark blue, and soft tissue interface between the ultrasound transducer and bone is denoted as dark red

sound data into bone, soft tissue, and acoustic shadow regions. Validation was performed on 2D ultrasound scans collected from seven health volunteers by scanning thoracic and lumbar regions of the spine. The proposed method achieve a classification rate of 85% for the spinous process, 92% for the acoustic shadow, and 91% for the soft tissue. In [58], local phase information, signal attenuation map, and bone shadow features were combined to create a new bone descriptor. Validation was performed on 3D ultrasound in vivo pelvic data collected from 18 trauma patients. The localization accuracy was obtained by measuring the surface fit error against the gold standard surfaces obtained from a preoperative CT data. The reported error results for all the 18 subjects were under 1 mm with a computation time of 0.26 s per slice. In [54], the segmentation problem was modeled as a graph modeling approach. The authors used local phase information, local patch image intensity statistics, shadowing, attenuation, local binary patterns, and speckle statistics as features. Validation was performed on 2D ultrasound data collected from the forearm (radius, ulna), shoulder (acromion, humerus tip), leg (fibula, tibia, malleolus), hip (iliac crest), jaw (mandible, rasmus), and fingers (phalanges). The reported accuracy was 86% for 1 mm error tolerance rate. Reported processing time was 2 min per slice.

10.4.4 Bone Segmentation Based on Machine Learning

With the increased success of machine learning-based medical image segmentation methods, some researchers have proposed new methods for segmenting bone surfaces from ultrasound data. In [6], the authors proposed random forest classification for segmentation of bone surfaces. The algorithm was validated on two large datasets: dataset 1 contained 162 2D ultrasound scans collected from 25 subjects, and dataset 2 contained 178 2D ultrasound scans collected from 21 subjects. The datasets were collected from two different research hospitals with a specific clinical focus on the spine. The reported segmentation, recall, and precision rates were 0.82 and 0.84, respectively, with a maximum computation time of 0.6 s per slice. In a recent work, same group has also investigated the use of deep learning-based methods for segmenting bone surfaces [7]. The authors used a modified version of the convolutional neural network (CNN) proposed in [62]. The quantitative comparison, against their random forest method, achieved improved segmentation results further validating the strength of deep learning methods over traditional machine learning approaches. A deep learning method, based on modification of [62], was also investigated by Salehi at al. [64]. Validation performed on 2D ultrasound data collected from healthy volunteers from femur, tibia, and pelvis bone surfaces achieved 0.87 precision and recall rates. Bone localization accuracy was not assessed.

10.5 Validation of Bone Segmentation Methods

As explained in previous sections, bone surface response in ultrasound has a certain thickness due to imaging physics and manual operation of the transducer. Figure 10.7 shows a typical bone surface response profile. The region inside the two surfaces shown in red denotes where the actual bone surface is expected to be located. Quantification of gold standard bone surface locations has been a difficult and challenging process due to the difficulty of estimating where exactly the actual bone surface is located inside this response. Despite this difficulty the use of manual expert segmentation still continues to be the main method of validation. Once the two surfaces are extracted, various distance metrics are used to report segmentation and/or localization errors. In Table 10.2 we list the distance metrics used during validation in literature. Among the metrics provided in Table 10.2, surface registration error should be avoided for reporting segmentation accuracy. We believe this metric is more suitable for reporting the accuracy of the registration method and not providing information about the accuracy

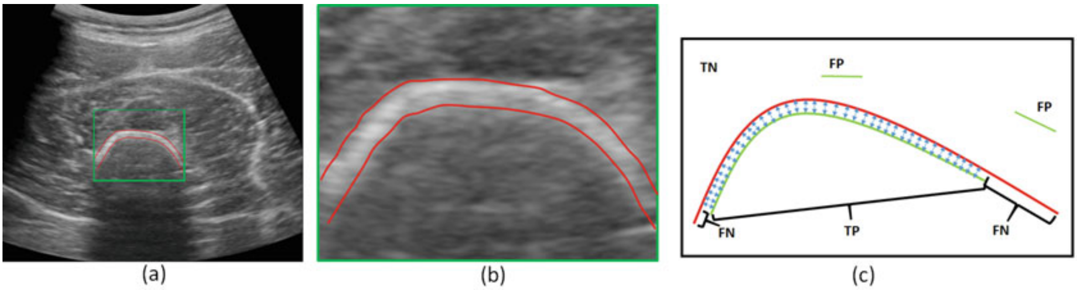

Fig. 10.7 Bone segmentation validation. (a) B-mode ultrasound image of femur bone obtained in vivo. Green rectangle is the region of interest where the bone surface response is located. (b) Zoomed-in region (shown in (a) inside the green rectangle). Region between the red lines represent the thick bone surface response where the actual bone surface resides. (c) Schematic plot for bone surface segmentation validation. Green and red curves represent automatically segmented and manual segmented bone surfaces, respectively

Table 10.2 Bone surface segmentation and/or localization error metrics used in proposed studies

Distance metric used	Reference
Euclidean root mean square distance	[58]
Surface registration error	[58, 64]
Root mean square error	[11, 48, 54]
Average euclidean distance	[3, 4, 28, 40]
Average signed distance	[30]
Hausdorff distance	[3, 4, 54, 79]

of the segmentation. If the proposed method involves the enhancement of the bone surfaces from the ultrasound data (not localization or segmentation), the surface registration error can be used.

In order to avoid the manual segmentation process, researchers have investigated the use of phantom setups. In [30], a phantom was constructed for validation of the bone enhancement method. The gold standard surfaces were extracted from the CT scan obtained by scanning the constructed phantom using an XtremeCT scanner (isometric resolution of 0.25 mm voxels). Gold standard surface was obtained by segmenting the CT scans. During the final step, the extracted gold standard surface was registered to the ultrasound data using a fiducial-based registration method. The challenge introduced during registration-based validation methods is the errors associated with the registration method which should be taken into consideration. Accuracy of bone segmentation from CT will also affect this kind of validation setup. Furthermore, phantom setups do not represent the full range of imaging characteristics and anatomical and pathological variations present in clinical data. Registration-based validation methods should report the errors associated with (1) the registration method used (target and fiducial registration errors), (2) segmentation error associated with segmenting bone surfaces from the CT data, and (3) surface matching error which represents the distance between the ultrasound bone surface and the gold standard CT bone surface.

Different groups have also investigated the use of tracked pointer devices for gold standard surface extraction. In [44], a localized pointer, tracked with an optical tracking system, was used to extract the gold standard surface information. However, this validation could only be performed on ex vivo bovine or cadaver experiments since the soft tissue interface connected to the bone surface needs to be removed for data collection which cannot be performed during in vivo scanning. Tracker system accuracy should also be considered during the pointer-based gold standard surface extraction.

Application of deep learning-based algorithms to medical data is a growing research area which is also investigated in the context of bone segmentation from ultrasound. Recently proposed machine learning-based methods [6, 7, 64] have only reported precision, recall, and F-scores of the proposed algorithm. Surface distance error related to the segmented surfaces were not reported. Specific attention should be given to report the segmentation errors of these methods. This is of special importance while investigating the overall accuracy of the proposed ultrasound-based CAOS system. Deep learning methods require a larger dataset with expert label annotations. Labels provided by experts for ultrasound bone segmentation have a certain uncertainty, and this will affect the accuracy of the deep learning methods. One potential solution to this could be to use multiple expert segmentations and provide a probability map as the label. Regions where the experts have mutual agreement can be represented with high probability, and regions where there is large disagreement can be represented by low probability.

During validation of the proposed segmentation methods, it is important to report one or more surface localization error metrics, provided in Table 10.2, together with precision and recall rates for the segmentation. In Fig. 10.7c we provide a schematic plot on how the precision and recall rates can be calculated from the true-negative (TN), true-positive (TP), false-positive (FP), and false-negative (FN) pixel values. In Fig. 10.7c automatically extracted surface is represented with green curves, while expert segmentation is represented with red curve. Since segmented bone surfaces do not always overlap with the gold standard surface, in order to calculate the TP values, a distance threshold can be chosen. Segmented pixels having a distance value below the threshold can be assigned as TP pixels and above the threshold value can be used as FP pixels. Bone segmentation error will contribute to the overall accuracy of the developed CAOS system the segmentation error. Therefore, during the selection of the threshold value, important consideration should be given to pick a small value (such as 1 or 0.5 mm) and avoid larger values (such as 2 mm).

10.6 Discussions and Future Trends

Imaging is one of the most important components in all of the CAOS systems. In this chapter we have described research efforts directed toward the application of ultrasound, as an intraoperative imaging modality, for various orthopedic procedures. We have also discussed efforts on non-surgical procedures, such as epidural anesthesia or scoliosis monitoring, where the main focus is on the use of this imaging modality for real-time guidance and diagnostic assessment. Despite the fact that ultrasound is one of the standard imaging modalities for neurosurgery [50,77] or biopsy procedures [35, 53], the clinical applicability of ultrasound in CAOS procedures is very few. The main reasons prohibiting the widespread acceptance of this modality in orthopedics are (1) difficulties faced during the imaging of bone surfaces, (2) high levels of speckle noise, (3) bone boundaries appearing several millimeters in thickness, and (4) limited field of view. Furthermore, the appearance of bone surface response profile in the ultrasound data differs for each anatomical bone region imaged. This can also be problematic while scanning the same bone surface due to the user-dependent imaging of ultrasound. Methods have been proposed by various groups in order to address some of these issues. In all the proposed ultrasound-based CAOS procedures, the segmented or enhanced bone ultrasound data was registered with a preoperative plan usually obtained from CT or MRI data. Promising initial results were reported for various applications. However, a robust and accurate bone segmentation or enhancement method able to work on various bone anatomy is still missing. Due to these difficulties, a commercially available ultrasound-guided CAOS system, validated on a large number of clinical trials, is currently not available.

One of the barriers remaining in the proposed segmentation methods is related to the limited number of validation studies performed. Most of the methods are validated on scans obtained from single anatomy bone region with a specific clinical focus. Once the anatomical region of interest changes, due to different clinical focus, the developed methods have difficulties in obtaining accurate segmentation results. One solution to overcome this would be the use of deep learning-based methods. A deep learning method trained on millions of ultrasound data might overcome majority of the difficulties mentioned earlier. Generalization of bone segmentation validation methods is also an important area which has not gained a lot of attention. The gold standard segmentation has a large standard deviation. As a result the accuracy of the segmentation will have an equal amount of deviation. A better validation could include the assessment of inter- and intra-user variability errors and define a new gold standard surface where the bone surface could be represented as a probabilistic surface rather than a single binary image. A joint effort in order to construct a publicly available database with gold standard expert segmentation should also be investigated. This effort might also result in the extension of the available number of expert segmentations providing a large database for improved assessment of inter-user variability errors.

Development of advanced ultrasound image acquisition and reconstruction algorithms is also another area investigated by various research groups and medical device companies. In [78], compressed sensing-based beamforming is proposed for reducing the sampling rate and processing time of image acquisition leading to sub-Nyquist sampling rate. In [47], ultrafast ultrasound image acquisition method is presented termed “functional ultrasound imaging.” The developed system can capture 20,000 frames per second, compared to the usual 50 frames per second in conventional ultrasound scanners. This promising direction will increase the widespread applicability of 3D ultrasound in orthopedic surgery as well.

Although access to radio-frequency (RF) ultrasound data is not available in most clinical ultrasound machines, some research has focused on the use of RF data for enhancement of bone data [80]. Another potential new direction can be the use of ultrasound strain imaging [37, 55]. Finally, with the new point of care ultrasound imaging research, ultrasound transducer technology is moving to a more mobile platform. Wireless or portable transducers pluggable to a USB port of a laptop are becoming more widespread. Integration of these portable transducers to an existing imaging platform will be more easy compared to a full ultrasound imaging system.

References

1. Amin DV, Kanade T, Digioia AM, Jaramaz B (2003) Ultrasound registration of the bone surface for surgical navigation. Comput Aided Surg 8(1): 1–16
2. Amiot LP, Lang K, Putzier M, Zippel H, Labelle H (2000) Comparative results between conventional and computer-assisted pedicle screw installation in the thoracic, lumbar, and sacral spine. Spine 25(5):606–614
3. Anas EMA, Seitel A, Rasoulian A, John PS, Pichora D, Darras K, Wilson D, Lessoway VA, Hacihaliloglu I, Mousavi P, Rohling R, Abolmaesumi P (2015) Bone enhancement in ultrasound using local spectrum variations for guiding percutaneous scaphoid fracture fixation procedures. Int J Comput Assist Radiol Surg 10(6):959–969
4. Anas EMA, Seitel A, Rasoulian A, John PS, Ungi T, Lasso A, Darras K, Wilson D, Lessoway VA, Fichtinger G, Rohling R, Abolmaesumi P (2016) Bone enhancement in ultrasound based on 3D local spectrum variation for percutaneous scaphoid fracture fixation. In: International conference on medical image computing and computer-assisted intervention. Springer, Cham, pp 465–473
5. Azhari H (2010) Basics of biomedical ultrasound for engineers. Wiley, Hoboken
6. Baka N, Leenstra S, van Walsum T (2017) Random forest-based bone segmentation in ultrasound. Ultrasound Med Biol 43(10):2426–2437
7. Baka N, Leenstra S, van Walsum T (2017) Ultrasound aided vertebral level localization for lumbar surgery. IEEE Trans Med Imaging 36(10):2138–2147
8. Barratt DC, Penney GP, Chan CS, Slomczykowski M, Carter TJ, Edwards PJ, Hawkes DJ (2006) Self-calibrating 3D-ultrasound-based bone registration for minimally invasive orthopedic surgery. IEEE Trans Med Imaging 25(3):312–323
9. Bäthis H, Perlick L, Tingart M, Lüring C, Zurakowski D, Grifka J (2004) Alignment in total knee arthroplasty. Bone Joint J 86(5):682–687
10. Beek M, Abolmaesumi P, Luenam S, Ellis RE, Sellens RW, Pichora DR (2008) Validation of a new surgical procedure for percutaneous scaphoid fixation using intra-operative ultrasound. Med Image Anal 12(2):152–162

11. Beitzel J, Ahmadi SA, Karamalis A, Wein W, Navab N (2012) Ultrasound bone detection using patient-specific ct prior. In: Proceedings of the 2012 annual international conference on the IEEE engineering in medicine and biology society. IEEE, Piscataway, pp 2664–2667
12. Berton F, Cheriet F, Miron MC, Laporte C (2016) Segmentation of the spinous process and its acoustic shadow in vertebral ultrasound images. Comput Biol Med 72:201–211
13. Boukerroui D, Noble JA, Brady M (2004) On the choice of band-pass quadrature filters. J Math Imaging Vis 21(1–2):53–80
14. Brendel B, Winter S, Rick A, Stockheim M, Ermert H (2002) Registration of 3D CT and ultrasound datasets of the spine using bone structures. Comput Aided Surg 7(3):146–155
15. Brudfors M, Seitel A, Rasoulian A, Lasso A, Lessoway VA, Osborn J, Maki A, Rohling RN, Abolmaesumi P (2015) Towards real-time, tracker-less 3D ultrasound guidance for spine anaesthesia. Int J Comput Assist Radiol Surg 10(6):855–865
16. Carrat L, Tonetti J, Merloz P, Troccaza J (2000) Percutaneous computer assisted iliosacral screwing: clinical validation. In: Proceedings of the Medical image computing and computer-assisted intervention–MICCAI 2000. Springer, Berlin/Heidelberg, pp 97–140
17. Chen TK, Abolmaesumi P, Pichora DR, Ellis RE (2005) A system for ultrasound-guided computer-assisted orthopaedic surgery. Comput Aided Surg 10(5–6):281–292
18. Daanen V, Tonetti J, Troccaz J (2004) A fully automated method for the delineation of osseous interface in ultrasound images. In: Proceedings of the international conference on medical image computing and computer-assisted intervention. Springer, Berlin/Heidelberg, pp 549–557
19. Ecker TM, Tannast M, Murphy SB (2007) Computed tomography-based surgical navigation for hip arthroplasty. Clin Orthop Relat Res 465:100–105
20. Felsberg M, Sommer G (2001) The monogenic signal. IEEE Trans Signal Process 49(12):3136–3144
21. Fenster A, Downey DB, Cardinal HN (2001) Three-dimensional ultrasound imaging. Phys Med Biolo 46(5):R67
22. Foroughi P, Boctor E, Swartz MJ, Taylor RH, Fichtinger G (2007) P6d-2 ultrasound bone segmentation using dynamic programming. In: Ultrasonics Symposium. IEEE, Piscataway, pp 2523–2526
23. Foroughi P, Song D, Chintalapani G, Taylor RH, Fichtinger G (2008) Localization of pelvic anatomical coordinate system using us/atlas registration for total hip replacement. In: Proceedings of the international conference on medical image computing and computer-assisted intervention. Springer, Berlin, pp 871–879
24. Ganz R, Parvizi J, Beck M, Leunig M, Nötzli H, Siebenrock KA (2003) Femoroacetabular impingement: a cause for osteoarthritis of the hip. Clin Orthop Relat Res 417:112–120
25. Grau V, Becher H, Noble JA (2007) Registration of multiview real-time 3-D echocardiographic sequences. IEEE Trans Med Imaging 26(9):1154–1165
26. Hacihaliloglu I (2017) Enhancement of bone shadow region using local phase-based ultrasound transmission maps. Int J Comput Assist Radiol Surg 12(6):951–960
27. Hacihaliloglu I (2017) Ultrasound imaging and segmentation of bone surfaces: a review. Technology 50(02):74–80
28. Hacihaliloglu I (2018) Localization of bone surfaces from ultrasound data using local phase information and signal transmission maps. In: Computational methods and clinical applications in musculoskeletal imaging. Springer, Cham, pp 1–11
29. Hacihaliloglu I, Abugharbieh R, Hodgson AJ, Rohling RN (2009) Bone surface localization in ultrasound using image phase based feature. Ultrasound Med Biol 35(9):1475–1487
30. Hacihaliloglu I, Abugharbieh R, Hodgson AJ, Rohling RN (2011) Automatic adaptive parameterization in local phase feature-based bone segmentation in ultrasound. Ultrasound Med Biol 37(10):1689–1703
31. Hacihaliloglu I, Abugharbieh R, Hodgson AJ, Rohling RN, Guy P (2012) Automatic bone localization and fracture detection from volumetric ultrasound images using 3-D local phase features. Ultrasound Med Biol 38(1):128–144
32. Hacihaliloglu I, Guy P, Hodgson AJ, Abugharbieh R (2015) Automatic extraction of bone surfaces from 3D ultrasound images in orthopaedic trauma cases. Int J Comput Assist Radiol Surg 10(8):1279–1287
33. Hacihaliloglu I, Rasoulian A, Rohling RN, Abolmaesumi P (2014) Local phase tensor features for 3-D ultrasound to statistical shape+ pose spine model registration. IEEE Trans Med Imaging 33(11):2167–2179
34. Herscovici D Jr, Sanders RW (2000) The effects, risks, and guidelines for radiation use in orthopaedic surgery. Clin Orthop Relat Res 375:126–132
35. Hodge KK, McNeal JE, Terris MK, Stamey TA (1989) Random systematic versus directed ultrasound guided transrectal core biopsies of the prostate. J Urol 142(1):71–74
36. Hott JS, Deshmukh VR, Klopfenstein JD, Sonntag VK, Dickman CA, Spetzler RF, Papadopoulos SM (2004) Intraoperative Iso-C C-Arm navigation in craniospinal surgery: the first 60 cases. Neurosurgery 54(5):1131–1137
37. Hussain MA, Hodgson AJ, Abugharbieh R (2017) Strain-initialized robust bone surface detection in 3-D ultrasound. Ultrasound Med Biol 43(3):648–661
38. Ionescu G, Lavallée S, Demongeot J (1999) Automated registration of ultrasound with CT images: application to computer assisted prostate radiotherapy and orthopedics. In: Proceedings of the international conference on medical image computing

and computer-assisted intervention. Springer, Berlin, pp 768–777
39. Jain AK, Taylor RH (2004) Understanding bone responses in B-mode ultrasound images and automatic bone surface extraction using a Bayesian probabilistic framework. In: Medical imaging 2004: ultrasonic imaging and signal processing, vol 5373. International Society for Optics and Photonics, pp 131–143, 28 Apr 2004
40. Jia R, Mellon SJ, Hansjee S, Monk A, Murray D, Noble JA (2016) Automatic bone segmentation in ultrasound images using local phase features and dynamic programming. In: 2016 IEEE 13th international symposium on biomedical imaging (ISBI). IEEE, Piscataway, pp 1005–1008
41. Joskowicz L, Milgrom C, Simkin A, Tockus L, Yaniv Z (1998) Fracas: a system for computer-aided image-guided long bone fracture surgery. Comput Aided Surg 3(6):271–288
42. Karamalis A, Wein W, Klein T, Navab N: Ultrasound confidence maps using random walks. Med Image Anal 16(6):1101–1112 (2012)
43. Koivukangas T, Katisko JP, Koivukangas JP (2013) Technical accuracy of optical and the electromagnetic tracking systems. SpringerPlus 2(1):90
44. Kowal J, Amstutz C, Langlotz F, Talib H, Ballester MG (2007) Automated bone contour detection in ultrasound b-mode images for minimally invasive registration in computer-assisted surgery an in vitro evaluation. Int J Med Rob Comput Assist Surg 3(4):341–348
45. Learmonth ID, Young C, Rorabeck C (2007) The operation of the century: total hip replacement. Lancet 370(9597):1508–1519
46. Linsenmaier U, Rock C, Euler E, Wirth S, Brandl R, Kotsianos D, Mutschler W, Pfeifer KJ (2002) Three-dimensional CT with a modified c-arm image intensifier: feasibility 1. Radiology 224(1):286–292
47. Macé E, Montaldo G, Cohen I, Baulac M, Fink M, Tanter M (2011) Functional ultrasound imaging of the brain. Nat Methods 8(8):662
48. Masson-Sibut A, Nakib A, Petit E, Leitner F (2011) Computer-assisted intramedullary nailing using real-time bone detection in 2D ultrasound images. In: International workshop on machine learning in medical imaging. Springer, Berlin/Heidelberg, pp 18–25, 18 Sept 2011
49. Mercier L, Langø T, Lindseth F, Collins LD (2005) A review of calibration techniques for freehand 3-D ultrasound systems. Ultrasound Med Biol 31(2):143–165
50. Moiyadi AV, Unsgård G (2016) Navigable ultrasound, 3D ultrasound and fusion imaging in neurosurgery. In: Intraoperative ultrasound (IOUS) in neurosurgery. Springer, Cham, pp 135–145 (2016)
51. Mulet-Parada M, Noble JA (2000) 2d+ t acoustic boundary detection in echocardiography. Med Image Anal 4(1):21–30
52. Noble JA, Boukerroui D (2006) Ultrasound image segmentation: a survey. IEEE Trans Med Imaging 25(8):987–1010
53. Nyland TG, Mattoon JS, Herrgesell EJ, Wisner ER (2002) Ultrasound-guided biopsy. Small Anim diagn Ultrasound 2:30–48
54. Ozdemir F, Ozkan E, Goksel O (2016) Graphical modeling of ultrasound propagation in tissue for automatic bone segmentation. In: Proceedings of the international conference on medical image computing and computer-assisted intervention. Springer, Cham, pp 256–264
55. Parmar BJ, Yang X, Chaudhry A, Shajudeen PS, Nair SP, Weiner BK, Tasciotti E, Krouskop TA, Righetti R (2015) Ultrasound elastography assessment of bone/soft tissue interface. Phys Med Biol 61(1):131
56. Penney GP, Barratt DC, Chan CS, Slomczykowski M, Carter TJ, Edwards PJ, Hawkes DJ (2006) Cadaver validation of intensity-based ultrasound to ct registration. Med Image Anal 10(3): 385–395
57. Peters T, Cleary K (2008) Image-guided interventions: technology and applications. Springer, New York
58. Quader N, Hodgson A, Abugharbieh R (2014) Confidence weighted local phase features for robust bone surface segmentation in ultrasound. In: Proceedings of the workshop on clinical image-based procedures. Springer, Cham, pp 76–83
59. Rasoulian A, Abolmaesumi P, Mousavi P (2012) Feature-based multibody rigid registration of CT and ultrasound images of lumbar spine. Med Phys 39(6):3154–3166
60. Rasoulian A, Seitel A, Osborn J, Sojoudi S, Nouranian S, Lessoway, VA, Rohling RN, Abolmaesumi P (2015) Ultrasound-guided spinal injections: a feasibility study of a guidance system. Int J Comput Assist Radiol Surg 10(9):1417–1425
61. Riley GM, McWalter EJ, Stevens KJ, Safran MR, Lattanzi R, Gold GE (2015) MRI of the hip for the evaluation of femoroacetabular impingement; past, present, and future. J Magn Reson Imaging 41(3):558–572
62. Ronneberger O, Fischer P, Brox T (2015) U-net: convolutional networks for biomedical image segmentation. In: Proceedings of the international conference on medical image computing and computer-assisted intervention. Springer, Cham, pp 234–241
63. Rose JL, Goldberg BB (1979) Basic physics in diagnostic ultrasound. Wiley, New York
64. Salehi M, Prevost R, Moctezuma JL, Navab N, Wein W (2017) Precise ultrasound bone registration with learning-based segmentation and speed of sound calibration. In: Proceedings of the international conference on medical image computing and computer-assisted intervention. Springer, Cham, pp 682–690
65. Sanders R, Fortin P, DiPasquale T, Walling A (1993) Operative treatment in 120 displaced intraarticular calcaneal fractures results using a prognostic computed tomography scan classification. Clin Orthop Relat Res 290:87–95

66. Schep NWL, Broeders I, van der Werken C (2003) Computer assisted orthopaedic and trauma surgery: state of the art and future perspectives. Injury 34(4):299–306
67. Schumann S (2016) State of the art of ultrasound-based registration in computer assisted orthopedic interventions. In: Proceedings of the computational radiology for orthopaedic interventions. Springer, Cham, pp 271–297
68. Slomczykowski MA, Hofstetter R, Sati M, Krettek C, Nolte LP (2001) Novel computer-assisted fluoroscopy system for intraoperative guidance: feasibility study for distal locking of femoral nails. J Orthop Trauma 15(2):122–131
69. Solberg OV, Lindseth F, Torp H, Blake RE, Hernes TAN (2007) Freehand 3D ultrasound reconstruction algorithms a review. Ultrasound Med Biol 33(7):991–1009
70. Stulberg SD, Loan P, Sarin V (2002) Computer-assisted navigation in total knee replacement: results of an initial experience in thirty-five patients. JBJS 84(suppl_2):S90–S98
71. Suetens P (2017) Fundamentals of medical imaging. Cambridge University Press, Cambridge
72. Suri JS (2008) Advances in diagnostic and therapeutic ultrasound imaging. Artech House, Boston/London
73. Talib H, Peterhans M, Garcia J, Styner M, Ballester MAG (2011) Information filtering for ultrasound-based real-time registration. IEEE Trans Biomed Eng 58(3):531–540
74. Tonetti J, Carrat L, Blendea S, Merloz P, Troccaz J, Lavallée S, Chirossel JP (2001) Clinical results of percutaneous pelvic surgery. Computer assisted surgery using ultrasound compared to standard fluoroscopy. Comput Aided Surg 6(4): 204–211
75. Turnbull DH, Foster FS (1992) Fabrication and characterization of transducer elements in two-dimensional arrays for medical ultrasound imaging. IEEE Trans Ultrason Ferroelectr Freq Control 39(4):464–475
76. Tyryshkin K, Mousavi P, Beek M, Ellis R, Pichora D, Abolmaesumi P (2007) A navigation system for shoulder arthroscopic surgery. Proc Inst Mech Eng Part H J Eng Med 221(7):801–812
77. Unsgaard G, Rygh O, Selbekk T, Müller T, Kolstad F, Lindseth F, Hernes TN (2006) Intra-operative 3d ultrasound in neurosurgery. Acta Neurochir 148(3):235–253
78. Wagner N, Eldar YC, Friedman Z (2012) Compressed beamforming in ultrasound imaging. IEEE Trans Signal Process 60(9):4643–4657
79. Wein W, Karamalis A, Baumgartner A, Navab N (2015) Automatic bone detection and soft tissue aware ultrasound–ct registration for computer-aided orthopedic surgery. Int J Comput Assist Radiol Surg 10(6):971–979
80. Wen X, Salcudean S (2007) Enhancement of bone surface visualization using ultrasound radio-frequency signals. In: IEEE Ultra. Symp, vol 1051, pp 2535–2538
81. Wendl K, Von Recum J, Wentzensen A, Grützner P (2003) Iso-C (3D0-assisted) navigated implantation of pedicle screws in thoracic lumbar vertebrae. Unfallchirurg 106(11):907–913
82. Yaniv Z, Cleary K (2006) Image-guided procedures: A review. Comput Aided Interv Med Robot 3: 1–63

11 A Novel Ultrasound-Based Lower Extremity Motion Tracking System

Kenan Niu, Victor Sluiter, Jasper Homminga, André Sprengers, and Nico Verdonschot

Abstract

Tracking joint motion of the lower extremity is important for human motion analysis. In this study, we present a novel ultrasound-based motion tracking system for measuring three-dimensional (3D) position and orientation of the femur and tibia in 3D space and quantifying tibiofemoral kinematics under dynamic conditions. As ultrasound is capable of detecting underlying bone surface noninvasively through multiple layers of soft tissues, an integration of multiple A-mode ultrasound transducers with a conventional motion tracking system provides a new approach to track the motion of bone segments during dynamic conditions. To demonstrate the technical and clinical feasibilities of this concept, an in vivo experiment was conducted. For this purpose the kinematics of healthy individuals were determined in treadmill walking conditions and stair descending tasks. The results clearly demonstrated the potential of tracking skeletal motion of the lower extremity and measuring six-degrees-of-freedom (6-DOF) tibiofemoral kinematics and related kinematic alterations caused by a variety of gait parameters. It was concluded that this prototyping system has great potential to measure human kinematics in an ambulant, non-radiative, and noninvasive manner.

Keywords

Joint motion tracking · A-mode ultrasound · Knee · Kinematics · Lower extremity · Gait analysis

11.1 Introduction

Measuring skeletal motion occurring in the human joints is important to understand the functions of human joints [1], to assist the pathological diagnoses [2] and to monitor the actual three-dimensional (3D) positions of bone segments during surgeries [3] (e.g., total hip arthroplasty [4] (THA), total knee arthroplasty [5, 6] (TKA)) and to assess the outcomes of treatments [7, 8]. Skeletal kinematic data may be used in motion analyses combined with biomechanical modeling, e.g., musculoskeletal models for inverse

K. Niu (✉) · V. Sluiter · J. Homminga
Laboratory of Biomechanical Engineering, MIRA Institute, University of Twente, Enschede, the Netherlands

A. Sprengers · N. Verdonschot
Orthopaedic Research Lab, Radboud University Medical Center, Nijmegen, the Netherlands

G. Zheng et al. (eds.), *Intelligent Orthopaedics*, Advances in Experimental Medicine and Biology 1093, https://doi.org/10.1007/978-981-13-1396-7_11

dynamics approaches [9, 10]. Hence, a valid representation of actual skeletal motion and an accurate skeletal kinematics estimation is important in the fields of orthopedic research and human motion analysis [11]. However, the fact is that human skeletal structures are not exposed to the outside environment but are surrounded by the soft tissues (the muscles, the fat, the skin, etc.). Therefore, an effective measuring technique that could directly or indirectly detect the motion of the bone is necessary to monitor and trace the movements of bone segments underlying the skin surface [12, 13].

Currently, skin-mounted markers are widely used in human motion analysis to estimate the motions of bones by assuming no relative motions between the skin and bone [14]. However, this method is subject to soft tissue artifacts (STA) because the markers attached on the skin cannot represent the actual motions of underlying bone segments [15]. It has been reported that STA can cause measurement errors of markers up to 30 mm in the thigh [16]. The propagation of STA to knee joint kinematics has been reported to lead to average rotational errors of up to 4.4° and 13.1° and average translational errors of up to 13.0 mm and 16.1 mm for walking and cutting motions, respectively [17]. Although many researchers attempted to compensate for the STA by computer modeling [13, 18–24], no significant improvement has been found in previous studies [12].

With the development of medical imaging technologies, fluoroscopic systems have been utilized to capture high accurate joint kinematics in the prosthetic measurement for TKA patients [25–27]. However, high cost, cumbersome setup, and limited field of view (FOV) impede routine usage in the clinical setting. Recently, several groups have been working on the development of mobile fluoroscopy systems [28, 29]. Although using a robotic trolley or gantry carrying the fluoroscopic system following the movement of subject extends the FOV, the radiation exposure to the subject remains inevitable. Recently advanced four-dimensional (4D) MRI [30–32] and CT [33, 34] techniques have been reported to track the bone motion and to quantify the respective joint kinematics inside the scanners [30–32]. The disadvantages of this method are the limited FOV, limited sample rate, and the inability to measure kinematics during daily activities.

Besides abovementioned image modalities, ultrasound serves as a noninvasive and nonradiative imaging method to observe the soft tissues and internal organs in various clinical applications [35]. In addition, ultrasound is also capable of detecting bone surfaces through multiple layers of soft tissues [36]. Utilization of an ultrasound transducer combined with a surgical navigation system to accomplish the intraoperative registration of bone segments has been reported in computer-assisted orthopedic surgeries [37–39]. Due to its capability of detecting a bone surface under dynamic motions, the combination of multiple ultrasound transducers with conventional motion capture markers provides a new approach to estimate the 3D positions and orientations of bone segments and to quantify related joint kinematics. The bone detections (i.e., depths from the skin to bone) accompanied with corresponding spatial positions (3D coordinates of the ultrasound transducers) provide sufficient information to reconstruct the 3D bone motion per time frame without the effect of STA that exists in skin-mounted marker measurements. In vitro validation of this concept has been investigated for the knee joint in a previous study [40], which showed a relative high accuracy on the estimated tibiofemoral kinematics. The comparison with conventional skin-mounted markers measurement also has been conducted to assess the performance against widely used skin markers measurements. The ultrasound tracking system showed high accuracy in estimated 3D bone positions and quantified six-degrees-of-freedom (6-DOF) joint kinematics (maximum root-mean-square (RMS) error 3.44° for rotations and 4.88 mm for translations). However, to evaluate the capability of tracking knee joint motions and quantifying 6-DOF tibiofemoral kinematics of a variety of daily activities for living subjects is a crucial step to explore its technical and clinical implementation.

The aim of this study was to demonstrate and assess the in vivo capability of our proposed ultrasound tracking system when healthy subjects performed several daily activities, including treadmill walking at three different speeds and stair descent. We expected that kinematics alterations caused by different imposed gait parameters could also be identified by the ultrasound tracking system.

11.2 Methods

11.2.1 Participants

Five subjects (five males, age 37 ± 10 years, height 180 ± 8 cm, weight 75.4 ± 14.1 kg) participated in this study. Although only one subject had a meniscus operation four years ago, there was no influence and/or complaints on performing exercises reflecting daily activities as conducted during this experiment. The other subjects have no history of injury, treatment, or disorder affecting knee and hip functions. All subjects gave written informed consent. Prior to the experiment, each subject had an MRI scan using a Philips INGENIA 3T (BEST, the Netherlands) with a voxel size of 0.5 mm × 0.5 mm × 1 mm at the Radiology Department of Academisch Medisch Centrum (AMC, Amsterdam, Netherlands). After the MRI scan, the obtained MRI images were segmented manually to generate subject-specific geometrical surface models of the femur and tibia using Mimics 17.0 (Materialise N.V., Leuven, Belgium), which were exported in STL format. The femoral and tibial anatomical reference frames (ARF) were then defined based on obtained bone geometries using a method previously described [41]. Approval of this study (2017-3578) was obtained from the Ethical Committee at the Radboud University Medical Center (RUMC).

11.2.2 Ultrasound Tracking System

The ultrasound tracking system consisted of a conventional motion tracking system and an ultrasound signal acquisition system. In this study, we used Visualeyez VZ4000v system (PTI Phoenix Technologies Inc., Vancouver, Canada) equipped with two trackers to provide spatial positioning (see Figs. 11.1 and 11.2) with less than 0.5 mm RMS error [42]. The ultrasound signal and marker positioning information was collected and synchronized in the Diagnostic Sonar FI Toolbox (Diagnostic Sonar Ltd, Livingston, UK) with 2.3 GHz CPU (Intel Core i7-3610QE) and 8GB RAM with a custom acquisition program written by LabVIEW (National Instruments, Austin, Texas, USA). Thirty A-mode ultrasound transducers (7.5 MHz,

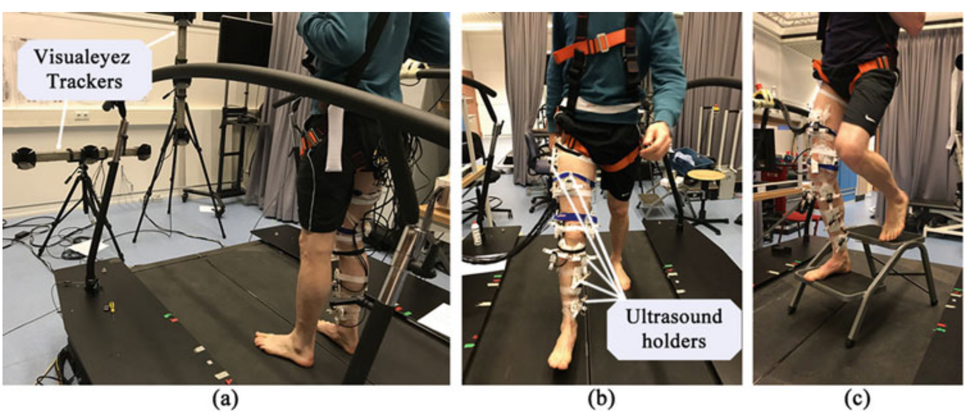

Fig. 11.1 (**a**) A side view of experimental setup, including two Visualeyez trackers to track the optical markers on ultrasound holder; (**b**) a front view of experimental setup, one subject wore all ultrasound holder and performed a treadmill walking task; (**c**) a subject performed stair descent with the ultrasound tracking system measurement

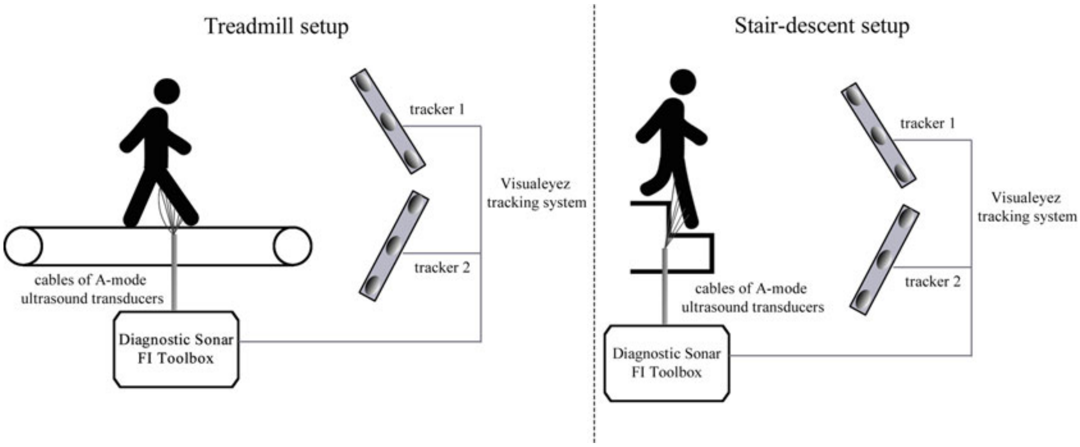

Fig. 11.2 A schematic representation of the experimental setups for treadmill walking (left) and stair descent (right). Two Visualeyez trackers were used to record the spatial information of attached ultrasound holders. Diagnostic Sonar FI Toolbox received all raw ultrasound signals and was synchronized with collected spatial information from Visualeyez trackers

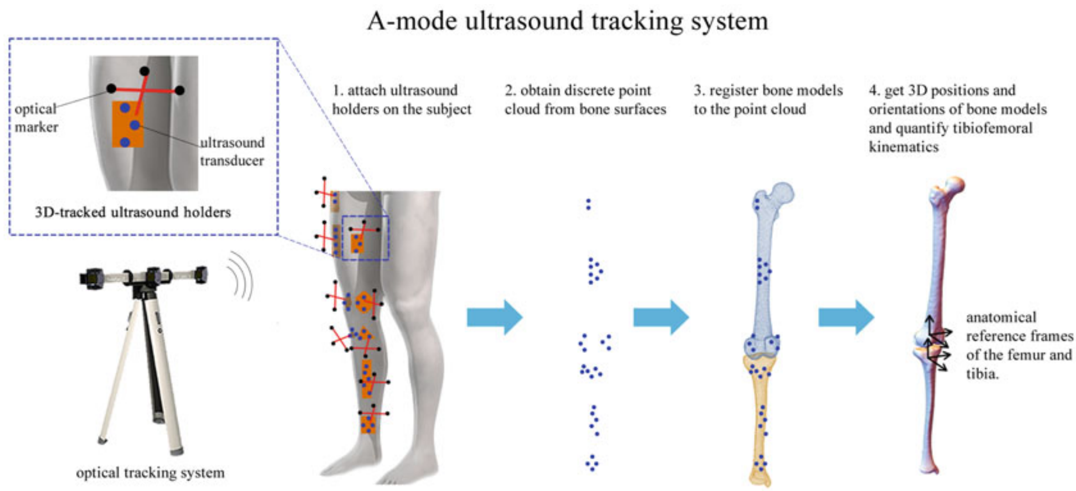

Fig. 11.3 A schematic representation of the A-mode ultrasound system to quantify tibiofemoral kinematics from obtained point cloud. Also shown is the placement of ultrasound holders on the right leg

focus at 2.5 cm, Imasonic SAS, Voray/l'Ognon, France) and 27 active optical markers (tracked by Visualeyez system) were installed into the custom ultrasound holders. The ultrasound holders cover various anatomical areas on the lower extremity, including ankle, middle shaft of tibia, tibial condyles, femoral epicondyles, middle thigh, and great trochanter (Fig. 11.3). The ultrasound holders were designed in SolidWorks (Waltham, Massachusetts, USA) and manufactured using polyamide powder material in 3D printer (EOS Formiga P110, EOS GmbH, Krailling, Germany) to insure high accuracy on their 3D geometrical structures for maintaining the strength, rigidity, and stability. Therefore, the spatial relations between each A-mode ultrasound transducer and each optical marker were known parameters. Hence no further physical calibration is required as this is build-in design.

The US transducers attached to the customized ultrasound holders reproduce the necessary information (i.e., the 3D discrete point cloud) to reconstruct bone motion through the obtained raw ultrasound signals and spatial information. A brief description of this processing can be found in our previous paper [40]. The ultrasound detected point can be digitalized through the known origin and pointing direction of each ultrasound transducers and the related spatial relation between each optical marker, when the depth of bone surface is obtained. For each subject, the anatomical landmarks (ankle, middle shaft of tibia, tibial condyles, femoral epicondyles, middle thigh, great trochanter) were manually digitalized in the segmented bone models, which will be used in point cloud registration. The yielded discrete point cloud was fed to a registration algorithm, using a modified weighted iterative closest point algorithm [43, 44] to get the transformations from the original geometrical surface models to the actual 3D positions and orientations of bone models in the laboratory coordinate system. The raw ultrasound signals from 30 (15 for the femur and 15 for the tibia) A-mode ultrasound transducers and the raw 3D coordinates of 27 optical markers were synchronized and recorded at 45 Hz sample rate. Thus the 3D discrete point cloud was reproduced in 45 Hz sample rate during experiment. The respective tibiofemoral kinematics were derived from the method based on the ISB recommendations [45, 46].

11.2.3 Experiments

The ultrasound holders were attached to the right leg of each subject and were fixated by using skin tapes in order to cover all needed anatomical areas without any hindrance during movements. After attaching all ultrasound holders, each subject performed two sets of trials: (1) walking at three different imposed speeds (1 km/h, 2 km/h, and 3 km/h) on the treadmill and (2) stair descent from two consecutive stairs (first stair, 18 cm height; second stair, 21cm height, next to the ground). For treadmill walking, at least five gait cycles were recorded for each trial. For the stair-descent trial, each subject was asked to repeat three times for stair-descent trial and was always asked to step the right leg at first for each stair. It took about one and a half hours to complete an experiment of one subject, including attachment of ultrasound holders to the subject, the calibration procedure, and all measurements of all trials.

11.2.4 Data Processing

After all experiments, 3D knee joint motions and 6-DOF tibiofemoral kinematics were calculated for all trials over all gait cycles and three repeated stair-descent cycles. The calculated 6-DOF tibiofemoral kinematics of treadmill walking were averaged across five subjects under imposed three treadmill speeds. The mean and standard deviation across five subjects of calculated 6-DOF tibiofemoral kinematics for the stair-descent cycles were illustrated as the functions of percentage of two-stair descending (100% represent one complete cycle of one-stair descending; thus completed cycle is 200%).

To demonstrate the capability of detecting the bony surfaces from different anatomical areas and the capability of detecting the changes of depth of detected bone surface caused by soft tissue deformation, several M-mode (motion mode) ultrasound images were generated. M-mode image is defined as motion display of the ultrasound wave along a chosen ultrasound line (in our case, a single ultrasound transducer element) during a time period. Its x-axis represents the number of samples. Its y-axis represents the intensity of received echo in a color map. It provides a two-dimensional view of the depth changes.

11.3 Results

The mean of 6-DOF tibiofemoral kinematics across five subjects under imposed three different treadmill speeds are illustrated in Fig. 11.4 The mean $\pm$ standard deviation of 6-DOF tibiofemoral kinematics across five subjects during stair descending is shown in Fig. 11.5.

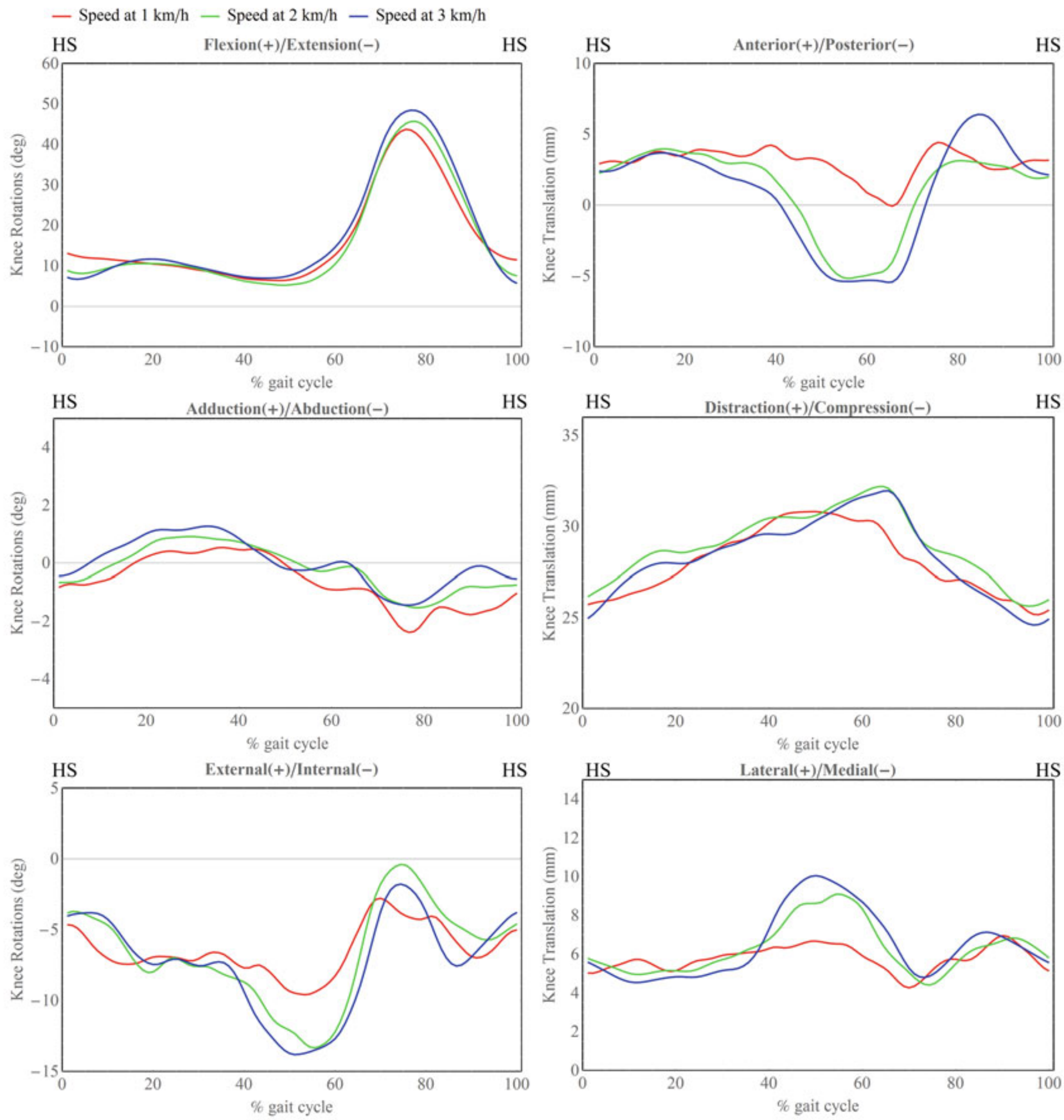

Fig. 11.4 Averaged 6-DOF tibiofemoral kinematics across five subjects for imposed three different speeds: 1 km/h (red line), 2 km/h (green line), and 3 km/h (blue line)

11.3.1 Treadmill Walking

The largest rotation motion was flexion-extension, followed by external-internal rotation and adduction-abduction. The peak knee flexion at the swing phase increased with increasing imposed speed. At heel strike, the knee was not fully extended (reach 0°) at all three imposed speeds. As the imposed treadmill speed increased, the extension angle of the knee joint increased at heel strike. The knee joint distraction started to increase from the heel strike and reached the peak until the swing phase started. Walking at the lowest imposed speed resulted in the smallest range of motion (ROM) for all 6-DOF kinematics compared to a higher imposed speed. We illustrated the M-mode images in two groups: (1) several anatomical areas at thesame

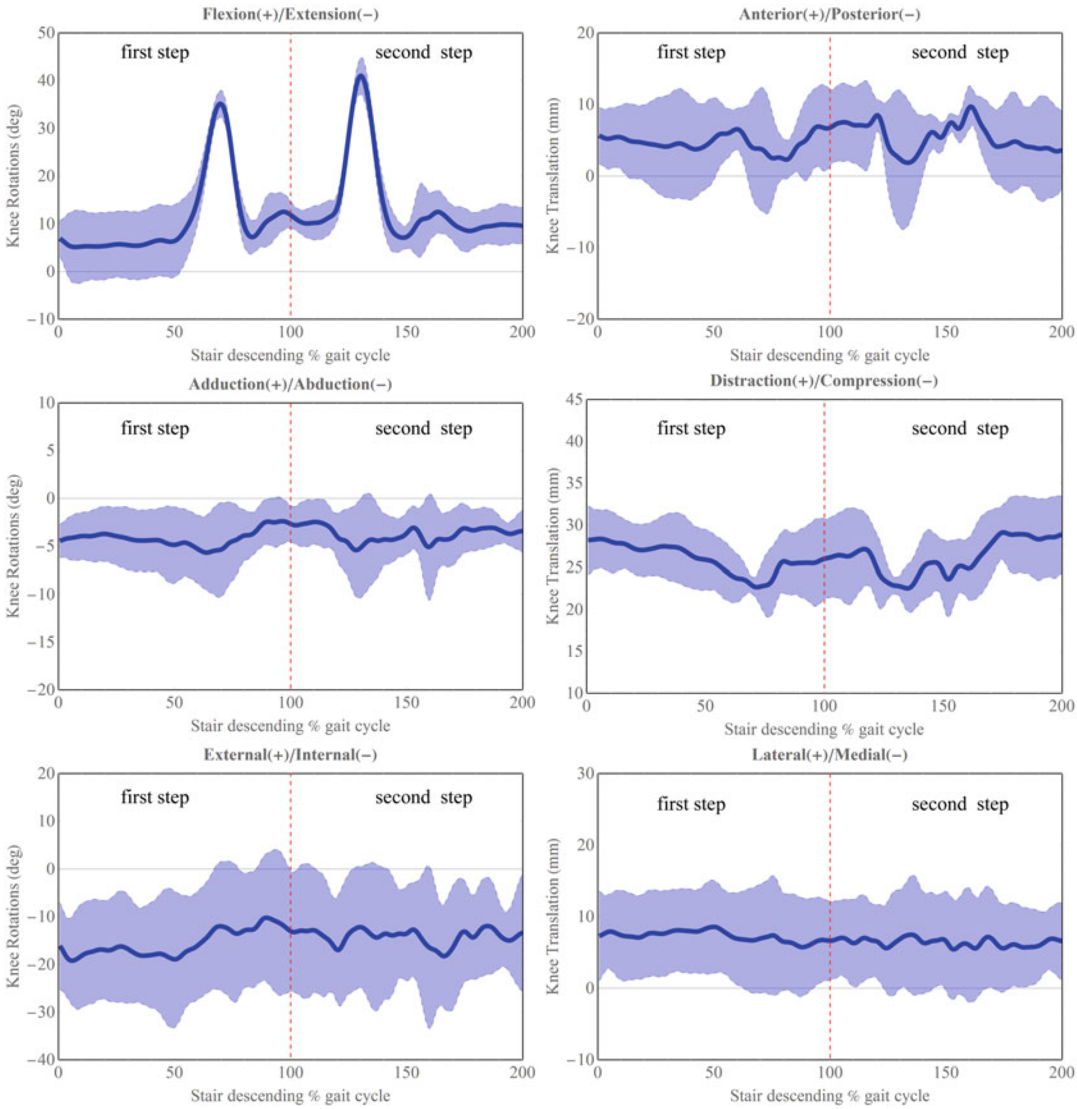

Fig. 11.5 6-DOF tibiofemoral kinematics for two consecutive stairs descending across five subjects. The solid line represents the mean data while the shaded areas represent ± 1 standard deviation from the mean. One hundred percent of stair descending cycle represents the completion of the first floor. Two hundred percent of stair descending cycle represents the completion of the second floor

treadmill speed (lateral side of middle femur, anterior side of middle femur, femoral lateral epicondyle, medial side of middle tibia at 1 km/h) and (2) three different treadmill speeds of an identical location (lateral side of middle femur at 1, 2, 3 km/h).

11.3.2 Stair Descending

The mean flexion angle across five subjects reached the first peak (35.1°) during stepping down the first stair (18 cm) and reached the second peak (41.0°) during stepping down the

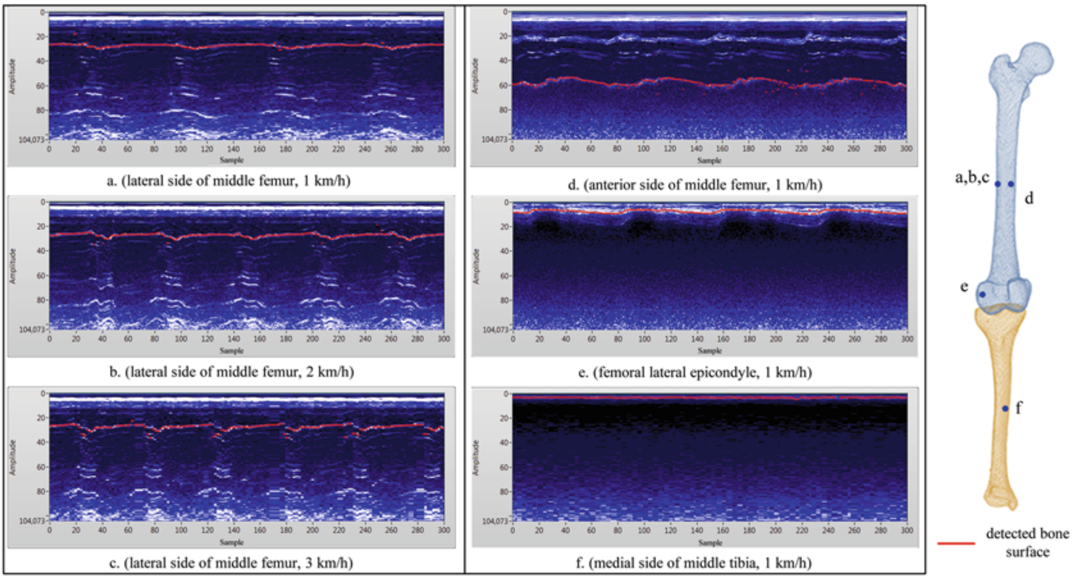

Fig. 11.6 Left: the examples of six M-mode images of one subject: x-axis of M-mode image represents the number of samples, y-axis of M-mode image represents the intensity of received ultrasound echo in a color map; (**a**, **b**, **c**) the M-mode images for lateral side of middle femur location at 1 km/h, 2 km/h, and 3km/h, respectively; (**d**) the M-mode image for anterior side of the middle femur at 1km/h; (e) the M-mode image for femoral lateral epicondyle at 1km/h; (**e**) the M-mode image for medial side of middle tibia at 1km/h; right: the illustration of abovementioned anatomical locations on the femur and tibia

second stair (21 cm). The knee joint distraction started to decrease when the right leg reached the next floor level and started to flex the knee to support the increasing pressure on the right knee. When the contralateral foot reached the same floor, the joint distraction began to increase until flexion angle was as the same as neutral standing. The similar changing pattern of joint distraction happened during stepping down to the second floor level.

11.3.3 M-mode Images

The examples of several M-mode images of one subject were illustrated in Fig. 11.6. The frequency of depth changing on the lateral side of middle femur was increased with the increase on the imposed treadmill speed. The changing range of depth also increased with the increases of speed. The depth changing at same speed was different for various anatomical locations. The depth changing of medial side of middle tibia had the smallest, since the thickness of soft tissue is the smallest compared to other locations. The anterior and lateral sides of the middle femur had the large variation in detected bone depth, as the thickness of soft tissue is the largest to other location.

11.4 Discussions

We presented a novel method to dynamically track the knee joint motion and to quantify 6-DOF tibiofemoral kinematics in a noninvasive and non-radiative manner. The combination of multiple A-mode ultrasound transducers with a conventional motion capture system provides an alternative method to capture skeletal motions and kinematics with mitigating the effect of STA. In this study, the in vivo capability of our proposed ultrasound tracking system to measure knee joint motion and to quantify 6-DOF tibiofemoral kinematics was demonstrated in two motor tasks of daily activities. The kinematic alterations caused by different gait parameters have also been identified by ultrasound tracking system. The peak flexion angle during swing phase on treadmill walking reduced apparently when participants walked at the slow imposed speed, which is in accordance with the findings in previous study [47]. Similarly, a smaller ROM was associated with a lower imposed speed during walking for all 6-DOF tibiofemoral kinematics [47]. The patterns of obtained 6-DOF tibiofemoral kinematics on the treadmill waking were in accordance with those of previous tibiofemoral kinematic outcome derived from a mobile fluoroscopy system [48]. For the stair descending, the peak flexion angle was correlated with the height of the stair level. The kinematic alterations caused by small changes of gait parameters could be recognized by our ultrasound tracking system, which proves a certain extent of sensitivity of ultrasound tracking system.

The novelty of this study lies in the secondary development of existed techniques, i.e., motion capture and ultrasound imaging. Taking advantage of ultrasound techniques extends the range of detection of a conventional motion capture system from superficial skin surface tracking to internal bony surface tracking. As a consequence, the sufficient spatial information (trajectories) of bony segments under the skin surface contributes to the accurate bone motion tracking and accurate kinematic estimation.

When comparing the ultrasound tracking system to the conventional skin-mounted markers measurement, the advantage is the removal of STA on the measurement data and its propagation on kinematic outcomes [49]. As demonstrated in the examples of M-mode images, A-mode ultrasound transducers has the capability of detecting the depth changing of bone surfaces on different anatomical areas. The capability could improve the validity of representing actual bone movement, since the trajectories of bone surfaces will be measured instead of superficial skin surfaces. A comparison with a skin-mounted marker measurement in a cadaveric setting has been conducted in our previous study. However, a critical comparison with a skin marker system under in vivo conditions is necessary, particularly if a ground truth method (e.g., an advanced mobile fluoroscopy system) [28, 29] can be incorporated. Currently, the FOV of our system is the same as the conventional motion capture systems, since it only depends on the FOV of the employed motion capture system. In addition, the length of the cables connected to the ultrasound transducers also restricts the maximum dynamic motion range. However, this aspect can be solved reasonably easy by extending the length of cables or employing an ambulant acquisition terminal instead of a stand-alone desktop computer on the side.

This work has several limitations:

Firstly, no "ground truth" measurement was employed during experiment. There is no a non-invasive and non-radiative method to obtain the ground truth of movements (walking and stair descent). Available methods like intracortical bone pins and fluoroscopic systems could potentially harm the subjects. An in vivo validation study will be completed in the near future so that the results would facilitate the improvements of current system and provide valuable comparisons with existed techniques.

Secondly, only five healthy subjects were involved in this study. Ideally, a cohort of living subject covering different patients and healthy groups with different sizes and BMIs accompanied with a ground truth measurements as a reference (e.g., advanced mobile fluoroscopy system) [28, 29] could provide more valuable information with regard to the pathological patterns on kinematics.

Thirdly, a standardized definition of the femoral and tibial ARF across different subjects is imperative for 6-DOF joint kinematics analysis. Since the discrepancies of the defined femoral and tibial ARF among different subjects caused the deviations on all 6-DOF kinematic outcomes and patterns for various motor tasks. In further study, a standardized definition of femoral and tibia ARF across different subjects should be proposed in order to eliminate the intrinsic variations among defined femoral and tibial ARF.

Fourthly, it has been shown that gait patterns on a treadmill are different to freely normal level walking [48]. However, in this study, the focus was on the demonstration of knee joint motion tracking during dynamic movements and detecting the kinematic alterations caused by different imposed treadmill speed and heights of staircase. Treadmill speed is a convenient parameter to change under a highly controlled scenario.

Fifthly, the cables and skin tapes may influence the nature gait pattern for individuals. In the future, we are aiming to develop a miniature and lightweight system toward a wearable measurement system that would facilitate its implementation in the clinic. Furthermore, future study will also focus on the improvement of designing the ultrasound holders in term of lighter, smaller, user friendly, and ergonomic design. These improvements on designs of ultrasound hold would be beneficial to popularize our system in a broader application field and to facilitate the usage among a cohort of subjects.

In summary, we developed an alternative, ultrasound tracking system that is capable of measuring knee joint motion. Hence, we conclude that this prototyping system has great potential to measure human kinematics in an ambulant, nonradiative, and noninvasive manner.

References

1. Ramsey DK, Wretenberg PF (1999) Biomechanics of the knee: methodological considerations in the in vivo kinematic analysis of the tibiofemoral and patellofemoral joint. Clin Biomech 14(9):595–611. https://doi.org/10.1016/S0268-0033(99)00015-7
2. Schilling C, Krüger S, Grupp TM, Duda GN, Blömer W, Rohlmann A (2011) The effect of design parameters of dynamic pedicle screw systems on kinematics and load bearing: an in vitro study. Eur Spine J 20(2):297–307. https://doi.org/10.1007/s00586-010-1620-6
3. Simon D. What is "registration" and why is it so important in CAOS
4. Sugano N, Sasama T, Sato Y, Nakajima Y, Nishii T, Yonenobu K et al (2001) Accuracy evaluation of surface-based registration methods in a computer navigation system for hip surgery performed through a posterolateral approach. Comput Aided Surg 6(4):195–203. https://doi.org/10.1002/igs.10011
5. Anderson KC, Buehler KC, Markel DC (2005) Computer assisted navigation in total knee arthroplasty: comparison with conventional methods. J Arthroplasty 20(7 Suppl 3):132–138. https://doi.org/10.1016/j.arth.2005.05.009
6. Mavrogenis AF, Savvidou OD, Mimidis G, Papanastasiou J, Koulalis D, Demertzis N et al (2013) Computer-assisted navigation in orthopedic surgery. Orthopedics 36(8):631–642. https://doi.org/10.3928/01477447-20130724-10
7. Kaiser JM, Vignos MF, Kijowski R, Baer G, Thelen DG (2017) Effect of Loading on In Vivo Tibiofemoral and Patellofemoral Kinematics of Healthy and ACL-Reconstructed Knees. Am J Sports Med 45(14):3272. https://doi.org/10.1177/0363546517724417
8. Zeng X, Ma L, Lin Z, Huang W, Huang Z, Zhang Y et al (2017) Relationship between Kellgren-Lawrence score and 3D kinematic gait analysis of patients with medial knee osteoarthritis using a new gait system. Sci Rep 7(1):4080. https://doi.org/10.1038/s41598-017-04390-5
9. Delp SL, Anderson FC, Arnold AS, Loan P, Habib A, John CT et al (2007) OpenSim: open-source software to create and analyze dynamic simulations of movement. IEEE Trans Biomed Eng 54(11):1940–1950. https://doi.org/10.1109/tbme.2007.901024
10. Gerus P, Sartori M, Besier TF, Fregly BJ, Delp SL, Banks SA et al (2013) Subject-specific knee joint geometry improves predictions of medial tibiofemoral contact forces. J Biomech 46(16):2778–2786. https://doi.org/10.1016/j.jbiomech.2013.09.005
11. Fuller J, Liu LJ, Murphy MC, Mann RW (1997) A comparison of lower-extremity skeletal kinematics measured using skin- and pin-mounted markers. Hum Mov Sci 16(2–3):219–242. https://doi.org/10.1016/S0167-9457(96)00053-X
12. Richard V, Cappozzo A, Dumas R (2017) Comparative assessment of knee joint models used in multi-body kinematics optimisation for soft tissue artefact compensation. J Biomech. https://doi.org/10.1016/j.jbiomech.2017.01.030
13. Andersen MS, Benoit DL, Damsgaard M, Ramsey DK, Rasmussen J (2010) Do kinematic models reduce the effects of soft tissue artefacts in skin marker-based motion analysis? An in vivo study of knee kinematics. J Biomech 43(2):268–273. https://doi.org/10.1016/j.jbiomech.2009.08.034
14. Lafortune MA, Cavanagh PR, Sommer HJ, Kalenak A (1992) Three-dimensional kinematics of the human knee during walking. J Biomech 25(4):347–357. https://doi.org/10.1016/0021-9290(92)90254-X
15. Cereatti A, Bonci T, Akbarshahi M, Aminian K, Barre A, Begon M et al (2017) Standardization proposal of soft tissue artefact description for data sharing in human motion measurements. J Biomech. https://doi.org/10.1016/j.jbiomech.2017.02.004

16. Akbarshahi M, Schache AG, Fernandez JW, Baker R, Banks S, Pandy MG (2010) Non-invasive assessment of soft-tissue artifact and its effect on knee joint kinematics during functional activity. J Biomech 43(7):1292–1301. https://doi.org/10.1016/j.jbiomech.2010.01.002
17. Benoit DL, Ramsey DK, Lamontagne M, Xu L, Wretenberg P, Renström P (2006) Effect of skin movement artifact on knee kinematics during gait and cutting motions measured in vivo. Gait Posture 24(2):152–164. https://doi.org/10.1016/j.gaitpost.2005.04.012
18. Bonnet V, Richard V, Camomilla V, Venture G, Cappozzo A, Dumas R (2017) Joint kinematics estimation using a multi-body kinematics optimisation and an extended Kalman filter, and embedding a soft tissue artefact model. J Biomech. https://doi.org/10.1016/j.jbiomech.2017.04.033
19. Cappozzo A, Cappello A, Croce UD, Pensalfini F (1997) Surface-marker cluster design criteria for 3-D bone movement reconstruction. IEEE Trans Biomed Eng 44(12):1165–1174. https://doi.org/10.1109/10.649988
20. Andersen MS, Damsgaard M, Rasmussen J (2009) Kinematic analysis of over-determinate biomechanical systems. Comput Methods Biomech Biomed Eng 12(4):371–384. https://doi.org/10.1080/10255840802459412
21. Bonnechère B, Sholukha V, Salvia P, Rooze M, Van Sint Jan S (2015) Physiologically corrected coupled motion during gait analysis using a model-based approach. Gait Posture 41(1):319–322. https://doi.org/10.1016/j.gaitpost.2014.09.012
22. Charlton IW, Tate P, Smyth P, Roren L (2004) Repeatability of an optimised lower body model. Gait Posture 20(2):213–221. https://doi.org/10.1016/j.gaitpost.2003.09.004
23. Duprey S, Cheze L, Dumas R (2010) Influence of joint constraints on lower limb kinematics estimation from skin markers using global optimization. J Biomech 43(14):2858–2862. https://doi.org/10.1016/j.jbiomech.2010.06.010
24. Lu TW, O'Connor JJ et al (1999) J Biomech 32(2):129–134. https://doi.org/10.1016/S0021-9290(98)00158-4
25. Bingham J, Li G (2006) An optimized image matching method for determining in-vivo TKA kinematics with a dual-orthogonal fluoroscopic imaging system. J Biomech Eng 128(4):588–595. https://doi.org/10.1115/1.2205865
26. Baka N, Kaptein BL, Giphart JE, Staring M, de Bruijne M, Lelieveldt BPF et al (2014) Evaluation of automated statistical shape model based knee kinematics from biplane fluoroscopy. J Biomech 47(1):122–129. https://doi.org/10.1016/j.jbiomech.2013.09.022
27. Gray HA, Guan S, Pandy MG (2017) Accuracy of mobile biplane X-ray imaging in measuring 6-degree-of-freedom patellofemoral kinematics during overground gait. J Biomech 57:152–156. https://doi.org/10.1016/j.jbiomech.2017.04.009
28. Guan S, Gray HA, Keynejad F, Pandy MG (2016) Mobile biplane x-ray imaging system for measuring 3D dynamic joint motion during overground gait. IEEE Trans Med Imaging 35(1):326–336. https://doi.org/10.1109/TMI.2015.2473168
29. List R, Postolka B, Schutz P, Hitz M, Schwilch P, Gerber H et al (2017) A moving fluoroscope to capture tibiofemoral kinematics during complete cycles of free level and downhill walking as well as stair descent. PLoS One 12(10):e0185952. https://doi.org/10.1371/journal.pone.0185952
30. Mazzoli V, Schoormans J, Froeling M, Sprengers AM, Coolen BF, Verdonschot N et al (2017) Accelerated 4D self-gated MRI of tibiofemoral kinematics. NMR Biomed. https://doi.org/10.1002/nbm.3791
31. Clarke EC, Martin JH, d'Entremont AG, Pandy MG, Wilson DR, Herbert RD (2015) A non-invasive, 3D, dynamic MRI method for measuring muscle moment arms in vivo: Demonstration in the human ankle joint and Achilles tendon. Med Eng Phys 37(1):93–99. https://doi.org/10.1016/j.medengphy.2014.11.003
32. Kaiser J, Bradford R, Johnson K, Wieben O, Thelen DG (2013) Measurement of 3D tibiofemoral kinematics using volumetric SPGR-VIPR Imaging. Magn Reson Med 69(5):1310–1316. https://doi.org/10.1002/mrm.24362
33. Forsberg D, Lindblom M, Quick P, Gauffin H (2016) Quantitative analysis of the patellofemoral motion pattern using semi-automatic processing of 4D CT data. Int J Comput Assist Radiol Surg 11(9):1731–1741. https://doi.org/10.1007/s11548-016-1357-8
34. Zhao K, Breighner R, Holmes D, Leng S, McCollough C, An K-N (2015) A technique for quantifying wrist motion using four-dimensional computed tomography: approach and validation. J Biomech Eng 137(7):0745011–0745015. https://doi.org/10.1115/1.4030405
35. Smistad E, Falch TL, Bozorgi M, Elster AC, Lindseth F (2015) Medical image segmentation on GPUs – A comprehensive review. Med Image Anal 20(1):1–18. https://doi.org/10.1016/j.media.2014.10.012
36. Wein W, Karamalis A, Baumgartner A, Navab N (2015) Automatic bone detection and soft tissue aware ultrasound–CT registration for computer-aided orthopedic surgery. Int J Comput Assist Radiol Surg 10(6):971–979. https://doi.org/10.1007/s11548-015-1208-z
37. Fieten L, Schmieder K, Engelhardt M, Pasalic L, Radermacher K, Heger S (2009) Fast and accurate registration of cranial CT images with A-mode ultrasound. Int J Comput Assist Radiol Surg 4(3):225–237. https://doi.org/10.1007/s11548-009-0288-z
38. Talib H, Peterhans M, Garcia J, Styner M, Gonzalez Ballester MA (2011) Information filtering for ultrasound-based real-time registration. IEEE Trans Biomed Eng 58(3):531–540. https://doi.org/10.1109/TBME.2010.2063703
39. Otake Y, Armand M, Armiger RS, Kutzer MD, Basafa E, Kazanzides P et al (2012) Intraoperative image-based multiview 2D/3D registration

for image-guided orthopaedic surgery: incorporation of fiducial-based C-arm tracking and GPU-acceleration. IEEE Trans Med Imaging 31(4):948–962. https://doi.org/10.1109/TMI.2011.2176555
40. Niu K, Sluiter V, Sprengers A, Homminga J, Verdonschot N (eds) (2017) A novel tibiafemoral kinematics measurement system based on multi-channel a-mode ultrasound system. In: CAOS 2017. 17th annual meeting of the international society for computer assisted orthopaedic surgery; 2017 June 13, EasyChair, Aachen
41. Miranda DL, Rainbow MJ, Leventhal EL, Crisco JJ, Fleming BC (2010) Automatic determination of anatomical coordinate systems for three-dimensional bone models of the isolated human knee. J Biomech 43(8):1623–1626. https://doi.org/10.1016/j.jbiomech.2010.01.036
42. Inc. PPT. VZ4000v technical specifications. http://www.ptiphoenix.com/products/trackers/VZ4000v. Accessed 3 Mar 2017
43. Maurer CR Jr, Maciunas RJ, Fitzpatrick JM (1998) Registration of head CT images to physical space using a weighted combination of points and surfaces. IEEE Trans Med Imaging 17(5):753–761. https://doi.org/10.1109/42.736031
44. Besl PJ, McKay HD (1992) A method for registration of 3-D shapes. IEEE Trans Pattern Anal Mach Intell 14(2):239–256. https://doi.org/10.1109/34.121791
45. Wu G, Cavanagh PR (1995) ISB recommendations for standardization in the reporting of kinematic data. J Biomech 28(10):1257–1261. https://doi.org/10.1016/0021-9290(95)00017-C
46. Grood ES, Suntay WJ (1983) A joint coordinate system for the clinical description of three-dimensional motions: application to the knee. J Biomech Eng 105(2):136–144
47. Mannering N, Young T, Spelman T, Choong PF (2017) Three-dimensional knee kinematic analysis during treadmill gait: Slow imposed speed versus normal self-selected speed. Bone Joint Res 6(8):514–521. https://doi.org/10.1302/2046-3758.68.bjr-2016-0296.r1
48. Guan S, Gray HA, Schache AG, Feller J, de Steiger R, Pandy MG (2017) In vivo six-degree-of-freedom knee-joint kinematics in overground and treadmill walking following total knee arthroplasty. J Orthop Res 35:1634–1643. https://doi.org/10.1002/jor.23466
49. Jia R, Monk P, Murray D, Noble JA, Mellon S (2017) CAT & MAUS: A novel system for true dynamic motion measurement of underlying bony structures with compensation for soft tissue movement. J Biomech. https://doi.org/10.1016/j.jbiomech.2017.04.015

12 Computer-Assisted Planning, Simulation, and Navigation System for Periacetabular Osteotomy

Li Liu, Klaus Siebenrock, Lutz-P. Nolte, and Guoyan Zheng

Abstract

Periacetabular osteotomy (PAO) is an effective approach for surgical treatment of hip dysplasia in young adults. However, achieving an optimal acetabular reorientation during PAO is the most critical and challenging step. Routinely, the correct positioning of the acetabular fragment largely depends on the surgeon's experience and is done under fluoroscopy to provide the surgeon with continuous live x-ray guidance. Our developed system starts with a fully automatic detection of the acetabular rim, which allows for quantifying the acetabular 3D morphology with parameters such as acetabular orientation, femoral head extrusion index (EI), lateral center-edge (LCE) angle, and total and regional femoral head coverage (FHC) ratio for computer-assisted diagnosis, planning, and simulation of PAO. Intraoperative navigation is conducted to implement the preoperative plan. Two validation studies were conducted on four sawbone models to evaluate the efficacy of the system intraoperatively and postoperatively. By comparing the preoperatively planned situation with the intraoperatively achieved situation, average errors of 0.6° ± 0.3°, 0.3° ± 0.2°, and 1.1° ± 1.1° were found, respectively, along three motion directions (flexion/extension, abduction/adduction, and external rotation/internal rotation). In addition, by comparing the preoperatively planned situation with the postoperative results, average errors of 0.9° ± 0.3° and 0.9° ± 0.7° were found for inclination and anteversion, respectively.

Keywords

Hip dysplasia · Periacetabular osteotomy (PAO) · Planning · Simulation · Navigation · Image-guided surgery · Joint preservation surgery

L. Liu (✉)
National-Regional Key Technology Engineering Laboratory for Medical Ultrasound, Guangdong Key Laboratory for Biomedical Measurements and Ultrasound Imaging, School of Biomedical Engineering, Health Science Center, Shenzhen University, Shenzhen, China

Institute for Surgical Technology and Biomechanics, University of Bern, Bern, Switzerland
e-mail: li.liu@szu.edu.cn

K. Siebenrock
Department of Orthopedic Surgery, Inselspital, University of Bern, Bern, Switzerland

L.-P. Nolte · G. Zheng
Institute for Surgical Technology and Biomechanics, University of Bern, Bern, Switzerland

G. Zheng et al. (eds.), *Intelligent Orthopaedics*, Advances in Experimental Medicine and Biology 1093, https://doi.org/10.1007/978-981-13-1396-7_12

12.1 Introduction

Developmental dysplasia of the hip joint is a prearthrotic deformity resulting in osteoarthritis at a very young age. Periacetabular osteotomy (PAO) is an effective approach for surgical treatment of painful dysplasia of the hip in younger patients [1]. The aim of PAO is to increase acetabular coverage of the femoral head and to reduce contact pressures by realigning the hip joint [2, 3]. However, insufficient reorientation leads to continued instability, while excessive reorientation correction would result in femoroacetabular impingement (FAI) [4, 5]. Therefore, a main important factor for clinical outcome and long-term success of PAO is to achieve an optimal acetabular reorientation [6]. The application of computer-assisted planning and navigation in PAO opens such an opportunity by showing its potential to improve surgical outcomes in PAO. Abraham et al. [7] reported an experimental cadaveric study to investigate the feasibility of preoperative 3D osteotomy planning and acetabular fragment repositioning in performing intraoperatively navigated PAOs. Hsieh et al. [8] assessed the efficacy of the navigated PAO procedure in 36 clinical cases using a commercially available navigation application for total hip arthroplasty (THA) (VectorVision, BrainLab Inc., Westchester, IL). Langlotz et al. [9] developed the first customized navigation system for PAO and applied it in 14 clinical cases. However, this system is only limited to intraoperative navigation and does not incorporate the preoperative planning module. More recently, Murphy et al. [10] developed a computer-assisted biomechanical guidance system (BGS) for performing PAO. The system combines geometric and biomechanical feedback with intraoperative tracking to guide the surgeon through the PAO procedure. In this paper, we present a validation study of a novel computer-assisted diagnosis, planning, simulation, and navigation system for PAO. It is hypothesized that the preoperative plan done with our system can be achieved by the navigated PAO procedure with a reasonable accuracy.

12.2 Materials and Methods

12.2.1 System Workflow

The computer-assisted diagnosis, planning, simulation, and navigation system for PAO consists of three modules as shown in Fig. 12.1.

- *Model generation module.* 3D surface models of the femur and the pelvis are generated by fully automatic segmentation of the preoperatively acquired CT data.
- *Computer-assisted diagnosis, planning, and simulation module.* The aim of this module is first to quantify the 3D hip joint morphology for a computer-assisted diagnosis of hip dysplasia and then to plan and simulate the reorientation procedure using the surface models generated from the model generation module. It starts with a fully automatic detection of the acetabular rim, which allows for computing important information quantifying the acetabular morphology such as femoral head coverage (FHC), femoral head extrusion index (EI), lateral center-edge (LCE) angle, version, and inclination. This module then provides a graphical user interface allowing the surgeon to conduct a virtual osteotomy and to further reorient the acetabular fragment until an optimal realignment is achieved.
- *Intraoperative navigation module*. Based on an optical tracking technique, this module aims for providing intraoperative visual feedback during acetabular fragment osteotomy and reorientation until the preoperatively planned orientation is achieved.

12.2.2 Fully Automatic Segmentation of Hip

In our study, given an unseen hip CT image of the target patient, the associated pelvic surface model and a set of acetabular rim points are obtained by using an in-house developed fully automatic hip CT segmentation method MASCG [11]. More specifically, in the first step, a multi-atlas fusion

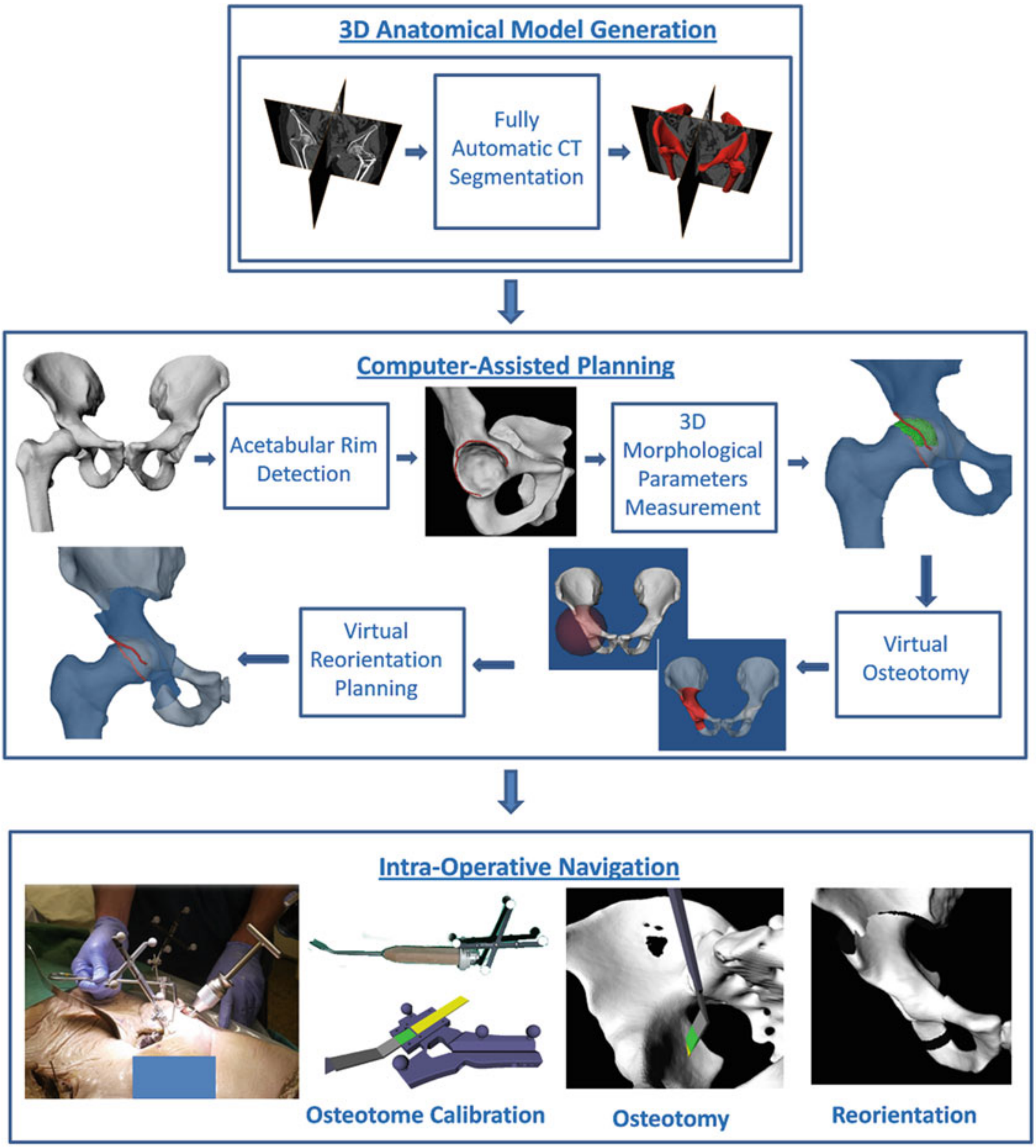

Fig. 12.1 Schematic view of our computer-assisted planning and navigation system for PAO

scheme is used to get an initial segmentation of the pelvis. Each atlas consists of a CT volume, manual segmentation of pelvis, and a set of predefined acetabular rim points. By performing registrations between the atlases and the target image using a hybrid registration method as described in [11], all the atlases can be aligned to the target image space. The initial segmentation of the pelvis is then obtained by deforming and fusing the manual segmentation of a selected subset of atlases. Similarly, the acetabular rim points are obtained by transforming and fusing the predefined rim point of these selected atlases. In the second step, by using a graph-cut constrained graph-search method, the initial segmentation of the pelvis is further modified, and from the modified binary segmentation, we generate the associated pelvic surface model which is used in the following study. Each acetabular rim point is also refined by replacing itself with the associated closet point on the generated pelvic surface model. For more details, we refer to [11].

12.2.3 Computer-Assisted Diagnosis of Hip Dysplasia

Accurate assessment of acetabular morphology and its relationship to the femoral head is essential for hip dysplasia diagnosis and PAO planning. After pelvic and femoral surface models are input to our system, the pelvic local coordinate systems is established using anatomical landmarks extracted from the CT data which is defined on the anterior pelvic plane (APP) using the bilateral anterior superior iliac spines (ASISs) and the bilateral pubic tubercles [12]. After local coordinate system is established, a fully automatic detection of the acetabular rim is conducted using an aforementioned method [26] (see Fig. 12.2a). As soon as acetabular rim points are extracted, least-squares fitting is used to fit a plane to these points (see Fig. 12.2b). The normal of the fitted plane is defined as the orientation of acetabulum $\vec{n}_{CT}$.The fitted plane then allows for computing acetabular inclination and anteversion [13] (see Fig. 12.2c, d). Additional hip morphological parameters such as the 3D LCE angle, the 3D femoral head EI, the FHC, the anterior coverage of femoral head (AC), and posterior coverage of femoral head (PC) are computed as well (see Fig. 12.2e–i). LCE is depicted as an angle formed by a line parallel to the longitudinal pelvic axis defined on the APP and by the line connecting the center of the femoral head with the lateral edge of the acetabulum according to Wiberg [14]. Femoral head EI is defined as the percentage of uncovered femoral head in comparison to the total horizontal head diameter according to Murphy et al. [15]. FHC is defined to be a ratio between the area of the upper femoral head surface covered by the acetabulum and the area of the complete upper femoral head surface from the weight-bearing point of view [16]. The 3D measurements of FHC used in this system are adapted from our previous method reported in [17]. The difference is that our current method [18] is based on native geometry of the femoral head. In contrast, our previous work assumed that the femoral head is ideally spherical [17]. In normal hips the assumption is valid since the femoral head is spherical or nearly so. However, in dysplastic hips, the femoral head may be elliptical or deformed [19]. Thus the method [18] used in this system is more accurate than the method that we introduced in [17]. Here the FHC is calculated with following algorithm. The inputs to this algorithm are femoral surface

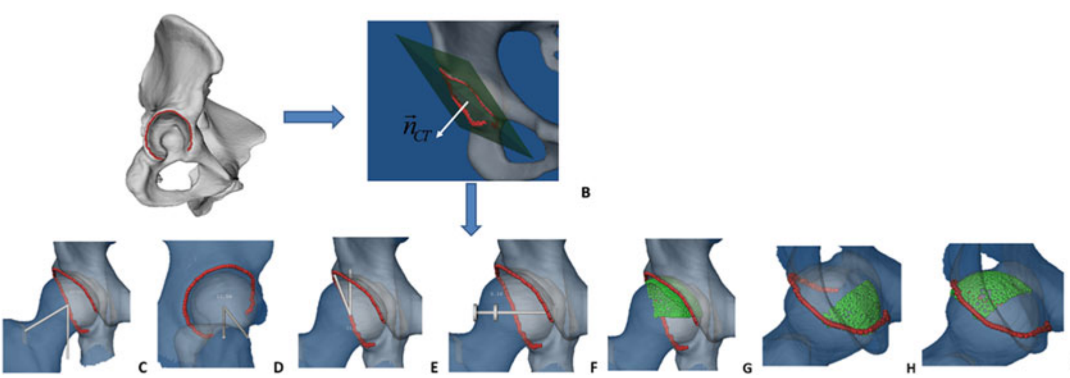

Fig. 12.2 Computing 3D morphological parameters of the hip joint. (**a**) Fully automatic acetabular rim detection; (**b**) least-squares fitting plane of acetabular rim and the orientation of acetabulum $\vec{n}_{CT}$; (**c**) acetabular inclination; (**d**) acetabular anteversion; (**e**) lateral center-edge angle (LCE); (**f**) femoral head extrusion index (EI); (**g**) femoral head coverage (FHC); (**h**) anterior coverage of femoral head (AC); (**i**) posterior coverage of femoral head (PC)

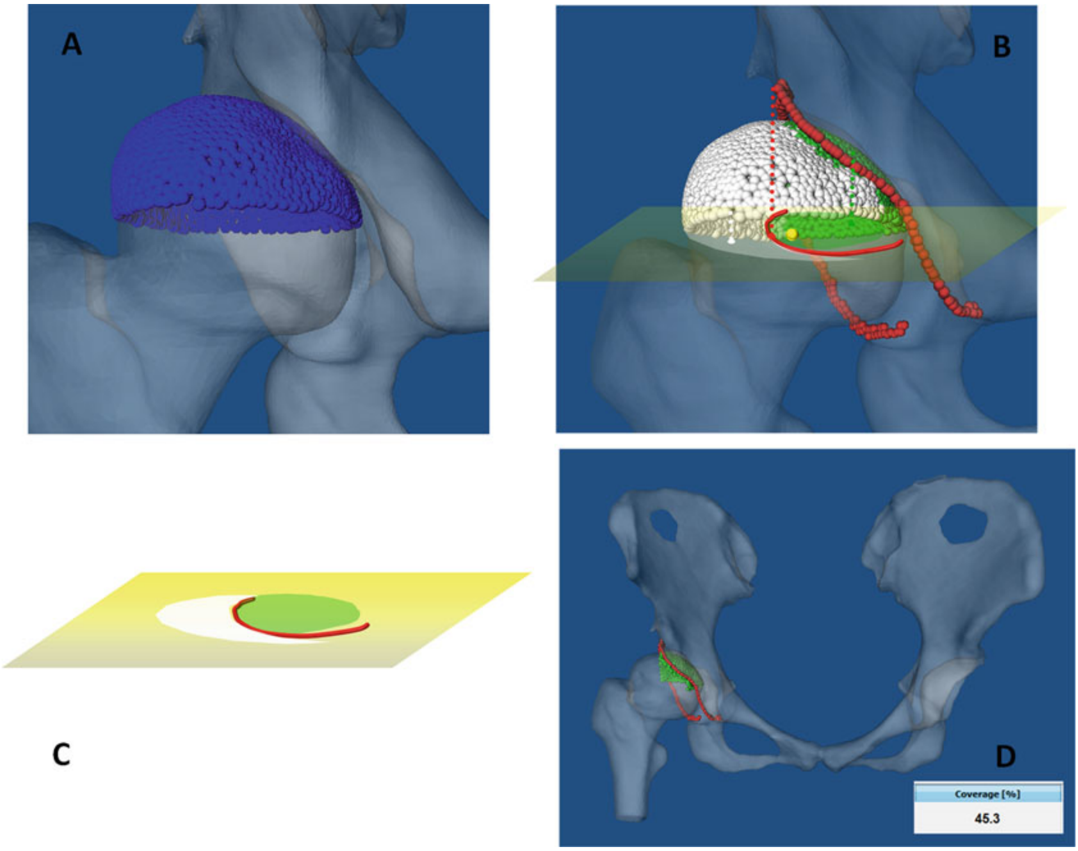

Fig. 12.3 3D measurement of the FHC. (**a**) The superior surface of the native femoral head (approximated with blue triangle meshes) and the opposing acetabular surface are major weight-bearing areas; (**b**) cranial rim points of the acetabulum and the superior hemisphere are projected onto the axial plane to produce a circle and a curved line (the projected acetabular rim contour) cutting across it; (**c**) a topographical image on the axial plane represents the femoral head with its covered (green area) and uncovered (white area) parts; (**d**) the percentage of FHC is calculated as a ratio between the green area and the sum of the green and the white areas on the femoral head

model, acetabular rim points, and the axial plane which is perpendicular to the APP and passes through the femoral head center.

- *Step 1:* Only the superior weight-bearing surface of the femoral head is used to estimate coverage as shown in Fig. 12.3a. The cranial rim points of the acetabulum and the superior hemisphere are both projected on to the axial plane to produce a circle and a curved line (the projected acetabular rim contour) cutting across it (Fig. 12.3b).
- *Step 2:* A topographical image is generated on the axial plane which represents the total femoral head. The covered and uncovered areas are separated by the projected acetabular rim contour. The green and white areas represent covered and uncovered parts, respectively, (Fig. 12.3c).
- *Step 3:* The percentage of FHC is calculated as a ratio between the area of covered part and the area of the total femoral head (see Fig. 3d for details).

12.2.4 Computer-Assisted Planning and Simulation of PAO Treatment

An in silico PAO procedure is conducted with our system as follows. First, since the actual osteotomies don't need to be planned as an exact trajectory, a sphere is used to simulate osteotomy operation. More specifically, the center of femoral head is taken as the center of the sphere whose radius and position can be interactively adjusted along lateral/medial, caudal/cranial, and dorsal/ventral directions, respectively, in order to approximate actual osteotomy operation (see Fig. 12.4a). After that, the in silico PAO procedure is conducted by interactively changing the inclination and the anteversion of the acetabulum fragment (see Fig. 12.4b). During the acetabulum fragment reorientation, 3D LCE angle, EI, FHC, AC, and PC are computed in real time based on the reoriented acetabulum fragment and showed at the bottom of the screen (see Fig. 12.4b). Once the morphological parameters of normal hip are achieved (inclination, 45° ± 4°, [37°–54°] [20]; anteversion, 17° ± 8°, [1°–31°] [20]; LCE > 25° [21]; FHC, 73% ± 4% [66–81%] [20]), the planned morphological parameters are stored and subsequently transferred to the navigation module as explained in details in the following section.

12.2.5 Intraoperative Surgical Navigation

Navigated PAO surgical intervention is described as follows: Before the acetabular fragment is osteotomized, the pelvis is attached with a dynamic reference base (DRB) in order to register the surgical anatomy to the pelvis surface model generated from a preoperatively acquired CT data (see Fig. 12.5a, b). After that, CT-patient registration based on a so-called restricted surface matching (RSM) algorithm [22] is conducted, which mainly consists of a paired point matching followed by a surface matching (see Fig. 12.5b). Specifically, the paired point matching is based on the alignment process of pairs of anatomical landmarks. In a preoperative step, four anatomical landmarks (bilateral ASISs and the bilateral pubic tubercles) are determined on the pelvic model segmented from CT data. Intraoperatively, the corresponding landmarks on the patient are digitized using a tracked probe. The digitized points are defined in the coordinate system of the DRB, which is rigidly fixed onto the pelvis. Then the surface matching computes the registration transformation based on 20–30 scattered points around the accessible surgical site that is matched onto a surface of a pelvic model (see Fig. 12.5b). After registration, the osteotomes are calibrated using a multi-tools calibration unit in order to determine the size and orientation of the blade plane (see Fig. 12.5c). The tip of the osteotome is shown in relation to the virtual bone model, axial, sagittal, and coronal views of the actual CT dataset. The cutting trajectory is visualized in real time by prolongation of the blade plane of the osteotome. Thus the osteotomies can be performed in a controlled manner, and complications such as intraarticular penetration and accidental transection of the posterior column can be avoided [2] (see Fig. 12.5d). After the acetabular fragment is mobilized from the pelvis, another DRB is anchored to the acetabulum area for intraoperative tracking, thereby the acetabular reorientation can be supported by the navigation module. The navigation system can provide interactive measurements of acetabular morphological parameters and image-guidance information, which instantaneously updates the virtual display, current position and orientation parameters of the acetabulum, and the planned situation (inclination and anteversion angles) derived from the preoperative planning module. The surgeon repositions the acetabulum by controlling its inclination and anteversion angle in order to determine whether the current position achieves the preoperatively planned position or further adjustment is required (see Fig. 12.5e).

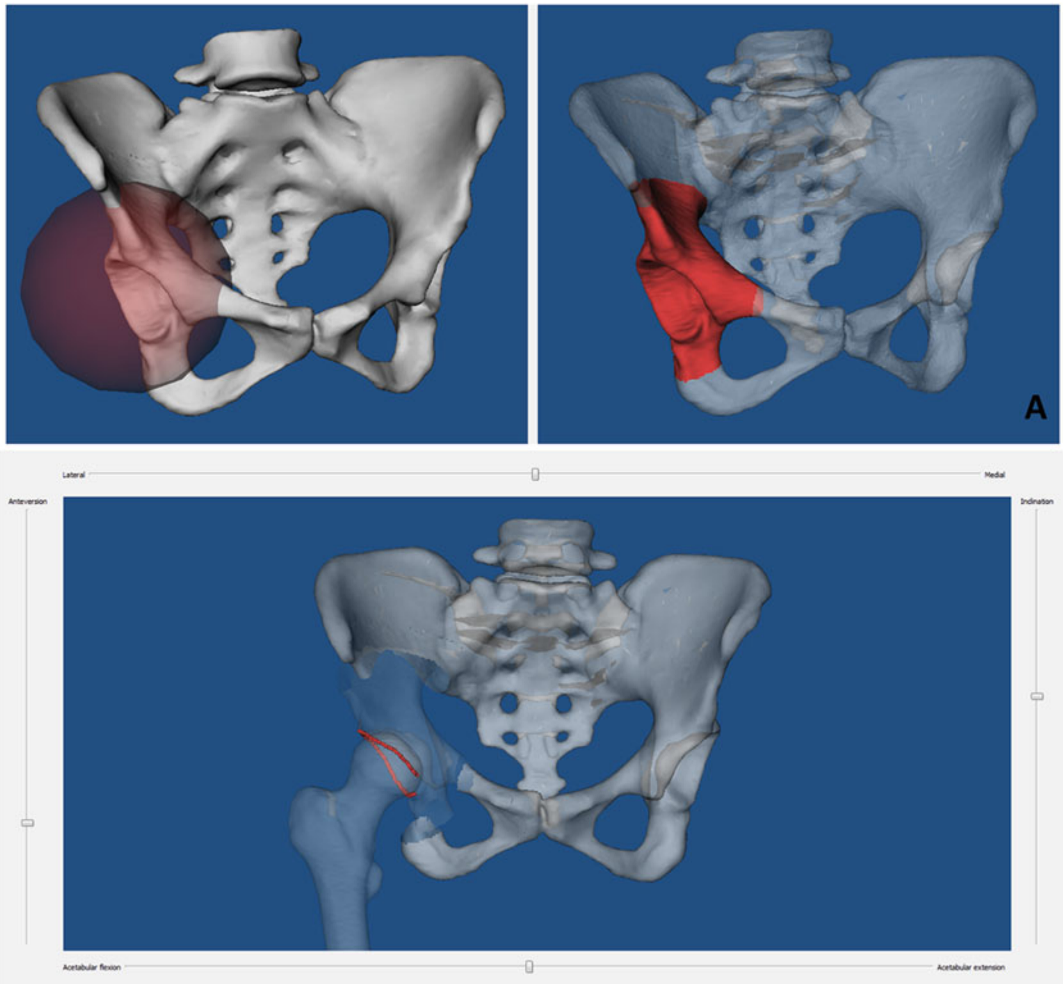

	Inclination	Anteversion	LCE	Extrusion Index	Coverage [%]	\nteriorCoverage [%	osteriorCoverage [%	Acetabular_rotation	Lateralization
Reference			26±5 [20-35]	0.23±0.05 [0.12-0.31]					
Original Situation	59.1	22.0	21.7	0.26	60.3	49.8	70.5	0.0	0.0
Planned Situation	49.1	13.0	32.0	0.17	72.47	70.53	74.33	0.0	0.0
Difference	-10.0	-9.0	10.3	-0.09	12.17	20.73	3.83	0.0	0.0

Fig. 12.4 In silico PAO surgical procedure in our PAO planning system. (**a**) Virtual osteotomy operation is done with a sphere, whose radius and position can be interactively adjusted; (**b**) virtual reorientation operation is done by interactively adjusting anteversion and inclination angle of the acetabulum fragment. The hip morphological parameters (inclination, anteversion, LCE, EI, FHC, AC, and PC) are then computed based on the reoriented acetabulum fragment and showed at the bottom of the screen

After successful repositioning, preliminary K-wire fixation and finally definitive screw fixation are conducted [23]. In this sawbone model study, a 3D articulated arm (Fisso 3D Articulated Gaging Arms, Switzerland) is employed to anchor the fragment for navigation accuracy validation (see Fig. 12.5a).

12.3 Study Design

In order to validate this newly developed planning and navigation system for PAO, two validation studies were designed and conducted on four sawbone models. The purpose of the first study is to evaluate the intraoperative accuracy

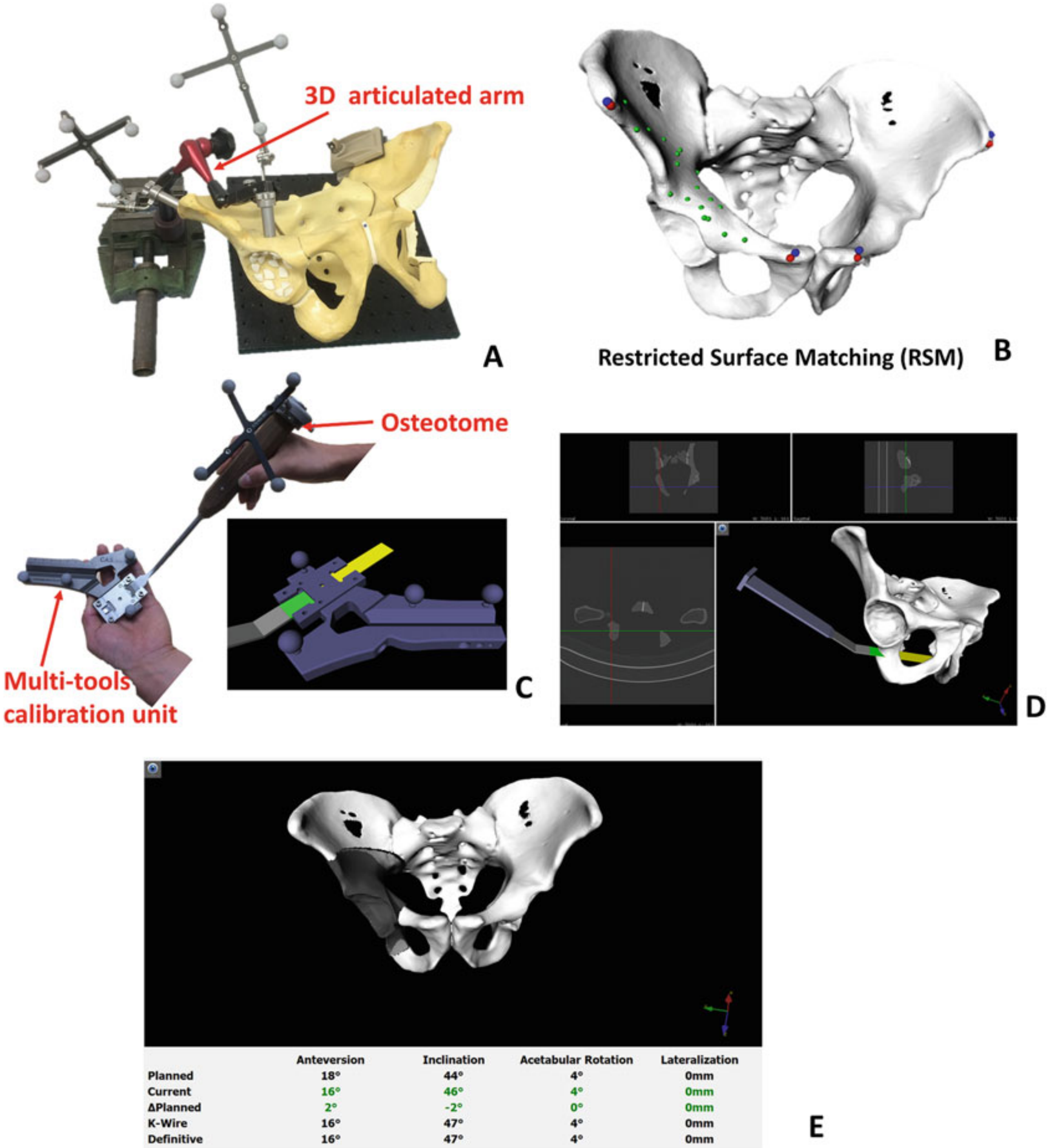

Fig. 12.5 Intraoperative PAO surgical navigation. (**a**) Setup of the navigated PAO surgery where two dynamic reference bases (DRBs) with reflective spheres are attached to both the iliac crest and the acetabular fragment; (**b**) the areas of the pelvis acquired with the tracked probe to perform the RSM registration; (**c**) osteotome calibration where the green part represents the blade plane of the osteotome and the yellow part represents the prolongation of the blade plane; (**d**) screenshot of CT-based osteotomy guidance where the tip of the osteotome is displayed on axial, sagittal, and coronal views of the CT dataset, and a cutting trajectory is displayed on the bony model; (**e**) screenshot of navigated reorientation procedure

and reliability of navigation system. The second study is designed to evaluate whether the acetabulum repositioning based on navigated PAO procedure can achieve the preoperative planned situation by comparing the measured acetabular orientation parameters between preoperative and postoperative CT data.

In the first study, preoperative planning was conducted with the PAO planning module. Subsequently the intraoperative navigation module was used to track acetabular and pelvic fragments, supporting and guiding the surgeon to adjust the inclination and anteversion angles of acetabulum interactively. Acetabular reorientation measured by the inclination and anterversion angles can be planned preoperatively and subsequently realized intraoperatively without significant difference. In order to assess the error difference between the preoperatively planned and the intraoperatively achieved acetabular orientation, we compared the decomposed rotation components derived from the acetabular fragment reorientation between the planned and intraoperative situations.

In the following, all related coordinate systems are first defined (see Fig. 12.6 for details) before the details about how to compute decomposed rotation components will be presented. During preoperative planning stage, the *Ref_CT* represents the preoperative CT data coordinate system, and the *(Ref_APP)^{Pre}* represents the local coordinate system defined on the APP that is extracted from the preoperative CT data. During intraoperative navigation stage, the *Ref_P* represents the intraoperative patient coordinate system defined on the pelvic DRB, the *Ref_A* represents the intraoperative acetabulum coordinate system defined on acetabular DRB, and the *(Ref_APP)^{Intra}* represents the local coordinate system defined on the intraoperative APP (see Fig. 12.6 for details). Following the definition of all related coordinate systems, details about how to compute decomposed rotation components are described below.

Step 1:

In order to register *Ref_CT* to *Ref_P*, the DRBs are fixated and a RSM algorithm [22] is applied before the osteotomies and the acetabular fragment tracking (see Fig. 12.6a). The transformation $\left(T_P^{APP}\right)_{Intra}$ between the *Ref_P* and the *(Ref_APP)^{Intra}* can be calculated by Eq.(12.1).

$$\left(T_P^{APP}\right)_{Intra} = \left(T_{CT}^{APP}\right)_{Pre} \cdot T_P^{CT} \qquad (12.1)$$

where T_P^{CT} is the rigid transformation between the *Ref_P* and the *Ref_CT* and $\left(T_{CT}^{APP}\right)_{Pre}$ is the transformation between the *Ref_CT* and the *(Ref_APP)^{Pre}*.

Step 2:

Before the fragment is moved, a snapshot of the neutral positional relationship $\left(T_A^P\right)_0$ between *Ref_A* and the *Ref_P* is recorded (Fig. 12.6a). At this moment, the orientation of the acetabulum $\left(\vec{n}_{APP}\right)_{Intra}^0$ with respect to the *(Ref_APP)^{Intra}* can be estimated by the following equation (see Fig. 12.6a):

$$\begin{aligned}\left(\vec{n}_{APP}\right)_{Intra}^0 &= \left(T_P^{APP}\right)_{Intra} \cdot \left(\vec{n}_P\right)_0 \\ &= \left(T_P^{APP}\right)_{Intra} \cdot \left(T_A^P\right)_0 \cdot \left(T_P^A\right)_0 \\ &\quad \cdot T_{CT}^P \cdot \vec{n}_{CT}\end{aligned} \qquad (12.2)$$

where $\vec{n}_{CT}$ denotes the orientation of acetabulum measured in the *Ref_CT* preoperatively. Equation (12.2) indicates that one can first compute the orientation of acetabulum $\left(\vec{n}_P\right)_0$ with respect to the *Ref_P* and then transform it to the *(Ref_APP)^{Intra}* through a transformation train.

Step 3:

Fragment mobility is measured by the navigation system, which records the instantaneous positional relationship $\left(T_A^P\right)_t$ between the *Ref_A* and the *Ref_P*. The neutral positional relationship $\left(T_A^P\right)_0$ obtained from *Step 2* is used to calculate the orientation of acetabulum $\left(\vec{n}_P\right)_t$ with respect to the *Ref_P* during motion. The instantaneous orientation of acetabulum $\left(\vec{n}_{APP}\right)_{Intra}^t$ with respect to the *(Ref_APP)^{Intra}* can be calculated by the following equation (see Fig. 12.6b):

$$\begin{aligned}\left(\vec{n}_{APP}\right)_{Intra}^t &= \left(T_P^{APP}\right)_{Intra} \cdot \\ \left(\vec{n}_P\right)_t &= \left(T_P^{APP}\right)_{Intra} \cdot \left(T_A^P\right)_t \cdot \left(T_P^A\right)_0 \\ &\quad \cdot T_{CT}^P \cdot \vec{n}_{CT}\end{aligned} \qquad (12.3)$$

Equation (12.3) indicates that one can first compute the instantaneous orientation of acetab-

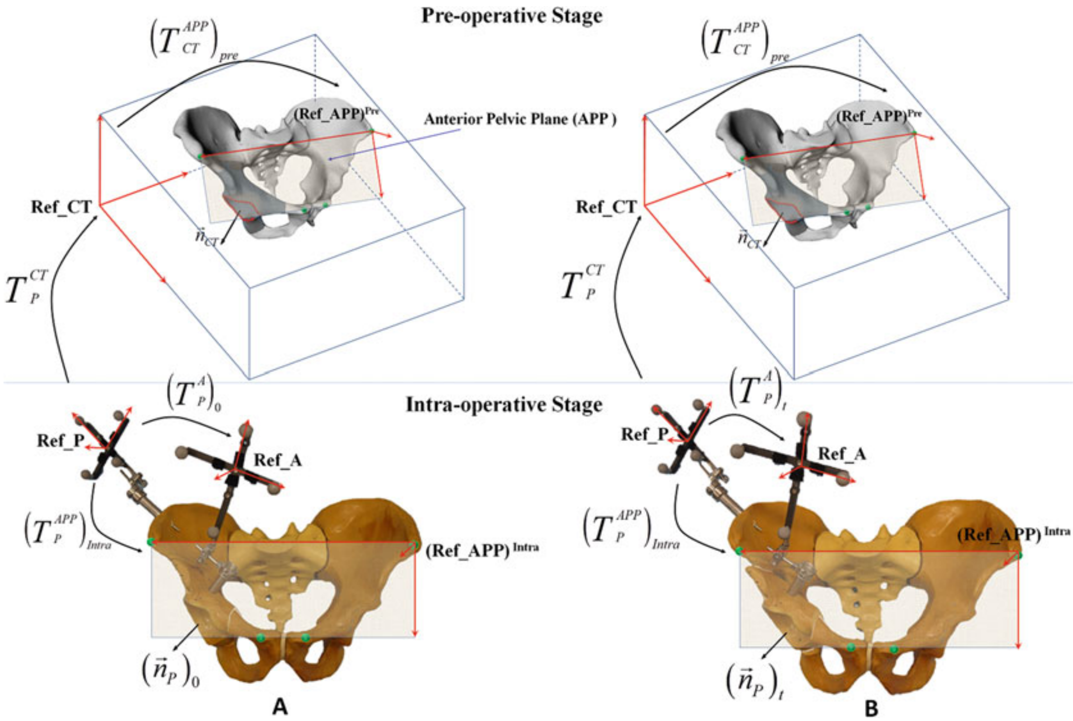

Fig. 12.6 Schematic representation of precise estimation of orientation change of acetabulum fragment after reorientation. (**a**) Estimation of orientation of acetabulum $\left(\vec{n}_{APP}\right)^{0}_{Intra}$ at the 0′ moment before reorientation procedure; (**b**) estimation of orientation of acetabulum $\left(\vec{n}_{APP}\right)^{t}_{Intra}$ at the t' moment during reorientation procedure

ulum $\left(\vec{n}_{P}\right)_{t}$ with respect to the *Ref_P* and then transform it to the *(Ref_APP)^{Intra}* through a transformation train.

Step 4:

The $\left(\vec{n}_{APP}\right)^{0}_{Intra}$ and $\left(\vec{n}_{APP}\right)^{t}_{Intra}$ can then be decomposed into three motion components (flexion/extension, external rotation/internal rotation, and abduction/adduction) along x, y, and z axis of the *(Ref_APP)^{Intra}*. The differences of respective decomposed rotation components were compared quantitatively between preoperative planned and intraoperative navigation situations in order to evaluate reorientation misalignment.

In the second study, we evaluated postoperatively the repositioning of the acetabular fragment and compared this with the preoperative planned acetabular orientation parameters. Specifically, the acetabular rim points after reorientation were digitized and transformed to preoperative CT space based on the aforementioned registration transformation T^{P}_{CT}. The transformed acetabular rim points were then imported into the computer-assisted PAO diagnosis module to quantify acetabular orientation parameters (inclination and anteversion) and compared them with the preoperatively planned acetabular orientation parameters.

12.4 Results

In the first intraoperative evaluation study, the decomposed rotation components of the acetabular fragment between the preoperatively planned situation and the intraoperatively achieved situation were compared. According to Tables 12.1, eight groups of acetabular reorientation data were obtained. It can be seen that the average errors along three motion components (flexion/extension, abduction/adduction,

Table 12.1 The difference (°) of decomposed motion components between preoperative planning and intraoperative navigation situations

		Mean error		
		Flex/Ext (°)	Abd/Add (°)	Ext Rot/Int Rot (°)
Sawbone 1	Left hip	0.9	0.1	3.6
	Right hip	0.5	0.5	0.7
Sawbone 2	Left hip	0.5	0.4	1.1
	Right hip	0.4	0.1	0.2
Sawbone 3	Left hip	0.9	0.1	1.2
	Right hip	0.4	0.5	1.2
Sawbone 4	Left hip	0.4	0.0	0.2
	Right hip	1.0	0.3	0.7
Mean ± Std. [Min, Max]		0.6 ± 0.3 [0.4, 1.0]	0.3 ± 0.2 [0.0, 0.5]	1.1 ± 1.1 [0.2, 3.6]

Table 12.2 The error of hip joint morphological parameters (*IN* inclination, *AV* anteversion) between preoperative planning and postoperative evaluation

Trial number		#1	#2	#3	#4	#5	#6	#7	#8	Average error
IN (°)	Preop	41.4	44.2	44.2	42.6	41.9	40.8	50.4	44.6	0.9 ± 0.3 [0.4, 1.2]
	Postop	42.6	45.3	44.6	43.8	41.1	40.0	49.3	45.3	
AV (°)	Preop	13.2	15.1	8.1	8.6	15.3	8.5	10.2	10.3	0.9 ± 0.7 [0.0, 1.7]
	Postop	15.2	16.1	9.6	6.9	15.9	8.5	10.5	10.6	

and external rotation/internal rotation) are $0.6° \pm 0.3°$, $0.3° \pm 0.2°$, and $1.1° \pm 1.1°$, respectively.

In the second postoperative evaluation study, the morphological parameters of hip joint between the preoperatively planned situation and postoperatively repositioned situation were compared. The results are shown in Table 12.2. From this table, it can be seen that the average errors of acetabular orientation parameters (inclination and anteversion angles) are $0.9° \pm 0.3°$ and $0.9° \pm 0.7°$, respectively. The results are accurate enough from a clinical point of view for PAO surgical intervention and verify the hypothesis that the preoperatively planned situation can be achieved by navigated PAO procedure with reasonable accuracy.

12.5 Discussion and Conclusions

In this paper, we present a computer-assisted planning, simulation, and navigation system for PAO, which allows for not only quantifying the 3D hip joint morphology with geometric parameters such as acetabular orientation (expressed as inclination and anteversion angles), LCE angle, and femoral head coverage for a computer-assisted diagnosis of hip dysplasia but also virtual PAO surgical planning and simulation. Intraoperatively navigation was performed to achieve the preoperative plan. A validation study was conducted on four sawbone models in order to evaluate the efficacy of navigated PAO intervention intraoperatively and postoperatively. The experimental results verified our hypothesis that the preoperative planned situation can be achieved intraoperatively with reasonable accuracy.

There exists a variety of studies in developing and validating PAO planning and navigation system. Langlotz et al. [9] developed the first generation of CT-based customized navigation system for PAO and applied it to 14 clinical cases. The osteotomes can be tracked and displayed on 3D pelvic model during osteotomies procedure. Acetabular reorientation can be achieved according to the angles in the sagittal, frontal, and transverse planes. However this system did not integrate the preoperative planning and the surgeon could not refer to standard parameters defining acetabular orientation (inclination and anteversion angle). Abraham et al. [7] reported an experimental cadaver study in order to prove the utility of preoperative 3D osteotomy planning and intraoperative acetabular repositioning in the navigated PAO surgery. The result of this study demonstrated considerably higher error (LCE, 4.9 ± 6° with maximum 12.4°). Moreover, in their system, in silico PAO reorientation was performed using commercially available image processing and editing software (Mimics, Materialise, Belgium). In contrast, our customized system can not only quantify the 3D hip morphology of hip dysplasia precisely but also provide virtual PAO surgical planning and simulation. Another application of CT-based navigation application for PAO was reported by Hsieh et al. [8], which has been successfully applied to 36 clinical cases. In their study they evaluated the efficiency of computer-assisted navigation in PAO by comparing with the conventional freehand approach. However, their study was conducted using a modified version of commercially available navigation program for THA (VectorVision, BrainLab Inc., Westchester, IL), with no preoperative planning function and which only allows for tool tracking of osteotomes. Once the acetabular fragment has been osteotomized and mobilized from the pelvis, the program does not allow for real-time tracking the fragment to guide the reorientation. In result, proper correction has to rely on the surgeon's own experience to find a new optimal position. In contrast, our PAO navigation system can track both pelvic and acetabular fragments in real time and guide the surgeon during acetabulum repositioning until the preoperative planned acetabular orientation was achieved. Jäger [24] et al. introduced a clinical trial based on a CT-based navigation system allowing for control of the acetabular fragment in 3D space. However no statistical evaluation of accuracy of acetabular repositioning was reported. In contrast, we conducted sawbone model-based studies to evaluate the accuracy and efficacy of navigation-based acetabular repositioning.Intraoperatively, we used decomposed rotation components (flexion/extension, abduction/adduction, and external rotation/internal rotation) to assess difference between the preoperatively planned and the intraoperatively navigated acetabular repositioning. Our experimental results demonstrated that sub-degree accuracy was achieved for the flexion/extension and abduction/adduction directions while slightly larger than 1 º error for the external rotation/internal rotation direction. Postoperatively, we used quantitative acetabular orientation parameters to assess the error between the preoperatively planned and the postoperatively achieved acetabular repositioning. Our experimental results demonstrated that the preoperative plan done with our system can be achieved by the navigated PAO procedure with a reasonable accuracy.

However, there are still limitations in the present validation experiment. The first limitation is that the developed system is only validated on sawbone models. However, the intraoperative navigation accuracy has been previously assessed in a cadaver experiment in order to investigate the technical feasibility of the pararectus surgical approach [25]. Another limitation is that the preoperative planning is only limited to increase FHC and does not consider aspects of impingement. The argument why we adopted such a strategy is that we are aiming to evaluate navigation accuracy in this study. In order to avoid impingement following PAO, the planned situation can be optimized with impingement simulation by making a trade-off between FHC and hip range of motion (ROM) reported in our previous work [17]. In addition, the transfer of this technique to the clinical setting has not yet been performed. A clinical trial is planned to further validate the efficacy of the developed system for PAO interventions.

Acknowledgments This work is supported in part by Natural Science Foundation of SZU (grant no. 2017089). This chapter was modified from the paper published by our group in *The 7th International Conference on Medical Imaging and Augmented Reality* (MIAR2016) (Li et al., MIAR2016; 15-26). The related contents were reused with permission.

References

1. Murphy SB, Millis MB, Hall JE (1999) Surgical correction of acetabular dysplasia in the adult. A Boston experience. Clin Orthop 363:38–44
2. Ganz R, Klaue K, Vinh T, Mast J (1988) A new periacetabular osteotomy for the treatment of hip dysplasia. Technique and preliminary results. Clin Orthop 232:26–36
3. Hipp JA, Sugano N, Millis MB, Murphy SB (1999) Planning acetabular redirection osteotomies based on joint contact pressures. Clin Orthop 364:134–142
4. Ziebarth K, Balakumar J, Domayer S et al (2011) Bernese periacetabular osteotomy in males: is there an increased risk of femoroacetabular impingement (FAI) after Bernese periacetabular osteotomy? Clin Orthop Relat Res 469:447–453
5. Myers SR, Eijer H, Ganz R (1999) Anterior femoroacetabular impingement after periacetabular osteotomy. Clin Orthop Relat Res 363:93–99
6. Crockaress J Jr, Trousdale RT, Cabanela ME, Berry DJ (1999) Early experience and results with the periacetabular osteotomy. The Mayo Clinic experience. Clin Orthop 363:45–53
7. Abraham C, Rodriguez J, Buckley JM, Diab M, Burch S (2010) An evaluation of the accuracy of computer assisted surgery in preoperatively three dimensionally planned periacetabular osteotomies. In: Proceedings of the 56th annual meeting of the Orthopaedic Research Society; 2010 Mar 6–9; New Orleans, USA
8. Hsieh PH, Chang YH, Shih CH (2006) Image-guided periacetabular osteotomy: computer-assisted navigation compared with the conventional technique: a randomized study of 36 patients followed for 2 years. Acta Orthop 77(4):591–597
9. Langlotz F, Bachler R, Berlemann U, Nolte LP, Ganz R (1998) Computer assistance for pelvic osteotomies. Clin Orthop 354:92–102
10. Murphy RJ, Armiger RS, Lepistö J, Mears SC, Taylor RH, Armand M (2014) Development of a biomechanical guidance system for periacetabular osteotomy. Int J Comput Assist Radiol Surg 10(4):497–508
11. Chu C, Bai J, Wu X, Zheng G (2015) Mascg: multi-atlas segmentation constrained graph method for accurate segmentation of hip ct images. Med Image Anal 26(1):173–184
12. Zheng G, Marx A, Langlotz U, Widmer KH, Buttaro M, Nolte LP (2002) A hybrid CT-free navigation system for total hip arthroplasty. Comput Aided Surg 7(3):129–145
13. Murray DW (1993) The definition and measurement of acetabular orientation. J Bone Joint Surg Br 75(B):228–232
14. Wiberg G (1939) The anatomy and roentgenographic appearance of a normal hip joint. Acta Chir Scand Suppl 83:7–38
15. Murphy SB, Ganz R, Muller ME (1995) The prognosis in untreated dysplasia of the hip. A study of radiographic factors that predict the outcome. J Bone Joint Surg Am 77:985–989
16. Konishi N, Mieno T (1993) Determination of acetabular coverage of the femoral head with use of a single anteroposterior radiograph. A new computerized technique. J Bone Joint Surg Am 75(9): 1318–1333
17. Liu L, Ecker TM, Schumann S, Siebenrock KA, Nolte LP, Zheng G (2014) Computer assisted planning and navigation of periacetabular osteotomy (PAO) with range of motion (ROM) optimization. Medical Image Computing and Computer-Assisted Intervention–MICCAI 2014. Springer, 2014: pp 643–650
18. Cheng H, Liu L, Yu W, Zhang H, Luo D, Zheng G (2015) Comparison of 2.5D and 3D quantification of femoral head coverage in normal control subjects and patients with hip dysplasia. Plos One (under review)
19. Steppacher SD, Tannast M, Werlen S, Siebenrock K (2008) Femoral morphology differs between deficient and excessive acetabular coverage. Clin Orthop Relat Res 466(4):782–790
20. Dandachli W, Kannan V, Richards R, Shah Z, Hall-Craggs M, Witt J (2008) Analysis of cover of the femoral head in normal and dysplastic hips: new CT-based technique. J Bone Joint Surg Br 90(11):1428–1434
21. Zou Z, Chavez-Arreola A, Mandal P, Board TN, Alonso-Rasgado T (2012) Optimization of the position of the acetabulum in a Ganz periacetabular osteotomy by finite element analysis. J Orthop Res 31(3):472–479
22. Bächler R, Bunke H, Nolte LP (2001) Restricted surface matching - numerical optimization and technical evaluation. Comput Aided Surg 6:143–152
23. Olson SA (2010) The Bernese periacetabular osteotomy: a review of surgical technique. Duke Orthop J 1(1):21–26
24. Jäger M, Westhoff B, Wild A, Krauspe R (2004) Computer-assisted periacetabular triple osteotomy for treatment of dysplasia of the hip. Z Orthop Ihre Grenzgeb 142(1):51–59
25. Liu L, Zheng G, Bastian JD, Keel MJB, Nolte LP, Siebenrock KA, Ecker TM (2015) Periacetabular osteotomy through the pararectus approach: technical feasibility and control of fragment mobility by a validated surgical navigation system in a cadaver experiment. Int orthop:1–8
26. Puls M, Ecker TM, Steppacher SD, Tannast M, Siebenrock KA, Kowal JH (2011) Automated detection of the osseous acetabular rim using three-dimensional models of the pelvis. Comput Biol Med 41(5):285–291

13 Biomechanical Optimization-Based Planning of Periacetabular Osteotomy

Li Liu, Klaus Siebenrock, Lutz-P. Nolte, and Guoyan Zheng

Abstract

Modern computerized planning tools for periacetabular osteotomy (PAO) use either morphology-based or biomechanics-based methods. The latter rely on estimation of peak contact pressures and contact areas using either patient-specific or constant thickness cartilage models. We performed a finite element analysis investigating the optimal reorientation of the acetabulum in PAO surgery based on simulated joint contact pressures and contact areas using patient-specific cartilage model. Furthermore we investigated the influences of using patient-specific cartilage model or constant thickness cartilage model on the biomechanical simulation results. Ten specimens with hip dysplasia were used in this study. Image data were available from CT arthrography studies. Bone models were reconstructed. Mesh models for the patient-specific cartilage were defined and subsequently loaded under previously reported boundary and loading conditions. Peak contact pressures and contact areas were estimated in the original position. Afterward we used validated preoperative planning software to change the acetabular inclination by an increment of 5° and measured the lateral center-edge angle (LCE) at each reorientation position. The position with the largest contact area and the lowest peak contact pressure was defined as the optimal position. In order to investigate the influence of using patient-specific cartilage model or constant thickness cartilage model on the biomechanical simulation results, the same procedure was repeated with the same bone models but with a cartilage mesh of constant thickness. Comparison of the peak contact pressures and the contact areas between these two different cartilage models showed that good correlation between these two cartilage models for peak contact pressures ($r = 0.634 \in [0.6, 0.8]$, $p < 0.001$) and contact areas ($r = 0.872 > 0.8$, $p < 0.001$). For both cartilage models, the largest contact

L. Liu (✉)
National-Regional Key Technology Engineering Laboratory for Medical Ultrasound, Guangdong Key Laboratory for Biomedical Measurements and Ultrasound Imaging, School of Biomedical Engineering, Health Science Center, Shenzhen University, Shenzhen, China

Institute for Surgical Technology and Biomechanics, University of Bern, Bern, Switzerland
e-mail: li.liu@szu.edu.cn

K. Siebenrock
Department of Orthopedic Surgery, Inselspital, University of Bern, Bern, Switzerland

L.-P. Nolte · G. Zheng
Institute for Surgical Technology and Biomechanics, University of Bern, Bern, Switzerland

G. Zheng et al. (eds.), *Intelligent Orthopaedics*, Advances in Experimental Medicine and Biology 1093, https://doi.org/10.1007/978-981-13-1396-7_13

areas and the lowest peak pressures were found at the same position. Our study is the first study comparing peak contact pressures and contact areas between patient-specific and constant thickness cartilage models during PAO planning. Good correlation for these two models was detected. Computer-assisted planning with FE modeling using constant thickness cartilage models might be a promising PAO planning tool when a conventional CT is available.

Keywords

Hip dysplasia · Periacetabular osteotomy (PAO) · Planning · Biomechanical simulation · Finite element analysis (FEA) · Image-guided surgery · Joint preservation surgery

13.1 Introduction

Periacetabular osteotomy (PAO) is an established surgical intervention for treatment of hip dysplasia and acetabular retroversion [1, 2]. During the procedure, the acetabulum is reoriented in order to optimize the containment of the femoral head and the pressure distribution between acetabulum and femoral head for reduction of the peak contact pressures within the joint. The goal of acetabular reorientation is to restore or to approximate normal acetabular geometry. In order to achieve this, two types of planning strategies have been reported, which can be divided into morphology-based planning methods and biomechanics-based planning methods. Morphology-based planning uses standard geometric parameters, which have shown their importance for quantification of acetabular under- or overcoverage [3]. Several authors have described different morphology-based planning methods which range from simplified two-dimensional planning [4–6] to complex three-dimensional planning applications [7–11]. Other authors presented biomechanics-based planning methods. Different approaches have been presented using, for example, discrete element analysis (DEA) [12] or the more sophisticated finite element analysis (FEA) [13, 14]. In literature, both constant thickness cartilage models [14] and patient-specific cartilage models [15] have been suggested. In the clinical routine, knowledge of patient specific cartilage is rarely available, since special imaging protocol (e.g., CT arthrography or MRI with dGEMRIC, T1rho or T2 mapping) is necessary to retrieve this information. One alternative could be constant thickness cartilage model that is virtually generated from bony surface models derived from conventional CT scans. However differences between these two different cartilage models in planning of PAO using FE simulation have never been investigated. Previously, we have developed a morphology-based 3D planning system for PAO [16]. This system allows for quantification of the hip joint morphology in three dimensions, using geometric parameters such as inclination and anteversion angle, the lateral center-edge (LCE) angle, and femoral head coverage. It also allows for virtual reorientation of the acetabulum according to these parameters. In the current study, we enhanced this application with an additional biomechanics-based method for estimation of joint contact pressures employing FEA. In this study, we investigated the following research questions:

1. What is the optimal position of the acetabulum based on simulated joint contact pressures using patient specific cartilage models in a FE analysis?

Are there significant differences in joint contact pressures between patient specific cartilage model and constant thickness cartilage model in the same hip model?

13.2 Materials and Methods

13.2.1 System Overview

The computer-assisted planning system for PAO uses 3D surface models of the pelvis and femur, generated out of DICOM (digital imaging and communication in medicine) data, using a commercially available segmentation program (AMIRA, Visualization Sciences Group, Burlington, MA). The system starts with a morphology-based method. Employing fully automated detection of the acetabular rim, parameters such as acetabular version, inclination, LCE angle, femoral head extrusion index (EI), and femoral head coverage can be calculated for a computer-assisted diagnosis [16]. Afterward, the system offers the possibility to perform a virtual osteotomy (Fig. 13.1a(1)) and reorientation of the acetabular fragment in a stepwise pattern. During the fragment reorientation, acetabular morphological parameters are recomputed in real time (Fig. 13.1a(2)) until the desired position is achieved. Our system is further equipped with a biomechanics-based FE prediction of changes of cartilage contact stresses, which occurs during acetabular reorientation. An optimal position of the acetabulum can be defined, once contact areas in the articulation are maximized, while at the same time peak contact pressures are minimized (Fig. 13.1b). The respective cartilage model for the biomechanics-based FE prediction is generated from either CT arthrography data (patient-specific) or using a virtually generated cartilage with predefined thickness (constant thickness).

13.2.2 Biomechanical Model of Hip Joint

13.2.2.1 Cartilage Models

In literature, both constant thickness cartilage models and patient-specific cartilage models have been employed. Zou et al. [14] used a constant thickness model and thus created a cartilage with a predefined thickness of 1.8 mm, a value derived from cartilage thickness data from the literature. In contrast Harris et al. [15] introduced a CT arthrography protocol allowing for excellent visualization of patient-specific cartilage. DICOM data of dysplastic hip joints, which have been CT scanned using this arthrography protocol, were provided by the open source dysplastic hips image data from the Musculoskeletal Research Laboratories, University of Utah [17]. The data provider has obtained IRB approval (University of Utah IRB #10983).We used our morphology-based planning system for calculation of the acetabular morphological parameters [18], verifying true dysplasia (Table 13.1). We used these datasets in order to retrieve the patient-specific cartilage models. The bony anatomy of the same ten specimens was then used to create the constant thickness cartilage models by expanding a constant 1.8 mm thickness using 3D dilation operation on the articular surface.

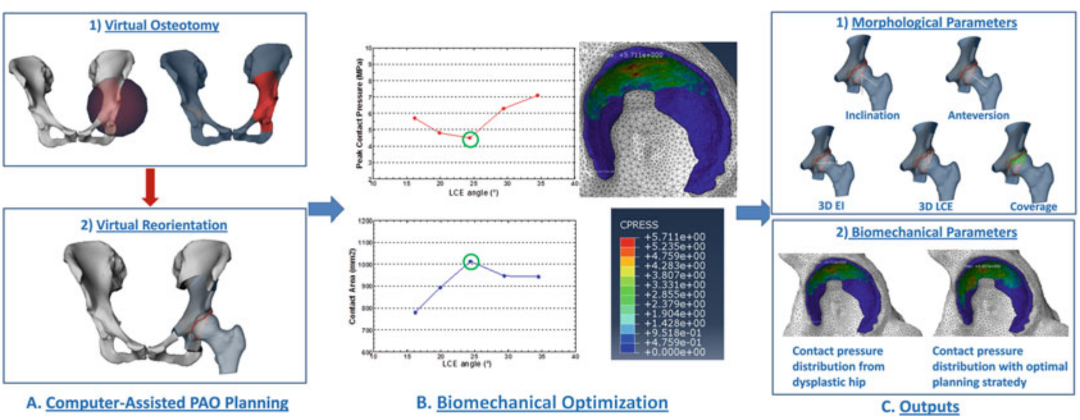

Fig. 13.1 The schematic workflow of computer-assisted planning of PAO with biomechanical optimization. (**a**) Computer-assisted morphology based PAO planning. Virtual osteotomy operation is done with a sphere, whose radius and position can be interactively adjusted, and virtual reorientation operation is done by interactively adjusting anteversion and inclination angle of the acetabulum fragment. (**b**) Biomechanical optimization. (**c**) The preoperative planning output

Table 13.1 Acetabular morphological parameters of ten specimens with hip dysplasia

	Inclination (°)	Anteversion (°)	LCE (°)	Extrusion index	Coverage (%)
#1	59.7	12.5	17.2	0.33	63.3
#2	57.2	10.9	17.1	0.34	62.6
#3	58.6	17.1	16.2	0.34	61.8
#4	59.0	18.9	19.8	0.31	60.4
#5	44.7	16.7	23.1	0.26	69.9
#6	59.6	26.7	17.7	0.35	57.4
#7	50.5	19.4	23.9	0.25	70.9
#8	56.3	23.6	21.0	0.27	66.3
#9	60.7	24.7	15.6	0.34	59.3
#10	57.4	18.6	18.6	0.30	56.5

13.2.2.2 Mesh Generation

Bone and cartilage surface models of the reoriented hip joints were imported into ScanIP software (Simpleware Ltd., Exeter, UK) as shown in Fig. 13.2a, c. Surfaces were discretized using tetrahedral elements (Fig. 13.2b, d). Since the primary focus was the joint contact stresses, a finer mesh was employed for the cartilage than for the bone. Refined tetrahedral meshes were constructed for the cartilage models (~135,369 elements for the femoral cartilage model and ~92,791 elements for the acetabular cartilage model, using the ScanFE module (Simpleware Ltd., Exeter, UK). Cortical bone surfaces were discretized using coarse tetrahedral elements (~149,120 elements for the femoral model and ~188,526 elements for the pelvic model). The trabecular bone was not included in the models, as it only has a minor effect on the predictions of contact pressure as reported in another study [19].

13.2.2.3 Material Property

Acetabular and femoral cartilage were modeled as homogeneous, isotropic, and linearly elastic material with Young's modulus $E = 15$ MPa and Poisson's ratio $\nu = 0.45$ [14]. The cortical bone of the pelvis and femur were modeled as homogeneous, isotropic material with elastic modulus $E = 17$ GPa and Poisson's ratio $\nu = 0.3$ [14].

13.2.2.4 Boundary Conditions and Loading

Tied and sliding contact constraints were used in Abaqus/CAE 6.10 (Dassault Systèmes Simulia Corp, Providence, RI, USA) to define the cartilage-to-bone and cartilage-to-cartilage interfaces, respectively. It has been reported that the friction coefficient between articular cartilage surfaces was very low (0.01–0.02) in the presence of synovial fluid, making it reasonable to neglect eventual frictional shear stresses [15, 20]. The top surface of pelvis and pubic areas were fixed, and the distal end of the femur was constrained to prevent displacement in the body x and y directions while being free in vertical z direction (Fig. 13.2e). The center of the femoral head was derived from a least-squares sphere fitting and was selected to be the reference node. The nodes of femoral head surface were constrained by the reference node via kinematic coupling. The fixed boundary condition model was then subjected to a loading condition as published before [21], representing a single leg stance situation with the resultant hip joint contact force acting at the reference node. Following the loading specifications suggested in another previous study [22](Fig. 13.2e), the components of joint contact force along three axes were given as 195 N, 92 N, and 1490 N, respectively. In order to remove any scaling

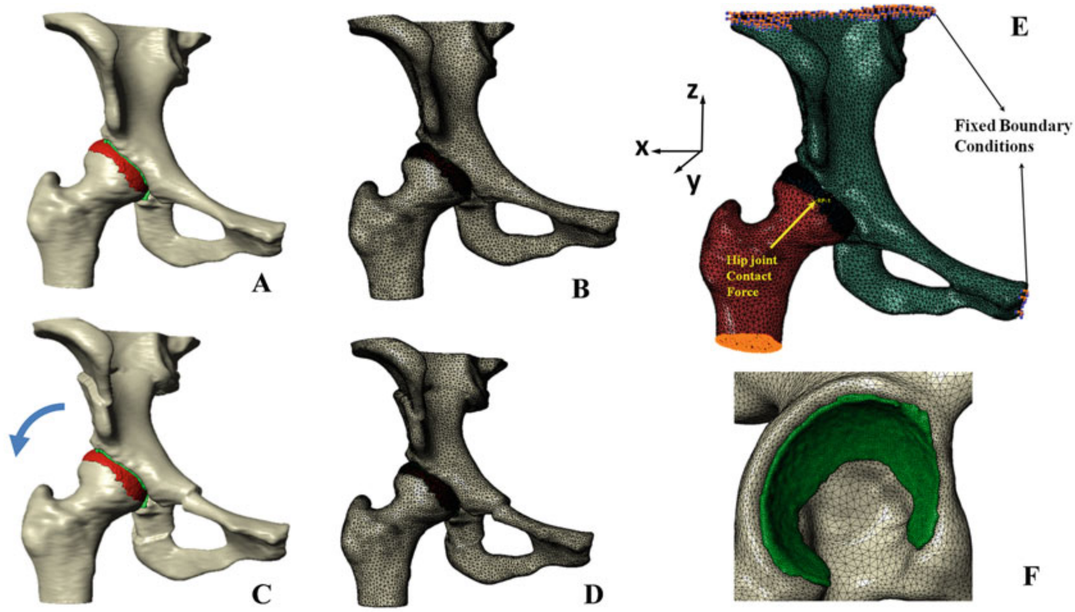

Fig. 13.2 Biomechanical simulation of contact pressure on acetabular cartilage. (**a**) Surface models of a dysplastic hip. (**b**) Volume meshes of a dysplastic hip. (**c**) Surface models for a planned situation after acetabulum fragment reorientation. (**d**) Volume meshes for the planned situation. (**e**) Boundary conditions and loading for biomechanical simulation. (**f**) Coarse meshes for bone models and refined meshes for cartilages

effect of body weight on the absolute value of the contact pressure, we defined a constant body weight of 650 N for all subjects. The resultant force was applied, based on anatomical coordinate system described by Bergmann et al. [21], whose local coordinate system was defined with the x axis running between the centers of the femoral heads (positive running from the left femoral head to the right femoral head), the y axis pointing directly anteriorly, and the z axis pointing directly superiorly.

13.2.2.5 Study 1: FE Simulation for Biomechanics-Based Planning of PAO Using Patient-Specific Cartilage Model

In order to find the optimal acetabular position, the acetabular fragment was now virtually rotated around the y axis (Fig. 13.2e) in 5° increments in relation to the anterior pelvic plane (APP). This deemed to imitate a decrease in acetabular inclination, as performed during actual PAO surgery (Fig. 13.2c). For each increment, the predicted peak contact pressure and total contact area were directly extracted from the output of Abaqus/CAE 6.10. The resulting peak contact pressures and contact areas in the different acetabular positions were then compared and the corresponding LCE angle was measured. Optimal orientation was determined by the position yielding the maximum contact area and the minimum peak contact pressure.

13.2.2.6 Study 2: Evaluation the Influences of Using Different Cartilage Models on the Simulation Results

After the peak pressures and contact areas had been simulated using the patient-specific cartilage models, the same procedure was performed using the constant thickness cartilage models. Finally, comparison between peak pressures and contact areas between patient-specific and constant thickness cartilage models was performed. Linear regression analysis was used to determine associations between the results for peak

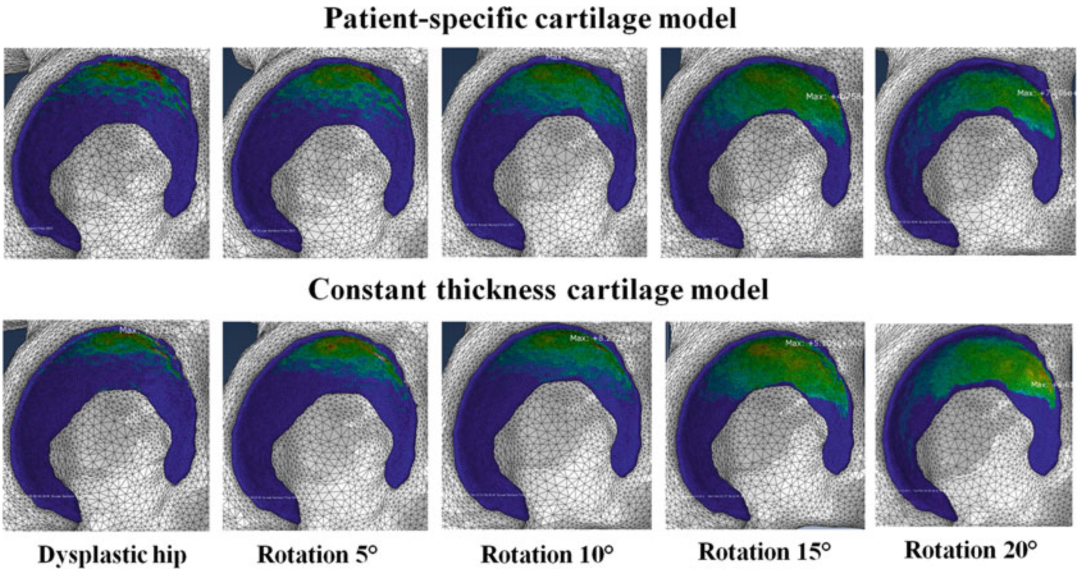

Fig. 13.3 Contact pressure distribution obtained by using two different cartilage models at different acetabular reorientation position

pressures and contact areas for both cartilage types. Thus, the values for the constant thickness models were the independent variables, whereas the values obtained by the patient-specific models represented the dependent variables. Pearson's correlation coefficient r was interpreted as "poor" below 0.3, "fair" from 0.3 to 0.5, "moderate" from 0.5 to 0.6, "moderately strong" from 0.6 to 0.8, and "very strong" from 0.8 to 1.0. Significance level was defined as $p < 0.05$.

13.3 Results

While the initial contact area in the dysplastic hip was primarily located in an eccentric superolateral region of the acetabulum, an increase in LCE angle led to an enlarged and more homogeneously distributed contact area (Fig. 13.3). At the same time, an increase in LCE angle resulted in decreased peak contact pressures. For each specimen, the optimal acetabular fragment reposition was defined as the position with minimum peak contact pressure and maximum contact area (Table 13.2).

Comparison of the peak contact pressures and the contact areas between the two different cartilage models showed similar results (Table 13.3). Regression analysis quantitatively showed that the results obtained by the constant thickness cartilage models have good correlation with those obtained by using the patient-specific cartilage models. Specifically, a moderately strong correlation was found between both cartilage models when analyzing peak contact pressures ($r = 0.634 \in [0.6, 0.8]$, $p < 0.001$) (Fig. 13.4), while a very strong correlation was also found when analyzing the contact areas between the two different cartilage models ($r = 0.872 > 0.8$, $p < 0.001$) (Fig. 13.4b). For both cartilage models, the largest contact areas and the lowest peak pressures were found at the same position (Table 13.3).

13.4 Discussion

We used a previously validated morphology-based PAO planning system [16] to perform virtual acetabular reorientation. An additional biomechanics-based module then estimated contact areas and peak contact pressures within the joint. First we used hip joint models with patient-specific cartilage models and changed

Table 13.2 Acetabular fragment reposition position with peak contact pressures and contact area

		R-0°	R-5°	R-10°	R-15°	R-20°
#1	LCE (°)	17.2	23.0	27.9	**32.9***	37.9
	Peak contact pressure (MPa)	14.1	9.5	7.1	4.8*	7.3
	Contact area (mm^2)	523	616	778	899*	860
#2	LCE (°)	17.1	21.7	**26.8***	**31.8***	36.8
	Peak contact pressure (MPa)	8.7	6.6	6.3*	7.0	9.8
	Contact area (mm^2)	625	655	698	741*	731
#3	LCE (°)	16.2	19.9	**24.4***	29.4	34.5
	Peak contact pressure (MPa)	5.7	4.8	4.5*	6.3	7.1
	Contact area (mm^2)	779	894	1013*	947	943
#4	LCE (°)	19.8	**23.5***	28.0	33.0	38.0
	Peak contact pressure (MPa)	7.1	6.2*	8.3	10.2	13.0
	Contact area (mm^2)	1166	1198*	1096	933	836
#5	LCE (°)	23.1	27.9	**32.9***	37.9	43.0
	Peak contact pressure (MPa)	5.5	5.2	4.8*	7.7	9.1
	Contact area (mm^2)	636	769	764*	587	523
#6	LCE (°)	17.7	21.5	**26.5***	**31.6***	36.6
	Peak contact pressure (MPa)	8.6	9	8.2*	8.8	11.1
	Contact area (mm^2)	466	493	517	565*	468
#7	LCE (°)	23.9	28.9	**33.9***	**38.9***	43.9
	Peak contact pressure (MPa)	11.3	9.8	10.0*	10.0*	15.0
	Contact area (mm^2)	441	521	586	590*	485
#8	LCE (°)	21.0	26.0	31.0	**36.0***	41.0
	Peak contact pressure (MPa)	15.0	10.2	10.8	9.9*	11.3
	Contact area (mm^2)	469	514	518	530*	505
#9	LCE (°)	15.6	19.6	24.6	**29.7***	34.7
	Peak contact pressure (MPa)	10.7	9.3	9.2	7.1*	8.5
	Contact area (mm^2)	425	381	411	480*	448
#10	LCE (°)	18.6	23.0	**28.0***	32.8	37.8
	Peak contact pressure (MPa)	6.6	6.0	4.7*	9.7	22.5
	Contact area (mm^2)	802	826	951*	750	699

the LCE angle in order to increase femoral head containment and to find the optimal position with the largest contact area and lowest peak contact pressure. The same operation was then conducted with the bone models of the same hip joints by replacing the patient-specific cartilage models with virtually generated constant thickness cartilage models. In the patient-specific cartilage models, an increase in LCE angle led to enlarged and more homogeneously distributed contact areas and decreased peak contact pressures. Comparison of the peak contact pressures and the contact areas between the two different cartilage models showed similar results. Regression analysis quantitatively showed moderately strong correlation between both models for peak contact pressures while very strong correlation for contact areas.

In the light of our findings, several aspects need to be discussed. We did not include the acetabular labrum in our FE analysis; however the role of the labrum during load distribution is debatable in literature. While some authors promoted inclusion of the labrum [23], other authors denied the importance of its inclusion [24]. More interestingly, Henak et al. [17] showed that

Table 13.3 Acetabular fragment reposition position with peak contact pressures and contact area (patient-specific cartilage model vs. constant thickness cartilage model)

		R-0°	R-5°	R-10°	R-15°	R-20°
#1	Patient-specific cartilage model					
	Peak contact pressure (MPa)	14.1	9.5	7.1	4.8*	7.3
	Contact area (mm^2)	523	616	778	899*	860
	Constant thickness cartilage model					
	Peak contact pressure (MPa)	17.2	9.9	8.3	5.1*	6.6
	Contact area (mm^2)	447	544	717	808*	865
#2	Patient-specific cartilage model					
	Peak contact pressure (MPa)	8.7	6.6	6.3*	7.0	9.8
	Contact area (mm^2)	625	655	698	741*	731
	Constant thickness cartilage model					
	Peak contact pressure (MPa)	10.3	9.8	9.2*	10.5	11.7
	Contact area (mm^2)	563	604	681*	709	684
#3	Patient-specific cartilage model					
	Peak contact pressure (MPa)	5.7	4.8	4.5*	6.3	7.1
	Contact area (mm^2)	779	894	1013*	947	943
	Constant thickness cartilage model					
	Peak contact pressure (MPa)	6.5	4.9	4.4*	5.5	6.3
	Contact area (mm^2)	839	958	1078*	1029	1073
#4	Patient-specific cartilage model					
	Peak contact pressure (MPa)	7.1	6.2*	8.3	10.2	13.0
	Contact area (mm^2)	1166	1198*	1096	933	836
	Constant thickness cartilage model					
	Peak contact pressure (MPa)	8.1	7.2*	7.4	8.0	8.1
	Contact area (mm^2)	1101	1200*	1151	1159	1046
#5	Patient-specific cartilage model					
	Peak contact pressure (MPa)	5.5	5.2	4.8*	7.7	9.1
	Contact area (mm^2)	636	769*	764	587	523
	Constant thickness cartilage model					
	Peak contact pressure (MPa)	6.3	5.2	5.0*	6.0	7.0
	Contact area (mm^2)	804	945	975*	848	836
#6	Patient-specific cartilage model					
	Peak contact pressure (MPa)	8.6	9.0	8.2*	8.8	11.1
	Contact area (mm^2)	466	493	517	565*	468
	Contact area (mm^2)	305	375	431	457*	369
#7	Patient-specific cartilage model					
	Peak contact pressure (MPa)	11.3	9.8	10.0	10.0*	15.0
	Constant thickness cartilage model					
	Peak contact pressure (MPa)	15.6	15.1	10.4	9.9*	14.7
	Contact area (mm^2)	441	521	586	590*	485
	Constant thickness cartilage model					
	Peak contact pressure (MPa)	11.0	7.7	5.7	5.2*	5.9
	Contact area (mm^2)	497	646	766	870*	807

(continued)

Table 13.3 (continued)

		R-0°	R-5°	R-10°	R-15°	R-20°
#8	Patient-specific cartilage model					
	Peak contact pressure (MPa)	15.0	10.2	10.8	9.9*	11.3
	Contact area (mm^2)	469	514	518	530*	505
	Constant thickness cartilage model					
	Peak contact pressure (MPa)	10.7	9.7	8.4	7.9*	8.0
	Contact area (mm^2)	398	531	584	630	661*
#9	Patient-specific cartilage model					
	Peak contact pressure (MPa)	10.7	9.3	9.2	7.1*	8.5
	Contact area (mm^2)	425	381	411	480*	448
	Constant thickness cartilage model					
	Peak contact pressure (MPa)	13.0	9.4	9.1	7.7*	8.8
	Contact area (mm^2)	383	481	412	515	558*
#10	Patient-specific cartilage model					
	Peak contact pressure (MPa)	6.6	6.0	4.7*	9.7	22.5
	Contact area (mm^2)	802	826	951*	750	699
	Constant thickness cartilage model					
	Peak contact pressure (MPa)	6.0	5.3	4.5*	9.3	18.5
	Contact area (mm^2)	909	990	1021*	879	775

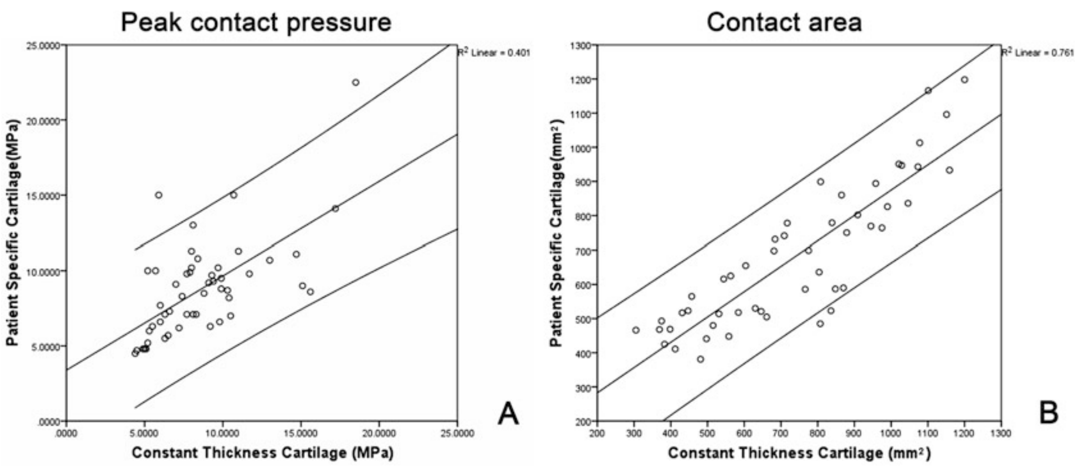

Fig. 13.4 (**a**) Scatter plot of peak contact pressure obtained by constant thickness cartilage models against those obtained by patient-specific cartilage models. (**b**) Scatter plot of contact area obtained by constant thickness cartilage models against those obtained by patient-specific cartilage models

the labrum has a far more significant role in dysplastic hip joints biomechanics than it does in normal hips, since it supports a large percentage of the load transferred across the joint due to the eccentric loading in dysplastic hips. The same study group in a previous study [25], however, found that the labrum only supported less than 3% of the total load across the joint in normal hips. The final goal of our study was not to measure peak contact pressures and contact areas in the originally dysplastic state of our specimen but to find an optimal position resembling a "normal" hip joint during PAO. Hence, for this purpose disregarding the labrum was acceptable.

Regarding loading conditions, a fixed body weight of 650 N [21] was used, which is not patient-specific. However, Zou et al. [14] justified the use of constant loading, since the relative change of contact pressure before and after PAO reorientation planning is assessed, regardless of the true patient weight. Also, the applied loading conditions were derived from in vivo data from patients who underwent total hip arthroplasty (THA) [21] and thus might be just an approximation to the true loading conditions in the native joint. For simplification reasons we also did not simulate typical motion patterns such as sitting-to-standing or gait cycle. Since we only performed static loading, the conchoid shape of the hip joint, which is important when performing dynamic loading, was also disregarded. This might be a limitation, when interpreting our results. Finally, although the CT scans were performed in the supine position and the loading condition is based on one-leg stance situation, this is not an infrequent practice, [26] and previous work [27] has shown that there was no significant difference between the contact pressure in the one-leg stance reference frame and those in the supine reference frame.

Our results are reflected conclusively in the current literature. Zhao et al. [13] conducted a 3D FE analysis investigating the changes of von Mises stress distribution in the cortical bone before and after PAO surgery. They showed the favorable stress distribution in the normal hips compared to dysplastic hips. One limitation of this study might be that the specimens were not truly dysplastic hips. The authors created dysplasia by deforming the acetabular rim of normal hip joints. Hence, their depiction of the stress distribution in the dysplastic joint is rather an approximation. Furthermore, they used a constant thickness cartilage model. They did not estimate pressure distribution in the cartilage model but in the underlying subchondral cortical bone. Another group developed a biomechanical guiding system (BGS) [12, 26, 28]. In 2009 they presented a manuscript reporting on three-dimensional mechanical evaluation of joint contact pressure in 12 PAO patients with a 10-year follow-up. They measured radiologic angles and joint contact pressures in these patients pre- and postoperatively. The authors were able to show that after a 10-year follow-up, peak contact pressures were reduced 1.7-fold and that lateral coverage increased in all patients. One limitation of their study is the use of discrete element analysis (DEA). Since the system was not only used for preoperative planning but also as an intraoperative guidance system, the DEA represents a computationally efficient method for modeling of cartilage stress by neglecting underlying bone stress. The cartilage models however remain largely approximated, since neither patient-specific nor constant cartilage models are used, but a simplified distribution of spring elements is employed for cartilage simulation. Recently, Zou et al. [14] also developed a 3D FE simulation of the effects of PAO on contact stresses. They validated their method on five models generated from CT scans of dysplastic hips and used constant thickness cartilage models. The acetabulum of each model was rotated in 5° increments in the coronal plane from the original position, and the relationship between contact area and pressure, as well as von Mises stress in the cartilage, was investigated, looking for the optimal position for the acetabulum. One limitation of this study is that acetabular reorientation was roughly performed with commercial FE analysis software (Abaqus1, Dassault Systèmes Simulia Corp, USA). Unlike our morphological-based planning application, their method is thus unvalidated and does not have a precise planning tool for an accurate quantification of patient specific 3D hip joint morphology.

In conclusion, our investigation contributes well to the current state of the art. First, to the best knowledge of the authors, this is the first study to use a patient-specific cartilage model for biomechanics-based planning of PAO allowing for estimation of changes of contact areas and peak pressures in truly dysplastic hips. Previous studies had investigated either normal or dysplastic hips, but never the true change during virtual reorientation of the latter. Furthermore, our results seem conclusive, since the optimal position with the largest contact areas and lowest peak pressures were found within the predefined normal values [3, 29] for the investigated LCE angle. This range for safe positioning is especially important, since in real-time surgery, reorientation toward the one "perfect" position might not be feasible. Finally, the comparison to constant thickness cartilage models is another novelty. Strong correlation was found for biomechanical optimization results between these two cartilage models. This is encouraging, since acquisition of patient-specific cartilage requires special multiplanar arthrography imaging (e.g., CT arthrography or MRI with dGEMRIC, T1rho or T2 mapping), while constant thickness cartilage is basically always available. Although our study has its limitations and further investigation is needed, computer-assisted planning with FE modeling using constant thickness cartilage might be a promising PAO planning tool providing conclusive and plausible results.

Acknowledgments This work was supported by the open source dysplastic hips image data from the University of Utah [17] and partially supported by Natural Science Foundation of SZU (grant no. 2017089) and Japanese-Swiss Science and Technology Cooperation Program.

This chapter was modified from the paper published by our group in *PLoS One* (Li et al., PLoS One 2016; 11(1):e0146452). The related contents were reused with permission.

References

1. Ganz R, Klaue K, Vinh TS, Mast JW (1988) A new Periacetabular osteotomy for the treatment of hip dysplasias technique and preliminary results. Clin Orthop Relat Res 232:26–36. PMID: 3383491
2. Steppacher SD, Tannast M, Ganz R, Siebenrock KA (2008) Mean 20-year followup of Bernese periacetabular osteotomy. Clin Orthop Relat Res 466(7):1633–1644. https://doi.org/10.1007/s11999-008-0242-3. PMID: 18449617
3. Tannast M, Hanke MS, Zheng G, Steppacher SD, Siebenrock KA (2015) What are the radiographic reference values for acetabular under-and overcoverage? Clin Orthop Relat Res 473(4):1234–1246. https://doi.org/10.1007/s11999-014-4038-3
4. Tannast M, Siebenrock KA, Anderson SE (2007) Femoroacetabular impingement: radiographic diagnosis—what the radiologist should know. Am J Roentgenol 188(6):1540–1552. https://doi.org/10.2214/AJR.06.0921. PMID: 17515374
5. Tannast M, Mistry S, Steppacher SD, Reichenbach S, Langlotz F, Siebenrock KA et al (2008) Radiographic analysis of femoroacetabular impingement with Hip2Norm-reliable and validated. J Orthop Res 26(9):1199–1205. https://doi.org/10.1002/jor.20653. PMID: 18404737
6. Clohisy JC, Carlisle JC, Trousdale R, Kim YJ, Beaule PE, Morgan P et al (2009) Radiographic evaluation of the hip has limited reliability. Clin Orthop Relat Res 467(3):666–675. https://doi.org/10.1007/s11999-008-0626-4. PMID: 19048356
7. Klaue K, Wallin A, Ganz R (1988) CT evaluation of coverage and congruency of the hip prior to osteotomy. Clin Orthop Relat Res 232:15–25. PMID: 3383480
8. Millis MB, Murphy SB (1992) Use of computed tomographic reconstruction in planning osteotomies of the hip. Clin Orthop Relat Res 274:154–159. PMID: 1729000
9. Dutoit M, Zambelli P (1999) Simplified 3D-evaluation of periacetabular osteotomy. Acta Orthop Belg 65(3):288–294. PMID: 10546351
10. Janzen D, Aippersbach S, Munk P, Sallomi D, Garbuz D, Werier J et al (1998) Three-dimensional CT measurement of adult acetabular dysplasia: technique, preliminary results in normal subjects, and potential applications. Skelet Radiol 27(7):352–358. https://doi.org/10.1007/s002560050397. PMID: 9730324
11. Dandachli W, Kannan V, Richards R, Shah Z, Hall-Craggs M, Witt J (2008) Analysis of cover of the femoral head in normal and dysplastic hips NEW CT-BASED TECHNIQUE. J Bone Joint Surg Br Vol 90(11):1428–1434. https://doi.org/10.1302/0301-620X.90B11.20073
12. Armand M, Lepistö J, Tallroth K, Elias J, Chao E (2005) Outcome of periacetabular osteotomy: joint contact pressure calculation using standing AP radiographs, 12 patients followed for average 2 years. Acta Orthop 76(3):303–313. PMID: 16156455
13. Zhao X, Chosa E, Totoribe K, Deng G (2010) Effect of periacetabular osteotomy for acetabular dysplasia clarified by three-dimensional finite element analysis. J Orthop Sci 15(5):632–640. https://doi.org/10.1007/s00776-010-1511-z. PMID: 20953924
14. Zou Z, Chávez-Arreola A, Mandal P, Board TN, Alonso-Rasgado T (2013) Optimization of the position of the acetabulum in a ganz periacetabular osteotomy by finite element analysis. J Orthop Res 31(3):472–479. https://doi.org/10.1002/jor.22245. PMID: 23097237
15. Harris MD, Anderson AE, Henak CR, Ellis BJ, Peters CL, Weiss JA (2012) Finite element prediction of cartilage contact stresses in nor-

mal human hips. J Orthop Res 30(7):1133–1139. https://doi.org/10.1002/jor.22040. PMID: 22213112

16. Liu L, Ecker T, Schumann S, Siebenrock K, Nolte L, Zheng G (2014) Computer assisted planning and navigation of periacetabular osteotomy with range of motion optimization. Springer, Heidelberg, pp 643–650
17. Henak CR, Abraham CL, Anderson AE, Maas SA, Ellis BJ, Peters CL et al (2014) Patient-specific analysis of cartilage and labrum mechanics in human hips with acetabular dysplasia. Osteoarthr Cartil 22(2):210–217. https://doi.org/10.1016/j.joca.2013.11.003. PMID: 24269633
18. Liu L, Ecker T, Xie L, Schumann S, Siebenrock K, Zheng G (2015) Biomechanical validation of computer assisted planning of periacetabular osteotomy: a preliminary study based on finite element analysis. Med Eng Phys. https://doi.org/10.1016/j.medengphy.2015.09.002
19. Anderson AE, Ellis BJ, Maas SA, Peters CL, Weiss JA (2008) Validation of finite element predictions of cartilage contact pressure in the human hip joint. J Biomech Eng 130(5):051008. https://doi.org/10.1115/1.2953472. PMID: 19045515
20. Caligaris M, Ateshian GA (2008) Effects of sustained interstitial fluid pressurization under migrating contact area, and boundary lubrication by synovial fluid, on cartilage friction. Osteoarthr Cartil 16(10):1220–1227. https://doi.org/10.1016/j.joca.2008.02.020. PMID: 18395475
21. Bergmann G, Deuretzbacher G, Heller M, Graichen F, Rohlmann A, Strauss J et al (2001) Hip contact forces and gait patterns from routine activities. J Biomech 34(7):859–871. https://doi.org/10.1016/S0021-9290(01)00040-9. PMID: 11410170
22. Phillips A, Pankaj P, Howie C, Usmani A, Simpson A (2007) Finite element modelling of the pelvis: inclusion of muscular andligamentous boundary conditions. Med Eng Phys 29(7):739–748. https://doi.org/10.1016/j.medengphy.2006.08.010
23. Ferguson S, Bryant J, Ganz R, Ito K (2003) An in vitro investigation of the acetabular labral seal in hip joint mechanics. J Biomech 36(2):171–178. https://doi.org/10.1016/S0021-9290(02)00365-2. PMID: 12547354
24. Konrath GA, Hamel AJ, Olson SA, Bay B, Sharkey NA (1998) The role of the acetabular labrum and the transverse acetabular ligament in load transmission in the hip. J Bone Joint Surg 80(12):1781–1788
25. Henak CR, Ellis BJ, Harris MD, Anderson AE, Peters CL, Weiss JA (2011) Role of the acetabular labrum in load support across the hip joint. J Biomech 44(12):2201–2206. https://doi.org/10.1016/j.jbiomech.2011.06.011. PMID: 21757198
26. Armiger RS, Armand M, Tallroth K, Lepistö J, Mears SC (2009) Three-dimensional mechanical evaluation of joint contact pressure in 12 periacetabular osteotomy patients with 10-year follow-up. Acta Orthop 80(2):155–161. https://doi.org/10.3109/17453670902947390. PMID: 19404795
27. Niknafs N, Murphy RJ, Armiger RS, Lepistö J, Armand M (2013) Biomechanical factors in planning of periacetabular osteotomy. Frontiers in bioengineering and biotechnology; 1. https://doi.org/10.3389/fbioe.2013.00020. PMID: 25152876
28. Lepistö J, Armand M, Armiger RS (2008) Periacetabular osteotomy in adult hip dysplasia–developing a computer aided real-time biomechanical guiding system (BGS). Suomen ortopedia ja traumatologia = Ortopedioch traumatologi i Finland = Finn J Orthop Traumatol 31(2):186. PMID: 20490364
29. Haefeli P, Steppacher S, Babst D, Siebenrock K, Tannast M (2015) An Increased Iliocapsularis-to-rectusfemoris Ratio Is Suggestive for Instability in Borderline Hips. Clin Orthop Relat Res 473(12):3725–3734. https://doi.org/10.1007/s11999-015-4382-y

14 Biomechanical Guidance System for Periacetabular Osteotomy

Mehran Armand, Robert Grupp, Ryan Murphy, Rachel Hegman, Robert Armiger, Russell Taylor, Benjamin McArthur, and Jyri Lepisto

Abstract

This chapter presents a biomechanical guidance navigation system for performing periacetabular osteotomy (PAO) to treat developmental dysplasia of the hip. The main motivation of the biomechanical guidance system (BGS) is to plan and track the osteotomized fragment in real time during PAO while simplifying this challenging procedure. The BGS computes the three-dimensional position of the osteotomized fragment in terms of conventional anatomical angles and simulates biomechanical states of the joint. This chapter describes the BGS structure and its application using two different navigation approaches including optical tracking of the fragment and x-ray-based navigation. Both cadaver studies and preliminary clinical studies showed that the biomechanical planning is consistent with traditional PAO planning techniques and that the additional information provided by accurate 3D positioning of the fragment does not adversely impact the surgery.

Keywords

Developmental dysplasia of the hip (DDH) · Periacetabular osteotomy (PAO) · Biomechanical guidance system · X-ray-based navigation

M. Armand (✉)
Johns Hopkins University Applied Physics laboratory, Laurel, MD, USA

Department of Mechanical Engineering, Johns Hopkins University, Baltimore, MD, USA

Department of Orthopaedic Surgery, Johns Hopkins University, Baltimore, MD, USA
e-mail: Mehran.Armand@jhuapl.edu

R. Grupp · R. Taylor
Department of Computer Science, Johns Hopkins University, Baltimore, MD, USA

R. Murphy · R. Armiger
Johns Hopkins University Applied Physics laboratory, Laurel, MD, USA

R. Hegman
Johns Hopkins University Applied Physics laboratory, Laurel, MD, USA

Department of Computer Science, Johns Hopkins University, Baltimore, MD, USA

B. McArthur
Dell Medical School at the University of Texas, Austin, TX, USA

J. Lepisto
Orton Orthopaedic Hospital, Helsinki, Finland

14.1 Introduction

Hip dysplasia is a condition in which the acetabulum is shallow and its roof is obliquely inclined laterally. As a result of this configuration,

G. Zheng et al. (eds.), *Intelligent Orthopaedics*, Advances in Experimental Medicine and Biology 1093, https://doi.org/10.1007/978-981-13-1396-7_14

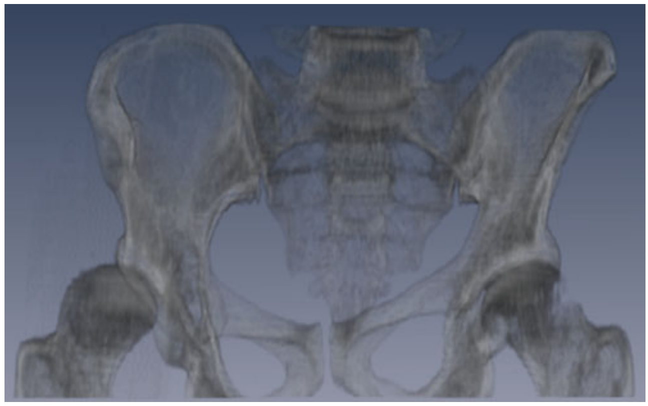

Fig. 14.1 Dysplastic right hip with inadequate coverage of the femoral head

the anterior and superior aspect of the articular cartilage of the femoral head is not adequately covered (Fig. 14.1). This leads to abnormally high stresses on the lateral edge of the acetabulum, a situation that may cause osteoarthritis [1, 2], fracture of the rim of the acetabulum due to excessive loading, and/or breakdown of the rim of the acetabular cartilage [3]. The symptoms of hip dysplasia usually occur in adolescents and young adults (<45 years) with seven times more incidence in females. If these patients were treated with total hip replacement (THR), they may require multiple revision surgeries during their lifetime. Each revision surgery will become substantially more invasive and challenging. Osteotomy of the hip, therefore, is commonly the surgery of choice for young adults suffering from dysplasia. Numerous outcome studies performed during the last 30 years have shown that performing periacetabular osteotomy (PAO) on young adults with dysplasia is a very effective surgery and prevents or delays osteoarthritis of the hip (e.g., [4, 5]).

The Bernese periacetabular osteotomy (PAO), one of the most popular techniques for periacetabular osteotomy, aims at achieving optimum coverage of the femoral head by recreating the relatively normal anatomy and mechanics for the dysplastic hip. This procedure can be performed without compromising pelvic ring stability (Fig. 14.2). It consists of a sequence of cuts through the ischium, pubis, and ilium. The procedure completely detaches the acetabulum from the rest of the pelvis (Fig. 14.2). The cup is then reoriented

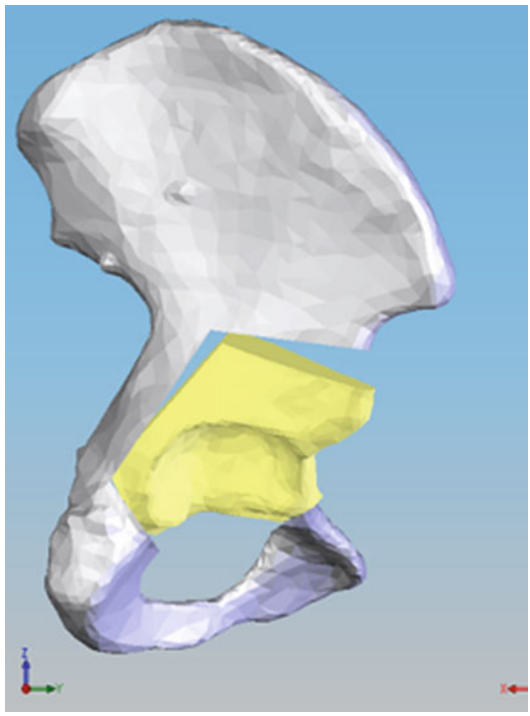

Fig. 14.2 Bernese PAO: the acetabular fragment (yellow) is osteotomized while maintaining pelvic stability

and fixed to the pelvis to improve the femoral head coverage and contact pressure distribution in the hip joint.

PAO is a technically challenging procedure with a steep learning curve [6–8]; the acetabular fragment must be detached with a limited line of sight and without fracture of the posterior column or damage to the hip joint (Fig. 14.2). There is always potential to damage the neural and vascular structures close to the site of surgical activity [9]. Correct intraoperative 3D joint alignment is especially difficult [10] and should be checked intraoperatively to improve survivorship [11, 12]. Conventional procedures rely on limited feedback (typically, C-arm x-ray images and surgeon experience) for optimal joint alignment during the procedure. Previous systems have been developed to navigate tools during PAO [13, 14], which can help the surgeon in making the difficult cuts that do not allow a direct line of sight. However, those systems only address the technical challenge of surgically releasing the acetabulum and do not provide information regarding achieving the surgical goals for intraoperative joint alignment. Because of the limited advantage, additional equipment cost, additional time needed during the intervention, and space constraints in the operating room (occluding the field of view for optical trackers), at this time, few surgeons in the world perform image-guided computer-assisted PAO.

Several studies have proposed computer-assisted surgery for PAO (e.g., [13–16]) and described a number of potential benefits, including preoperative planning, and visual feedback combined with intraoperative navigation. However, the main limitation of each system is either the lack of fragment tracking or the inability to intraoperatively assess fragment location. Real-time feedback of the joint alignment and simulated joint contact pressures has the potential to provide the surgeon with necessary information to select and achieve optimal joint alignment [12, 17–20].

In this chapter, we describe our efforts in the development of a navigation system enabling tracking of the detached bone fragment and algorithms performing real-time biomechanical and geometrical analysis, providing the surgeon with anatomical measurements previously unavailable [21–25]. To this end, the system has successfully been used in 12 clinical investigations by Dr. Lepisto at Orton Orthopaedic Hospital, Helsinki, Finland, and 10 clinical investigations by Dr. Kjeld Soballe at Aarhus University Hospital, Denmark. We further discuss our more recent efforts to address the disadvantages due to the use of optical tracking by applying x-ray-based biomechanical navigation and 3D fragment tracking.

14.2 Overview of the System Architecture

The workflow of the biomechanical guidance system (BGS) workstation is shown in Fig. 14.3 and described below. Preoperatively, the partial CT around the hip joint and a standing radiograph of the full pelvis is acquired (Fig. 14.3a). Using the statistical atlas of dysplastic pelves, the 3D model of the (full) pelvis of the patient is reconstructed (Fig. 14.3b) [26, 27, 29]. The BGS workstation segments and reconstructs the acetabular cartilage from CT data and automatically calculates the radiographic angles [22] (Figs. 14.3c and 14.4). The workstation will also calculate the contact pressure distribution around the joint for simulated walking, standing, and sitting scenarios [18] (Fig. 14.3c). In the BGS simulation/visualization environment, the surgeon can manually or automatically find the optimized joint position for the PAO surgery and plan the osteotomy lines (Fig. 14.3h). Intraoperatively, The BGS can use two different methods for tracking the position of osteotomized bone fragment.

1. *Navigation using optical tracking:* The BGS can use an optical tracking system for tracking the fragment position and calculating the anatomical realignment angles. The surgeon creates at least three bone burs on the fragment and finds its position using a digitizer probe tracked by an optical tracker (Polaris, NDI Inc.) (Fig. 14.3e1) with respect to a reference rigid body attached to the pelvis. The details of the approach can be found in [30].
2. *X-ray-based navigation:* Before performing the osteotomy and after making skin incisions, the surgeon can inject 1 mm diameter tantalum radiopaque fiducials (shown as dots in Fig. 14.3e2) into the pelvis in the ilium (sta-

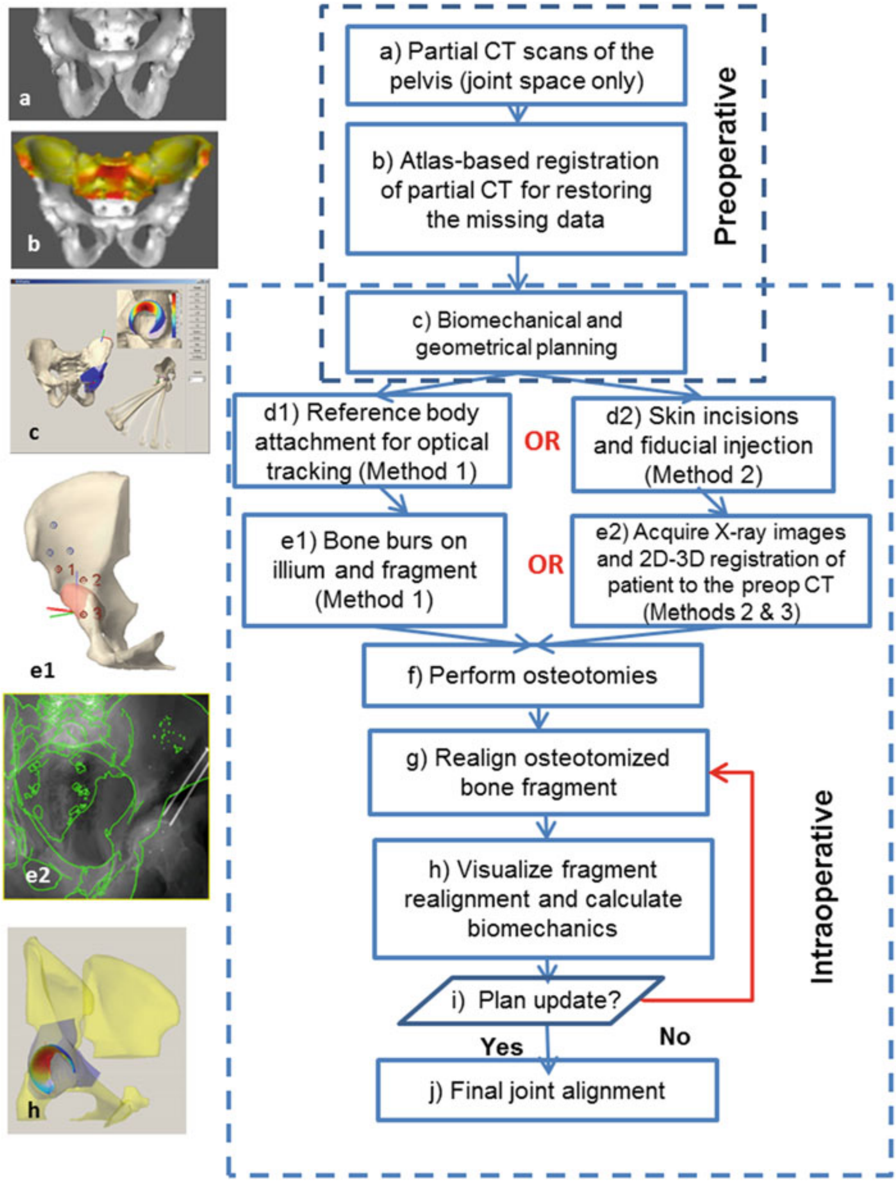

Fig. 14.3 BGS workflow with the use of two different methods for intraoperative navigation: (1) use of optical tracker, (2) x-ray-based navigation with fiducials

tionary fragment) and into the bone around the acetabular joint (the detached acetabular fragment) using a bead injector (Halifax Biomedical Inc.). The surgeon will then acquire two x-ray images, and the BGS workstation will perform 2D-3D registration to register the x-ray image to the preoperative 3D model of the pelvis and localize the fiducials on the model coordinates frames (Fig. 14.3e2). At any time after performing the osteotomies, the surgeon can acquire an x-ray image and the BGS workstation will then register the image to the 3D model using the fiducials on the stationary fragment. It will also determine the change in relative coordinates of the fiducials on the detached fragment with respect to the fiducials in the stationary fragment and use the information to calculate the joint realignment angles and simulate the joint contact pressures (Fig. 14.3h) [31].

In general, the surgeon may need to consider trade-offs and revise the surgical plan (Fig. 14.3i) for a variety of reasons (e.g., patient bone quality, the strength of soft tissues around the joint, variability of the bone fracture line due to chiseling). The BGS will allow the surgeon to update the plan and recalculate the biomechanics and new joint angles when using any of the above approaches. In the following we describe the BGS modules and the evaluation experiments performed for each module and the overall system.

14.3 Planning Module

The planning module performs three tasks: (1) estimates the full pelvis shape from the partial CT scans of the pelvis around the hip joint with the help of a statistical atlas of dysplastic hips, (2) automatically calculates the conventional anatomical angles (Fig. 14.4) and simulated contact pressures (Fig. 14.3h) used for diagnosis of dysplasia, and (3) determines the desired joint realignment and osteotomy lines based on optimizing anatomical angles and joint contact pressure.

14.3.1 Pelvis Shape Estimation

The hip osteotomy patient demographic consists mainly of young (likely less than 45 years old) females without arthritis [9, 32]. Excess radiation is a cause for concern among all patients, especially those in this demographic group. Ideally, for the diagnosis of dysplasia and conventional planning of PAO, a partial CT around the hip joint is required. However, for biomechanical planning and intraoperative registration as used for computer-aided surgery procedures, a full pelvis CT will be more desirable.

We have developed two approaches for extrapolating the missing pelvis anatomy using statistical atlases. In the approach described in [26], we performed a study by constructing a statistical atlas of 104 normal male pelves using the process described in [33]. In this study the model representation for the atlas consisted of a tetrahedral mesh parameterizing the anatomical shape and Bernstein polynomials approximating CT intensities [34, 35]. We created partial CT data from the full CT by manually segmenting the partial volume and randomly sampling the segmented volume. The registration of partial CT to the statistical atlas consisted of rigid registration and principal component mode matching. We also used an image-based 2D-3D registration method with a standing AP radiograph with the 3D predicted model to see the effect of additional information on estimation accuracy. Using leave-out experiments, simulation results show that the accuracy of the atlas-extrapolated model improved and was comparable with the full CT model when x-ray images were used [26].

One of the issues with the above model is the discontinuity in transition from the actual CT data to the interpolated portion of the data. To address this issue, we developed a smooth extrapolation technique leveraging a partial pelvis CT and a statistical shape model of the full pelvis in order to estimate a patient's complete pelvis. Unknown anatomy was simulated by keeping the axial slices of the patient's acetabulum intact and varying the amount of the superior iliac crest retained, from 0 to 15% of the total pelvis extent. The smooth technique showed an average improvement over the cut-and-paste method of 1.31 mm and 3.61 mm, in RMS and maximum surface error, respectively [29, 36].

As another approach, we developed a robust, automated atlas-to-patient registration algorithm by using statistics of the voxel-wise *displacement* learned from computed deformation vectors on a training dataset. This allows direct translation of the template image to the patient image. Also, the voxel-wise displacement approach is a more natural fit for the goal of extrapolation of missing data from the atlas since it does not require the intermediate step of modifying/manipulating

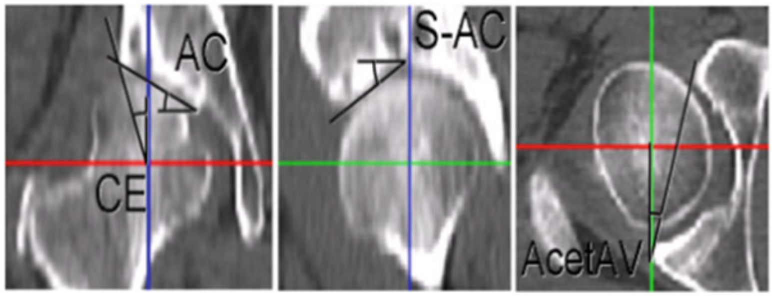

Fig. 14.4 Characteristic anatomical angles for diagnosis of dysplasia and conventional planning of PAO

the tetrahedral meshes. The details of the approach were reported in [27]. Briefly the leave-one-out experiments demonstrated 4.13 mm error with respect to the true displacement fields.

14.3.2 Geometrical and Biomechanical Planning

The BGS uses meshed surface models generated from the segmented CT scans of the pelvis to visualize patient anatomy and plan the location of the osteotomies. The articular surface of the cartilage model is developed on reformatted oblique CT slices extending radially from the center of femoral head as described in [22]. The biomechanical model uses linear [18] or nonlinear [37] discrete element analysis (DEA), with and without the measure of the cartilage thickness [25] to estimate contact pressures. Briefly, this approach models the cartilage region with a series of elastic compressive elements assuming no deformation of the acetabular bone in response to load. Loads are applied through the center of the femoral head to simulate standing [17] and the peak forces during walking and sitting down [38]. The parameters calculated in the mechanical analysis include metrics for both the location and magnitude of the peak contact pressure, as well as the hip range of motion (Fig. 14.3c). The biomechanical planning system was evaluated on 12 patients with developmental hip dysplasia. Consistent with 2-year outcome studies, the results showed that in all but one patient, the peak contact pressure significantly reduced postoperatively. The range of contact pressures reported preoperatively was 1.9 to 7.7 MPa, while postoperatively the range showed an improvement of 1.4 to 3.2 MPa. The details of this study were reported in [18].

The BGS also performs geometric characterization of the acetabulum using radiographic angles measured through CT reformats and x-ray projections (Fig. 14.4). The angles include the center edge (CE), acetabular inclination (AC) in the frontal plane, superior-anterior coverage (S-AC) in the sagittal plane, and the acetabular anteversion (AcetAV) in the transverse plane (Fig. 14.4). The detail of the calculations of these angles by the BGS is reported in [30].

14.4 Navigation Module

The BGS tracks the osteotomized fragment throughout the procedure. In addition to visualization, the BGS quantitatively reports the position of the fragment and updates and compares the mechanical analysis with that of the plans. The two approaches used for the BGS navigation is as follows:

14.4.1 Navigation with Optical Tracker

For this approach, the surgeon mounts a reference rigid body (NDI Inc. Waterloo, Canada) to either the contralateral or ipsilateral iliac crest using a 20 × 4 mm bone pin (Stryker, Kalamazoo, MI, USA). The BGS uses a two-stage process to register the subject-specific pelvis computer model developed from CT data to the patient. First, a coarse registration is performed by selecting anatomical landmarks in the CT model and by touching the corresponding landmarks on the patient's pelvis using a navigated digitizer probe.

Next, surface points are collected from patient's accessible bony regions using the navigated digitizer probe, and a fine point to surface registration is performed using iterative closest points (ICP) [39] or unscented Kalman filter (UKF) [40] technique. After registration, the surgeon creates and digitizes four burrs on the expected fragment (Fig. 14.3e1) to localize the fragment throughout the surgery. As the surgeon positions the fragment, at any time during the operation, he/she can touch the burs using the digitizing probe. The software will then recalculate and visualize the fragment position, simulate the magnitude and position of the peak contact pressure, and report both desired and actual anatomical characteristic angles. We performed a set of 19 cadaver studies to evaluate the system accuracy and refine the surgical protocol. Postoperative CT scans of the cadavers were obtained, and the accuracy of the intraoperative calculation of the angles was compared against the postoperative CT data. The results showed strong agreement (about 2 degrees) among intra- and postoperative angles in all three dimensions. The details of the work can be found in [30].

14.4.1.1 X-ray-Based Navigation

While the optical trackers have been shown to be reliable tools for the development of navigation systems for tracking the surgical tools in real time and tracking the detached bone fragment as discussed above, they suffer some disadvantages:

1. Surgeons are most accustomed to x-ray images and trust the images obtained by x-ray more than the visualization created from augmented reality using CT models and optical tracking.
2. Optical tracking requires additional reference bodies attached to the bone as well as specifically modified surgical tools.
3. Recent less invasive PAO surgeries with less than 10 cm skin incision (e.g., Dr. Soballe's approach [41]) will impose serious challenges to the use of optical trackers,especially for surface registration methods requiring exposure of considerable amount of pelvic bone surface.
4. The visualization based on optical tracking cannot substitute the need for x-ray images, as surgeons cannot reliably monitor some of the more challenging posterior osteotomy cuts via chiseling when using the virtual model.

The BGS can use an alternative approach for tracking the fragment and performing biomechanical guidance using x-ray images only. Tracking the acetabular fragment is essential to automated measurements of the anatomical angles and intraoperative biomechanical analysis without disrupting surgical workflow and eliminating the need for external tracking devices.

For x-ray-based navigation, after performing the skin incisions, the surgeon injects a series of radiopaque fiducials (1.0 mm diameter tantalum beads) to the stationary pelvis fragment (e.g., iliac wing) and the acetabular (moving) fragment similar to the approach approved for Roentgen stereometric analysis (RSA) using a bead injector (Halifax Biomedical Inc., Halifax, Canada) (Fig. 14.5). With the acetabulum intact and fiducials affixed, the surgeon acquires two to three x-ray images. A 2D-3D registration framework estimates the relative pose of the x-ray images and registering the patient anatomy of interest to the preoperative model obtained from CT scanner. Briefly, the registration framework is as follows:

1. Preoperatively acquired diagnostic CT data is converted into a volume image represented by line attenuation coefficients.
2. An initial estimate of the relative pose between each x-ray image and CT data will be used to start the registration process. This is achieved by determining some anatomical landmarks on the pelvis anatomy (e.g., ASIS, ISIS, etc.) and performing a point-based registration.
3. Digitally reconstructed radiographs (DRRs) will be generated from preoperative CT data using GPU-based implementation of the DRR using trilinear interpolation algorithm [42].

Fig. 14.5 The tantalum 1 mm beads (black dots) injected into the ilium and the detached acetabular fragment

4. A measure of similarity between x-ray images and DRR images (e.g., normalized cross-correlation of 2D Sobel gradients (Grad-NCC), gradient information (GI), or mutual information (MI)) is used as an objective function. A multi-resolution optimization approach maximizes the similarity between images.
5. After registration the corresponding location of each fiducial can be localized on the CT image, and the exact geometry of each of the two sets of fiducials (on stationary and moving fragments) can be determined.

For the first x-ray image set prior to osteotomy, the fiducials on the stationary fragment (ilium) define a common reference frame for future images, and the acetabular fragment fiducials define the initial fragment position. For intraoperative data, we can perform a feature-based registration [43] between the fiducials on the stationary fragment to align the current imaging frame with the preoperative imaging frame. The transformation of the fiducials on the acetabular fragment between pre- and intraoperative imaging frames quantifies the motion of the acetabular fragment. The system additionally provides the visualization of the current fragment location compared with the preoperative and planned location.

As mentioned above, the anatomical angles and biomechanics will be determined based on the new position of the acetabular fragment. If needed, the surgeon can update the surgical plan (due to the potential constraints), and the BGS workstation will intraoperatively update the target anatomical angles and biomechanics and allow the surgeon make the necessary trade-offs.

In a preliminary study, we attached eight stainless steel fiducials (four on the ilium and four around the hip joint) to a high-density plastic sawbone and performed PAO cuts around the hip joint. We obtained CBCT from the pelvis prior (preop) and after moving the acetabular fragment (postop). On four arbitrary x-ray images, we performed 2D-3D registration to find the transformation between the preop 3D model and the x-ray images. We then backprojected the fiducials in the x-ray images to obtain their 3D coordinates and compared it to the location of the fiducials on the acetabular (moving) fragment in postop CBCT (ground truth). We found a rotation error of 1.4 degrees which is within the acceptable error range (<3 degrees) for acetabular fragment placement [31].

14.5 Clinical Experience

In addition to multiple cadaver studies, the BGS with optical tracking has been used to perform a series of 12 consecutive PAO surgeries on 11 patients (including a bilateral PAO) at Orton Orthopaedic Hospital in Helsinki, Finland (approved by JHM IRB #NA_00001257), by Dr. Jyri Lepisto [44]. The patient cohort included 3 males and 8 females with the mean age of 34 (ranging from 22 to 28 years). For this study patients with concurrent femoral pathologies such as slipped capital femoral epiphysis or Legg-Calve-Perthes syndrome were excluded from the study.

For this study, the CT scans of pelves with 2 mm spacing between slices were obtained prior to the surgeries. The CT images were then resampled and segmented with 1 mm slices. The points along acetabular rim were then digitized to develop the acetabular contact surface using lunate trace method as described in [22].

For these surgeries, following an incision on the iliac crest, the surgeon attached a removable rigid body (RB) to the contralateral iliac crest using an anchoring pin. Prior to any osteotomy, the surgeon digitized three landmarks on the pelvis (the ASIS and AIIS on the ipsilateral side and the ASIS on the contralateral side) that were previously defined in the CT model. After osteotomizing the anterior inferior iliac spine as part of the exposure, a bone burr was used to create a set of four 1.5 mm concavities on the iliac cortex (so-called confidence points similar to Fig. 14.3e). A coarse registration was then performed using the above three landmarks. Next, the surgeon collected a series of points on the exposed portions of pelvis. The data acquired was used to perform fine registration using iterative closest point [39] and/or unscented Kalman filters [40]. After registration the surgeon created two osteotomy cuts without repositioning the fragment. He then created four additional bone burrs on the osteotomized fragment. After performing osteotomies, the surgeon released and repositioned the fragment. He then assessed the position of the fragment by placing a digitizing probe on each of the four bone burr concavities in the fragment. The BGS used this data to calculate the 3D position of the fragment, the anatomical angles (Fig. 14.4), and the simulated contact pressure distribution on the articular joint (Fig. 14.3e1). The data was then compared with the preoperative plan.

To validate the BGS tracking, we compared intraoperative measurements to postoperative CT scans taken at least 4 months after each surgery. Overall, the BGS data acquisition did not introduce any major difficulties for the surgeon. The surgical time was comparable to the conventional approach (ranging from 95 to 210 min). The BGS measured fragment positioning was in good agreement with the postoperative CT measurements performed 4 months later (mean 3.7 degrees). The details of the clinical experience were reported in [44].

14.6 Limitations and Ongoing Work

The BGS addresses some of the existing challenges in performing PAO including steep learning curve, limited line of sight, limitation of current conventional methods for three dimensional tracking of the osteotomized fragment position, and lack of intraoperative biomechanical analysis tools. Notably, the system allows the surgeon to perform real-time analysis and update of the surgical plan as needed. Several aspects of the BGS can be improved with additional research. The biomechanical analysis is based on the simulation of the contact pressure. Our biomechanically based simulation for the correction of the joint position is commonly in agreement with the established ideal ranges for characteristic angles (current gold standards). The simulation methods used, however, can be considered the first order of approximation of the acetabular joint contact pressure. Addition of more details to the biomechanical model (e.g., modeling the effect of labrum, cartilage thickness, etc.) may further help to improve the accuracy of the outcome predictions. Moreover, the addition of details to the model must be validated against more sophisticated cadaveric experimentations and multiyear outcome studies on patients undergoing PAO.

The BGS supports navigation using both optical trackers and fluoroscopic C-arm. Our ongoing work has shown the promise of x-ray-based navigation with fiducials. However, image-based navigation system without the use of fiducials seems to be a more promising approach. Our very recent work demonstrates that if the PAO cuts closely follow that of the preoperative plan, the osteotomized fragment position can be successfully tracked at any time during the surgery by performing 2D-3D registration on 2–3 x-ray images. Furthermore, our current work focuses on showing that approaches for intraoperatively updating the preoperatively planned PAO cuts may also help in eliminating the use of fiducials by improving the fragment model accuracy. The accuracy of the latter technique is currently under investigation.

Acknowledgments The human subject research and cadaver studies were approved by Johns Hopkins Medicine JHM IRB NA_00001257 and JHM IRB1 #05-09-02-01.The study was supported by grant number R01 EB60389 and R21 EB020113 from the National Institute for Biomedical Imaging and Bioengineering (NIH/NIBIB) and two JHU/APL graduate student scholarships.

References

1. Wiberg G (1939) Studies on dysplastic acetabula and congenital subluxation of the hip joint with special reference to the complication of osteoarthritis. Acta Chir Scand 83
2. Cooperman DR, Wallensten R, Stulberg SD (1983) Acetabular dysplasia in the adult. Clin Orthop Relat Res:79–85
3. Matta JM, Stover MD, Siebenrock K (1999) Periacetabular osteotomy through the smith-Petersen approach. Clin Orthop Relat Res:21–32
4. Siebenrock KA, Scholl E, Lottenbach M, Ganz R (1999) Bernese periacetabular osteotomy. Clin Orthop Relat Res:9–20
5. Trumble SJ, Mayo KA, Mast JW (1999) The periacetabular osteotomy. Minimum 2 year followup in more than 100 hips. Clin Orthop Relat Res:54–63
6. Davey JP, Santore RF (1999) Complications of periacetabular osteotomy. Clin Orthop Relat Res:33–37
7. Hussell JG, Rodriguez JA, Ganz R (1999) Technical complications of the Bernese periacetabular osteotomy. Clin Orthop Relat Res:81–92
8. Trousdale RT, Cabanela ME (2003) Lessons learned after more than 250 periacetabular osteotomies. Acta Orthop Scand 74:119–126
9. Ganz R, Klaue K, Vinh TS, Mast JW (1988) A new periacetabular osteotomy for the treatment of hip dysplasias. Technique and preliminary results. Clin Orthop Relat Res:26–36
10. Troelsen A (2009) Surgical advances in periacetabular osteotomy for treatment of hip dysplasia in adults. Acta Orthop Suppl 80:1–33
11. Albers CE, Steppacher SD, Ganz R, Tannast M, Siebenrock KA (2013) Impingement adversely affects 10-year survivorship after periacetabular osteotomy for DDH. Clin Orthop Relat Res 471: 1602–1614
12. Troelsen A, Elmengaard B, Soballe K (2009) Medium-term outcome of periacetabular osteotomy and predictors of conversion to total hip replacement. J Bone Joint Surg Am 91:2169–2179
13. Langlotz F, Stucki M, Bachler R, Scheer C, Ganz R, Berlemann U et al (1997) The first twelve cases of computer assisted periacetabular osteotomy. Comput Aided Surg 2:317–326
14. Mayman DJ, Rudan J, Yach J, Ellis R (2002) The Kingston periacetabular osteotomy utilizing computer enhancement: a new technique. Comput Aided Surg 7:179–186
15. Akiyama H, Goto K, So K, Nakamura T (2010) Computed tomography-based navigation for curved periacetabular osteotomy. J Orthop Sci 15:829–833
16. Hsieh PH, Chang YH, Shih CH (2006) Image-guided periacetabular osteotomy: computer-assisted navigation compared with the conventional technique: a randomized study of 36 patients followed for 2 years. Acta Orthop 77:591–597
17. Armand M, Lepisto J, Tallroth K, Elias J, Chao E (2005) Outcome of periacetabular osteotomy: joint contact pressure calculation using standing AP radiographs, 12 patients followed for average 2 years. Acta Orthop 76:303–313
18. Armiger RS, Armand M, Tallroth K, Lepisto J, Mears SC (2009) Three-dimensional mechanical evaluation of joint contact pressure in 12 periacetabular osteotomy patients with 10-year follow-up. Acta Orthop 80:155–161
19. Hipp JA, Sugano N, Millis MB, Murphy SB (1999) Planning acetabular redirection osteotomies based on joint contact pressures. Clin Orthop Relat Res 364:134–143
20. Tsumura H, Kaku N, Ikeda S, Torisu T (2005) A computer simulation of rotational acetabular osteotomy for dysplastic hip joint: does the optimal transposition of the acetabular fragment exist? J Orthop Sci 10:145–151
21. Armand M, Armiger R, Waites M, Mears S, Lepisto J, Minhas D, et al (2006) A guidance system for intraoperatively updating surgical-plans during Periacetabular osteotomy: development and cadaver tests. In: CAOS, Montreal, Canada, 2006
22. Armiger RS, Armand M, Lepisto J, Minhas D, Tallroth K, Mears SC et al (2007) Evaluation of a computerized measurement technique for joint alignment before and during periacetabular osteotomy. Comput Aided Surg 12:215–224
23. Armand M, Lepistö J, Merkle A, Tallroth K, Liu X, Taylor R et al (2004) Computer-aided Orthopaedic surgery with near real-time biomechanical feedback. APL Tech Dig 25:242–252
24. Lepisto J, Armand M, Armiger R (2008) Periacetabular osteotomy in adult hip dysplasia - developing a computer aided real-time biomechanical guiding system (BGS). Suomen Ortopedia ja Traumatologia 31:186–190
25. Niknafs N, Murphy RJ, Armiger RS, Lepisto J, Armand M (2013) Biomechanical factors in planning of periacetabular osteotomy. Frontiers in bioengineering and biotechnology, vol 1
26. Chintalapani G, Murphy R, Armiger R, Lepisto J, Otake Y, Sugano N, et al (2010) Statistical Atlas based extrapolation of Ct data. In: SPIE medcial

imaging: visualization, image-guided procedures, and modeling, vol 7625

27. Otake Y, Murphy R, Grupp R, Sato Y, Taylor R, Armand M (2015) Comparison of optimization strategy and similarity metric in atlas-to-subject registration using statistical deformation model. In: SPIE medical imaging, Orlando, pp 94150Q-94150Q-6
29. Grupp R, Otake Y, Murphy R, Parvizi J, Armand M, Taylor R (2016) Pelvis surface estimation from partial CT for computer-aided pelvic osteotomies. Bone Joint J 98:55–55
30. Murphy RJ, Armiger RS, Lepisto J, Mears SC, Taylor RH, Armand M (Apr 2015) Development of a biomechanical guidance system for periacetabular osteotomy. Int J Comput Assist Radiol Surg 10: 497–508
31. Murphy R, Otake Y, Lepisto J, Armand M (2013) Computer-assisted x-ray image-based navigation of periacetabular osteotomy with fiducial based 3D acetabular fragment tracking. In: Proceedings of 13th annual meeting of the international society for computer assited orthopaedic surgery, Orlando, pp 59–61
32. Sierra RJ, Trousdale RT, Ganz R, Leunig M (Dec 2008) Hip disease in the young, active patient: evaluation and nonarthroplasty surgical options. J Am Acad Orthop Surg 16:689–703
33. Chintalapani G, Ellingsen LM, Sadowsky O, Prince JL, Taylor RH (2007) Statistical atlases of bone anatomy: construction, iterative improvement and validation. Med Image Comput Comput Assist Interv 10:499–506
34. Yao J, Taylor RH (2003) Non-rigid registration and correspondence finding in medical image analysis using multiple-layer flexible mesh template matching. Int J Pattern Recognit Artif Intell 17(7):1145–1165
35. Sadowsky O, Cohen JD, Taylor RH (2006 July) Projected tetrahedra revisited: a barycentric formulation applied to digital radiograph reconstruction using higher-order attenuation functions. IEEE Trans Vis Comput Graph 12:461–473
36. Grupp R, Chiang H, Otake Y, Murphy R, Gordon C, Armand M, et al (2015) Smooth extrapolation of unknown anatomy via statistical shape models. In SPIE medical imaging, Orlando, pp 941524–941524-10
37. Volokh KY, Chao EY, Armand M (Jun 2007) On foundations of discrete element analysis of contact in diarthrodial joints. Mol Cell Biomech 4:67–73
38. Heller M, Bergmann G, Deuretzbacher G, Durselen L, Pohl M, Claes L et al (2001) Musculo-skeletal loading conditions at the hip during walking and stair climbing. J Biomech 34:883–893
39. Besl PJ, McKay ND (1992) A method for registration of 3-D shapes. In: IEEE Trans Pattern Anal Mach Intell 14:239–256
40. Moghari MH, Abolmaesumi P (2005) A novel incremental technique for ultrasound to CT bone surface registration using unscented Kalman filtering. Med Image Comput Comput Assist Interv 8:197–204
41. Troelsen A, Elmengaard B, Soballe K (Mar 2008) A new minimally invasive transsartorial approach for periacetabular osteotomy. J Bone Joint Surg Am 90:493–498
42. Otake Y, Armand M, Armiger R, Kutzer M, Basafa E, Kazanzides P et al (2012) Intraoperative image-based multi-view 2D/3D registration for image-guided Orthopaedic surgery: incorporation of fiducial-based C-arm tracking and GPU-acceleration. IEEE Trans Med Imaging 31:948–962
43. Kang X, Armand M, Yoshito O, YAU W, Cheung P, Hu Y et al (2014) Robustness and accuracy of feature-based single image 2D-3D registration without correspondences for image-guided intervention. IEEE Trans Biomed Eng 61:149–161
44. Murphy RJ, Armiger RS, Lepistö J, Armand M (2016) Clinical evaluation of a biomechanical guidance system for periacetabular osteotomy. J Orthop Surg Res 11:36

15 Gravity-Assisted Navigation System for Total Hip Arthroplasty

Guoyan Zheng

Abstract

In this chapter we propose a new system that allows reliable acetabular cup placement in total hip arthroplasty (THA) when the surgery is operated in lateral approach. Conceptually it combines the accuracy of computer-generated patient-specific morphology information with an easy-to-use mechanical guide, which effectively uses natural gravity as the angular reference. The former is achieved by using a statistical shape model-based 2D-3D reconstruction technique that can generate a scaled, patient-specific 3D shape model of the pelvis from a single conventional anteroposterior (AP) pelvic X-ray radiograph. The reconstructed 3D shape model facilitates a reliable and accurate co-registration of the mechanical guide with the patient's anatomy in the operating theater. We validated the accuracy of our system by conducting experiments on placing seven cups to four pelvises with different morphologies. Taking the measurements from an image-free navigation system as the ground truth, our system showed an average accuracy of $2.1 \pm 0.7°$ for inclination and an average accuracy of $1.2 \pm 1.4°$ for anteversion.

G. Zheng (✉)
Institute for Surgical Technology and Biomechanics, University of Bern, Bern, Switzerland
e-mail: guoyan.zheng@istb.unibe.ch

Keywords

Total hip arthroplasty (THA) · Gravity-assisted navigation system (GANS) · Statistical shape model · 2D-3D reconstruction · Smart instrumentation · Mechanical guide

15.1 Introduction

Total hip arthroplasty (THA) is one of the most frequent orthopedic surgical interventions. Proper positioning, in particular angulation of the acetabular cup, is essential for improving the success of total hip arthroplasty. Previous studies [1–6] demonstrate that higher rates of pelvis osteolysis and component migration have all been well-associated with the malpositioning of the acetabular component, and surgical experience indicates that improper orientation of the acetabular component in terms of anteversion and inclination is the major cause of dislocation. As the risk of dislocation is significantly higher in those who have already experienced dislocation or after revision surgery [6], obtaining proper cup orientation during primary surgery is crucial.

G. Zheng et al. (eds.), *Intelligent Orthopaedics*, Advances in Experimental Medicine and Biology 1093, https://doi.org/10.1007/978-981-13-1396-7_15

Optimal ranges for angular cup position in terms of anteversion and inclination of the acetabular component have been extensively debated in the literature. Several so-called safe zones have been suggested. Lewinnek et al. described a safe zone of 5°–25° for anteversion and 30°–50° for inclination [5]. They found that acetabular cups placed outside this safe zone were approximately four times as likely to dislocate. Consequently optimal cup positioning requires that the surgeon attains adequate and reproducible angulations of the acetabular component with respect to the patient's individual pelvic morphology.

State-of-the-art mechanical guides, which are used in the vast majority of THAs, are easy to handle but cannot be registered to the individual pelvic morphology. Angular orientation is gained from reference objects in space-fixed coordinates and may be corrected/optimized through the surgeon's expert knowledge. A study conducted by DiGioia et al. [7], in which they used navigation technology to evaluate the performance of mechanical guides, found that 78% of the inserted cups would have been implanted outside the safe zone as suggested by Lewinnek et al. [5].

The search for alternatives was unsuccessful until modern optoelectronic tracking robotic technology was introduced to the field of orthopedics. Previously, a variety of image-based and image-free so-called navigation systems have been introduced for THA [8–13], which for the first time allowed co-registration of the patient's pelvic morphology. Despite encouraging results of smaller clinical trials and an early widespread enthusiasm, some drawbacks of navigation technology have been identified, which prevent their widespread use in clinical routine. Current criticism focuses on (a) significant investments required for acquisition and running costs for maintenance and use (training of users, additional operating room (OR) time, disposable markers, etc.); (b) all navigation systems proposed to date, no matter what image modality is used, have difficulty when the THA is operated in lateral approach, which is the approach of choice for more than 80% of THAs worldwide [13]; (c) the steep learning curve and the system complexities, which may result in 10–20% failure cases [12]; (d) optoelectronic tracking technology used in most navigation systems requires a straight line of sight, which is often difficult to maintain during surgery without paying additional efforts and time; (e) CT-based systems require CT scan, usually not performed for diagnosis, generating unnecessary radiation exposure to the patient and significant additional cost; (f) for image-free navigation systems, significant intra- and interobserver variability caused by variations during digitization of the anatomical landmarks, especially the one in the pubic region, was observed [14]; and (g) fluoroscopy-based navigation systems [12] have the advantage of eliminating a CT scan and achieving an equivalent accuracy. However, such a technology requires calibration of the image intensifier, and it was judged to be too cumbersome and time-consuming to intraoperatively manipulate the C-arm device for multiple image acquisition [12].

Recently, several groups [15–17] described methods to use the constant direction of the force of gravity as a reference in THA. Asayama et al. [15, 16] introduced a three-direction indicator to control intraoperative pelvic motion during THAs. The three-direction indicator incorporates a digital compass with two goniometers, as well as a pendulum and target apparatus. It allows for controlling only pelvic motion by measuring the three-dimensional (3D) angle formed by the gravitational direction and the Steinmann pin inserted into the iliac bone to fix the direction indicator. No control of acetabular cup placement was considered with this device. Echeverri et al. [17] described a gravity-assisted system to control both the pelvic motion and the acetabular component placement. Like any other mechanical guide, this system is simple to use, but it is also highly flawed. This is due to the fact that the alignment system developed by Echeverri et al. was placed in a fixed orientation relative to the shaft of a cup placement instrument, which in the best case scenario can be understood as being calibrated with respect to the morphology of a fixed pelvis without considering the morphological difference between the future pelvis to be navigated and the fixed pelvis used for calibration. It simply does not work due to the inherent morphological variations in human being. A recent simulation study of this device on 48 patient data revealed a maximum anteversion error of as high as 15° [18].

To address the limitations in the existing gravity-based systems, we developed a new gravity-assisted navigation system termed as "patient-specific, gravity-assisted navigation system" or "PS-GANS" in abbreviation. Conceptually it combines the accuracy of computer-generated patient-specific morphology information with an easy-to-use mechanical guide, which effectively uses natural gravity as the angular reference. Unlike the existing gravity-based systems, our system allows for calibration of the mechanical guide with respect to the patient-specific morphology, which is obtained by using a statistical shape model-based 2D-3D reconstruction technique that can generate a scaled, patient-specific 3D shape model of the pelvis from a single conventional anteroposterior (AP) X-ray radiograph. The reconstructed 3D shape model facilitates a reliable and accurate co-registration of the mechanical guide with the patient's anatomy in the operating theater.

15.2 Materials and Methods

15.2.1 Notations

Throughout the paper, we always establish a local coordinate system of a rigid body on a local reference plane of the entity. Thus, without explicitly stating, we always name the local coordinate system after the local reference plane. Furthermore, a vector $\mathtt{v}$ that is defined in a local coordinate system X will be noted as $\mathtt{v}^{\mathtt{X}}$. But if we would like to know the axis $\mathtt{v}$ of a local coordinate system $\mathtt{X}$ in another local coordinate system $\mathtt{Y}$, we will note it as $\mathtt{v}_{\mathtt{X}}^{\mathtt{Y}}$. A rigid body transformation from a local coordinate system $\mathtt{X}$ to another local coordinate system $\mathtt{Y}$ will be noted as $\mathtt{T}_{\mathtt{X}}^{\mathtt{Y}}$. The inverse of this transformation will be recorded as $\mathtt{T}_{\mathtt{Y}}^{\mathtt{X}}$. As in most of the time, we are only interested in knowing the orientation of a vector in a local coordinate system; knowing the rotational part $\mathtt{R}_{\mathtt{X}}^{\mathtt{Y}}$ of the rigid body transformation $\mathtt{T}_{\mathtt{X}}^{\mathtt{Y}}$ is enough for our purpose.

15.2.2 System Overview

Our system requires three bull's-eye bubble levels, as shown in Fig. 15.1. The first one is called witness bubble level that is fixed on the iliac

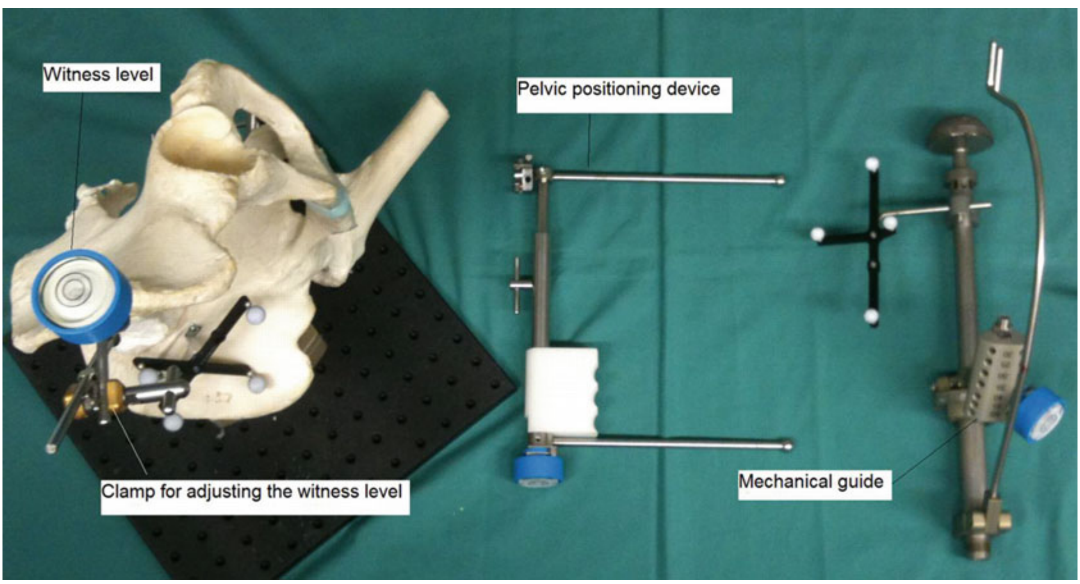

Fig. 15.1 An overview of the PS-GANS system

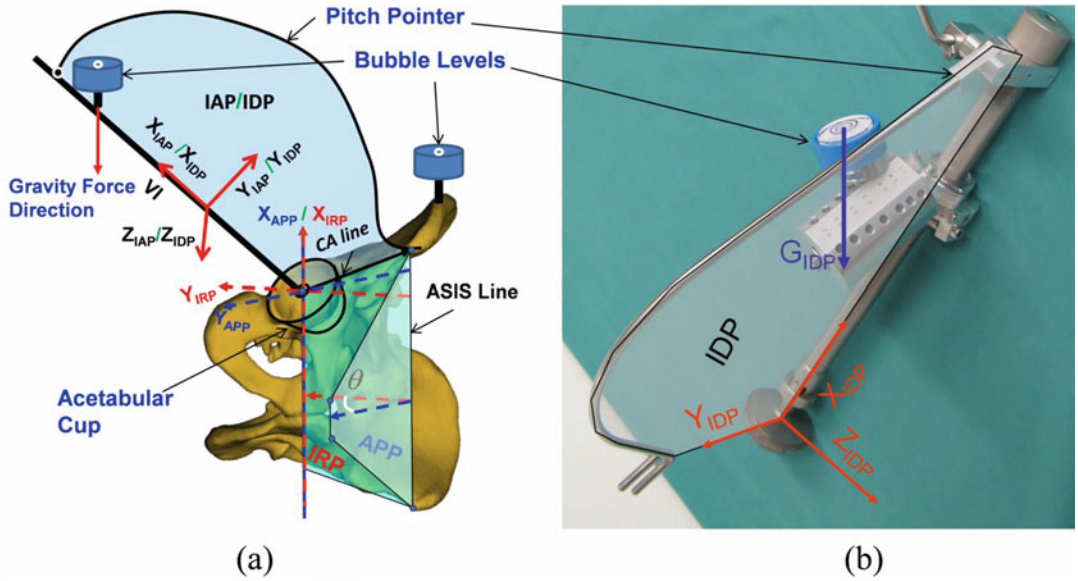

Fig. 15.2 (**a**) Schematic view of the relationship between the APP, the IRP, and the IAP (IDP) when the cup is placed in the desired orientation. (**b**) The mechanical guide attached to the cup placement instrument and the definition of the IDP

crest and is designed together with the one on the pelvic positioning device to place the pelvis to strict lateral decubitus. As soon as the pelvis is placed at strict lateral decubitus by using the pelvic positioning device, one can adjust a standard clamp to set the witness level's bubble to the center and move away the pelvic positioning device (see below for details). The witness level then acts as a witness, identifying the strict lateral decubitus position of the pelvis throughout the operation. The third one is called the instrument bubble level that is placed on a mechanical guide that is rigidly attached to the cup placement instrument for controlling cup orientation to the desired anteversion and inclination. Please keep it in mind that all the passive markers appearing in Fig. 15.1 are only for our validation purpose and are not required to use our system.

15.2.3 Coordinate Systems

Before we describe the details about how the patient-specific system calibration is done, we would like to first present a summary of all four local reference planes as well as their associated local coordinate systems that will be used in the calibration. See Fig. 15.2a for an overview.

Jamaraz et al. [10] introduced the anterior pelvic plane (APP) concept for measuring anteversion and inclination of the acetabular cup in their computer-assisted acetabular cup placement system. The APP is a reference plane of the human pelvis and, thus, allows the exact definition of a corresponding 3D local coordinate system as shown in Fig. 15.2a. It is based on three landmarks: bilateral anterior superior iliac spines (ASIS) and the geometric center of two pubic tubercles. The APP x-axis points to the patient's operating side, parallel with the line between the iliac spine points. The y-axis points inferior. The angular orientation of the acetabular component can be directly put into relation to the APP.

It is difficult, if it is not impossible, to locate the orientation of the APP without using a positional tracking device, largely due to the difficulty in mechanically aligning the geometric center of two pubic tubercles. In this work, we propose and use a new reference plane that is called intraoperative reference plane (IRP), which is defined by two lines that can be mechanically aligned with the design of our system: the line connecting the bilateral ASISs (we named it as the ASIS line) and the line CA from the cup center of the operating side to the ASIS of the operating side (we named it as the CA line). Similar to how we establish a 3D local coordinate system on the APP, we also establish a 3D local coordinate system on the IRP, as shown in Fig. 15.2a, where we translate the origins of both coordinate systems to the acetabular center of the operating side. As we are only interested in the orientation of the acetabular component, such a translation does not affect our analysis and computation below. The x-axis of the IRP local coordinate system has the same orientation as the x-axis of the APP local coordinate system, while the y-axis of the IRP local coordinate system is chosen to be a vector that is inside the IRP and perpendicular to the x-axis. The z-axis of the IRP local coordinate system can be computed from the cross product of the x-axis and the y-axis of the IRP local coordinate system.

The so-called instrument design plane (IDP) is a plane that is defined by the design of the mechanical guide as shown in Fig. 15.2b. Physically, it is defined by the instrument axis and a curved metal rod called the pitch pointer, as shown in Fig. 15.2b. The pitch pointer is calibrated to be always inside the IDP and to be freely rotated around a fixed axis at the distal end of the cup placement instrument. We could establish a local coordinate system on the IDP as follows. The origin of this local coordinate system is chosen to be the center of the attached cup; the x-axis is chosen to be the instrument axis, and the y-axis is defined as a vector that is inside the IDP and perpendicular to the x-axis. The z-axis of the IDP local coordinate system can be computed from the cross product of the x-axis and the y-axis of the IDP local coordinate system.

Given a desired orientation of the cup (e.g., a typically desired orientation of the cup is 20° anteversion and 45° inclination with respect to the APP), we can construct a virtual instrument axis with respect to the APP of the pelvis using the method introduced by Murray [19], and we call its direction as VI^{APP}. This axis together with the CA line defines the instrument alignment plane (IAP), to which the IDP should be aligned in order to place the cup in the desired orientation using the method described below. Thus, similar to how we define a local coordinate system on the IDP, we also establish a local coordinate system on the IAP (see Fig. 15.2a for a schematic view of how the local coordinate system of the IAP is established). More specifically, we take the virtual instrument axis as the x-axis of the IAP local coordinate system. The y-axis is defined as a vector that is inside the IAP and perpendicular to the x-axis.

15.2.4 System Calibration

System calibration here means to define the orientation of the instrument bubble level as shown in Fig. 15.2b with respect to the local coordinate system of the IDP for a given pelvis whose morphology is known (the exact morphological information that our system requires will be described below), so that when all system requirements are satisfied (see below for the details about our system requirements) and when the bubble of the instrument level is oriented to the center, the axis of the cup placement instrument should be aligned with the virtual instrument axis that is constructed according to the desired orientation of the cup.

Without loss of generality, let's assume that the x-axis of the IRP of the given pelvis is $[1\ 0\ 0]^T$, the y-axis of the IRP is $[0\ 1\ 0]^T$, and the z-axis is $[0\ 0\ 1]^T$. As the morphology of this pelvis is given, we assume that we know the angle θ between its APP and its IRP, and we further assume that we know the orientation of the CA line in the local coordinate system of the IRP, which is defined as CA^{IRP}. Using angle θ, we can find the rotation between the local coordinate system of the IRP and the local coordinate system of the APP, R_{APP}^{IRP}, and the inverse rotation R_{IRP}^{APP} as well. With rotation matrix R_{APP}^{IRP}, one can transform the vector VI^{APP} from the local coordinate system of APP to the local coordinate system of IRP and denote it as VI^{IRP}.

$$VI^{IRP} = R_{APP}^{IRP}(\theta) \cdot VI^{APP} \tag{15.1}$$

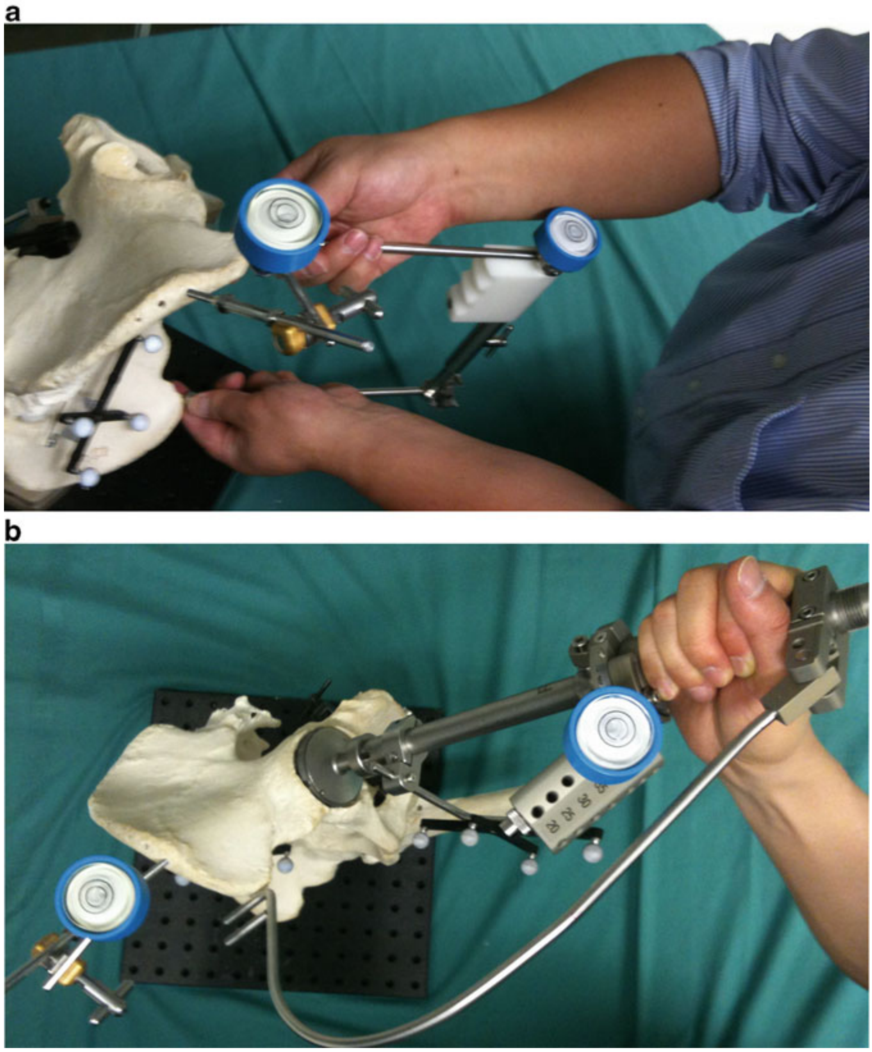

Fig. 15.3 (**a**) This image shows how to use the pelvic positioning device to place the pelvis in strict lateral decubitus and then to set the witness level at zero; (**b**) this image illustrates the touch of the pitch pointer on the ASIS of the operating side during cup placement navigation

When our system would be used for the navigation of the cup placement, additionally we require that (A) the pelvis should be placed in strict lateral decubitus, which means that the ASIS line should be parallel to the constant direction of the force of gravity (but with opposite direction). This is realized intraoperatively by using the pelvic positioning device and the witness level, as shown in Fig. 15.3a, following the procedure introduced by Echeverri et al. [17]; and (B) the pitch pointer should touch on the ASIS of the operating side of the pelvis, as shown in Fig. 15.3b. As only a thin layer of soft tissue exists on top of the ASIS of the operating side, this landmark can be easily palpatable by a surgeon [13].

According to the requirement (A), the constant direction G of the force of gravity in the IRP coordinate system can now be represented as:

$$G^{IRP} = [-1\ 0\ 0]^T \qquad (15.2)$$

When the cup would be placed in the desired orientation by the cup placement instrument and at the same time when the requirement (B) is satisfied, the IDP would be aligned with the IAP (see Fig. 15.2a for details). Thus, at this moment, the orientations of the axes of the local coordinate system of the IDP (or the IAP, as the IDP is aligned with the IAP) with respect to the local coordinate system of the IRP of the pelvis are:

$$\begin{cases} x_{IDP}^{IRP} = VI^{IRP} \\ z_{IDP}^{IRP} = \frac{VI^{IRP} \times CA^{IRP}}{|VI^{IRP} \times CA^{IRP}|} \\ y_{IDP}^{IRP} = z_{IDP}^{IRP} \times x_{IDP}^{IRP} \end{cases} \tag{15.3}$$

where "×" means the cross product of two vectors.

And the rotation from the local coordinate system of the IRP to the local coordinate system of the IDP is:

$$R_{IRP}^{IDP} = [R_{IDP}^{IRP}]^T = [x_{IDP}^{IRP} \; y_{IDP}^{IRP} \; z_{IDP}^{IRP}]^T \tag{15.4}$$

We thus can transform the constant direction of the force of gravity from the local coordinate system of the IRP to the local coordinate system of the IDP:

$$G^{IDP} = R_{IRP}^{IDP} \cdot G^{IRP} \tag{15.5}$$

We could then further compute the three angles between G^{IDP} with all three axes of the local coordinate system of the IDP. Given an arbitrary fixation point on the cup placement instrument, these three angles will uniquely determine an alignment direction along which the instrument bubble level should be placed such that when the bubble is placed to the center by orienting the cup placement instrument and its attached level and when the above two requirements are satisfied, the cup will be placed in the desired orientation. This principle has been used to design a mechanical guide as shown in Figs. 15.2b and 15.3b. The mechanical guide has an intraoperatively exchangeable steel block with a set of pre-manufactured holes, where each hole defines an alignment orientation along with which the instrument bubble level should be placed. Intraoperatively, according to the desired cup orientation and the patient-specific morphological information, the surgeon can choose the right steel block with the correctly oriented hole to place the instrument bubble level.

15.2.5 2D-3D X-ray Radiograph Reconstruction-Based Morphological Information Derivation

As clearly indicated in the above calibration procedure, the system calibration is a patient-specific task. Given a desired cup orientation, the exact decomposition of the constant direction of the force of gravity with respect to the three axes of the local coordinate system of the IDP depends on two patient-specific morphological parameters: (a) the angle θ between the APP and the IRP of the pelvis and (b) the orientation of the CA line in the local coordinate system of the IRP of the pelvis. Both parameters can be easily obtained from a CT or a MRI scan. However, these have the disadvantages that they are expensive, time-consuming, and/or induce high-radiation doses to the patient. More importantly, they are not part of the standard treatment loop of every patient in clinical routine. In this paper, we propose to use a statistically deformable 2D-3D reconstruction technique [20], which can reconstruct a scaled, patient-specific 3D model from a single conventional AP pelvic X-ray radiograph based on a statistical shape model of the pelvis. The reconstructed model can then be used to extract all the required morphological parameters. Figure 15.4 shows one example of applying this technique to reconstruct a 3D surface model of the pelvis from a conventional AP pelvic X-ray radiograph. Another example of the single image-based 2D-3D reconstruction of a pelvis used in our experiment which has different morphology from the one shown in Fig. 15.4 is presented in Fig. 15.5. As we are only interested in the angular or orientational information, a scaled, patient-specific 3D model will be accurate enough for our purpose.

Fig. 15.4 One convention AP pelvic X-ray radiograph of a pelvis used in our experiment (left) and the model reconstructed from the radiograph (right)

Fig. 15.5 Another example of the single image-based 2D-3D reconstruction of a pelvis used in our experiment which has different morphology from the one shown in Fig. 15.4. Left: a convention AP pelvic X-ray radiograph of the pelvis; right: the model reconstructed from the radiograph

15.3 Experiments and Results

We designed and conducted two studies on placing seven cups to four pelvises with different morphologies (four left sides and three right sides) to validate the accuracy of the present system. As all the pelvises were dry bones, we implemented an image-free navigation system following the principles introduced by Dorr et al. [13] to get the ground truth measurement for each experiment. Every time when the bubble of the instrument level is placed at the center, we recorded the measurements of the image-free navigation system. For all the experiments, the desired cup orientation is set to be 45° inclination and 20° anteversion.

For the first study, we acquired one conventional AP X-ray radiograph for each pelvis. The morphological information extracted from a surface model that was reconstructed from the X-ray radiograph of the associated pelvis was used to calibrate our system. This study was designed to validate the accuracy of the present system in

Table 15.1 Difference between the desired cup orientation and the cup orientation actually achieved by the present system

Angle	B_01, L	B_01, R	B_02, L	B_02, R	B_03, L	B_03, R	B_04, L	Mean
Anteversion (°)	0.1	0.4	0.8	3.4	0.2	3.0	0.6	1.2 ± 1.4
Inclination (°)	1.6	1.8	1.8	2.2	1.4	3.4	2.6	2.1 ± 0.7

Table 15.2 Difference between the desired cup orientation and the actually achieved one when different X-ray radiographs were used

Angle	Img_01	Img_02	Img_03	Img_04	Img_05	Mean
Anteversion (°)	1.4	0.8	0.7	1.1	0.0	0.8 ± 0.5
Inclination (°)	2.3	1.9	2.3	2.0	2.2	2.1 ± 0.2

placing the acetabular cups to different pelvises with different morphologies. For this purpose, every time when the bubble of the instrument level was placed at the center and when both system requirements were satisfied, the recorded measurements from the image-free navigation system were compared to the desired cup orientation. Table 15.1 summarizes the placement errors where an average accuracy of $2.1 \pm 0.7°$ was found for inclination and an average accuracy of $1.2 \pm 1.4°$ was found for anteversion.

The second study was designed to validate how sensitive the present system is to the orientation of the pelvis with respect to the X-ray table during image acquisition. For this purpose, one pelvis ($B04$) was chosen, and the pelvis was placed in different orientations with respect to the X-ray plate. Starting from an initial position, which we defined as the 0° position, we tilted the pelvis around the acetabular center line in one direction with an incremental interval of 5° until 20°, and at each orientation we acquired one X-ray radiograph. We thus obtained five X-ray radiographs of the same pelvis. We then reconstructed a surface model of the pelvis from each X-ray radiograph and used the reconstructed model to derive morphological parameters for the instrument calibration. Based on the calibration, we performed the similar experiments as we did in the first study. Table 15.2 shows the placement errors when different X-ray radiographs were used to derive the patient-specific morphological parameters.

15.4 Discussions and Conclusions

In this paper, we presented a patient-specific, gravity-assisted navigation system for high-precision placement of acetabular cup for THA operated in lateral approach. It starts with a 2D-3D reconstruction of a scaled, patient-specific 3D surface model of the pelvis from one conventional AP pelvis X-ray radiograph. The reconstructed 3D model facilitates a reliable and accurate co-registration of a gravity-assisted mechanical guide with the patient's anatomy in the operating theater. We validated the accuracy of our system by conducting experiments on placing seven cups to four pelvises with different morphologies. The experimental results demonstrated the efficacy of the present system.

The rationale of using the measurements of an image-free navigation system as the ground truth in our experiment should be discussed. Previously, several studies [21–23] have suggested that CT-based solutions seem to be the most reliable method for noninvasive postoperative assessment of the acetabular cup orientation with experienced and trained observers. Probably this is true for those studies where there are no direct bone access to the anatomical landmarks that are required to precisely calculate the postoperative cup orientation. In such a situation, all the required landmarks have to be digitized percutaneously, which lead to errors in determining the cup orientation. In contrast, in the present study, all pelvises used in our experiment are dry bones. We can thus do direct bone digitization with our image-free navigation system, which may result in more accurate ground truth than the CT-based method according to what have been reported by Lin et al. [24].

Our system offers several advantages in comparison to other existing systems. First, instead of using a positional tracker, whose price ranges from several thousand Euros to dozens of thousand Euros, our system uses a mechanical guide with bull's eye-bubble level indicators, taking advantage of the constant direction of the natural gravity force as a globally available reference for acetabular cup placement. Second, unlike most previously introduced mechanical alignment units, our system allows for a calibration with respect to the patient's individualized morphology. Furthermore, in our system the patient-specific morphological information is derived from a 3D surface model of the pelvis that is reconstructed from a conventional AP X-ray radiograph using a statistically deformable 2D-3D registration approach. No CT/MRI scan is required. Our system is completely integrated with the standard treatment protocol.

Acknowledgements This chapter was modified from the paper published by our group in *the 2011 International Conference on Information Processing in Computer Assisted Interventions (IPCAI 2011)* (Zheng et al., IPCAI 2011:101–112). The related contents were reused with the permission.

References

1. Ali Kahn AMA, Brakenbury PH, Reynolds IS (1981) Dislocation following total hip replacement. J Bone Joint Surg 63B:214–218
2. McCollum DE, Gray WJG (1990) Dislocation after total hip arthroplasty. Causes and Prevention. Clin Orthop 261:159–170
3. Sarmiento A, Ebramzadeh E, Gogan WJ, McKellop HA (1990) Cup containment and orientation in cemented total hip arthroplasties. J Bone Joint Surg 72B:996–960
4. Bader RJ, Steinhauser E, Willmann G, Gradinger R (2001) The effects of implant position, design and wear on the range of motion after total hip arthroplasty. Hip Int 11:80–90
5. Lewinnek GE, Lewis JL, Tarr R, Compere CL, Zimmerman JR (1978) Dislocation after total hip-replacement arthroplasties. J Bone Joing Surg 60A:217–220
6. Kotwal RS, Ganapathi M, John A, Maheson M, Jones SA (2009) Outcome of treatment for dislocation after primary total hip replacement. J Bone Joint Surg 91B:321–326
7. Digioia AM III, Jaramaz B, Plakseychuk AY, Moody JE Jr, Nikou C, Labarca RS, Levison TJ, Picard F (2002) Comparison of a mechanical acetabular alignment guide with computer placement of the socket. J Arthroplasty 17:359–364
8. DiGioia AM III, Jaramaz B, Blackwell M, Simon DA, Morgan F, Moody JE, Nikou C, Colgan BD, Aston CA, Labarca RS, Kischell E, Kanade T (1998) The Otto Aufranc award: image-guided navigation system to measure intraoperatively acetabular implant alignment. Clin Orthop 355:8–22
9. Bargar WL, Bauer A, Börner M (1998) Primary and revision total hip replacement using the Robodoc systems. Clin Orthop 354:82–91
10. Jaramaz B, DiGioia AM 3rd, Blackwell M, Nikou C (1998) Computer assisted measurement of cup placement in total hip replacement. Clin Orthop 354:70–81
11. Taylor RH, Joskowicz L, Williamson B, Guéziec A, Kalvin A, Kazanzides P, Van Vorhis R, Yao J, Kumar R, Bzostek A, Sahay A, Börner M, Lahmer A (1999) Computer-integrated revision total hip replacement surgery: concept and preliminary results. Med Image Anal 3:301–319
12. Zheng G, Marx A, Langlotz U, Widmer KH, Buttaro M, Nolte LP (2002) A hybrid CT-free navigation system for total hip arthroplasty. Comput Aided Surg 7:129–145
13. Dorr LD, Hishiki Y, Wan Z, Newton D, Yun A (2005) Development of imageless computer navigation for acetabular component position in total hip replacement. Iowa Orthop J 25:1–9
14. Spencer JM, Day RE, Sloan KE, Beaver RJ (2006) Computer navigation of the acetabular component: a cadaver reliability study. J Bone Joint Surg 88B: 972–975
15. Asayama I, Akiyoshi Y, Naito M, Ezoe M (2004) Intraoperative pelvic motion in total hip Arthroplasty. J Arthroplasty 19:992–997
16. Ezoe M, Naito M, Asayama I, Ishiko T, Fujisawa M (2005) Pelvic motion during total hip Arthroplasty with translateral and posterolateral approaches. J Orthop Sci 10:167–172
17. Echeverri S, Leyvraz PF, Zambelli PY, Jolles BM (2006) Reliable acetabular cup orientation with a new gravity-assisted guidance system. J Arthroplasty 21:413–419
18. Dong X, Nolte LP, Zheng G (2008) Acetabular cup orientation using a statistical data based calibration table. In: Proceedings of CAOS 2008, Hongkong, 4–7 June 2008, pp 262–265

19. Murray DW (1993) The definition and measurement of acetabular orientation. J Bone Joint Surg 75: 228–232
20. Zheng G (2010) Statistically deformable 2D/3D registration for estimating post-operative cup orientation from a single standard X-ray radiograph. Ann Biomed Eng 38:2910–2927
21. Arai N, Nakamura S, Matsushita T, Suzuki S (2010) Minimal radiation dose computed tomography for measurement of cup orientation in total hip arthroplasty. J Arthroplasty 25:263–267
22. Beckmann J, Lüring C, Tingart M, Anders S, Grifka J, Köck FX (2009) Cup positioning in THA: current status and pitfalls. A systematic evaluation of the literature. Arch Orthop Trauma Surg 129: 863–872
23. Kalteis T, Handel M, Herold T, Perlick L, Paetzel C, Grifka J (2006) Position of the acetabular cup – accuracy of radiographic calculation compared to CT-based measurement. Eur J Radiol 58:294–300
24. Lin F, Lim D, Wixson RL, Milos S, Hendrix RW, Makhsous M (2008) Validation of a computer navigation system and a CT method for determination of the orientation of implanted acetabular cup in total hip arthroplasty: a cadaver study. Clin Biomech 23:1004–1011

3D Visualization and Augmented Reality for Orthopedics

16

Longfei Ma, Zhencheng Fan, Guochen Ning, Xinran Zhang, and Hongen Liao

Abstract

Augmented reality (AR) techniques play an important role in the field of minimally invasive surgery for orthopedics. AR can improve the hand–eye coordination by providing surgeons with the merged surgical scene, which enables surgeons to perform surgical operations more easily. To display the navigation information in the AR scene, medical image processing and three-dimensional (3D) visualization of the important anatomical structures are required. As a promising 3D display technique, integral videography (IV) can produce an autostereoscopic image with full parallax and continuous viewing points. Moreover, IV-based 3D AR navigation technique is proposed to present intuitive scene and has been applied in orthopedics, including oral surgery and spine surgery. The accurate patient-image registration, as well as the real-time target tracking for surgical tools and the patient, can be achieved. This paper overviews IV-based AR navigation and the applications in orthopedics, discusses the infrastructure required for successful implementation of IV-based approaches, and outlines the challenges that must be overcome for IV-based AR navigation to advance further development.

Keywords

Three-dimensional visualization · Augmented reality · Integral videography · Orthopedics

16.1 Introduction

Image-guided techniques are important in orthopedic surgery for helping surgeons to understand the real-time spatial relationships between different detailed anatomical structures and surgical targets and tools better. It can guarantee the safety and accuracy of the surgery by using the image-guided techniques [1, 2]. Image-guided techniques have been applied widely in orthopedic procedures, and intuitive visualization is vital for surgeons to guide their surgical operation. However, navigation information in common image-guided systems are always displayed on a two-dimensional (2D) display screen away from the surgical site. This setup leads a hand–eye coordination problem for surgeons' operation. The operations' efficiency as well as accuracy is sig-

L. Ma · Z. Fan · G. Ning · X. Zhang · H. Liao (✉)
Department of Biomedical Engineering, School of Medicine, Tsinghua University, Beijing, China
e-mail: liao@tsinghua.edu.cn

G. Zheng et al. (eds.), *Intelligent Orthopaedics*, Advances in Experimental Medicine and Biology 1093, https://doi.org/10.1007/978-981-13-1396-7_16

nificantly reduced because that surgeons have to keep switching focus between the screen and the surgical site [3]. It is difficult to confirm the correct direction and position between the tools, the surgical target, and the anatomical structure.

Augmented reality (AR) techniques are applied to solve the above problem. AR refers to a fusion of virtual computer-generated information and real objects. Several AR display techniques have been used to create a dynamic fused virtual and real image in real time [4]. Direct augmentation technique uses projectors to directly present the virtual information on the surfaces of real objects in the three-dimensional (3D) real environment [5]. Head-mounted displays (HMDs) are coupled with the human eye and usually equipped with micro-displays to present images by employing optical or video see-through technology [6]. However, additional hardware is usually uncomfortable to wear. Video see-through technique employs a video camera to capture the real environment and provides the user with the captured video blended with the rendering of the virtual information. The video see-through approach is suitable for applications such as laparoscopy and arthroscopy [7]. Optical see-through technique enables observers to see overlaid AR scene of the real object and the reflected virtual image through a half-silvered mirror. Thus, observers can directly perceive the real environment while simultaneously receive the reflected virtual content [8].

Precise depth perception is essential to medical AR navigation systems. It makes surgeons to observe the 3D object directly with depth information, providing adequate spatial accuracy for safe and efficient treatment [9]. The 3D AR approach with precise depth perception can be realized through an autostereoscopic image overlay using integral videography (IV) technique [8, 10]. This 3D AR approach uses the optical see-through technique to provide a more comfortable visual perception and a larger viewing angle for multiple observers. Moreover, accurate patient-image registration and real-time target tracking are necessary to ensure that the reflected autostereoscopic image can be overlaid on the correct position. In this chapter, we overview the 3D visualization and AR techniques for orthopedics.

16.2 3D Visualization for Orthopedics

Virtual models are generated by image segmentation from the medical image of the patient, and up to now, several different image segmentation methods have been proposed. Furthermore, the virtual models are required to accurately register with the real objects for 3D visualization. To realize 3D visualization, a good 3D rendering and display technology is important to accurately present the same geometric structure as the real objects, and IV is a promising 3D autostereoscopic display technique.

16.2.1 Medical Image Segmentation

Medical image segmentation and registration play a dominating part in medical imaging processing, which is of great significance in developing a surgical navigation system, improving surgical accuracy, and illness monitoring [11]. Medical image segmentation is the basic work for the medical image registration and choosing personalized orthopedic implant [12].

Medical image segmentation refers to dividing the image into several subregions that do not overlap each other, so that the characteristics of the same subregion have similar similarity and the characteristics of different subregions show an obvious difference [13]. But there is no specific segmentation algorithm that can be applied to all kinds of medical image so far due to some drawbacks like ambiguity, complexity, and individual differences in medical image. Traditional medical image segmentation methods include threshold method, boundary detection method, region method, and so on. Most of the traditional methods are based on algebraic computation [14]. The ultra-pixel-based image segmentation method can improve the efficiency by taking the processing of group pixel with similar characteristics, so that the image block contains image content information that is not available for a single pixel. According to the principle of the algorithm implementation, the ultra-pixel method can be classified as graph-based method and clustering method. In line with clustering method, the medical image segmentation is regarded as the classification problem of the single pixel of the image. The neural network (NN), logistic regression (LR), and support vector machine (SVM) [15] and other classifiers are trained by tagged images which are considered as a training set and then training the classifier to classify the pixel. The image segmentation result is acquired on the basis of pixel classification result. The classification method is a supervised learning algorithm that requires a large number of annotation images as a sample training classifier, but it's a time-consuming and laborious work to label the image at pixel level.

Deep convolutional neural networks (CNNs) and fully convolutional networks (FCNs) have developed rapidly in medical image analysis [16–18], and improved networks can be applied for specific medical applications. Automatic femur segmentation from CT volume is essential for orthopedic surgeries, but it is challenging due to the inherent blur of CT images, a variety of legs' postures and positions, the density and shape variations of femurs, and so on [19–21]. To address these challenges, Chen et al. presented a novel 3D feature-enhanced network to achieve fast and accurate femur segmentation from CT volume [22]. Two feature enhancement modules were used. First, the edge detection task module was embedded into the common FCN to optimize femur segmentation from CT volume and overcome the challenging of narrow joint space and weak femur boundary. Second, the multi-scale features fusion module processed the large variations in leg postures and femur shape and density via both local and global contexts. The experimental results demonstrated that the proposed method achieved a high Dice similarity coefficient of 96.88% and took computation time of about 0.93 s to segment a CT volume for accurate 3D femur segmentation. The qualitative CT femur volume segmentation results are illustrated in Fig. 16.1. The adjacent anatomical structures with a weak boundary is successfully segmented (Fig. 16.1b, c), and the segmentation result can delineate the femur volume accurately compared with manual segmentation (Fig. 16.1d).

16.2.2 3D Image Rendering

To display 3D medical data intuitively for orthopedics, 3D autostereoscopic display techniques are in desperate demand for displaying spatial information without supplementary glasses, compared with 2D display techniques. As a promising 3D autostereoscopic display technique, IV can provide a 3D image with spatial information as if it exists in the space. Observers can view the reconstructed 3D image with naked eyes from different aspects limited in the viewing area. Moreover, the IV-based 3D autostereoscopic display technique holds other benefits, including full parallax, full color, and simple structure. Main components in IV device include a micro-convex lens array) and an elemental image array. Light rays from the 3D medical image are modified by the micro-convex lens array and recorded on the elemental image array, as shown in Fig. 16.2. Since firstly proposed by Lipmann in 1908 [23], integral photography (IP) technique has been improved and optimized for the specific situation. Researches focused on 3D image rendering methods and improving the performance of 3D autostereoscopic display, such as the viewing angle, display depth, and image quality. Conventionally, IV mainly uses optical pickup devices to render the elemental image array.

With the development of 3D medical image acquisition method, such as MRI, CT, and computer graphics technique, the rendering process can be operated by simulating the light rays from the 3D medical image on the computer. For the 3D image rendering process, each light ray emitting from 3D medical image acquired by 3D data scanners is simulated to pass through centers of the lenses in micro-convex lens array and recorded on the corresponding elemental images. Moreover, information over the range of the corresponding elemental image is abandoned. During operation, 2D flat displays are widely applied to provide medical information. Therefore, a high-resolution 2D flat display with micro-convex lens array attached can be utilized for 3D autostereoscopic display. According to the reversibility of the ray tracing, rays emitting from the pixel layer are modulated by the micro-

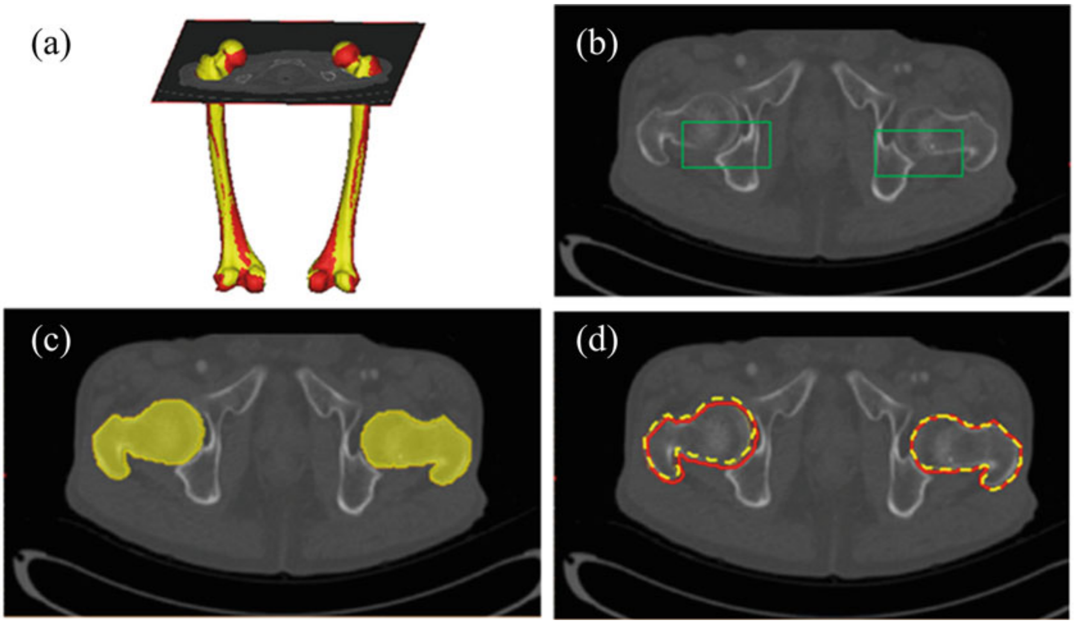

Fig. 16.1 (**a**) Segmentation results (yellow) and 3D ground truth (red) overlap visualization; (**b**) weak boundary of adjacent anatomical structures (green box indicated); (**c**) the segmented femur volume in 2D slice; (**d**) the contour of segmented femur volume (yellow line indicated) compared with manual segmentation (red line indicated) [22]

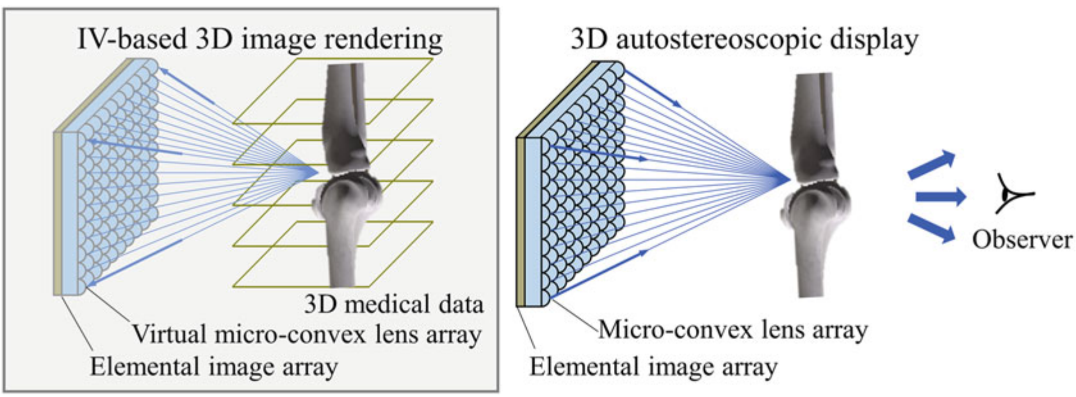

Fig. 16.2 Principal of IV-based 3D image rendering and display

convex lens array to reconstruct the 3D medical image.

Different computer generation algorithms of elemental image array were proposed, including the point ray-tracing rendering algorithm [24], real-time pickup method [25], multiview rendering algorithm [26, 27], lens-based rendering algorithm [28], etc. As a common computer-generated integral videography (CGIV) rendering algorithm, the point ray-tracing rendering algorithm consists of the volume rendering-based point ray-tracing rendering algorithm and the surface rendering-based point ray-tracing rendering algorithm and can be chosen according to actual demands. 3D medical image data should be preprocessed for 3D image rendering. Firstly, the important target anatomical structures should be segmented and reconstructed. Then, the target medical data can be processed in volume or surface data for volume rendering-based IV algorithm or surface-based IV algorithm.

Due to demand on real-time 3D rendering and display, a flexible IV rendering pipeline using graphics processing unit (GPU) [29] can be utilized to accelerate 3D image rendering rate. Moreover, to achieve higher frame rates and better image quality without pixel resampling or view interpolation, a lens-based rendering algorithm is proposed [28]. Both fixed and programmable graphics pipelines are taken into consideration to accelerate CGIV rendering and exploit inter-perspective antialiasing. The proposed lens-based rendering method outperforms state-of-the-art CGIV algorithms in rendering speed and image quality with the super-multiview hardware configurations. Evaluation and comparison experiments between the proposed method and multiple cluster ray rendering method were operated. The interactivity of a super-multiview display using the proposed algorithm was revealed by a series of demonstration experiments [28].

In the fields of surgical navigation and intervention, 3D autostereoscopic medical images with accurate spatial information are in desperate demand. In IV technique, the discrepancy between the actual optical apparatus setups and the simulated rendering model is the main influencing factor. The discrepancy comprises (1) the alignment error between the elemental image array and micro-convex lens array and (2) the actual apparatus between the elemental image array and micro-convex lens array [30]. Measuring the rotational alignment and translational alignments between the elemental image array and the micro-convex lens array directly is difficult, considering the size of each small component. Therefore, a rotational alignment calibration method using the moiré fringes [31, 32] and a translational alignment calibration method by encoding pixels periodically in a certain direction [30] is proposed. The quantitative calibration result can be calculated to rectify the actual optical apparatus. Furthermore, the main parameter of the actual apparatus between the elemental image array and micro-convex lens array can be evaluated using a dedicated calibration pattern through quantitative calibration [30]. Using the rendering model considering the actual optical apparatus and the evaluated parameter, 3D medical images with accurate spatial information can be reconstructed.

With the assistance of the IV-based 3D autostereoscopic display, surgeons can easily observe the spatial information of the anatomical structures intuitively without visual and physical fatigue during the procedures of surgical planning and operation.

16.3 AR Navigation

16.3.1 3D AR System for Navigation

3D AR systems can provide intuitive 3D images with accurate spatial information for surgical planning and operation to overcome the hand–eye coordination problem. Despite of binocular-based 3D AR systems assisted by supplementary glasses, 3D autostereoscopic AR systems can provide a 3D image directly for multiviewers. IV-based 3D autostereoscopic AR system is the promising one due to its full parallax and continuous viewing points [24]. Surgeons can observe a “see-through” 3D medical image, which overlaid onto the real surgical scene intuitively without assistant tracking devices or special glasses.

The IV-based 3D autostereoscopic AR system mainly includes 3D image processing and rendering, 3D image overlay, and real-time target tracking, as shown in Fig. 16.3. With 3D image processing, the important anatomical structures can be segmented and reconstructed. By utilizing IV-based 3D image rendering algorithms, the 3D medical image can be displayed with full parallax. The 3D image overlay device mainly utilizes a half-silver mirror to reflect the reconstructed 3D image and present the real surgical scene simultaneously. Surgeons can easily look through the half-silvered mirror to observe the AR scene. To ensure that the overlaid 3D medical image can be fused on the target area, real-time target tracking and accurate patient-image registration methods are of great importance. The targets, such as patients, 3D overlay device and surgical

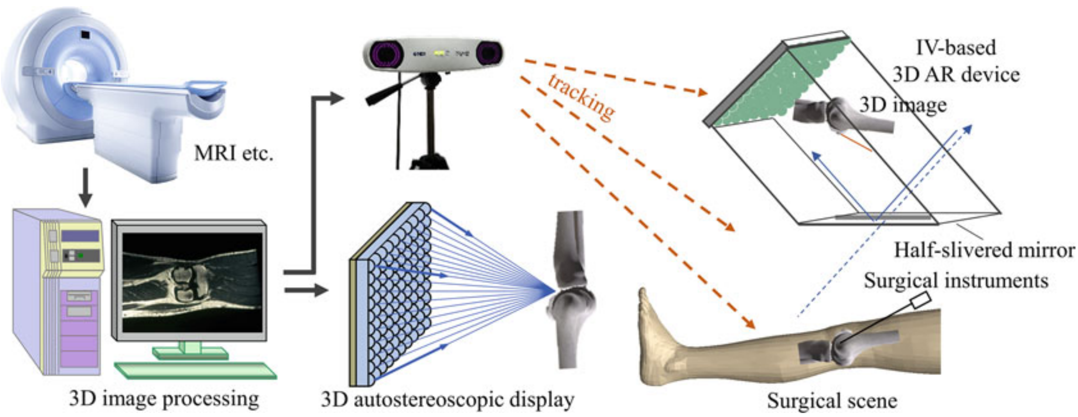

Fig. 16.3 IV-based 3D autostereoscopic AR system

instruments, etc., are tracked, and the spatial information of the displayed 3D medical images is refreshed in real time. With the assistance of the IV-based 3D AR system, surgeons can operate flexibly and accurately based on the intuitive 3D AR image.

16.3.2 Medical Image Registration for Orthopedics

The definition of medical image registration is finding an optimal spatial transformation to make the feature points from two associated images into the same spatial and anatomical position [33]. The results should make the two images to achieve matching through the anatomical points with diagnostic significance. Based on the geometric transformation method, the classification of the medical image registration method can be divided into two classes: rigid registration and nonrigid registration. The main aim of rigid registration is to ensure the target image corresponds to the feature points on the source image on the basis of finding the free transformation of six degrees of space. In comparison, nonrigid registration is a nonlinear transformation; the transformation process contains the polynomial method, physical model simulation, and so on.

Registration is critical, and rigid registration is commonly used in orthopedic navigation guidance. There are implicit registration methods that directly acquire the volumetric image of the patient with a dynamic reference frame (DRF) as well as the imaging device's DRF. The two DRFs are both tracked by a spatial tracking system. So, automated transformation from volumetric image to physical space is done without external intraoperative registration. For example, an implicit registration can be performed by using an O-arm system via factory calibration [34]. However, there are some limitations among them. First, these systems may cause radiation dose to the patient. Second, the quality of the visual guidance may be decreased, due to the lower quality of the volumetric image than that of diagnostic image. Third, the high cost of these systems needs to be considered. Hence, the implicit registration methods have not been popularized because of the above limitations.

Most commonly, registration is utilized for alignment of preoperative data to the physical world. Registration accuracy directly affects the accuracy of the intervention in orthopedics. To introduce a feasible registration workflow to the clinic, several factors, which determine the clinical acceptance, need to be considered, such as high target registration accuracy, high robustness, low computation time, avoiding the extra complexity, and no detrimental side effects [34]. For the optimal clinical workflow, the last two factors are very important. For example, although the ROBODOC system for total hip replacement had a high and robust registration accuracy by using implanted fiducials, it resulted in significant collateral damage caused by the pin implantation [35]. In orthopedics, paired-point algorithms use three or more corresponding points to compute the rigid transformation between image coordinate system and physical coordinate system. However, the surgeon has to indicate the corresponding points because of the explicit pairing in paired-point algorithms. To overcome this problem, surface-based registration is a solution, and the rigid transformation is obtained by matching intraoperative surface to preoperative surface. The preoperative surface can be obtained from CT, MRI, etc. The intraoperative surface can be segmented from ultrasound (US) image as a noninvasive method of surface acquisition. Automated segmentation of the bone surface from US image is critical, and several segmentation algorithms are proposed [36, 37]. A preoperative surface model of a patient can also be created by using a statistical shape model in orthopedics, without the need of a 3D scan. Statistical surface model-based registration has primarily used the diffeomorphic demons method [38] and the free-form deformation method [39]. This approach was also recently applied in the 2D/2D registration process for a proximal femur model [40].

To reduce radiation dose, 2D US is a promising navigation method instead of intraoperative 2D X-ray image [41]. However, there are limitations like poor image quality and limited imaging field in US image. Hence, the combination of 2D US with preoperative 3D CT image is studied as an available solution. Chen et al. have proposed a novel 2D US and 3D CT registration method [42]. Rough image registration is performed by using convolutional neural network (CNN) classification of US image reported for the first time. Local registration refinement is further finished by applying a new orientation code mutual information metric. The accuracy of the proposed 2D US and 3D CT registration algorithm is validated on the clinical dataset from in vivo human spine. Finally, 2D US and 3D CT registration for multiple vertebras (L2–L4) are achieved without an appropriate initial alignment. As a demonstration, three examples of registration trials are shown in Fig. 16.4, and the corresponding 2D US image is registered with the 3D CT image of the spine according to the bone edges. The experimental results showed that the proposed method successfully aligned 2D US image and 3D CT image. Totally 50 registration trials between US images from multiple vertebras (L2-L4) and 3D CT images were performed, and the mean target registration error was 2.3 mm, which was clinically acceptable. In the future work, the registration process will be accelerated using C++, and the time consumption will be evaluated. Without needing appropriate initial registration position, the proposed registration method potentially takes less time consumption. Moreover, this method can achieve precise registration.

16.3.3 Real-Time Target Tracking

Real-time target tracking can detect the spatial position of the targets to render corresponding 3D autostereoscopic images. Currently, the tracking methods in medicine mainly consist of image-based tracking method [43], optical tracking method, and electromagnetic tracking method. Each of the tracking methods has both advantages and disadvantages and can be chosen according to the demands. Electromagnetic tracking systems (EMTS) can be utilized in vivo without occlusion, while it easily suffers from magnetic interference. Compared with EMTS, optical tracking systems (OTS) can avoid the magnetic interference and increase the accuracy of tracking. However, optical occlusion exists in OTS. Complicated real-time tracking systems are considered by combining two or more tracking techniques to improve tracking performance and enlarge working space.

To superimpose the 3D image with accurate spatial position, an optical tracking system is utilized in the IV-based 3D AR system. Each coordinate of the target should be related and transferred into one coordinate to interconnect

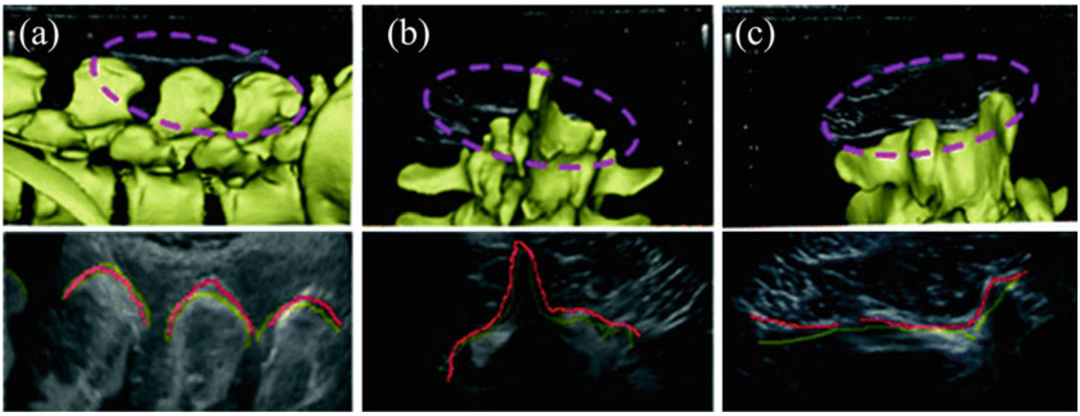

Fig. 16.4 (**a**), (**b**), and (**c**) are three examples of registration trials. The bone edges in US images (red line) were registered with the bone edges in CT images (yellow line) [42]

the patient, the displayed 3D image and the surgical instruments. The patient and the displayed 3D image can be correlated by patient-image registration. Patient-image registration can be fulfilled by marker-based registration method or markerless-based registration method. Marker-based registration method mainly uses external fiducial markers attached to the target, while markerless-based registration method mainly detects the anatomical features, such as points, boundary, or surface.

The coordinate transformation for accurate 3D AR is shown in Fig. 16.5 [44]. The coordinate system of the 3D position tracking system is the reference frame. Two optical markers are mounted on the 3D IV AR device and the patient, respectively. Their positions and orientations can be obtained through T_{Mar}^{Tra} and T_{Pat}^{Tra}, respectively. The transformation T_{Dis}^{Mar} between the 3D display and the optical marker mounted on the 3D IV AR device can be derived by using a calibration marker overlaid with its reflected 3D image. An optical marker is fixed on surgical instrument, and the 3D image of the surgical instrument can be localized by

$$T_{Dis}^{Sur} = T_{Dis}^{Mar} \cdot T_{Mar}^{Tra} \cdot T_{Tra}^{Sur} \tag{16.1}$$

From accurately superimposing the 3D image of the important anatomic structures onto the patient, the patient-image registration needs to be performed. First, the transformation T_{Pat}^{3D} from the preoperative 3D image to patient under optical tracking is calculated. Therefore, the 3D image of the patient can be localized by

$$T_{Dis}^{3D} = T_{Dis}^{Mar} \cdot T_{Mar}^{Tra} \cdot T_{Tra}^{Pat} \cdot T_{Pat}^{3D} \tag{16.2}$$

16.3.4 AR Visualization for Navigation

To provide abundant navigation information with flexible operation, a specific navigation interface is needed in the IV-based 3D AR system. Preoperatively, the operation path can be planned and determined. Therefore, surgeons can operate under the guidance of the 3D medical image and the planned operation path. As shown in Fig. 16.6, the navigation interface in 3D AR system consists of two parts. One is used for displaying AR image, such as the preoperative 3D medical data, the simulated surgical instruments, and the planning path to guide the operation. The other is used for normal 2D display to present navigation information in different directions.

Moreover, a real-time prompt is designed to intuitively guide surgeons to operate accurately. When the path of the surgical instrument is far from the planned operation path, the surgical instrument is displayed as red. Surgeons should adjust the position or direction of the interven-

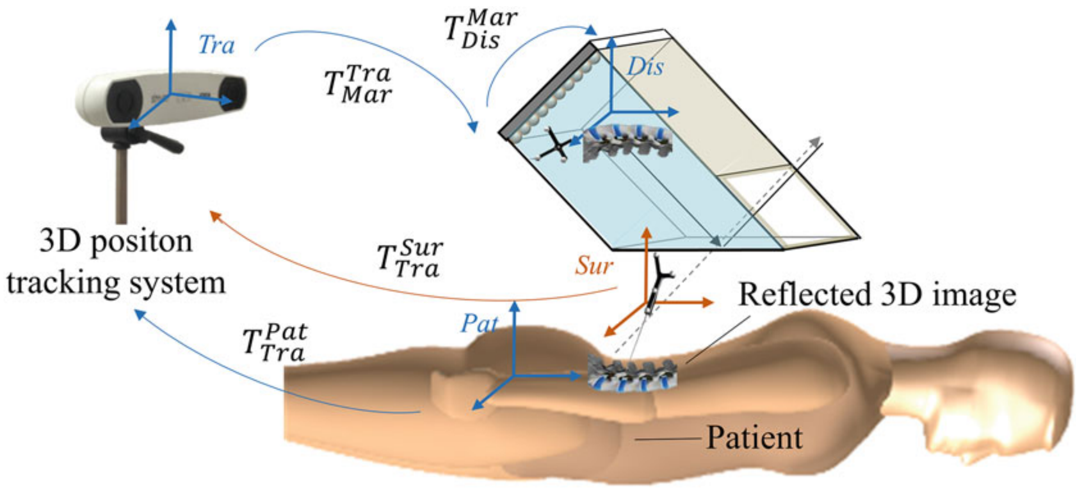

Fig. 16.5 Coordinate transformation for accurate 3D AR

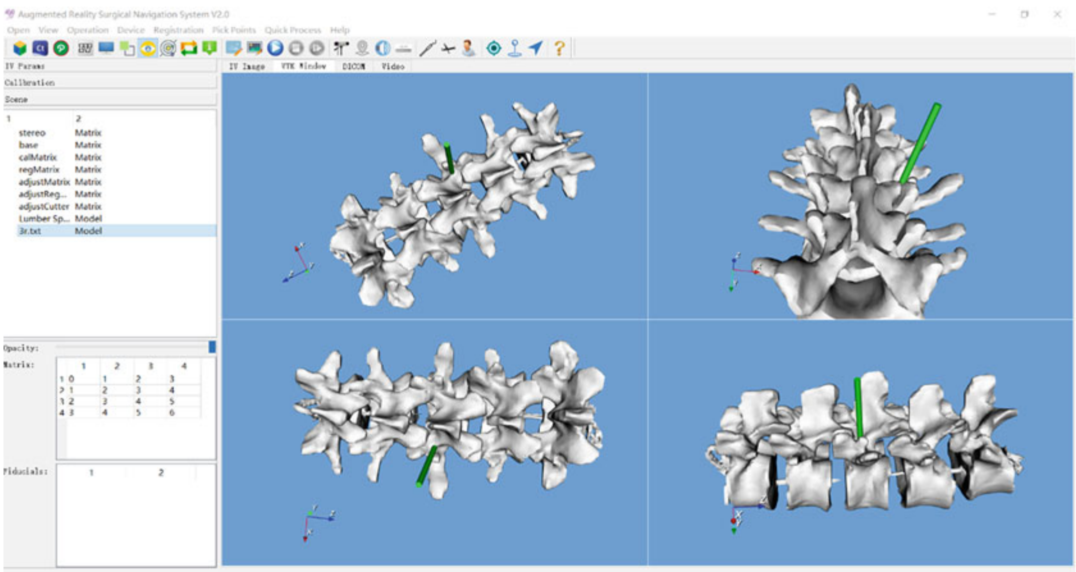

Fig. 16.6 Navigation interface in IV-based 3D autostereoscopic AR system

tion until the surgical instrument is displayed as green. Moreover, other surgeons can constantly pay attention to the current surgical scene through the normal 2D display and propose comments. With the guidance of the IV-based 3D AR system, invasiveness of the surgery can be reduced, and the surgical accuracy can be ensured.

16.4 Application of 3D Visualization and AR in Orthopedics

Because of the intuitive AR scene with full parallax, and the simplified operation, the IV-based 3D visualization and AR are the promising solutions in oral surgery, knee surgery, spine surgery, and other orthopedic surgeries.

16.4.1 3D AR-Guided Oral Surgery

It is challenging to achieve oral surgeries with high accuracy, because these operations are limited by a narrow space and high risk tissues such as dental nerves and blood vessels need to be avoided [45]. Moreover, surgical targets are hard to view because they might be hidden by surrounding structures. The real-time image-guided navigation technologies are more helpful to assist dentists to achieve highly precise operations, since dentists can monitor the relative positions between surgical instruments and the important anatomical structures accurately in real time. However, current surgical navigation systems lack hand–eye coordination and depth perception, due to their visual guidance information are always displayed far from the surgical area. The above shortcomings in the current navigation systems can be overcome by using the IV-based 3D AR navigation systems for dental surgery proposed by Tran et al. and Wang et al. [46, 47]. The proposed system employs a vision-based automatic marker-free image registration method and uses a stereo camera for tracking patients and instruments. As a result, the 3D images of the patient's anatomy and the surgical instruments generated by using IV technology are overlaid on the surgical region through a half-silvered mirror, which forms an AR scene to guide the surgeon to observe the hidden anatomy and the surgical instruments intuitively. Experiments have demonstrated that the overlay error of the system was 0.71 mm [47]. With the help of intuitive 3D information with depth perception proposed by the AR system, surgeons can perform the surgical operation more easily.

16.4.2 3D AR-Guided Spine Surgery

Percutaneous pedicle screw placement is a particularly challenging therapy [48]. Under the traditional condition, intraoperative fluoroscopy is used to access indirectly the positions of the instruments and the lumbar pedicles of patients. Moreover, to reduce the intraoperative radiation doses, image-guided navigation systems have been used widely in orthopedics based on preoperative CT or MRI [49]. However, the 2D display in the current surgical navigation systems may increase the difficulty of operation, owing to the lack of image depth, and be situated away from the operative field. To solve the hand–eye coordination problem, we introduced the IV-based AR surgical navigation system for the medical field of pedicle screw placement [44]. Owing to soft tissue deformation, low accuracy of patient registration using landmarks on the skin may be encountered. To eliminate this problem, this paper proposed a US-assisted registration method by using rigid anatomical landmarks inside the body, and each vertebra can be registered individually (Fig. 16.7a). After registration, accurate 3D images of the spine as well as the surgical instruments are overlaid on the surgical area to guide the surgical operation intuitively (Fig. 16.7b). The feasibility of the proposed system was finally evaluated by using an agar phantom and a sheep cadaver.

16.4.3 Enhanced 3D IV AR for Microsurgery

A high-quality and high-accuracy 3D IV image display method is designed to overcome the resolution and viewing angle limitation of autostereoscopic 3D display for precision surgery [50]. Compared with above IV-based AR system, a dedicated optical image enhancement module is added and arranged between the surgical scene and observers to magnify the actual surgical scene with reflected 3D surgical guidance information. The magnified and merged AR scene can be acquired for observers with naked eyes. The optical magnifier module consists of optical lenses, which can cause the scale and position changes of the patient and the image, so a novel patient-image registration method is operated. With this method, the submillimeter accuracy of the proposed system can be reached up, and the viewing angle can be enlarged. The magnified surgical scene is shown in Fig. 16.8, which can provide surgeons with high-quality 3D AR scene and help them to perform precise operations.

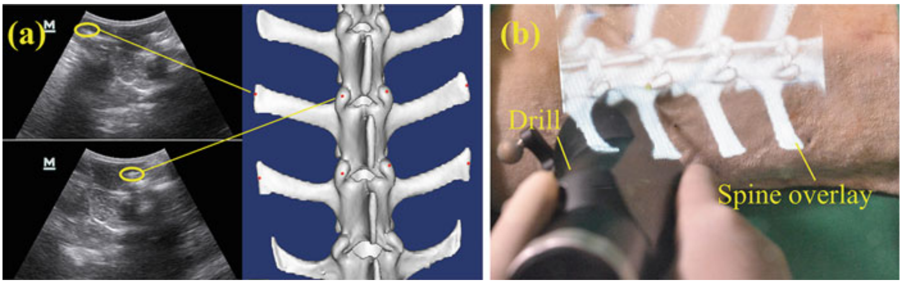

Fig. 16.7 (**a**) US-assisted registration method by using rigid anatomical landmarks inside the body; (**b**) 3D AR-guided spine surgery by using a sheep cadaver [44]

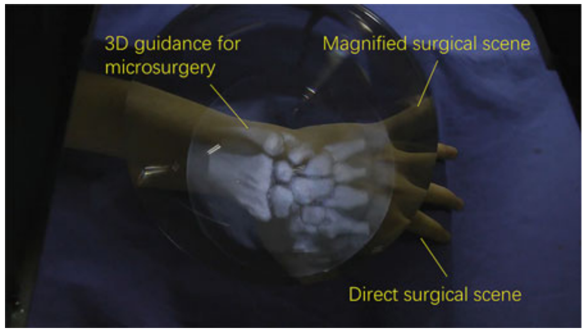

Fig. 16.8 Magnified 3D AR surgical scene for microsurgery [50]

16.5 Discussion and Conclusion

To realize real-time accurate 3D AR navigation for orthopedics, advanced 3D visualization algorithms, precise patient-image registration techniques, and reliable tracking methods [51] are critical. In this paper, we describe an IV-based 3D visualization and AR method for orthopedics. The IV technique can provide a 3D image with full parallax and help surgeons directly observe the hidden anatomical structure with naked eyes, and the hand–eye coordination problem is avoided. The GPU-accelerated IV image can be rendered in real time and generated from preoperative data and intraoperative data, such as CT/MRI and US. The proposed IV-based AR systems with different patient-image registration methods have been used for oral surgery, spine surgery, etc. and meet desired clinical demands. Moreover, an enhanced 3D IV AR system is proposed to provide surgeons high-quality magnified 3D AR scene, especially for precision surgery [52]. The spatial resolution of the IV-based 3D display could be further improved [53]. To achieve a high-quality autostereoscopic image with a wide viewing angle, a high-resolution display with a high-performance micro-convex lens array is needed. We have been actively promoting the clinical application of our AR system and have completed a sheep cadaver experiment for pedicle screw placement. To apply our AR system in clinic, it needs to meet the requirements of clinical safety, disinfection, ethics, and so on. With further improvements and evaluations, the 3D visualization and AR technology are valuable in the field of orthopedics.

Acknowledgments The authors acknowledge supports from National Natural Science Foundation of China (81427803, 81771940), National Key Research and Development Program of China (2017YFC0108000), Beijing Municipal Science and Technology Commission (Z151100003915079), Beijing National Science Foundation (7172122, L172003), and Soochow–Tsinghua Innovation Project (2016SZ0206).

References

1. Cleary K, Peters TM (2010) Image-guided interventions: technology review and clinical applications. Annu Rev Biomed Eng 12(1):119–142

2. Fan Z, Weng Y, Chen G, Liao H (2017) 3D interactive surgical visualization system using mobile spatial information acquisition and autostereoscopic display. J Biomed Inform 71:154–164
3. Peters TM, Cleary K (2008) Image-guided interventions: technology and applications. Springer, New York (3):e50
4. Tang R, Ma L, Rong Z, Li M, Zeng J, Wang X, Liao H, Dong J (2017) Augmented reality technology for preoperative planning and intraoperative navigation for hepatobiliary surgery: a review of current methods. Hepatobiliary Pancreat Dis Int. https://doi.org/10.1016/S1499-3872(18)60093-1
5. Raskar R, Welch G, Low KL, Bandyopadhyay D (2000) Shader lamps: animating real objects with image-based illumination. Eurographics: 89–102
6. Cakmakci O, Rolland J (2006) Head-worn displays: a review. J Disp Technol 2(3):199–216
7. Lamata P (2010) Augmented reality for minimally invasive surgery: overview and some recent advances. Intech
8. Liao H, Nakajima S, Iwahara M et al (2000) Development of real-time 3D navigation system for intra-operative information by integral videography. J Japan Soc Comput Aided Surg 2(4):245–252
9. Zhao D, Ma L, Ma C, Tang J, Liao H (2016) Floating autostereoscopic 3D display with multidimensional images for telesurgical visualization. Int J Comput Assist Radiol Surg 11(2):207–215
10. Tang R, Ma L, Xiang C, Wang X, Li A, Liao H, Dong J (2017) Augmented reality navigation in open surgery for hilar cholangiocarcinoma resection with hemihepatectomy using video-based in situ three-dimensional anatomical modeling: a case report. Medicine 96(37):e8083. https://doi.org/10.1097/MD.0000000000008083
11. Oliveira FP, Tavares JM (2014) Medical image registration: a review. Comput Methods Biomech Biomed Eng 17(2):73–93
12. Chen F, Zhao Z, Gao C, Liu J, Su X, Zhao J, Tang P, Liao H (2017) Clustering of morphological features for identifying femur cavity subtypes with difficulties of intramedullary nail implantation. IEEE J Biomed Health Inf:1. https://doi.org/10.1109/JBHI.2017.2761980
13. Gooya A, Liao H, Sakuma I (2012) Generalization of geometrical flux maximizing flow on riemannian manifolds for improved volumetric blood vessel segmentation. Comput Med Imaging Graph 36(6):474–483
14. Gooya A, Liao H, Matsumiya K, Masamune K, Masutani Y, Dohi T (2008) A variational method for geometric regularization of vascular segmentation in medical images. IEEE Trans Image Process. A Publication of the IEEE Signal Processing Society 17(8):1295–1312
15. Shinde S, Lendal A, Bajaj N, Shelar Y (2014) Content based image retrieval and classification using support vector machine. Int J Comput Applications 92(7):8–12
16. Litjens G, Kooi T, Bejnordi BE, Setio AAA, Ciompi F, Ghafoorian M et al (2017) A survey on deep learning in medical image analysis. Med Image Anal 42(9):60
17. Goceri E, Goceri N (2017) Deep learning in medical image analysis: recent advances and future trends. In: The International conferences computer graphics, visualization, computer vision and image processing 2017 (CGVCVIP 2017), pp 305–311, 20–23 2017
18. Milletari F, Navab N, Ahmadi SA (2016) V-net: fully convolutional neural networks for volumetric medical image segmentation. In: Fourth international conference on 3D vision, pp 565–571
19. Almeida DF, Ruben RB, Folgado J, Fernandes PR, Audenaert E, Verhegghe B, Beule M (2016) Fully automatic segmentation of femurs with medullary canal definition in high and in low resolution ct scans. Med Eng Phys 38(12):1474–1480
20. Casper DS, Kim GK, Parvizi J, Freeman TA (2012) Morphology of the proximal femur differs widely with age and sex: relevance to design and selection of femoral prostheses. J Orthop Res 30(7):1162–1166
21. Ito M, Nakata T, Nishida A, Uetani M (2011) Age-related changes in bone density, geometry and biomechanical properties of the proximal femur: CT-based 3D hip structure analysis in normal postmenopausal women. Bone 48(3):627–630
22. Chen F, Liu J, Zhao Z, Zhu M, Liao H (2017) 3D feature-enhanced network for automatic femur segmentation. IEEE J Biomed Health Inform:1. https://doi.org/10.1109/JBHI.2017.2785389
23. Lippmann G (1908) Epreuves reversibles donnant la sensation du relief. Journal De Physique Théorique Et Appliquée 7(1):821–825
24. Liao H, Hata N, Nakajima S, Iwahara M, Sakuma I, Dohi T (2004) Surgical navigation by autostereoscopic image overlay of integral videography. IEEE Trans Inform Technol Biomed. A Publication of the IEEE Eng Med Biol Soc 8(2):114
25. Okano F, Hoshino H, Arai J, Yuyama I (1997) Real-time pickup method for a three-dimensional image based on integral photography. Appl Opt 36(7):1598
26. Liao H, Nomura K, Dohi T (2006) Long visualization depth autostereoscopic display using light field rendering based integral videography. In: IEEE conference on virtual reality. vol 2006, pp 314. IEEE computer society
27. Liao H, Dohi T, Nomura K (2011) Autostereoscopic 3D display with long visualization depth using referential viewing area based integral photography. IEEE Trans Vis Comput Graph 17(11):1690–1701
28. Chen G, Ma C, Fan Z, Cui X, Liao H (2017) Real-time lens based rendering algorithm for super-multiview integral photography without image resampling. IEEE Trans Vis Comput Graph:1. https://doi.org/10.1109/TVCG.2017.2756634
29. Wang J, Liao H (2013) Real-time 3D medical imaging using GPU-based integral videography. Med Image Tech 31:159–166

30. Fan Z, Chen G, Xia Y, Huang T, Liao H (2017) Accurate 3D autostereoscopic display using optimized parameters through quantitative calibration. J Opt Soc Am A Opt Image Sci Vis 34(5):804
31. Hutley MC, Hunt R, Stevens RF, Savander P (1994) The moire magnifier. Pure Appl Opt J Eur Opt Soc A 3(2):133
32. Hirsch M, Lanman D, Wetzstein G, Raskar R (2013) Construction and calibration of optically efficient LCD-based multi-layer light field displays. In J Phys: Conference Series 415:012071
33. Maintz JBA, Viergever MA (1998) A survey of medical image registration. Med Image Anal 2(1):1–36
34. Yaniv Z (2016) Registration for orthopaedic interventions. Computational radiology for orthopaedic interventions. Springer 23:41–70
35. Nogler M, Maurer H, Wimmer C, Gegenhuber C, Bach C, Krismer M (2001) Knee pain caused by a fiducial marker in the medial femoral condyle. Acta Orthop Scand 72(5):477–480
36. Schumann S, Nolte LP, Zheng G (2012) Determination of pelvic orientation from sparse ultrasound data for THA operated in the lateral position. Int J Med Robot Comput Assist Surg 8(1):107–113
37. Talib H, Peterhans M, Garća J, Styner M, Ballester MAG (2011) Information filtering for ultrasound-based real-time registration. IEEE Trans Biomed Eng 58(3):531–540
38. Vercauteren T, Pennec X, Perchant A, Ayache N (2009) Diffeomorphic demons: efficient non-parametric image registration. NeuroImage 45(1, supplement 1):S61–S72
39. Rueckert D, Sonoda LI, Hayes C, Hill DLG, Leach MO, Hawkes DJ (1999) Non-rigid registration using free-form deformations: application to breast MR images. IEEE Trans Med Image 18(8):712–721
40. Xie W, Franke J, Chen C, Grützner PA, Schumann S, Nolte L, Zheng G (2014) Statistical model-based segmentation of the proximal femur in digital antero-posterior (AP) pelvic radiographs. Int J Comput Assist Radiol Surg 9(2):165–176
41. Chen F, Liu J, Liao H (2016) Ultrasound navigation for transcatheter aortic stent deployment using global and local information. Appl Sci 6(12):391
42. Chen F, Wu D, Liao H (2016) Registration of CT and ultrasound images of the spine with neural network and orientation code mutual information. In: International conference on medical imaging and virtual reality. Springer, Cham, pp 292–301
43. Chen F, Liu J, Liao H (2017) 3D catheter shape determination for endovascular navigation using a two-step particle filter and ultrasound scanning. IEEE Trans Med Imaging 36(3):685–695
44. Ma L, Zhao Z, Chen F, Zhang B, Fu L, Liao H (2017) Augmented reality surgical navigation with ultrasound-assisted registration for pedicle screw placement: a pilot study. Int J Comput Assist Radiol Surg 12(12):2205–2215
45. Hassfeld S, Mühling J (2001) Computer assisted oral and maxillofacial surgery–a review and an assessment of technology. Int J Oral Maxillofac Surg 30(1):2–13
46. Tran HH, Suenaga H, Kuwana K, Masamune K, Dohi T, Nakajima S, Liao H (2011) Augmented reality system for oral surgery using 3D auto stereoscopic visualization. In: Medical image computing and computer-assisted intervention–MICCAI 2011. Springer, Berlin pp 81–88
47. Wang J, Suenaga H, Hoshi K, Yang L, Kobayashi E, Sakuma I, Liao H (2014) Augmented reality navigation with automatic marker-free image registration using 3D image overlay for dental surgery. IEEE Trans Biomed Eng 61(4):1295–1303
48. Laine T, Lund T, Ylikoski M, Lohikoski J, Schlenzka D (2000) Accuracy of pedicle screw insertion with and without computer assistance: a randomised controlled clinical study in 100 consecutive patients. Eur Spine J 9(3):235–240
49. Manbachi A, Cobbold RS, Ginsberg HJ (2014) Guided pedicle screw insertion: techniques and training. Spine J Off J North Am Spine Soc 14(1):165–179
50. Zhang X, Chen G, Liao H (2017) High quality see-through surgical guidance system using enhanced 3D autostereoscopic augmented reality. IEEE Trans Biomed Eng 64(8):1815–1825
51. Fan Z, Chen G, Wang J, Liao H (2018) A spatial position measurement system for surgical navigation using 3-D image marker-based tracking tools with compact volume. IEEE Trans Biomed Eng 65(2):378–389
52. Liao H, Inomata T, Sakuma I, Dohi T (2010) 3-D augmented reality for MRI-guided surgery using integral videography autostereoscopic image overlay. IEEE Trans Biomed Eng 57(6):1476–1486
53. Fan Z, Zhang S, Weng Y, Chen G, Liao H (2017) 3D quantitative evaluation system for autostereoscopic display. J Disp Technol 12(10):1185–1196

17

Intelligent HMI in Orthopedic Navigation

Guangzhi Wang, Liang Li, Shuwei Xing, and Hui Ding

Abstract

The human-machine interface (HMI) is an essential part of image-guided orthopedic navigation systems. HMI provides a primary platform to merge surgically relevant pre- and intraoperative images from different modalities and 3D models including anatomical structures and implants to support surgical planning and navigation. With the various input-output techniques of HMI, surgeons can intuitively manipulate anatomical models generated from medical images and/or implant models for surgical planning. Furthermore, HMI recreates sight, sound, and touch feedback for the guidance of surgery operations which helps surgeons to sense more relevant information, e.g., anatomical structures and surrounding tissue, the mechanical axis of limbs, and even the mechanical properties of tissue. Thus, with the help of interactive HMI, precision operations, such as cutting, drilling, and implantation, can be performed more easily and safely.

Classic HMI is based on 2D displays and standard input devices of computers. In contrast, modern visual reality (VR) and augmented reality (AR) techniques allow the showing more information for surgical navigation. Various attempts have been applied to image-guided orthopedic therapy. In order to realize rapid image-based modeling and to create effective interaction and feedback, intelligent algorithms have been developed. Intelligent algorithms can realize fast registration of image to image and image to patients, and the algorithms to compensate the visual offset in AR display have been investigated. In order to accomplish more effective human-computer interaction, various input methods and force sensing/force reflecting methods have been developed. This chapter reviews related human-machine interface techniques for image-guided orthopedic navigation, analyzes several examples of clinical applications, and discusses the trend of intelligent HMI in orthopedic navigation.

Keywords

Intelligent human-machine interface · Visual reality (VR) · Augmented reality (AR) · Orthopedic navigation

G. Wang (✉) · L. Li · S. Xing · H. Ding
Department of Biomedical Engineering, School of Medicine, Tsinghua University, Beijing, People's Republic of China
e-mail: wgz-dea@mail.tsinghua.edu.cn; lil17@mails.tsinghua.edu.cn; xsw16@mails.tsinghua.edu.cn; dinghui@tsinghua.edu.cn

G. Zheng et al. (eds.), *Intelligent Orthopaedics*, Advances in Experimental Medicine and Biology 1093, https://doi.org/10.1007/978-981-13-1396-7_17

17.1 Preoperative Image Visualization Interfaces

Preoperative medical images play important roles in diagnosis and planning. X-ray projection (XP), X-ray computed tomography (XCT), magnetic resonance (MR), and ultrasound (US) images are used to make individualized surgical solution in orthopedic navigation system. As visual interfaces are critical to the surgical planning, many visualization methods have been proposed in clinical practice.

17.1.1 Visualization Interfaces of XP Images

X-ray projection (XP) images are the most widely used medical image modality in orthopedic navigation. Because an XP image is a 2D image, it can be easily and fully presented by a 2D monitor, and it is convenient to add auxiliary and planning lines on images. XP images acquired from at least two different views could offer 3D spatial information. If the spatial position of a projection is known, the 3D position of landmarks can be computed by selecting the corresponding points in different XP images. For surgical planning, these procedures are usually conducted by intelligent algorithms.

As an example, Fig. 17.1 shows the planning interface of a biplane robot-assisted femoral neck fracture fixation surgery. This interface contains a pair of femoral neck XP images from orthogonal views. Solid lines of different color indicate different screw paths, while dashed lines indicate the space constraints. The constraints of corresponding auxiliary lines are computed by the navigation system automatically to establish 3D guiding lines. Any correction of the auxiliary lines is immediately updated to another XP image [1]. Thus, physicians can select an appropriate screw and conduct the placement.

17.1.2 Visualization Interfaces of Volume Images

Usually, it is hard to establish a clear 3D view of the bony and damaged structures only based on multi-view XP images. 3D anatomy of patients can be directly represented by XCT images or MR images, but additional processing is necessary to visualize 3D volume data on a 2D monitor. There are three ways to achieve these kinds

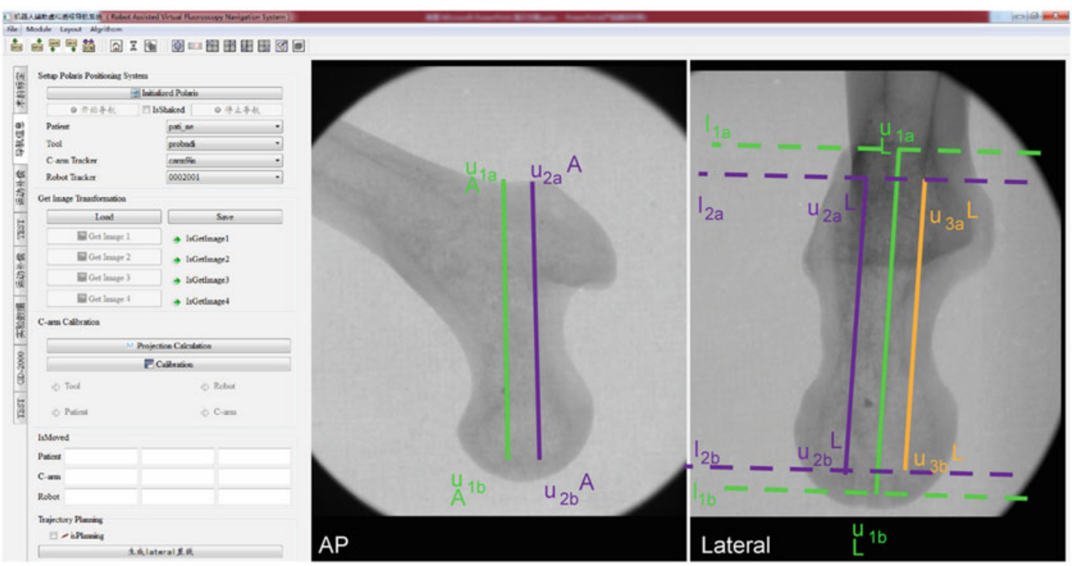

Fig. 17.1 Visualization based on XP images

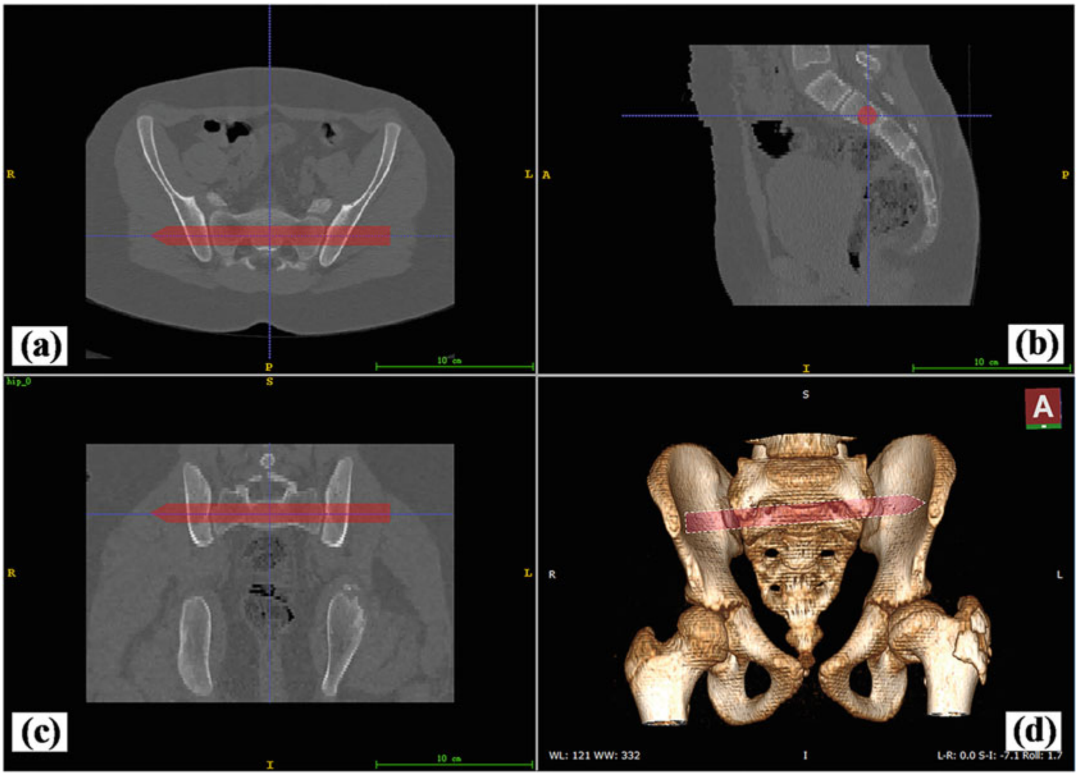

Fig. 17.2 Visualization based on volume image; axial slice (**a**); sagittal slice (**b**); coronal slice (**c**); 3D rendering (**d**)

of visual interfaces: (1) multi-planar rendering (MPR), which shows the slices of the volume image along three orthogonal axes separately; (2) surface rendering (SR), which renders the surface segmented from a volume image in different directions; and (3) direct volume rendering (DVR), which renders the volume image data directly.

Each visualization method has its own advantages. MPR shows the volume data in the same format as diagnosis images, which is a popular way to illustrate the detail of the anatomical structure. It is convenient to get the 3D anatomical structure with the SR model, but the accuracy of the structure depends on the segmentation process of the images. DVR is the most intuitive way to show 3D volume data, but the calculation costs are much higher than other rendering methods. Different visualization methods are selected according to the application situation, and some of the methods can be combined to get a better effect.

For surgical planning and implants, measurement rulers and auxiliary planes for evaluating the cutting pathway are usually labeled in a visualization interface. Surgeons' planning operation in a viewport can be corresponded to other viewports automatically, which is helpful to identify the relative space relationship between implants and patients' anatomy. Figure 17.2 shows a visualization interface of an XCT image-guided sacroiliac joint fixation surgery. The red shapes indicate the virtual screw, while the solid lines are the auxiliary lines for planning.

17.1.3 Visualization Interfaces of Partial Cross-Sectional Images

Due to space and cost limitations, lightweight real-time imaging devices are commonly used in the operating room. As a result, only regional images with relatively poor imaging quality can be acquired, which makes navigation difficult. A good solution is to visualize these images together with high-quality preoperative diagnostic images. To achieve this, an accurate registration procedure is necessary [2].

17.1.4 Visualization Interfaces of Multimodal Images

Multimodal images can show abundant anatomy, pathology, and function information. Fusion of different modal images can provide more effective visual guidance information for the surgeon. An intelligent image registration process is necessary to match the images in space in real time. Images are merged for visualization, and the opacity or color can be adjusted to enhance the visual ability of each image modality. Surgeons make the surgical plan in a main modal image and refine the surgical plan in combination with other modal images.

Multimodal images are able to present soft tissues much better than single-modal images [3]. Figure 17.3 shows MR-XCT fusion images of a patient with a mandible defect. The CT-MRI registration was made based on normalized mutual information automatically. Then, the 3D mandible model was segmented from CT, and the surrounding soft tissue can be visualized in MR slices.

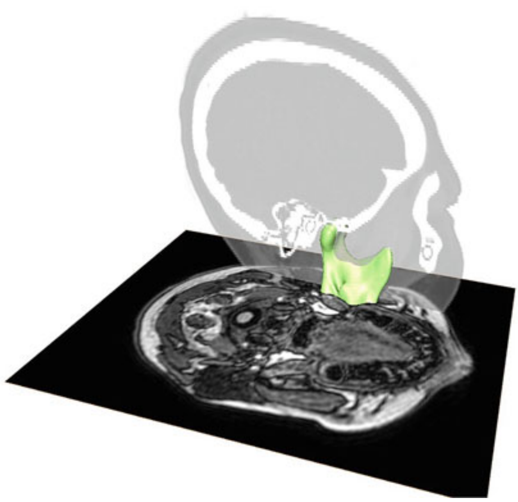

Fig. 17.3 Visualization based on MR-XCT fusion images

17.1.5 Visualization Interfaces of Digitized Models

Digitized surfaces can be used to guide the registration of operating space with the image/implant model space. It is achieved by picking up anatomic landmarks or the joint surface of a specific anatomy region using the tip of a 3D digitizer [4]. The visualization of the digitized point cloud represents the selected anatomy surface, which helps the surgeons perform and validate the registration.

17.2 Interactive Interfaces of Preoperative Planning

In addition to visualization interfaces for observing bone and peripheral tissue structure, flexible interaction interfaces of images and models are necessary for surgeons. Operations on images and models such as rotation, translation, and zooming can be conducive to the visualization of key surgical areas and surgeons' observation habits. Comprehensive patient anatomy information is also usually contained in different slices and images of different modalities; therefore switching between different images is essential. Furthermore, operations in surgical planning such as defect/trauma measurement, cutting arrangement, and implantation process simulation also need to be carried out by using interactive interfaces. All of these require navigation systems to provide efficient and accurate interactive interfaces.

17.2.1 Information Input System

An information input system, which is the core of any navigation system, can obtain surgeons' operating intentions. Keyboard, mouse, touchscreen, and other PC input devices are widely used in orthopedic navigation systems. As two-dimensional (2D) input devices, mouse and touchscreen are effective for 2D interaction. Interactions based on 2D image viewport, such as anatomical measurements or trajectory planning, can be done easily.

Due to the dimensional differences between 2D input devices and three-dimensional (3D) objects, it is difficult to measure or draw graphics in 3D models directly and accurately only using 2D input devices. Projection or slice conversion is needed before making a surgical plan in 3D space. Joysticks can overcome this problem to some degree. With this 3D input device, surgeons' intentions can be directly expressed in 3D space, so surgeons can obtain a more intuitive surgical planning experience. Kovler et al. [5] designed a 3D interactive system based on Phantom Omni (Sensable Technologies Inc., USA) haptic devices, in cooperation with the 3D image display of CT data and 3D interaction of force feedback. They achieved preoperative planning of fracture surgery and verified the feasibility of this system experimentally. However, the interaction of 3D devices cannot fully meet the surgeons' needs on the operation on real objects without a 3D image display. Literature shows that at present, the efficiency of 3D information input devices is not as good as traditional 2D information input devices [6].

17.2.2 Interactions for Image Measurement

In orthopedic surgeries such as arthroplasty and trauma, the most ideal outcome is to make the lesion part heal as well as possible. In order to achieve this goal, the precise geometric information on the patient's skeletal anatomy is needed for both implant size selection and the planning of the resection site. Easy-to-use image measurement tools are important for the acquisition of geometric information. Before interaction with image measurement tools, navigation systems usually convert the 3D mode into a two-dimensional view under a specific perspective to facilitate the operation. During measurement operations, surgeons use the pointing device to specify the end point of the line segment, or the angle of the vertex in the 2D image. Then the system can calculate the relevant lengths, angles, and axes of the patient's skeletal anatomy. For common orthopedic parameter measurements, semi-customized measurement templates are usually provided by navigation systems [7]. By using those templates, surgeons only need to specify the location of the critical anatomic landmark in patient's image. Then all commonly used anatomical parameters of the patients will be automatically displayed in the screen.

17.2.3 Interactions in Preoperative Surgical Planning

Based on the pre-measurement and observation, a suitable prosthesis or implants can be selected. The implantation path and resection area can also be planned preoperatively. In order to adapt to different forms of orthopedic surgery, navigation systems provide several surgical planning interactions for surgeons. The interactive interfaces can be divided into 2D and 3D interactive planning methods based on images' dimensions.

In 2D planning, common computer graphic tools are used to make a surgical plan in 2D images directly. The 2D images are generally from patients' radiographs or axial, sagittal, and coronal views of CT or MRI scans. Surgeons can use the graphic tool in the system to perform basic planning operations such as auxiliary line settings and path settings. In order to reduce the surgeons' workload, the navigation system provides a smart planning method based on an interactive template. The interactive template is a set of standard surgical plan graphics. During planning of the surgical path, surgeons first import the template into the 2D images, then make a minor adjustment to the template according to the patient's specific anatomy, after which the surgical planning is complete. In the template-based planning approach, the computer performs repeatable tasks such as drawing and plotting, and surgeons only need to set and validate key sections. This method enhances the interaction efficiency and lightens the surgeons' workload. However, template-based surgical planning is only suitable for operations with standardized procedures such as joint replacement. For complex orthopedic surgery such as trauma restoration, manual planning by surgeons is still required.

3D planning allows surgeons to interact with patients' 3D images directly. There are several advantages to 3D planning. First of all, patients' images that are displayed in 3D space conform more to the real operation, and the planning can be rapidly visually verified. Lonner et al. [4] reports a planning interface of the Navio PFS navigation system for semi-knee replacement surgery. The 3D display can visually show the degree of coincidence of the implant with patients' actual anatomy. The position adjustment of the implant can also be directly visualized. Second, for some complex traumatic fractures, it is difficult to express three-dimensional surgical planning through two-dimensional images. By using 3D planning methods, the fractured parts can be visualized in 3D mode, and the optimal recovery path and fixation plan can also be determined and simulated. Wang et al. [8] report their method for preoperative planning on pelvic fractures. The fractured fragments of skeleton are shown in different colors. Each part can be controlled by a pointing device to move and rotate to form a fracture reduction program. It is also possible to help surgeons choose the appropriate internal implant and determine which bone fragments need to be retained or removed (Fig. 17.4).

Giulio Dagnino et al. [9] demonstrate the potential of the integration of robotic assistance and 3D image guidance to overcome fracture malreduction. They proposed an image-guided surgical robotic system for the percutaneous treatment of knee joint fractures. The preoperative planning was performed based on a CT model in 3D space, and guidance was established by registration of an intraoperative fluoroscopic image and a CT model. A Leap Motion was used to capture the gesture of the operator and move the fracture pieces in 3D space. Simultaneous manipulation of two bone fragments, safer robot-bone fixation, and a traction performing robotic manipulator were tested in clinic. Figure 17.5 illustrates the interface of 2D image, 3D model, and the surgeon using the interactive GUI to virtually reduce the fracture.

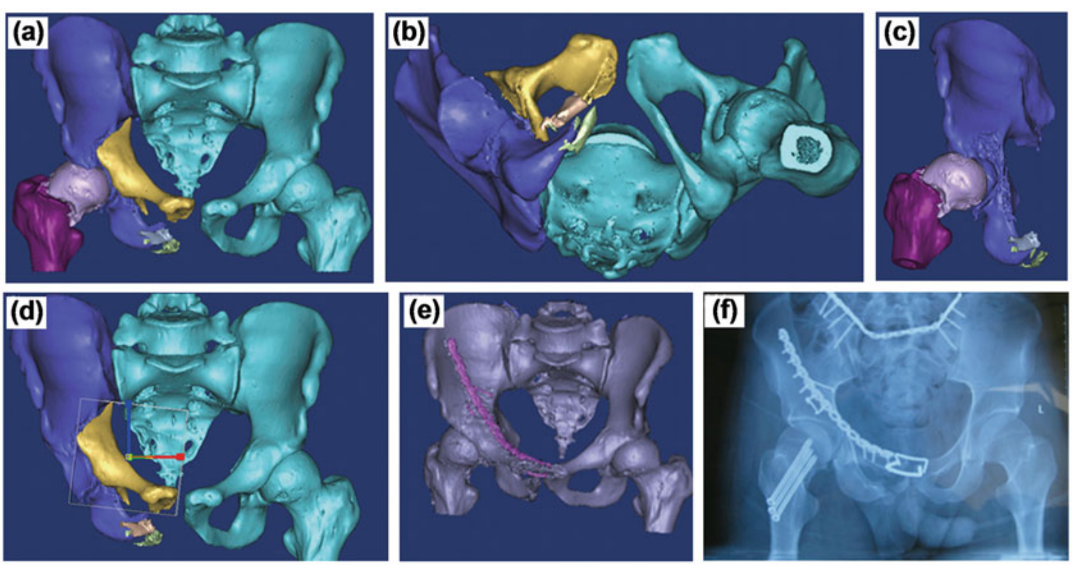

Fig. 17.4 Preoperative planning of pelvic fracture; model of fractured pelvis (**a**); the model could be rotated (**b**); every fragment could be subtracted and moved (**c**, **d**); anteroposterior radiograph of the postoperative (**e**); 3D rendering of the postoperative CT (**f**). (Courtesy of Dr. Guang-Ye Wang)

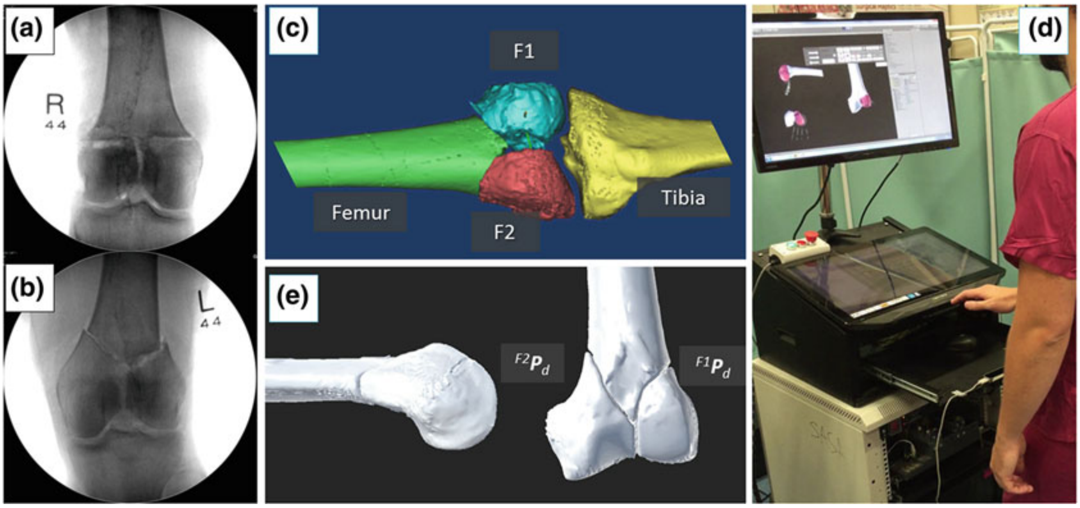

Fig. 17.5 Preoperative planning with CT-generated 3D models of a Y-shape fracture of a cadaveric specimen; articular Y-shape and T-shape fractures (**a**, **b**); 3D models of each bone fragment (**c**); the surgeon virtually reduces the fracture using the GUI (**d**); the desired final (**d**); poses for fragments with respect to the femur (**e**). (Courtesy of Dr. Giulio Dagnino)

17.3 Interactive Manipulation During Surgery

To complete an image-guided orthopedic surgery, the surgeons need to perform diagnosis and then design the surgery plan based on preoperative images. The surgery plan is very important for precise operation. The preoperative planning images, organ model, implant model, and interactive HMI are still helpful during surgery. Due to the limitations of the operation room environment and operational constraints, more convenient, reliable, and contactless HMI is necessary. At the same time, more effective registration methods are expected to obtain the accurate transform between the preoperative plan and intraoperative space. With these registration methods, surgeons can easily observe and compare the intraoperative scene with the preoperative plan and can achieve more precise surgery. Therefore, 3D visualization techniques, virtual reality, and augmented reality have attracted a lot attention. Comprehensive tests have been performed, making some of these techniques accepted in practice.

17.3.1 Visual Interfaces with 2D Flat Panel Monitor

2D display devices are widely used in the operation room for image-guided surgery. These devices can guide the surgeons to perform precise orthopedic operations by showing patients' images, implants, and surgical tools simultaneously.

For example, operations like fracture healing and bone nail implantation can be safely performed with the guidance of 2D visualization. The surgeon can adjust surgical tools according to the guidance of 2D trajectory guiding lines overlapped on the images. The spatial relationship between the surgical tools and the planned trajectory, implantation orientation and depth of pedicle screw, and so on can be clearly illustrated by multiple 2D views. However, 2D display lacks depth information. Surgeons have to use two or more images from different viewpoints to guarantee guidance accuracy. As a result, precise operation mainly relies on the surgeons' spatial visualization ability. Meanwhile, the registration methods affect the alignment of surgical tools and image. To make the surgery more accurate, effective techniques like intraoperative imaging and motion tracking are used. Then patients' position and surgery tool position can be obtained simultaneously to calculate the transform between the image space and surgery space. The displayed image slices can be updated automatically with the surgery tool's motion. This will reduce the need for manual adjustment and viewpoints tuning.

To make the visual interface more intuitive, 3D visualization of medical images are widely used. After 3D reconstruction of patients' volume images, the surgical object, implants, and surgical tools can be combined and visualized in any given viewpoint. To make sure that it shows the right spatial relationship between surgical objects and implants, accurate intelligent registration algorithms are the most important fundamental for image-guided orthopedic surgery. For orthopedic operations, the skeleton is usually considered as rigid body; thus rigid registration is often used. In practice, two registration methods are commonly applied. The first one acquires the spatial positions of anatomic landmarks of the bone picked up by a motion tracking probe. Then the corresponding positions are picked on the 3D bone model using a graphic user interface. The optimal registration based on the corresponding points can then be performed. If necessary, a point cloud can be acquired and used to perform point-to-surface registration. The other more reliable method is to acquire the intraoperative images of patients with attached tracking markers. Transformation between the surgical tools and the images can be established automatically according to tracing markers, and the surgeons only need to evaluate the registration accuracy on the basis of HMI [10].

17.3.2 Visual Interfaces Based on Mobile Devices

From a HMI point of view, the visual interfaces mentioned above prevent common hand-eye coordinated manipulation. Surgeons must switch between looking at the screen and the surgical region. Therefore, some researchers combined the surgery tool with mobile devices to optimize the form of HMI.

Marien et al. [11] developed a system with a movable tablet display. As shown in Fig. 17.6, this system can be adjusted to a proper position according to the surgical environment and surgeons' requirement. The CT image shown in the display is registered with patients by using an embedded tracking sensor, and surgical tools with a tracking sensor can be mapped into the image space. Compared with the HMI mentioned above, this kind of visual interface is more suitable for eye-hand coordination.

17.3.3 Visual Interfaces Based on Augmented Reality

Although the two types of HMI mentioned above have been optimized, the visual object and the therapeutic object are still in separate spaces. The rapid development of AR and mixed reality (MR) technologies provides opportunities to realize an ideal form of HMI.

Zeng et al. [12] developed a vision enhancement image-guided surgery robot system. They designed a projector-camera system (PCS) to realize registration and AR simultaneously. As shown in Fig. 17.7, the PCS attached to the distal flange of a robot arm can obtain the point clouds of the patient's surface, which are utilized for patient-to-image registration. Then see-through AR is produced by merging real-time video of the patient and the preoperative three-dimensional (3D) operational planning model. In addition, spatial AR is implemented by projecting the planning electrode trajectories and local anatomical structure onto the patient's skin. A demonstration of the system was performed using a lumbar vertebra phantom. The phantom (Lumbar Training Phantom Model 034, America) was scanned with CT ($512 \times 512 \times 336$, 0.41 mm $\times$ 0.41 mm $\times$ 1 mm). Then the surface and internal spine structure were extracted. The PCS was used to obtain the point cloud of the surface for registration. Finally, the see-through AR was implemented by projecting the internal spine structure to the phantom surface.

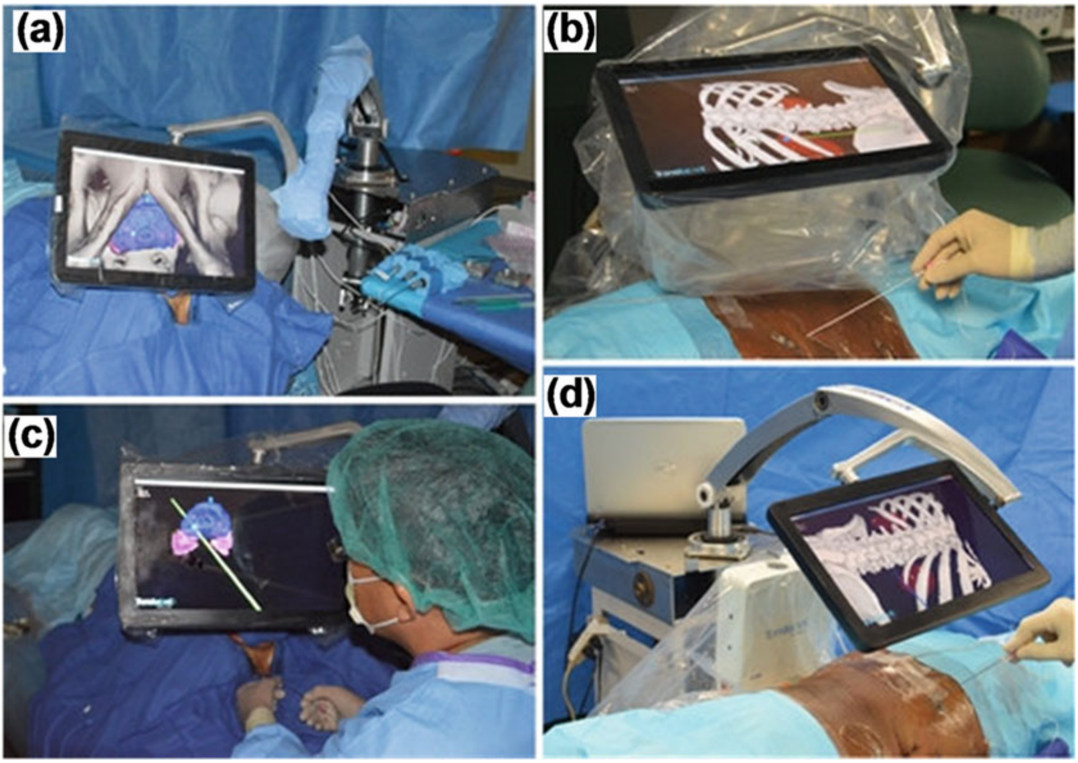

Fig. 17.6 Image-guided system with a movable tablet display; real-time navigation for percutaneous puncture in the prostate (**a**, **c**) and kidney (**b**, **d**). (Courtesy of Dr. Arnaud Marien)

Zhang et al. [13] developed an enhanced 3D autostereoscopic AR system. It can realize high-quality see-through surgical guidance and is expected to be used as in situ guidance for orthopedic surgery. The visual interfaces of this study are shown in Fig. 17.8.

With the advent of novel commercial AR devices and mixed reality devices, new solutions are emerging for visual interfaces in surgical operations. Golab et al. [14] designed an AR system on Google Glass (Google, Inc., Mountain View, Calif, USA.) for spine surgery. During selective dorsal rhizotomy neurosurgical procedures, the doctor wearing the AR system can observe the real-time response of neural electrical signals. Perkins et al. [15] and Tepper et al. [16] demonstrated the great potential of mixed reality based on Microsoft HoloLens (Microsoft Corp., Redmond, Wash, USA.) in orthopedics.

These new visual interfaces (AR, VR, and MR) showed great advantages in intraoperative interaction, but for real clinical applications, there are some technical issues which need to be further studied, such as display latency, imaging accuracy, registration accuracy, etc. [17].

17.3.4 Interactive Control During the Surgery

During image-guided or robot-assisted surgery, it is necessary for surgeons to adjust the displayed images or surgical instruments. Then they can manipulate the tools or control the robot to perform high-quality surgery.

Traditionally, to keep the surgery environment sterilized, surgeons can only accomplish some simple operations by the switch equipped on surgical tools. But in order to perform complex

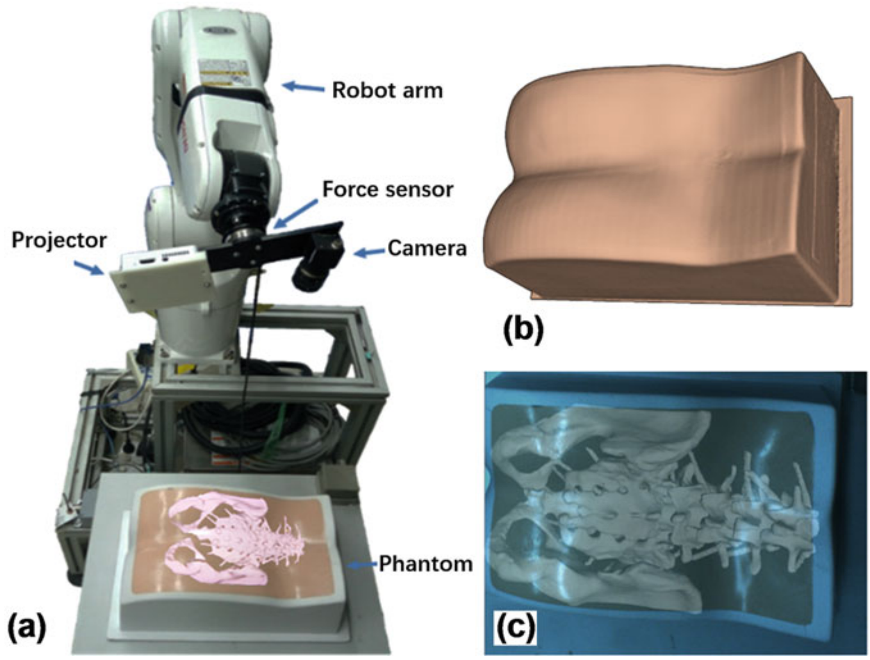

Fig. 17.7 Experiment using lumbar vertebra phantom; (**a**) experiment scene; surface extracted from phantom CT images (**b**); internal structure of the phantom (**c**)

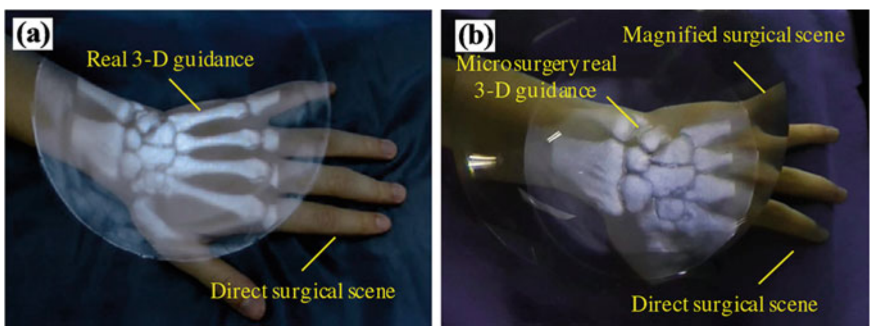

Fig. 17.8 Enhanced 3D autostereoscopic AR system; demo for microsurgery in orthopedic operations (**a**); magnified surgical sense in orthopedic operations (**b**). (Courtesy of Dr. Liao HG)

adjustment of the navigation system, surgeons need close cooperation with their assistants. Although this interactive form allows for collaboration between the surgeon and his assistants, this requires them to be experienced working together.

Touchless interactive HMI makes it possible for surgeons to control the equipment via gesture, posture, or voice without touching. Touchless interactive HMI at present mainly utilizes mature commercial interactive devices and is designed for specific surgery needs. The widely used interactive devices include the Kinect (Microsoft Corp., Redmond, Wash, USA.), Leap Motion (Leap Motion Inc., San Francisco, USA), and similar kinds of detectors.

Lopes et al. [18] developed a touchless interface controlled via hand gestures and body posture to rapidly rotate and position images in three dimensions. Mewes et al. [19] utilized Leap Motion to toggle and operate images during image-guided intervention.

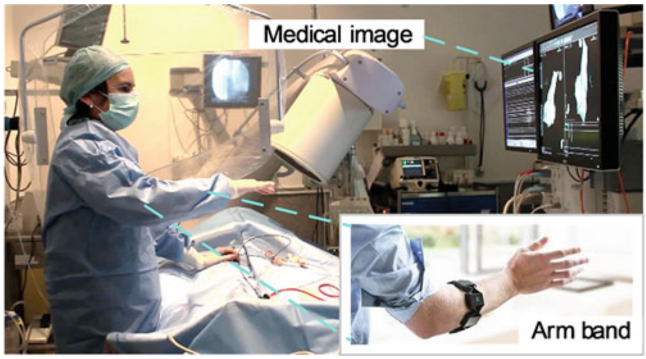

Fig. 17.9 Wearable interactive devices based on Myo™ Armband for image control (the Myo gesture control armband from Thalmic Labs)

Wearable interactive devices based on inertial navigation and myoelectricity can also be applied in HMI. It is worth mentioning that these devices have no occlusion issues and are not limited to working in the field of view of tracking systems. As shown in Fig. 17.9, a myoelectricity-based wearable armband was worn on the surgeon's arm, and instructions from arm movements can be instantly recognized. By using this device, surgeons can control image information in real time without touching anything [20].

Currently touchless interactive HMI is mainly studied in laboratories. Although some have been validated in a surgery environment, the robustness and accuracy of touchless control is still limited and cannot replace the present operation mode. So far, there is no mature touchless interactive HMI that can be widely accepted by surgeons [21].

17.4 Interfaces of Intraoperative Operation Status Monitoring and Feedback

Orthopedic navigation or surgical robot systems use tracking equipment to obtain the relative position of surgical tools and the patient's anatomy. In order to guide surgeons to manipulate surgical tools in an invisible surgical field, the relative positional relationship between tools and patients is usually displayed by the navigation system. However, the interactive interface based on the visual feedback device only allows surgeons to visually inspect the relative position of surgical tools and bone. Due to the limitation of having to pass all the guide information through the visual interfaces, nonvisual intraoperative status information has not been well applied in orthopedic navigation systems. By detecting and identifying specific signals during the surgery, the interaction of surgical tools and dissecting tissue can be monitored. In this way, surgeons can receive multidimensional guidance, and better treatment results can be achieved. However, the material and anatomy of the human skeleton is quite complex, and orthopedic instruments are usually running at a very high speed. There are still considerable challenges to make a comprehensive, accurate, and reliable state detection in orthopedic surgery.

17.4.1 Force Signal Monitoring and Feedback

During manual operation in orthopedic surgery, surgeons need to determine the interaction force between instruments and the patient's bone to make corresponding adjustments of the tools in real time. This places high demands on the surgeons' level of experience. Since the force signal during surgery can be digitized by the sensor, and the status of the surgical instrument can be automatically recognized by an intelligent signal analysis algorithm, this problem can be partially addressed by passing the surgical instrument's state to surgeons via HMI. Kastelov et al. [22–25] designed a special automatic and/or semiautomatic bone drilling by monitoring the thrust force during orthopedic drilling. They can monitor the type and depth of bone tissue during drilling. A visual interface was used to display real-time information. The risk of far cortex damage during drilling can be avoided by this approach. Hu et al. [26–28] studied thrust force and torque signal during the bone drilling with the force sensing; five key states, including the initial state, the outer cortical state, the cancellous state, the transitional state, and the inner cortical state, can be recognized.

17.4.2 Audio and Vibration Signal Monitoring and Feedback

In surgical operations, acoustics and vibrations are generated when high-speed rotating tools contact different tissues and bone structures. The status of the surgical instruments are also included in acoustic and vibration signals. Due to differences in personal experience, it is hard for surgeons to determine the status from this kind of signal accurately. Some researchers monitor these signals to identify the status of instruments during surgery. Dai et al. [29] collected the tissue's vibration and acceleration signals during bone milling. They can monitor different tissue structures in robotic-assisted bone milling. Their device was verified on porcine spines, which successfully discriminated the tissues in the operation field such as bone, spinal cord, and muscle. Hu et al. [30, 31] collected acoustic signals during drilling to identify the state of the drilling. They can identify different bone tissue structures that may potentially prevent drilling through the spine during surgery.

17.4.3 Spatial Distance Signal Monitoring and Feedback

In orthopedic surgery, it is not only necessary to ensure accurate excision of the target tissue but also important to protect the normal tissues and vital organs around the excised area. In operation, the positional relationship between the surgical instrument and the patient's anatomy can be obtained by the registered navigation system in real time. The real-time positional relationship can be passed to surgeons through the man-machine interface. In this way, surgeons' mistakes may be avoided. For example, in orthopedic drilling surgery, the position of drilling tool's end point can be modeled and monitored by the navigation system, and a safe area for peripheral nerves can be set, as shown in Fig. 17.10. When the distance

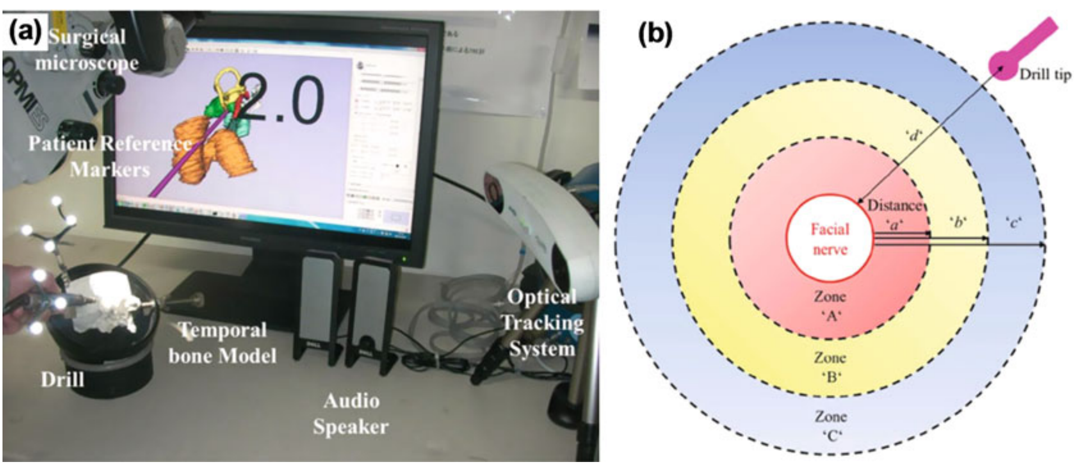

Fig. 17.10 Warning navigation system using real-time safe region monitoring for otologic surgery; prototype system (**a**); the degree of risk when the drill tip approached the surface of the facial nerve (**b**). (Courtesy of Dr. J. Hong)

between the drilling point and the nerve tissue exceeds the safety threshold, an audible alarm is triggered to alert the surgeons [32–34]. In addition, monitored spatial location information can also be conveyed using a certain parameter of sound such as frequency. Thus, guiding information such as distance can be fed back to surgeons though the sound interface in real time [35].

17.5 Surgical Simulation and Training

With the development of human-machine interface technologies, such as VR, AR, and haptic feedback, many novel simulation methods have emerged for the training of novice surgeons. These novel methods not only have advantages in operating space, reduced surgery times, and surgical reproducibility but also show real 3D images of body anatomy or haptic feedback. Unlike relatively mature simulation systems, such as those for endoscopy or needle insertion, simulators for orthopedic surgery have lagged behind simulators from other fields over the past 20 years [36]. The emergence of new human-machine interfaces marks a turning point for orthopedic simulation. Lots of orthopedic simulation systems created by research institutes or companies have been carried out.

Mithra et al. [37] classified orthopedic simulation into three groups: non-interactive simulators, interactive simulators based on visual feedback, and interactive simulators based on visual and haptic feedback. Non-interactive simulation is the most widely used way to train surgeons before the application of novel interfaces. Nowadays, both interactive simulators based on vision and interactive simulators based on haptic and vision have become mainstream. As for hardware equipment, besides traditional interfaces, various commercial products are available. These products can accomplish operations freely in three-dimensional space and provide users with haptic feedback.

17.5.1 Vision-Based Feedback

Virtual reality technology can show us a vivid scene by rendering and simulating users' operations. Using VR technology, orthopedic simulation systems can provide trainees real three-dimensional anatomy structures from individuals and reduce the cost of training. At the same time, it has a great advantage in improving trainees' understanding of complex bone structures. Cecil et al. [38] developed an orthopedic simulator for less invasive stabilization system (LISS) plating orthopedic surgery based on VR technology. Operators can interact with the virtual environment by operating the device and perform some surgical tasks such as fracture reduction, LISS plate positioning, and fixation. Finally, learning assessments consisting of qualitative and quantitative tests were conducted by surgeons and students and showed the significance of using VR technology in LISS plating surgery.

In surgical simulation, AR is even more effective. Shen et al. [39] developed a preoperative system for unilateral pelvic and acetabular fracture reduction and internal fixation surgery. This system consists of two subsystems: a semi-automatic 3D fracture reduction system and a simulation system based on AR. While the semi-automatic 3D fracture reduction system aims to repair the broken pelvic according to pelvic symmetry and plan, the surgical path simulation system made trainees more proficient on specified surgical tasks by matching the implant in real and virtual space. Six clinical trials were conducted to verify the feasibility of this system.

In addition to VR and AR, mixed reality technology also brings us novel surgical simulation solutions. As shown in Fig. 17.11, the patient's anatomy can be directly matched to the human body model by using the Microsoft HoloLens. What is more significant is that the real-time images obtained by the ultrasound device can be superimposed in situ on the virtual anatomy and the human body model. This kind of surgical simulation can greatly enhance the authenticity and intuition of the doctor and is more conducive to developing the doctor's understanding [40].

Fig. 17.11 Mixed reality ultrasound simulation solution with Microsoft HoloLens. (The picture is from CAE Healthcare)

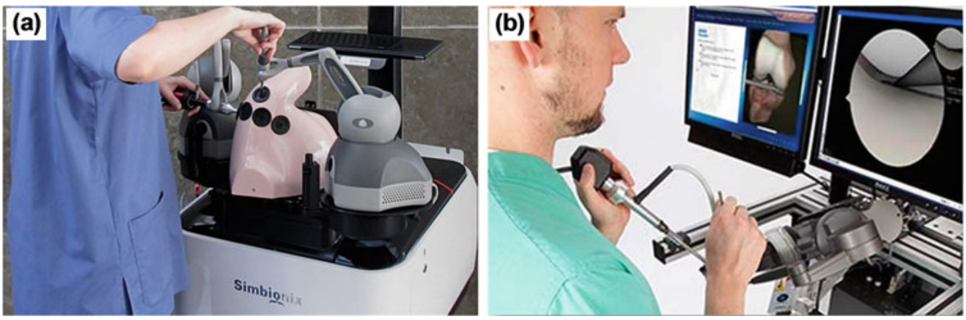

Fig. 17.12 Commercial products: ARTHRO Mentor™ (**a**) and ArthroSim Arthroscopy Simulator (**b**) (Simbionix ARTHRO Mentor from 3D systems, ArthroSim Arthroscopy Simulator from Touch of Life Technologies Inc.)

17.5.2 Haptic and Vision-Based Interaction

In surgical simulation, the absence of haptic feedback is a potential drawback for simulation [41]. Jecobi et al. [42] have concluded that the simulation based on haptic and vision has great advantages in execution time and training precision. A few haptic feedback simulators were developed. Figure 17.12 gives two examples of orthopedic simulators. These systems allow trainees to acquire true-to-life hands-on experience with haptic feedback by utilizing a realistic set of tools. Although the effectiveness of haptic feedback in surgical simulation is still debated, several studies [41, 43, 44] have shown that surgical simulation with haptic feedback can provide more realistic feedback and reduce the learning curve of surgical simulation.

Bone drilling is considered the most basic operation in orthopedic surgery. The effectiveness of some operations, such as implanting screws, depends on the accuracy of pre-drilling of bones. Mithra et al. [37] designed a bone drilling simulator based on the Phantom Desktop™ device. Using the simulator, they carried out two experiments with haptic feedback and reported the feasibility of the simulator.

Spinal surgery is a high-risk operation in orthopedic surgery because of the spine's proximity to surrounding nerves and soft tissues. In the research by Cristian et al. [45], an immersive touch augmented virtual reality system was developed for pedicle implantation. The system generates high-resolution VR and AR and provides real-time force feedback. A test on 51 participants was conducted, which concluded that the participants' accuracy of implanting virtual pedicle screws was comparable to the accuracy of implanting actual screws reported in the literature.

Due to the use of novel human-machine interfaces such as AR, VR, and haptic feedback, there have been huge changes in the form of orthopedic simulation. Although some commercial products have appeared on the market, the applications of these new interfaces in surgical simulation are still in their infancy. As surgical simulation and human-machine interfaces support each other, intelligent human-machine interfaces will provide a higher fidelity environment both for simulation training and orthopedic operations in the near future.

17.6 The Trends of Intelligent HMI in Orthopedic Navigation

Modern orthopedic surgery is increasingly dependent on the support of advanced medical equipment. HMI serves as a bridge between surgeons and medical devices, which allows for smooth interaction between them. HMI needs to accurately transfer the patient's anatomy, navigation information, and other intraoperative signals to the surgeons and also needs to obtain the surgeons' operational intentions and give timely feedback. HMI in orthopedics shows the following trends.

In terms of information output, virtual reality [5, 38], augmented reality [12, 13, 39], and mixed reality [15, 16] have been continuously introduced into clinical research, such as preoperative planning, intraoperative guidance, and surgical simulation. New commercial display devices such as Google Glass and Microsoft HoloLens have also been gradually adopted in the field of orthopedic navigation [14, 16]. With this new 3D display technology, finer orthopedic anatomy will be presented to surgeons in a more realistic way. In addition, the presentation of surgical information will not only be limited to visual feedback, but comprehensive multidimensional sensory feedback, such as auditory, tactile, and force perception, which will bring more comprehensive guidance to surgeons [35]. Consequently, the spatial positional relationship between surgical instruments and tissue will not be the only guidance information that the navigation system can provide. The force interaction between the device and tissue, anatomical changes, and other physical or physiological nonvisual information can all be presented to the surgeon through the man-machine interface for more precise surgical guidance [28, 32].

In terms of information input, in addition to traditional input devices, contactless interaction such as gesture interaction and voice interaction also show the potential in the operating room. Contactless interaction technology based on gesture recognition has the advantages of sterility and being more in line with the surgeons' intuition when operating a 3D model. This technique has considerable advantages in both surgical planning and intraoperative imaging control [19, 46]. Voice interaction allows surgeons to use natural language to convey operational intent to the device [47, 48]. This approach is similar to the interaction between people and will be more conducive to collaboration between surgeons and navigation systems.

The new HMI technology offers considerable advantages and potential in orthopedics, both at the input and output levels of information. However, these new technologies still need to be further improved in terms of practicability, reliability, and safety so as to truly meet the needs of the operating room. Another potential problem is that current HMI technology is still independently developed toward different directions. Only single interaction modes (such as visual, auditory, tactile, gestures, etc.) are considered, and most studies are about a single interaction technique application in orthopedic navigation. This is necessary at early stages of technological development. However, ideally surgeons need be able to interact more naturally and habitually with the surgical equipment by systematically invoking their sensory and operating organs. Therefore, the question of how to integrate various advanced HMI technologies together to achieve multidimensional interaction is still a problem that needs to be further explored.

With the rapid development of technologies in display, sensor, and artificial intelligence, it is foreseeable that medical devices will have more power to understand surgeons' operational intentions and the effect of feedback is more in line with surgeons' intuition. In the future, surgeons' gestures, voice, and even eye movements are likely to be the means to communicate with medical devices [49], and the degree of understanding between surgeons and medical devices can reach the level of Tri-Co (Coexisting-Cooperative-Cognitive) [50].

References

1. Song J, Ding H, Han W et al (2016) A motion compensation method for bi-plane robot-assisted internal fixation surgery of a femur neck fracture. Proc Inst Mech Eng H J Eng Med 230(10):942–948. https://doi.org/10.1177/0954411916663582
2. Hacihaliloglu I, Wilson DR, Gilbart M et al (2013) Non-iterative partial view 3D ultrasound to CT registration in ultrasound-guided computer-assisted orthopedic surgery. Int J Comput Assist Radiol Surg 8(2):157–168. https://doi.org/10.1007/s11548-012-0747-9
3. Wong KC (2016) Image fusion for computer-assisted bone tumor surgery. In: Zheng G, Li S (eds) Computational radiology for Orthopaedic interventions. Springer, Cham, pp 217–230. https://doi.org/10.1007/978-3-319-23482-3_11
4. Lonner JH (2015) Robotically assisted unicompartmental knee arthroplasty with a handheld image-free sculpting tool. Orthop Clin North Am 25(2):104–113. https://doi.org/10.1016/j.ocl.2015.08.024
5. Kovler I, Joskowicz L, Weil YA et al (2015) Haptic computer-assisted patient-specific preoperative planning for orthopedic fractures surgery. Int J Comput Assist Radiol Surg 10(10):1535–1546. https://doi.org/10.1007/s11548-015-1162-9
6. Hettig J, Saalfeld P, Luz M et al (2017) Comparison of gesture and conventional interaction techniques for interventional neuroradiology. Int J Comput Assist Radiol Surg 12(9):1643–1653. https://doi.org/10.1007/s11548-017-1523-7
7. Stefanou MA, Pasparakis D, Mastrokalos D et al (2014) Radiographic assessment of lower limb lengthening in achondroplastic patients, using the ilizarov frame: a 5-19 year follow up study. Int J Orthop 1(4):140–145. https://doi.org/10.6051/j.issn.2311-5106.2014.01.33
8. Wang GY, Huang WJ, Song Q et al (2016) Computer-assisted virtual preoperative planning in orthopedic surgery for acetabular fractures based on actual computed tomography data. Comput Assist Surg 21(1):160–165. https://doi.org/10.1080/24699322.2016.1240235
9. Dagnino G, Georgilas I, Morad S et al (2017) Image-guided surgical robotic system for percutaneous reduction of joint fractures. Ann Biomed Eng 45(11):2648–2662. https://doi.org/10.1007/s10439-017-1901-x
10. Lonner JH, Smith JR, Picard F et al (2015) High degree of accuracy of a novel image-free handheld robot for unicondylar knee arthroplasty in a cadaveric study. Clin Orthop Relat Res 473(1):206–212. https://doi.org/10.1007/s11999-014-3764-x
11. Marien A, Al DCA, Desai M et al (2015) Three-dimensional navigation system integrating position-tracking technology with movable tablet display for percutaneous targeting. BJU Int 115(4):659–665. https://doi.org/10.1111/bju.12948
12. Zeng BW, Meng FL, Ding H et al (2017) A surgical robot with augmented reality visualization for stereoelectroencephalography electrode implantation. Int J Comput Assist Radiol Surg 12(8):1355–1368. https://doi.org/10.1007/s11548-017-1634-1
13. Zhang XR, Chen GW, Liao HG (2017) High-quality see-through surgical guidance system using enhanced 3-d autostereoscopic augmented reality. IEEE Trans Biomed Eng 64(8):1815–1825. https://doi.org/10.1109/tbme.2016.2624632
14. Golab MR, Breedon PJ, Vloeberghs M (2016) A wearable headset for monitoring electromyography responses within spinal surgery. Eur Spine J 25(10):3214–3219. https://doi.org/10.1007/s00586-016-4626-x
15. Perkins SL, Lin MA, Srinivasan S et al (2017) A mixed-reality system for breast surgical planning. In: 2017 IEEE International Symposium on Mixed and Augmented Reality (ISMAR-Adjunct) Proceedings pp 269–274. https://doi.org/10.1109/ISMAR-Adjunct.2017.92
16. Tepper OM, Rudy HL, Lefkowitz A et al (2017) Mixed reality with HoloLens: where virtual reality meets augmented reality in the operating room. Plast Reconstr Surg 140(5):1066–1070. https://doi.org/10.1097/prs.0000000000003802
17. Vavra P, Roman J, Zonca P et al (2017) Recent development of augmented reality in surgery: a review. J Healthc Eng 9. https://doi.org/10.1155/2017/4574172
18. Lopes DS, Parreira PDD, Paulo SF et al (2017) On the utility of 3D hand cursors to explore medical volume datasets with a touchless interface. J Biomed Inform 72(2017):140–149. https://doi.org/10.1016/j.jbi.2017.07.009

19. Mewes A, Saalfeld P, Riabikin O et al (2016) A gesture-controlled projection display for CT-guided interventions. Int J Comput Assist Radiol Surg 11(1):157–164. https://doi.org/10.1007/s11548-015-1215-0
20. Phil (2014) See the Myo armband in surgery. http://blog.thalmic.com/myo-armband-surgery/. Accessed 5 Feb 2018
21. Mewes A, Hensen B, Wacker F et al (2017) Touchless interaction with software in interventional radiology and surgery: a systematic literature review. Int J Comput Assist Radiol Surg 12(2):291–305. https://doi.org/10.1007/s11548-016- 1480-6
22. Boiadjiev T, Boiadjiev G, Delchev K et al (2017) Far cortex automatic detection aimed for partial or full bone drilling by a robot system in orthopaedic surgery. Biotechnol Biotechnol Equip 31(1):200–205. https://doi.org/10.1080/13102818.2016.1234947
23. Boiadjiev T, Boiadjiev G, Delchev K et al (2015) Eliminating of far pedicle cortex perforation by automatic spine drilling. Appl Mech Mater 799-800:505–508. https://doi.org/10.4028/www.scientific.net/AMM.799-800.505
24. Boiadjiev T, Zagurski K, Boiadjiev G et al (2011) Identification of bone structure during automatic drilling in orthopedic surgery. Mech Based Des Struc 39(2):285–302. https://doi.org/10.1080/15397734.2011.550863
25. Boiadjiev G, Kastelov R, Boiadjiev T et al (2013) Design and performance study of an orthopaedic surgery robotized module for automatic bone drilling. Int J Med Robot Comput 9(4):455–463. https://doi.org/10.1002/rcs.1479
26. Jin HY, Hu Y, Deng Z et al (2014) Model-based state recognition of bone drilling with robotic orthopedic surgery system. In: 2014 IEEE International Conference on Robotics and Automation ICRA, Hong Kong, China, 31 May–7 June 2014. IEEE International Conference on Robotics and Automation ICRA. IEEE, pp 3538–3543. https://doi.org/10.1109/ICRA.2014.6907369
27. Hu Y, Jin HY, Zhang LW et al (2014) State recognition of pedicle drilling with force sensing in a robotic spinal surgical system. IEEE/ASME Trans Mechatronics 19(1):357–365. https://doi.org/10.1109/tmech.2012.2237179
28. Tian W, Han XG, Liu B et al (2014) A robot-assisted surgical system using a force-image control method for pedicle screw insertion. PLoS One 9(1):9. https://doi.org/10.1371/journal.pone.0086346
29. Dai Y, Xue Y, Zhang JX (2016) Milling state identification based on vibration sense of a robotic surgical system. IEEE Trans Ind Electron 63(10):6184–6193. https://doi.org/10.1109/tie.2016.2574981
30. Jin HY, Hu Y, Gao P et al (2014) Intraoperative control for robotic spinal surgical system with audio and torque sensing. In: Processing of 2014 International conference on multisensor fusion and information integration for intelligent systems (Mfi), Beijing, China, 28–29 Sept. 2014 2014. IEEE, p 6. https://doi.org/10.1109/MFI.2014.6997711
31. Sun Y, Jin HY, Hu Y et al (2014) State recognition of bone drilling with audio signal in robotic orthopedics surgery system. In: 2014 IEEE/RSJ International Conference on Intelligent Robots and Systems, Chicago, IL, USA, 14–18 Sept. 2014. IEEE International Conference on Intelligent Robots and Systems. IEEE, pp 3503–3508. https://doi.org/10.1109/IROS.2014.6943051
32. Cho B, Oka M, Matsumoto N et al (2013) Warning navigation system using real-time safe region monitoring for otologic surgery. Int J Comput Assist Radiol Surg 8(3):395–405. https://doi.org/10.1007/s11548-012-0797-z
33. Cho B, Matsumoto N, Komune S et al (2014) A surgical navigation system for guiding exact cochleostomy using auditory feedback: a clinical feasibility study. Biomed Res Int 2014(3):769659. https://doi.org/10.1155/2014/769659
34. Dixon BJ, Daly MJ, Chan H et al (2014) Augmented real-time navigation with critical structure proximity alerts for endoscopic skull base surgery. Laryngoscope 124(4):853–859. https://doi.org/10.1002/lary.24385
35. Woerdeman PA, Willems PW, Noordmans HJ et al (2009) Auditory feedback during frameless image-guided surgery in a phantom model and initial clinical experience. J Neurosurg 110(2):257–262. https://doi.org/10.3171/2008.3.17431
36. Vaughan N, Dubey VN, Wainwright TW et al (2016) A review of virtual reality based training simulators for orthopaedic surgery. Med Eng Phys 38(2):59–71. https://doi.org/10.1016/j.medengphy.2015.11.021
37. Vankipuram M, Kahol K, McLaren A et al (2010) A virtual reality simulator for orthopedic basic skills: a design and validation study. J Biomed Inform 43(5):661–668. https://doi.org/10.1016/j.jbi.2010.05.016
38. Cecil J, Gupta A, Pirela-Cruz M (2018) An advanced simulator for orthopedic surgical training. Int J Comput Assist Radiol Surg 13(2):305–319. https://doi.org/10.1007/s11548-017-1688-0
39. Shen F, Chen B, Guo Q et al (2013) Augmented reality patient-specific reconstruction plate design for pelvic and acetabular fracture surgery. Int J Comput Assist Radiol Surg 8(2):169–179. https://doi.org/10.1007/s11548-012-0775-5
40. MedGadget (2017) CAE Healthcare announces first mixed reality ultrasound simulation solution with Microsoft HoloLens. https://www.medgadget.com/2017/01/cae-healthcare-announces-first-mixed-reality-ultrasound-simulation-solution-with-microsoft-hololens.html. Accessed 10 Feb 2018
41. Enayati N, De ME, Ferrigno G (2016) Haptics in robot-assisted surgery: challenges and benefits. IEEE Rev Biomed Eng 9:49–65. https://doi.org/10.1109/RBME.2016.2538080

42. Jacobs S, Holzhey D, Strauss G et al (2007) The impact of haptic learning in telemanipulator-assisted surgery. Surg Laparosc Endosc Percutan Tech 17(5):402–406. https://doi.org/10.1097/SLE.0b013e3180f60c23
43. Tholey G, Desai JP, Castellanos AE (2005) Force feedback plays a significant role in minimally invasive surgery: results and analysis. Ann Surg 241(1):102–109. https://doi.org/10.1097/01.sla.0000149301.60553.1e
44. van der Meijden OAJ, Schijven MP (2009) The value of haptic feedback in conventional and robot-assisted minimal invasive surgery and virtual reality training: a current review. Surg Endosc 23(6):1180–1190. https://doi.org/10.1007/s00464-008-0298-x
45. Luciano CJ, Banerjee PP, Bellotte B et al (2011) Learning retention of thoracic pedicle screw placement using a high-resolution augmented reality simulator with haptic feedback. Oper Neurosurg 69(suppl_1):14–19. https://doi.org/10.1227/NEU.0b013e31821954ed
46. Indraccolo C, Paolis LT (2017) Augmented reality and MYO for a touchless interaction with virtual organs.Paper presented at the augmented reality, virtual reality and computer graphics. In: 4th international conference, AVR 2017, Ugento, Italy, 12–15 June 2017
47. Mentis HM, O'Hara K, Gonzalez G et al (2015) Voice or gesture in the operating room. In: ACM Conference Extended Abstracts on Human Factors in Computing Systems, Seoul, Republic of Korea, 18–23 April 2015. pp 773–780. https://doi.org/10.1145/2702613.2702963
48. Hotker AM, Pitton MB, Mildenberger P et al (2013) Speech and motion control for interventional radiology: requirements and feasibility. Int J Comput Assist Radiol Surg 8(6):997–1002. https://doi.org/10.1007/s11548-013-0841-7
49. Mylonas GP, Kwok KW, James DRC et al (2012) Gaze-contingent motor Channelling, haptic constraints and associated cognitive demand for robotic MIS. Med Image Anal 16(3):612–631. https://doi.org/10.1016/j.media.2010.07.007
50. Ding H, Yang X, Zheng N et al (2017) Tri-co robot: a Chinese robotic research initiative for enhanced robot interaction capabilities. Natl Sci Rev 0(0):1–3. https://doi.org/10.1093/nsr/nwx148

18 Patient-Specific Surgical Guidance System for Intelligent Orthopaedics

Manuela Kunz and John F. Rudan

Abstract

Clinical benefits for image-guided orthopaedic surgical systems are often measured in improved accuracy and precision of tool trajectories, prosthesis component positions and/or reduction of revision rate. However, with an ever-increasing demand for orthopaedic procedures, especially joint replacements, the ability to increase the number of surgeries, as well as lowering the costs per surgery, is generating a similar interest in the evaluation of image-guided orthopaedic systems. Patient-specific instrument guidance has recently gained popularity in various orthopaedic applications. Studies have shown that these guides are comparable to traditional image-guided systems with respect to accuracy and precision of the navigation of tool trajectories and/or prosthesis component positioning. Additionally, reports have shown that these single-use instruments also improve operating room management and reduce surgical time and costs. In this chapter, we discuss how patient-specific instrument guidance provides benefits to patients as well as to the health-care community for various orthopaedic applications.

Keywords

Patient-specific instrument guidance · Total knee arthroplasty (TKA) · Computer-assisted surgery (CAS) · Cartilage defect repair · Planning

18.1 Introduction

The introduction of x-ray technology as a medical image modality by William Conrad Röntgen in 1895 marked the beginning of image-guided surgery. Within months of Prof. Röntgen publishing his findings, x-ray images were not only used as a diagnostic tool but also to navigate surgical procedures [1, 2]. One of the first reported cases was performed by Dr. Robert Jones in Liverpool to remove a small bullet which was embedded in a boy's wrist [2]. In this case, x-ray images of the affected anatomy allowed the surgeon to better understand the complex anatomy of the patient,

M. Kunz (✉) · J. F. Rudan
Department of Surgery, Queen's University, Kingston, ON, Canada
e-mail: kunz@queensu.ca

G. Zheng et al. (eds.), *Intelligent Orthopaedics*, Advances in Experimental Medicine and Biology 1093, https://doi.org/10.1007/978-981-13-1396-7_18

plan a suitable approach and help to transfer this plan into their surgical actions [3]. This basic workflow for an image-guided intervention is still used today in many orthopaedic interventions.

In general, image-guided surgery provides a link between a plan based on an image of the affected anatomy and the intraoperative action of the surgeon. The challenge in every image-guided procedure is to link the intraoperative situation to the medical image of the affected anatomy. This step requires a registration of the real anatomy to the representation of the anatomy in the image. In traditional image-guided interventions, this 2D (x-ray) to 3D (anatomy) registration is performed by the surgeon and relies on his or her clinical expertise.

In the early 1990s, computer-assisted surgery (CAS) systems were introduced for orthopaedic applications. CAS systems are image-guided surgery systems in which the link between image and anatomy is created using a navigator. CAS systems can be classified as freehand systems or instrument-guided systems. This characterization is based on the style of the instrument handling. In freehand systems the surgeon is guiding the surgical instrument, and the CAS system is providing visual feedback to navigate the instrument position and trajectory. In instrument-guided systems, the surgical tool is physically guided by the CAS system. Robotic-assisted systems are one example of such instrument-guided CAS systems.

A novel method of instrument-guided computer-assisted surgery was introduced in 1998 by Prof. Rademacher [4]. Patient-specific instrument guides, also known as patient-specific guides, or patient-specific instrumentations, provide a unique way of registration. While "conventional" CAS systems registration is performed by applying computer algorithms intraoperatively to virtually align the image with the anatomy, in patient-specific instrument guides, the registration is structurally integrated into a physical component of an instrument guide.

The basic steps for the patient-specific instrument-guided procedure are image acquisition, surgical planning, surgical guide design and creation, registration and instrument tracking.

In the image acquisition step, a 3D image (computed tomography (CT) or magnetic resonance imaging (MRI)) of the affected anatomy is obtained, and image analysis methods are applied to create 3D isosurface models of the anatomy (Fig. 18.1a). Using these 3D models, a surgical plan is generated. Depending on the surgical intervention, this plan may contain entrance point, trajectory and/or insertion depth of one or more surgical instruments. Furthermore, for arthroplasty cases, the type and size of prosthesis components may be planned (Fig. 18.1b). Surgical planning and 3D isosurface anatomical models are then used to design a patient-specific instrument guide. Each guide contains one or more registration components, as well as one or more tool guidance components. The registration component(s) are shaped to fit uniquely onto areas of the 3D anatomical model which will be accessible during the surgical intervention. To ensure a stable and unique registration, anatomical areas with distinct features are chosen, such as bone protuberances or unique curvatures. Instrument guidance components (such as cylinders or slots) are integrated into the guide in such a way to reproduce the surgical planning (Fig. 18.1c). A physical model of the patient-specific instrument guide is created using prototyping technology. The majority of patient-specific instrument guides are currently produced using an additive manufacturing process, also referred to as 3D printing, in which a part is created by depositing material, layer-by-layer [5]. These guides are then packaged, and sterilized, and sent to the surgery room. During the surgery, a surgical exposure is performed, and the guide is fitted to the corresponding anatomical surface (Fig. 18.1d). With the guide in the predefined (registered) position on the anatomy, surgical instruments are navigated using the guidance components in the guide (Fig. 18.1e). After all tools are navigated, the guide is removed from the anatomy and discarded.

Although the implementation of tool navigation in patient-specific instrument guides is very different to the above-mentioned robotic CAS systems, both systems can be classified as instrument-guided CAS systems. In both meth-

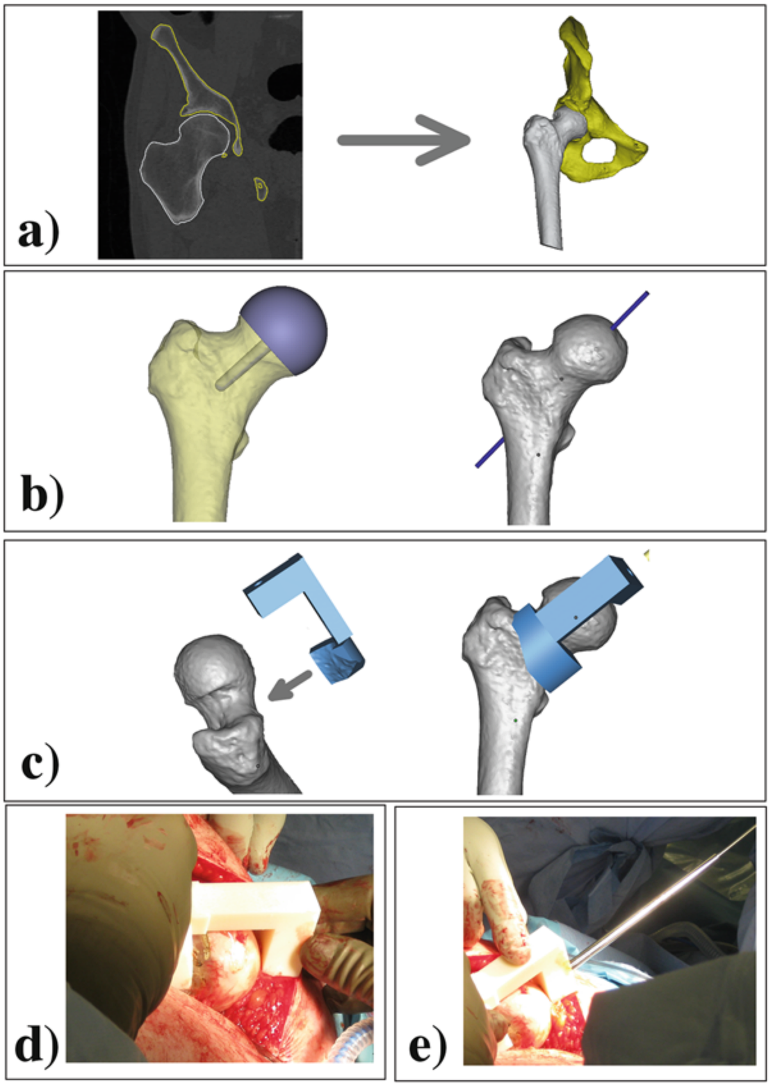

Fig. 18.1 Basic steps for patient-specific instrument-guided procedures. This example shows a patient-specific guide for the femoral central pin placement during a hip resurfacing procedure: (**a**) segmentation and 3D model generation from a preoperative CT scan; (**b**) surgical planning of component size and central pin alignment; (**c**) guide design, surface area around the femoral neck is used to register the guide to the anatomy; (**d**) intraoperative registration of the patient-specific instrument guides; (**e**) a medially attached guidance component is used to drill the pin into the bone following the preoperative planned central pin trajectory

ods, the surgeon manually performs the registration: in robotic-CAS systems, by selecting and digitizing appropriate anatomical features; in patient-specific instrument guides, by fitting the guide to the corresponding anatomical surface. Following registration, in both systems, the surgical tool(s) are guided along a preoperatively defined tool trajectory.

Currently, the majority of applications for patient-specific guides are in total knee arthroplasty. Other applications include hip and shoulder arthroplasty, osteotomies, and cartilage repair. In the following sections, we will focus on knee applications. We will also examine the effect of patient-specific instrument guides on operating room efficiency, costs and infection rates. We will conclude this chapter with a discussion of challenges and future developments in the area of patient-specific instrument guides.

18.2 Patient-Specific Instrument Guides for Total Knee Arthroplasty

Total knee arthroplasty (TKA) is a well-established surgical treatment for patients with advanced knee osteoarthritis. It is predicted that the number of primary TKA cases in the USA will be over 1.3 Million in 2020, which reflects a 300% increase compared to 2005 [6]. Other countries predict a similar increase in demand for this procedure [7, 8]. Although the complication rate for the procedure is considered low, due to the number of procedures performed, revision surgeries are still a burden for healthcare systems.

The malalignment of prosthesis components during the surgical intervention is considered a major factor for implant failure. In particular, outliers in the overall coronal leg alignment are associated with a higher rate of revisions compared to well-aligned knees [9]. Computer-assisted surgery systems are applied to TKA procedures with the goal of increasing the accuracy and reliability in prosthesis component alignment. CAS systems for TKA procedures were introduced by Delp et al. in 1998 [10]. Although many studies have shown an improvement in component alignment using CAS as compared to conventional TKA procedures [10], their effect on the long-term success of the procedure has prompted controversial discussion for many years. However, in 2016, the Australian National Joint Registry reviewed their long-term results and reported a significant decrease in revisions for the CAS-TKA system relative to conventional TKA procedures [11], indicating that the improved component alignment resulted in a better long-term clinical outcome.

The application of patient-specific instrument guides for TKA has seen rapid growth in recent years. Various commercial products implement the concept of patient-specific instrument guides for TKA cases. The current leading products on the market are the PSI Knee System and the Signature System from Zimmer Biomet (Warsaw, IN, USA), the TruMatch Personalized Solution from DePuy Synthes (Warsaw, IN, USA) and the Visionaire Patient Matched Instrumentation from Smith & Nephew (London, UK).

In general, patient-specific instrumentations for the TKA procedure contain a set of two patient-specific guides: one femur and one tibial guide. These guides are designed to be used with standard surgical approaches, such as medial parapatellar arthrotomy. The registration surface of the femur guides contains part of the anterior ridge as well as part of the distal condyles. The tibia guides are fitted to the anterior medial tibial cortex and medial and/or lateral plateaus.

Patient-specific instrument guides in TKA are employed to navigate the femoral and tibial bony resections. The guidance components contain either slots to directly navigate the saw to perform these bony cuts or contain cylinders to navigate the insertion of pins. These pins are then used to position a standard prosthesis cutting block onto the bone, which subsequently guides the saw for the bony resections.

In recent years, various studies have reported on the short- and midterm outcomes of patient-specific guided TKAs compared to conventional TKA procedures. So far, there is no common conclusion as to whether the guides provide higher accuracy and/or precision in achieving optimal prosthesis component alignment. While some studies found that patient-specific instrument guided cases had a significantly better and/or more reliable overall leg alignment [12–17], other studies did not find a significant difference in the neutral leg alignment [18–24]. Similarly, some studies found that the use of patient-specific instrument guides increased the accuracy and/or reliability for femoral component rotation [25–27], while other studies did not see a significant difference in femoral component rotation between the use of patient-specific instrument guides and the conventional technique [28, 29]. Some studies have found that the application of patient-specific instrument guides might result in less accurate and reliable alignment for the tibial component [21, 30]. On the other hand, Heyse et al. found that the use of patient-specific instrument guides improved the tibial component rotation significantly compared to conventional technique [31]. Sliva et al. and Ng et al. found significantly smaller deviations for tibial component rotation using patient-specific guides [25, 32].

Notably, only a minority of the above-mentioned studies used a 3D image modality, such as CT or MRI, for the postoperative evaluation of the alignment errors [14, 15, 22, 25, 27, 31, 32]. More often, the measurements were performed on plain radiographs and might be affected by projection errors.

The majority of studies have reported no significant differences in patient-reported short- or midterm clinical outcomes. However, Nabavi et al. published significantly higher Oxford Knee Scores in the 1-year postoperative follow-up for patients treated with patient-specific instrument guides compared to conventional instruments [33].

Unlike conventional TKA instrumentations, patient-specific instrument guides do not require the opening of the femoral intramedullary canal. This, together with the reduced surgery time discussed below, is believed to be the reason for significantly reduced blood loss, which some researchers observed when comparing conventional and patient-specific guided procedures [33–36].

Commercial patient-specific instrument guide systems for TKA procedures use either MRI or CT scans as preoperative image modalities. The authors of a recently published meta-analysis concluded that CT-based guides had a slightly but significantly higher incidence rate of outliers in the coronal overall limb alignment compared to MRI-based guides [37].

Many authors of the above-mentioned studies discussed limitations, including low case numbers, single-surgeon observations and absent long-term evaluations. Further studies are required to fully evaluate the effect of patient-specific instrument guides on the clinical outcome for total knee arthroplasties.

18.3 Operating Room Efficiency, Cost and Infections

Although the effect of patient-specific instrument guides on postoperative alignment of prosthesis components is still uncertain, there is less controversy about the effect of these guides on the operating room efficiency.

Studies have shown a significant decrease of surgical time compared to conventional procedures [12, 13, 23, 24, 35, 38–41]. The average decrease in surgical time varied between 3 min [23] and 18.5 min [12]. Some authors also reported a significant decrease in the overall operating room time, ranging between 8.6 min [13] and 20.4 min [38].

In contrast, Hamilton et al. did not find a significant decrease in surgical time, but did report a significant decrease in the number of surgical trays opened during the procedure. The group measured the average number of trays opened during a conventional procedure as 7.3, which was significantly reduced to 2.5 using patient-specific guides [42]. Significant reductions of opened trays during the surgery were also found by other researchers [13, 17, 29].

Conventional instrumentations for performing bone resections during TKA procedures adapt to differences between patients by accommodating instruments and instrument parts of various sizes, angles, distances etc. Often, these instruments are modular, requiring assembly in the operating room. Patient-specific instrument guides make many of the conventional instruments obsolete, simplifying and streamlining the intraoperative procedure. These changes are reflected in the published reduction in surgical time and number of trays opened during the procedure.

The correlation between the number of opened trays during the surgery and a faster room turnover time was measured in a study by DeHaan et al. [38]. The authors of this study found that the average turnover time for conventional TKA surgery was significantly reduced from 21.6 min to 15.2 min using patient-specific instrument guides. DeHaan and co-authors also analysed the costs and savings associated with patient-specific instrument guides for TKA surgeries in a single US institution. Added costs for patient-specific guides, including preoperative imaging and the guide itself, were documented to be in a range of \$930–\$1860. The average cost saving was calculated as \$1566 per case, which included the savings from reduced operating room time and sterilization of fewer trays. The authors concluded that, depending upon which imaging centre is used, the use of patient-specific instrument guides for TKA procedures can result in significant cost savings.

A more comprehensive cost analysis was performed by Tibesku et al. using an activity-based costing model [43]. The authors of this study also concluded that the additional costs per case for the guide and the preoperative imaging were offset by an increase in the efficiency of the procedure which led to cost savings due to reduction in OR time and reduced surgical tray utilization. The activity-based cost model applied by the authors of this study showed an annual OR time savings of 10,500 min. By utilizing these gains in OR time to perform surgeries other than TKA, the model estimated the additional gross margin for the hospital per year as 78,240 Euros. The study concluded that if saved OR time can be used effectively to perform additional procedures, the use of patient-specific instrument guides can result in incremental revenue for the hospital.

Furthermore, it is speculated that the preoperative planning of prosthesis component sizes might result in decreased storage and loaner costs for instruments, which, in turn, might also result in additional cost savings for the hospital and health-care system.

Due to their individualized character, patient-specific instrument guides are single-use instruments. In general, single-use instruments are considered safer with respect to infection control compared to reusable instruments, since cross-contamination can be avoided [44–46]. The effect of using patient-specific instruments during TKA procedures on the postoperative infection rate should be investigated further, as surgical site contamination can lead to periprosthetic infections, a serious complication with prolonged and expensive treatment [47]. It stands to reason that lowering the infection rate can not only have a huge benefit for the patient but can also result in significant lowering of costs for hospitals and health-care systems.

18.4 Patient-Specific Instrument Guides for Large Osteochondral Cartilage Defect Repair

Clinical studies have demonstrated superior outcomes for osteochondral autologous transplantations (OAT) as a treatment option for osteochondral cartilage defects [48, 49]. In this procedure, one or more autologous osteochondral cylindrical grafts are harvested from minimal weight-bearing areas in the joint and transplanted in a weight-bearing area where cartilage is damaged. Unlike alternative treatment options, OAT is a single-stage treatment with restoration of mature hyaline cartilage and fast native bone-to-bone subchondral healing. On the other hand, various studies have demonstrated the importance of creating a congruent, continuous joint surface when using OAT to optimize outcomes [50, 51]. Donor site accessibility and the variation in the radius of the femoral condyle curvature make re-creation of a congruent joint surface challenging when using multiple small grafts. Furthermore, the limited donor site availability often restricts conventional OAT treatment to lesions less than 4 cm^2 [49]. However, the combination of advances in 3D preoperative planning and accurate and reliable intraoperative guidance also makes this preferred treatment option available for larger defects.

Here we describe a case of a 17-year old woman with a 6.9 cm^2 full-thickness cartilage defect in the medial femoral condyle of her right knee, who was treated with a patient-specific instrument-guided OAT procedure. Prior to the surgery, a CT arthrogram scan of the treatment knee was obtained. Three-dimensional surface models of the bony anatomy and the cartilage were created (Fig. 18.2).

These models were imported into our custom-designed image-guided planning software [52]. In consultation with the orthopaedic surgeon, a

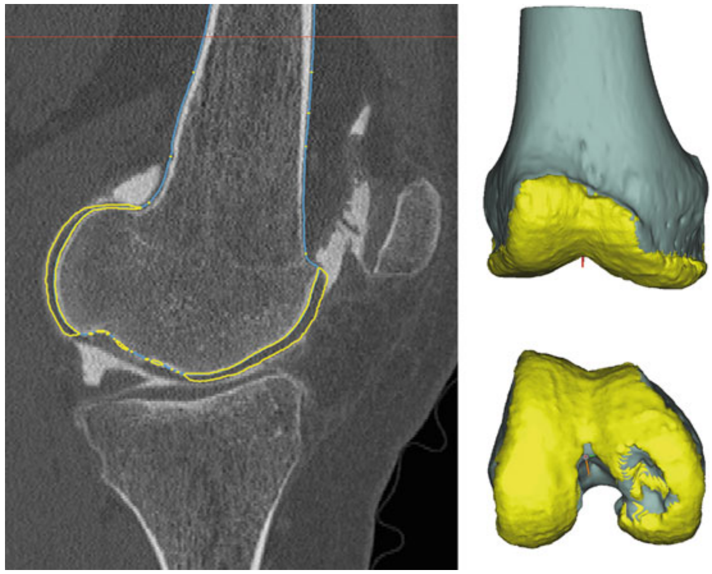

Fig. 18.2 Left side shows a sagittal CT arthrogram slice of the medial condyle. Blue contours mark the outline of bone; yellow contours mark the outline of cartilage. Right side shows the isosurface models for bone and cartilage created from the segmented CT arthrogram

patient-specific surgical plan was developed. The surgical plan consisted of a set of five osteochondral grafts (plugs) positioned in the defect site and their corresponding harvest sites. The plugs could be rotated axially allowing the sloped surface at the harvest site to match that of the defect site. Furthermore, by displaying the bone and/or cartilage 3D model transparently, the bone plug interference in the recipient and harvest sites could be identified and corrected. Based on the intraoperatively available harvest and delivery tools, plug diameters were planned with three plugs with a diameter of 10 mm and two plugs with an 8 mm diameter. Figure 18.3 shows the final surgical plan.

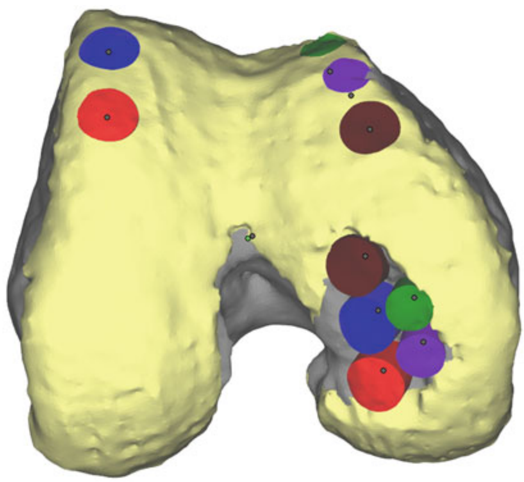

Fig. 18.3 A set of 3 × 10 mm and 2 × 8 mm grafts were planned. For each graft, the planned harvest site and corresponding recipient site are marked with the identical colour

Using the patient's surgical plan, a set of individualized guides were designed and prototype printed using a thermoplastic ABS material. For each osteochondral graft in the surgical plan, a guide was constructed containing the following three components: a positioning template, a harvest guide cylinder and a delivery guide cylinder (Fig. 18.4).

The undersides of the positioning templates were shaped to the surface of the femoral condyles surrounding the defect as well as the patellar groove and were designed to fit into a conventional surgical exposure of the knee (Fig. 18.4-1). For the preparation of the delivery site, a guide cylinder was positioned directly over the planned recipient site (Fig. 18.4-2), which guided a chisel tool to prepare the cylindrical recipient hole. A harvest guide cylinder was integrated into the template to allow positioning and orienting of a conventional harvester over the planned harvest site (Fig. 18.4-3). The delivery of the harvested graft plug was guided through the delivery guide cylinder (Fig. 18.4-4). Small

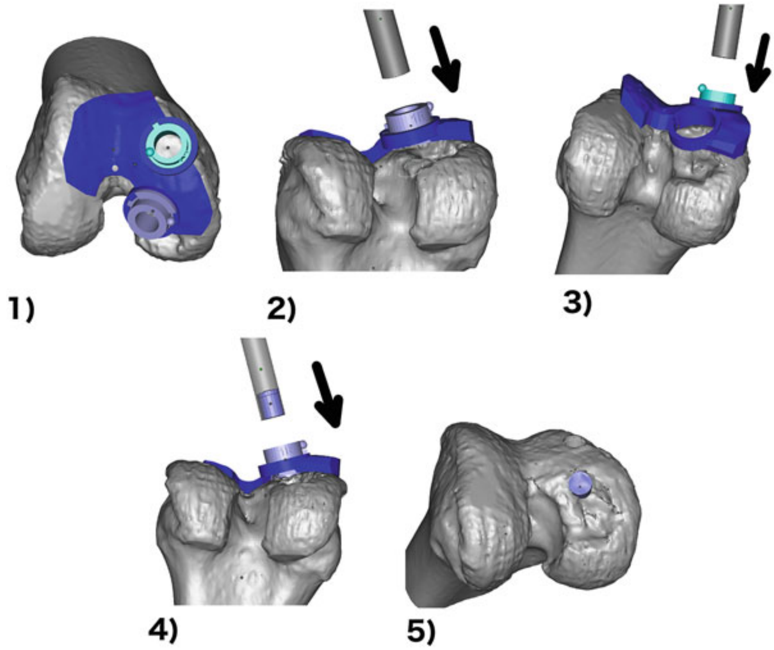

Fig. 18.4 Patient-specific instrument-guided harvesting and delivery of one osteochondral graft

spherical rotation marks attached to the harvest cylinder, as well as the delivery cylinder, allowed insertion of the graft following the planned rotation and ensured that the slope of the graft consistent with the medial condyle curvature. To ensure that the prepared delivery hole and the height of the cylinder matched, the depth of the chisel insertion was navigated using a predefined mark on the chisel tool. The planned depth of tool insertion was reached when this mark was aligned with the top of the guidance cylinder.

After delivery of the graft, the patient-specific instrument guide was removed (Fig. 18.4-5). The same procedure was repeated for the remaining four grafts, each with their own specific guide tool.

Preoperatively, as well as 3 months, 6 months and 1 year postoperatively, the patient documented pain and function using the Knee Injury and Osteoarthritis Outcome Score (KOOS) and the Western Ontario and McMaster Universities Osteoarthritis index (WOMAC). Figure 18.5 shows the KOOS sub-scores for symptoms, knee-related quality of life, pain, function in daily living (ADL) and function in sports and recreation (Sportsrec). Overall, the sub-scores showed a continuous improvement during the follow-up period. Similarly, the WOMAC sub-scores[1] for pain, stiffness and function showed a steady improvement over the 1-year postoperative follow-up time.

Using conventional surgical techniques, OAT is considered technically demanding for larger lesions due to the potential for incongruous surface, gapping between the plugs with fibrocartilaginous fill and donor site morbidity [49]. Therefore, it is often only used to treat defects which can be filled with two to three plugs. By using accurate and high-resolution 3D preoperative images, combined with medical image analysis methods, a precise and careful preoperative planning of plug position, orientation and optimal harvest sides can be performed.

Such virtual planning can provide unique features, such as investigation of graft intersections, and measurements for defect coverage. Furthermore, a preoperative planning allows for a trial-and-repeat process to establish an optimal graft pattern, which is impossible in an ad hoc surgical approach. We have shown in an earlier study that our preoperative planning

[1] Sub-scores were transformed to a 0–100 scale, with higher scores reflecting better quality of life.

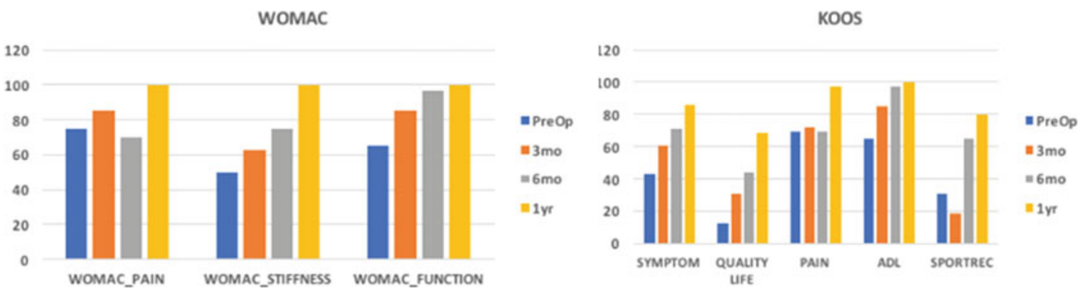

Fig. 18.5 WOMAC and KOOS sub-scores for preoperative, 3-month, 6-month and 1-year postoperative evaluations

can achieve reproduction of natural cartilage curvature with an Root Mean Square (RMS) error of 0.31 mm, a defect coverage of 84% and an overlap between the graft plugs of 16% [52]. In the same study, we were also able to show that large parts of the planning procedure can be performed automatically with similar or better results than those of a human operator with substantially faster planning time.

After creating a preoperative plan which optimizes the use of available harvest areas, patient-specific instrument guides were employed to precisely transfer this plan into the intraoperative situation. By using guidance cylinders, combined with rotational marks and depth navigation, it was possible to guide tool trajectories with 6 degrees of freedom. Accuracy and precision of this patient-specific instrument-guided technique was investigated in a laboratory study [53]. By using patient-specific guides, it was found that the surgeons were able to significantly more accurately reconstruct surface congruency over the defect, have better coverage of the defect area and reduce the number of grafts which were proud or recessed compared to using the conventional surgical technique. Furthermore, the patient-specific instrument-guided procedures were significantly faster, not only compared to the conventional technique but also compared to a freehand CAS method. An animal trial showed that this higher accuracy and precision during the intraoperative procedure directly related to a better short-term healing response in the transplanted cartilage [54]. Both of these studies have shown that the patient-specific instrument-guided methods were comparable to freehand CAS methods with respect to accurate reconstruction of the cartilage surface over the defect. However, differences between the two CAS systems were seen with respect to procedure time, which was significantly longer for the freehand CAS system. Furthermore, the animal trial revealed a significantly smaller cyst volume in the patient-specific instrument-guided group compared to the conventional, a difference which was not observed for the freehand CAS group. It is considered that subchondral cysts might be the result of synovial fluid penetrating into the gap between the graft and the subchondral bone. Since patient-specific instrument guides are an instrument-guided CAS system, which holds the chisel tool or drill in a steady trajectory during the preparation of the delivery hole, it may provide a more tightly fitting plug, reducing the fluid penetration. With the conventional and freehand CAS-guided techniques, the tools are hand-held without external support and can result in a hole that is less cylindrical.

A unique combination of preoperative planning and easy-to-use and precise intraoperative guidance provides the ability to extend the technically demanding procedure of OAT to patients with larger defects of over 4 cm^2.

18.5 Other Applications for Patient-Specific Instrument Guides for Orthopaedic Interventions

About 10 years ago, rapid prototype technology started to be more widely available, which accelerated the research and development in patient-specific instrument guides. Around the same time, newly developed materials proved to significantly increase the long-term survival rate of hip resurfacing implants, which created a renewed interest in using hip resurfacing arthroplasty (HRA) as a treatment option for hip osteoarthritis. However, HRA is deemed a technically challenging procedure with a significant learning curve [55], and interest in image-guided methods for HRA procedures were soon expressed. Consequentially, researchers saw the opportunity to introduce patient-specific instrument guides for HRA procedures. The preparation of the proximal femur and the resulting alignment of the femur component allow for only a small margin of error, and the majority of patient-specific instrument guides in hip resurfacing are designed to navigate femoral component placement. In hip resurfacing systems, the placement of the femoral central pin (also known as the guide wire) is a crucial step for the accuracy of femoral component alignment since it identifies the final femoral component orientation, as well as 2 of the 3 degrees of freedom for femoral component positioning. Various research groups have published methods and results for patient-specific femoral central pin guidance tools. Figure 18.1 shows a patient-specific guide for the femoral central pin placement. We tested the accuracy of this patient-specific guide design in various studies [56, 57] and found in the most recent study that the alignment error for the central pin was 0.05° in the frontal plane and 2.8° in the transverse plane. We found errors in the entrance point for the central pin of 0.47 mm in the frontal plane and 2.6 mm in the transverse plane. Other research groups have compared similar patient-specific instrument-guided solutions to conventional central pin placements techniques and found significantly improved accuracy for the patient-specific guided pins [58–60].

Recently, researchers have also proposed and evaluated solutions for patient-specific instrument guides for total hip replacement (THR). Various groups developed and tested patient-specific instrument guides for acetabular cup placement [61–65]. When compared with conventional surgical methods, these guides have shown to significantly improve acetabulum cup alignment [61, 62, 65]. Similarly, patient-specific instrument guides which were developed to navigate the femoral stem placement showed improved precision compared to conventional methods [66, 67].

Other joint arthroplasty applications for patient-specific instrument guides include total shoulder arthroplasty [68–71] and total ankle arthroplasty [72].

Bone abnormalities as a result of trauma or disease may result in pain and limited mobility of the adjacent joints. Osteotomy, a surgical procedure in which a reduction of bone towards a healthy anatomy is performed, is a joint-preserving treatment option for such cases. Osteotomy not only allows for angular correction in three different planes (varus/valgus, extension/flexion and internal/external rotation) but also for displacement correction in three directions (lengthening/shortening, medial/lateral, dorsal/ventral). This 3D complexity means these procedures profit greatly from a 3D planning [73]. Since the misalignments (as a result of fractures or deformities) are unique, each patient also has a unique osteotomy resection(s). It is, therefore, very difficult to provide any "standard guidance" instruments, and conventional procedures rely heavily on intraoperative imaging and surgeon experience. Instead, various research groups have suggested navigating these complex procedures using patient-specific instrument guides and have published promising results in early studies. So far, the suggested applications for patient-specific instrument guides range from lower limb osteotomies [74–76] and upper limb osteotomies [77–79], to osteotomies to improve joint functions [80–85]. Furthermore, patient-specific instrument guides are utilized to navigate pelvic tumour resections to ensure sufficient margin resections as well as to avoid unnecessary loss of joint function [86–89].

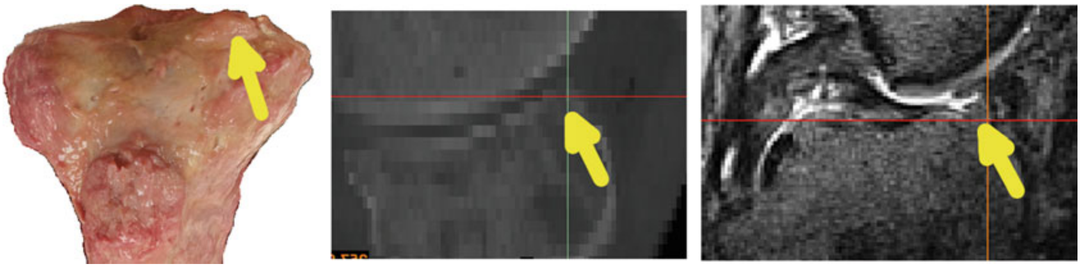

Fig. 18.6 Depiction of a proximal tibia with a partly cartilaginous osteophyte (yellow arrow). Left: dissection of the proximal tibia. Middle: CT slice in sagittal view with 120 KvP voltage and 2.5 mm slice distance. Right: Sagittal T1-weighted MRI slice

18.6 Challenges and Future Work

Patient-specific instrument guides are a relatively newly developed computer-assisted technology, and their application for orthopaedic surgical interventions is in the beginning phase. As with many new developments, patient-specific guides still have some challenges to overcome to achieve a full transition into routine clinical use. In this section, we will discuss some of these limitations and some future and current work which may overcome these challenges.

18.7 Preoperative Image Modalities

Patient-specific instrument guides rely on a preoperative 3D model of the affected anatomy which accurately represents the patient's anatomy, especially in the registration areas. The bases for such accurate models are medical images of the anatomy which depict the anatomical surface exactly. Particularly in patients with osteoarthritis, this consideration might be critical, because the disease is characterized by the breakdown of articular cartilage accompanied by the changing of local bone anatomy [90]. One example of such bone alterations is the development of osteophytes – abnormal osteocartilaginous tissue that grows along joint borders [91]. Their high variability in density and composition might interfere with an accurate depiction in medical image modalities.

Figure 18.6 shows the depiction of a partly cartilaginous osteophyte on a proximal tibia (left), in a CT scan (middle), and a MRI scan (right).

Various studies have hypothesized that osteophytes may be related to increased postoperative errors for image-guided interventions. In an accuracy study for patient-specific instrument-guided total knee arthroplasties, Seon et al. suggested that outliers resulted from large osteophytes which interfered with the fit of the guide [92]. An observational study on patient-specific guides for hip resurfacing procedures found that osteophytes, not accurately identified in a preoperative CT scan with standard segmentation protocols, could potentially result in errors up to 2.8° between the planned and final achieved tool trajectories [93]. Results for this study also showed that 78% of the surface points collected from osteophytes were depicted in the CT scan with a Hounsfield unit below the usual bone threshold and would therefore be missed with segmentation methods using the standard threshold.

In addition to osteophytes, motion artefacts during image acquisition might result in insufficient image quality. Kosse et al. reported that 4% of the patients had visible motion artefacts in the preoperatively acquired MRIs and needed to be excluded from the study [28]. All of these studies indicate that future work in the careful selection of image modalities, custom-made imaging protocols, as well as improved segmentation protocols might improve the reliability of patient-specific instrument guides. It can be speculated that inaccurate depiction of the anatomy might be the reason for some of the reported outliers in the above-mentioned clinical follow-up studies.

Some researchers have raised concerns about the requirement of preoperative CT or MRI scans due to the additional cost, time and radiation exposure [18, 94]. Cerveri et al. published early results of a feasibility study to replace the preoperative 3D image with 2 to 5 x-rays [95]. The authors proposed a method in which these x-ray images of a patient are used to morph a statistical shape atlas for a distal femur with severe cartilage damage into a patient-specific model. The results of this feasibility study are promising, and future work in this area might eliminate or reduce the need for costly and/or invasive preoperative imaging.

18.8 Preoperative Planning

Patient-specific instrument guides are a tool to transfer preoperatively planned resections into the surgical situation. As such, the quality of the preoperative planning plays an important role in the postoperative outcome of the procedure and should be performed with great care by the surgeon. Although many commercial systems provide an "initial plan" based on image analysis for tibial and femoral resection, these plans might not reflect optimal outcome from a clinical point of view. A study found that 91.1% of initial plans for patient-specific instrument-guided TKA procedures required at least one correction by the surgeon [96]. A similar study found that surgeons corrected the initial plan for the size of the femoral component in 16% of the cases and the size of the tibial component in 48% of the cases. The initial planned rotation for the tibial component was changed by the surgeon in all of the 50 investigated cases (100%), and the initial planned flexion of the femoral component was manipulated by the surgeon in 46% of cases [97]. Goyal and Stulberg evaluated the precision of surgical planning systems for patient-specific instrumented TKA by comparing plans from two different commercial systems and found significant differences in the determination of the mechanical axis, in the planning of femoral and tibial component sizes, as well as in the resection heights of four of the six bone resections [98].

The findings of these studies show that future developments into more advanced preoperative planning methods might help to improve the clinical translation for patient-specific instrument guides.

18.9 Intraoperative Validation

An important step for every computer-assisted surgery system is the registration between the intraoperative instrument position and the medical image used for planning. In patient-specific instrument guides, this registration is achieved by fitting the guide to the corresponding anatomical surface during the surgical intervention. An accurate fit between guide and anatomy depends on many factors, including the accuracy of the preoperative images of the anatomy as discussed above. Furthermore, the design of the registration component might influence the fit of the guide. The selected anatomical registration areas need to be not only accurately depicted but also must have a sufficient number of registration features. Kwon et al. published the results of a comparison study between two different patient-specific instrument guide designs for TKA and found that minor expansions of the registration area for both guides (femur and tibia) resulted in an improved rotational stability of these guides. This improved fit directly translated into better alignment of the prosthesis components and shorter surgery times [12]. However, an expansion to a larger registration area is not always clinically feasible or desired. For example, increasing the registration area of a tibial cutting guide during a TKA procedure would require removal of larger parts of the tuberosity. Such increase in invasiveness could directly affect the recovery time of the patient. Furthermore, larger registration areas do not necessarily guarantee improved fit of the guide. A study on patient-specific guides for hip resurfacing showed an improvement in tool guidance accuracy when the registration surface of the guide was reduced [57]. In this study, articular surface and osteophyte-prone areas were removed, which resulted in a decrease of depiction uncertainty. Selection of the optimal registration surface is currently made by researchers and technicians manually. However, promising research in this area could provide mathematical methods to support this part of the guide design process. Van den Broeck et al. published an algorithm to analyse the registration stability of guides based on the anatomical geometry [99]. Such methods might help to optimize guide designs preoperatively in the future.

18.10 Summary and Conclusions

Patient-specific instrument guides are a unique way of performing computer-assisted orthopaedic surgeries, in which a prototype-printed part is the navigator which links a preoperative plan to surgical action. Similar to other CAS systems, the guides rely on an accurate 3D preoperative image of the affected anatomy, a clinically optimal surgical plan, a reliable registration procedure and a precise tool guidance method.

Prototype technologies are currently one of the most rapidly advancing new technologies. Patient-specific instrument guides take advantage of these innovations without the need to bring new technology into the surgery room. This simplifies clinical transition for these guides. For a hospital, no great initial investments are required to purchase equipment and/or hire technical staff.

Unlike other CAS solutions, patient-specific instrument guides have shown to improve efficiency in the surgery room, and there are good indications that these guides can achieve cost savings. In a time where health-care costs are steadily rising and the number of orthopaedic procedures is expected to multiply in coming years, it is sensible to also evaluate the economic benefit of new technologies.

Orthopaedic surgery and computer-assisted orthopaedic surgery are rapidly evolving fields, with new developments and discoveries frequently improving current methods and standards. Such developments include novel prosthesis designs, new recommendations for component positioning and new and improved algorithms for segmentation or registration. An advantage of patient-specific instrument guides is a seamless integration of changes into the clinical routine. While freehand and robotic CAS systems often require software and/or hardware updates to implement new or improved features, for users of patient-specific instrument guides, no update procedure is necessary. For these users, evidence of change is having an improved guide delivered to the surgery room.

Patient-specific instrument guides require sufficient access to the registration area of the anatomy. Therefore, for minimally invasive procedures, patient-specific instrument guides are not the optimal image-guided technology. For example, the articular cartilage repair case we presented above was chosen because of the very large defect size. Large defects require extensive access to harvest sites and are therefore not candidates for arthroscopic procedures. Consequently, patient-specific guides were an optimal navigation method. Smaller cartilage defects are more likely treated in an arthroscopic manner, and freehand or robotic CAS systems are better options for intraoperative navigation for these cases. Another limitation in the use of patient-specific instrument guides is the requirement of a final preoperative planning of instrument trajectories. In contrast, freehand CAS systems can provide intraoperative planning methods, which might allow the surgeon to adapt to a situation which can only be sufficiently judged intraoperatively.

In general, we believe that the easy integration of patient-specific instrument guides into operating room procedures as discussed above is a major advantage of this CAS method. However, it also makes this relatively new technology vulnerable to an insufficient research period. Many hospitals have adapted the technology for TKA procedures and have published early results. Although motivation to integrate this new method into clinical practice is encouraging, results should be seen as possible input into further improvements and not necessarily as "make-or-break" validation studies. Kwon et al. described their experiences with patient-specific instrument guides for TKA procedures before and after small modifications were made to the guides' designs and found that these small changes in the second generation of guides significantly improved axis alignment and surgical time [12]. Similarly, we found that changes in the guide design for hip resurfacing procedures improved our accuracy from 4.5° [56] in the transverse plane to 2.8° [57]. There might not be much of a learning curve in the application of the guide for the surgeon and operating room team, but there might be a learning curve for researchers and technicians in the design of the guides. Effects of this learning curve might only be evident in a delayed reaction in the clinical outcome.

In conclusion, patient-specific instrument guides provide a method to 3D plan a surgical intervention and transfer this plan into the surgical field in an effective, user-friendly and time- and instrument-efficient way.

References

1. Toledo-Pereyra LH (2009) X-rays surgical revolution. J Investig Surg 22(5):327–332
2. Hagy M (2004) "Keeping up with the Joneses"–the story of Sir Robert Jones and Sir Reginald Watson-Jones. Iowa Orthop J 24:133–137
3. Azagury DE, Dua MM, Barrese JC, Henderson JM, Buchs NC, Ris F, Cloyd JM, Martinie JB, Razzaque S, Nicolau S, Soler L, Marescaux J, Visser BC (2015) Image-guided surgery. Curr Probl Surg 52(12):476–520. https://doi.org/10.1067/j.cpsurg.2015.1010.1001 Epub 2015 Oct 1022
4. Radermacher K, Portheine F, Anton M, Zimolong A, Kaspers G, Rau G, Staudte HW (1998) Computer assisted orthopaedic surgery with image based individual templates. Clin Orthop Relat Res 354:28–38
5. Conner BP, Manogharan GP, Martof AN, Rodomsky LM, Rodomsky CM Jordan DC. Limperos JW 1-4:64. https://doi.org/10.1016/j.addma.2014.08.005
6. Kurtz SM, Ong KL, Lau E, Bozic KJ (2014) Impact of the economic downturn on total joint replacement demand in the United States: updated projections to 2021. J Bone Joint Surg Am 96(8):624–630. https://doi.org/10.2106/JBJS.M.00285
7. Nemes S, Rolfson O, Annette WD, Garellick G, Sundberg M, Karrholm J, Robertsson O (2015) Historical view and future demand for knee arthroplasty in Sweden. Acta Orthop 86(4):426–431. https://doi.org/10.3109/17453674.17452015.11034608 Epub 17452015 Mar 17453625
8. Patel A, Pavlou G, Mujica-Mota RE, Toms AD (2015) The epidemiology of revision total knee and hip arthroplasty in England and Wales: a comparative analysis with projections for the United States. A study using the National Joint Registry dataset. Bone Joint J 97-B(8):1076–1081. https://doi.org/10.1302/0301-1620X.1097B1078.35170
9. Fang DM, Ritter MA, Davis KE (2009) Coronal alignment in total knee arthroplasty: just how important is it? J Arthroplasty 24(Suppl 6):39–43. https://doi.org/10.1016/j.arth.2009.1004.1034 Epub 2009 Jun 1024
10. Delp SL, Stulberg SD, Davies B, Picard F, Leitner F (1998) Computer assisted knee replacement. Clin Orthop Relat Res 354:49–56
11. https://aoanjrr.sahmri.com/annual-reports-2016. (2016). Accessed 7 Dec 2017
12. Kwon OR, Kang KT, Son J, Suh DS, Heo DB, Koh YG (2017) Patient-specific instrumentation development in TKA: 1st and 2nd generation designs in comparison with conventional instrumentation. Arch Orthop Trauma Surg 137(1):111–118. https://doi.org/10.1007/s00402-00016-02618-00402 Epub 02016 Dec 00422
13. Renson L, Poilvache P, Van den Wyngaert H (2014) Improved alignment and operating room efficiency with patient-specific instrumentation for TKA. Knee 21(6):1216–1220. https://doi.org/10.1016/j.knee.2014.1209.1008 Epub 2014 Oct 1230
14. Anderl W, Pauzenberger L, Kolblinger R, Kiesselbach G, Brandl G, Laky B, Kriegleder B, Heuberer P, Schwameis E (2016) Patient-specific instrumentation improved mechanical alignment, while early clinical outcome was comparable to conventional instrumentation in TKA. Knee Surg Sports Traumatol Arthrosc 24(1):102–111. https://doi.org/10.1007/s00167-00014-03345-00162 Epub 02014 Oct 00119
15. Pfitzner T, Abdel MP, von Roth P, Perka C, Hommel H (2014) Small improvements in mechanical axis alignment achieved with MRI versus CT-based patient-specific instruments in TKA: a randomized clinical trial. Clin Orthop Relat Res 472(10):2913–2922. https://doi.org/10.1007/s11999-11014-13784-11996 Epub 12014 Jul 11915
16. Ivie CB, Probst PJ, Bal AK, Stannard JT, Crist BD, Sonny Bal B (2014) Improved radiographic outcomes with patient-specific total knee arthroplasty. J Arthroplasty 29(11):2100–2103. https://doi.org/10.1016/j.arth.2014.2106.2024 Epub 2014 Jun 2128
17. Noble JW Jr, Moore CA, Liu N (2012) The value of patient-matched instrumentation in total knee arthroplasty. J Arthroplasty 27(1):153–155. https://doi.org/10.1016/j.arth.2011.1007.1006 Epub 2011 Sep 1019

18. Zhu M, Chen JY, Chong HC, Yew AKS, Foo LSS, Chia SL, Lo NN, Yeo SJ (2017) Outcomes following total knee arthroplasty with CT-based patient-specific instrumentation. Knee Surg Sports Traumatol Arthrosc 25(8):2567–2572. https://doi.org/10.1007/s00167-00015-03803-00165 Epub 02015 Sep 00126
19. Sharareh B, Schwarzkopf R (2015) Review article: patient-specific versus standard instrumentation for total knee arthroplasty. J Orthop Surg (Hong Kong) 23(1):100–106. https://doi.org/10.1177/230949901502300123
20. Mannan A, Smith TO, Sagar C, London NJ, Molitor PJ (2015) No demonstrable benefit for coronal alignment outcomes in PSI knee arthroplasty: a systematic review and meta-analysis. Orthop Traumatol Surg Res 101(4):461–468. https://doi.org/10.1016/j.otsr.2014.1012.1018 Epub 2015 Mar 1020
21. Shen C, Tang ZH, Hu JZ, Zou GY, Xiao RC, Yan DX (2015) Patient-specific instrumentation does not improve accuracy in total knee arthroplasty. Orthopedics 38 (3):e178-e188. https://doi.org/10.3928/01477447-20150305-01477454
22. Nam D, Park A, Stambough JB, Johnson SR, Nunley RM, Barrack RL (2016) The mark Coventry award: custom cutting guides do not improve Total knee arthroplasty clinical outcomes at 2 years Followup. Clin Orthop Relat Res 474(1):40–46. https://doi.org/10.1007/s11999-11015-14216-y
23. Fu H, Wang J, Zhou S, Cheng T, Zhang W, Wang Q, Zhang X (2015) No difference in mechanical alignment and femoral component placement between patient-specific instrumentation and conventional instrumentation in TKA. Knee Surg Sports Traumatol Arthrosc 23(11):3288–3295. https://doi.org/10.1007/s00167-00014-03115-00161 Epub 02014 Jun 00111
24. Nunley RM, Ellison BS, Ruh EL, Williams BM, Foreman K, Ford AD, Barrack RL (2012) Are patient-specific cutting blocks cost-effective for total knee arthroplasty? Clin Orthop Relat Res 470(3):889–894. https://doi.org/10.1007/s11999-11011-12221-11993 Epub 12011 Dec 11920
25. Ng CTJ, Newman S, Harris S, Clarke S, Cobb J (2017) Patient-specific instrumentation improves alignment of lateral unicompartmental knee replacements by novice surgeons. Int Orthop 41(7):1379–1385. https://doi.org/10.1007/s00264-00017-03468-00264 Epub 02017 May 00213
26. Mannan A, Smith TO (2016) Favourable rotational alignment outcomes in PSI knee arthroplasty: a level 1 systematic review and meta-analysis. Knee 23(2):186–190. https://doi.org/10.1016/j.knee.2015.1008.1006 Epub 2016 Jan 1015
27. Heyse TJ, Tibesku CO (2014) Improved femoral component rotation in TKA using patient-specific instrumentation. Knee 21(1):268–271. https://doi.org/10.1016/j.knee.2012.1010.1009 Epub 2012 Nov 1018
28. Kosse NM, Heesterbeek PJC, Schimmel JJP, van Hellemondt GG, Wymenga AB, Defoort KC (2017) Stability and alignment do not improve by using patient-specific instrumentation in total knee arthroplasty: a randomized controlled trial. Knee Surg Sports Traumatol Arthrosc 26:4792–4793
29. Huijbregts HJ, Khan RJ, Sorensen E, Fick DP, Haebich S (2016) Patient-specific instrumentation does not improve radiographic alignment or clinical outcomes after total knee arthroplasty. Acta Orthop 87(4):386–394. https://doi.org/10.1080/17453674.17452016.11193799 Epub 17452016 Jun 17453671
30. Zhang QM, Chen JY, Li H, Chai W, Ni M, Zhang ZD, Yang F (2015) No evidence of superiority in reducing outliers of component alignment for patient-specific instrumentation for total knee arthroplasty: a systematic review. Orthop Surg 7(1):19–25. https://doi.org/10.1111/os.12150
31. Heyse TJ, Tibesku CO (2015) Improved tibial component rotation in TKA using patient-specific instrumentation. Arch Orthop Trauma Surg 135(5):697–701. https://doi.org/10.1007/s00402-00015-02157-00402 Epub 02015 Apr 00401
32. Silva A, Sampaio R, Pinto E (2014) Patient-specific instrumentation improves tibial component rotation in TKA. Knee Surg Sports Traumatol Arthrosc 22(3):636–642. https://doi.org/10.1007/s00167-00013-02639-00160 Epub 02013 Aug 00129
33. Nabavi A, Olwill CM (2015) Early outcome after total knee replacement using computed tomography-based patient-specific cutting blocks versus standard instrumentation. J Orthop Surg (Hong Kong) 23(2):182–184. https://doi.org/10.1177/230949901502300213
34. Leon VJ, Lengua MA, Calvo V, Lison AJ (2017) Use of patient-specific cutting blocks reduces blood loss after total knee arthroplasty. Eur J Orthop Surg Traumatol 27(2):273–277. https://doi.org/10.1007/s00590-00016-01893-00595 Epub 02016 Dec 00520
35. Vide J, Freitas TP, Ramos A, Cruz H, Sousa JP (2017) Patient-specific instrumentation in total knee arthroplasty: simpler, faster and more accurate than standard instrumentation-a randomized controlled trial. Knee Surg Sports Traumatol Arthrosc 25(8):2616–2621. https://doi.org/10.1007/s00167-00015-03869-00160 Epub 02015 Nov 00119
36. Rathod PA, Deshmukh AJ, Cushner FD (2015) Reducing blood loss in bilateral total knee arthroplasty with patient-specific instrumentation. Orthop Clin North Am 46(3):343–350

37. Wu XD, Xiang BY, Schotanus MGM, Liu ZH, Chen Y, Huang W (2017) CT- versus MRI-based patient-specific instrumentation for total knee arthroplasty: a systematic review and meta-analysis. Surgeon 15(6):336–348. https://doi.org/10.1016/j.surge.2017.1006.1002 Epub 2017 Jul 1026
38. DeHaan AM, Adams JR, DeHart ML, Huff TW (2014) Patient-specific versus conventional instrumentation for total knee arthroplasty: peri-operative and cost differences. J Arthroplasty 29(11):2065–2069. https://doi.org/10.1016/j.arth.2014.2006.2019 Epub 2014 Jun 2028
39. Chan WC, Pinder E, Loeffler M (2016) Patient-specific instrumentation versus conventional instrumentation in total knee arthroplasty. J Orthop Surg (Hong Kong) 24(2):175–178. https://doi.org/10.1177/1602400211
40. Chareancholvanich K, Narkbunnam R, Pornrattanamaneewong C (2013) A prospective randomised controlled study of patient-specific cutting guides compared with conventional instrumentation in total knee replacement. Bone Joint J 95-B(3):354–359. https://doi.org/10.1302/0301-1620X.1395B1303.29903
41. Boonen B, Schotanus MG, Kerens B, van der Weegen W, van Drumpt RA, Kort NP (2013) Intra-operative results and radiological outcome of conventional and patient-specific surgery in total knee arthroplasty: a multicentre, randomised controlled trial. Knee Surg Sports Traumatol Arthrosc 21(10):2206–2212. https://doi.org/10.1007/s00167-00013-02620-y Epub 02013 Aug 00169
42. Hamilton WG, Parks NL (2014) Patient-specific instrumentation does not shorten surgical time: a prospective, randomized trial. J Arthroplasty 29(7):1508–1509. https://doi.org/10.1016/j.arth.2014.1501.1029 Epub 2014 Jan 1530
43. Tibesku CO, Hofer P, Portegies W, Ruys CJ, Fennema P (2013) Benefits of using customized instrumentation in total knee arthroplasty: results from an activity-based costing model. Arch Orthop Trauma Surg 133(3):405–411. https://doi.org/10.1007/s00402-00012-01667-00404 Epub 02012 Dec 00415
44. Bhadra AK, Kwiecien GJ, Harwin SF, Johnson AJ, Mont MA, Malkani AL (2012) Procedure simplification: the role of single-use instruments in total knee arthroplasty. Surg Technol Int 22:326–330
45. Siu J, Hill AG, MacCormick AD (2017) Systematic review of reusable versus disposable laparoscopic instruments: costs and safety. ANZ J Surg 87(1–2):28–33. https://doi.org/10.1111/ans.13856. Epub 12016 Nov 13823
46. Litrico S, Recanati G, Gennari A, Maillot C, Saffarini M, Le Huec JC (2016) Single-use instrumentation in posterior lumbar fusion could decrease incidence of surgical site infection: a prospective bi-centric study. Eur J Orthop Surg Traumatol 26(1):21–26. https://doi.org/10.1007/s00590-00015-01692-00594 Epub 02015 Sep 00591
47. Osmon DR, Berbari EF, Berendt AR, Lew D, Zimmerli W, Steckelberg JM, Rao N, Hanssen A, Wilson WR (2013) Executive summary: diagnosis and management of prosthetic joint infection: clinical practice guidelines by the Infectious Diseases Society of America. Clin Infect Dis 56(1):1–10. https://doi.org/10.1093/cid/cis1966
48. Horas U, Pelinkovic D, Herr G, Aigner T, Schnettler R (2003) Autologous chondrocyte implantation and osteochondral cylinder transplantation in cartilage repair of the knee joint. A prospective, comparative trial. J Bone Joint Surg Am 85-A(2):185–192
49. Sherman SL, Thyssen E, Nuelle CW (2017) Osteochondral autologous transplantation. Clin Sports Med 36(3):489–500. https://doi.org/10.1016/j.csm.2017.1002.1006 Epub 2017 Apr 1026
50. Pearce SG, Hurtig MB, Clarnette R, Kalra M, Cowan B, Miniaci A (2001) An investigation of 2 techniques for optimizing joint surface congruency using multiple cylindrical osteochondral autografts. Arthroscopy 17(1):50–55. https://doi.org/10.1053/jars.2001.19966
51. Koh JL, Wirsing K, Lautenschlager E, Zhang LO (2004) The effect of graft height mismatch on contact pressure following osteochondral grafting: a biomechanical study. Am J Sports Med 32(2):317–320. https://doi.org/10.1177/0363546503261730
52. Inoue J, Kunz M, Hurtig MB, Waldman SD, Stewart AJ (2011) Automated planning of computer assisted mosaic arthroplasty. In: Fichtinger G, Martel A, Peters T (eds) Medical image computing and computer-assisted intervention – MICCAI 2011: 14th international conference, Toronto, Canada, September 18–22, 2011, proceedings, Part I. Springer, Berlin/Heidelberg, pp 267–274. https://doi.org/10.1007/978-3-642-23623-5_34
53. Sebastyan S, Kunz M, Stewart AJ, Bardana DD (2016) Image-guided techniques improve accuracy of mosaic arthroplasty. Int J Comput Assist Radiol Surg 11(2):261–269. https://doi.org/10.1007/s11548-11015-11249-11543 Epub 12015 Jul 11547
54. Kunz M, Devlin SM, Hurtig MB, Waldman SD, Rudan JF, Bardana DD, Stewart AJ (2013) Image-guided techniques improve the short-term outcome of autologous osteochondral cartilage repair surgeries: an animal trial. Cartilage 4(2):153–164. https://doi.org/10.1177/1947603512470683
55. Siebel T, Maubach S, Morlock MM (2006) Lessons learned from early clinical experience and results of 300 ASR hip resurfacing implantations. Proc Inst Mech Eng H 220(2):345–353. https://doi.org/10.1243/095441105X095469079

56. Kunz M, Rudan JF, Xenoyannis GL, Ellis RE (2010) Computer-assisted hip resurfacing using individualized drill templates. J Arthroplasty 25(4):600–606. https://doi.org/10.1016/j.arth.2009.1003.1023 Epub 2009 May 1022
57. Kunz M, Rudan JF, Wood GC, Ellis RE (2011) Registration stability of physical templates in hip surgery. Stud Health Technol Inform 163:283–289
58. Du H, Tian XX, Li TS, Yang JS, Li KH, Pei GX, Xie L (2013) Use of patient-specific templates in hip resurfacing arthroplasty: experience from sixteen cases. Int Orthop 37(5):777–782. https://doi.org/10.1007/s00264-00013-01842-00264 Epub 02013 Mar 00262
59. Zhang YZ, Lu S, Yang Y, Xu YQ, Li YB, Pei GX (2011) Design and primary application of computer-assisted, patient-specific navigational templates in metal-on-metal hip resurfacing arthroplasty. J Arthroplasty 26(7):1083–1087. https://doi.org/10.1016/j.arth.2010.1008.1004 Epub 2010 Oct 1086
60. Kitada M, Sakai T, Murase T, Hanada T, Nakamura N, Sugano N (2013) Validation of the femoral component placement during hip resurfacing: a comparison between the conventional jig, patient-specific template, and CT-based navigation. Int J Med Robot 9(2):223–229. https://doi.org/10.1002/rcs.1490 Epub 2013 Mar 1005
61. Buller L, Smith T, Bryan J, Klika A, Barsoum W, Iannotti JP (2013) The use of patient-specific instrumentation improves the accuracy of acetabular component placement. J Arthroplasty 28(4):631–636. https://doi.org/10.1016/j.arth.2012.1012.1001
62. Zhang YZ, Chen B, Lu S, Yang Y, Zhao JM, Liu R, Li YB, Pei GX (2011) Preliminary application of computer-assisted patient-specific acetabular navigational template for total hip arthroplasty in adult single development dysplasia of the hip. Int J Med Robot 7(4):469–474. https://doi.org/10.1002/rcs.1423 Epub 2011 Oct 1007
63. Schwarzkopf R, Schnaser E, Nozaki T, Kaneko Y, Gillman MJ (2016) Novel, patient-specific instruments for acetabular preparation and cup placement. Surg Technol Int XXIX:309–313
64. Spencer-Gardner L, Pierrepont J, Topham M, Bare J, McMahon S, Shimmin AJ (2016) Patient-specific instrumentation improves the accuracy of acetabular component placement in total hip arthroplasty. Bone Joint J 98-B(10):1342–1346. https://doi.org/10.1302/0301-620X.1398B1310.37808
65. Small T, Krebs V, Molloy R, Bryan J, Klika AK, Barsoum WK (2014) Comparison of acetabular shell position using patient specific instruments vs. standard surgical instruments: a randomized clinical trial. J Arthroplasty 29 (5):1030–1037. doi: 10https://doi.org/10.1016/j.arth.2013.1010.1006. Epub 2013 Oct 1016
66. Sakai T, Hamada H, Takao M, Murase T, Yoshikawa H, Sugano N (2017) Validation of patient-specific surgical guides for femoral neck cutting in total hip arthroplasty through the anterolateral approach. Int J Med Robot 13(3). https://doi.org/10.1002/rcs.1830 Epub 2017 May 1008
67. Ito H, Tanaka S, Tanaka T, Oshima H, Tanaka S (2017) A patient-specific instrument for femoral stem placement during Total hip arthroplasty. Orthopedics 40(2):e374–e377. https://doi.org/10.3928/01477447-20161108-01477406 Epub 01472016 Nov 01477414
68. Lau SC, Keith PPA (2018) Patient-specific instrumentation for total shoulder arthroplasty: not as accurate as it would seem. J Shoulder Elb Surg 27(1):90–95. https://doi.org/10.1016/j.jse.2017.1007.1004 Epub 2017 Sep 1015
69. Gomes NS (2016) Patient-specific instrumentation for total shoulder arthroplasty. EFORT Open Rev 1(5):177–182. https://doi.org/10.1302/2058-5241.1301.000033 eCollection 002016 May
70. Gauci MO, Boileau P, Baba M, Chaoui J, Walch G (2016) Patient-specific glenoid guides provide accuracy and reproducibility in total shoulder arthroplasty. Bone Joint J 98-B(8):1080–1085. https://doi.org/10.1302/0301-1620X.1098B1088.37257
71. Dallalana RJ, McMahon RA, East B, Geraghty L (2016) Accuracy of patient-specific instrumentation in anatomic and reverse total shoulder arthroplasty. Int J Shoulder Surg 10(2):59–66. https://doi.org/10.4103/0973-6042.180717
72. Berlet GC, Penner MJ, Lancianese S, Stemniski PM, Obert RM (2014) Total ankle arthroplasty accuracy and reproducibility using preoperative CT scan-derived, Patient-Specific Guides. Foot Ankle Int 35(7):665–676. https://doi.org/10.1177/1071100714531232 Epub 1071100714532014 Apr 1071100714531239
73. Zdravkovic V, Bilic R (1990) Computer-assisted preoperative planning (CAPP) in orthopaedic surgery. Comput Methods Prog Biomed 32(2):141–146
74. Munier M, Donnez M, Ollivier M, Flecher X, Chabrand P, Argenson JN, Parratte S (2017) Can three-dimensional patient-specific cutting guides be used to achieve optimal correction for high tibial osteotomy? Pilot study. Orthop Traumatol Surg Res 103(2):245–250. https://doi.org/10.1016/j.otsr.2016.1011.1020 Epub 2017 Jan 1027
75. Hoekstra H, Rosseels W, Sermon A, Nijs S (2016) Corrective limb osteotomy using patient specific 3D-printed guides: a technical note. Injury 47(10):2375–2380. https://doi.org/10.1016/j.injury.2016.2307.2021 Epub 2016 Jul 2321

76. Arnal-Burro J, Perez-Mananes R, Gallo-Del-Valle E, Igualada-Blazquez C, Cuervas-Mons M, Vaquero-Martin J (2017) Three dimensional-printed patient-specific cutting guides for femoral varization osteotomy: do it yourself. Knee 24(6):1359–1368. https://doi.org/10.1016/j.knee.2017.1304.1016 Epub 2017 Oct 1351
77. Ranalletta M, Bertona A, Rios JM, Rossi LA, Tanoira I, Maignon GD, Sancineto CF (2017) Corrective osteotomy for malunion of proximal humerus using a custom-made surgical guide based on three-dimensional computer planning: case report. J Shoulder Elbow Surg 26(11):e357–e363. https://doi.org/10.1016/j.jse.2017.1008.1002
78. Bauer AS, Storelli DAR, Sibbel SE, McCarroll HR, Lattanza LL (2017) Preoperative computer simulation and patient-specific guides are safe and effective to correct forearm deformity in children. J Pediatr Orthop 37(7):504–510. https://doi.org/10.1097/BPO.0000000000000673
79. Vlachopoulos L, Schweizer A, Graf M, Nagy L, Furnstahl P (2015) Three-dimensional postoperative accuracy of extra-articular forearm osteotomies using CT-scan based patient-specific surgical guides. BMC Musculoskelet Disord 16:336. https://doi.org/10.1186/s12891-12015-10793-x
80. Kunz M, Ma B, Rudan JF, Ellis RE, Pichora DR (2013) Image-guided distal radius osteotomy using patient-specific instrument guides. J Hand Surg Am 38(8):1618–1624. https://doi.org/10.1016/j.jhsa.2013.1605.1018
81. Hirsiger S, Schweizer A, Miyake J, Nagy L, Furnstahl P (2017) Corrective osteotomies of phalangeal and metacarpal Malunions using patient-specific guides: CT-based evaluation of the reduction accuracy. Hand 1(1558944717726135):1558944717726135
82. Weigelt L, Furnstahl P, Hirsiger S, Vlachopoulos L, Espinosa N, Wirth SH (2017) Three-dimensional correction of complex ankle deformities with computer-assisted planning and patient-specific surgical guides. J Foot Ankle Surg 56(6):1158–1164. https://doi.org/10.1053/j.jfas.2017.1105.1025 Epub 2017 Jun 1128
83. Zhou Y, Kang X, Li C, Xu X, Li R, Wang J, Li W, Luo H, Lu S (2016) Application of a 3-dimensional printed navigation template in Bernese periacetabular osteotomies: a cadaveric study. Medicine (Baltimore) 95(50):e5557. https://doi.org/10.1097/MD.0000000000005557
84. Schweizer A, Mauler F, Vlachopoulos L, Nagy L, Furnstahl P (2016) Computer-assisted 3-dimensional reconstructions of scaphoid fractures and nonunions with and without the use of patient-specific guides: early clinical outcomes and postoperative assessments of reconstruction accuracy. J Hand Surg Am 41(1):59–69. https://doi.org/10.1016/j.jhsa.2015.1010.1009
85. Schweizer A, Furnstahl P, Nagy L (2013) Three-dimensional correction of distal radius intra-articular malunions using patient-specific drill guides. J Hand Surg Am 38(12):2339–2347. https://doi.org/10.1016/j.jhsa.2013.2309.2023 Epub 2013 Nov 2331
86. Sallent A, Vicente M, Reverte MM, Lopez A, Rodriguez-Baeza A, Perez-Dominguez M, Velez R (2017) How 3D patient-specific instruments improve accuracy of pelvic bone tumour resection in a cadaveric study. Bone Joint Res 6(10):577–583. https://doi.org/10.1302/2046-3758.1610.BJR-2017-0094.R1301
87. Jentzsch T, Vlachopoulos L, Furnstahl P, Muller DA, Fuchs B (2016) Tumor resection at the pelvis using three-dimensional planning and patient-specific instruments: a case series. World J Surg Oncol 14(1):249. https://doi.org/10.1186/s12957-12016-11006-12952
88. Chen X, Xu L, Wang Y, Hao Y, Wang L (2016) Image-guided installation of 3D-printed patient-specific implant and its application in pelvic tumor resection and reconstruction surgery. Comput Methods Programs Biomed 125:66–78. https://doi.org/10.1016/j.cmpb.2015.1010.1020 Epub 2015 Dec 1012
89. Roner S, Vlachopoulos L, Nagy L, Schweizer A, Furnstahl P (2017) Accuracy and early clinical outcome of 3-dimensional planned and guided single-cut osteotomies of Malunited forearm bones. J Hand Surg Am 42(12):1031.e1031–1031.e1038. https://doi.org/10.1016/j.jhsa.2017.1007.1002 Epub 2017 Sep 1036
90. Turmezei TD, Poole KE (2011) Computed tomography of subchondral bone and osteophytes in hip osteoarthritis: the shape of things to come? Front Endocrinol (Lausanne) 2:97. https://doi.org/10.3389/fendo.2011.00097 eCollection 02011
91. Gelse K, Soder S, Eger W, Diemtar T, Aigner T (2003) Osteophyte development–molecular characterization of differentiation stages. Osteoarthr Cartil 11(2):141–148
92. Seon JK, Park HW, Yoo SH, Song EK (2014) Assessing the accuracy of patient-specific guides for total knee arthroplasty. Knee Surg. Sports Traumatol. Arthrosc 24:3678. https://doi.org/10.1007/s00167-014-3429-z
93. Kunz M, Balaketheeswaran S, Ellis RE, Rudan JF (2015) The influence of osteophyte depiction in CT for patient-specific guided hip resurfacing procedures. Int J Comput Assist Radiol Surg 10(6):717–726. https://doi.org/10.1007/s11548-11015-11200-11547 Epub 12015 Apr 11511
94. Sassoon A, Nam D, Nunley R, Barrack R (2015) Systematic review of patient-specific instrumentation in total knee arthroplasty: new but not improved. Clin Orthop Relat Res 473(1):151–158. https://doi.org/10.1007/s11999-11014-13804-11996
95. Cerveri P, Sacco C, Olgiati G, Manzotti A, Baroni G (2017) 2D/3D reconstruction of the dis-

tal femur using statistical shape models addressing personalized surgical instruments in knee arthroplasty: a feasibility analysis. Int J Med Robot 13(4). https://doi.org/10.1002/rcs.1823 Epub 2017 Apr 1007

96. Okada Y, Teramoto A, Suzuki T, Kii Y, Watanabe K, Yamashita T (2017) Preoperative corrections are required for planning of patient-specific instrumentation in total knee arthroplasty. Knee 24(6):1492–1497. https://doi.org/10.1016/j.knee.2017.1409.1008 Epub 2017 Oct 1416
97. Pietsch M, Djahani O, Hochegger M, Plattner F, Hofmann S (2013) Patient-specific total knee arthroplasty: the importance of planning by the surgeon. Knee Surg Sports Traumatol Arthrosc 21(10):2220–2226. https://doi.org/10.1007/s00167-00013-02624-00167 Epub 2013 Aug 00113
98. Goyal N, Stulberg SD (2015) Evaluating the precision of preoperative planning in patient specific instrumentation: can a single MRI yield different preoperative plans? J Arthroplasty 30(7):1250–1253. https://doi.org/10.1016/j.arth.2015.1202.1021 Epub 15 Feb 1226
99. Van den Broeck J, Wirix-Speetjens R, Vander Sloten J (2015) Preoperative analysis of the stability of fit of a patient-specific surgical guide. Comput Methods Biomech Bomed Eng 18(1):38–47. https://doi.org/10.1080/10255842.10252013.10774383 Epub 10252013 Apr 10255829

Intelligent Control for Human-Robot Cooperation in Orthopedics Surgery

19

Shaolong Kuang, Yucun Tang, Andi Lin, Shumei Yu, and Lining Sun

Abstract

Cooperation between surgeon and robot is one of the key technologies that limit the robot to be widely used in orthopedic clinics. In this study, the evolution of human-robot cooperation methods and the control strategies for typical human-robot cooperation in robot-assisted orthopedics surgery were reviewed at first. Then an intelligent admittance control method, which combines the fuzzy model reference learning control with the virtual constraint control, is proposed to solve the requirements of intuitive human-robot interaction during orthopedics surgery. That is, a variable damping parameter model of the admittance control based on fuzzy model learning control algorithm is introduced to make the robot move freely by using the reference model of surgeon's motion equation with the minimum jerk trajectory. And the virtual constraint control method based on the principle of virtual fixture is adopted to make the robot move within the pre-defined area so as to perform more safe surgery. The basic principle and its realization of this intelligent control method are described in details. At last, a test platform is built based on our designed 6 DOF articulated robot. Experiments of safety and precision on acrylic model with this method show that the robot has the ability of better intuitive interaction and the high precision. And the pilot experiment of bone tumor resection on sawbone model shows the effectiveness of this method.

Keywords

Human-robot intuitive interaction · Admittance control · Variable damping control · Fuzzy model reference learning · Virtual constraint

19.1 Introduction

Robot-assisted surgery is an evolving technology that has gained more and more attentions from the research fields of biomedicine, engineering, and marketing because it has the advantages of more minimally invasive abilities with reliable and repeatable outcomes compared with conventional surgery. Robot in orthopedics surgery

S. Kuang (✉) · Y. Tang · A. Lin · S. Yu · L. Sun (✉)
Robotics and Micro-Systems Center, Soochow University, Suzhou City, Jiangsu Province, People's Republic of China
e-mail: slkuang@suda.edu.cn; lnsun@hit.edu.cn

G. Zheng et al. (eds.), *Intelligent Orthopaedics*, Advances in Experimental Medicine and Biology 1093, https://doi.org/10.1007/978-981-13-1396-7_19

is the most popular in surgical robot research fields as the bone has some characteristics like metal materials and it can be easily realized by integrating some advanced manufacturing technologies (Miller [23]). Several commercial robot-assisted orthopedics surgery (RAOS) systems had been approved by the US Food and Drug Administration (FDA) such as ROBODOC (now TCAT, THINK Surgical, Inc.), Acrobot (now Sculptor, Acrobot Company Ltd.), Mako RIO (Stryker, USA), ROSA Spine (Medtech S.A.), and SpineAssist (now Renaissance, Mzor Robotics, Israel). The RAOS systems are the largest number of robotic surgical systems that FDA approved as we know from literature reported. However, the RAOS systems have not gained so much widespread use compared to endoscopic surgery robot systems, such as Da Vinci system.

Robot in orthopedics surgery is mainly to help surgeon to do drilling, milling, and cutting tasks for minimized invasive surgical incision, enhancing surgical accuracy, improving surgical output performance, and better ergonomics of surgeon. The early RAOS systems, like ROBODOC and CASPAR system, are active type and complete the surgical task autonomously (Sugano [29]). However, it was found that the highly automatic systems bring more mental pressure in clinical use, even though they were safer than manual work (Hancock et al. [8]). The key to the problem is who is in charge of the procedure: the surgeon or the computer programmer (Baena and Davies [1]). That is, besides good output of robotic surgery, the issues of safety, controllability, and usability of the system during the operation are more important things for surgeon to choose the robot for surgery. And surgeons want to control the robot timely and directly to gain more safe surgery. In general, the cooperation and interaction mode between surgeon and robot is a key point in clinical use.

From the aspect of human-robot cooperation, the orthopedics robots are divided into passive robots, active robots, semi-active /cooperation robots, and teleoperation robots (Sugano [29], Langlotz and Nolte [16], Cinquin [3]) despite their complexity for establishing the robot systems. Passive robots have the advantages of safety and can be easily accepted by surgeon from the viewpoint of human-robot cooperation (Leung et al. [20], [32]), but the robots eventually fail to spread to the clinical use due to the accuracy, which is eventually guaranteed by doctors' manual adjustment, and it's a time-consuming thing (Troccaz and Delnondedieu [32]). Active robots have always been in the awkward situations because of the safety issue that is doubted by surgeon during surgical procedures. Eventually, this kind of active robots, such as ROBODOC (Fig. 19.1a), had to adopt a technology of compliance control for better man-machine cooperation to fulfill the clinical need of safety (Taylor et al. [31]). Based on this, another type of robot was designed with the ability of compliance control (such as BRIGIT (Maillet et al. [21])) (Fig. 19.1b) which was used as a positioning, supporting, and guiding tool to enhance the safety during surgical procedures. This type of robot is positioned in the mode of compliant control operated by surgeon and performs surgery in traditional mode that is

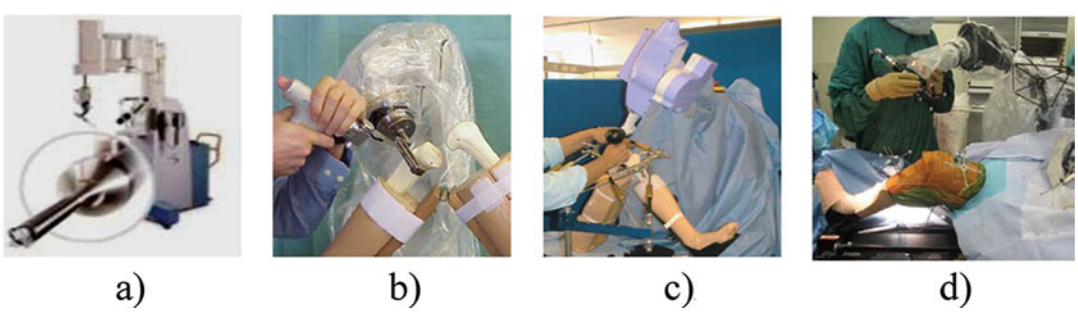

Fig. 19.1 Typical orthopedics robots. (**a**) ROBODOC, (**b**) BRIGIT, (**c**) Acrobot, (**d**) Mako RIO

controlled by doctor under the restriction of mechanical fixture, which is installed at the end of the robot. It's an acceptable design as to the active robot in surgery.

In fact, the robot itself has the excellent ability of motion control and high precision of trajectory positioning. If the fixture technology is designed by a kind of software and used to substitute some kinds of functions of the mechanical fixture during the operation, the robot then shall have the flexible ability to fulfill kinds of surgery without using different mechanical fixture. This kind of fixture technology is called virtual fixture. Acrobot (Jakopec et al. [11]) (Fig. 19.1c) is such a kind of robot developed for total knee replacement (TKR), which extends the idea of human-robot cooperation of ROBODOC by using compliant control during the entire surgery procedures and combined with a so-called hands-on method of active constraint control algorithm [30]. It is a kind of semi-active robot and has gained good acceptance by many surgeons and hospitals because of the good human-robot cooperation ability (Baena and Davies [1]). Another semi-active robot is Mako RIO (Kazanzides et al. [13]) (Fig. 19.1d), which has the ability of real-time tracking and position adjusting between the robot and the surgical space through the navigation, which can overcome some disadvantages of the early semi-active machine. The system is also known as the Tactile Guidance System (TGS) (Banks [2] because the RIO robot has the tactile (force) feedback during the operation of surgeons.

The development and evolution of human-robot cooperation in orthopedics surgical robot presented above mainly focus on the guiding force exerted by the surgeon and the corresponding control strategies to achieve successful surgery with high safety (Haidegger et al. [7]). This kind of control method that the robot generates corresponding motion according to the given force is called as admittance control (Newman [24], Kwon et al. [15]). The compliant motion control of ROBODOC (Kazanzides et al. [13]), active constraint control of Acrobot (Ho et al. [9]), and haptics interactive control of Mako RIO (Quaid et al. [26]) are some kinds of admittance control which regulate the dynamic behavior of the robot by modifying the parameters of virtual stiffness, damping, and inertia of the controller (Cruces and Wahrburg [4], Ott et al. [25]). Under this control strategy, the surgical area is usually classified into free zone, transition zone, and restricted zone (Ho et al. [9], Kapoor et al. [12]). And each zone has the different safety level according to the requirement of operation, which is used to regulate the gains of parameters of the admittance control for better motion compliance and good output performance.

Actually, the human-robot cooperation process of the semi-active orthopedics robot is a control process with variable admittance control (Cruces and Wahrburg [4]). The gains of parameters of variable admittance control are determined by using experimental methods. The ROBODOC robot proposed two kinds of damping parameter models including linear gains and nonlinear gains to realize the compliance motion in teach pendant process. And the Acrobot uses constant damping parameter and variable stiffness parameter to achieve the goal of stiffness control. On the other hand, the human-robot cooperation models of orthopedics robots mentioned above are a typical interaction mode of physical human-robot interaction (pHRI). And the current research of pHRI is concentrating on how to adjust the virtual damping, the most dominant parameters of admittance control to achieve more intuitive interaction (Ikeura and Inooka [10], Duchaine and Gosselin [6], Lecours et al. [19]). In summary, the performance and stability of the admittance control are determined by how to design the admittance control parameters (Ott et al. [25]). And the current challenge of this method is how to get better human-robot intuitive interaction during the process of RAOS (Robotics [28]).

In this study, an intelligent control of human-robot cooperation is introduced to realize the intuitive interactive abilities of the orthopedics robots and meet the requirements on performance and stability during orthopedics surgery. That is, a variable admittance control of fuzzy model reference learning control (FMRLC) (Layne and Passino [18]) is proposed to combine with the technology of virtual fixture (Kwon et al. [15], Kapoor et al. [12]). During the operation, the surgeon can move the robot freely from installed position to surgical zone with the FMRLC method for intuitive interaction under the control strategy of dynamic behavior of human arms. The virtual constraint based on virtual fixture is proposed during cutting, milling, and drilling of the robotic surgery for the better performance and stability.

19.2 Variable Admittance Control for HRI in Orthopedics Surgery

19.2.1 Requirement of HRI in Orthopedics Surgery

To illustrate the requirements of HRI during orthopedics surgery, a robotic surgery scene is modeled as in Fig. 19.2. When the robot is ready to perform operation after power on, the doctor shall drag the robot from positioning point P1 that outside the surgical field to point P2 that in the surgical Zone I. In this process, the doctor must freely drag the robot according to surgeon's guiding force exerted on the end effector of the robot. This operation process is defined as process S1 in this study.

The surgical zone is divided into three zones, i.e., free zone (I), transition zone (II), and forbidden zone (III). In Zone I, the doctor can freely drag the robot to milling focal bone tissue with the help of surgical navigation system. Zone II is the transition area that needs to be milled by the robot. Zone III is the outside space compared to the planned surgery area. In this zone, the end of the tool shall not reach the boundary of Zone III for safety. So the boundary between Zone II and Zone III (defined as critical boundary here) is the most critical area for safety and precision. During the operation, if the robot moves from Zone II to Zone III, it is possible to reach Zone III due to the shaking of human hands, which can drop the operation precision and cause safety issue. Therefore, the transition Zone II shall be significantly designed to improve the surgical precision and operational safety.

19.2.2 Admittance Control and Its Control Strategy

Admittance control establishes a dynamical relationship between the end effector motion (position/velocity) and force, which can provide precise motion control in the condition of high transmission such as harmonic-driven robotic system. In admittance control, the controller is admittance and the manipulator is impedance (Ott et al. [25]). The equation of the robot admittance controller can be described as follows:

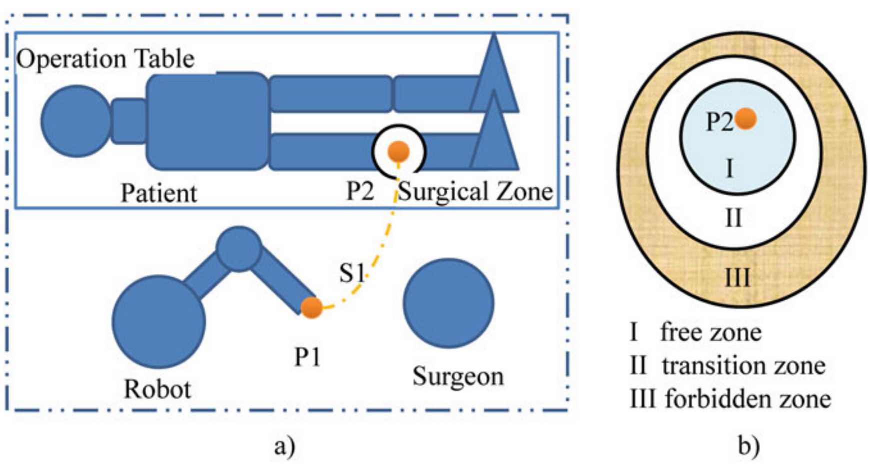

Fig. 19.2 Illustration of human-robot interaction process of robotic orthopedics surgery (**a**) Robotic surgical system. (**b**) Surgical zone

$$M_d\left(\ddot{x}_d-\ddot{x}_0\right)+B_d\left(\dot{x}_d-\dot{x}_0\right)+K_d\left(x_d-x_0\right)=F_h \tag{19.1}$$

where M_d, B_d, and K_d are virtual inertia, virtual damping, and virtual stiffness, respectively. And F_h is the guiding force exerted by the surgeon on the robot. Moreover, virtual damping is the most dominant parameter of HRI admittance control. When the robot is not in contact with the external environment, M_d and K_d are ignored (Marayong et al. [22]) to establish the admittance control model based on velocity (Eq.(19.2)). Therefore, the choice of virtual damping is the core of variable admittance control based on velocity.

$$B_d V = F_h \tag{19.2}$$

During the operation in stage S1 (Fig. 19.2a), the doctor drags the robot freely, that is, the robot shall move according to the intention of the doctor to gain the ability of intuitive interaction. Many researchers had proposed to use the minimum jerk trajectory model of human (Rahman et al. [27]) to construct the dynamics control of the RHI to achieve the intuitive HRI. Based on this, Dimeas and Aspragathos [5] proposed a method of FMRLC to gain the suitable damping parameter of admittance control for investigating the performance of pHRI with linear motion. In this study, the minimum jerk trajectory model is adopted to derive robot's motion equation according to the characteristic of surgeon's movement. Then the reference model of FMRLC, which is called fuzzy model reference learning variable admittance control (FMRLVAC), is proposed based on the motion equation to get variable virtual damping parameter model.

During the operation as in Fig. 19.2b, the surgeon can drag the robot to move freely, but the speed of operation in this zone is very slow for the sake of smooth motion. However, from Zone II to Zone III, besides the stable guiding force, the error and tremble of the surgeon must be considered to prevent the robot from going in to Zone III. Under this condition, the virtual fixture constraint model is often used to solve this problem (Ho et al. [9], Kwon et al. [15]). Therefore, the virtual fixture constraint model based on admittance control is proposed here to fulfill the requirements of operation in this stage.

19.2.3 Fuzzy Model Reference Learning Variable Admittance Control

19.2.3.1 Structure and Principle of the FMRLVAC

Dimeas and Aspragathos [5] and Layne and Passino [17] had done the great example of using FMRLC to solve the control issue on high-order, nonlinear, time variable of the complex system. FMRLC shall not need to know the exact model of the control system. The good performance of the controller is achieved by setting up the rules of fuzzy control based on the reference model of experts or operators and regulating the fuzzy rules and controller parameters through its self-learning abilities. It's very useful to regulate the damping parameters of the admittance control of the HRI. Based on these, the FMRLVAC method is proposed in this study. The structure of FMRLVAC is composed of five elements: human in the loop, reference model, learning mechanism, fuzzy controller, and the controlled plant (robot), as shown in Fig. 19.3.

In this control system, the input of the admittance controller is the guiding force F_h exerted on the robot. The output of the controlled plant is velocity V of the tool end of the robot, and the output of admittance controller is velocity V_{ref}. The output of reference model is also a velocity variable V_{jerk}. The inputs of the fuzzy controller are F_h and V, while the output of the fuzzy controller is damping parameter B_d, which is also the input of the admittance controller. The learning mechanism, one part of this control system, includes knowledge-base modifier and fuzzy inverse model. The input of the fuzzy inverse model is error y_e, and the rate of change of the error y_c, y_e denotes the error between the output of the reference model and the output of the controller plant. The output of the fuzzy inverse model is p, which denotes the modified value of the knowledge base. The output of that is C_m, which is used to modify the damping parameters of the admittance control.

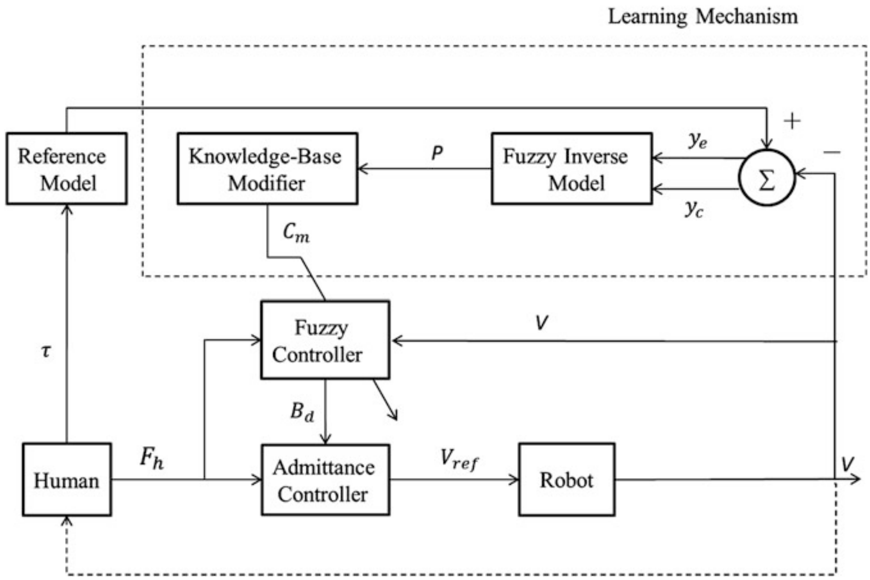

Fig. 19.3 Structure of the FMRLVAC

The fuzzy control system outputs B_d by using fuzzy inference according to the input of F_h and V. The learning mechanism acquires a corrected value p according to the error y_e and the rate of change of the error y_c. The knowledge base is modified by p, which makes the system deviation y_e quickly approach zero.

19.2.3.2 Design of the Fuzzy Controller

The input of the fuzzy controller is $F_h(KT)$ and the velocity $V(KT)$ of the robot movement, where T denotes the sampling period in the discrete time domain. The output of the fuzzy controller is damping parameter $B_d$of the admittance control. A multiple-input and single-output (MISO) fuzzy controller is used here, whose reasoning rules are set as the following form:

$$\begin{aligned}
&\text{If } \tilde{F}_{h1}\ is\ A_1^j \text{ and} \cdots \tilde{F}_{hs} \text{ is } A_s^k \quad \text{and} \\
&\tilde{V}_1\ is\ D_1^l \text{ and} \cdots \tilde{V}_s \text{ is } D_s^m \\
&\text{Then } \tilde{B}_{dn} \text{ is } E_n^{j,\ldots,k,l,\ldots,m}
\end{aligned} \tag{19.3}$$

where $\tilde{F}_{hb}$ and$\tilde{V}_b$(b = 1, ... ,s) denote the linguistic variables associated with fuzzy controller inputs F_h and V, respectively. $\tilde{B}_{dn}$ denotes the linguistic variable associated with the fuzzy controller output B_d, A_1^a and D_1^a denote the a[th] linguistic value associated with $\tilde{F}_{h1}$ and $\tilde{V}_1$, and $E_n^{j,\ldots,k,l,\ldots,m}$ denotes the consequent linguistic value associated with $\tilde{B}_{dn}$. So fuzzy implication relation of MISO system can be expressed as

$$\begin{aligned}
R_n^{j,\ldots,k,l,\ldots,m} &= \left(A_1^j \times \cdots A_s^k\right) \times \\
&\left(D_1^l \times \cdots \times D_s^m\right) \times E_n^{j,\ldots,k,l,\ldots,m}
\end{aligned} \tag{19.4}$$

The MISO fuzzy control system fuzzy relationship is

$$R_n = \cup_{j,\ldots,k,l,\ldots,m} R_n^{j,\ldots,k,l,\ldots,m} \tag{19.5}$$

Assuming that the maximum and minimum values of force F_h are F_{max} and F_{min}, respectively, the maximum and minimum values of speed V are V_{max} and V_{min}, and the values of F_h and V are, respectively, in their domain $[F_{min}, F_{max}]$ and $[V_{max}, V_{min}]$ are divided into nine levels, i.e., F_h and V consist of nine triangular-shaped membership functions, respectively. The input fuzzy sets are as follows:

$$\tilde{F}_{hb} = \{-4, -3, -2, -1, 0, 1, 2, 3, 4\} \tag{19.6}$$

$$\tilde{V}_b = \{-4, -3, -2, -1, 0, 1, 2, 3, 4\} \tag{19.7}$$

Table 19.1 The initial rules of fuzzy controller

		$\tilde{F}_{hb}$								
$\tilde{B}_{dn}$		4	3	2	1	0	1	2	3	4
$\tilde{V}_b$	4	1	1	2	2	3	3	4	4	5
	3	1	2	2	3	3	4	4	5	4
	2	2	2	3	3	4	4	5	4	4
	1	2	3	3	4	4	5	4	4	3
	0	3	3	4	4	5	4	4	3	3
	1	3	4	4	5	4	4	3	3	2
	2	4	4	5	4	4	3	3	2	2
	3	4	5	4	4	3	3	2	2	1
	4	5	4	4	3	3	2	2	1	1

Assuming that the maximum and minimum values of admittance B_d are B_{dmax} and B_{dmin}, respectively, B_d is divided into five fuzzy subsets on its domain $[B_{dmin}, B_{dmax}]$ as the following fuzzy sets:

$$\tilde{B}_{dn} = \{1, 2, 3, 4, 5\} \tag{19.8}$$

And the selected rules form a complete and consistent rule base, meaning that there is a valid conclusion for every possible input.

Fuzzy controller rules can be explained by the following sentences:

- *If force is high ($-4or4$) and velocity is high ($-4or4$), then damping is very low (1).*
- *If force is middle ($-2or2$) and velocity is middle ($-2or2$), then damping is middle (3).*
- *If force is low (0) and velocity is high (0), then damping is very high (5).*

The complete set of control rules for the fuzzy controller is shown in Table 19.1.

19.2.3.3 Reference Model

V_{jerk} denotes the output value of the reference model. The minimum jerk trajectory minimizes the change in acceleration of the motion of the human arm. According to reference (Rahman et al. [27]), this model can be obtained by the following formula:

$$X(\tau) = X_0 + \left(X_f - X_0\right)\left(A\tau^5 + B\tau^4 + C\tau^3 + D\tau^2 + E\tau\right) \tag{19.9}$$

where τ is the normalized value of moving time, $\tau = {}^{t}\!/_{t_f}$, $0 \le \tau \le 1$, and X_0 and X_f are the initial and final positions, respectively. A, B, C, D, and E are all the constant.

By differentiating the above equation, the following equation can be obtained:

$$V_{jerk} = \frac{dX(t)}{dt} \tag{19.10}$$

The error between the reference model and the output value of the controlled object is

$$y_e(KT) = V_{jerk} - V \tag{19.11}$$

As long as the learning mechanism can satisfy $y_e(KT) \approx 0$ at $t \ge KT$, it is considered that the ideal behavior of the controlled object has arrived, and the learning mechanism will not make any big adjustment to the parameters of the fuzzy controller.

19.2.3.4 Design of Fuzzy Learning Mechanism

The input of the fuzzy inverse model is

$$\begin{cases} y_e(KT) = V_{jerk} - V \\ y_c(KT) = \left(y_e(KT) - y_e(KT - T)\right)/T \end{cases} \tag{19.12}$$

The output is $P(KT)$. Similar to the fuzzy controller, the knowledge base of fuzzy inverse model can be expressed by fuzzy rules (where $n = 1, \ldots, r$):

$$\text{If } Y_{e1}^{j} \text{ and} \cdots Y_{es}^{k} \text{ and } Y_{c1}^{l} \cdots \text{and } Y_{cs}^{m} \quad \text{Then } P_n^{j,\ldots,k,l,\ldots,m}$$

where Y_{ea}^{b} and Y_{ca}^{b} denote the b^{th} linguistic value associated with y_{ea} and y_{ca}. $P_n^{j,\ldots,k,l,\ldots,m}$ denotes the consequent linguistic value, which reflects the adjustment of the fuzzy controller output value.

Table 19.2 Fuzzy inverse control rules

		Y_c										
P		−5	−4	−3	−2	−1	0	1	2	3	4	5
Y_e	−5	1	1	0.8	0.8	0.6	0.6	0.4	0.4	0.2	0.2	0
	−4	1	0.8	0.8	0.6	0.6	0.4	0.4	0.2	0.2	0	−0.2
	−3	0.8	0.8	0.6	0.6	0.4	0.4	0.2	0.2	0	−0.2	−0.2
	−2	0.8	0.6	0.6	0.4	0.4	0.2	0.2	0	−0.2	−0.2	−0.4
	−1	0.6	0.6	0.4	0.4	0.2	0.2	0	−0.2	−0.2	−0.4	−0.4
	0	0.6	0.4	0.4	0.2	0.2	0	−0.2	−0.2	−0.4	−0.4	−0.6
	1	0.4	0.4	0.2	0.2	0	−0.2	−0.2	−0.4	−0.4	−0.6	−0.6
	2	0.4	0.2	0.2	0	−0.2	−0.2	−0.4	−0.4	−0.6	−0.6	−0.8
	3	0.2	0.2	0	−0.2	−0.2	−0.4	−0.4	−0.6	−0.6	−0.8	−0.8
	4	0.2	0	−0.2	−0.2	−0.4	−0.4	−0.6	−0.6	−0.8	−0.8	−1
	5	0	−0.2	−0.2	−0.4	−0.4	−0.6	−0.6	−0.8	−0.8	−1	−1

Fuzzy inverse controller rules can be explained by the following sentences:

- *If y_e is zero and y_c is zero, then P is zero.*
- *If y_e is positive and y_c is positive, then P is negative.*
- *If y_e is negative and y_c is negative, then P is positive.*

The complete set of control rules for the fuzzy controller is shown in Table 19.2.

The relationship between learning mechanism and fuzzy controller is

$$C_m(KT) = B_d(KT - T) + P(KT) \quad (19.13)$$

where $C_m(KT)$ is the modified value of B_d.

Assume that some uniformly partitioned membership functions are defined in the domain of the output variable of the Fuzzy Controller. Use $C_m^{j,\ldots,k,l,\ldots,m}(t)$ to represent the central value of the fuzzy set $E_n^{j,\ldots,k,l,\ldots,m}$ membership function.

The degree of contribution for a particular fuzzy implication whose fuzzy relation is denoted $R_n^{j,\ldots,k,l,\ldots,m}$ determined by its "activation level", defined as

$$\delta_n^{j,\ldots,k,l,\ldots,m}\mathrm{t} = \min\left\{m_{A_1^j}\left(\tilde{F}_{h1}(t)\right), \ldots, m_{A_s^k}\right.$$
$$\left.\times\left(\tilde{F}_{hs}(t)\right), m_{D_1^j}\left(\tilde{V}_1(t)\right), \ldots, m_{D_s^k}\left(\tilde{V}_s(t)\right)\right\} \quad (19.14)$$

Where m_B denotes the membership function of the fuzzy set B.

Only those rules whose activation level $\delta_n^{j,\ldots,k,l,\ldots,m}(kT - T) > 0$ are modified, The rest do not change.

19.2.4 Virtual Constraint Model for Admittance Control

19.2.4.1 Linear Gain of Admittance Control

During the operation in surgical zone (Fig. 19.2 b), the doctor performs operation very slowly and carefully. After investigation of the doctor's manual operation, it is found that the surgeon's motion is at almost a constant speed and with less force changing. In this condition, a linear admittance controller with constant damping parameter can fulfill the operation's needs of HRI (Eq.(19.15)).

In order to prevent too fast velocity of the robot from overload force exerted by the surgeon, the threshold of the guiling force is set and defined as F_{max}. And the dead zone of guiding force is also considered as F_{dz} to prevent over sensitive of the force sensor.

$$\begin{cases} B_d V = -F_{max} & F_h \le -(F_{max} + F_{dz}) \\ B_d V = F_h + F_{dz} & -(F_{max} + F_{dz}) < F_h \le -F_{dz} \\ B_d V = 0 & -F_{dz} < F_h < F_{dz} \\ B_d V = F_h - F_{dz} & F_{dz} \le F_h < (F_{max} + F_{dz}) \\ B_d V = F_{max} & F_h \ge (F_{max} + F_{dz}) \end{cases} \quad (19.15)$$

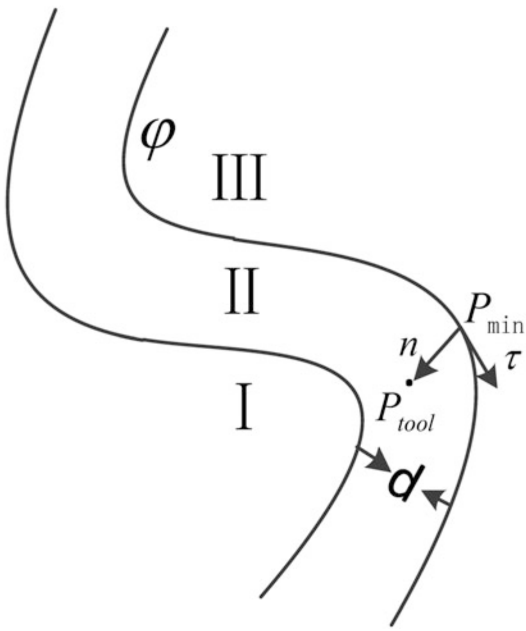

Fig. 19.4 The illustration of virtual constraint

19.2.4.2 Virtual Constraint Control Strategy

The surgical zone is an irregular 3D shape, but surgeon always removes materials layer by layer like material cutting in mechanical engineering. Based on this, the virtual constraint can be designed by different 2D models in different layers. Thus the virtual constraint model in 2D space can be illustrated in Fig. 19.4.

In Fig. 19.4, φ is the restrained boundary curve, d is the distance from the restrained boundary to the inner boundary, P_{tool} is the position of the end of the robot, and P_{min} is the nearest point from P_{tool} to curve φ. The guiding force F_h can be decomposed into two components along the directions of tangent and normal of P_{min} in curve φ.In this area, the admittance control in Eq. (19.2) can be written as

$$B_d V = F_\tau + F_n \tag{19.16}$$

Because the movement of robot in normal direction may cause safety problems, it is necessary to correct the normal direction component of the guiding force. Here the correction coefficient $c_n (\in [0, 1])$ is introduced, and then Eq.(19.16) can be written as follows:

$$B_d V = F_\tau + c_n F_n \tag{19.17}$$

In region I, c_n is set to be 1 to ensure robot moves freely according to surgeon's guiding force. In region II, c_n is defined as a liner model to prevent robot from moving out of the critical boundary. In region III, c_n is set to be 0. Thus the c_n can be described as follows:

$$\begin{cases} c_n = 1 & P_{\text{tool}} \in \Omega_{\text{I}} \text{ or } (P_{\text{tool}} \in \Omega_{\text{II}} \text{ and } \\ & \quad F_h \cdot n > 0) \\ c_n = 1 - x/d & P_{\text{tool}} \in \Omega_{\text{II}} \text{and } F_h \cdot n \le 0 \\ c_n = 0 & P_{\text{tool}} \in \Omega_{\text{III}} \end{cases} \tag{19.18}$$

where x is the distance in the normal direction between the inner boundary and the robot.

It is more safe to operate in the tangential direction than that in normal direction. The algorithm used in this study was proposed by Marayong et al. (Marayong et al. [22]).

19.3 Experiments and Results

An experiment platform is built to verify the proposed intelligent control method of variable admittance control combined with virtual constraint for robotic orthopedics surgery, as in Fig. 19.5. The robot is developed by the authors for orthopedics surgery named iSA (intelligent Surgical Assist). An optical tracking device (NDI Polaris Spectra, North Digital Inc., Canada) is used here to get the poses (positions and orientations) of the surgical tool at the end of the robot iSA and surgical object (sawbone) by using two position trackers. Thus it is easy to get the pose relationships between robot iSA and the surgical object. All the following experiments are based on this platform.

19.3.1 Experiment on FMRLVAC

19.3.1.1 Reference Model

In this study, the experimental platform (Fig. 19.6) based on Fig. 19.5 is established to

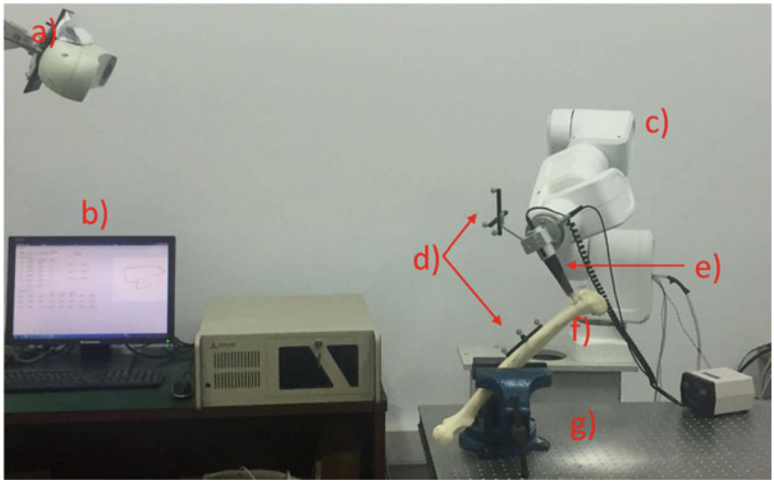

Fig. 19.5 (**a**) NDI Polaris Spectra optical tracking device. (**b**) Robot control system. (**c**) Robot for orthopedics surgery. (**d**) Position tracker. (**e**) Surgical tool. (**f**) Sawbone. (**g**)Test table

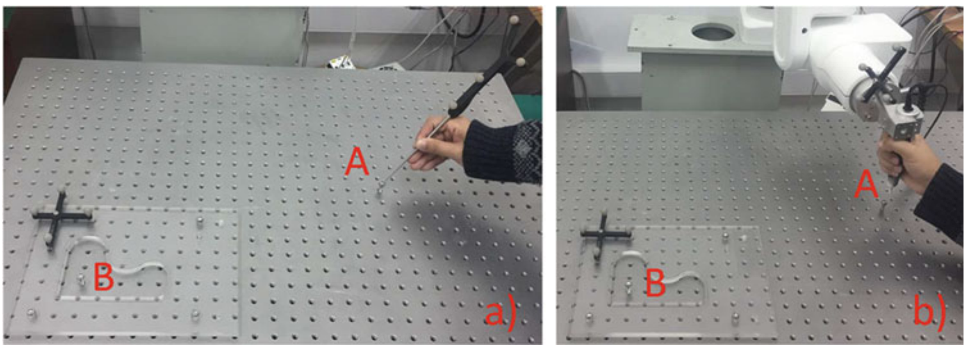

Fig. 19.6 Testing platform for reference model experiments (**a**) Human movement. (**b**) Robot movement

obtain the surgeon's reference motion features. Assuming Points A and B here are Points P1 and P2 in Fig. 19.2 a, respectively, the surgeon's moving time and position are tracked and recorded in an interval of 10 ms with the help of NDI optical tracker. After conducting experiments repeatedly, the reference motion model is fit based on the records. In the experiments, the distance of AB is 450 mm.

The operating data of five interns are collected for this experiment. Each subjects operated 10 times and total 50 sets of experimental data are obtained. Firstly, the operating time of every intern is counted by calculating average value and standard deviation (Table 19.3), and the time data are normalized to range of 0 to 1. Since this study only studies the motion in a plane, the equation of plane position and τ can be deduced from the minimum jerk model (Eq.(19.19)).

Table 19.3 Average operator time and standard deviation

No.	Average time T (ms)	Standard deviation σ (ms)
1	5605	60.95
2	5493	64.97
3	5312	56.47
4	4997	79.75
5	5583	68.26

$$\begin{cases} x(\tau) = x_0 + \left(x_f - x_0\right) \\ \left(a_0 + a_1\tau + a_2\tau^2 + a_3\tau^3 + a_4\tau^4 + a_5\tau^5\right) \\ y(\tau) = y_0 + \left(y_f - x_0\right) \\ \left(b_0 + b_1\tau + b_2\tau^2 + b_3\tau^3 + b_4\tau^4 + b_5\tau^5\right) \end{cases} \tag{19.19}$$

In the experiment, A and B denote the initial position and the end position of the movement. The experiment only studies the point-to-point movement of A to B, so the connection between A and B points is taken as the x-axis that can get the following formula:

$$x(\tau) = x_0 + (x_f - x_0)(a_0 + a_1\tau + a_2\tau^2 + a_3\tau^3 + a_4\tau^4 + a_5\tau^5) \tag{19.20}$$

Here, $x_0 = 0$, $x_f = 450$mm. Then the motion reference model is fitted by the data collected above, the formula Eq.(19.21) is obtained, and the fitting curve is shown in Fig. 19.7.

$$x(\tau) = x_0 + (x_f - x_0)(0.25\tau + 4.79\tau^2 - 7.71\tau^3 + 6.38\tau^4 - 2.22\tau^5) \tag{19.21}$$

19.3.1.2 Offline Training

The main purpose of the surgeon collaborating with robot during the process S1 is to let robot go into the surgical zone with high safety. It is not a high-precision work and just follows the surgeon's motion with intuitive interaction. So the variable damping parameters can be determined through offline training. The training process and the scene are the same as that of the reference model, except that the surgical robot is used to assist the surgeon (Fig. 19.6b). The training processes are as follows:

A Input and Output Fuzzification

The variable range of each input and output must be determined before fuzzification. F_h is the input of fuzzy controller and fuzzy inverse model in FMRLVAC. First, the range of the F_h is determined by the testing of five interns, who are selected to test how much force they expected to apply on the robots. It is found that the appropriate range is $3 \sim 5$ N, and the largest force of F_h can hardly be over 7 N. Considering the inverse force, the F_h range is set at [-7 N, 7 N]. The range of velocity, which is in [−150 mm/s, 150 mm/s], is gotten from the reference model. y_e and y_c in the fuzzy inverse model are determined by the change rate relative to that in the reference model.

B_d is the output of the fuzzy controller. The range of B_d also can be acquired from tests above. By accumulating many experiments, the range of B_d can be obtained that is in [0.05 N.s/mm, 0.5 N.s/mm].

The fuzzy sets are defined for each controller input and output such that the membership functions are triangular shaped and evenly distributed on the appropriate universes of discourse.

B Training on the RHI Task

According to the reference model, the minimum jerk model was trained into the fuzzy controller. The subject collaborated with the robot to move from the starting point A to the end point B for the adaptation process. During the movement, the fuzzy controller constantly calculates a corresponding damping according to the current velocity and force. The learning mechanism measures the deviation y_e from the minimum jerk trajectory.

The training is finished until the subject cannot feel any change of the performance improvement. The trajectories of the 1st, 15th, and 30th training were analyzed shown in Fig. 19.8.

The four curves in Fig. 19.8 are the motion trajectories of the human-robot motions according to the minimum jerk model movement. It can be found that the motion trajectory is very close to the trajectory of the minimum jerk model after 30 times training. The maximum error e_{max} between the 1st curve and the 30th curve is at $\tau = 0.67$, and the maximum error $e_{max} \approx 16.64$mm.

19.3.2 Simulation on Virtual Constraint Control

19.3.2.1 Coefficients of Linear Gain Admittance Control

According to the range of guiding force tested above, the maximum operating force of the doctor is set at 5 N to ensure safety, which is

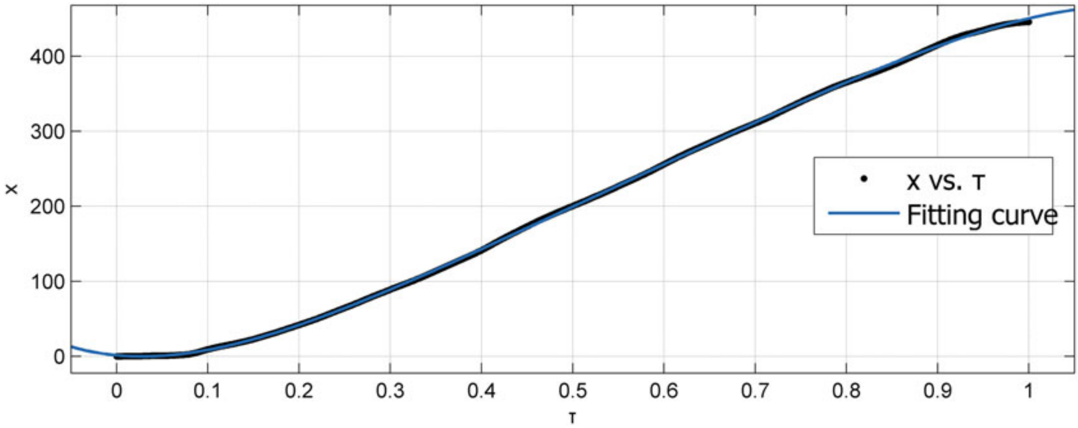

Fig. 19.7 Minimum jerk model equation of motion fitting curve

Fig. 19.8 Trajectories of training during operation during process S1

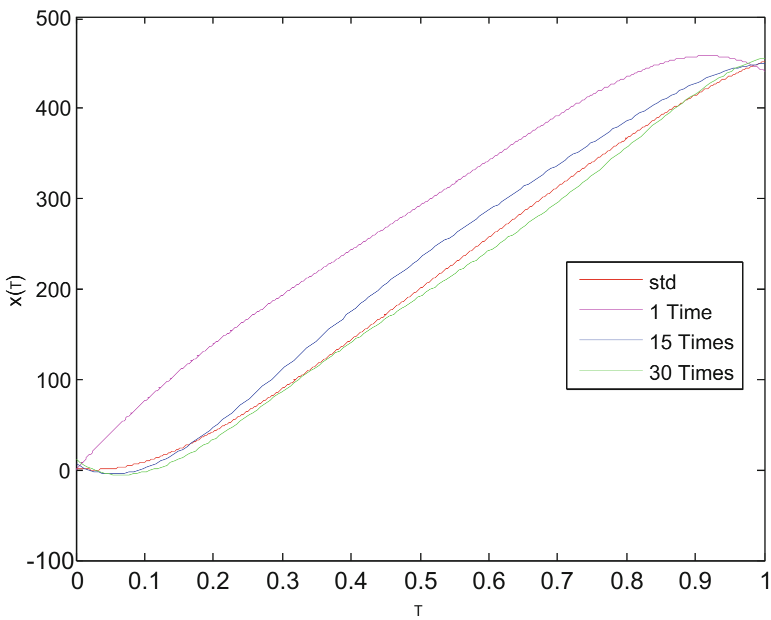

$F_{max} = 5$, and the dead zone operating force is set at 0.5 N, i.e., $F_{dz} = 0.5$, to prevent the sensor from overly sensitive and the inadvertent operation of surgeon.

In addition, the velocity of doctors moving the surgical tools in surgical zone is recorded through observing conventional bone resection surgery, and it is less than 10 mm/s under normal condition.

Let $V = 10mm/s$, $F_h = 5N$, and put them into Eq.(19.2), and then get $B_d = 0.5N \cdot s/mm$. Now Eq.(19.15) transforms to the following:

$$\begin{cases} V = -10 & F_h \leq -5.5 \\ V = 2\left(F_h + 0.5\right) & -5.5 < F_h \leq -0.5 \\ V = 0 & -0.5 < F_h < 0.5 \\ V = 2\left(F_h - 0.5\right) & 0.5 \leq F_h < 5.5 \\ V = 10 & F_h \geq 5.5 \end{cases} \tag{19.22}$$

The velocity-force curve of the linear gain admittance control is shown in Fig. 19.9.

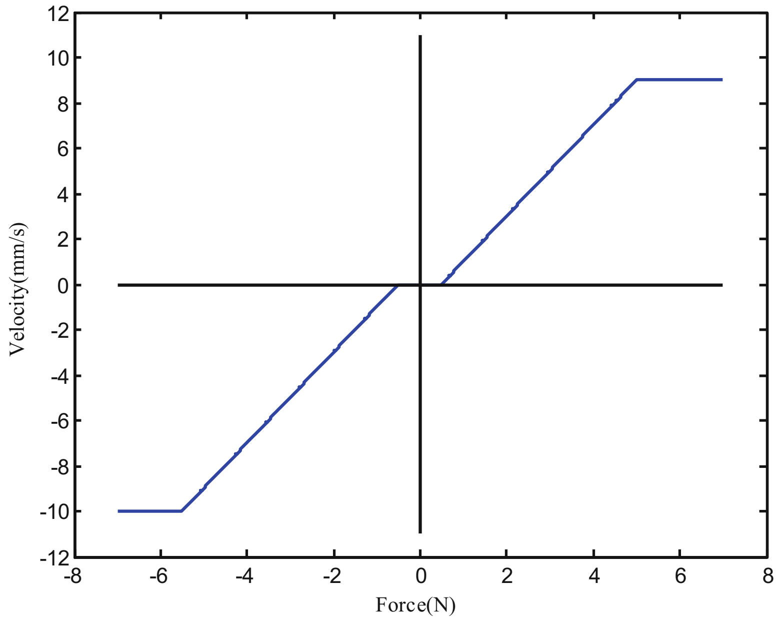

Fig. 19.9 The velocity-force curve of linear gain admittance control in surgical zone

19.3.2.2 Simulation on Virtual Constraint Control Strategy

Three types of force model for simulation and a real force exerted during experiment are carried out to find out how the velocity of the robot varies under the guiding force in the normal direction. In Fig. 19.4 the distance *d* of virtual constraint is set to 5 mm. Assume that the value of guiding force at the starting point is 3 N, and the value of guiding force eventually reaches to 7 N at the end point. The velocity slows down as the guiding force increases and then the surgeon feels the increased discomfort.

In addition, the increase of force is assumed as a kind of linear, square, or third power function of distance, respectively, in this study, which is used to verify the convergence of the speed at the critical boundary. Table 19.4 lists the force function defined here for simulating. Result shows that the velocity converges to zero, as shown in Fig. 19.10.

At last, the actual experiment on this control strategy is also shown in Fig. 19.10. It shows that the Cartesian velocity of the robot can converge to zero when reaching the restrained boundary no matter how the guiding force changed.

Table 19.4 Simulation force for virtual constraint on normal direction

Simulation	Force simulation model related to distance (N)
1	$F_n = 3 + (0.8 * x)$
2	$F_n = 3 + (0.4 * x)^2$
3	$F_n = 3 + (0.31748 * x)^3$

19.3.2.3 Virtual Constraint Control Testing with Acrylic Model

Tests on the efficiency of virtual constraint control are shown in Fig. 19.11. Three different zones are designed in acrylic board model, and a NDI position tracker is installed onto it to determine the relationship between position of robot and the acrylic board. Then the milling experiment is done under the guidance of the interns.

In this kind of experiments, the width of region II is designed to 5 mm. The starting point of the robot is set at Point A in Zone I. First, the operator drags the robot from the region I into the region II to reach to the restrained boundary. Then the operator drags the robot around the restrained boundary with the outward force.

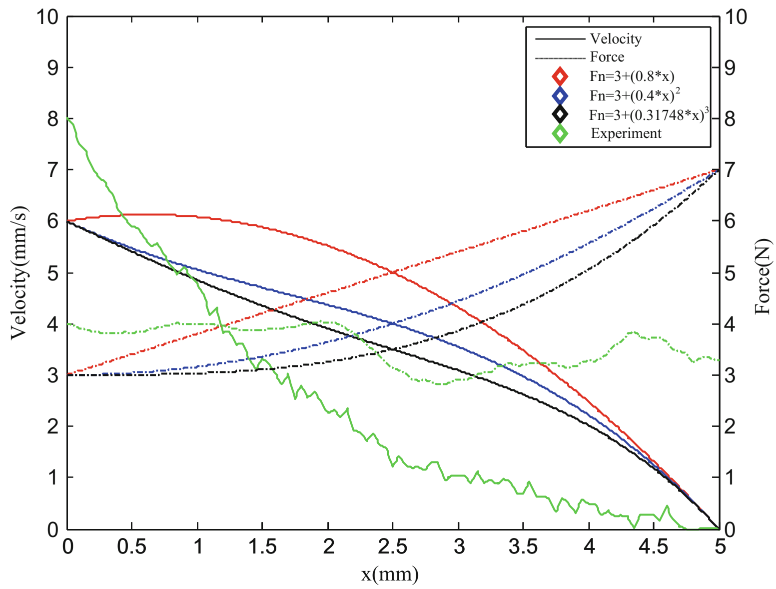

Fig. 19.10 Simulation of convergence of the speed by virtual constraint on normal direction

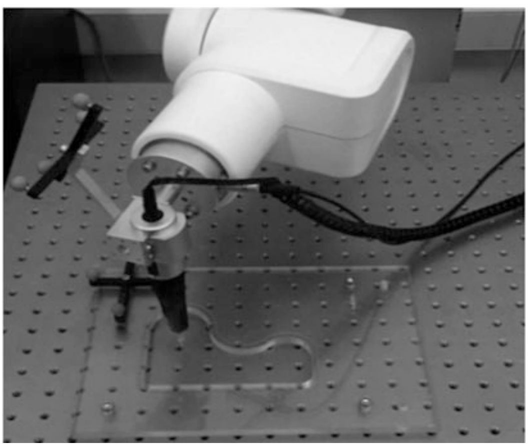

Fig. 19.11 Test of virtual constraint of the RHI control with acrylic model

At last, the operator drags the robot across every region repeatedly. During the operation, the position in the target coordinate system of the robot's end is recorded by the NDI tracking device shown in Fig. 19.5, and the trajectory is shown in Fig. 19.12. The trajectory is divided into three corresponding sections: AB, BC, CD for different motion tests.

Errors were calculated relative to the critical boundary in sections BC to verify the actual performance of virtual constraint control. The average error was 0.439 mm, and the root mean square error was 0.348, with the maximum error of 0.612 mm. We can know that the precision of the system can meet the actual surgical needs.

The guiding force is also recorded by a force/torque sensor. Figure 19.13 shows the magnitude of the guiding force and robot's velocity in tangential direction and normal direction, respectively.

In Fig. 19.13, F_n is the actual guiding force applied in the normal direction by the operator, and $c_n F_n$ is the guiding force in normal direction which restricted by virtual constraint.

In Fig. 19.14, comparing the velocity and force of AB section in Zone II, it is found that after entering Zone II, the force increases obviously at start, but the velocity of the robot decreases and eventually converges to zero. Therefore, the virtual constraint algorithm is stable and feasible for surgical robots.

19.3.3 Pilot Study on Sawbone Femur Model

Robotic assist is very useful in bone tumor resection surgery because of the highly cutting

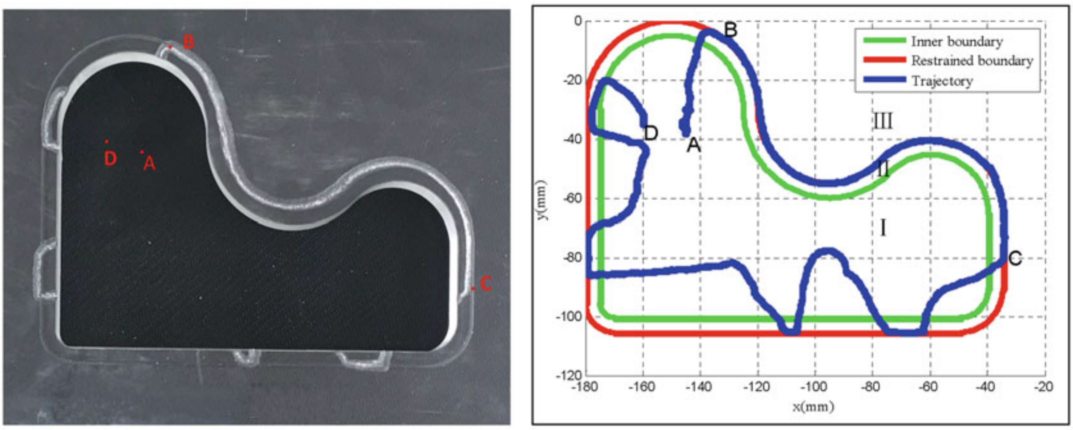

Fig. 19.12 Acrylic model for virtual constraint testing

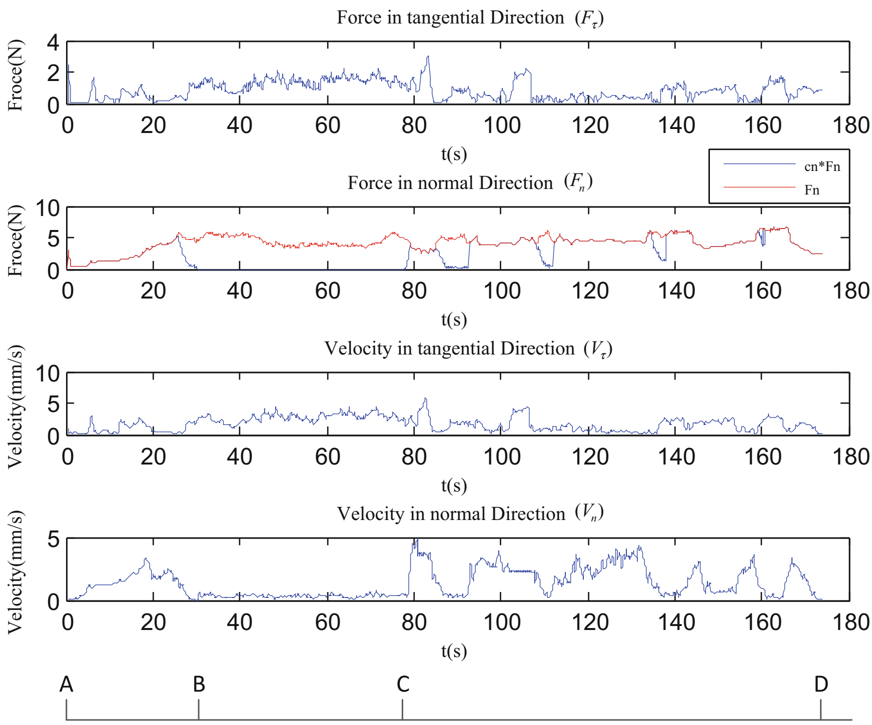

Fig. 19.13 Guiding force and velocity recorded

precision needed for the convenient of prosthesis implantation. Khan et al. had conducted the pilot study on bone tumor resection with Mako RIO robot (Khan et al. [14]).

In this study, the bone tumor cutting platform is build up as in Fig. 19.5. The operation processes are the following:

1. A position tracker is installed onto the sawbone for establishing the position relationship with the robot.
2. The focal bone area that must be cut was marked out on the sawbone (Fig. 19.15a). Then the positions of the marked area's boundary on the sawbone surface

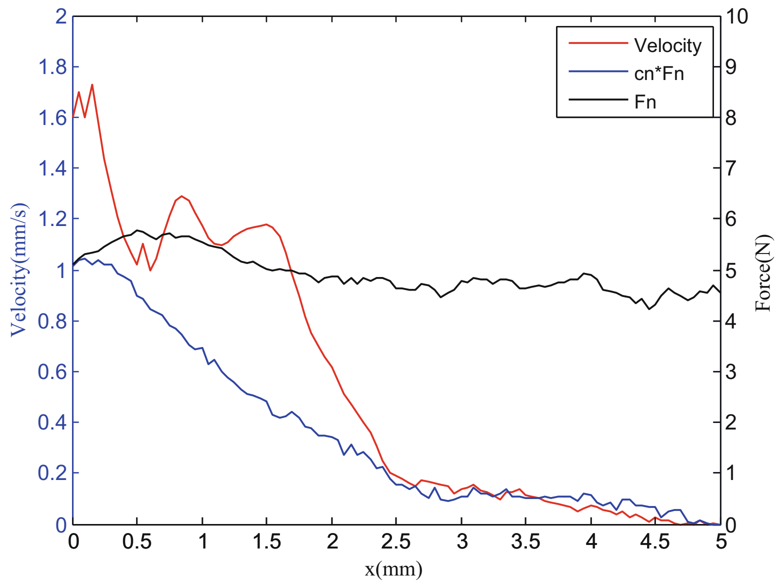

Fig. 19.14 Convergence of the velocity to critical boundary with virtual constraint

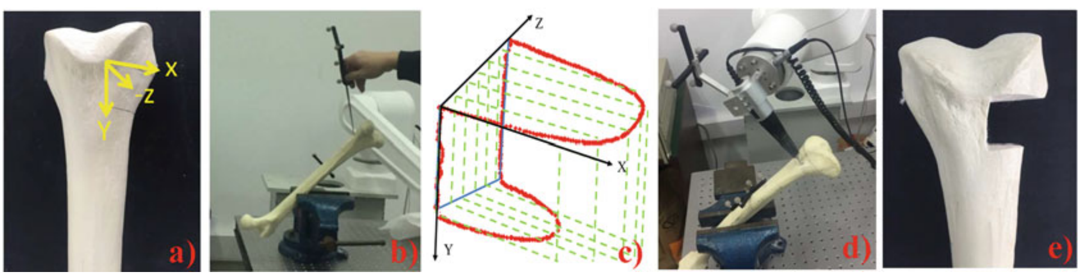

Fig. 19.15 The Results of the Bone Milling Experiments on Sawbone. (**a**) Mark the focal bone area. (**b**) Collecting the positions of the boundary on the sawbone. (**c**) Virtual constraint planned from the surface 3D model. (**d**) Performs the operation. (**e**) Result of the bone cut.

were sampled by the NDI tracking device (Fig. 19.15b).

3. The surface 3D model is reconstructed by the tracked points. And the virtual constraint is planned layer by layer from the surface 3D model (Fig. 19.15c).
4. At last, the surgeon performs the operation with the assist of robot (Fig. 19.15d).
5. Result of the bone cut by using the intelligent control method we proposed (Fig. 19.15e).

Three tests were done on sawbones to verify the effectiveness of this intelligent control method, and the results were shown in Fig. 19.15. It can be concluded that the method we proposed is useful for bone cutting in orthopedics surgery. More tests shall be done to obtain the effective data for evaluating the robotic surgical system in the future.

19.4 Conclusions

In this study, an intelligent admittance control method is proposed based on fuzzy model reference learning control that combined with the virtual constraint control according to the requirements of human-robot interaction during orthopedics surgery. The main purpose of this study is to solve the issues of intuitive interaction between surgeon and surgical robot and to fulfill the needs of more compliance, more safety, and high precision during robotic surgery. Preliminary experiments show that the proposed method is a useful solution based on surgeon's guiding force.

Nevertheless, developing a robotic system for surgery is a challenging work. A suitable surgical navigation system shall be integrated into this robot system later for performing more practical test, such as test on animal or cadaver bone. And more data shall be collected for further analysis to validate the effectiveness and performance of the surgery performed by robot assisted.

On the other hand, the robot in surgery has the trend of more and more instrumentalization for easy using. Accordingly, the better interactive ability between surgeon and the robot is a key factor for surgeon to select the robot in the future. A good interactive method or useful control strategy will make the robot more easily acceptable in practice. Maybe to model the robots' behavior based on that of humans' is a good method to solve this kind of issues.

Acknowledgments This work has been supported by many individuals and organizations. In particular, we would like to thank Dr. HU Yan from Jinan University and Dr. GAN Minfeng and Dr. ZHOU Xiaofei from First Affiliated Hospital of Soochow University for their valuable suggestions during our research. This project was supported by the National Natural Science Foundation of China (No. 61375090, U1613224) and National High-tech R&D Program (863 Program) (No. 2015AA043204).

References

1. Baena F, Davies B (2010) Robotic surgery: from autonomous systems to intelligent tools. Robotica 28(2):163–170
2. Banks SA (2009) Haptic robotics enable a systems approach to design of a minimally invasive modular knee arthroplasty. Am J Orthop 38(2):23–27
3. Cinquin P (2011) How today's robots work and perspectives for the future. J Visc Surg 148(5):12–18
4. Cruces RA, Wahrburg J (2007) Improving robot arm control for safe and robust haptic cooperation in orthopaedic procedures. Int J Med Robot Comp Assist Surg 3(4):316–322
5. Dimeas F, Aspragathos N (2014) Fuzzy learning variable admittance control for human-robot cooperation. Paper presented at the international conference on the intelligent robots and systems (IROS), 4770–4775 September 2014
6. Duchaine V, Gosselin CM (2007) General model of human-robot cooperation using a novel velocity based variable impedance control. Paper presented at the euro haptics symposium on haptic interfaces for virtual environment and Teleoperator systems, 446–451 March 2007
7. Haidegger T, Benyó B, Kovács L et al (2009) Force sensing and force control for surgical robots. IFAC Proc 42(12):401–406
8. Hancock PA, Billings DR, Schaefer KE et al (2011) A meta-analysis of factors affecting trust in human-robot interaction. Hum Factors 53(5):517–527
9. Ho SC, Hibberd RD, Davies BL (1995) Robot assisted knee surgery. IEEE Eng Med Biol Mag 14(3):292–300
10. Ikeura R, Inooka H (1995). Variable impedance control of a robot for cooperation with a human. Paper presented at the international conference on the Robotics and Automation (ICRA), 3097–3102 May 1995
11. Jakopec M, Baena FR, Harris SJ et al (2003) The hands-on Orthopaedic robot "Acrobot": early clinical trials of Total knee replacement surgery. Trans Robot Autom 19(5):902–911
12. Kapoor A, Li M, Taylor RH (2006) Constrained control for surgical assistant robots. Paper presented at the international conference on the Robotics and Automation (ICRA), 231-236 May 2006
13. Kazanzides P, Zuhars J, Mittelstadt B, et al (1992) Force sensing and control for a surgical robot. Paper presented at the international c on the robotics and automation, 612–617 May 1992
14. Khan F, Pearle A, Lightcap C et al (2013) Haptic robot-assisted surgery improves accuracy of wide resection of bone tumors: a pilot study. Clin Orthop Relat Res 471(3):851–859
15. Kwon DS, Yoon YS, Lee JJ et al (2001) ARTHROBOT: a new surgical robot system for total hip arthroplasty. Intell Robot Syst 2:1123–1128
16. Langlotz F, Nolte LP (2004) Technical approaches to computer-assisted orthopedic surgery. Eur J Trauma 30(1):1–11
17. Layne JR, Passino KM (1993) Fuzzy model reference learning control for cargo ship steering. IEEE Control Syst 13(6):23–34
18. Layne JR, Passino KM (1996) Fuzzy model reference learning control. J Intell Fuzzy Syst 4(1):33–47
19. Lecours A, Mayer-St-Onge B, Gosselin C (2012) Variable admittance control of a four-degree-of-freedom intelligent assist device. Paper presented at the international conference on the Robotics and Automation (ICRA), 3903-3908 May 2012
20. Leung KS, Ning TANG, Cheung LW et al (2008) Robotic arm in orthopaedic trauma surgery–early clinical experience and a review. Spinal Surg 1(2): 3–4
21. Maillet P, Nahum B, Blondel L, et al (2005) BRIGIT, a robotized tool guide for orthopedic surgery. Paper presented at the international conference on the Robotics and Automation, 211–216 April 2005
22. Marayong P, Li M, Okamura AM., Hager GD (2003) Spatial motion constraints: theory and demonstra-

tions for robot guidance using virtual fixtures. Paper presented at the 3rd international conference on the Robotics and Automation, 1954–1959 September 2003

23. Miller L (2011) Robotics in orthopedic surgery: 6 points on the present and future. In: Becker's orthopedic, Spine & Pain Management Review. http://www.beckersorthopedicandspine.com/orthopedic-spine-device-mplant-news/item/4201-robotics-in-orthopedic-surgery-6-points-on-the-present-and-future. Accessed 1 Jan 2013
24. Newman WS (1992) Stability and performance limits of interaction controllers. J Dyn Syst Meas Control 114(4):563–570
25. Ott C, Mukherjee R, Nakamura Y (2010) Unified impedance and admittance control. Paper presented at the international conference on the robotics and automation (ICRA), 554–561 May 2010
26. Quaid AE, Kang H, Moses D et al (2014) Haptic guidance method. United State Patent No. 8911499B2
27. Rahman MM, Ikeura R., Mizutani K (1999) Investigating the impedance characteristic of human arm for development of robots to co-operate with human operators. Paper presented at the 99th international conference on the *Systems,* Man, and Cybernetics, 676–681 1999
28. Robotics VO (2013) A roadmap for US robotics: from internet to robotics. Robotics Virtual Organization
29. Sugano N (2003) Computer-assisted orthopedic surgery. J Orthop Sci 8(3):442–448
30. Taylor RH (2006) A perspective on medical robotics. Proc IEEE 94(9):1652–1664
31. Taylor RH, Mittelstadt BD, Paul HA et al (1994) An image-directed robotic system for precise orthopaedic surgery. Trans Robot Autom 10(3): 261–275
32. Troccaz J, Delnondedieu Y (1996) Semi-active guiding systems in surgery. A two-dof prototype of the passive arm with dynamic constraints (PADyC). Mechatronics 6(4):399–421

20 Multilevel Fuzzy Control Based on Force Information in Robot-Assisted Decompressive Laminectomy

Xiaozhi Qi, Yu Sun, Xiaohang Ma, Ying Hu, Jianwei Zhang, and Wei Tian

Abstract

The lumbar spinal stenosis (LSS) is a kind of orthopedic disease which causes a series of neurological symptom. Vertebral lamina grinding operation is a key procedure in decompressive laminectomy for LSS treatment. With the help of image-guided navigation system, the robot-assisted technology is applied to reduce the burdens on surgeon and improve the accuracy of the operation. This paper proposes a multilevel fuzzy control based on force information in the robot-assisted decompressive laminectomy to improve the quality and the robotic dynamic performance in surgical operation. The controlled grinding path is planned in the medical images after 3D reconstruction, and the mapping between robot and images is realized by navigation registration. Multilevel fuzzy controller is used to adjust the feed rate to keep the grinding force stable. As the vertebral lamina contains different components according to the anatomy, it has different mechanical properties as the main reason causing the fluctuation of force. A feature extraction method for texture recognition of bone is introduced to improve the accuracy of component classification. When the inner cortical bone is reached, the feeding operation needs to stop to avoid penetration into spinal cord and damage to the spinal nerves. Experiments are conducted to evaluate the dynamic stabilities of the control system and state recognition.

Keywords

Decompressive laminectomy · Surgical robot · Multilevel fuzzy control · State recognition

X. Qi · Y. Sun · X. Ma · Y. Hu (✉)
Shenzhen Key Laboratory of Minimally Invasive Surgical Robotics and System, Shenzhen Institutes of Advanced Technology, Chinese Academy of Sciences, Shenzhen, China
e-mail: xz.qi@siat.ac.cn; yu.sun@siat.ac.cn; 954373276@qq.com; ying.hu@siat.ac.cn

J. Zhang
University of Hamburg, Hamburg, Germany
e-mail: zhang@informatik.uni-hamburg.de

W. Tian
Beijing Jishuitan Hospital, Beijing, China
e-mail: tianweijst@vip.163.com

20.1 Introduction

Lumbar spinal stenosis (LSS) is the most common spinal disease in older individuals, which will cause pain and numbness in the lower limbs

G. Zheng et al. (eds.), *Intelligent Orthopaedics*, Advances in Experimental Medicine and Biology 1093, https://doi.org/10.1007/978-981-13-1396-7_20

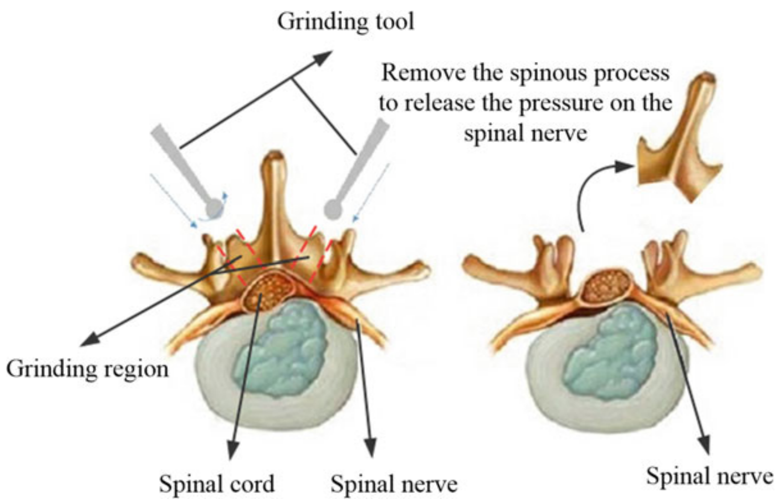

Fig. 20.1 The laminectomy operation

[2, 32]. And it is one of the most common reasons to perform spinal surgery at an advance age [37]. Laminectomy is an effective operation for severe cases [13], and vertebral lamina grinding is the key procedure of this operation. Figure 20.1 shows the operation of laminectomy. It requires an experienced surgeon hands grinding instrument to mill out slots with the help of navigation equipment until an acceptable thickness is removed from vertebral lamina to release the pressure on the spinal nerve. However, the long-time operation can cause surgeon tired and hands trembling, which will bring the risk of harming the vital tissues. For the vital arteries and nerves distributed in spinal canal [31], any damage to these tissues would cause irreparable side effects to the patients, such as long-time pain, paralysis, and death. Although the application of piezosurgery in laminectomy reduces the invasiveness, it has a high maintenance cost. For these reasons, the robot can be used to assist surgeons to complete the grinding operation quickly with ensuring the accuracy and safety.

In order to achieve high-quality operation, a few techniques are applied in clinical-assisted robot including the image-based navigation dynamic and safety control [1]. Navigation system just like the robot's eyes which guided it completes planned operation at planned location. Since 1995, the first report on the successful clinical application is an image navigation system for pedicle screw placement in the lumbar spine [21, 22], after which the image-based navigation has a great development in minimally invasive spinal surgery [39]. This technology helps surgeons perform surgeries in a limited space. The virtual fluoroscopy and CT-based and 3D fluoroscopy-based strategies are often used in image guidance [11]. Virtual fluoroscopy can provide intraoperative images, which is usually applied in computer-assisted orthopedic surgery [10, 23]. However, it has the limitation that the patient and surgeons will be affected by X-ray radiation for many times. The 2D/3D registration, such as the registration of intraoperative X-ray images and preoperative CT, is a main procedure in image-based navigation to build the mapping between patients and medical images. The intensity-based or feature-based registration algorithm is a very common method as the condition of similarity metrics. The former is mostly adopted because of its higher identification for the anatomical structures with less invasiveness in spinal surgery [19, 20]. Siddon, R L [30] proposed a fast calculation algorithm for exacting radiological path for a three-dimensional CT array, which raises the efficiency of the DDRs. Jacobs, Filip et al. [36] improved Siddon's algorithm, resulting in a considerable speedup. Russakoff [26] and Chen [4] et al. improved the computational efficiency for the automatic registration of orthogonal X-ray images with volumetric CT data. Luan et al. [18]

proposed a 3D navigation and monitor method for spinal grinding operation, which alerts the surgeon to stop operation before penetrating the lamina.

Although image navigation technology has enough accuracy applied in clinical environment, there is a long learning curve for surgeons to accomplish. The minor inaccuracies in the handling might translate into major surgical errors. The reference paper [39] shows that the accuracy may be lost in the interaction between surgeons and the image-guidance system because of the deformation of the spine and other factors. However, robot and image-guidance system can exchange data with a high accuracy and efficiency.

Recently, more and more attention has been paid on robot-assisted spinal surgery with the image-based navigation system. Kwoh et al. [14, 15] originally combined navigation and industry robot PUMA200 to discuss experiments for the future high-technology neurosurgical stereotactic procedures, which opened a new research direction of robot in medical field. Sautot et al. [27, 28] firstly applied the image navigation system to guide a PUMA260 which hands a laser emitter to assist the surgery accomplish pedicle screw placement along planned path. Taylor et al. [38] developed an image-directed robotic system to augment the performance of human surgeons in surgery. Shoham et al. [29] developed a miniature robot for the surgical procedure, which can guide the path of the pedicle with a few intraoperative fluoroscopic X-ray images. The SPINEBOT robot is designed by Chung et al. [5–7], which can be planned in three dimensions. The new version SPINEBOT V2 can detect the patient and instrument positions by processing the fluoroscopic images with 2D/3D registration algorithm. Yen et al. [43, 44] came up with a CT-free surgical planer for the knee replacement which uses the probe to measure specific anatomical features positions under an optical tracking device to generate the cutting boundary. Sugita et al. [35] used the sculpted joint surface to fit the shape of an artificial joint, and the grinding path was planned preoperatively by setting the instrument path data in discrete coordinates. Inoue et al. [12] developed a robotic system for total knee arthroplasty, which can transfer the CT series images to 3D model to plan grinding path in the CAM system. However, the related studies of vertebral lamina are still scarce.

For the vertebral lamina, there are irregular surface and different tissues constraints. Therefore, the grinding procedure always requires dynamic control to enhance the system stability. Sugita et al. [12, 33, 34] developed a force control system for grinding operation. Yen et al. [43, 44] proposed an impedance force control between the robot and the surgeon to maintain the safety, stability, and accuracy in bone resection process. Inoue et al. [12] developed a robotic-assist system for knee arthroplasty which can estimate the bone hardness to adjust the feed rate. Deng et al. [8] proposed a grinding force control based on fuzzy logic controller, which can shorten the grinding time and stabilize the contact force. Fan et al. [9] designed a closed-loop system to control the feed velocity based on force signals.

This paper presents a new interactive method to achieve robot-assisted vertebral lamina grinding operation with high accuracy, efficiency, and safety. The mapping between the image and real spaces is established by registration algorithm, and a rapid planning method based on BSP tree in 3D image is proposed. The fuzzy controller is designed to control the robot motion state to keep the system have a good dynamic performance. A feature extraction method for bone texture classification is proposed to improve the classification accuracy.

The rests of the paper are organized as follows. Section 20.2 illustrates the registration and grinding trajectory planning. Section 20.3 proposes an adaptive fuzzy logic controller for grinding control, and the experiments are applied to test its effect. The bone texture feature extraction method is introduced in Sect. 20.4, and its effect with original feature for bone texture classification based on SVM is contrasted. Section 20.5 is the conclusion.

20.2 Grinding Path Planning and 2D/3D Registration

In order to achieve the automated grinding procedure by robot and guarantee the grinding quality, a well preoperative planning is essential. For the decompressive laminectomy, robot needs to follow a pre-planned path to finish the operation. A grinding path generator is proposed which generates path based on the surface outline of the vertebral lamina in the reconstructed model from volumetric data. The planned path data can be transformed to the coordinate system of the robot by 2D/3D registration to navigate the robot to accomplish precise grinding. When the grinding is finished, the remainder bone will keep uniform thickness because the grinding path is parallel with the spinal canal wall, which ensured the grinding instrument do not penetrate into the spinal and damage the spinal nerve.

20.2.1 Grinding Path Generator

For robot-assisted operation, the grinding area should be well planned with image information. The interactive software is designed for this function. By this software, one 3D model of the spinal bone can be reconstructed based on CT series images. Surgeon adjusts the interactive box to set the operating area as shown in Fig. 20.2.

As shown in Fig. 20.3, the upper (outer cortex) and lower (inner cortex) surfaces are marked by discrete points calculated by ray casting and BSP tree methods. They will generate a set of grids with n points and the length-width ratio of grid region is t. w is the number of points located on short edge, l is the number of points located on long edge, which satisfy $n = w \times l$ and $t = l/w$. Therefore, w and l are calculated from the formula (20.1):

$$\begin{cases} w = \left\lfloor \frac{\sqrt{(t-1)^2+4nt}-t-1}{2t} \right\rfloor \\ l = \left\lfloor \frac{n}{w+1} \right\rfloor - 1 \end{cases} \tag{20.1}$$

The red points **PD** in the inner wall of spinal canal are used to interpolate the trajectory and generate a security layer to constrain the motion of the robot. For improving the grinding efficiency, a series of points is filtered out to prevent grinding in invalid area above the green points **PU**. The point-sets of **PD** and **PU** can be expressed as follows:

$$\mathbf{PU} : \begin{pmatrix} \mathbf{pu}_{11} & \cdots & \mathbf{pu}_{1l} \\ \vdots & \ddots & \vdots \\ \mathbf{pu}_{w1} & \cdots & \mathbf{pu}_{wl} \end{pmatrix} \tag{20.2}$$

$$\mathbf{PD} : \begin{pmatrix} \mathbf{pd}_{11} & \cdots & \mathbf{pd}_{1l} \\ \vdots & \ddots & \vdots \\ \mathbf{pd}_{w1} & \cdots & \mathbf{pd}_{wl} \end{pmatrix} \tag{20.3}$$

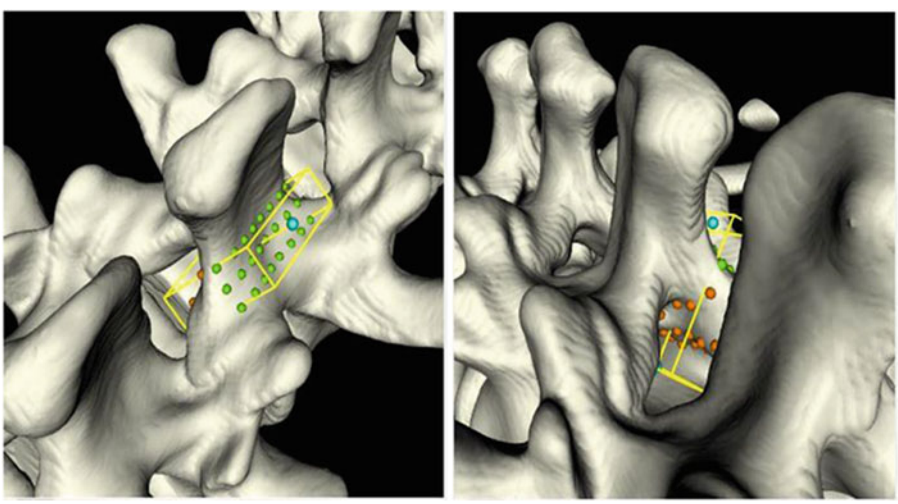

Fig. 20.2 The grid of points of grinding region

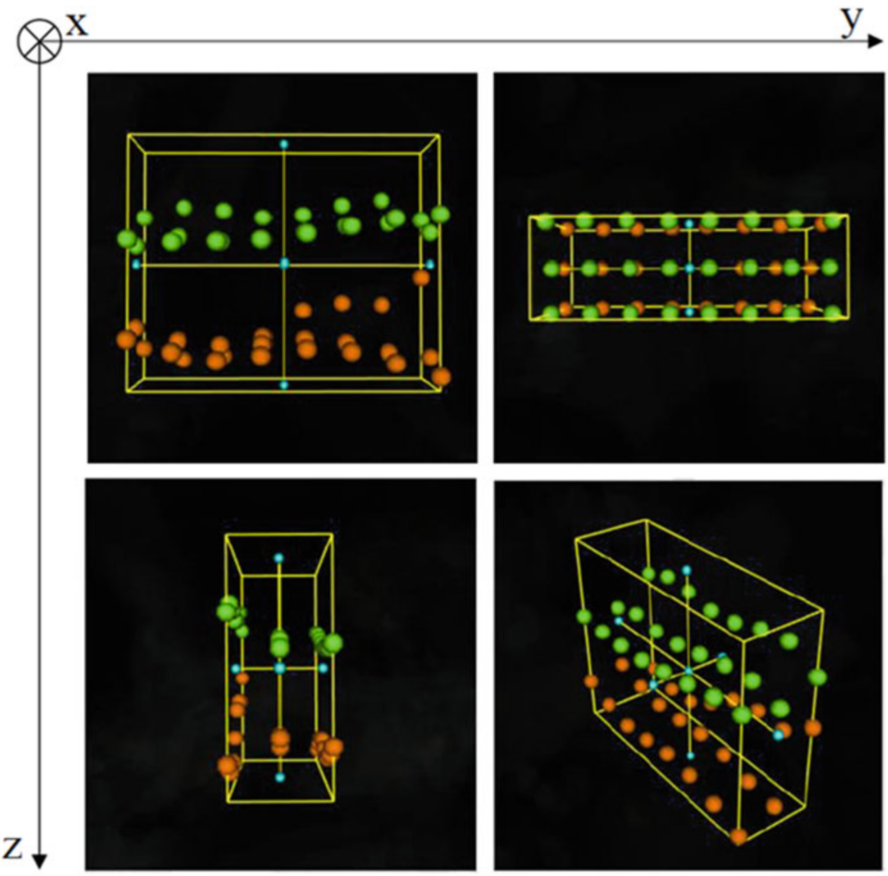

Fig. 20.3 The upper and lower points on vertebral lamina

Based on the point-sets of lower surface, a security constraint layer of points **PD’** expressed as the formula (20.4) is generated, which is also the last layer needed to be milled.

$$\mathbf{PD}' : \begin{pmatrix} \mathbf{pd}_{11}{}' & \cdots & \mathbf{pd}_{1l}{}' \\ \vdots & \ddots & \vdots \\ \mathbf{pd}_{w1}{}' & \cdots & \mathbf{pd}_{wl}{}' \end{pmatrix} \tag{20.4}$$

The coordinates of the point-sets can be obtained by the formula (20.5) as follows:

$$\mathbf{pd}_{ij}{}' = \mathbf{pd}_{ij} + Z_{\text{safe}} \cdot \mathbf{e}_{\text{p}}, \quad i \in [1, 2, \ldots, w], \; j \in [1, 2, \ldots, l] \tag{20.5}$$

where Z_{safe} is the safety margin and $\mathbf{e}_{\text{p}}$ is the projection unit direction vector.

Then the k-th layer’s cutting point-sets $\mathbf{PC}^k$ can be calculated from the formulas (20.6) and (20.7):

$$\mathbf{PC}^k : \begin{pmatrix} \mathbf{pc}_{11}{}^k & \cdots & \mathbf{pc}_{1l}{}^k \\ \vdots & \ddots & \vdots \\ \mathbf{pc}_{w1}{}^k & \cdots & \mathbf{pc}_{wl}{}^k \end{pmatrix} \tag{20.6}$$

$$\mathbf{pc}_{ij}{}^k = \mathbf{pd}_{ij}{}' + k \cdot Z_{\text{feed}} \cdot \mathbf{e}_{\text{p}} \tag{20.7}$$

where Z_{feed} is the depth of the feed.

Well, the generated grinding path points contain some invalid points, which must be filtered out when $T_{ij}{}^k < 0$, where $T_{ij}{}^k$ is the discrimination function whether the point is valid or not, which is calculated as follows:

$$T_{ij}^k = \operatorname{sgn}\left(\left(\mathbf{pu}_{ij} - \mathbf{pc}_{ij}{}^k\right) \cdot \mathbf{e}_{\text{p}}\right) \tag{20.8}$$

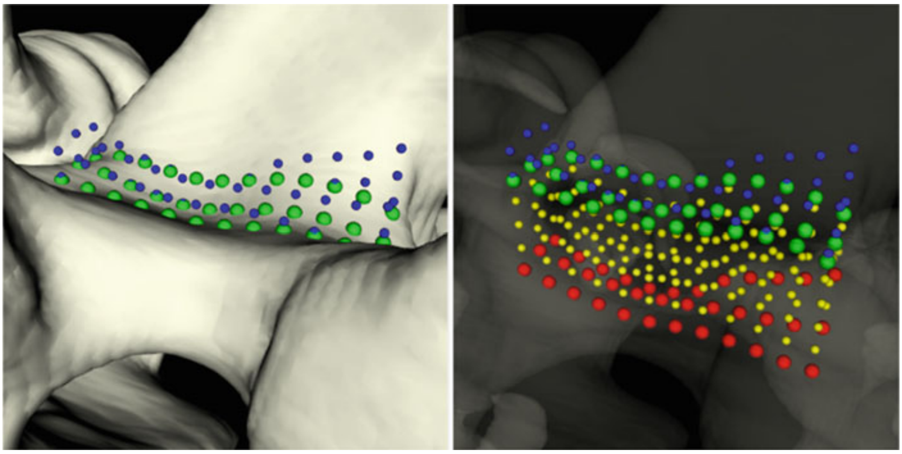

Fig. 20.4 The generated and filtered path with 36 points per layer

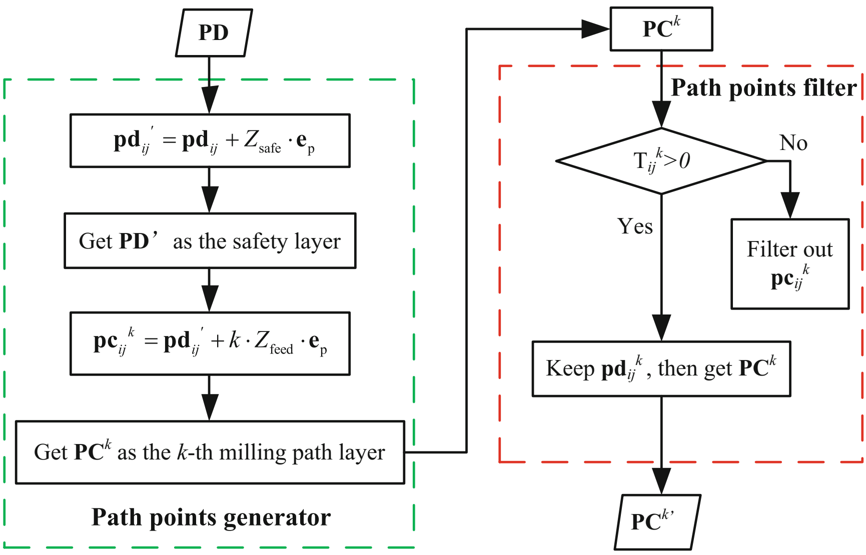

Fig. 20.5 Progress of grinding path generator

Finally, the generated and filtered path with at least 36 points per layer is shown in Fig. 20.4, and BSP tree is used to generate these balls to search the intersection between the cast ray and the image data with only one pixel thickness. The blue ones are invalid points and the yellow ones are the layers of path points reserved.

From the above, the progress of grinding path generator is shown in Fig. 20.5, which is based on the surface outline of the vertebral lamina in the reconstructed model from volumetric data. The planned path data can be transformed to the coordinate system of the robot by 2D/3D registration to navigate the robot to accomplish precise grinding.

20.2.2 2D/3D Registration for Grinding Navigation

The preoperative CT images have higher resolution and contain 3D information, but 2D X-ray images are often used to position the grinding instruments during operation. And the planned

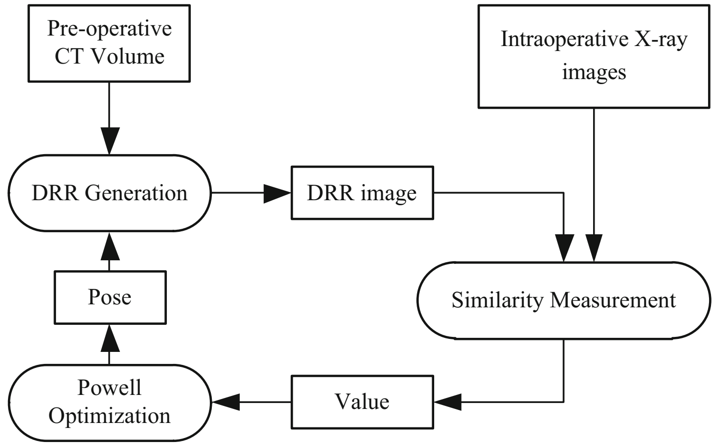

Fig. 20.6 The procedures of 2D/3D registration

data are under the coordinate system of the CT volume. Therefore, registration is needed to make sure 3D information can be used during the operation. The CT and X-ray images contain different dimension information, so we need to calculate the simulated X-ray projection images called digitally reconstructed radiographs (DRRs). And then, the maximum intensity projection (MIP) can be used to get the DRRs, which has high resolution to bone with high intensity [19]. For evaluating the effect of registration, mutual information (MI) is used as a measure of the similarity of objects [24, 25]. In this paper, we use the distance coefficient mutual information (DCMI) [17, 40] algorithm. Additionally, Powell optimization is applied to find the optimal results. The process of registration is showed in Fig. 20.6.

The original *MI* is given in the formula (20.9):

$$MI = \sum_{x,y} p(x, y) \log\left(\frac{p(x, y)}{p(x)p(y)}\right) \tag{20.9}$$

where $p(x)$ and $p(y)$ are the probability distributions in individual images, while $p(x, y)$ is the joint probability distribution.

Well, *DCMI* is given in the formula (20.10), which is improved by applying a coefficient $S(x)$ calculated in the formula (20.11):

$$DCMI = \sum_{x,y} p(x, y) \log\left(\frac{p(x, y)}{p(x)p(y)}\right) S(x) \tag{20.10}$$

$$S(x) = \frac{1}{1 + d(x)^2 d(y)^2} \tag{20.11}$$

where $d(\cdot)$ is the difference between the distances of the same intensities ($I_{x,y}$ and $J_{x,y}$) in X-ray image and DRR image and they can be obtained by the formula (20.12):

$$\begin{cases} d(x) = \left\| \sum \sqrt{\left(RI_x{}^2 + RJ_x{}^2\right)} - \sum \sqrt{\left(FI_x{}^2 + FJ_x{}^2\right)} \right\| \\ d(y) = \left\| \sum \sqrt{\left(RI_y{}^2 + RJ_y{}^2\right)} - \sum \sqrt{\left(FI_y{}^2 + FJ_y{}^2\right)} \right\| \end{cases} \tag{20.12}$$

Ultimately, the distance coefficient mutual information (*DCMI*) can be obtained from the formula (10, 11, 12), which is used as the iterative termination condition while optimizing the projection angles.

20.3 Grinding Force Control Based on an Adaptive Fuzzy Controller

The anatomical structure of the vertebral lamina is consisted of cortical and cancellous bone. The cortical bone is much denser than the cancellous bone, which forms the hard exterior of bones, while the cancellous bone has a porous trabecular structure which makes it soft and weak but flexible. In vertebral lamina grinding

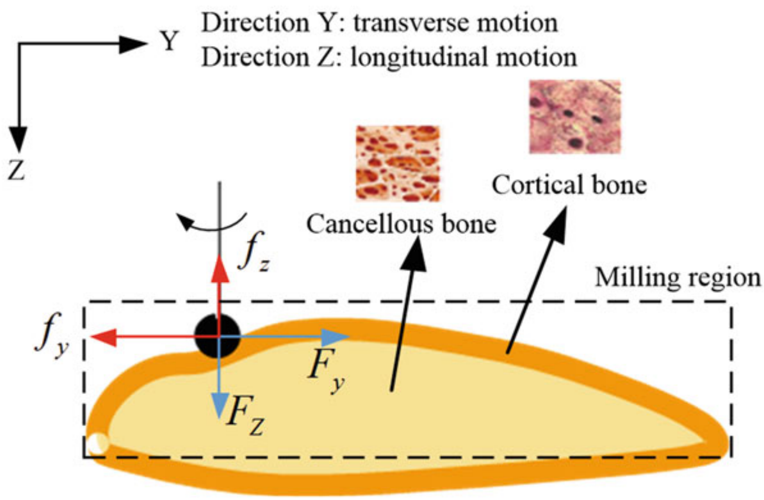

Fig. 20.7 The contact force during grinding procedure

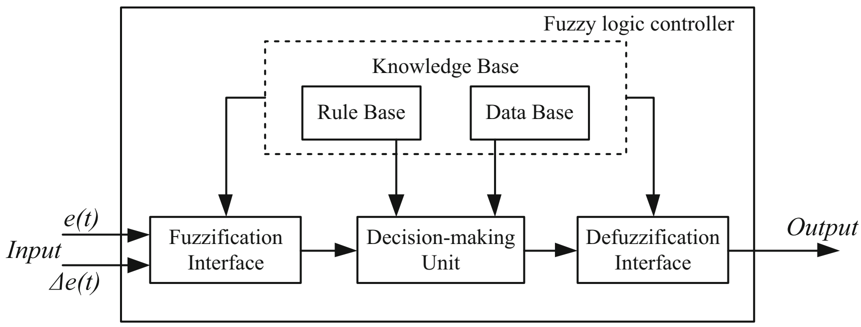

Fig. 20.8 Traditional fuzzy logic controller

operation, the bone conditions and instrument movements are time-varying for the irregular surface and the different tissues constraints. For this reason, the vertebral lamina and the grinding instruments produce vibration and a change in temperature which can lead to the imbalance between osteoblast and osteoclast to cause tissue damage around the operating area. Therefore, the adaptive parameters are necessary for the robot system controller to adjust the grinding speed automatically, and it is regular to use the force sensors feedback as the inputs.

As shown in Fig. 20.7, the contact force acting on the grinding bit can be decomposed in a dynamic coordinate which Y axis is time-varying according to the velocity direction. The decomposed forces include longitudinal force f_z and transverse force f_y. In order to improve the dynamic performance, an adaptive fuzzy controller will be used to adjust the grinding speed based on the transverse force f_y.

20.3.1 Multilevel Fuzzy Control System

As the irregular features of the vertebral lamina, the nonlinear process should be controlled to perform good dynamic performance. The fuzzy logic control technique can be used in the model-unpredictable control system with the controller parameters obtained from linguistic information based on human's experience rather than a mathematical model. The control algorithm framework [16] is shown in Fig. 20.8.

However, the control rules of fuzzy logic controller (FLC) is predefined and fixed during the control. The parameters of FLC may not always adapt time-varying conditions. Therefore, an adaptive FLC is required to be applied in vertebral lamina grinding.

The multilevel fuzzy controller (MLFC) system is a kind of adaptive FLC proposed by Xu et al. [41, 42], which has simpler structure and

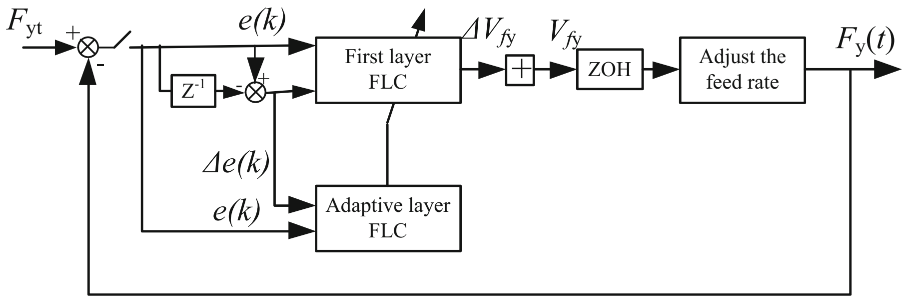

Fig. 20.9 MLFC for transverse contact force control

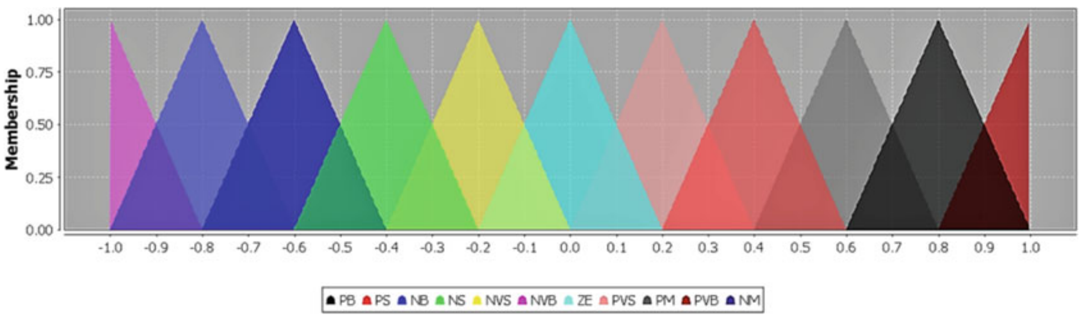

Fig. 20.10 Membership function of inputs

lower computation compared with some other FLCs. MFLC has two FLC layers, as shown in Fig. 20.9. The first layer is designed based on human's experience, and the second layer is an adaptive layer to compensate the effect of loads. Compared with traditional FLC, MLFC has higher adaptability for the high nonlinearities and time-varying system.

20.3.2 MLFC for Vertebral Lamina Grinding

A MLFC is designed to keep the transverse contact force to a desired value by controlling the transverse feed rate. When the cortical bone is milled, the transverse feed rate will be slower than cancellous bone to adapt to the compact structure and reduce heat generation.

The first layer of MLFC is a basic two-input and single-output controller designed based on experience. The error $e(k)$ which is calculated from the desired force f_{yt} and the feedback force $f_y(k)$ as shown in the formula (20.13) and the time difference $\Delta e(k)$ are set as the inputs, while the output u is the regulating value to the feed rate:

$$e(k) = \left[f_{yt} - f_y(k)\right] \cdot GE \tag{20.13}$$

The GE and GC are the scaling factors which map the $e(k)$ and $\Delta e(k)$ into the interval of $[-1{,}1]$, and then, the inputs and outputs are fuzzified to linguistic values by triangular membership functions shown in Fig. 20.10 and Fig. 20.11 as negative very big (NVB), negative big (NB), negative middle (NM), negative small (NS), negative very small (NVS), zero (ZE), positive very small (PVS), positive small (PS), positive middle (PM), positive big (PB), and positive very big (PVB). The corresponding rules based on these spaced triangular are listed in Table 20.1.

There are 121 control rules at all. Each one of the rules can be defined as the following form:

$$\text{R : if } e \text{ is } Ei \text{ and } \Delta e \text{ is } Ej\text{, t hen } u \text{ is } U\text{n}\,(i,\ j)$$

where e is the error $e(k)$ at time instant k, Δe is its change, u is the regulating value $u(k)$ at instant k, and E_i, E_j, $U_n(i,j)$ are corresponding linguistic values.

Use Mamdani's minimum fuzzy implication and center average defuzzification to get control signal from the formula (20.14):

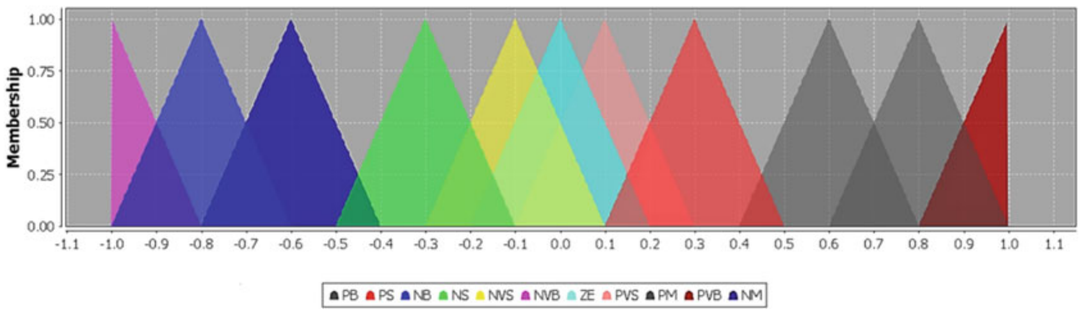

Fig. 20.11 Membership function of outputs

Table 20.1 Fuzzy control rules of first layer FLC

Change of error											
Error		NVB	NB	NM	NS	NVS	ZE	PVS	PS	PM	PB	PVB
	NVB	PVB	PVB	PVB	PVB	PVB	PVB	PB	PM	PS	PVS	ZE
	NB	PVB	PVB	PVB	PVB	PVB	PB	PM	PS	PVS	ZE	NVS
	NM	PVB	PVB	PVB	PVB	PB	PM	PS	PVS	ZE	NVS	NS
	NS	PVB	PVB	PVB	PB	PM	PS	PVS	ZE	NVS	NS	NM
	NVS	PVB	PVB	PB	PM	PS	PVS	ZE	NVS	NS	NM	NB
	ZE	PVB	PB	PM	PS	PVS	ZE	NVS	NS	NM	NB	NVB
	PVS	PB	PM	PS	PVS	ZE	NVS	NS	NM	NB	NVB	NVB
	PS	PM	PS	PVS	ZE	NVS	NS	NM	NB	NVB	NVB	NVB
	PM	PS	PVS	ZE	NVS	NS	NM	NB	NVB	NVB	NVB	NVB
	PB	PVS	ZE	NVS	NS	NM	NB	NVB	NVB	NVB	NVB	NVB
	PVB	ZE	NVS	NS	NM	NB	NVB	NVB	NVB	NVB	NVB	NVB

$$u = \frac{\sum_{i,j} \left[\mu_{E_i}(e) \cap \mu_{E_j}(\Delta e) \, U_{n(i,j)} \right]}{\sum_{i,j} \left[\mu_{E_i}(e) \cap \mu_{E_j}(\Delta e) \right]} GU \tag{20.14}$$

where GU is the scaling factor which maps the output u from the interval $[-1,1]$ to its real interval.

The second layer of MLFC is used to imitate the process of human learning to compensate the model uncertainties, time-varying parameters, and sensor noises. The system adaptability and stability will be enhanced for complex procedure of vertebral lamina grinding. Compared with the first layer, the second one has the same inputs but different output and fuzzy control rules, whose output is used to adjust center of first layer's output MFs. The corresponding rules are listed in Table 20.2.

As the same as the first layer, the second layer also has 121 control rules shown in Table 20.2, and each one of them can be defined as the following form:

$$\mathrm{R}: \text{if } e \text{ is } E_i \text{ and } \Delta e \text{ is } E_j, \text{ then } c \text{ is } Cn\,(i,\, j)$$

where e is the error $e(k)$ at time instant k, Δe is its change, C is the correction value to change the center of output MFs of first layer at instant k, and E_i, E_j, $C_m(i,j)$ are the corresponding linguistic values.

Use Mamdani's minimum fuzzy implication and center average defuzzification to get control signal corrected linguistic output $U_n(i,j)$ from the formula (20.15).

$$U_{n(i,j)} = U_{n(i,j)} + \frac{\sum_{i,j}\left[\mu_{E_i}(e) \cap \mu_{E_j}(\Delta e)\, C_{m(i,j)}\right]}{\sum_{i,j}\left[\mu_{E_i}(e) \cap \mu_{E_j}(\Delta e)\right]} GU \tag{20.15}$$

Finally, the new feed rate can be adjusted in the formula (20.16 and 20.17).

$$v_{\mathrm{f}}(k) = v_{\mathrm{f}}(k-1) + u(k) \tag{20.16}$$

$$u(k) = \frac{\sum_{i,j}\left[\mu_{E_i}(e) \cap \mu_{E_j}(\Delta e)\left(U_{n(i,j)} + \frac{\sum_{i,j}\left[\mu_{E_i}(e)\cap\mu_{E_j}(\Delta e) C_{m(i,j)}\right]}{\sum_{i,j}\left[\mu_{E_i}(e)\cap\mu_{E_j}(\Delta e)\right]} GU\right)\right]}{\sum_{i,j}\left[\mu_{E_i}(e) \cap \mu_{E_j}(\Delta e)\right]} GU \tag{20.17}$$

20.3.3 MLFC Grinding Experiments

20.3.3.1 Experiment Setup

The experimental platform consists of a host computer system, which runs our software for interaction, signal acquisition, and robot controller; a speed control grinding instrument system, which provides given rotation rate grinding motion; a three coordinate robot system, which receives and implements control instructions from the host computer system to achieve the feed of bone grinding instrument; and a bone clamp with three coordinate force collection system, which feeds back the contact force to the host computer system.

20.3.3.2 Experiment Method

In order to contrast the effects between normal bone grinding and MLFC grinding, three groups of experiments are performed, each of which contains a normal grinding procedure and a MLFC grinding procedure, and the two procedures are carried out in adjacent area on the bone. Normal grinding and MLFC grinding are explained as follows:

- 1) Normal grinding, free control under constant transverse feed velocity at 1 mm/s without MLFC.
- 2) MLFC grinding, MLFC controller was used to adjust the transverse feed rate to keep the transverse contact force to a desired value at 1.5 N, 2 N and 2.5 N.

Table 20.2 Fuzzy control rules of second layer FLC

Change of error												
Error		NVB	NB	NM	NS	NVS	ZE	PVS	PS	PM	PB	PVB
	NVB	PVB	PVB	PVB	PVB	PVB	PB	ZE	ZE	ZE	ZE	ZE
	NB	PVB	PVB	PVB	PVB	PB	PM	ZE	ZE	ZE	ZE	ZE
	NM	PVB	PVB	PVB	PB	PM	PS	ZE	ZE	ZE	ZE	ZE
	NS	PVB	PVB	PB	PM	PS	PVS	ZE	ZE	ZE	ZE	ZE
	NVS	PVB	PB	PM	PS	PVS	ZE	ZE	ZE	ZE	ZE	ZE
	ZE	PB	PM	PS	PVS	ZE	ZE	ZE	NVS	NS	NM	NB
	PVS	ZE	ZE	ZE	ZE	ZE	ZE	NVS	NS	NM	NB	NVB
	PS	ZE	ZE	ZE	ZE	ZE	NVS	NS	NM	NB	NVB	NVB
	PM	ZE	ZE	ZE	ZE	ZE	NS	NM	NB	NVB	NVB	NVB
	PB	ZE	ZE	ZE	ZE	ZE	NM	NB	NVB	NVB	NVB	NVB
	PVB	ZE	ZE	ZE	ZE	ZE	NB	NVB	NVB	NVB	NVB	NVB

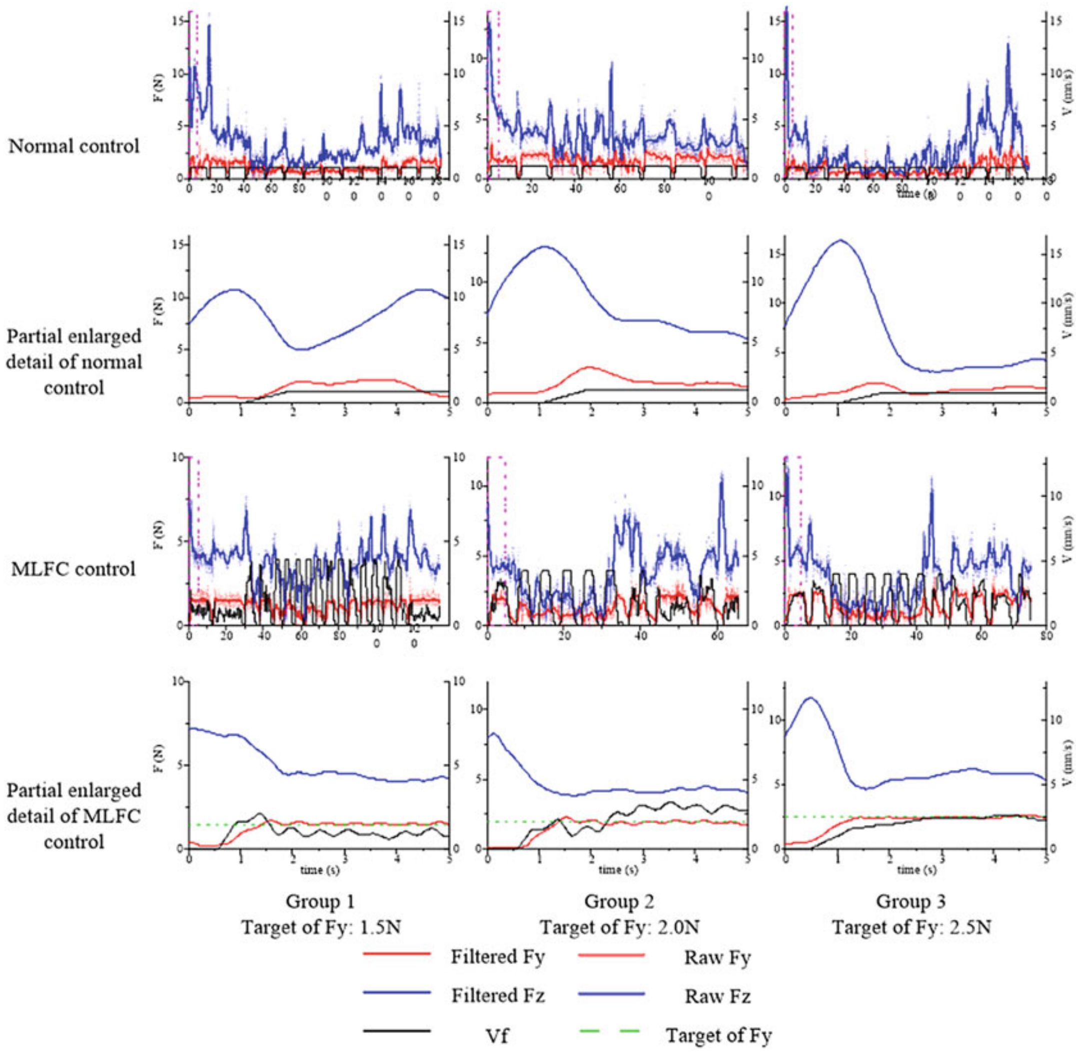

Fig. 20.12 Experiment result

In the experiments, a piece of scapula bone of pig was milled through by the two control strategies as mentioned above. A ball end grinding cutter was used as the grinding instrument; the grinding depth was set as 0.5 mm every layer; the rotation rate of grinding instrument was set as 20,000 r/min.

20.3.3.3 Experiment Result

Figure 20.12 shows the experiment results. From the three figures in the fourth rows, it can be seen that the transverse contact force can float at desired values when the cortical bone is milled compared with normal grinding. From the three figures in the third rows, it can be seen that the feed rate can be adjusted to given maximum value when cancellous bone is milled. Figure 20.13 shows the box figure of Fy when the first layer (cortical bone) is milled; it can be found that all the variation range of Fy can be reduced significantly.

In Table 20.3, the consumed time for grinding through the vertebral lamina and coefficient of variation of Fy during the first layer are compared between normal grinding and MLFC grinding. The consumed time can be meanly reduced over 45%, and the coefficient of variation can be meanly reduced over 80%.

Fig. 20.13 Box figure of Fy

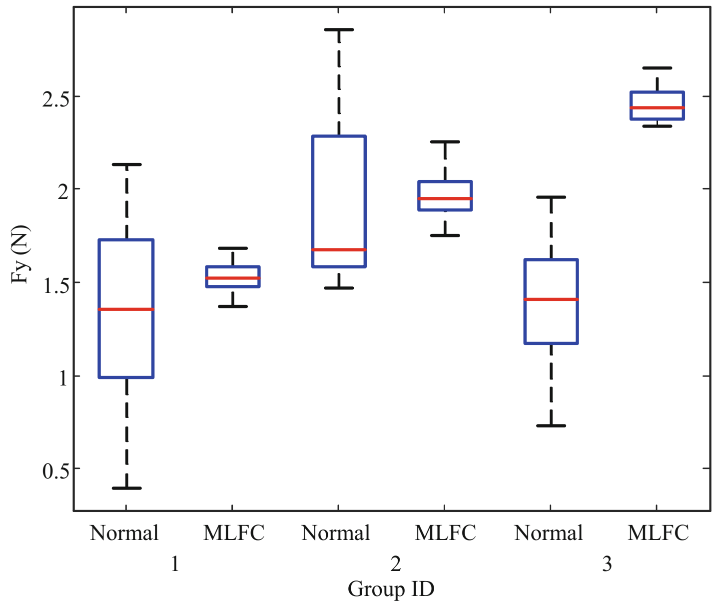

Table 20.3 Experiment results

Group ID		1	2	3
Consumed time (s)	Normal grinding	230	118	167
	MLFC grinding	135	68	78
Coefficient of variation	Normal grinding	0.343	0.237	0.239
	MLFC grinding	0.048	0.060	0.035

So the efficiency and safety of the assisted robot can be improved when MLFC is applied.

20.4 Safety Control Method Based on Bone Texture Recognition

In order to avoid the vital nerves in spinal canal harmed, the grinding procedure must be halted before the inner cortical bone is milled through. In this paper, we propose a feature extraction method for bone texture recognition under alterative feed rate.

20.4.1 Bone Texture Feature

The signals which are used for bone texture recognition contain transverse contact force Fy, axial contact force Fz, and transverse feed rate Vy. Fy is positively related to Vy and the hardness of the bone. When MLFC is applied to control transverse contact force, the transverse feed rate must be adjusted. In order to distinguish the bone texture based on the three signals, we must find a feature transform method to get a feature which is as far as possible related to the hardness of the bone but Vy. Here, this paper comes up with a method called energy consumed density (ECD) feature extraction, which is gotten from the energy consumed to mill off unit volume.

In this chapter, the feature $R = (Fy, Fz, Vy)^T$ from the raw signal can be called as the original feature, and then, the new feature $E = (E1, E2, E3)^T$ transformed by the method is called as ECD feature. Therefore, the ECD feature can be calculated according to the procedure as follows:

As for a sample, window contains n samples.

- A. Kinetic energy from robot's transverse feed

$$E_y = T \sum_{i=1}^{n} F_{yi} \cdot v_{yi} \tag{20.18}$$

- B. Dissipative heat energy during transverse feed

$$Q_{\mathrm{fy}} = \mu T \sum_{i=1}^{n} F_{zi} \cdot v_{yi} \tag{20.19}$$

- C. Deformation potential energy in grinding instrument

$$E_{\mathrm{k}} = \frac{{F_{yn}}^2 - {F_{y1}}^2}{2k} \tag{20.20}$$

- D. Volume of bone milled off

$$V_{\mathrm{y}} = T \cdot S_{\mathrm{z}} \sum_{i=1}^{n} v_{yi} \tag{20.21}$$

where T is the sample period, n is the number of samples in the sample window, μ is the friction coefficient, k is the distortion coefficient, and S_{z} is the cross-sectional area of grinding instrument.

Then, the energy consumed to mill the unit volume of bone is calculated in the formula (20.22):

$$w_{\mathrm{y}} = \frac{E_{\mathrm{y}} - E_{\mathrm{k}} - Q_{\mathrm{fy}}}{V_{\mathrm{y}}} = \frac{\sum_{i=1}^{n} F_{yi} \cdot v_{yi}}{S_{\mathrm{z}} \sum_{i=1}^{n} v_{yi}} - \frac{\mu \sum_{i=1}^{n} F_{zi} \cdot v_{yi}}{S_{\mathrm{z}} \sum_{i=1}^{n} v_{yi}} - \frac{{F_{yn}}^2 - {F_{y1}}^2}{2kT S_{\mathrm{z}} \sum_{i=1}^{n} v_{yi}} \tag{20.22}$$

Although there are some unknown coefficients, the ECD feature can be obtained by the formula (20.23).

$$\mathbf{E}_{\mathrm{ECD}} = (\mathbf{E}_1, \mathbf{E}_2, \mathbf{E}_3)^{\mathrm{T}} = \left(\frac{\sum_{i=1}^{n} F_{yi} \cdot v_{yi}}{\sum_{i=1}^{n} v_{yi}}, \frac{\sum_{i=1}^{n} F_{zi} \cdot v_{yi}}{\sum_{i=1}^{n} v_{yi}}, \frac{{F_{yn}}^2 - {F_{y1}}^2}{\sum_{i=1}^{n} v_{yi}} \right)^{\mathrm{T}} \tag{20.23}$$

Thestandardized original feature and ECD feature in 3D figures are plotted as shown in Fig. 20.14 and Fig. 20.15 for 1000 cortical bone, 1000 cancellous bone, and 1000 transition layer (where grinding instrument is between cortical bone and cancellous bone). In ECD feature space, the feature points from the same class gather together but disperse away from different classes compared with original feature space, which increases the separability.

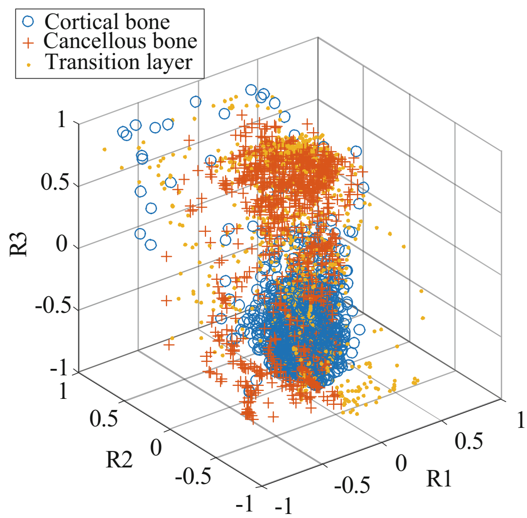

Fig. 20.14 Original feature space

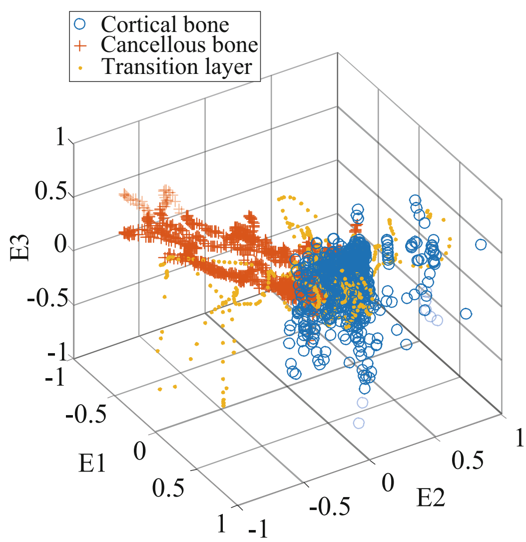

Fig. 20.15 ECD feature space

Table 20.4 Test result of SVM trained from original feature space

Sample class (300 each)	Classify results			Accuracy (%)	Comprehensive accuracy (%)
	cortical bone	cancellous bone	transition layer		
Cortical bone	268	12	20	89.33	75.89
Cancellous bone	15	236	49	78.67	
Transition layer	86	35	179	59.67	

Table 20.5 Test result of SVM trained from ECD feature space

Sample class (300 each)	Classify results			Accuracy (%)	Comprehensive accuracy (%)
	cortical bone	cancellous bone	transition layer		
Cortical bone	271	4	25	90.33	88.11
Cancellous bone	7	281	12	93.67	
Transition layer	41	18	241	80.33	

20.4.2 Bone Texture Recognition Based on SVM

In order to test the ECD feature's significance in bone texture classification, this paper applied the original feature and ECD feature to train and test SVM. We collected 1000 samples for each class, 700 of which are as train samples and 300 of which are as test samples. The libSVM [3] is used to achieve SVM and choose RBF as kernel function. The grid search method is applied to find the optimum parameters to train SVM. Then the test results of two SVMs trained from two feature spaces are shown in Table 20.4 and Table 20.5. It can be seen that the recognition accuracy has been improved significantly when ECD feature are used. The classified results based on original feature space have a low accuracy, especially for transition layer. Moreover, the transition layer is the key position to control the grinding process which affects the safety of the main tissues directly. On the other hand, the ECD feature shows a better result for classification. The method used in our experiment can recognize the different components effectively, which means the robot can be controlled to stop in time when the instrument reaches the inner cortical bone.

20.5 Conclusion

In this paper, some key technologies in vertebral lamina grinding are studied. 3D reconstruction from CT images is used to preoperatively plan the grinding path. 2D/3D registration is used to navigate the grinding instrument achieve preplanned grinding path. Multilevel fuzzy controller (MLFC) is applied to stabilize the transverse contact force and enhance the grinding efficiency. The effects of normal grinding and MLFC grinding are contrasted by the grinding experiments. The results show that MLFC grinding is more stable and efficient than the normal grinding. ECD feature extraction method is proposed to apply to improve separability for bone texture, which guarantees the safety during grinding procedure. This study proposes a strategy for robot-assisted vertebral lamina grinding, which covers the method from preoperative planning and intraoperative navigation to grinding force control. Although this study is aimed at vertebral lamina grinding, the method proposed in this paper can also be applied on other types of orthopedic surgery.

Acknowledgments This work is financially supported by the National Natural Science Foundation of China (Grant Nos. U1613224, U1713221 and 61573336) and the National Key R&D Program of China (Grant No. 2017YFC0110600), in part by Shenzhen Fundamental Research Funds (Grant Nos. JCYJ20150529143500954, JCYJ20160608153218487, JCYJ20170307170252420 and JCYJ20160229202315086) and Shenzhen Key Laboratory Project (Grant No. ZDSYS201707271637577).

References

1. Bertelsen A, Melo J, Sánchez E, Borro D (2013) A review of surgical robots for spinal interventions. Int J Med Robot 9:407–422. https://doi.org/10.1002/rcs.1469
2. Chad DA (2007) Lumbar spinal stenosis. Neurol Clin 25:407–418
3. Chang C-C, Lin C-J (2011) LIBSVM: a library for support vector machines. ACM Trans Intell Syst Technol 2(27):1–27
4. Chen X, Varley MR, Shark LK, Shentall GS, Kirby MC (2008) A computationally efficient method for automatic registration of orthogonal x-ray images with volumetric CT data. Phys Med Biol 53: 967–983
5. Chung GB, Lee SG, Oh SM, Yi BJ (2004) Development of SPINEBOT for spine surgery. In: IEEE/RSJ international conference on intelligent robots and systems, vol 4, pp 3942–3947
6. Chung GB, Lee SG, Kim S, Yi BJ, Kim WK, Oh SM, Kim YS, Park JI, Oh SH (2005) A robot-assisted surgery system for spinal fusion. In: IEEE/RSJ International Conference on Intelligent Robots and Systems. pp 3015–3021
7. Chung GB, Kim S, Lee SG, Yi BJ, Kim W, Oh SM, Kim YS, So BR, Park JI, Oh SH (2006) An image-guided robotic surgery system for spinal fusion. Int J Control Autom Syst 4:30–41
8. Deng Z, Jin H, Hu Y, He Y, Zhang P, Tian W, Zhang J (2016) Fuzzy force control and state detection in vertebral lamina grinding. Mechatronics 35:1–10
9. Fan L, Gao P, Zhao B, Sun Y, Xin X, Hu Y, Liu S, Zhang J (2016) Safety control strategy for vertebral Lamina grinding task. Caai Trans Intell Technol
10. Foley K, Simon D, Rampersaud Y (2001) Virtual fluoroscopy: computer-assisted fluoroscopic navigation. Spine 26:347
11. Holly LT (2006) Image-guided spinal surgery. Int J Med Robot 2:7–15
12. Inoue T, Sugita N, Mitsuishi M, Saito T (2010) Optimal control of cutting feed rate in the robotic grinding for total knee arthroplasty. In: IEEE Ras and Embs International Conference on Biomedical Robotics and Biomechatronics. pp 215–220
13. Kim EH, Kim HT (2009) En bloc partial laminectomy and posterior lumbar interbody fusion in Foraminal spinal stenosis. Asian Spine J 3:66–72. https://doi.org/10.4184/asj.2009.3.2.66
14. Kwoh YS (1985) A new computerized tomographic aided robotic stereotactic system. Robot Age 7:17–21
15. Kwoh YS, Hou J, Jonckheere EA, Hayati S (1988) A robot with improved absolute positioning accuracy for CT guided stereotactic brain surgery. IEEE Trans Biomed Eng 35:153
16. Lee CC (1990) Fuzzy logic in control systems: fuzzy logic. Parts I and II, IEEE Trans. IEEE Trans Syst Man Cybern 20:404–418
17. Lei W, Xin G, Qiang F (2013) A novel mutual information-based similarity measure for 2D/3D registration in image guided intervention. In: International Conference on Orange Technologies. pp 135–138
18. Luan S, Wang T, Li W, Liu Z, Jiang L, Hu L (2012) 3D navigation and monitoring for spinal grinding operation based on registration between multiplanar fluoroscopy and CT images. Comput Methods Prog Biomed 108:151–157
19. Markelj P, Tomaževič D, Likar B, Pernuš F (2012) A review of 3D/2D registration methods for image-guided interventions. Med Image Anal 16:642–661
20. Mclaughlin RA, Hipwell J, Hawkes DJ, Noble JA, Byrne JV, Cox TCS (2002) A comparison of 2D-3D intensity-based registration and feature-based registration for Neurointerventions. Med Image Comput Comput-Assist Interv 2489:517–524
21. Nolte LP, Visarius H, Arm E, Langlotz F, Schwarzenbach O, Zamorano L (1995a) Computer-aided fixation of spinal implants. J Image Guid Surg 1:88–93
22. Nolte LP, Zamorano L, Visarius H, Berlemann U, Langlotz F, Arm E, Schwarzenbach O (1995b) Clinical evaluation of a system for precision enhancement in spine surgery. Clin Biomech 10:293
23. Nolte LP, Slomczykowski MA, Berlemann U, Strauss MJ, Hofstetter R, Schlenzka D, Laine T, Lund T (2000) A new approach to computer-aided spine surgery: fluoroscopy-based surgical navigation. Eur Spine J 9:S078–S088
24. P MFCAVDMGS (1997) Multimodality image registration by maximization of mutual information. IEEE Trans Med Imaging 16:187–198
25. Pluim JP, Maintz JB, Viergever MA (2003) Mutual-information-based registration of medical images: a survey. IEEE Trans Med Imaging 22:986–1004
26. Russakoff DB, Rohlfing T, Mori K, Rueckert D, Ho A, Adler JR, Maurer CR (2005) Fast generation of digitally reconstructed radiographs using attenuation fields with application to 2D-3D image registration. IEEE Trans Med Imaging 24:1441
27. Santos-Munné JJ, Peshkin MA, Mirkovic S, Stulberg SD, Iii TCK (1995) A stereotactic/robotic system for pedicle screw placement
28. Sautot P, Cinquin P, Lavallee S, Troccaz J (1992) Computer assisted spine surgery: a first step toward clinical, application in orthopaedics. In: Engineering

in Medicine and Biology Society, 1992 International Conference of the IEEE. pp 1071–1072
29. Shoham M, Burman M, Zehavi E, Joskowicz L (2003) Bone-mounted miniature robot for surgical procedures: concept and clinical applications. Robot Autom IEEE Trans On 19:893–901
30. Siddon RL (1985) Fast calculation of the exact radiological path for a three-dimensional CT array. Med Phys 12:252
31. Singh K, Vaccaro AR (2012) Pocket atlas of spine surgery. Stuttgart Georg Thieme Verlag
32. Stephane Genevay SJA (2010) Lumbar Spinal Stenosis. Best Pract Res Clin Rheumatol 24:253–265
33. Sugita N, Genma F, Nakajima Y, Mitsuishi M (2007) Adaptive controlled grinding robot for orthopedic surgery. In: IEEE International Conference on Robotics and Automation. pp 605–610
34. Sugita N, Nakano T, Nakajima Y, Fujiwara K, Abe N, Ozaki T, Suzuki M, Mitsuishi M (2009) Dynamic controlled grinding process for bone machining. J Mater Process Technol 209:5777–5784
35. Sugita N, Nakano T, Kato T, Nakajima Y, Mitsuishi M (2010) Instrument path generator for bone machining in minimally invasive orthopedic surgery. IEEEASME Trans Mechatron 15: 471–479
36. Sundermann E, Jacobs F, Christiaens M, Sutter BD, Lemahieu I (1998) A fast algorithm to calculate the exact radiological path through a pixel or voxel space. J Comput Inf Technol 6:89–94
37. Szpalski M, Gunzburg R (2003) Lumbar spinal stenosis in the elderly: an overview. Eur Spine J 12:S170–S175
38. Taylor RH, Mittelstadt BD, Paul HA, Hanson W, Kazanzides P, Zuhars JF, Williamson B, Musits BL, Glassman E, Bargar WL (1994) An image-directed robotic system for precise orthopaedic surgery. IEEE Trans Robot Autom 10:261–275
39. Tjardes T, Shafizadeh S, Rixen D, Paffrath T, Bouillon B, Steinhausen ES, Baethis H (2010) Image-guided spine surgery: state of the art and future directions. Eur Spine J 19:25–45
40. Wang L, Gao X, Zhang R, Xia W (2014) A comparison of two novel similarity measures based on mutual information in 2D/3D image registration. In: IEEE International Conference on Medical Imaging Physics and Engineering. pp 215–218
41. Xu C, Shin YC (2005) Design of a multilevel fuzzy controller for nonlinear systems and stability analysis. IEEE Trans Fuzzy Syst 13:761–778
42. Xu C, Shin YC (2008) An adaptive fuzzy controller for constant cutting force in end-grinding processes. J Manuf Sci Eng 130:683–695
43. Yen PL, Hung SS (2010) An intelligent bone cutting instrument in robot-assisted knee replacement. In: Sice conference 2010, proceedings of. pp 1894–1899
44. Yen PL, Tsai CH (2007) Cooperative force control of a knee surgical robot for lateral grinding of bone. In: IEEE Workshop on Advanced Robotics and ITS Social Impacts. pp 1–6

21 Potential Risk of Intelligent Technologies in Clinical Orthopedics

Yajun Liu

Abstract

Nowadays, the intelligent technologies are getting more and more attention, and the surgical robot is one of the most typical representatives. Orthopedic robots have revolutionized orthopedic surgery, but there are also risks. The risks can be categorized into those directly related to the use of the robotic system and the general risks of the operative procedure. This paper analyzes the potential risks of intelligent technologies in clinical orthopedics from three aspects, including surgical planning and strategies, spatial registration, and robotic guidance and navigation. Through these summaries, we hope to help clinical doctors better understand intelligent orthopedic techniques and promote a wide range of clinical applications of intelligent orthopedics. Besides, we also indicate the future research direction of intelligent orthopedic techniques, such as risk analysis, safety assessment, and risk management system.

Y. Liu (✉)
Department of Spine Surgery, Beijing Jishuitan Hospital, Beijing, China

Keywords

Risk analysis · Intelligent technologies · Surgical robot · Minimally invasive surgery · Precision surgery · Intelligent orthopedics

21.1 Introduction

In recent years, intelligent technologies represented by computer-assisted diagnosis, medical image automatic recognition and segmentation, and surgical robotics have been well developed and popularized in various clinical fields. Among them, the surgical robot is one of the most typical representatives of intelligent technology and also is the convergence of cutting-edge medical technologies. In the field of orthopedics, trauma, spine, and joint surgery have their own dedicated surgical robotic platform to achieve the clinical goal such as minimally invasive surgery and precision surgery, improving operative efficiency, reducing intraoperative fluoroscopies, and reducing postoperative complications. Currently, the technical framework of orthopedic robots is based on image-guided/image-free robotic-assisted surgical navigation, mainly including three key aspects: surgical planning

G. Zheng et al. (eds.), *Intelligent Orthopaedics*, Advances in Experimental Medicine and Biology 1093, https://doi.org/10.1007/978-981-13-1396-7_21

and strategies, spatial registration, and robotic guidance and navigation. Each step adopts the latest intelligent technologies at various levels, but it also may increase more potential risks, which may ultimately affect patient safety and their clinical benefits. However, since intelligent orthopedic robotics is still in its infancy and has not been yet widely used in clinical applications, there is no systematic analysis and assessment of these potential risks, and the sophisticated patient safety and risk management system has not yet been developed. At present, only a few literatures report relevant information [1–3].

Therefore, the risk assessment and management of the intelligent orthopedic technologies is a new topic and challenging. This paper attempts to summarize the potential risks of intelligent technologies in clinical orthopedics based on three key aspects of the intelligent orthopedic robots.

21.2 The Potential Risks of Surgical Planning and Strategies

Surgical planning and strategies are recognized as a fundamental aspect of orthopedic practice and an indispensable part of any successful surgical procedure. For orthopedic robotic surgery, normally during preoperative or intraoperative period, in the robotic planning software or platform, the surgeon designs the surgical planning such as implant trajectory, and also they make surgical strategies which describe a step-by-step guide to the operation including the planned patient position, surgical approach, and operation logistics [4]. Such robotic software platforms typically include multimodal medical image processing, surgical approaches or implant placement planning, surgical simulation, and patient management modules, which all contain varying degrees of intelligence (Fig. 21.1). In medical image processing, automatic segmentation and extraction of anatomical structures based on deep learning and big data, automatic fusion of multimodal images, and automatic calculation of kinematics parameters have reached a certain degree of automation and precision so far, but most still need to be verified, fine-tuned, or manually planned by surgeon. Also, image modalities and image correction processing may affect planning efficiency or accuracy. For example, traumatic orthopedics often use biplane fluoroscopy images as screw planning images, two-dimensional fluoroscopic images themselves lacking three-dimensional information and image

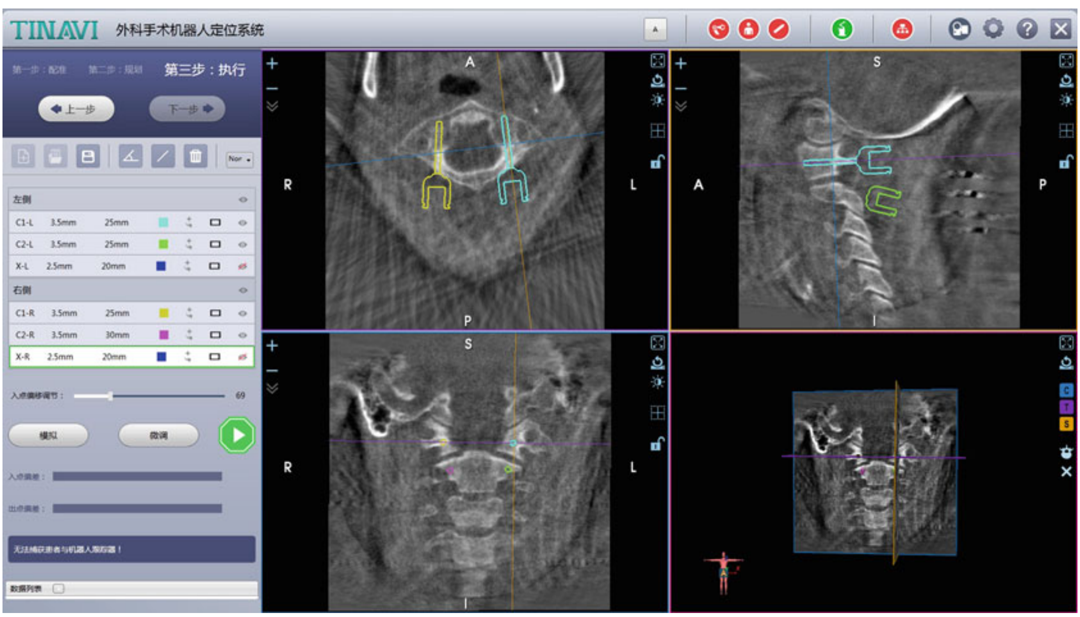

Fig. 21.1 TiRobot Spine cervical screws planning interface

edge distortion, making the planning trajectory often could not be automatically generated or not optimal and safe design. Spinal surgery often uses intraoperative CBCT image as guidance images. Due to poor quality of the image itself and the metal artifacts, automatic segmentation and recognition or visual identification of anatomy structures such as pedicle channel is difficult, which makes the intraoperative planning time-consuming. CT-based 3D automatic reconstruction used by hip and knee arthroplasty may loss the small bone structures, which perhaps affect components placement accuracy. Currently, 2D and 3D multimodal image fusion has been largely automated, but for complex cases it may take longer or fail to achieve satisfactory accuracy. In the design of implants, whether it is the pedicle screw system for scoliosis or hip and knee components, it mainly depends on manual planning and lacks the intelligent evaluation and verification based on kinematics and soft tissue balancing. In surgical simulations, such as complex cervical spinal surgery, the surgeon can "fly through" their patients' anatomy and perform complex operations in virtual reality using VR medical visualization solution. In the field of patient data management and treatment solutions, there is still a lack of big data such as images supported by evidence-based medicine or labeled by professional physicians, which have true practical values in clinical decision-making.

In general, there is a lack of a sophisticated and robust software and hardware platform in orthopedic surgery planning and strategies including planning software of orthopedic robots, to help doctors to optimally manage the full treatment process and clinical decision-making from preoperative diagnosis to postoperative rehabilitation. Otherwise, all these current surgical planning software are generally poor in usability and have steep learning curves; most surgeons who have not been comprehensively trained in medical image processing and robotic surgery could not learn their use in a short period of time and could not use these data for innovative medical research. In addition, the vast majority of orthopedic surgeons are undergoing heavy surgical tasks, often leaving little time to perform delicate surgical planning and optimal surgical strategies.

21.3 The Potential Risks of Spatial Registration

The spatial registration of intelligent orthopedic surgical robotic platform refers to the robotic work space and patients' image space or physical space coordinates matching, which is the central operation of orthopedic robotic surgery and one of the most important limiting factors for end-to-end clinical accuracy. There are three types of spatial registration methods for orthopedic robots, including fiducial-based registration, surface-based registration, and fiducial- and surface-based hybrid registration. Fiducial-based registration has normally been automated, and the accuracy mostly is satisfactory but may still need manual adjustment for very few complicated cases, mainly used in spinal surgery and traumatic orthopedics (Fig. 21.2). For surface-based registration or hybrid registration, it is often necessary for the surgeon to hold a hand-held optical navigation probe to acquire a certain number of bone surface points to match with the 3D surface reconstructed by preoperative CT images. Surface-based registration has a similar or lower accuracy compared with fiducial-based registration, and it is often experience-depending and time-consuming, mainly used in hip and knee arthroplasty. In the actual clinical applications of orthopedic robots, there are many potential risk factors which lead to poor registration accuracy, registration failure, or repeated registrations, including optical camera failure, reference arrays loose or damaged, sight-light obstruction, relative displacement of bone structure or respiratory motion, the operator registration process error, image fiducial-similar artifacts, and other factors, and these may affect the fluency of the procedure or result in the termination of the procedure. Notably in hip and knee arthroplasty, errors in registration can have serious consequences due to the proximity of neurovascular structures around

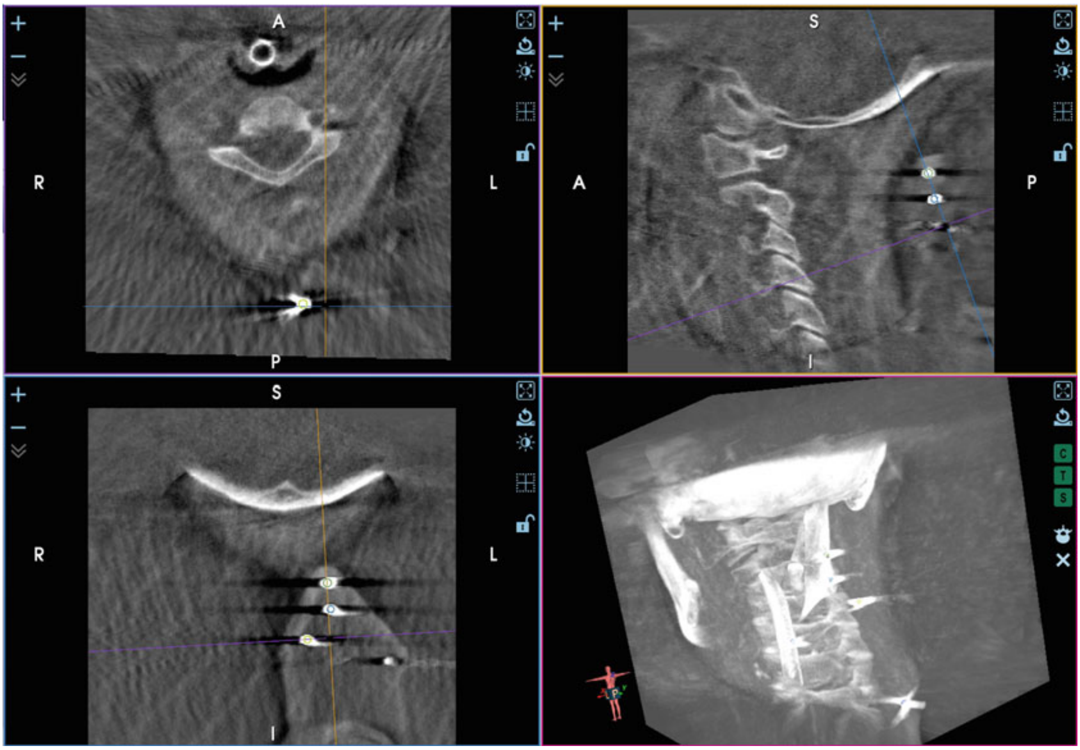

Fig. 21.2 TiRobot Spine fiducial-based automatic registration

the hip and knee and have the potential to damage them in addition to the inaccuracies of bone milling [6].

At present, new registration method and strategies such as optical 3D scanning registration, automatic registration refresh, and elastic registration between vertebral bodies have not been effectively applied in orthopedics, which need further study and clinical testing.

21.4 The Potential Risks of Robotic Guidance and Navigation

After spatial registration has completed, the surgeon performs the main orthopedic surgical task such as stereotaxy, guidance, drilling, milling, and cutting with the guidance of robots and optical navigation. This step highlights the automatic or intelligent technologies and also may introduce the biggest and most complex potential risks. The orthopedic surgery environmental difficulty, the complexity of the operational tasks, and the surgeon independence directly affect the human-robot interaction strategies or automation realization of the orthopedic robot [7]. In general, percutaneous minimally invasive surgery needs smaller incision which causes soft tissue pressure to implanted screws and rods, and thus is more difficult than open surgery. Robotic spinal surgery theoretically has the potential to achieve high automation but it needs high clinical accuracy due to the fact that the surgical field is adjacent to important blood vessels and nerves. This is especially true for the cervical surgery, making it difficult to achieve high automation (Fig. 21.3). In traumatic orthopedics, the surgical area is relatively large and the patient positioning varies. The main surgical mission is complicated. The difficulty of placement of the implants varies greatly and often relies on intraoperative fluoroscopy to repeatedly verify the position of the implants. Therefore, robotic trauma orthopedic

Fig. 21.3 TiRobot Spine-assisted cervical screw placement surgery environment

surgery theoretically is difficult to achieve a high automation. In the field of hip and knee arthroplasty, open surgery is generally performed, and the surgical area is relatively small and limited. Surgeons have a large number of complicated surgical missions, and the placement of the implants is generally difficult considering the kinematic parameters and soft tissue balance and other factors, so the degree of automation to achieve is low, but in some bone milling or cutting operations, because there is no soft tissue involved and relatively safe, in theory, robotic hip and knee arthroplasty can achieve a high automation.

At present, the dominant traumatic orthopedic robots, spinal surgical robot, and hip and knee arthroplasty robots all use multi-DOF robotic arms combined with optical navigation technology. The most foundational functions of robotic arms are stereotactic guidance, such as positioning, drilling, and cutting, and milling is the continuous operation of drilling. In traumatic orthopedics and spinal surgery, the end-effector of robotic arm carries various tools, mainly performing a single drilling or cutting function. The human-robot interaction mode is relatively simple. For example, TiRobot, Mazor X, ROSA Spine, and Excelsius GPS all mainly work in automatic movement mode [8] [9] [10] [11] (Fig. 21.4). And Mazor X end-effector carrying a laser scanner allows 3D reconstruction of the patients' surface surgical areas for safer automated operation and intelligent obstacle avoidance. In the field of hip and knee arthroplasty, Mako robotic arm carrying power drill, saw blade, or acetabular reamers to perform drilling, milling, cutting, and other complex surgical tasks, and MAKO need surgeon work in collaboration with robot, that is, once the work begins on the bone, the surgeon provides the force, while the robot provides guidance [12]. In addition, Mako sets up several robotic arm safety margin and stereotactic space for complex operations such as milling more safely and accurately.

Compared with surgical planning and spatial registration steps, robotic guidance has the greatest potential risks. In traumatic orthopedics especially hip and pelvis surgery, the soft tissue through implant placement such as the muscle fascia is thick and high pressure; the robotic arm may undergo a protective shutdown due to insufficient load. In addition, for example, the trajectory of the acetabular anterior columnar screw is steep. The guidance sleeve may deviate from the planned path due to the high soft tissue pressure, and the movement trajectory of the robotic arm may be limited by the C-

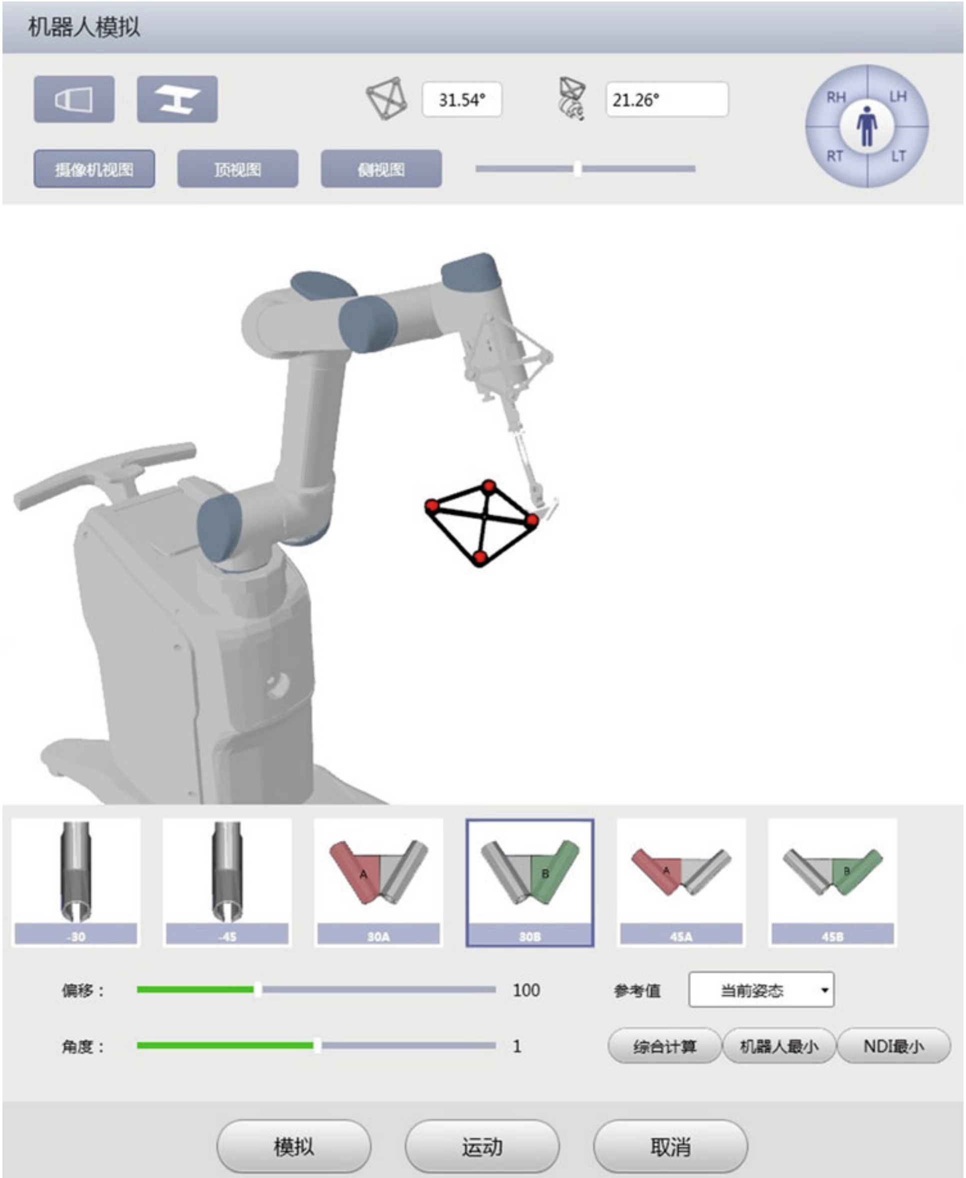

Fig. 21.4 TiRobot Spine automatic movement simulation

arm positioning and cannot be quickly realized obstacle avoidance during the intraoperative C-arm fluoroscopy verification. In the field of spinal surgery, pedicle screw entry point is often at a steep bone surface, the guidance sleeve is easily skidding and deviates from the planning path, and, because adjacent vertebral body is a fine motion joint especially the cervical spine, the surgeon performing a large surgical operation may lead to the displacement of the vertebral body, thus affecting the positioning accuracy and injuring important neurovascular structures. In addition, the thoracic and lumbar vertebral body largely affects with respiratory motion, which may result in poor positioning accuracy. In the field of hip and knee robotic arthroplasty, technical complications may include fissuring of the femur, milling of a defect in the greater trochanter and damage to the acetabulum, and damage to the patellar tendon during milling [13].

In clinical applications, there are various adverse events related with the usage of robotic arms, which include: the robotic arm is short-circuited or unexpectedly shut down; the robotic arm is not moved as planned simulation; the robotic arm cannot be stopped or work in place; the guidance sleeve is subjected to stress and bending; potential risks such as damaging collisions with patients, surgeons, or other devices; delays in manipulator operation; inadequate sterile protection of end-effector; control software crashes; errors in software tool parameters; and so on. All these adverse events may eventually result in surgical procedures interrupted or terminated, affecting the clinical accuracy, and even endanger human life.

In general, none of the dominant commercial orthopedic robots currently have an integrity of operational risk management systems for robotic arm movement, especially in soft tissue stress feedback, complex path operation simulation and intelligent obstacle avoidance, and emergency arm power supply. To some extent, it affects and limits its own clinical application and promotion.

21.5 Summary

Risks of robotic surgery can be categorized into those directly related to the use of the robotic system and the general risks of the operative procedure. Compared with the master-slave control mode, which is mainly represented by Da Vinci surgical system, orthopedic robots take more automatic or semiautomatic mode under the supervision of the surgeon, and the level of automation is constantly improving. Thus, if we would like to compare the master-slave model with the automatic model, we don't known which model would have a higher surgical risk. In fact, there is relatively little research on the management of adverse events and risk management, both for master-slave control robots and for automatic or semiautomatic robots. A retrospective analysis of adverse surgical events using Da Vinci surgical robots revealed that 10,624 adverse events occurred in 1.75 million operations over a 14-year period, 75% of which were equipment failures, and 1.4% of deaths were mainly caused by surgical inherent risks and complications as well as the doctor's mistake caused [14]. In the two literatures of spinal robot up to 1000 cases of surgical operation, the robot failure rate and registration failure rate were about 1%, while 85.7% of the factors affecting the surgical accuracy were related to surgeons' operation [15] [16] . Therefore, in reducing the risk, with the exception of robust and reliability and intelligence of robotic system, the surgeon's basic surgical operation training and robot training is also very important. A risk management framework for robotic surgery has been proposed, recommending that medical device regulatory agency, surgical robot manufacturers, and healthcare providers should work together to reduce the risk of design-related defects and to reduce the risk of lack of training as well as reduce the risk caused by the lack of application guidance information [17].

In short, for the emerging intelligent orthopedic robots, it urgently needs to establish a comprehensive and systematic risk analysis, safety assessment, and risk management system, which thus may promote a wide range of clinical applications and promote the development of a new era of intelligent orthopedic.

References

1. Korb W et al (2003) Risk analysis for a reliable and safe surgical robot system. Int Congr Ser 1256:766–770
2. Korb W et al (2005) Risk analysis and safety assessment in surgical robotics: A case study on a biopsy robot. Minim Invasive Ther 14(1):23–31
3. Morandi A et al A methodological framework for the definition of patient safety measures in robotic surgery: the experience of SAFROS project. Intell Auton Syst 12(AISC 194):155–164
4. Atesok K et al (2015) Preoperative Planning in Orthopaedic Surgery Current Practice and Evolving Applications. Bull Hosp Joint Dis 73(4):257–268
6. Shenoy R et al (2017) Evidence for robots. SICOT J 3:38
7. Moustris GP et al (2011) Evolution of autonomous and semi-autonomous robotic surgical systems: a review of the literature. Int J Med Robot Comput Assist Surg 7:375

8. TiRobot Spine product brochures.www.tinavi.com
9. Mazor X product brochures. www.mazor robotic.com
10. ROSA Spine product brochures. www.medtech surgical.com
11. Excelsius GPS product brochures. www.globus medical.com
12. MAKO product brochures. www.stryker.com
13. Waddell BS (2017) Technology in arthroplasty: are we improving value? Curr Rev Musculoskelet Med 10:378–387
14. Alemzadeh H et al Adverse events in robotic surgery: a retrospective study of 14 years of FDA data. PLoS One 11(4):e0151470
15. Devito DP et al (2010) Clinical Acceptance and Accuracy Assessment of Spinal Implants Guided with SpineAssist Surgical Robot: Retrospective Study. Spine 35(24):2109–2115
16. Tsai T-H et al (2017) Pedicle screw placement accuracy of bone-mounted miniature robot system. Medicine 96:3
17. Brisbois BR. Patient lives in our [Robotic] hands: risks and implications of robotic surgery, 19th AVENUE N.E., SEATTLE, WA 98115 | www.anniesearle.com | 206.453.4386 Page 1 of 11

22 Clinical Application of Navigation in the Surgical Treatment of a Pelvic Ring Injury and Acetabular Fracture

Masaki Takao, Hidetoshi Hamada, Takashi Sakai, and Nobuhiko Sugano

Abstract

The purpose of this chapter is to review current evidence on indications, techniques, and outcomes of computer-navigated surgical treatment of pelvic ring injuries and acetabular fractures, particularly computer-navigated screw fixation.

Iliosacral screw fixation of pelvic ring injury using navigation is attracting attention because the biomechanical stabilization of posterior pelvic ring disruption is of primary importance and is widely indicated because it does not require complete reduction of the fracture site. A cadaver study with a simulated zone II sacral fracture demonstrated a substantial compromise in the space available for iliosacral screws with displacements greater than 10 mm. It is possible to reduce the fracture fragment prior to intraoperative imaging in 2D or 3D fluoroscopic navigation. The use of 3D fluoroscopic navigation reportedly results in lower rates of iliosacral screw malpositioning than the use of the conventional technique or 2D fluoroscopic navigation. Moreover, compared with the conventional technique, it reduces radiation exposure and lowers revision rates. However, the malposition rate associated with 3D fluoroscopic navigation ranges from 0% to 31%, demonstrating that there is still room to improve the navigation performance.

Conversely, complete articular surface reduction is required when treating a displaced acetabular fracture to prevent residual hip pain and subsequent osteoarthritic changes. Treating a severely displaced acetabular fracture by screw fixation is very challenging, even with the use of 3D fluoroscopic navigation, because of the difficulty in performing closed anatomical reduction. The indication for percutaneous screw fixation is limited to cases with a small articular displacement. Using 3D fluoroscopic navigation for open surgeries reportedly improves the quality of radiographic fracture reduction, limits the need for an extended approach, and lowers the complication rate.

In conclusion, percutaneous screw fixation for pelvic ring injuries is widely indicated, and navigation makes these procedures safe and reliable. The indication for percutaneous screw fixation of acetabular fractures is limited to cases with a small articular displacement. Using 3D fluoroscopic navigation when

M. Takao (✉) · N. Sugano
Department of Orthopaedic Medical Engineering, Osaka University Graduate School of Medicine, Suita, Japan
e-mail: masaki-tko@umin.ac.jp

H. Hamada · T. Sakai
Department of Orthopaedic Surgery, Osaka University Graduate School of Medicine, Suita, Japan

G. Zheng et al. (eds.), *Intelligent Orthopaedics*, Advances in Experimental Medicine and Biology 1093, https://doi.org/10.1007/978-981-13-1396-7_22

performing open surgeries is reported to be useful in evaluating fracture reduction and screw position.

Keywords
Pelvic ring injury · Acetabular fracture · 2D fluoroscopic navigation · 3D fluoroscopic navigation · CT-based navigation · Iliosacral screw · Anterior column screw · Posterior column screw · Supraacetabular screw

22.1 Introduction

A pelvic ring injury and acetabular fracture are life-threatening injuries caused by high-energy trauma, which are often accompanied by multiple organ damage [1]. Early stabilization of the pelvic ring and acetabulum is required to prevent further bleeding from the fracture sites and facilitate early functional recovery. Thus, it is ideal to perform minimally invasive surgery as soon after the injury as possible. In developed countries, the number of high-energy accidents such as a motor vehicle crashes or falls from great heights at construction sites is slowly decreasing, while due to the increase of an aging population, the number of fragility fractures of the pelvis is reportedly increasing [2]. Conservative treatment is a standard option for fragility fractures of the pelvis, but this approach is often accompanied by immobility-associated complications such as loss of waking function, pneumonia, decubitus, and venous thromboembolism. Rommens et al. [2] classified these fractures to the localization of the instability. They recommended a minimally invasive surgical treatment, except for isolated anterior pelvic ring lesions, in order to achieve stable fixation and earlier mobilization [3].

Percutaneous screw fixation under fluoroscopic guidance, including that of an iliosacral screw, transsacral screw, posterior column screw, anterior column (or pubic) screw, and supraacetabular screw, is a good minimally invasive treatment option, but it requires detailed knowledge and experience to correlate the osseous landmarks of the pelvic ring and acetabulum with their corresponding fluoroscopic images and find a secure screw corridor by rotating fluoroscopic views. In order to make these procedures safe and reliable, various types of navigation systems have been applied, including computed tomography (CT)-based navigation [4–6], two-dimensional (2D) fluoroscopic navigation [5, 7–17], and three-dimensional (3D) fluoroscopic navigation [5, 8, 12–14, 18–23]. Their indication and efficacy in surgical treatments of pelvic ring injuries and acetabular fractures are now being debated [13, 24, 25]. The 3D intraoperative imaging modalities and image-based navigation have also been applied to open surgeries for pelvic ring injury and acetabular fracture, and their efficacy in fracture reduction and screw position has been focused on [26–28]. The purpose of this chapter is to review current evidence on the indications, techniques, and outcomes of computer-navigated surgical treatment of pelvic ring injuries and acetabular fractures and especially computer-navigated screw fixation.

22.2 Navigated Iliosacral Screw Fixation for the Surgical Treatment of a Pelvic Ring Injury

22.2.1 Indications and Outcomes

Iliosacral screw fixation under fluoroscopic guidance has become a popular technique to stabilize unstable pelvic ring fractures [29–31] because the biomechanical stabilization of a posterior pelvic ring disruption is of most importance in the treatment of pelvic ring injury. The use of percutaneous iliosacral screw fixation has minimized the risk of operative blood loss, skin necrosis, and infection associated with open procedures fractures [31–33]. Due to the complex 3D sacral anatomy, percutaneous iliosacral screw insertion is a technically demanding procedure because the placement corridors are narrow and variable [34, 35]. It is sometimes difficult to achieve clear and optimal fluoroscopic sacral

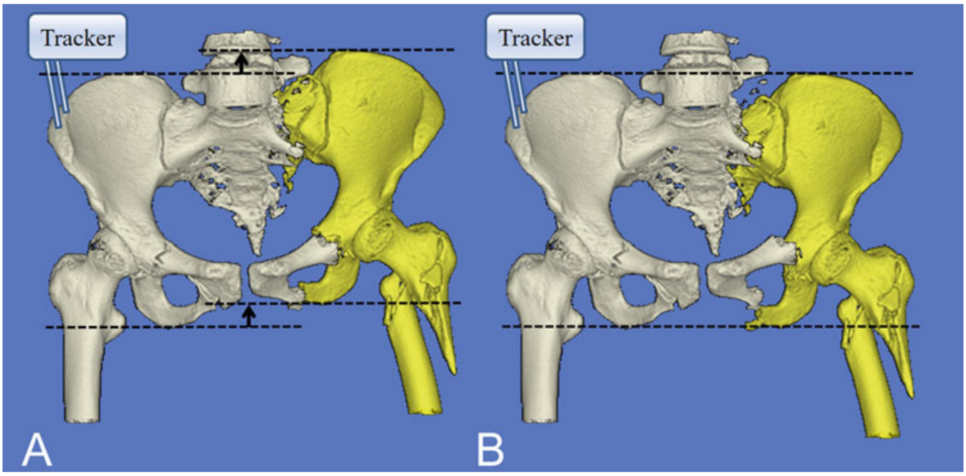

Fig. 22.1 The schema shows the pelvic ring before (**a**) and after manipulative fracture reduction (**b**). Displaced and reduced bone fragments are colored yellow. The navigation system can track the movement of the sacrum even after reduction because the reference tracker is fixed to the contralateral iliac crest. The black arrows indicate vertical displacement of bone fragments before manipulative fracture reduction. (Reprinted with permissions from [47])

visualization due to excessive bowel gas, obesity, and/or osteoporosis [36, 37]. Screw malposition rates with fluoroscopic guidance have been reported to range from 2% to 68% [18, 19, 38, 39], with an incidence of neurologic injury between 0.5% and 7.9% [38, 39]. This method requires detailed knowledge and experience to correlate the osseous landmarks of the sacrum with their corresponding fluoroscopic images and to determine a secure screw corridor by rotating the inlet, outlet, and lateral fluoroscopic views [36]. A trigonometric analysis of patients' CT data suggested that a deviation of the surgeon's hand by as little as 4° could direct iliosacral screws either into the S1 foramina or through the anterior cortex of the sacrum [35]. Several factors reportedly increase the risk of screw malpositioning such as the presence of a dysmorphic sacrum [34], the use of S2 screws [38], the number of S1 screws used [9], the extent of the dislocation [9], and the surgeon's experience [9, 40].

To make iliosacral screw fixation under fluoroscopic guidance safe and reliable, various types of computer-assisted techniques, including CT-based navigation [4–6], 2D fluoroscopic navigation [5, 7–14, 17], and 3D fluoroscopic navigation systems [5, 8, 12–14, 18–20], have been developed. It has also been reported that the use of intraoperative 3D imaging modalities in an assessment of iliosacral screws was effective in improving screw position [41, 42]. Iliosacral screw fixation using CT-based navigation is indicated for a minimally displaced pelvic ring injury of 5 mm or less because it is not possible to reduce the fracture. In 2D or 3D fluoroscopic navigation, it is possible to reduce the fracture fragment if the navigation tracker was fixed on the contralateral ilium (Fig. 22.1). A cadaver study with a simulated zone II sacral fracture demonstrated a substantial compromise of the space available for iliosacral screws with displacements greater than 10 mm [43]. Thus, the indication of iliosacral screw fixation using 2D or 3D fluoroscopic navigation could be extended to a displacement of 10 mm or more if a traction table or some special device which could assist and maintain the fracture reduction is used.

On the other hand, even with the use of 2D and 3D fluoroscopic navigation, the procedure requires substantial experience and detailed anatomical knowledge to find the proper entry point and trajectory of a guide-wire on 2D and 3D fluoroscopic images [9, 20]. Using

3D fluoroscopic navigation reportedly results in lower rates of malpositioning of iliosacral screws compared with conventional fluoroscopic guidance [18, 19, 44] and 2D fluoroscopic navigation [44, 45]. In addition, it has been reported that 3D fluoroscopic navigation reduces radiation time and dose [18] and lowers the revision rate [19] as compared with conventional navigation. However, the malposition rate associated with 3D fluoroscopic navigation reportedly ranged from 0% to 31% when malpositioning was defined as perforation of grade 1 or more [18, 19, 44, 46] (Table 22.1). This means that there is still room for improvement in the accuracy of 3D fluoroscopic navigation for the insertion of iliosacral screws. In most studies, screw perforations were graded according to an established classification method used for pedicle screw placement: grade 0 indicated no perforation, grade 1 indicated a perforation of less than 2 mm, grade 2 indicated a perforation of 2–4 mm, and grade 3 indicated a perforation greater than 4 mm [14].

The navigation system guides the sleeve device for guide-wire insertion, not the guide-wire or the screw itself, which could be a cause of screw malposition. In addition, the flexibility of the guide-wire is a concern. The guide-wire diameter of standard iliosacral screws is 2.8–3.2 mm. Richter et al. [46] reported greater screw perforation rates for transsacral screws (45%) than for standard iliosacral screws (4.4%) inserted using navigation combined with robot arm-assisted 3D fluoroscopy. Greater guide-wire flexibility is therefore one possible reason for the greater degree of positional error using transsacral long screws.

Grossterlinden et al. [20] reported that the surgeon experience affected the malposition rates in screw placement in cadaveric pelvises, even when using 3D fluoroscopic navigation. It is difficult for less experienced surgeons to find a safe corridor in the multiple reconstructed planes of 3D fluoroscopic images [40]. We hypothesized that 3D fluoroscopic navigation combined with a preoperative CT-based plan could assist even less experienced surgeons to perform iliosacral screw insertion safely and reliably [40, 47]. A 3D fluoroscopic navigation system using the flat-panel detector-equipped C-arm has made it possible to overlap the preoperative CT-based plan on intraoperative 3D fluoroscopic images of the pelvis with an accuracy of 0.8 mm [48, 49]. In the previous cadaveric study, guide-wires were inserted bilaterally across the ilia into the S1 and S2 vertebral bodies by four novice orthopedic surgeons using fluoroscopic guidance and 3D fluoroscopic navigation with and without CT-based preoperative planning. They could not avoid perforation of the guide-wires, even using 3D fluoroscopic navigation, but the combination of 3D fluoroscopic navigation and CT-based preoperative planning enabled them to insert a guide-wire successfully with a single short. This result showed that the "3D cognitive" skill required to recognize bone structure and position of a guide-wire by viewing 2D or 3D fluoroscopic images is very difficult for trainees to acquire in percutaneous iliosacral screw insertion. Training is necessary for novice orthopedic surgeons to find a proper corridor for the guide-wire viewing either 2D or 3D fluoroscopic images. We initially reported on six cases of pelvic ring injury treated by percutaneous iliosacral screw guided by CT-3D-fluoroscopy matching navigation [47].

The 3D intraoperative imaging modality and image-based navigation have also been applied to open surgeries to evaluate fracture reduction and screw position. We applied CT-3D-fluoroscopy matching navigation to anterior sacroiliac plate fixation through the anterior approach for a type C1 pelvic ring fracture. Intraoperative lumbosacral nerve visualization using computer navigation was useful to recognize the "at risk area" for nerve injury during anterior sacroiliac plate fixation [26] (Fig. 22.2).

22.2.2 Surgical Technique

Surgical procedures for iliosacral screw fixation using 3D fluoroscopic navigation combined with CT-based plan are summarized in the flowchart shown in Fig. 22.3. The navigation procedure was performed using a computer navigation system (Stryker Navigation System

Table 22.1 Clinical reports of navigation use for iliosacral screw insertion for pelvic ring injuries

Author (year)	Mode of navigation	Number of patients	Number of screws	Mean operation time (minutes)	Mean radiation time (seconds)	Mean radiation dose (cGy/cm2)	Perforation rate	Screw perforation grade[a] (0/1/2/3)	Diagnostic modality
Mosheiff (2004)	2D fluoroscopy	24	27	NA	NA	NA	0%[b]	NA	2D fluoroscopy
Zwingmann (2009)	3D fluoroscopy	24	26	72	63[c]	822[c]	31%[c]	18/4/2/2	CT
	Non-navigation	32	35	69	141[c]	1848[c]	60%[c]	14/13/4/4	
Zwingmann (2010)	3D fluoroscopy	54	63	NA	NA	NA	19%[c]	51/7/2/3	CT
	Non-navigation	87	131				58%[c]	55/29/28/17	
Gras (2010)	2D fluoroscopy	44	56 IS, 29 pubic	62 per screw	123 per screw	NA	6%	NA	CT
Grossterlinden (2011)	2D fluoroscopy	46	82	39.2 per screw[c]	62.8 per screw[c]	NA	3%[c]	NA	CT
	Non-navigation	36	65	29.4 per screw[c]	103.1 per screw[c]		15%[c]		
Peng (2013)	Intraoperative CT	13	13	21.2 per screw	NA	51.9 mGy	0%	NA	CT
Takao (2014)	3D fluoroscopy	6	12	65 (33 per screw)	NA	NA	0%	12/0/0/0	CT
Matityahu (2014)	2D fluoroscopy	18	25	NA	NA	NA	32%[c]	NA	CT
	3D fluoroscopy	54	78				0%[c]		
	Non-navigation	58	95				17%[c]		
Richter (2016)	3D fluoroscopy	61	65	69 (44 per screw)	NA	NA	17%	54/4/5/2	3D fluoroscopy

2D two dimensional, 3D three dimensional, CT computed tomography, IS iliosacral screw, NA not available

[a]The numbers indicate the number of screws used in each grade. Perforations were graded as follows: grade 0, no perforation; grade 1, perforation <2 mm; grade 2, perforation 2–4 mm; and grade 3, perforation >4 mm

[b]The percentage of screw demonstrated a deviation >2 mm or > 5° on fluoroscopic images

[c]There was a statistically significant difference between the navigation group and the non-navigation group

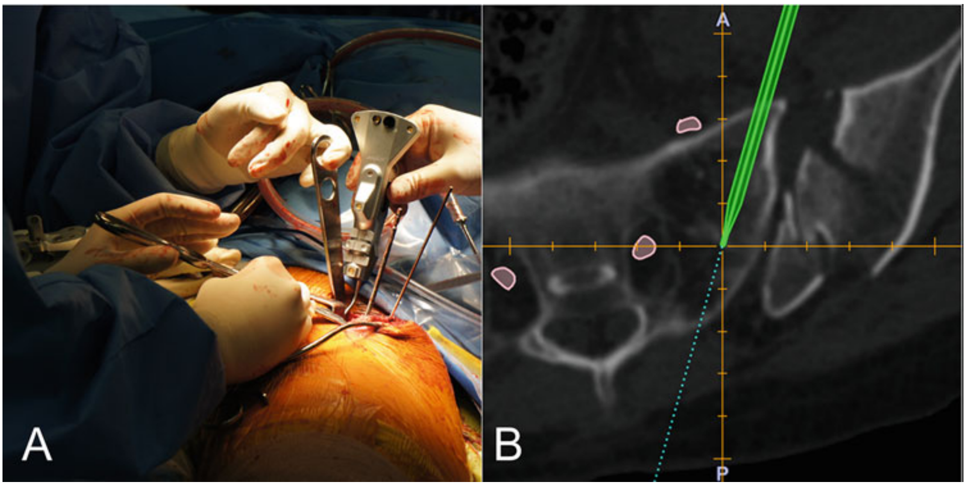

Fig. 22.2 For an anterior sacroiliac plate fixation, the direction and depth of screw drilling were checked by inserting the navigation pointer to the drilled holes in the sacral ala instead of fluoroscopic imaging through an anterior approach to the sacroiliac joint (**a**). A navigation monitor image shows that there is no perforation to the sacral canal, neural foramen, or sacroiliac joint. The navigation pointer is colored green and the lumbosacral nerves are white (**b**). (Reprinted with permissions from [26])

II-Cart; Stryker, Kalamazoo, MI, USA) and a mobile 3D C-arm equipped with a flat-panel detector (Ziehm Vision FD Vario 3D; Ziehm Imaging, Nuremberg, Germany). The screw position was planned preoperatively using a CT-based planning software (OrthoMap 3D; Stryker) within the navigation unit. During preoperative CT-based planning, three orthogonal reconstructions were viewed along the planned screw axis. In the sagittal-reconstructed plane passing through the nerve root tunnel, the screw position was adjusted to keep a safety margin of more than 3 mm from the upper cortical alar and the S1 and S2 nerve root tunnels (Fig. 22.4).

The patients were placed in a supine or prone position on a radiolucent operating table or traction table (Fig. 22.5). The navigation computer was placed at each patient's caudal side. The mobile 3D C-arm approached from the opposite side to the operating surgeon. A reference tracker was fixed to the contralateral anterior or posterior iliac crest using the external fixation device. The C-arm was connected to the navigation system and calibrated by registering three points on the detector using a pointing device. A 3D fluoroscopy scan of the sacrum was performed intraoperatively with the scan center aimed at the S2 vertebral body. Image matching between preoperative CT data and intraoperative 3D fluoroscopic image volume was done using an image registration technique (Fig. 22.6) [47] after the image data were transferred to the navigation system.

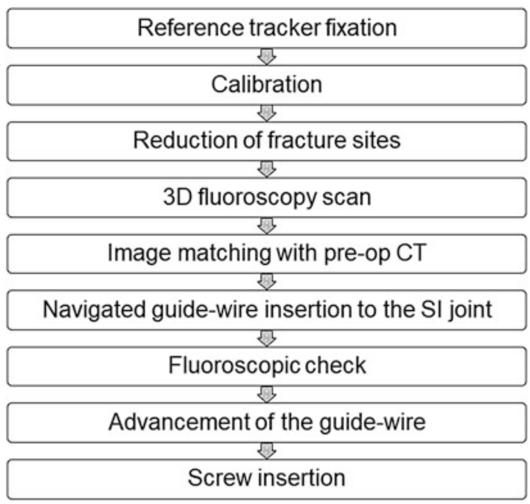

Fig. 22.3 Flowchart showing surgical procedures for iliosacral screw fixation using 3D fluoroscopic navigation combined with CT-based plan

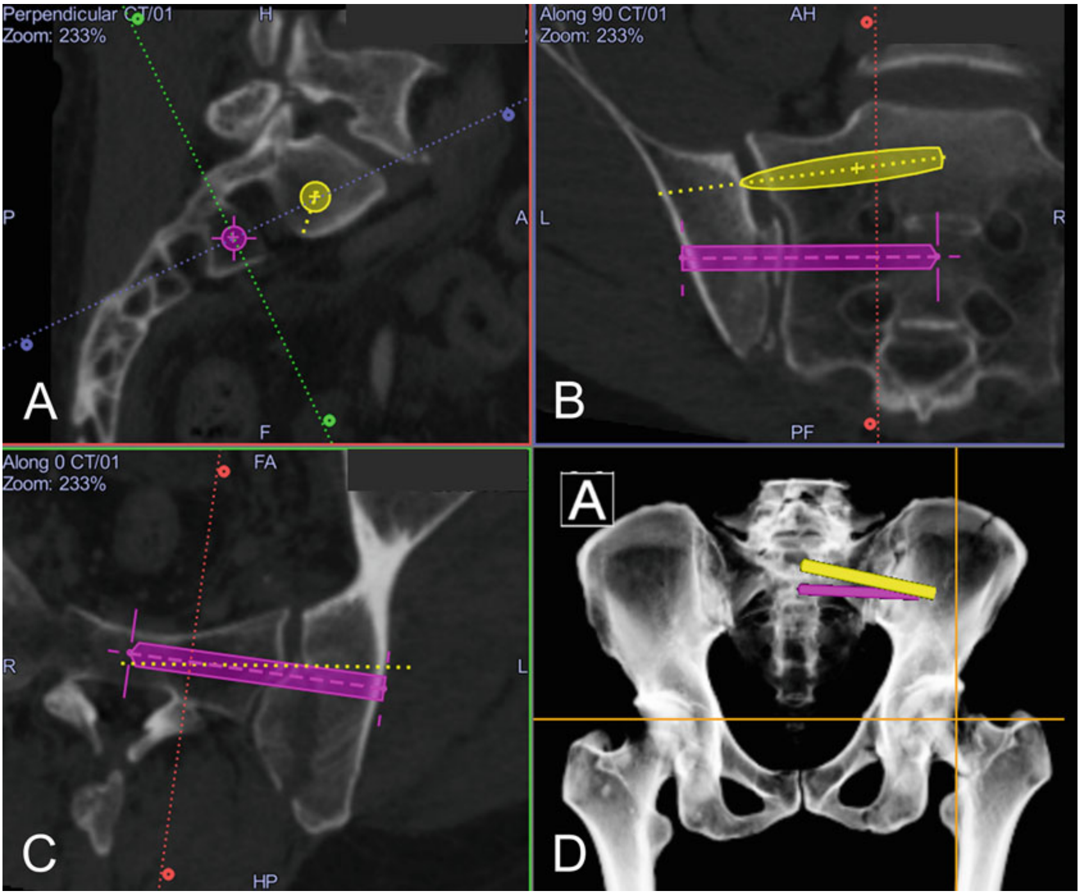

Fig. 22.4 Three orthogonal reconstructions along the planned screw axis were viewed on a CT-based navigation workstation. The screw position was adjusted to gain a sufficient margin on the sagittal-reconstructed plane (**a**) passing throughout the nerve root tunnel. Screw direction and length were determined on coronal (**b**) and axial (**c**) planes parallel or perpendicular to the sacrum. Each screw was advanced just beyond the sacral midline

The guide-wire sleeve was calibrated, and a guide-wire was then placed into the S1 and S2 vertebrae according to the preoperative plan with the navigation sleeve while viewing the navigation monitor (Fig. 22.7). It was also possible to perform screw insertion viewing intraoperative 3D fluoroscopic images (Fig. 22.8). The guide-wire was advanced until it penetrated the iliosacral joint. The wire placement was checked fluoroscopically on the inlet and outlet views. For iliosacral screw fixation, the guide-wire was advanced up to the center of the vertebral body because bone density is higher around the vertebral body center [50]. For transsacral screw fixation, the guide-wire was advanced to penetrate the contralateral sacroiliac joint. Drilling and tapping were performed on the ipsilateral sacroiliac joint, and a cannulated 6.5 or 8.0 mm in diameter threaded screw was inserted.

22.3 Navigated Periacetabular Screw Fixation for the Surgical Treatment of an Acetabular Fracture

22.3.1 Indications and Outcomes

Treatment of a displaced acetabular fracture requires complete reduction of the articular surface to prevent residual hip pain and subsequent osteoarthritic changes. An open reduction and in-

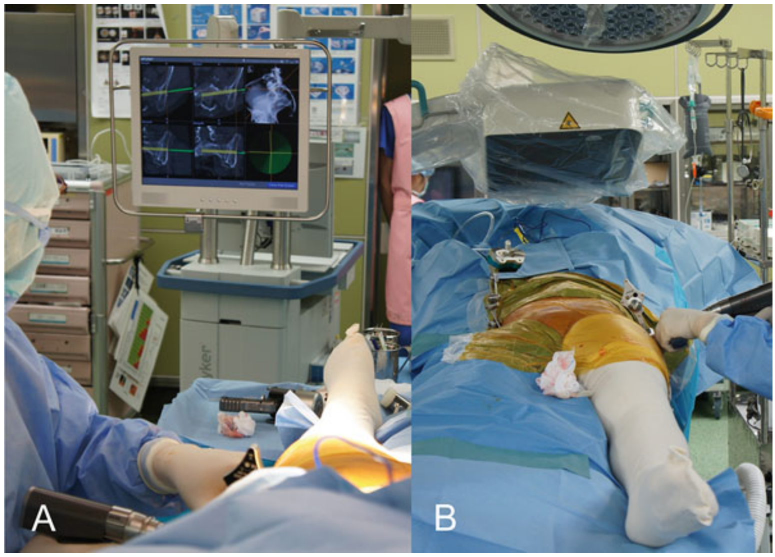

Fig. 22.5 Setup of percutaneous iliosacral screw fixation with the patient supine on a radiolucent operating table. The navigation computer was placed at the patient's caudal side (**a**). The mobile 3D C-arm approached from the opposite side to the operating surgeon (**b**). A reference tracker was fixed to the contralateral anterior iliac crest using the external fixation device (**b**)

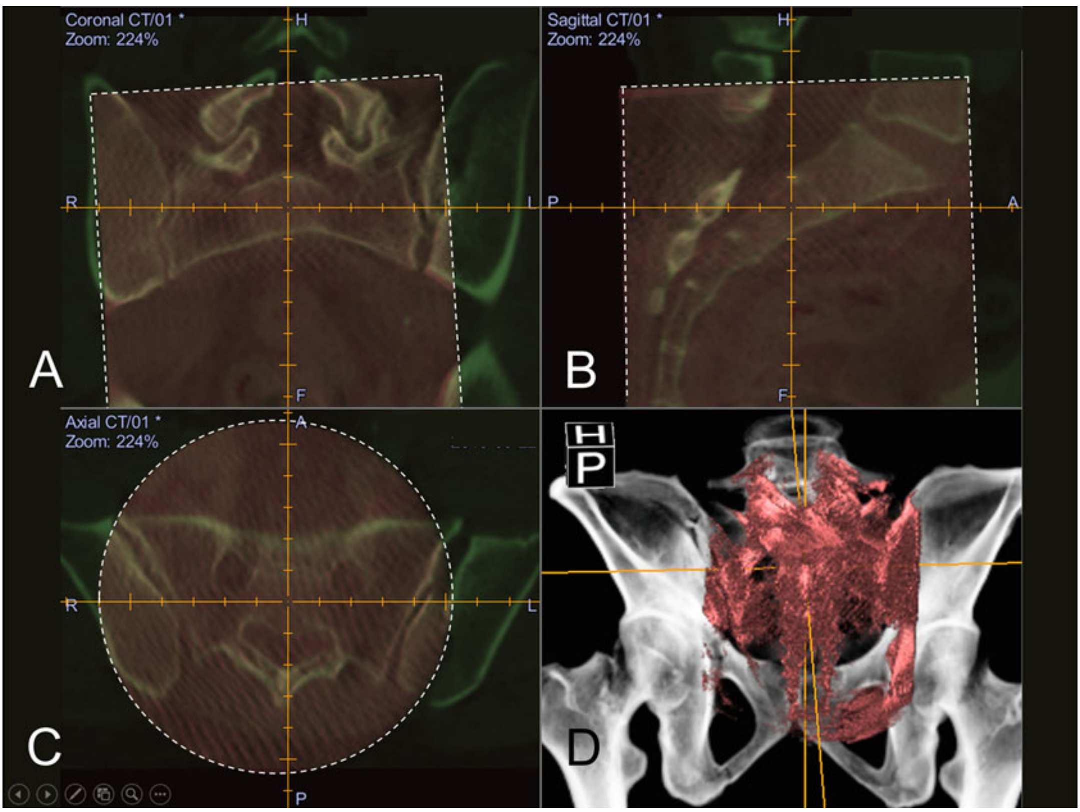

Fig. 22.6 Image matching between preoperative CT data and intraoperative 3D fluoroscopic image volume (broken lines) was done using an image registration technique. The accuracy of image matching can be visually assessed on coronal (**a**), sagittal (**b**), axial (**c**), and digitally reconstructed radiographic images (**d**)

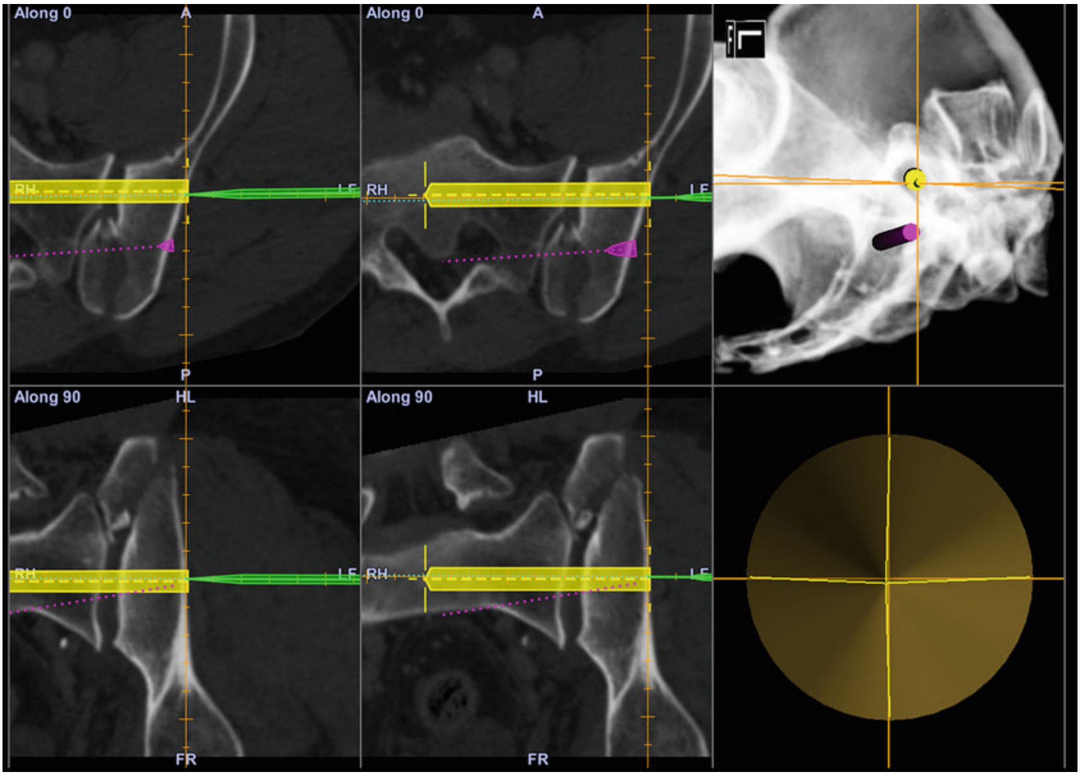

Fig. 22.7 Intraoperative view of CT-3D-fluoroscopy matching navigation shows the preoperative planned screw position on CT images (yellow screw). The surgeon inserted the guide-wire with the navigated guide-wire sleeve while viewing the guidance cone (right bottom)

ternal fixation is the standard treatment option for displaced acetabular fractures. It remains difficult even in the hands of experts, and good postoperative results cannot always be guaranteed. Matta et al. [21] graded the reduction according to one of four categories: anatomical (0–1 mm displacement), imperfect (2–3 mm displacement), poor (>3 mm displacement), or surgical secondary congruence (the acetabulum is reduced anatomically, but displacements in the innominate bone alter the position of the joint) on an anteroposterior and 45° oblique (Judet) radiograph. The reduction was graded as anatomical in 185 of 262 hips (71%), and the quality of the reduction was strongly associated with the clinical result. Giannoudis et al. [51] reported in a meta-analysis of operative treatment of displaced fractures of the acetabulum that if the reduction was satisfactory (≤2 mm displacement), the incidence of osteoarthritis was 13.2%. However, if the reduction was not satisfactory (>2 mm displacement), it increased to 43.5%.

In an experimental study of navigated periacetabular screws using artificial pelvis models and human cadaver specimens, the screw deviation severity from the predefined placement was reportedly significantly lower using a 3D fluoroscopic navigation compared to a 2D fluoroscopic navigation and the conventional technique [13]. In the real clinical setting, it is challenging to treat a displaced acetabular fracture by percutaneous screw fixation even with the use of 3D fluoroscopic navigation because of the difficulty of an anatomical reduction in a closed manner. The indication of percutaneous screw fixation should be limited to cases with a small articular displacement or impaired general condition not allowing for general anesthesia regardless of the amount of fracture displacement. Patients unable to maintain partial weight bearing due

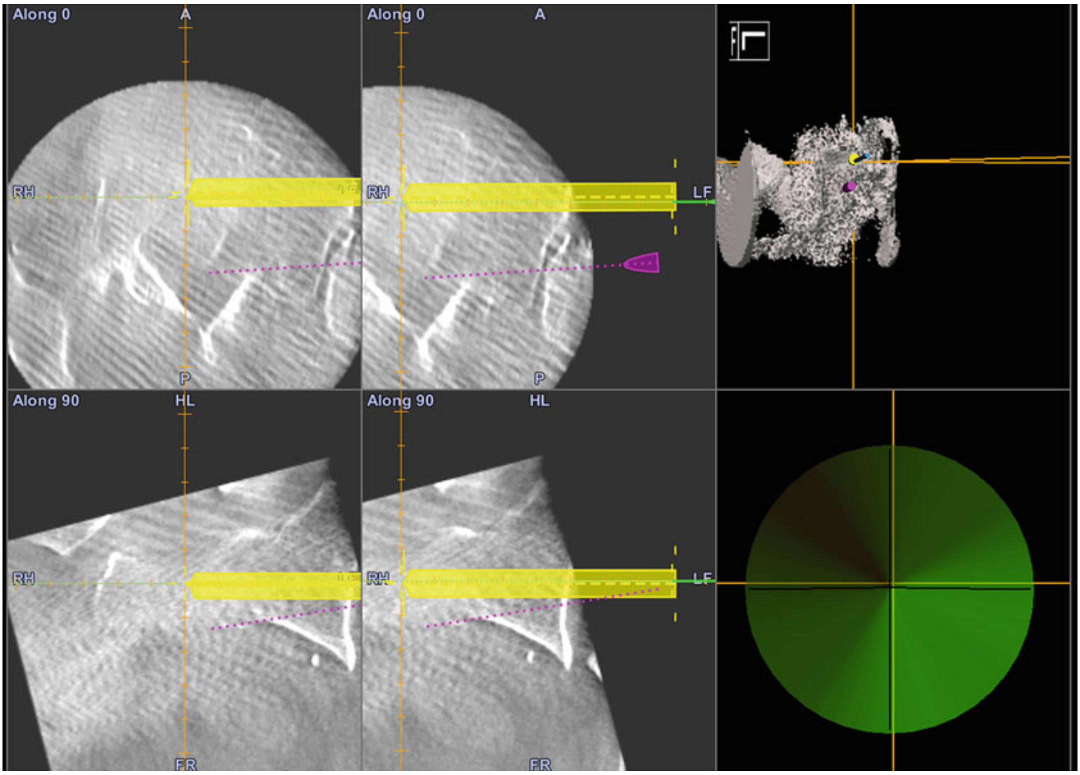

Fig. 22.8 Intraoperative view of the 3D fluoroscopic navigation mode shows 3D fluoroscopic images and the superimposed planned screw (yellow screw)

to dementia or other psychological disorders are also a good indication given that a non-operative treatment would necessitate several weeks of bed rest with an increased risk of complications such as venous thromboembolism or pneumonia. Schwabe et al. [22] reported very good radiographic and functional outcome of acetabular fractures treated with closed reduction and percutaneous 3D fluoroscopy-based navigated screw fixation. They excluded patients with a fragment displacement >1 cm, comminution, isolated or combined wall fractures, associated both-column fractures, or mildly displaced fractures with intraarticular fragments. Another advantage of percutaneous screwing is that it allows surgery to be performed as soon as possible after the injury due to its inherent minimal invasiveness, which allows for an easy reduction of fractures. Mears et al. [52] reported that if surgery was delayed for more than 11 days after injury, there were significantly fewer anatomical reductions.

The 3D intraoperative imaging modality and image-based navigation have been applied to open surgeries to evaluate fracture reduction and screw position. Oberst et al. [27] compared an acetabular fracture treatment before and after the introduction of a navigation system and a 3D image intensifier. They reported that 25% of the patients with acetabular fractures could be treated with percutaneous screwing using the navigation. The remaining patients were treated by open surgery. Using a navigation system in combination with a 3D image intensifier for open reduction and internal fixation of displaced acetabular fractures led to a significant increase in skin-to-skin time, but the 3D fluoroscopic navigation improved the quality of radiographic fracture reduction, limited the need for an extended approach, and lowered the complication rate. It has been also reported that the use of intraoperative 3D imaging modalities in the treatment of a displaced acetabular fractures led to an improvement in fracture reduction and screw position [28].

After the introduction of the 3D fluoroscopic navigation system, 17 patients with a displaced acetabular fracture were treated operatively in our hospital. Acetabular fractures were classified according to the Judet–Letournel classification as posterior wall in three patients, anterior column in one patient, transverse in one patient, transverse and posterior wall in three patients, anterior column and posterior hemi-transverse in five patients, and both-column in four patients. Five patients (29%) were treated with percutaneous periacetabular screw fixation guided by CT-3D-fluoroscopic navigation. The fracture type was posterior wall in one patient, anterior column in one patient, transverse and posterior wall in one patient, and both-column in two patients. We excluded patients with a fragment displacement >1 cm, comminution, dislocation, or mildly displaced fractures with intraarticular fragments. In the postoperative CT-based analysis, there was no articular or cortical perforation by the screws. The maximal gap of the acetabular articular surface was reduced from 4.8 to 2.5 mm, and the maximal step of the acetabular articular surface changed from 0.2 to 0 mm. These results were comparable to those of other reports (Table 22.2) [15–17, 22, 23, 27].

22.3.2 Surgical Technique

Surgical procedures for retrograde pubic screw fixation using 3D fluoroscopic navigation combined with CT-based plan are summarized in the flowchart shown in Fig. 22.9. In preoperative CT-based planning, three orthogonal reconstructions were viewed along the planned screw axis (Fig. 22.10). The screw position was adjusted to avoid articular penetration and cortical perforation. The patients were placed in a supine or prone position on a radiolucent operating table or traction table. The navigation computer was placed at each patient's caudal side. The mobile 3D C-arm approached from the opposite side to the operating surgeon. A reference tracker was fixed to the contralateral or ipsilateral and anterior or posterior iliac crest using the external fixation device. The C-arm was connected to the navigation system and calibrated by registering three points on the detector using a pointing device. A 3D fluoroscopy scan of the pelvis was performed intraoperatively with the scan center aimed at the screw entry point. Image matching between the preoperative CT data and the intraoperative 3D fluoroscopic image volume was performed using an image registration technique [47] after the image data were transferred to the navigation system.

In the supraacetabular screw and retrograde posterior column screw insertion, a guide-wire was placed into the anterior inferior iliac spine or ischial tuberosity using the navigated drilling sleeve (Fig. 22.11). In retrograde pubic screw insertion, the pubic cortex at an entry point was penetrated using a navigated awl because the screw trajectory is almost parallel to the cortical surface, and a guide-wire tends to be placed extracortically (Fig. 22.12). A navigated pedicle feeler was inserted into the superior pubic ramus to prepare the screw corridor without cortical perforation. The guide-wire was inserted into the hole and the wire placement was checked fluoroscopically. Cannulated 5.0, 6.5, or 8.0 mm in diameter partial thread screws were inserted.

22.4 Discussion

Advantages and disadvantages of a CT-based system as well as 2D and 3D fluoroscopic navigation systems are summarized in Table 22.3. A systematic review reported malpositioning and revision rates using different iliosacral screw fixation techniques including the conventional technique, 2D or 3D fluoroscopic navigation, and CT-based navigation [24]. CT-based navigation had the lowest rate of screw malposition, and 2D/3D fluoroscopic navigation showed a slightly lower rate of complications than the conventional technique; however, the difference was not statistically significant. It is difficult to compare the performance of different navigation systems by systematic review because the indication for navigation in treating pelvic and acetabular fractures

Table 22.2 Clinical reports of navigation use for periacetabular screw fixation of acetabular fracture

Author (year)	Mode of navigation	No. of patients	Screw type[a]	Percutaneous screwing/open surgery	Mean operation time (minutes)	Mean radiation time (seconds)	Screw perforation rate	Mean (range) preoperative displacement (mm)	Mean (range) postoperative displacement (mm)
Crowl (2002)	CT guided	10	Periacetabular	23/0	NA	NA	NA	6.1	2.2
	2D fluoroscopy	9				<45		12	2.4 (0 to 6)
	Non-navigation	4				73		8.3	2.8
Mosheiff (2004)	2D fluoroscopy	29[a]	IS 27, pubic15, supraacetabular 1, posterior column 2	21/8	NA	NA	0%[b]	NA	NA
Hong (2010)	2D fluoroscopy	18	Anterior column 21	18/0	24.6	28.4	0%	Gap 10 (2 to 22), step 4 (0 to 4)	Gap 3 (0 to 5), step 2 (0 to 4)
			Posterior column screw 9						
Oberst (2012)	3D fluoroscopy	31	NA	7/24	306[c]	NA	NA	Gap 11.6, step 6.8	Gap 2.1, step 0.3[c]
	Non-navigation	37		0/37	264[c]			Gap 9.6, step 7.2	Gap 1.6, step 1.5[c]
Schwabe (2014)	3D fluoroscopy	12	Periacetabular 22	12/0	NA	NA	0%	Gap 4.1, step 1.2	Gap 0.4, step 0.2
He (2016)	3D fluoroscopy	10	Retrograde anterior column screw	10/0	34	26.9[c]	0%	NA	NA
	Non-navigation	12		12/0	35	80.7[c]	16.7%		
Authors' series	3D fluoroscopy	5	Supraacetabular 3, pubic 2, posterior column 2, posterior wall 2	5/0	140	NA	0%	Gap 4.8 (1.8 to 8.9), step 0.2 (0 to 0.7)	Gap 2.5 (0.7 to 6.6), step 0

2D two dimensional, 3D three dimensional, CT computed tomography, IS iliosacral screw, NA not available
[a]The subjects included 24 patients with pelvic fractures, 5 with acetabular fracture, and 1 with both fractures
[b]The percentage of screw demonstrated a deviation >2 mm or > 5° on fluoroscopic images
[c]There was a statistically significant difference between the navigation group and the non-navigation group

is different among navigation systems because of the differences in their own performance. In addition, the definition and diagnostic imaging modality of screw perforation differ among studies. A prospective, randomized clinical study and/or a well-designed cadaveric study is necessary to compare the performance of navigation systems in the treatment of pelvic and acetabular fractures.

The current navigation system has three possible drawbacks that call for improvement. First, guidance of the screw itself is not possible with the commercially available system, which further reduces the incidence of screw perforation and fluoroscopic time and dose. Second, no navigation system can guide fracture reduction maneuvers, although the level of fracture reduction is a critical factor in determining postoperative outcomes [21, 51]. To accomplish this, it would be necessary to collect quantitative data on fracture reduction maneuvers by skillful surgeons and develop an artificial intelligence system specifically for fracture reduction. Third, surgeons must learn how to use the navigation system to utilize it in surgery. Few studies have evaluated the learning curve of computer-assisted techniques. Peng et al. used intraoperative CT with an integrated navigation system in percutaneous iliosacral screw fixation, reporting that the operation time decreased to half after the first five procedures and further decreased to one-third after the tenth procedure [6]. A training system using virtual reality technology and an easy-to-use device, such as a smartphone, would be required.

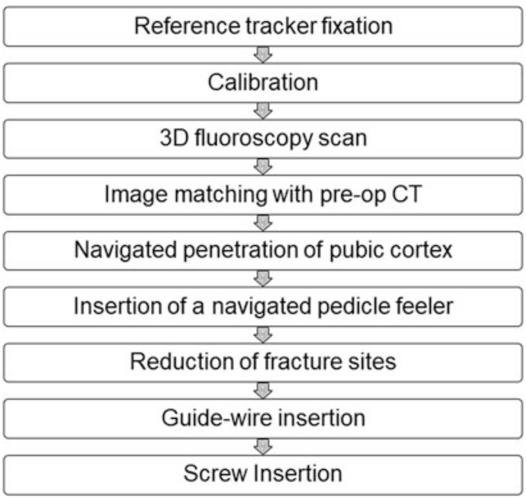

Fig. 22.9 Flowchart showing surgical procedures for retrograde pubic screw fixation using 3D fluoroscopic navigation combined with CT-based plan

22.5 Conclusion

The indication of percutaneous screw fixation for pelvic ring injuries is relatively wide, and the navigation has made these procedures safe and reliable. In particular, the efficacy of 3D fluoroscopic navigation in iliosacral screw insertion has been noted. The indication of percutaneous screw fixation for acetabular fractures is limited to cases with a small articular displacement;

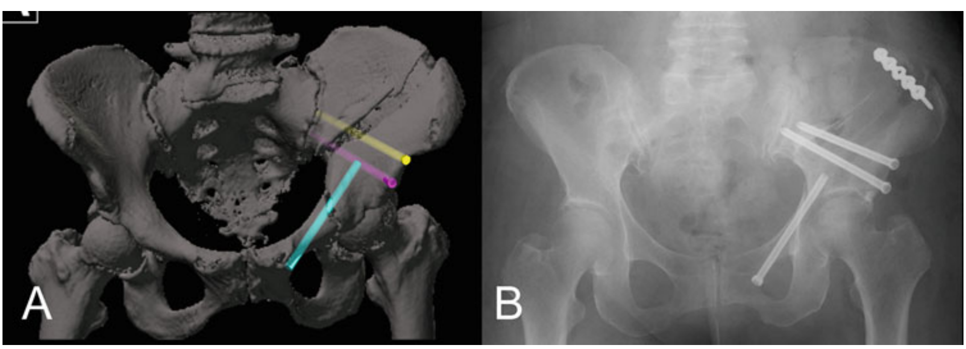

Fig. 22.10 Preoperative CT-based plan of an acetabular fracture shows the planned position of a retrograde anterior column screw and two supraacetabular screws (**a**). Postoperative anteroposterior radiograph of the pelvis was similar to the preoperative plan (**b**)

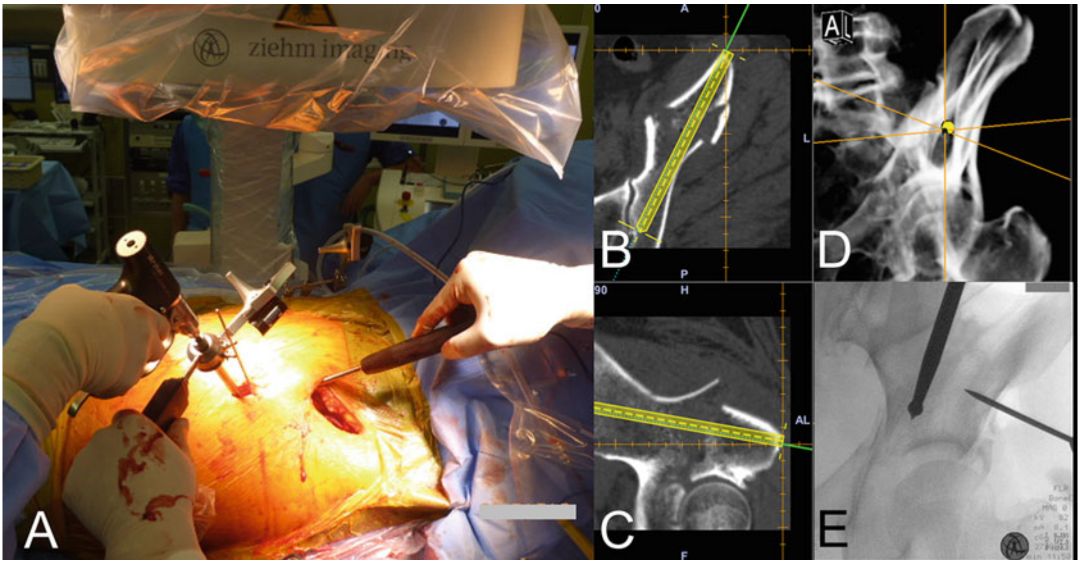

Fig. 22.11 For supraacetabular screw placement, a guide-wire was placed into the anterior inferior iliac spine using the navigated sleeve (**a**) while viewing the orthogonal screw trajectory (**b** and **c**) and digitally reconstructed radiograph (**d**). Reduction of the acetabular fracture was performed through a mini-incision using a reduction bar viewing intraoperative fluoroscopy (**e**)

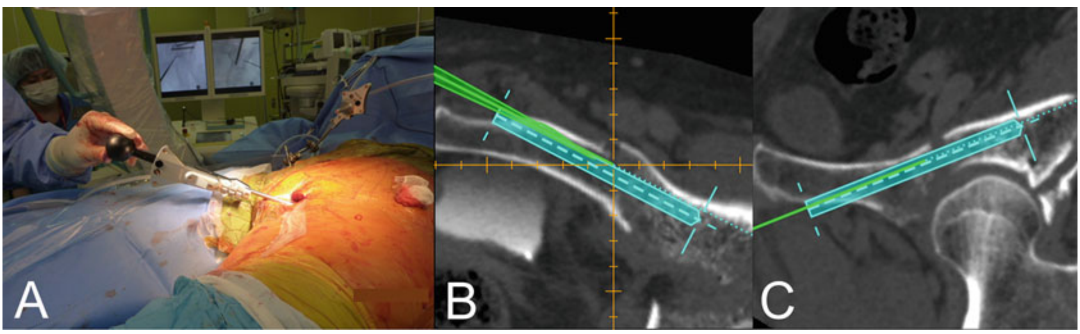

Fig. 22.12 For retrograde anterior column screw placement, the pubic cortex as an entry point was penetrated using a navigated awl. A navigated pedicle feeler (**a**) was inserted into the superior pubic ramus while viewing orthogonal screw trajectory views, which showed the feeler position in real time (**b** and **c**). The guide-wire was inserted into the hole

therefore, there are few reports regarding the use of navigation. The application of 3D fluoroscopic navigation to open surgeries is reported to evaluate fracture reduction and screw position. In the future, development of a navigation system which can guide fracture reduction is expected.

Table 22.3 Advantages and disadvantages of navigation systems using different imaging modalities

	Advantages	Disadvantages
CT-based	3D image-based system	Fracture reduction is not possible
	Preoperative planning	Paired point or surface patient-to-image registration by the surgeon's hand
	Wide field of view	
2D-fluoroscopic	Simultaneous two directional radiographic images	2D image-based system
	Fracture reduction is possible before imaging	Intraoperative planning
	Automatic patient-to-image registration	
3D-fluoroscopic	3D image-based system	Limited field of view
	Fracture reduction is possible before imaging	Intraoperative planning
	Automatic patient-to-image registration	
	Intraoperative 3D evaluation of screw position and fracture reduction	

References

1. Hauschild O, Strohm PC, Culemann U, Pohlemann T, Suedkamp NP, Koestler W, Schmal H (2008) Mortality in patients with pelvic fractures: results from the German pelvic injury register. J Trauma 64(2): 449–455
2. Rommens PM, Hofmann A (2013) Comprehensive classification of fragility fractures of the pelvic ring: recommendations for surgical treatment. Injury 44(12):1733–1744
3. Wagner D, Ossendorf C, Gruszka D, Hofmann A, Rommens PM (2015) Fragility fractures of the sacrum: how to identify and when to treat surgically? Eur J Trauma Emerg Surg 41(4):349–362
4. Arand M, Kinzl L, Gebhard F (2004) Computer-guidance in percutaneous screw stabilization of the iliosacral joint. Clin Orthop Relat Res 422:201–207
5. Briem D, Linhart W, Lehmann W, Begemann PG, Adam G, Schumacher U, Cullinane DM, Rueger JM, Windolf J (2006) Computer-assisted screw insertion into the first sacral vertebra using a three-dimensional image intensifier: results of a controlled experimental investigation. Eur Spine J 15(6):757–763
6. Peng KT, Li YY, Hsu WH, Wu MH, Yang JT, Hsu CH, Huang TJ (2013) Intraoperative computed tomography with integrated navigation in percutaneous iliosacral screwing. Injury 44(2):203–208
7. Gras F, Marintschev I, Wilharm A, Klos K, Muckley T, Hofmann GO (2010) 2D-fluoroscopic navigated percutaneous screw fixation of pelvic ring injuries–a case series. BMC Musculoskelet Disord 11:153
8. Behrendt D, Mutze M, Steinke H, Koestler M, Josten C, Bohme J (2012) Evaluation of 2D and 3D navigation for iliosacral screw fixation. Int J Comput Assist Radiol Surg 7(2):249–255
9. Grossterlinden L, Rueger J, Catala-Lehnen P, Rupprecht M, Lehmann W, Rucker A, Briem D (2011) Factors influencing the accuracy of iliosacral screw placement in trauma patients. Int Orthop 35(9): 1391–1396
10. Collinge C, Coons D, Tornetta P, Aschenbrenner J (2005) Standard multiplanar fluoroscopy versus a fluoroscopically based navigation system for the percutaneous insertion of iliosacral screws: a cadaver model. J Orthop Trauma 19(4):254–258
11. Hinsche AF, Giannoudis PV, Smith RM (2002) Fluoroscopy-based multiplanar image guidance for insertion of sacroiliac screws. Clin Orthop Relat Res 395:135–144
12. Gras F, Marintschev I, Klos K, Muckley T, Hofmann GO, Kahler DM (2012) Screw placement for acetabular fractures: which navigation modality (2-dimensional vs. 3-dimensional) should be used? An experimental study. J Orthop Trauma 26(8):466–473
13. Ochs BG, Gonser C, Shiozawa T, Badke A, Weise K, Rolauffs B, Stuby FM (2010) Computer-assisted periacetabular screw placement: comparison of different fluoroscopy-based navigation procedures with conventional technique. Injury 41(12):1297–1305
14. Smith HE, Yuan PS, Sasso R, Papadopolous S, Vaccaro AR (2006) An evaluation of image-guided technologies in the placement of percutaneous iliosacral screws. Spine (Phila Pa 1976) 31(2):234–238
15. Crowl AC, Kahler DM (2002) Closed reduction and percutaneous fixation of anterior column acetabular fractures. Comput Aided Surg 7(3):169–178
16. Mosheiff R, Khoury A, Weil Y, Liebergall M (2004) First generation computerized fluoroscopic navigation in percutaneous pelvic surgery. J Orthop Trauma 18(2):106–111
17. Hong G, Cong-Feng L, Cheng-Fang H, Chang-Qing Z, Bing-Fang Z (2010) Percutaneous screw fixation of acetabular fractures with 2D fluoroscopy-based computerized navigation. Arch Orthop Trauma Surg 130(9):1177–1183

18. Zwingmann J, Konrad G, Kotter E, Sudkamp NP, Oberst M (2009) Computer-navigated iliosacral screw insertion reduces malposition rate and radiation exposure. Clin Orthop Relat Res 467(7): 1833–1838
19. Zwingmann J, Konrad G, Mehlhorn AT, Sudkamp NP, Oberst M (2010) Percutaneous iliosacral screw insertion: malpositioning and revision rate of screws with regards to application technique (navigated vs. conventional). J Trauma 69(6):1501–1506
20. Grossterlinden L, Nuechtern J, Begemann PG, Fuhrhop I, Petersen JP, Ruecker A, Rupprecht M, Lehmann W, Schumacher U, Rueger JM, Briem D (2011) Computer-assisted surgery and intraoperative three-dimensional imaging for screw placement in different pelvic regions. J Trauma 71(4):926–932
21. Matta JM (1996) Fractures of the acetabulum: accuracy of reduction and clinical results in patients managed operatively within three weeks after the injury. J Bone Joint Surg Am 78(11):1632–1645
22. Schwabe P, Altintas B, Schaser KD, Druschel C, Kleber C, Haas NP, Maerdian S (2014) Three-dimensional fluoroscopy-navigated percutaneous screw fixation of acetabular fractures. J Orthop Trauma 28(12):700–706 discussion 706
23. He J, Tan G, Zhou D, Sun L, Li Q, Yang Y, Liu P (2016) Comparison of Isocentric C-arm 3-dimensional navigation and conventional fluoroscopy for percutaneous retrograde screwing for anterior column fracture of acetabulum: an observational study. Medicine (Baltimore) 95(2):e2470
24. Zwingmann J, Hauschild O, Bode G, Sudkamp NP, Schmal H (2013) Malposition and revision rates of different imaging modalities for percutaneous iliosacral screw fixation following pelvic fractures: a systematic review and meta-analysis. Arch Orthop Trauma Surg 133(9):1257–1265
25. Zwingmann J, Sudkamp NP, Konig B, Culemann U, Pohlemann T, Aghayev E, Schmal H (2013) Intra- and postoperative complications of navigated and conventional techniques in percutaneous iliosacral screw fixation after pelvic fractures: results from the German pelvic trauma registry. Injury 44(12): 1765–1772
26. Takao M, Nishii T, Sakai T, Sugano N (2014) Navigation-aided visualization of lumbosacral nerves for anterior sacroiliac plate fixation: a case report. Int J Med Robot 10(2):230–236
27. Oberst M, Hauschild O, Konstantinidis L, Suedkamp NP, Schmal H (2012) Effects of three-dimensional navigation on intraoperative management and early postoperative outcome after open reduction and internal fixation of displaced acetabular fractures. J Trauma Acute Care Surg 73(4):950–956
28. Eckardt H, Lind D, Toendevold E (2015) Open reduction and internal fixation aided by intraoperative 3-dimensional imaging improved the articular reduction in 72 displaced acetabular fractures. Acta Orthop 86(6):684–689
29. Vanderschot PM, Broens PM, Vermeire JI, Broos PL (1999) Trans iliac-sacral-iliac bar stabilization to treat bilateral sacroiliac joint disruptions. Injury 30(9):637–640
30. Matta JM, Saucedo T (1989) Internal fixation of pelvic ring fractures. Clin Orthop Relat Res 242: 83–97
31. Routt ML Jr, Kregor PJ, Simonian PT, Mayo KA (1995) Early results of percutaneous iliosacral screws placed with the patient in the supine position. J Orthop Trauma 9(3):207–214
32. Shuler TE, Boone DC, Gruen GS, Peitzman AB (1995) Percutaneous iliosacral screw fixation: early treatment for unstable posterior pelvic ring disruptions. J Trauma 38(3):453–458
33. Templeman D, Goulet J, Duwelius PJ, Olson S, Davidson M (1996) Internal fixation of displaced fractures of the sacrum. Clin Orthop Relat Res 329:180–185
34. Gardner MJ, Morshed S, Nork SE, Ricci WM, Chip Routt ML Jr (2010) Quantification of the upper and second sacral segment safe zones in normal and dysmorphic sacra. J Orthop Trauma 24(10):622–629
35. Templeman D, Schmidt A, Freese J, Weisman I (1996) Proximity of iliosacral screws to neurovascular structures after internal fixation. Clin Orthop Relat Res 329:194–198
36. Ziran BH, Wasan AD, Marks DM, Olson SA, Chapman MW (2007) Fluoroscopic imaging guides of the posterior pelvis pertaining to iliosacral screw placement. J Trauma 62(2):347–356 discussion 356
37. Sagi HC, Lindvall EM (2005) Inadvertent intraforaminal iliosacral screw placement despite apparent appropriate positioning on intraoperative fluoroscopy. J Orthop Trauma 19(2):130–133
38. van den Bosch EW, van Zwienen CM, van Vugt AB (2002) Fluoroscopic positioning of sacroiliac screws in 88 patients. J Trauma 53(1):44–48
39. Routt ML Jr, Simonian PT, Mills WJ (1997) Iliosacral screw fixation: early complications of the percutaneous technique. J Orthop Trauma 11(8): 584–589
40. Takao M, Nishii T, Sakai T, Sugano N (2013) CT-3D-fluoroscopy matching navigation can reduce the malposition rate of iliosacral screw insertion for less-experienced surgeons. J Orthop Trauma 27(12): 716–721
41. Beck M, Krober M, Mittlmeier T (2010) Intraoperative three-dimensional fluoroscopy assessment of iliosacral screws and lumbopelvic implants stabilizing fractures of the os sacrum. Arch Orthop Trauma Surg 130(11):1363–1369
42. Kim JW, Oh CW, Oh JK, Lee HJ, Min WK, Kyung HS, Yoon SH, Mun JU (2013) Percutaneous iliosacral screwing in pelvic ring injury using three-dimensional fluoroscopy. J Orthop Sci 18(1):87–92
43. Reilly MC, Bono CM, Litkouhi B, Sirkin M, Behrens FF (2003) The effect of sacral fracture malreduction on the safe placement of iliosacral screws. J Orthop Trauma 17(2):88–94

44. Matityahu A, Kahler D, Krettek C, Stockle U, Grutzner PA, Messmer P, Ljungqvist J, Gebhard F (2014) Three-dimensional navigation is more accurate than two-dimensional navigation or conventional fluoroscopy for percutaneous sacroiliac screw fixation in the dysmorphic sacrum: a randomized multicenter study. J Orthop Trauma 28(12): 707–710
45. Thakkar SC, Thakkar RS, Sirisreetreerux N, Carrino JA, Shafiq B, Hasenboehler EA (2017) 2D versus 3D fluoroscopy-based navigation in posterior pelvic fixation: review of the literature on current technology. Int J Comput Assist Radiol Surg 12(1): 69–76
46. Richter PH, Gebhard F, Dehner C, Scola A (2016) Accuracy of computer-assisted iliosacral screw placement using a hybrid operating room. Injury 47(2):402–407
47. Takao M, Nishii T, Sakai T, Yoshikawa H, Sugano N (2014) Iliosacral screw insertion using CT-3D-fluoroscopy matching navigation. Injury 45(6): 988–994
48. Takao M, Yabuta K, Nishii T, Sakai T, Sugano N (2011) Accuracy of a 3D fluoroscopic navigation system using a flat-panel detector-equipped C-arm. Comput Aided Surg 16(5):234–239
49. Takao M, Nishii T, Sakai T, Sugano N (2012) Application of a CT-3D fluoroscopy matching navigation system to the pelvic and femoral regions. Comput Aided Surg 17(2):69–76
50. Wagner D, Kamer L, Sawaguchi T, Richards RG, Noser H, Rommens PM (2016) Sacral bone mass distribution assessed by averaged three-dimensional CT models: implications for pathogenesis and treatment of fragility fractures of the sacrum. J Bone Joint Surg Am 98(7):584–590
51. Giannoudis PV, Grotz MR, Papakostidis C, Dinopoulos H (2005) Operative treatment of displaced fractures of the acetabulum. A meta-analysis. J Bone Joint Surg Br 87(1):2–9
52. Mears DC, Velyvis JH, Chang CP (2003) Displaced acetabular fractures managed operatively: indicators of outcome. Clin Orthop Relat Res 407:173–186

23 Patient-Specific Surgical Guide for Total Hip Arthroplasty

Takashi Sakai

Abstract

Three-dimensional printing technique has been adapted for orthopedic surgery, and a patient-specific surgical guide (PSG) has been introduced as a convenient surgical instrument and implicated in the ideal positioning of the components, including acetabular and femoral components in total hip arthroplasty (THA). PSG is designed and manufactured based on preoperative imaging data, mainly computed tomography (CT) data. PSGs for implantation in THA are classified into three types: PSG for guidewire insertion, PSG for bone cutting, and PSG for bone reaming and implant fixation. PSG positioning accuracy depends on the PSG design and surgical preparation in contact area on the bone surface. PSGs for the acetabular component, for the conventional femoral component, and for the resurfacing femoral component have been clinically used. To achieve precise implantation, precise PSG setting needs and careful surgical preparation of soft tissues are important.

Keywords

Patient-specific surgical guide · Total hip arthroplasty · Guidewire insertion · Bone cutting · Accuracy

23.1 Introduction

Patient-specific surgical guide (PSG) for the orthopedic surgery has been introduced as a computer-assisted surgical tool in 1998 [1]. In the total hip arthroplasty (THA) procedure, ideal orientation and positioning of hip implants are necessary to prevent postoperative dislocation [2, 3], satisfactorily perform daily living activities [4], and enhance implant longevity [5]. In combination with the advancements of three-dimensional printing, a PSG for hip arthroplasty is a convenient surgical instrument and has been implicated in the ideal positioning of the acetabular components and femoral components, based on preoperative planning (Fig. 23.1) [6–15]. In the present chapter, PSGs for THA have been reviewed and the validation of PSGs is elucidated.

T. Sakai (✉)
Department of Orthopaedic Surgery, Osaka University Graduate School of Medicine, Suita, Japan
e-mail: tsakai-osk@umin.ac.jp

G. Zheng et al. (eds.), *Intelligent Orthopaedics*, Advances in Experimental Medicine and Biology 1093, https://doi.org/10.1007/978-981-13-1396-7_23

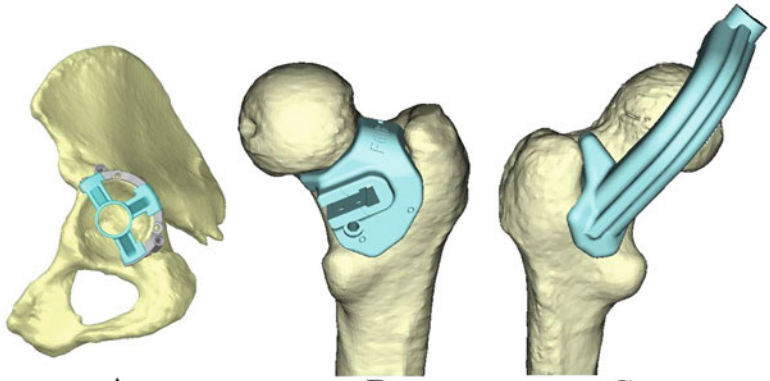

Fig. 23.1 PSG for total hip arthroplasty. (**a**) PSG for acetabular component, (**b**) PSG for femoral neck cut, (**c**) PSG for resurfacing total hip arthroplasty

23.2 Design and Manufacturing of PSG

A PSG is designed to match the surface of the three-dimensional bone models based on either preoperative computed tomography (CT) data or magnetic resonance imaging data. PSGs are made by various materials, including resin, nylon, and metal. We used the helical CT data, reconstructed at 1-mm intervals and transferred to a workstation in STL format. The following standardized protocol was used: 130kv, 56–112 mA, collimation 1.0 mm, pitch 1, and rotation length 1.0 s. Reconstructions were obtained using 1.0-mm sections, 0.5-mm increment, 216-mm field of view, and 512 x 512 matrix. PSGs for THA were designed based on preoperative planning using an image-processing software (Mimics, Materialise, Leuven, Belgium). PSGs are made from resins and produced by a machine (FORMIGA, EOS GmbH, Krailling, Germany) using a rapid prototyping method. It takes about 3 hours for making one PSG from CT data preparing to manufacturing. The interoperator error of producing PSGs is 0.048 ± 0.25 mm [14].

23.3 Function of PSGs for THA

PSGs for THA are mainly classified into three types: PSG for guidewire insertion [6–15], PSG for bone cutting [14], and PSG for bone reaming and implant fixation [14]. PSGs for guidewire insertion have been used to regulate the direction of the acetabular component and the resurfacing femoral component. These guides do not regulate the three-dimensional position of the component but regulate the two-dimensional position and direction. For example, PSG for acetabular component regulates inclination and anteversion, but it does not regulate three-dimensional position including acetabular depth. While the guidewire of the resurfacing femoral component is at the center of the component and regulates the two-dimensional position and the direction of the component [8, 9, 11, 13, 14], there are two types of guidewire of the acetabular components. The first type of guidewire regulates the center of the component and the direction of the acetabular component as the resurfacing femoral component [10, 12]. The second type of guidewire regulates the direction of the acetabular component only [6, 7, 15]. In the second type, surgeons attempt to fix acetabular components parallel to the inserted guidewire around the acetabular rim.

PSGs for bone cutting have been used for femoral neck cutting in conventional THA. These guides regulate the neck-cut height and the direction, such as neck-cut angle on the coronal and sagittal plane [14]. When the surgeons insert and fix the femoral component, some guides have additional parts to regulate the stem anteversion.

PSGs for bone reaming and implant fixation have been particularly reported for acetabular reaming and acetabular component fixation [14]. Although these guides are set around the acetabular rim, these guides are influenced and moved by the tremor of the reamer and impaction of the socket holder.

23.4 PSG Positioning on the Bone Surface

To achieve the accurate positioning of THA implants using PSGs, accurate PSG positioning on the bone surface based on preoperative planning is necessary. The soft tissue covering the bony surface where PSGs will contact, including the joint capsule, acetabular limbus, and synovium, has to be removed completely. Otherwise, PSGs cannot be set on the bony surface accurately, and guidewire insertion and/or bone cutting cannot be performed precisely based on preoperative planning. Additionally, surgeons must confirm that PSGs are placed on the bony surface without any gaps, except the gaps PSG design allows between PSG and bone surface. Sometimes, longer incision, not minimum incision, is needed to confirm no gap between PSG and bone surface. Because of the removal of soft tissues and preparation needed to confirm PSG setting, PSGs for THA do not always mean minimal invasive surgery.

There are no clinical data concerning the accuracy of PSG positioning on the bone surface in THA. In a cadaver study [14], PSGs had four metal sphere markers (2 mm in diameter) for the evaluation of the accuracy of PSG positioning on the bone surface. The preoperative bone model and the intraoperative or postoperative bone model based on CT data were matched using automatic segmentation and semiautomatic registration and compared between these two bone models. The accuracy between preoperative planning and PSG positioning depends on the design and the contact area of PSGs.

In PSGs for the femoral neck cut through the posterior approach, there were no significant differences in PSG positioning between the wide-base-contact type and the narrow-base-contact type [14]. The absolute errors (wide vs. narrow) are $1.6 \pm 0.7°$ vs. $1.6 \pm 1.3°$ in the neck-cut angle on the coronal plane, $1.0 \pm 0.4°$ vs. $0.7 \pm 0.7°$ in the neck-cut angle on the sagittal plane, and 1.2 ± 0.8 mm vs. 0.8 ± 0.5 mm in the medial neck-cut height.

In PSGs for the femoral neck cut through the anterior approach, there were significant differences in the neck-cut angle on the sagittal plane between the wide-base-contact type and the narrow-base-contact type [18]. The absolute errors (wide vs. narrow) are $0.9 \pm 0.3°$ vs. $1.3 \pm 1.3°$ in the neck-cut angle on the coronal plane, $1.7 \pm 0.8°$ vs. $5.5 \pm 2.8°$ in the neck-cut angle on the sagittal plane ($p = 0.03$), and 1.0 ± 0.6 mm vs. 1.6 ± 1.1 mm in the medial neck-cut height.

In PSGs for acetabular component implantation, all rim contact types showed more accuracy in PSG positioning than non-anterior rim contact types [14]. The absolute errors (all rim contact vs. non-anterior contact) are $1.0 \pm 0.9°$ vs. $3.4 \pm 2.4°$ in the inclination angle and $1.7 \pm 1.1°$ vs. $3.6 \pm 2.8°$ in the anteversion angle ($p = 0.03$).

23.5 PSGs for the Acetabular Component

There are three types of PSGs according to the functional classification: (1) guidewire outside the acetabulum (acetabular rim) to regulate the direction (inclination and anteversion) of the acetabular component [6, 7, 15], (2) guidewire inside the acetabulum to regulate the direction and the two-dimensional position of the acetabular component [10, 12], and (3) PSGs to regulate the direction and the three-dimensional position of the acetabular component [14]. The accuracy between the preoperative planning and cup implantation is shown in Table 23.1.

23.5.1 Type 1: Guidewire Insertion Around the Acetabular Rim

The PSG design is matched with the bony surface of the acetabular rim and/or the bony surface inside the acetabulum, avoiding contact with the remaining degenerative cartilages [6, 7, 15]. PSG has one hole for guidewire insertion around the acetabular rim. This guidewire regulates the di-

Table 23.1 Comparison of accuracy of PSG[a] for cup implantation in THA[b]

	Subjects (hips)	PSG^{+} type	Inclination (°)	Anteversion (°)
Hananouchi et al. [6]	Clinical (24)	Type 1. Outside parallel guidewire	2.8 ± 2.1	3.7 ± 2.7
Hananouchi et al. [7]	Clinical (38)	Type 1. Outside parallel guidewire	3.2 ± 2.3	3.7 ± 2.7
Zhang et al. [10]	Clinical (11)	Type 2. Reaming guidewire	1.6 ± 0.4	1.9 ± 1.1
Buller et al. [12]	Model bone (14)	Type 2. Cup holder guidewire	1.4 ± 0.2	5.2 ± 5.5
Sakai et al. [14]	Cadaveric (8) cadaveric (8)	Type 3. Non-anterior rim contact	6.7 ± 4.2	8.4 ± 4.8
		Type 3. Anterior rim contact	3.4 ± 2.1	6.6 ± 4.7
Small et al. [15]	Clinical (18)	Type 1. Parallel guidewire	−1.96 ± 7.3	−0.22 ± 6.9

Values are mean ± standard deviation
[a]Patient-specific surgical guide
[b]Total hip arthroplasty

rection, namely, inclination and anteversion of the acetabular component, based on preoperative planning. After reaming the acetabular bone and preparing the acetabular component, the cup holder is parallel to the guidewire, and the surgeons hit the cup holder to implant the acetabular component. The accuracy between the preoperative planning and cup implantation is determined by comparing the preoperative and postoperative CT data, and the absolute errors have been reported to be 3.2 ± 2.3° in the inclination of the acetabular component and 3.7 ± 2.7° in the anteversion of the acetabular component [7].

23.5.2 Type 2: Guidewire Inside the Acetabulum

PSG is designed and manufactured as the above-mentioned type. PSG has one hole for guidewire insertion or for the reaming handle/cup holder inside the acetabulum [10, 12]. This guidewire regulates the two-dimensional position and the direction (inclination and anteversion) of the acetabular component based on preoperative planning. Surgeons use the hollow reamer holder through the guidewire and prepare the acetabular component implantation. After reaming, surgeons use the hollow cup holder through the guidewire and implant the acetabular component. The accuracy between the preoperative planning and cup implantation is determined by comparing the preoperative and postoperative CT data, and the absolute errors have been reported to be 1.6 ± 0.4° in the inclination of the acetabular component and 1.9 ± 1.1° in the anteversion of the acetabular component [10].

23.5.3 Type 3: Reaming Guide and Cup Holder in the Acetabulum (Fig. 23.2)

The PSG design is matched with the bony surface of the acetabular rim, avoiding contact with the remaining degenerative cartilages. PSG has one hole where the reamer handle and the cup holder pass [14]. It regulates both the two-dimensional position and the direction (inclination and anteversion) of the reamer handle and cup holder based on preoperative planning. Although this PSG can theoretically regulate the three-dimensional position including the depth of the acetabular component, cup impaction affects the PSG setting. In a cadaver study, the absolute errors have been reported to be 3.4 ± 2.1° in the inclination of the acetabular component and 6.6 ± 4.7° in the anteversion of the acetabular component [14]. These PSGs have the risk of moving because of the tremor of the reamer and the cup impactor, and it is difficult to use clinically.

23.6 PSGs for the Conventional Femoral Component (Fig. 23.3)

There are two types of PSGs according to the functional classification: (1) a PSG that regulates the height and the direction of the neck cutline

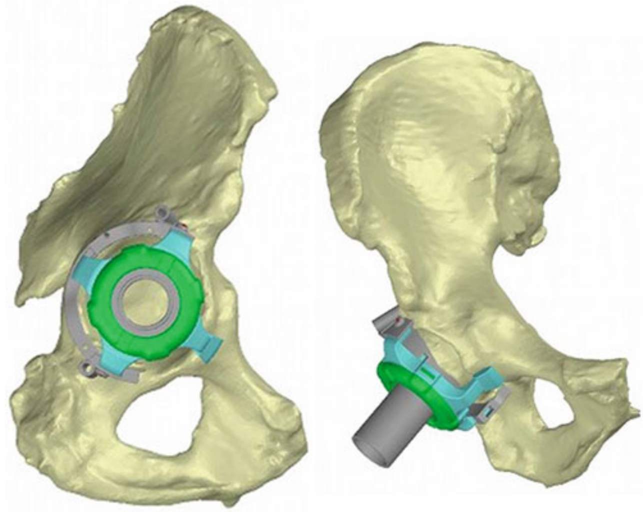

Fig. 23.2 PSG for acetabular component. This PSG regulates the direction and three-dimensional position of the reaming guide and the cup holder in the acetabulum

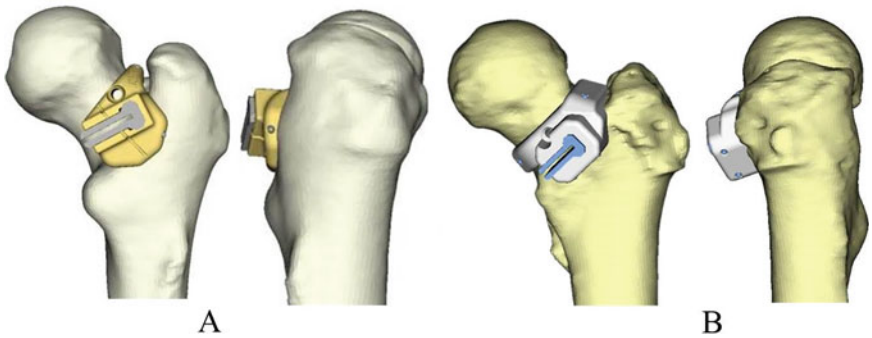

Fig. 23.3 PSG for the conventional femoral component. PSG regulates the height and the direction of the neck cutline. (**a**) PSG for the posterolateral approach, (**b**) PSG for the anterior approach

[14, 18] and (2) a PSG that regulates the coronal/sagittal alignment and the anteversion of the femoral component.

23.6.1 Type 1: PSG Regulates the Height and the Direction of the Neck Cutline

The PSG design is matched with the bony surface of the femoral neck [14]. The posterior aspect is chosen as the PSG positioning area in the posterior approach, while the anterior aspect is chosen in the anterior approach [18]. PSG regulates the height and direction of the neck cutline. Through the metal slit, the blade contacts the bony surface and cuts the femoral neck. After the neck cut, the conventional stem is inserted and fixed based on the neck cutline, including height and direction. In the cadaver study, the absolute errors between the preoperative planning and postoperative stem implantation, by comparing the preoperative and postoperative CT data, are 1.4 ± 0.8° for the coronal alignment (varus/valgus), 3.0 ± 1.4° for the sagittal alignment (flexion /extension), and 0.7 ± 0.5 mm for the medial neck-cut height in posterior THA [14]. The absolute errors are 0.6 ± 0.6° for the coronal alignment (varus/valgus), 1.0 ± 0.9° for the sagittal alignment (flexion /extension), and 1.0 ± 1.1 mm for the medial neck-cut height in anterior THA, and there were significant differences in the sagittal alignment and medial neck-cut height compared with control (without PSG) [18].

23.6.2 Type 2: PSG Regulates the Coronal/Sagittal Alignment and the Anteversion of the Femoral Component

PSG is designed and manufactured as the above-mentioned type. This PSG regulates the height, the coronal/sagittal alignment, and the anteversion using the additional part attached to the neck-cut plane. After the neck cut, the conventional stem is inserted and fixed based on the neck cutline, including height and direction as well as the anteversion direction.

23.7 PSG for the Resurfacing Femoral Component (Fig. 23.1c)

The PSG design is matched with the bony surface of the posterior aspect of the femoral neck and the saddle. This PSG regulates the position on the femoral head and the direction (stem-shaft angle and anteversion) of the guidewire insertion. PSG for the resurfacing femoral component is most practical [8, 9, 11, 13, 14], and optimal results have been reported (Table 23.2). The precision of the procedure using PSG has been reported to be as excellent as the CT-based navigation system [13].

23.8 PSG for the Corrective and Shortening Osteotomy Combined with THA

In some hip osteoarthritis patients who underwent preoperative femoral osteotomy, THA combined with the corrective and shortening osteotomy is needed. For such cases, PSG is useful like PSGs in the corrective osteotomy for the deformed upper extremities [19]. The PSG design is matched with the bony surface of the deformed femur. This PSG regulates the angle of the corrective osteotomy and the shortening distance.

23.9 Discussion

To confirm PSG setting as the preoperative planning, namely, without no gap between PSGs and the bone surface in every direction, the removal of soft tissues and preparation is necessary. On the other hand, in CT-based navigation system [17], because the tip of the probe that acquires the bone surface information can reach to the bone surface through the soft tissue, the complete removal of soft tissues is not necessary. Compared with CT-based navigation system, PSGs for THA do not always mean minimal invasive surgery.

Table 23.2 Comparison of accuracy of PSG[a] for femoral guidewire insertion in resurfacing THA[b]

	Subjects (hips)	PSG design	Stem-shaft angle (°)	Anteversion (°)	Insertion point (mm)
Kunz et al. [8]	Clinical (45)		1.14	4.49	
Raaijmaakers et al. [9]	Clinical (5)			2.02 (1.5 2.9)	1.84 (1.6 2.1)
Andenaert et al. [11]	Clinical (6)			4.1 ± 1.8	2.7 ± 2.0
Sakai et al. [14]	Cadaveric (8)	Narrow-base-contact	2.6 ± 2.8	2.4 ± 1.8	3.7 ± 2.6
	Cadaveric (8)	Wide-base-contact	0.8 ± 0.6	1.7 ± 2.0	2.6 ± 1.5

Values are mean ± standard deviation
[a]Patient-specific surgical guide
[b]Total hip arthroplasty

The accuracy of PSG setting depends on the PSG design, including the width of bone contact surface. In PSGs for the femoral neck cut through the anterior approach [18], PSG setting accuracy was worse in the narrow-based PSG than wide-based PSG, while there were no significant differences in PSGs for the neck cut through the posterior approach [14]. In PSGs for acetabular component implantation, the absolute errors were significantly worse in the inclination angle and the anteversion of the cup in non-anterior contact type than in all-contact type [14].

The PSGs for reaming and fixation of the acetabular component have the risk of moving because of the tremor of the reamer and the cup impactor. The absolute errors of cup inclination and anteversion in the cup fixation were significantly larger than PSG setting errors [14], and it is difficult to use practically. PSGs for the acetabular component that indicate inclination and anteversion of the acetabular component [6, 7, 10, 12, 15] showed lower errors as other computer-assisted devices such as mechanical navigation instrument (inclination, $1.3 \pm 3.4°$; anteversion, $1.0 \pm 4.1°$) [16] and CT-based navigation (inclination, $1.5 \pm 3.5°$; anteversion, $1.4 \pm 5.6°$) [17], and they may be practical in clinical use.

The PSGs for femoral neck cut in conventional THA [14, 18] and those for resurfacing [8, 9, 11, 13, 14] were practical in clinical use because the accuracy of PSGs is reasonable, and the skin incision is not necessarily extended longer than 10 cm.

23.10 Conclusion

PSG for THA is a convenient surgical instrument and implicated in the ideal positioning of the acetabular and femoral components. PSG based on preoperative CT data is dominated over MRI. PSG for guidewire insertion and PSG for bone cutting were practical in clinical use. PSG positioning accuracy depends on the PSG design with bone contact area and surgical preparation in contact area on the bone surface.

References

1. Radermacher K, Portheine F, Anton M, Zimolong A, Kaspers G, Rau G, Staudte HW (1998) Computer assisted orthopaedic surgery with image based individual templates. Clin Orthop Relat Res 354:28–38
2. Widmer KH, Zurfluh B (2004) Compliant positioning of total hip components for optimal range of motion. J Orthop Res 22:815–821
3. Miki H, Yamanashi W, Nishii T, Sato Y, Yoshikawa H, Sugano N (2007) Anatomic hip range of motion after implantation during total hip arthroplasty as measured by a navigation system. J Arthroplast 22:946–952
4. Jolles BM, Zangger P, Leyvraz PF (2002) Factors predisposing to dislocation after primary total hip prosthesis. J Arthroplast 17:282–288
5. Kennedy JG, Rogers WB, Soffe KE, Sullivan RJ, Griffen DG, Sheehan LJ (1998) Effect of acetabular component orientation on recurrent dislocation, pelvic osteolysis, polyethylene wear, and component migration. J Arthroplast 13:530–534
6. Hananouchi T, Saito M, Koyama T, Hagio K, Murase T, Sugano N, Yoshikawa H (2009) Tailor-made surgical guide based on rapid prototyping technique for cup insertion in total hip arthroplasty. Int J Med Robot 5:164–169
7. Hananouchi T, Saito M, Koyama T, Sugano N, Yoshikawa H (2010) Tailor-made surgical guide reduces incidence of outliers of cup placement. Clin Orthop Relat Res 468:1088–1095
8. Kunz M, Rudan JF, Xenoyannis GL, Ellis RE (2010) Computer-assisted hip resurfacing using individualized drill templates. J Arthroplast 25:600–606
9. Raaijmaakers M, Gelaude F, De Smedt K, Clijmans T, Dille J, Mulier M (2010) A custom-made guidewire positioning device for hip surface replacement arthroplasty: description and first results. BMC Musculoskelet Disord 11:161–167
10. Zhang YZ, Chen B, Lu S, Yang Y, Zhao JM, Liu R, Li YB, Pei GX (2011) Preliminary application of computer-assisted patient-specific acetabular navigational template for total hip arthroplasty in adult single development dysplasia of the hip. Int J Med Robot Comput Assist Surg 7:469–474
11. Andenaert E, De Smedt K, Gelaude F, Clijmans T, Pattyn C, Geebelen B (2011) A custom-made guide for femoral component positioning in hip resurfacing arthroplasty: development and validation study. Comput Aided Surg 16:304–309
12. Buller L, Smith T, Bryan J, Klika A, Barsoum W, Iannti JP (2013) The use of patient-specific instrumentation improves the accuracy of acetabular component placement. J Arthroplast 28:631–636
13. Kitada M, Sakai T, Murase T, Hanada T, Nakamura N, Sugano N (2013) Validation of the femoral component placement during hip resurfacing: a comparison between the conventional jig,patient-specific

template, and CT-based navigation. Int J Med Robot 9:223–229

14. Sakai T, Hanada T, Murase T, Kitada M, Hamada H, Yoshikawa H, Sugano N (2014) Validation of patient specific surgical guides in total hip arthroplasty. Int J Med Robot 10:113–120
15. Small T, Krebs V, Molloy R, Bryan J, Klika AK, Barsoum WK (2014) Comparison of acetabular shell position using patient specific instruments vs. standard surgical instruments: a randomized clinical trial. J Arthroplast 29:1030–1037
16. Steppacher SD, Kowal JH, Murphy SB (2011) Improving cup positioning using a mechanical navigation instrument. Clin Orthop Relat Res 469:423–428
17. Kitada M, Nakamura N, Iwana D, Kakimoto A, Nishii T, Sugano N (2011) Evaluation of the accuracy of computed tomography–based navigation for femoral stem orientation and leg length discrepancy. J Arthroplast 26:674–679
18. Sakai T, Hamada H, Takao M, Murase T, Yoshikawa H, Sugano N (2017) Validation of patient-specific surgical guides for femoral neck cutting in total hip arthroplasty through the anterolateral approach. Int J Med Robot 13(3). https://doi.org/10.1002/rcs.1830 Epub 2017 May 8
19. Murase T, Oka K, Moritomo H, Goto A, Yoshikawa H, Sugamoto K (2008) Three-dimensional corrective osteotomy of malunited fractures of the upper extremity with use of a computer simulation system. J Bone Joint Surg Am 90:2375–2389

24 Computer Navigation in Orthopaedic Tumour Surgery

Kwok-Chuen Wong, Xiaohui Niu, Hairong Xu, Yuan Li, and Shekhar Kumta

Abstract

In orthopaedic bone tumour surgery, surgeons perform malignant bone tumour resections with tumour-free margin. The bone defects following the resections have to be reconstructed to restore limb function. An inaccurate resection with positive surgical margin increased the risk of local recurrence and compromised patients' survival. Conventionally, orthopaedic tumour surgeons analyse two-dimensional (2D) imaging information and mentally integrate to formulate a three-dimensional (3D) surgical plan. It is difficult to translate the surgical plan to the operating room in complex cases.

Computer-assisted tumour surgery (CATS) has been developed in orthopaedic oncology for the last decade. The technique may enable surgeons' 3D surgical planning and image-guided bone resection as planned. The technique may apply to difficult surgery in pelvic or sacral tumours, limited resection in joint-preserving tumour surgery or bone defect reconstruction using CAD prostheses or allograft.

Early results suggested that the technique may help in safe tumour resection and improve surgical accuracy by replicating the preoperative planning. The improved surgical accuracy may offer clinical benefits.

Surgeons have to be aware of the potential errors of the technique that may result in inaccurate bone resections with possible adverse clinical outcomes. Given that bone sarcoma is rare, the published reports from different tumour centres could only analyse relatively small patient population with the heterogeneous histological diagnosis. Multicentre comparative studies with long-term follow-up are necessary to confirm its clinical efficacy.

This chapter provides an overview of computer navigation in orthopaedic tumour surgery over the past decade. It (1) describes the current workflow, (2) reports the clinical indications and results and (3) discusses its limitations and future development.

Keywords

Computer navigation · Computer-assisted tumour surgery (CATS) · Image fusion · Pelvic tumour · Sacral tumour · Joint-preserving surgery · Surgical accuracy · Orthopaedic oncology · Surgical planning · Image-guided bone resection

K.-C. Wong (✉) · S. Kumta
Orthopaedic Oncology, Prince of Wales Hospital, The Chinese University of Hong Kong, Hong Kong, China
e-mail: skcwong@ort.cuhk.edu.hk

X. Niu · H. Xu · Y. Li
Orthopaedic Oncology, Jishuitan Hospital, Beijing, China

G. Zheng et al. (eds.), *Intelligent Orthopaedics*, Advances in Experimental Medicine and Biology 1093, https://doi.org/10.1007/978-981-13-1396-7_24

24.1 Introduction

In orthopaedic bone tumour surgery, surgeons perform malignant bone tumour resections with tumour-free margin. The bone defects following the resections have to be reconstructed to restore limb function. An inaccurate resection with positive surgical margin increased the risk of local recurrence and compromised patients' survival [1–3]. On the other hand, bone resections with incorrect orientation may affect the matching of prostheses or allograft to the resection defects, leading to inferior limb function. Therefore, accurate surgical planning and implementation of the bone resection and reconstruction are crucial to bone tumour surgery.

Conventionally, orthopaedic tumour surgeons analyse all the two-dimensional preoperative images and have to integrate and formulate a three-dimensional surgical plan mentally. The mental planning and its translation to the operating room are difficult, particularly in cases with complex anatomy and proximity to nearby neurovascular structures, like pelvic or sacral tumours, or technically demanding operations, like geometric or joint-preserving tumour resections. In an experimental study, four experienced tumour surgeons operated on simulated pelvic models. An experienced surgeon could obtain a 10-mm surgical margin with a 5-mm tolerance above or below in a probability of only 52% (95% CI 37–67). Also, the host-graft contact for reconstruction was reported to be poor [4]. Surgeons may tend to resect more healthy tissue than oncologically necessary to ensure adequate surgical margins. Thus it may result in less favourable reconstruction and limb functions. Therefore, tumour surgeons need to embrace new techniques that can improve surgical accuracy by replicating the intended bone resections in the operating rooms.

Computer navigation surgery connects between the patient's imaging information and anatomy through the use of tracking and registration of the preoperative and/or intraoperative acquired images. Studies showed that computer navigation technology improves the accuracy of various orthopaedic surgical procedures, such as pedicle screw placement in spine surgery, joint replacement and trauma surgery [5–11]. This computer-assisted approach has created considerable interest among orthopaedic tumour surgeons after the use of CT-based navigation first reported in assisting pelvic and sacral tumour resection in 2004 [12, 13]. The reports suggested that the computer-assisted approach can potentially increase accuracy in tumour resections with anatomic and surgical complexity [13]. However, neither MR images that are essential for planning bone tumour surgery nor any specific planning process was used for tumour surgery in the reports. Since then, computer-assisted tumour surgery (CATS) has been developed rapidly for the last decade. This chapter provides an overview of the emerging techniques in computer-assisted surgery in bone tumour surgery over the past decade. It (1) describes the current workflow, (2) reports the clinical indications and results and (3) discusses the limitations and future development of orthopaedic malignant bone tumour surgery.

24.2 Clinical Workflow of CATS

The CATS workflow consists of the essential steps for performing a complex bone tumour resection and reconstruction, from preoperative planning to intraoperative implementation (Fig. 24.1). Preoperative computer-assisted planning is emphasised in the workflow. It is equally important as the computer navigation that is used initially as an intraoperative tool to locate the surgical anatomy [14]. The more detailed the planning is, the higher chance the surgical goals can be attained. The CT-based navigation has been adopted as the image-based navigation system to implement the 3D surgical plan in bone tumour surgery.

24.2.1 Preoperative Navigation Planning

In contrast to the surgical plan in other orthopaedic disciplines, bone tumour surgery

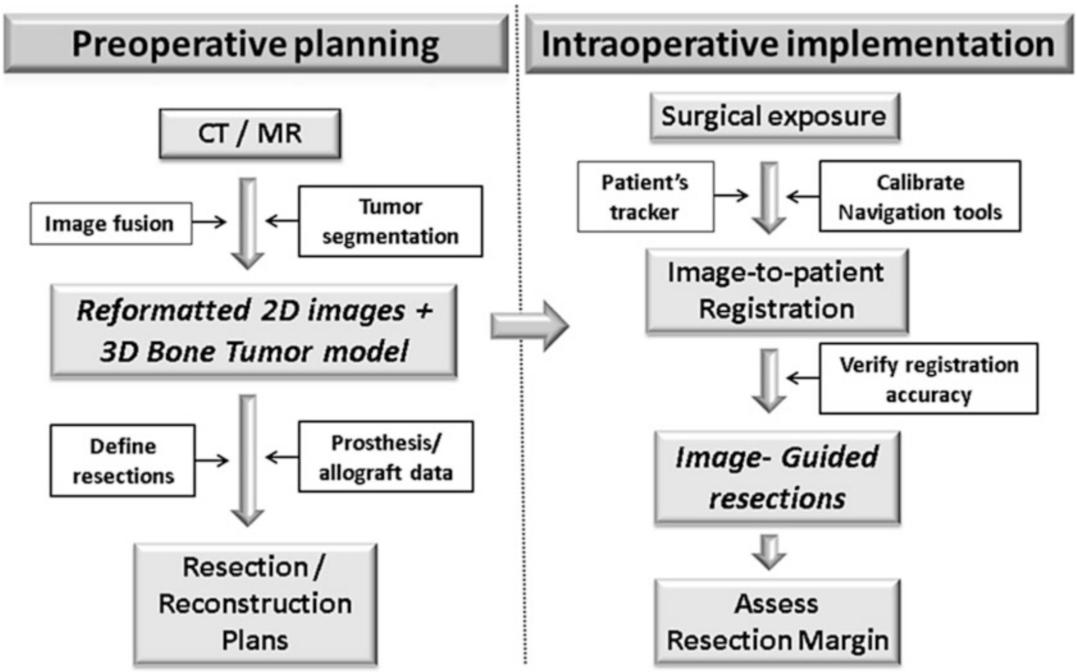

Fig. 24.1 Summarises the clinical workflow of CATS from preoperative planning to intraoperative implementation

involves analysis of multimodal preoperative images to determine the amount of resection and the choice of bone reconstruction. 3D surgical planning has been described in the navigation system that might facilitate the process of the complex surgical planning [15–18]. CT and MR images are both essential preoperative images for planning a bone tumour resection. CT provides good bony details, whereas MR images are better at indicating the extent of a tumour and its relationship with nearby vital structures. Overlapping MRI over CT images with the same coordinates produces fusion images that combine the characteristics of each imaging modality [19] (Fig. 24.2a–d). Tumour extent is outlined on MR images, whereas a 3D bone model is produced by adjusting the contrast level of the CT images. The 3D bone model and the segmented tumour volume then create a 3D bone tumour model (Fig. 24.3a, b). Surgical approach and the sites of bone resections can be planned, based on the reformatted 2D fused images and the 3D bone tumour model in the navigation system (Fig. 24.3a, b). As the navigation system only accepts medical imaging data in Digital Imaging and Communications in Medicine (DICOM) format, it does not offer complex surgical simulation on these data. A technique of integrating computer-aided design (CAD) planning, like virtual resections, CAD implants or allograft bone models into the CATS planning, has been developed [20]. CAD planning and CAD custom prostheses can be translated and visualised in the navigation system (Fig. 24.4b–e). It greatly enhances the capability of navigation planning in bone tumour surgery.

24.2.2 Intraoperative Implementation

After the bone tumours are exposed using traditional surgical techniques, a patient's tracker is placed in the operated bone. A navigation probe is calibrated with the navigation system. Surgeons then performed an image-to-patient registration that is the most critical operative step for the overall accuracy of CATS technique. The

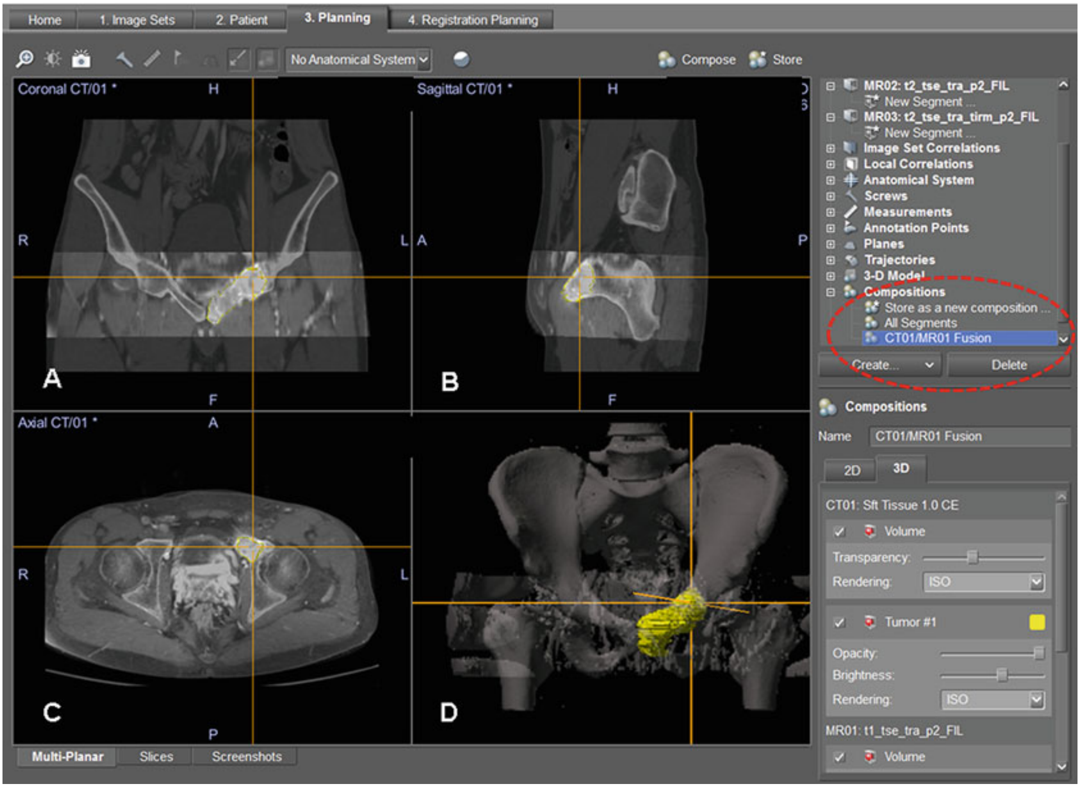

Fig. 24.2 (**a–d**) CT/MR fusion images are shown in the navigation display in a 30-year-old patient with low-grade osteosarcoma at left superior pubic rami and part of an anterior column of the left acetabulum. The contour of pelvic bone from both CT and MR images coincides with <1 mm error. Pelvic bone was created after adjusting the threshold level of CT images. The extent of the tumour (yellow) was also outlined from MR images. All the reformatted, fused coronal image (**a**), sagittal image (**b**) and axial image (**c**) and the 3D bone tumour model (**d**) were used for the bone resection planning

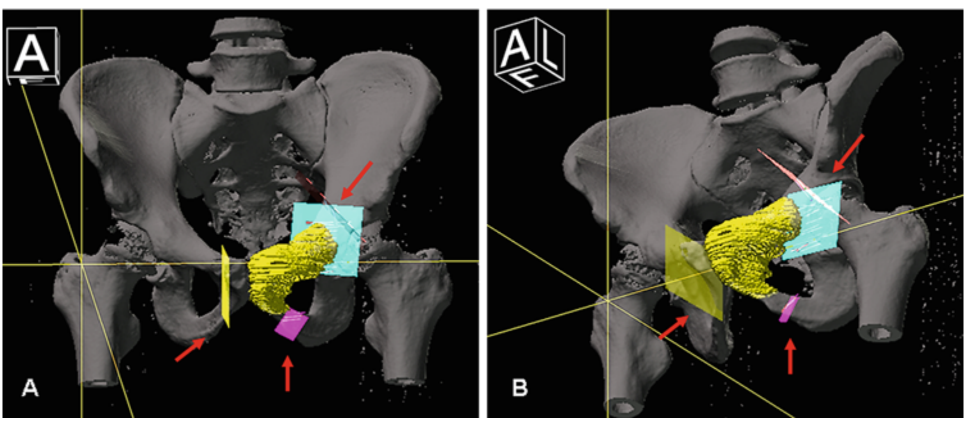

Fig. 24.3 Shows the planes of bone resection (red arrows) in the 30-year-old patient with low-grade osteosarcoma at the left superior pubic ramus and the anterior column of the left acetabulum. The 3D bone tumour model (**a** in the frontal view and **b** in left oblique view) facilitated the resection planning with tumour-free margin, whereas the limited resection could preserve the posterior column of the left acetabulum for better function

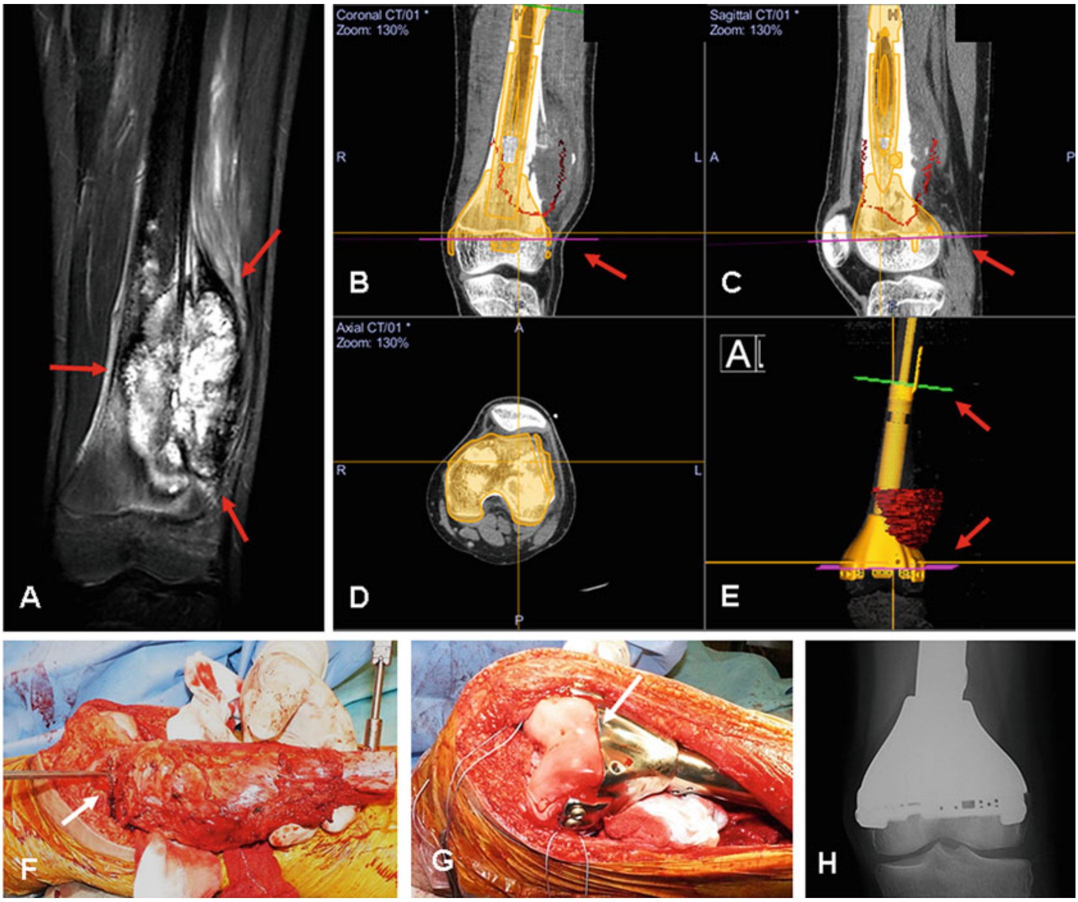

Fig. 24.4 Illustrates CATS in a 14-year-old boy with high-grade osteosarcoma at the metaphysis of the left distal femur undergone a joint-preserving tumour resection and reconstruction with a custom prosthesis. (**a**) shows the intra- and extraosseous extent of osteosarcoma (red arrows) at the left distal femur on the coronal view of MR images. Coronal view (**b**), sagittal view (**c**), axial view (**d**) of CT images and 3D model (**e**) show the integration of CAD model of the custom implant that matched to the planned bone resections (red arrows) in the navigation display. (**f**) A patient's tracker was placed at 2 cm above the proximal tumour edge after the distal femur was surgically exposed via an anterolateral approach. The entry sites of the planned bone resections were identified by a navigation pointer under the real-time navigation guidance and were marked by a diathermy (white arrow). The bone resection was then completed by an oscillating saw or thin osteotomes along an orientation guided by the navigation pointer. (**g**) shows good matching of the CAD prosthesis to the epiphysis of the knee joint (white arrow). (**h**) shows the plain radiograph of his knee joint with good osseointegration of the distal epiphysis to the prosthesis 2.5 years after the surgery

registration is a process in which the preoperatively acquired imaging data is linked to the patient's anatomy of the operative site. Manual registration using paired points and surface matching is performed. In addition to the registration error generated from the navigation machine, the registration accuracy is further verified by checking some anatomical landmarks or tracing the exposed bone surface with a navigation pointer (Fig. 24.5a–d). Only if patients' operative anatomy can be matched to their preoperative images and the operated bones can be physically tracked by the navigation system, surgeons can trust and rely on the virtual images to execute their 3D surgical plans. As the current navigation system cannot integrate a navigated saw, the sites of intended osteotomies are identified by the navigation. The osteotomies are then made

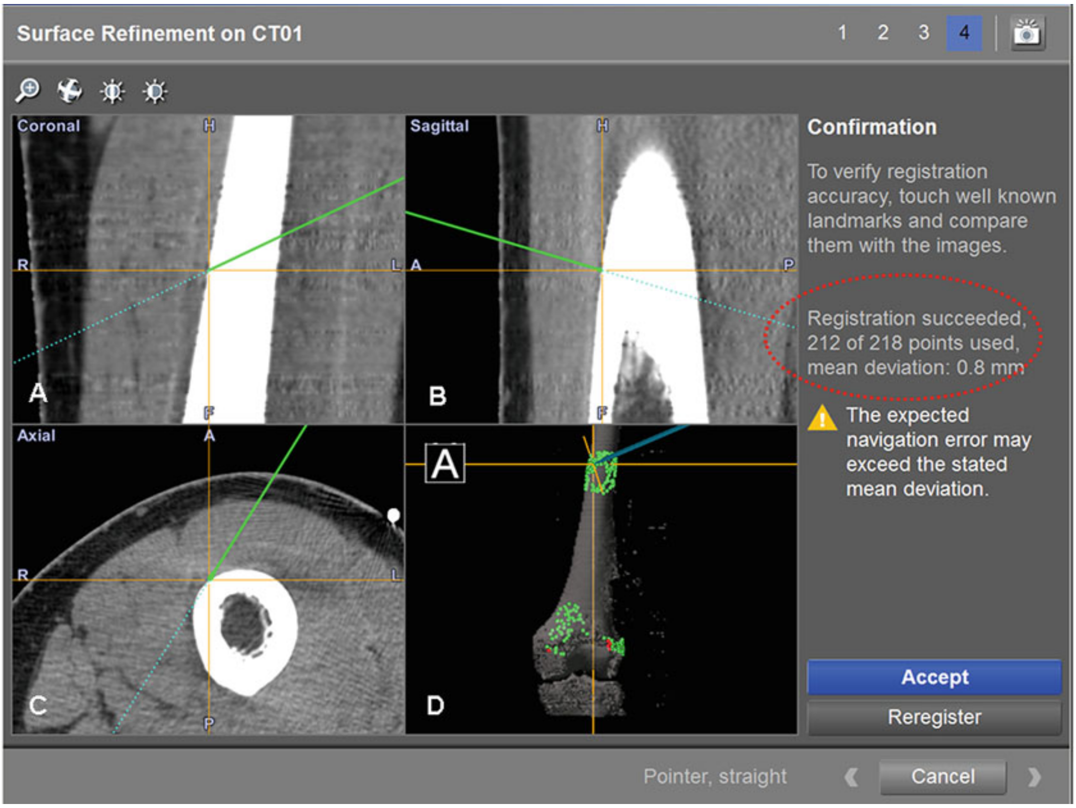

Fig. 24.5 (**a**–**d**) The intraoperative navigation screen shows the surface matching in the 14-year-old boy with high-grade osteosarcoma at the metaphysis of the left distal femur undergone a joint-preserving tumour resection and reconstruction with a custom prosthesis. The registration error was 0.8 mm after 218 bone surface points were collected from the bone surface. The virtual tip (orange cross) of the navigation pointer (green line) was exactly on the bone surface on the coronal view (**a**), sagittal view (**b**), axial view (**c**) of CT images and 3D bone model (**d**) while the surgeon moved the tip of the navigation pointers on the bone surface. It represented the real-time matching between the virtual images and the patient's anatomy. The registration was considered to be accurate for subsequent implementation of the navigation planning

manually, while the orientation of the saw blade is guided by the navigation pointer. Surgeons can also assess the resection margin with the navigation system. As the patient's trackers are still attached to the tumour specimens or remaining bones following tumour resection, the image-to-patient registration is valid. By placing the tip of the navigation probe at the planes of the achieved bone resection, surgeons can visualise their achieved bone resections with regard to the planned resections and intraosseous tumour edge. It is in stark contrast to intraoperative frozen sections that only gives positive or negative resection margins.

24.3 Clinical Indications and Results

Given the complexity of 3D surgical planning and the additional resources required for intraoperative implementation, the CATS technique is not for routine use in bone tumour surgery but may be applied in malignant bone tumours if (1) there are difficulties in achieving an accurate tumour resection with tumour-free margin, (2) in obtaining a correct resection to accommodate a custom tumour implant or (3) in an allograft shaping to reconstruct a bone defect after resection [14, 15].

24.3.1 Pelvic or Sacral Tumour Resection [Figs. 24.6a–i and 24.7a–i]

Pelvic or sacral tumour surgery is challenging due to complex anatomy and proximity to nearby neurovascular structures. The local recurrence after pelvic tumour resection (70%) [21] was higher than that after extremity tumour resection (14%) [2]. In the recent studies from Cho et al. [22] and Wong and Kumta [23], 10 and 12 patients, respectively, with pelvic or sacral tumours underwent tumour resections with the CATS technique. Negative resection margins could be achieved in all cases. With a minimum of 3 years of follow-up, the local recurrence rates were 20% (2 of 10) and 25% (3 of 12), respectively. The results were better when compared with 70% (47 of 67) in a report of 67 pelvic osteosarcomas operated on with conventional surgical techniques [21]. Jeys et al. supported the finding in a series of 31 patients with pelvic or sacral malignant bone tumours undergoing resection with CATS technique. The intralesional resection was mitigated from 29 to 8.7% [24]. The same centre conducted a retrospective case-control study of 21 patients with the posterior ilium and sacrum sarcoma. It also supported that the technique has increased the patient safety and allows for a better oncological outcome [25]. Also, CATS may help preserve unaffected sacral nerve roots for sphincter function during sacral tumour resection [22–24]. Therefore, early results of the CATS technique suggested that the method may help in safe tumour resection with no specific complications. It may improve surgical accuracy by replicating the preoperative planning at difficult anatomic locations, such as the pelvis and sacrum, and it may offer clinical benefits.

24.3.2 Joint-Preserving Tumour Resection [Fig. 24.4a–h]

As CATS enables surgeons to perform complex osteotomies, more technically demanding operations such as joint-preserving operations [26–28] or multiplanar tumour resections [17, 22, 23] are possible. More conservative resections that preserve native joints and ligaments may allow bone reconstruction with better joint function. In paediatric patients with joint-preserving tumour resections, the bone and its nearby capsular and ligamentous attachments are no need to be fully exposed for marking the resection plane; the preserved blood supply to the remaining joint can support its continual growth [28].

24.3.3 Reconstruction with Custom CAD Prosthesis

CATS may replicate bone resections with tumour-free margins and correct planes to match prefabricated CAD prostheses. As surgeons can define the surgical requirements and the resection bone defect in the navigation planning quantitatively, the implant engineers can design and fabricate CAD prostheses that are both patient- and tumour-specific. Also, incorporation of CAD data of prostheses into the navigation system greatly facilitates the resection planning and custom prosthetic reconstruction [20]. Therefore, the technique may thus allow one-stage operation from planning, complex implant fabrication and tumour resection to implant placement (Fig.24.8a–f).

24.4 Limitations

As surgeons use virtual images to assist bone resections, surgeons should clearly understand the potential errors of CATS technique. The success of the method depends on how surgeons can minimise the errors. Incorrect interpretation of the navigation information may result in inaccurate bone resections with possible adverse clinical outcomes. CATS errors have been described before [28]. CATS technique has been criticised for being difficult to learn. In a study of 78 bone tumour patients undergoing resection with CATS, intraoperative technical problems resulted in the navigation part not being completed in only 4 of 78 patients (5%), which occurred during the first

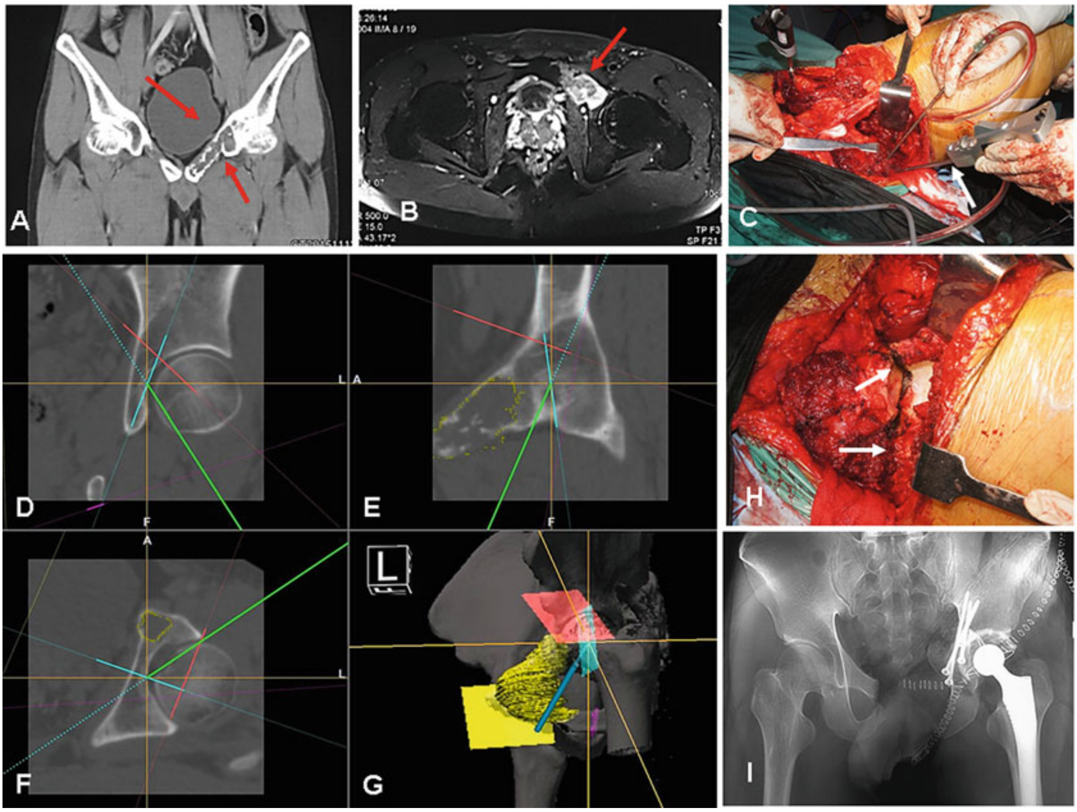

Fig. 24.6 Illustrates CATS in the 30-year-old patient with low-grade osteosarcoma of the left pelvis undergone partial acetabular resection. The coronal view of CT image (**a**) shows an osteolytic lesion (red arrows) at the left superior pubic ramus extending to the anterior column of the left acetabulum. The axial view of MR image (**b**) shows the tumour (red arrow) involving the anterior column of the left acetabulum. (**c**) After ilioinguinal surgical exposure with the protection of femoral neurovascular bundle, the sites of partial resection at the anterior column were identified under navigation guidance by a navigation pointer (white arrow). The navigation display shows that the tip and trajectory of the navigation pointer (green line) were at the planned resection (blue line) at the left acetabulum on the coronal view (**d**), sagittal view (**e**), axial view (**f**) of CT images and 3D bone tumour model (**g**). (**h**) The sites of partial acetabular resection (white arrows) were marked by diathermy at the acetabular cartilage, whereas the posterior column of the left acetabulum could be preserved for the reconstruction. (**i**) shows the postoperative radiograph of his pelvis after tumour resection and hip reconstruction. The acetabular defect was built with the ipsilateral femoral head, and a conventional total hip replacement was performed to restore the hip function

20 cases of the utilisation of the technology [29]. Soft tissue deforms and its spatial coordinates change after surgical exposure and is different from that of preoperative imaging. Therefore, CATS technique only improves the accuracy of bone resection but not soft tissue resection that requires traditional surgical technique. The performance of the CATS technique is only as good as raw imaging data. Better quality of each imaging modality and shorter time between imaging and surgery to avoid a change in tumour size are crucial to navigation planning. The chance of achieving an accurate resection as planned will be higher [19].

24.5 Future Developments of CATS

Given that primary malignant bone tumour is rare, the published reports from different tumour centres could only analyse relatively small pa-

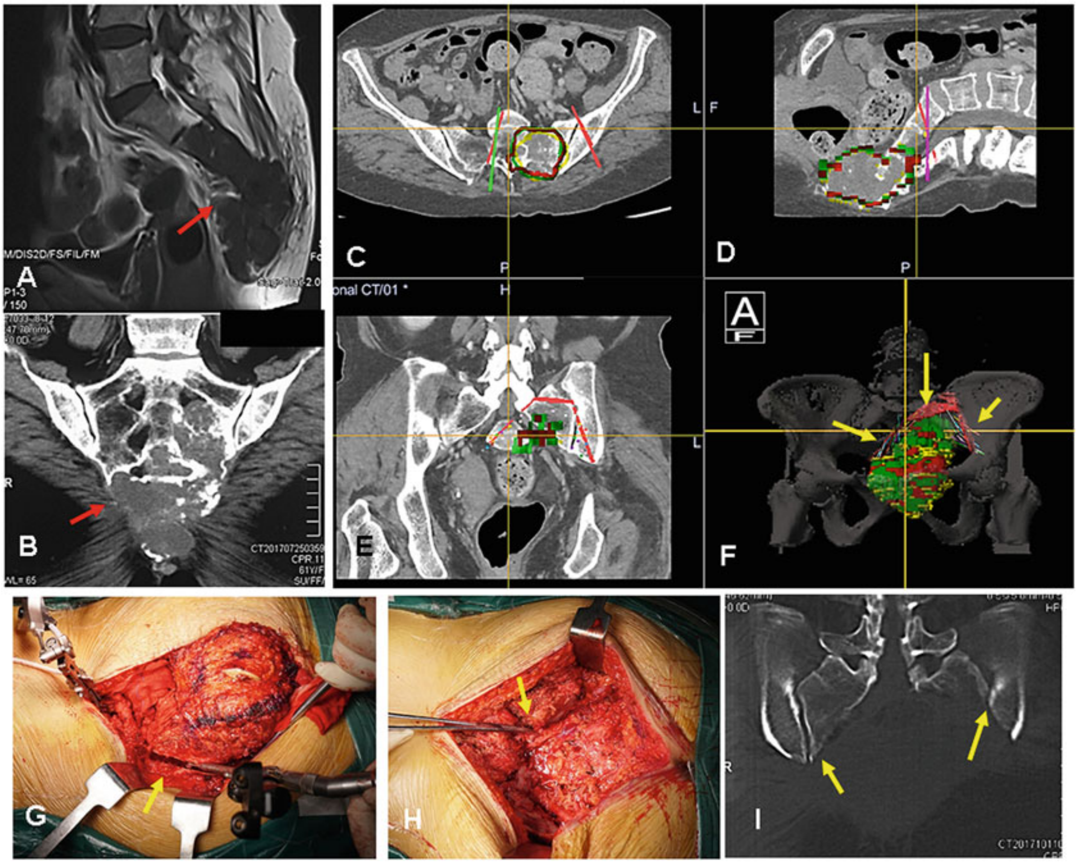

Fig. 24.7 Illustrates CATS in a 61-year-old patient with sacral chordoma (S1 and below) undergone subtotal sacrectomy. The sagittal view of MR image (**a**) shows sacral tumour extending proximally to the S2 vertebral body (red arrow). The coronal view of CT image (**b**) shows the tumour involving S2 and left S1 vertebral bodies. The navigation display shows the planning of subtotal sacrectomy with tumour-free margin on the axial view (**c**), sagittal view (**d**), coronal view (**e**) and 3D bone tumour model (**f**) (yellow arrows). (**g**) The posterior sacrum was exposed, and a navigated bone burr was used to identify and resect part of the left sacroiliac joint (yellow arrow). (**h**) Right S1 nerve root (yellow arrow) was preserved after subtotal sacrectomy. (**i**) shows the coronal view of postoperative CT image. Besides the S1 nerve root, both sacroiliac joint could be retained for the pelvic and sacral continuity in which lumbopelvic reconstruction might have been required if total sacrectomy was contemplated

tient population with the heterogeneous histological diagnosis. The retrospective nature of the studies and the inconsistent method of assessing margins and surgical accuracy of the technique make the comparison difficult. These prevent researchers from drawing a solid conclusion on the clinical efficacy of the technique in bone sarcoma surgery.

As the navigation-assisted technique involves multiple steps from preoperative planning on acquired medical images to the intraoperative implementation of the surgical plans, the surgical accuracy of the method regarding the errors from each step should be defined. The deviation errors can be calculated when the planes of the achieved bone resections are compared with that of the planned resections [18, 23]. As the technique involves digital data, a more comprehensive data on surgical margin, including the spatial relationship to tumour extent, may be obtained. The clinical efficacy can be better investigated if researchers are using the same method of measuring surgical accuracy and margins in the context of navigation-assisted tumour surgery.

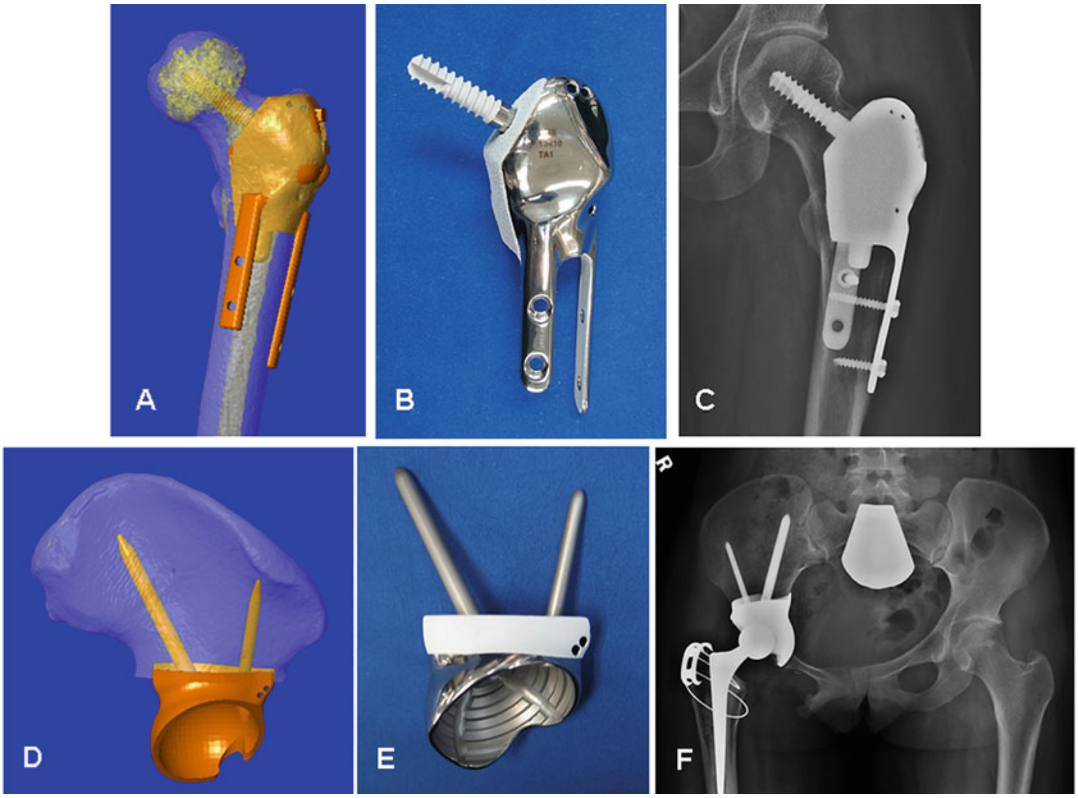

Fig. 24.8 In a 21-year-old patient with left proximal femur low-grade chondrosarcoma undergoing one-staged limited resection with preservation of hip joint, a CAD block prosthesis (**a**, **b**) was used for the reconstruction. (**c**) shows the radiograph of her left hip 9 years after surgery. In a 16-year-old patient with right acetabular osteosarcoma undergoing one-staged right acetabulum resection, a CAD pelvic prosthesis (**d**, **e**) was used for the hip reconstruction. (**f**) shows the radiograph of her pelvis 10 years after surgery

The navigation-assisted technique requires large and costly navigation facilities and the presence of an operator in the operating theatre and lacks the industrial support of making a reliable navigated saw or osteotome [20, 30, 31]. An alternative of using 3D printed patient-specific instrument (PSI) has been reported to replicate bone resections, and surgeons can focus on the operative field rather than looking at the virtual images on the navigation display while performing bone resections [20]. One criticism on PSI-guided tumour resection is the possible error in placing the PSI on the predetermined bone surface. In contrast to the navigation-assisted tumour resection that we can intraoperatively verify the registration accuracy, it is not possible to perform similar verification in PSI placement. We can only assess subjectively if the PSI had an identical fit on the patient's bone surface and the 3D printed bone model surface. Further studies are required to determine how much bone contact surface is necessary for the consistently accurate placement of the PSI [32]. One recent cadaveric simulation study comparing navigation- and PSI-assisted pelvic bone resections showed that both techniques could achieve similar accuracy with a mean deviation error of 2 mm, but the PSI technique required less resection time [32]. The exact clinical efficacy of the two methods remains to be seen in bone tumour surgery in the future.

As the current navigation system cannot provide the advanced surgical planning, like virtual resection, prosthetic/allograft reconstruction and direct exchange of the digital planning data with implant engineers, a unified computing platform should be developed to enable a seamless communication among involved care providers for customised patient treatment. Surgeons may choose which tools are more suitable for their patients [14].

24.6 Conclusion

Computer-assisted technology for orthopaedic bone tumours surgery has advanced rapidly for the last decade. Current evidence suggests that CATS may enable surgeons to replicate planned bone resections in bone tumours in an accurate and precise manner. It may result in better clinical outcomes. Given the complexity of CATS planning, additional time for intraoperative setup and unproven superior clinical efficacy than the traditional method, the technique may apply to difficult anatomical sites such as pelvic or sacral tumours, limited resection in joint-saving tumour surgery or complex reconstruction with CAD prostheses or allograft. Multicentre comparative studies with long-term follow-up are necessary to confirm its clinical efficacy.

Conflict of Interest Kwok-Chuen Wong, Xiaohui Niu, Hairong Xu, Yuan Li and Shekhar Kumta declared no conflict of interest. The Stryker, Materialise and Stanmore Implants Limited and companies did not fund or sponsor this research.

References

1. Fuchs B, Hoekzema N, Larson DR, Inwards CY, Sim FH (2009) Osteosarcoma of the pelvis: outcome analysis of surgical treatment. Clin Orthop Relat Res 467:510–518
2. Bertrand TE, Cruz A, Binitie O, Cheong D, Letson GD (2016 Mar) Do surgical margins affect local recurrence and survival in extremity, nonmetastatic, high-grade osteosarcoma? Clin Orthop Relat Res 474(3):677–683
3. He F, Zhang W, Shen Y, Yu P, Bao Q, Wen J, Hu C, Qiu S (2016) Effects of resection margins on local recurrence of osteosarcoma in extremity and pelvis: Systematic review and meta-analysis. Int J Surg 36(Pt A):283–292
4. Cartiaux O, Docquier PL, Paul L, Francq BG, Cornu OH, Delloye C et al (2008) Surgical inaccuracy of tumor resection and reconstruction within the pelvis: an experimental study. Acta Orthop 79(5):695–702
5. Sugano N (2003) Computer-assisted orthopedic surgery. J Orthop Sci 8(3):442–448
6. Laine T, Lund T, Ylikoski M, Lohikoshi J, Schlenzja D (2000) Accuracy of pedicle screw insertion with and without computer assistance: a randomized controlled clinical study in 100 consecutive patients. Eur Spine J 9:235–240
7. Anderson KC, Buehler KC, Markel DC (2005) Computer assisted navigation in total knee arthroplasty: comparison with conventional methods. J Arthroplast 20(Suppl 3):132–138
8. Grutzner PA, Suhm N (2004) Computer aided long bone fracture treatment. Injury 35(Suppl 1):S-A57–S-A64
9. Gebhard F, Weidner A, Liener UC, Stockle U, Arand M (2004) Navigation at the spine. Injury 35(Suppl 1):S-A35–S-A45
10. Chauhan SK, Scott RG, Breidahl W, Beaver RJ (2004) Computer-assisted knee arthroplasty versus a conventional jig-based technique. A randomised, prospective trial. J Bone Joint Surg 86:372–377
11. Wixson RL, MacDonald MA (2005) Total hip arthroplasty through a minimal posterior approach using imageless computer-assisted hip navigation. J Arthroplast 20(Suppl 3):51–56
12. Krettek C, Geerling J, Bastian L, Citak M, Rucker F, Kendoff D, Hufner T (2004) Computer aided tumor resection in the pelvis. Injury 35(Suppl 1):S-A79–S-A83
13. Hűfner T, Kfuri M Jr, Galanski M, Bastian L, Loss M, Pohlemann T, Krettek C (2004) New indications for computer-assisted surgery: tumor resection in the pelvis. Clin Orthop Relat Res 426:219–225
14. Wong KC, Kumta SM (2014) Use of computer navigation in orthopaedic oncology. Curr Surg Rep 2:47
15. Wong KC, Kumta SM, Chiu KH et al (2007) Precision tumour resection and reconstruction using image-guided computer navigation. J Bone Joint Surg Br 89:943–947
16. Wong KC, Kumta SM, Chiu KH, Cheung KW, Leung KS, Unwin P, Wong MC (2007) Computer assisted pelvic tumor resection and reconstruction with a custom-made prosthesis using an innovative adaptation and its validation. Comput Aided Surg 12(4):225–232
17. Aponte-Tinao LA, Ritacco LE, Ayerza MA, Muscolo DL, Farfalli GL (2013) Multiplanar osteotomies guided by navigation in chondrosarcoma of the knee. Orthopedics 36(3):e325–e330
18. Ritacco LE, Milano FE, Farfalli GL, Ayerza MA, Muscolo DL, Aponte-Tinao LA (2013) Accuracy of 3-D planning and navigation in bone tumor resection. Orthopedics 36(7):e942–e950
19. Wong KC, Kumta SM, Antonio GE, Tse LF (2008) Image fusion for computer-assisted bone tumor surgery. Clin Orthop Relat Res 466: 2533–2541
20. Wong KC, Kumta SM, Leung KS, Ng KW, Ng EW, Lee KS (2010) Integration of CAD/CAM planning

into computer assisted orthopaedic surgery. Comput Aided Surg 15:65–74
21. Ozaki T, Flege S, Kevric M et al (2003) Osteosarcoma of the pelvis: experience of the cooperative osteosarcoma study group. J Clin Oncol 21: 334–341
22. Cho HS, Oh JH, Han I, Kim HS (2012) The outcomes of navigation assisted bone tumour surgery: minimum three-year follow-up. J Bone Joint Surg Br 94(10):1414–1420
23. Wong KC, Kumta SM (2013) Computer-assisted tumor surgery in malignant bone tumors. Clin Orthop Relat Res 471(3):750–761
24. Jeys L, Matharu GS, Nandra RS, Grimer RJ (2013) Can computer navigation-assisted surgery reduce the risk of an intralesional margin and reduce the rate of local recurrence in patients with a tumour of the pelvis or sacrum? Bone Joint J 95-B(10):1417–1424
25. Laitinen MK, Parry MC, Albergo JI, Grimer RJ, Jeys LM (2017) Is computer navigation when used in the surgery of iliosacral pelvic bone tumours safer for the patient? Bone Joint J Feb 99-B(2):261–266
26. Cho HS, Oh JH, Han I, Kim HS (2009) Joint-preserving limb salvage surgery under navigation guidance. J Surg Oncol 100(3):227–232
27. Li J, Wang Z, Guo Z, Chen GJ, Yang M, Pei GX (2012) Irregular osteotomy in limb salvage for juxta-articular osteosarcoma under computer-assisted navigation. J Surg Oncol 106(4):411–416
28. Wong KC, Kumta SM (2013) Joint-preserving tumor resection and reconstruction using image-guided computer navigation. Clin Orthop Relat Res 471(3):762–773
29. Farfalli GL, Albergo JI, Ritacco LE, Ayerza MA, Milano FE, Aponte-Tinao LA (2017 Mar) What is the expected learning curve in computer-assisted navigation for bone tumor resection? Clin Orthop Relat Res 475(3):668–675
30. Gouin F, Paul L, Odri GA, Cartiaux O (2014) Computer-assisted planning and patient-specific instruments for bone tumor resection within the pelvis: a series of 11 patients. Sarcoma, Article ID 842709, 9 pages
31. Wong KC, Kumta SM, Geel NV, Demol J (2015) One-step reconstruction with a 3D-printed, biomechanically evaluated custom implant after complex pelvic tumor resection. Comput Aided Surg 20(1):14e23
32. Wong KC, Sze KY, Wong IO, Wong CM, Kumta SM (2016) Patient specific instrument can achieve same accuracy with less resection time than navigation assistance in periacetabular pelvic tumor surgery: a cadaveric study. Int J Comput Assist Radiol Surg 11(2):307e316

Sensor-Based Soft Tissue Balancing in Total Knee Arthroplasty

25

Jimmy Chow, Tsun Yee Law, and Martin Roche

Abstract

Total knee arthroplasty (TKA) is a highly successful procedure with utilization expected to grow substantially over the coming decades. However, the revision burden has not concurrently improved, with over 30% of revisions related to technical imperfections (Mulhall KJ, Ghomrawi HM, Scully S, Callaghan JJ, Saleh KJ, Clin Orthop Relat Res 446:45, 2006; Sharkey PF, Hozack WJ, Rothman RH, Shastri S, Jacoby SM, Clin Orthop Relat Res 404:7, 2002; Wylde V, Hewlett S, Learmonth ID, Dieppe P, Pain 152(3):566, 2011). Accurate alignment and soft tissue balancing have been identified as important factors in mitigating these risks. Historically, accuracy relating to soft tissue balance has relied upon surgeon experience and subjective tactile feel. This chapter will explore the utilization of intraoperative sensors related to soft tissue balancing in total knee arthroplasty.

J. Chow
Hedley Orthopaedic Institute, Phoenix, AZ, USA

T. Y. Law · M. Roche (✉)
Holy Cross Orthopedic Institute, Fort Lauderdale, FL, USA
e-mail: martin@mroche.com

Keywords

Total knee arthroplasty (TKA) · Intraoperative sensor · Soft tissue balance · Sensor-assisted surgery · Surgical robotics

25.1 Introduction

Total knee arthroplasty (TKA) is one of the most successful and cost-effective joint replacement procedures currently performed. Despite this, risk for failure requiring revision at 10 years postoperatively is nearly 5%, with patients reporting dissatisfaction nearly 20% of the time [4, 5]. Infection, instability, pain, and stiffness have been implicated as the leading causes for revision and dissatisfaction [2, 5, 6]. Requirements for a successful TKA are thought to include both neutral alignment and soft tissue balancing [7, 8]. Recent interest in various alignment parameters on soft tissue balance and potentially improved outcomes (Anatomic, Kinematic) are being investigated [9]. Historically achieving proper soft tissue balance relies heavily upon the surgeon's subjectively perceived tactile feel of ligamentous tension, surgical training, operative experience, and overall skill [10].

G. Zheng et al. (eds.), *Intelligent Orthopaedics*, Advances in Experimental Medicine and Biology 1093, https://doi.org/10.1007/978-981-13-1396-7_25

Newly emerging intraoperative load-bearing sensor technology has enabled surgeons to mitigate the inherent drawbacks of subjective knee balancing. This sensor provides dynamic load pressures visualized through a graphical user interface display. The surgeon can visualize the effects of implant rotation and limb alignment on soft tissue balance through a range of motion. The surgeon can receive real-time dynamic information as they adjust rotation, alignment, and the effects of selective soft tissue releases. Knee stability, with inter-compartmental balance, has been shown to be the most important contributor to improved postoperative outcomes, and the ability to visualize objective load data is highly important [4, 11]. There are presently two commercial disposable intra-op devices that utilize load data during a TKA.

25.2 Intraoperative Load-Bearing Sensors

Verasense (Verasense Knee System, Orthosensor Inc., Dania Beach, FL) is a sensorized device that replicates the specific design of the final polyethylene insert. It is implant agnostic and presently compatible with Stryker, Zimmer Biomet, and Smith & Nephew implants. During trialing, the device replaces the standard tibial insert trial. The surgeon utilizes the data through a full range of motion with the patella and capsule reduced. The wireless device measures inter-compartmental load pressures, implant congruency, kinetic rollback, and flexion stability. The pressure differentials, combined with knee position, guide the surgeon on the specific adjustments related to implant rotation, bony realignments, and selective soft tissue releases. The system can be utilized during trialing, cementation, and post-cementation to confirm knee stability in the coronal, rotational, and flexion space, with static and dynamic outputs. The data can be saved and linked to the patients' implant, post-op PROMS, and functional scores (Fig. 25.1).

25.2.1 Benefits of Sensor-Guided TKA

Current projection models show an exponential increase in the incidence of TKA which necessitates the development of new technologies to improve patient outcomes [12, 13]. The use of quantified intra-op data related to knee balance and stability is necessary if we are to address revisions related to imprecise technical factors and patient dissatisfaction in TKAs.

The use of intraoperative sensors was found to significantly improve patient-reported outcomes (Knee Society Score (KSS) and Oxford Knee Score) in a comparative cohort study of 114 patients (57 manual, 57 sensor assisted) who received a primary TKA with a 6-month follow-up [14]. Similarly, in a cohort of 135 sensor-assisted TKA with a minimum 1-year follow-up found excellent KSS and Western Ontario and McMaster Universities Osteoarthritis Index (WOMAC) scores of 179.3 and 10.4 in KSS and WOMAC, respectively [11]. Furthermore, soft tissue imbalance is a known contributing factor to many of the complications leading to revision including pain (44%), instability (21%), and joint stiffness (17%) [1–3]. Soft tissue imbalance may be due to the subjective nature and static measurements of manual TKA techniques that rely upon static instruments, surgeon experience, and tactile feel [15, 16]. In a randomized clinical trial (RCT), when blinding surgeons to data outputs, the correlation between their subjective feel of a balanced knee was correct only approximately 50% of the time [17, 18].

The intraoperative sensor mitigates the surgeon's imprecise knowledge of three-dimensional soft tissue stability through real-time dynamic quantitative and objective load data. As described in one study, the sensor outputs allowed for targeted ligament balancing with an average of two to three corrections being needed to achieve ligament balance, thereby decreasing loading variability and ligament imbalance [19]. In addition, studies

Fig. 25.1 Surgeon evaluates implant rollback and soft tissue pressures on computer screen through a full ROM

have shown a significant reduction in the rate of postoperative arthrofibrosis/stiffness and subsequent manipulation under anesthesia when utilizing intraoperative sensor assistance during TKA [14, 20]. Further studies on safe zones of bony alignment (+/− 3 degrees coronal plane) have found that soft tissue balance obtained with 1–2 degrees of bone adjustments may reduce the risk of destabilization from an over-released soft tissue envelope [21, 22].

The sensor can be utilized during revision surgery to help define the root cause of a painful knee where x-rays and work-up are negative. This enables a potentially modified revision leading to less morbidity and economic resource expenditure (Fig. 25.2).

25.2.2 Surgical Technique

The TKA is performed as per the usual fashion, with the sensor being utilized during the trialing phase. After initial trial component placement, the trial tibial insert is substituted with the sensor insert. Shims are used to account for thicker insert sizes.

Tibiofemoral rotational congruency is then evaluated (determined as the position of the tibia in relation to the femoral contact point); positive contact point angles were indicative of internal rotation, while a negative value indicates external rotation. Once congruency is obtained, the patella is then reduced and the capsule closed with towel

Fig. 25.2 Surgeon identifies malrotation and an over-tensioned lateral compartment in a painful TKA. Revision was modified to address both issues and a balanced knee was obtained

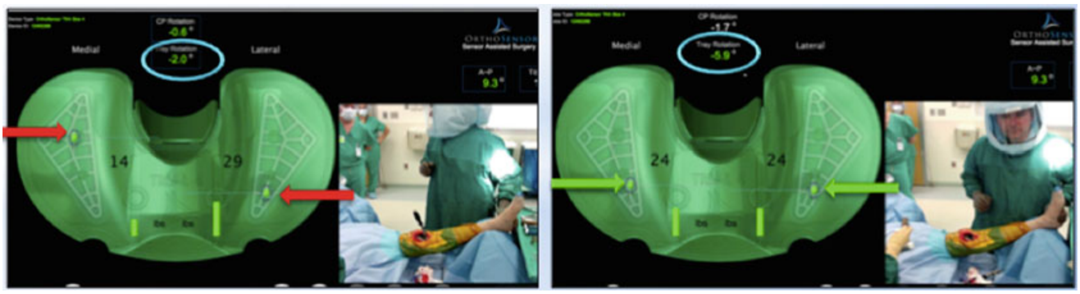

Fig. 25.3 Surgeon rotates the tibia from IR position to obtain congruency and achieves equalized inter-compartmental balance

clips prior to range of motion (ROM) as this has been shown to affect load outputs [23] (Fig. 25.3).

Soft tissue tension is best defined at 10°, 45°, and 90° of flexion, with the hip and leg in a neutral position during ROM. A balanced knee is determined when a mediolateral loading differential of $\leq$15 lbs through the ROM with absolute loading pressures falls between 10 and 40 lbs along with a stable end point (minimal translation <2 mm) on posterior drawer testing [11, 24, 25]. Of note, it is important to reference load pressures during cementation, as elements of imbalance were observed in 44% of patients during initial cementing techniques [26].

25.3 Intraoperative Force Measurement Device

The other commercially available device is the eLIBRA® dynamic knee balancing system (DKBS) (Synvasive Technology, Zimmer® Warsaw, IN). This knee system allows for measured balanced resection utilizing an electronic force measurement device along with an adjustable femoral component device to achieve a symmetrical flexion gap. This system was designed to account for patient variability that may produce irregularities that occur with standard techniques that depend upon empirical anatomical bone landmarks [27]. However, this device does not measure pressures or tensions and is only compatible with Zimmer knee systems and instrumentation.

25.3.1 Benefits of Force Measurement TKA Flexion Gap

The force measurement system is designed to address intraoperative flexion instability with objective dynamic measurements of inter-compartmental soft tissue forces allowing patient-specific femoral component rotation [28]. In a study of 75 force measurement-assisted TKA patients, postoperative cone beam computed tomography (CBCT) found that there was optimal orientation of the femoral component with a mean of 2.18° of external rotation [29]. This study also found an improvement in KSS clinical and functional scores (preoperative means of 48.35 and 47.53; postoperative means of 88.03 and 91.2 ($p < 0.001$ for both aspects)) [29].

25.3.2 eLIBRA Surgical Technique

The TKA is approached as per the surgeon's usual preferred technique with a modified trial femur and sensor inserted following the distal femur and proximal tibia resections with care to reducing the patella. Alternatively, the force plate may also be inserted under the trial insert or gap spacer paddle. The femoral posterolateral implant is then adjusted to obtain load pressures. The sensors are outfitted with force transducers on both the medial and lateral sides which are represented on a graphical user interface (Fig. 25.4).

The values depicted can range from 1 through 20 with each unit representing approximately 15 newtons (3.4 lbs of force). Following adequate symmetrical balancing, the femoral rotation is marked, the trial femoral block is inserted, and the TKA is completed as usual. The force plate can be used under the tibial trial for final evaluation.

25.4 Robotic- and Sensor-Assisted Surgery Synergy

The future integration of sensors that quantify the patient's soft tissue tension, and knee stability through a full range of motion, enables the robot to make incremental implant and bone readjustments to allow true customization of a patient's total knee soft tissue balance and alignment.

25.5 Conclusion

Intraoperative load-bearing sensors deliver real-time dynamic and objective load-bearing data to the surgeon through a full range of motion. This assists the surgeon in accurately and consistently balancing the knee during TKA. The surgeon can now minimize subjective decisions that can lead to inconsistent surgical

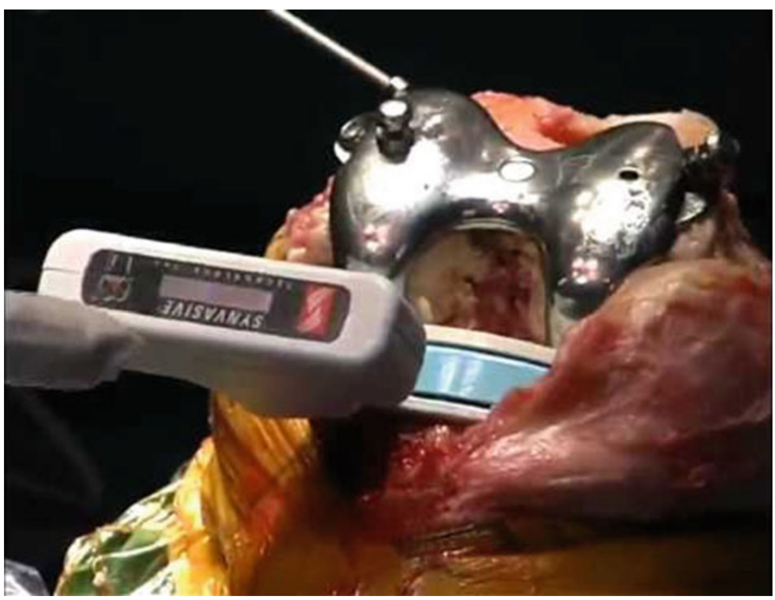

Fig. 25.4 *eLIBRA* device

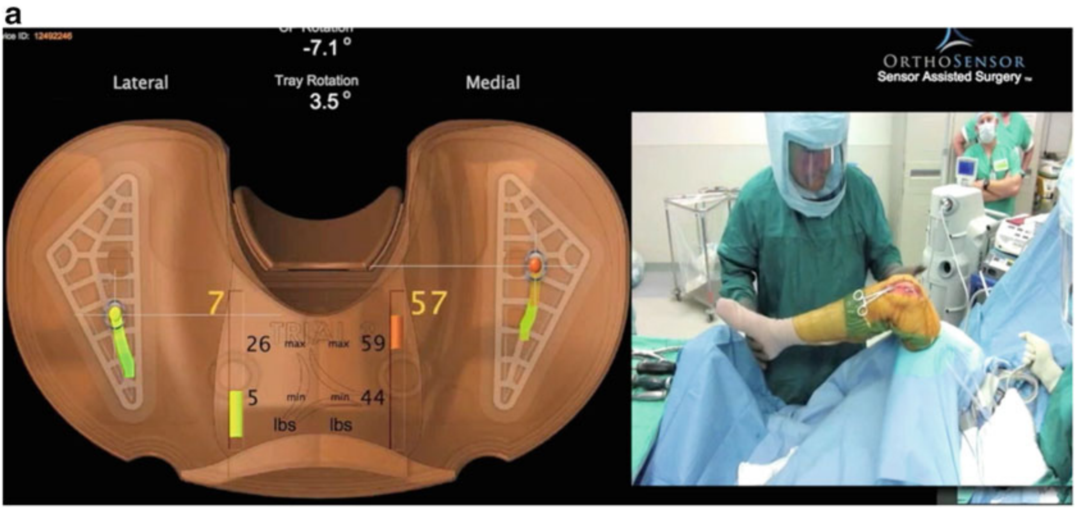

Fig. 25.5 Sensor depicts an over-tension MCL in flexion

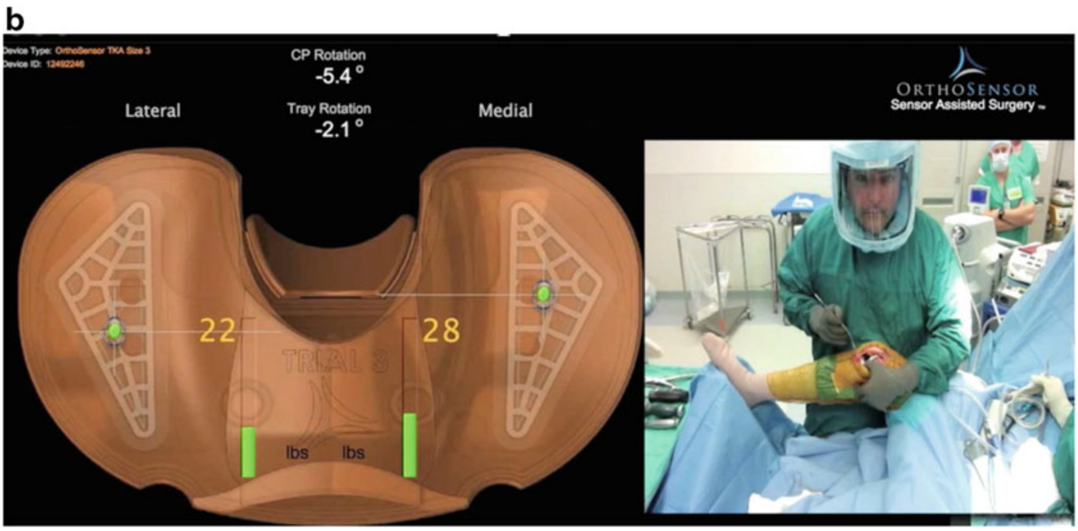

Fig. 25.6 Surgeon dynamically pie-crusts the anterior MCL until inter-compartmental balance is obtained

outcomes. The knowledge of the implant design and how the implants need to be coupled in a congruent manner through a full range of motion enables the surgeon to minimize malrotation as a confounding variable. The safety of pie-crusting to selectively elongate the soft tissue enables the surgeon to titrate their releases with resultant real-time soft tissue tension outputs [30, 31] (Figs. 25.5a and 25.5b).

The evolution of robotics into the TKA field now enables surgeons to perform accurate bony adjustments while obtaining soft tissue balance within known acceptable alignment parameters. This is the first step to customize our surgery to the individual's specific alignment and soft tissue signatures. Knowledge of the knee's kinetics (force + motion) in three planes will continue to evolve the mastery of our surgical techniques to achieve our evolving data endpoints (Fig. 25.6).

As machine learning advances, surgeons will be provided consistent zones and outputs, with data-driven techniques to improve our outcomes and potentially match our patient expectations.

Fig. 25.7 Computer screen displays the alignment, gaps, rotation, and kinetic rollback of the knee during surgery

References

1. Mulhall KJ, Ghomrawi HM, Scully S, Callaghan JJ, Saleh KJ (2006) Current etiologies and modes of failure in total knee arthroplasty revision. Clin Orthop Relat Res 446:45
2. Sharkey PF, Hozack WJ, Rothman RH, Shastri S, Jacoby SM (2002) Insall Award paper. Why are total knee arthroplasties failing today? Clin Orthop Relat Res 404:7
3. Wylde V, Hewlett S, Learmonth ID, Dieppe P (2011) Persistent pain after joint replacement: prevalence, sensory qualities, and postoperative determinants. Pain 152(3):566
4. Gustke KA, Golladay GJ, Roche MW, Jerry GJ, Elson LC, Anderson CR (2014) Increased satisfaction after total knee replacement using sensor-guided technology. Bone Joint J 96-b(10):1333
5. Khan M, Osman K, Green G, Haddad FS (2016) The epidemiology of failure in total knee arthroplasty: avoiding your next revision. Bone Joint J 98-b(1 Suppl A):105
6. Le DH, Goodman SB, Maloney WJ, Huddleston JI (2014) Current modes of failure in TKA: infection, instability, and stiffness predominate. Clin Orthop Relat Res 472(7):2197
7. Lombardi AV Jr, Berend KR, Ng VY (2011) Neutral mechanical alignment: a requirement for successful TKA: affirms. Orthopedics 34(9):e504

8. Peters CL, Jimenez C, Erickson J, Anderson MB, Pelt CE (2013) Lessons learned from selective soft-tissue release for gap balancing in primary total knee arthroplasty: an analysis of 1216 consecutive total knee arthroplasties: AAOS exhibit selection. J Bone Joint Surg Am 95(20):e152
9. Roth JD, Howell SM, Hull ML (2017) An improved tibial force sensor to compute contact forces and contact locations in vitro after total knee arthroplasty. J Biomech Eng 139(4)
10. Jarvelin J, Hakkinen U, Rosenqvist G, Remes V (2012) Factors predisposing to claims and compensations for patient injuries following total hip and knee arthroplasty. Acta Orthop 83(2):190
11. Gustke KA, Golladay GJ, Roche MW, Elson LC, Anderson CR (2014) Primary TKA patients with quantifiably balanced soft-tissue achieve significant clinical gains sooner than unbalanced patients. Adv Orthop 2014:628695
12. Inacio MCS, Paxton EW, Graves SE, Namba RS, Nemes S (1797) Projected increase in total knee arthroplasty in the United States – an alternative projection model. Osteoarthr Cartil 25(11):2017
13. Kurtz S, Ong K, Lau E, Mowat F, Halpern M (2007) Projections of primary and revision hip and knee arthroplasty in the United States from 2005 to 2030. J Bone Joint Surg Am 89(4):780
14. Chow JC, Breslauer L (2017) The use of intraoperative sensors significantly increases the patient-reported rate of improvement in primary Total knee arthroplasty. Orthopedics 40(4):e648
15. Elmallah RK, Mistry JB, Cherian JJ, Chughtai M, Bhave A, Roche MW, Mont MA (2016) Can we really "feel" a balanced Total knee arthroplasty? J Arthroplast 31(9 Suppl):102
16. D'Lima DD, Patil S, Steklov N, Colwell CW Jr (2007) An ABJS best paper: dynamic intraoperative ligament balancing for total knee arthroplasty. Clin Orthop Relat Res 463:208
17. Golladay GJ (2017) Is a surgeon-defined balanced knee following total knee arthroplasty really balanced? In: ISTA
18. MacDessi S (2017) Accuracy of manual surgeon defined assessment of soft tissue balance in TKA in comparison to Verasense sensor-guided measures – can we detect an unbalanced knee? In: AOA
19. Gustke KA, Golladay GJ, Roche MW, Elson LC, Anderson CR (2017) A targeted approach to ligament balancing using kinetic sensors. J Arthroplast 32(7):2127
20. Geller JA, Lakra A, Murtaugh T (2017) The use of electronic sensor device to augment ligament balancing leads to a lower rate of Arthrofibrosis after total knee arthroplasty. J Arthroplast 32(5):1502
21. Allen MM, Pagnano MW (2016) Neutral mechanical alignment: is it necessary? Bone Joint J 98-b(1 Suppl A):81
22. Verstraete MA, Meere PA, Salvadore G, Victor J, Walker PS (2017) Contact forces in the tibiofemoral joint from soft tissue tensions: implications to soft tissue balancing in total knee arthroplasty. J Biomech 58:195
23. Su EP, Su SL, Della Valle AG (2010) Stiffness after TKR: how to avoid repeat surgery. Orthopedics 33(9):658
24. Gustke KA, Golladay GJ, Roche MW, Elson LC, Anderson CR (2014) A new method for defining balance: promising short-term clinical outcomes of sensor-guided TKA. J Arthroplast 29(5):955
25. Roche M, Elson L, Anderson C (2014) Dynamic soft tissue balancing in total knee arthroplasty. Orthop Clin North Am 45(2):157
26. Chow J, Wang K, Elson L, Anderson C, Roche M (2017) Effects of cementing on ligament balance during total knee arthroplasty. Orthopedics 40(3):e455
27. Olcott CW, Scott RD (2000) A comparison of 4 intraoperative methods to determine femoral component rotation during total knee arthroplasty. J Arthroplast 15(1):22
28. Camarata DA (2014) Soft tissue balance in total knee arthroplasty with a force sensor. Orthop Clin North Am 45(2):175
29. D'Angelo F, Puricelli M, Binda T, Surace MF, Floridi C, Cherubino P (2015) The use of an electronic system for soft tissue balancing in primary Total knee arthroplasties: clinical and radiological evaluation. Surg Technol Int 26:261
30. Verdonk PC, Pernin J, Pinaroli A, Ait Si Selmi T, Neyret P (2009) Soft tissue balancing in varus total knee arthroplasty: an algorithmic approach. Knee Surg Sports Traumatol Arthrosc 17(6):660
31. Clarke HD, Fuchs R, Scuderi GR, Scott WN, Insall JN (2005) Clinical results in valgus total knee arthroplasty with the "pie crust" technique of lateral soft tissue releases. J Arthroplast 20(8):1010

26

Implant Orientation Measurement After THA Using the EOS X-Ray Image Acquisition System

Kunihiko Tokunaga, Masashi Okamoto, and Kenji Watanabe

Abstract

We investigated the accuracy of measuring implant orientation after THA in standing position using EOS system (EOS Imaging Inc., Paris, France). Ninety patients who underwent THA were subjected to this study by comparing angles measured by EOS system and those measured from CT scans using 3D image analyzing software, ZedHip (LEXI, Tokyo, Japan). The radiographic cup inclination and anatomical cup anteversion were measured with respect to the anterior pelvic plane (APP) coordinate. The femoral stem antetorsion was analyzed by measuring the angles between the stem neck axis and the post-condylar axis in the femoral functional axis coordinate.

The differences (mean ± SD) (range of 95%CI) between angles measured by EOS system and those from CT scans in the cup inclination, cup anteversion, and stem antetorsion were $-2.3° \pm 2.7°$ ($-2.8° \sim -1.7°$), $-0.1° \pm 5.0°$ ($-1.2° \sim 0.9°$), and $-1.3° \pm 6.5°$ ($-2.7° \sim 0.1°$), respectively. Cup inclination measured on 14 hips, cup anteversion measured on 28 hips, and stem antetorsion measured on 27 hips were classified as outliers whose differences were over 5°. Difficulties in defining the reference points for APP correlated with the incidences of the outliers in cup orientation measurements.

We could not set new reference points on the 3D bone surface models reconstructed by EOS system, so we have to use reference points defined on 2D images. In addition, the APP coordinate in EOS system was not the same as the standard definition. EOS system may not be used to measure the implant positions after THA until these problems will be improved.

Keywords

Total hip arthroplasty (THA) · Postoperative evaluation · Implant orientation · EOS system · Validation

K. Tokunaga (✉)
Niigata Hip Joint Center, Kameda Daiichi Hospital, Niigata City, Japan
e-mail: ktokunagajp@yahoo.co.jp

M. Okamoto
Department of Radiology, Kameda Daiichi Hospital, Niigata City, Japan

K. Watanabe
Department of Orthopedic Surgery, Kameda Daiichi Hospital, Niigata City, Japan

G. Zheng et al. (eds.), *Intelligent Orthopaedics*, Advances in Experimental Medicine and Biology 1093, https://doi.org/10.1007/978-981-13-1396-7_26

26.1 Introduction

EOS X-ray imaging acquisition system has sensitive ionization chamber detectors and X-ray source collimated in a narrow beam. Two co-linked pairs of linear radiation source and detector are placed perpendicular to each other, in frontal and lateral positions. Anteroposterior and lateral X-ray images can be obtained in standing, squatting, or sitting positions with high-quality resolution and reduced X-ray exposure [1]. 3D bone surface models are created using reference points interactively defined on these two-dimensional (2D) X-ray images (Fig. 26.1). We started our THA analysis using EOS system for the first time in Japan since April 2014.

The gold standard for accurate measurement of the acetabular cup angles, as well as the femoral stem angles, is to use CT images, in which implant angles were directly measured on the postoperative CT images using 3D image analyzing software [2–5]. HipMatch provided accurate implant measurement after THA using preoperative pelvic CT images and a regular postoperative anteroposterior pelvic X-ray film by 2D-3D matching registration [6]. Hip CAS (LEXI, Tokyo, Japan) enabled us to measure THA implants with patients in standing positions by 2D-3D matching procedure between preoperative CT images and postoperative biplanar X-ray images [7]. However, CT scan has several problems including radiation exposure and costs. In addition, it is still time consuming to achieve accurate 3D measurements with CT scan images. Even though the radiation dose of current CT scanners has been reduced less than those of conventional ones, postoperative routine analysis using CT scan has not been widely used by most orthopedic surgeons in the world, except for a small group of hip surgeons who have preferred to use computer-assisted orthopedic surgery.

Recently, several applications using EOS system have been introduced in various orthopedic interventions including spine, hip, and lower extremities [1]. Applications to hip interventions using EOS system were reported [8–12] in which EOS system was reported to be a powerful tool to obtain accurate 3D information of patients in not only standing but also sitting or squatting positions. However, there were few clinical studies to investigate the accuracy of measuring implant orientation after THA using EOS system. The purpose of this study is to investigate the accuracy of THA implant angles measured by EOS systems on Japanese patients taking those measured from postoperative CT scan as the ground truth.

26.2 Materials and Methods

Ninety Japanese THA patients (75 females and 15 males, average operative age was 60 years old) who underwent CT-based navigation surgery were subjected to this study. These patients were informed about the study and written informed

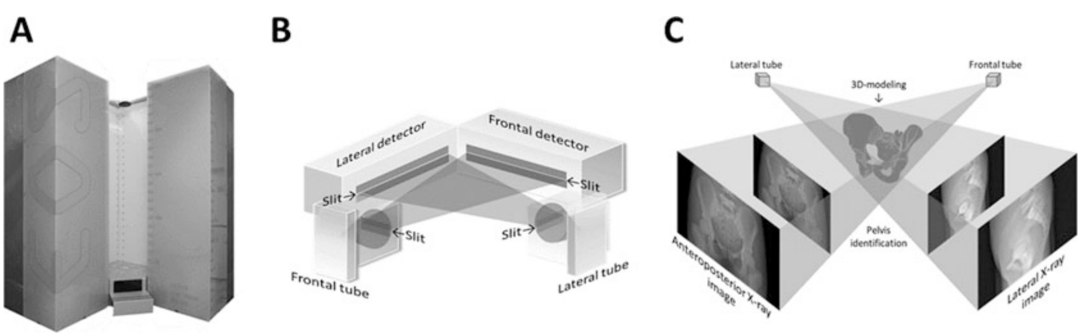

Fig. 26.1 The EOS system. (**a**) Outward form. (**b**) Sensitive ionization chamber detectors and X-ray sources collimated in a narrow beam. Two radiographic image acquisition systems are mounted at right angles to each other. (**c**) By digitizing the reference points on 2D images, a 3D statistical bone model is created semiautomatically

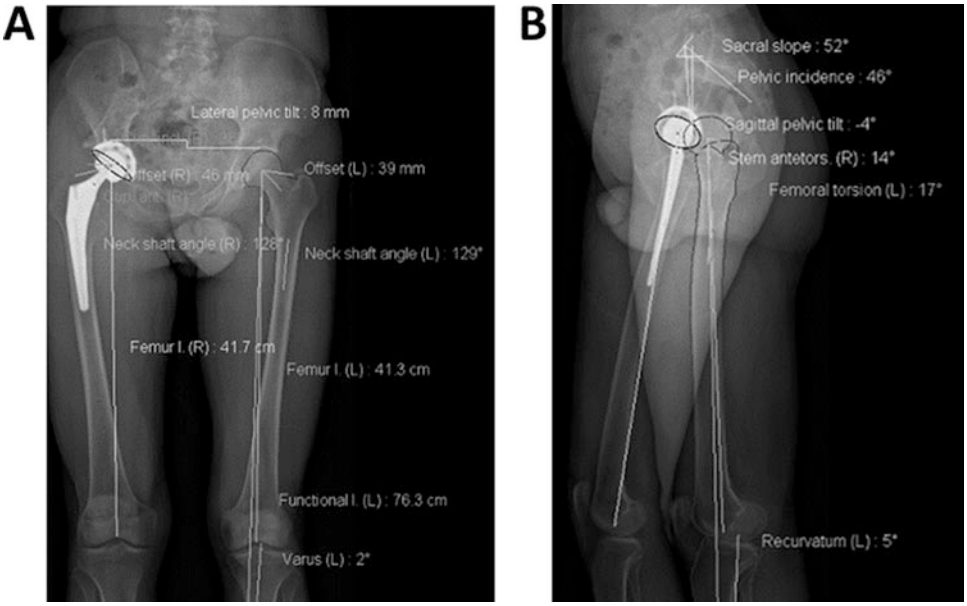

Fig. 26.2 Measurements of THA implants using EOS system. (**a**) Anteroposterior X-ray image and (**b**) lateral X-ray image. The sterEOS software implemented in EOS system demonstrated acetabular cup and femoral stem angles, as well as several parameters of pelvic and lower limb alignments

consents were obtained. The study protocol was approved by the Kameda Daiichi Hospital review board. The implanted prostheses were 50 of Trident cups and Accolade TMZF stems (Stryker, Michigan, USA), 37 of Continuum cups and CLS stems (Zimmer, Indiana, USA), and 3 of AMS cups and PerFix stems (Kyocera Medical, Osaka, Japan). We measured acetabular cup and femoral stem angles using EOS system in standing positions at 3 months after surgeries. Cup and stem angles were measured by the sterEOS 3D software (EOS Imaging Inc., Paris, France) implemented in EOS system. Specified reference points on 2D anteroposterior and lateral X-ray images were digitized according to the manufacturer's protocol. The sterEOS software displayed cup and stem angles in its specified coordinates (Fig. 26.2).

These measurements were compared with the associated angles measured with the 3D image analyzing software, ZedHip, from postoperative CT images in supine positions acquired by an Aquilion PRIME 80-slice CT scanner (Toshiba, Tokyo, Japan). The CT images were obtained at 6 weeks after surgeries. Digitally reconstructed radiograph (DRR) procedure implemented in ZedHip was used to sharpen the implant contours, by which we could get clear edges of acetabular cups or the stem necks without any metal halation. Computer-assisted design (CAD) models of the acetabular cups or of the femoral stems were superimposed on contours of the implants in multiplanar reconstructed images of the postoperative CT images according to the manufacturer's protocol. Then, ZedHip displayed the acetabular cup or stem neck angles in its specified coordinate (Figs. 26.3 and 26.4).

According to the cup angle definition of EOS system, we measured radiographic inclination and anatomical anteversion of the acetabular cups [13] with respect to the APP coordinate in both measurements by EOS system and CT scan. The stem antetorsion was defined as the angle between the neck shaft axis and the post-condylar axis on the profile view of the plane perpendicular to the functional femoral axis (Fig. 26.4a). The angle differences between EOS system and CT scan were compared to evaluate the accuracy of EOS system to measure implant angles after THA.

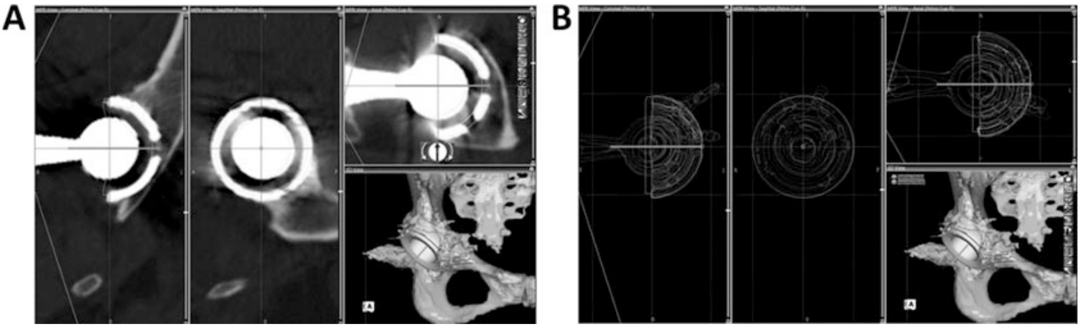

Fig. 26.3 Measurement of acetabular cup angles using CT scan images and 3D image analyzing software; ZedHip. (**a**) The CAD of acetabular cup was superimposed on the contour of acetabular cup in multiple slices of postoperative CT images. (**b**) The edge of the acetabular cup in the postoperative CT was sharpened using DRR procedure implemented in ZedHip

Fig. 26.4 The femoral coordinate for stem antetorsion. (**a**) Definition of the functional femoral axis coordinate in ZedHip. (**b**) The femoral stem CAD was superimposed on the contours of femoral stem in multiple slices of the postoperative CT. (**c**) The contours of stem neck was sharpened using DRR procedure implemented in ZedHip

We defined "outlier" as over 5° difference between the measurements obtained from EOS system and those measured from CT scan. Based on whether there is outlier angle or not, the data were divided into four groups as "all inlier," "cup," "stem," and "both." The "all inlier" group (36 hips) showed differences less than 5° in both cup and stem measurements between EOS system and CT scan. The "cup" group (31 hips) showed differences over 5° only in cup measurements. The "stem" group (17 hips) showed differences over 5° only in stem measurements. The "both" group (six hips) showed differences over 5° in both cup and stem measurements. Then we analyze effects of several parameters on outliers. Analyzed parameters were pelvic asymmetry, pelvic sagittal tilt angles in standing and supine positions (the inclination of the APP against the perpendicular axis in EOS system and against the CT table in CT scan), femoral deformity, difficulty in defining the APP, difficulty in defining cup contours, mismatch of femoral head, and mismatch of statistical 3D bone modeling (Figs. 26.5 and 26.6). Kruskal-Wallis one-way analysis of variance (KW analysis) was used to analyze the correlation between pelvic sagittal tilt angles and outliers. Chi square analysis was used to investigate the correlation between other parameters and outliers. Spearman's rank correlation was used to analyze correlation of measurement values between EOS system and CT scan. P values less than 0.05 were considered to be statistically significant. JMP 5.0.1a (SAS Institute Inc. North Carolina, USA) was used for statistical analyses.

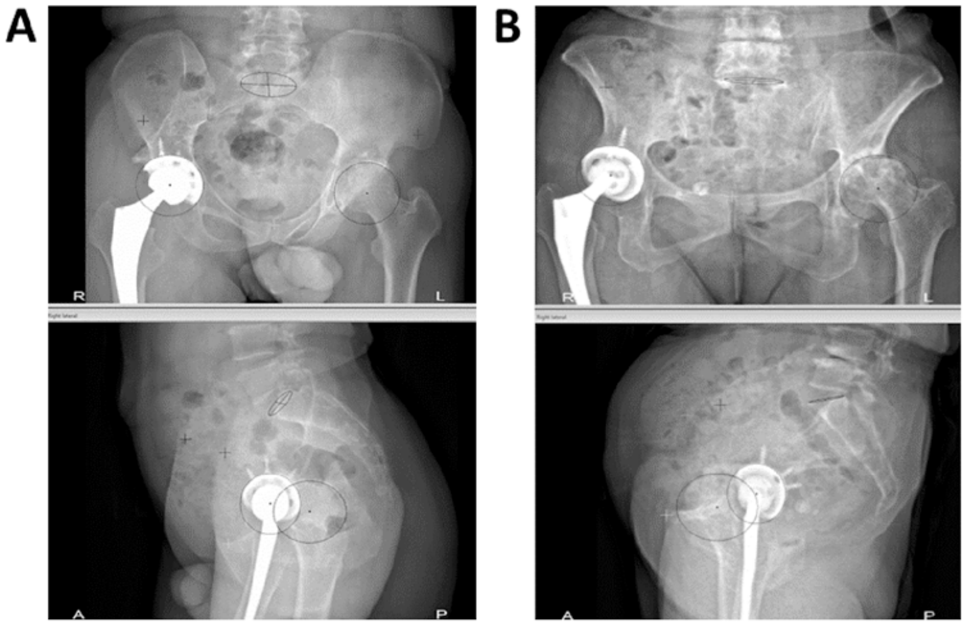

Fig. 26.5 Pelvic asymmetry and pelvic sagittal tilt. To digitize optimum reference points was sometimes difficult on a pelvis with pelvic asymmetry (**a**) or pelvic sagittal tilt (**b**)

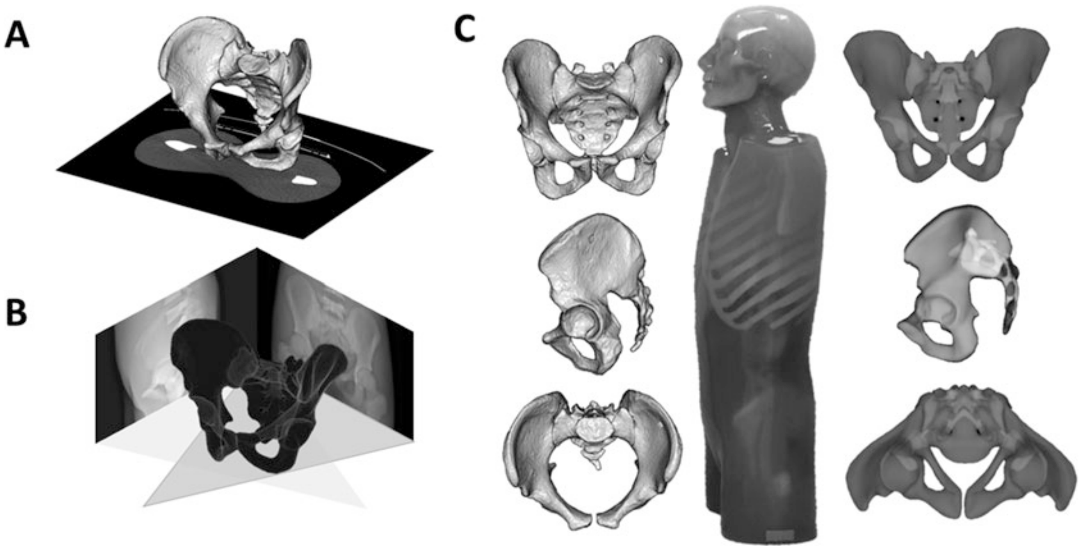

Fig. 26.6 Mismatch of statistical 3D bone modeling. (**a**) CT volume rendering using multiple CT slices. (**b**) EOS modeling using biplanar X-ray images. (**c**: 3D pelvic models were created using a CT torso phantom (Kyoto Kagaku. Co. Ltd., Kyoto, Japan). Pelvic models in the left column were by CT volume rendering, and the ones in the right column were by EOS statistical bone modeling. The shapes of the ilium, acetabulum, and ischium were different between CT volume rendering and EOS modeling

26.3 Results

The radiographic inclination (mean ± SD) of acetabular cups were 40.3° ± 3.6° by EOS system and 42.6° ± 3.5° by CT scan, respectively. The anatomical anteversion (mean ± SD) of acetabular cups were 21.9° ± 11.3° by EOS system and 22.0° ± 9.5° by CT scan, respectively. The neck antetorsion (mean ± SD) of femoral stems were 30.6° ± 13.4° by EOS system and 31.9° ± 11.9° by CT scan, respectively (Table 26.1 and Fig. 26.7). The differences between EOS system and CT scan (mean ± SD, range of 95% CI) were (−2.3° ± 2.7°, −2.8°∼ − 1.7°) in cup radiographic inclination, (−0.1° ± 5.0°, −1.2°∼0.9°) in cup anatomical anteversion, and (−1.3° ± 6.5°, −2.7° ∼0.1°) in stem antetorsion, respectively (Table 26.1).

The correlation coefficients (rho) between the values measured by EOS sys-tem and by CT scan were 0.6973 ($p < 0.0001$) in cup radiographic inclination, 0.763 ($p < 0.0001$) incup anatomical anteversion, and 0.8861 ($p < 0.0001$) in stem antetorsion (Table1), respectively.

The incidences of outliers (differences between values measured by EOS system and CT scan >5°) were 14/90 in cup radiographic inclination, 28/90 in cup anatomical anteversion, and 27/90 in stem antetorsion (Table 26.1 and Fig. 26.7).

The SDs of the cup anteversion and the stem antetorsion were larger than those of the cup inclination. There were strong correlations in each measurement between EOS system and CT scan. However, the scattered grams showed some outliers in each measurement, especially, in the cup anteversion and stem antetorsion, demonstrating over 30% outliers (Table 26.1 and Fig. 26.7).

In the study of the outliers, there were no significant differences ($p > 0.05$) in pelvic asymmetry, femoral deformity, difficulty in defining cup contours, mismatch of femoral head, and mismatch of statistical 3D bone modeling, as well as pelvic sagittal tilt angles instanding and

Table 26.1 Implants angles measured by EOS system and CT scan

	Cup inclination	Cup anteversion	Stem antetorsion
EOS system	40.3±3.6	21.9±11.3	30.6±13.4
CT scan	42.6±3.5	22.0±9.5	31.9±11.9
Differences(EOS-CT)	−2.3±2.7	−0.1±5.0	−1.3±6.5
95% CI of differences	−2.8∼−1.7	−1.2∼0.9	−2.7∼0.1
Spearman's correlation coefficients (rho)	0.6973 (p<0.0001)	0.763 (p<0.0001)	0.8861 (p<0.0001)
Outlier(difference>5°)	14/90 (17%)	28/90 (34%)	27/90 (31%)

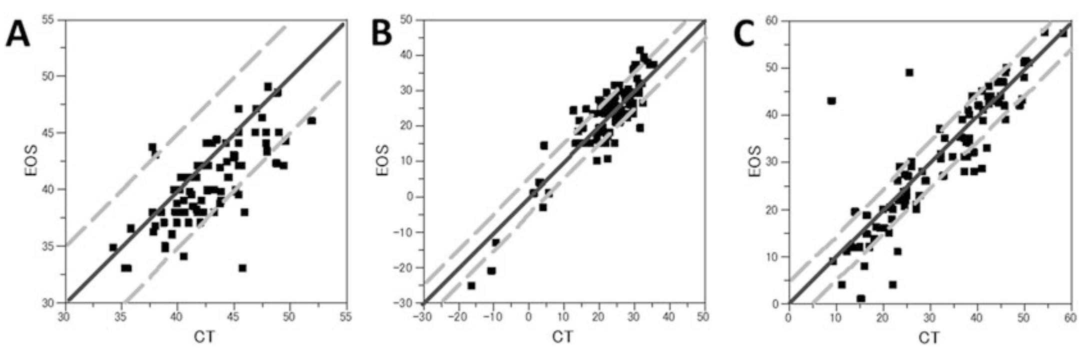

Fig. 26.7 Implant angles measured by EOS system and CT scan. (**a**) Radiographic inclination of the acetabular cups. (**b**) Anatomical anteversion of the acetabular cups. (**c**) Stem antetorsion. X-axis, CT scan measurement; Y-axis, EOS measurement; black solid line, y = x; dotted lines indicated ±5^0 from y = x

Table 26.2 Effects of pelvic sagittal tilt in standing and supine positions on outliers

	All inlier	Cup	Stem	Both	KW analysis
EOS system (standing)	0.31±8.1	−0.67±13.8	−1.5±9.1	−2.4±18.3	p = 0.8772
CT scan (supine)	2.5±6.3	2.3±9.7	2.0±8.3	4.8±10.2	p = 0.7300
N	36	31	17	6	

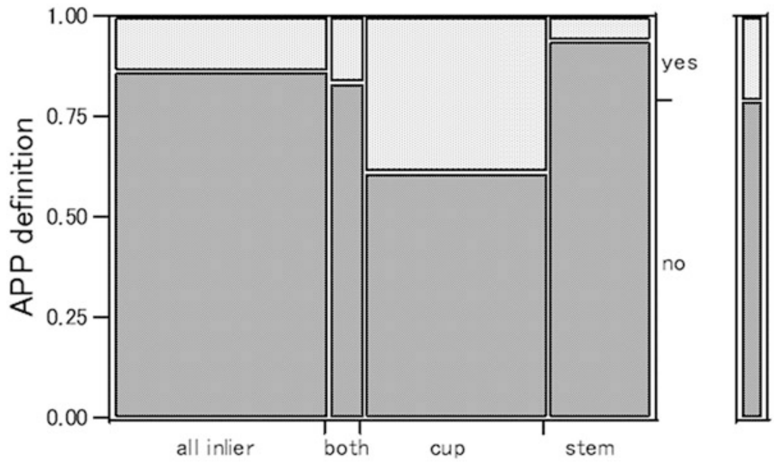

Fig. 26.8 Effects of difficulty of APP definition, X2: p = 0.0252

supine positions (Table 26.2). However, difficulty in defining APP demonstrated significant differences (p = 0.0252) (Fig. 26.8).

26.4 Discussions

There are a few modalities which provide 3D skeletal information of patients in standing position. HipCAS is one of the modality by which we can measure 3D hip alignments using biplanar X-ray images in a standing position and preoperative CT scan images with 2D-3D registration procedure [7]. However, biplanar X-ray images in HipCAS are obtained sequentially which may cause mismatch of 2D-3D registration if there is patient's movement during radiography. EOS system solved this problem by using of two pairs of perpendicular-positioned radiation sources and detectors which allow simultaneous capture of anteroposterior and lateral radiographs. These biplanar X-ray images enable us to create a precise 3D reconstruction of skeletal system because the images are captured in a spatially calibrated manner [1]. In this study, we successfully measured implant angles after THA in standing positions by using of EOS system. There were strong correlations in measurement values between EOS system and CT scan. However, we identified non-negligible (over 30%) outliers, especially in cup anteversion and stem antetorsion, showing over 5° differences between EOS system and CT scan (Table 26.1 and Fig. 26.7).

Journe et al. [14] compared angles of an acetabular cup implanted into a single cadaveric pelvis between EOS system and CT scan. The errors of EOS system in comparison with CT scan were 2.6° in inclination and 6.6° in anteversion, respectively. However, the pelvic coordinate systems used to measure the inclination and anteversion were not the same between EOS system and CT scan [14]. Guenoun et al. [15] reported a basic study for the stem implanted into the femoral model bones by comparing measurements obtained by EOS system and those measured from CT scan. Acceptable averages ± SDs of crude measurement values, strong correlation between measurements obtained by EOS system and those measured from CT scan, and reproducibility of the measurement procedures were presented. However, there were no description about differences of each measurement between EOS system and CT scan [15]. From their data, the previous basic accuracy studies using cadaveric or model bones were not reliable to understand real accuracy of 3D measurement after THA using EOS system.

Several factors which may affect outliers were investigated in this study. Difficulties to define APP demonstrated statistically significant differences. We used APP coordinate because the coordinate for angle measurements should be the same in both modalities. Even though EOS system provided biplanar anteroposterior and lateral images with high resolution, in some cases, it was quite difficult to identify bilateral anterior superior iliac spines or symphysis pubis on 2D X-ray images, especially in the patients with asymmetric pelvis or with sagittal pelvic tilt (Fig. 26.5).

The accuracy studies showed that the 3D spine or femoral models created from the biplanar X-ray images in EOS system provided clinically acceptable accuracies [16] [17]. Even though we can create 3D bone surface models by digitizing reference points on EOS X-ray images, these bone models were sometimes quite different from the 3D bone models created from CT images. So far, we could not find accuracy studies of 3D pelvic bone model created by EOS system. Surprisingly, non-negligible differences were detected when we compared the 3D bone surface models created by EOS system and those created from a CT scan using a CT torso phantom (Kyoto Kagaku Co. Ltd., Kyoto, Japan) (Fig. 26.6). The second weak point of these 3D bone models created by EOS system is that we cannot place any reference points on the 3D bone models. Therefore, only 2D information can be used when we collect reference points for measurements.

After discussion about these outliers in measurements of the implant alignment after THA with engineers from EOS Imaging Inc., we realized that the APP coordinate in EOS system was different from the standard APP definition. In EOS system, the X-axis for measurements was always shifted to be parallel to the line between the acetabular centers. Namely, the X-axis of each APP coordinate in EOS system was not the X-axis of the standard APP definition. Therefore, we could not make conclusion about accuracy in acetabular cup measurements by EOS system.

For the femoral coordinate in EOS system, the Z-axis was the functional femoral axis in which femoral head center was used. The femurs of Japanese patients who are suffering from secondary osteoarthritis due to developing dysplasia of the hip often show deformed femoral head. In such cases, it is difficult to identify the real femoral head center. Thus, many Japanese hip surgeons using computer-assisted surgery prefer to use the post-condylar tabletop coordinate for femoral measurements, such that the femoral head center is not used. We also realized that the distal points of the functional femoral axes were different between EOS system and ZedHip. The intercondylar notch was used in EOS system while the midpoint between the bilateral epicondyles was used in ZedHip. The definition for the distal point of femoral axes is still open for discussion [18–21]. When the femur rotates around the Z-axis, to define the intercondylar notch in 2D X-ray images is sometimes difficult. Because 3D bone models created from CT images are available for us, we prefer to use the midpoint between the bilateral epicondyles to define the functional femoral axis.

To reduce errors during 3D measurements, Kai proposed full automatic approach to decide reference points [22]. Uemura et al. presented automated 2D-3D registration between preoperative CT images and postoperative anteroposterior X-ray films to measure pelvic sagittal tilt in a large cohort [23]. The EOS system provides non-distorted clear biplanar X-ray images. Using 2D-3D registration techniques with preoperative CT images, we will be able to improve the accuracy of measurements by EOS system.

In conclusion, EOS system could not overcome the accuracy of 3D implant measurements after THA using CT scans. To improve measurement accuracy, 2D-3D registration between the 2D biplanar X-ray images and preoperative CT images should be considered. In addition, the pelvic and femoral coordinates in EOS system should be standardized according to the standard definitions.

Acknowledgments The authors gratefully acknowledged Mr. Antoine Mousnier for his advices about the coordinates in EOS system.

Conflict of Interest The authors declare that they have no conflict of interest.

References

1. Illes T, Somoskeoy S (2012) The EOS™ imaging system and its uses in daily orthopaedic practice. Int Orthop (SICOT) 36:1325–1331
2. Iwana D, Nakamura N, Miki H et al (2013) Accuracy of angle and position of the cup using computer tomography-based navigation system in total hip arthroplasty. Comput Aided Surg 18(5–6):187–194
3. Schwarzkopf R, Vigdorchik JM, Miller TT et al (2017) Quantification of imaging error in the measurement of cup position: a cadaveric comparison of radiographic and computed tomography imaging. Orthop 40(6):952–958
4. Hayashi S, Nishiyama T, Fujishiro T et al (2013) Evaluation of the ac-curacy of femoral component orientation by the CT-based fluoro-matched navigation system. Int Orthop (SICOT) 37:1063–1068
5. Kim TH, Lee SH, Yang JH et al (2012) Computed tomography assessment of image-free navigation-assisted cup placement in THA in an Asian population. Orthop 35(Suppl 10):13–17
6. Steppacher SD, Tannast M, Zheng G et al (2009) Validation of a new method for determination of cup orientation in THA. J Orthop Res 27:1583–1588
7. Kobayashi K, Kai S, Sakamoto M et al (2014) Image registration method for assessing 3D hip alignment and implant position during standing posture. J Biomech Sci Eng 9(2):162–170
8. Bendaya S, Anglin C, Lazennec JY et al (2016) Good vs poor results after total hip arthroplasty: an analysis method using implant and anatomic parameters with the EOS imaging system. J Arthroplast 31:2043–2052
9. Polkowski GG, Nunley RM, Ruh EL et al (2012) Does standing affect acetabular component inclination and version after THA? Clin Orthop Relat Res 470:2988–2994
10. Lazennec JY, Rousseau MA, Rangel A et al (2011) Pelvis and total hip arthroplasty acetabular component orientations in sitting and standing positions: measurements reproducibility with EOS imaging system versus conventional radiographies. Orthop & Trauma: Surg & Res 97:373–380
11. Lazennec JY, Rousseau MA, Brusson A et al (2015) Total hip prostheses in standing, sitting and squatting positions: an overview of our 8 years practice using the EOS imaging technology. Open Orthop J 9: 26–44
12. Monazzam S, Agashe M, Hosalkar HS (2013) Reliability of over-coverage parameters with varying morphologic pincer features: comparison of EOS and radiography. Clin Orthop Relat Res 471:2578–2585
13. Murray DW (1993) The definition and measurement of acetabular orientation. J Bone Joint Surg Br 75(2):228–232
14. Journe A, Sadaka J, Belicourt C et al (2012) New method for measuring acetabular component positioning with EOS imaging: feasibility study on dry bone. Inter Orthop (SICOT) 36: 2205–2209
15. Guenoun B, Hajj FE, Biau D et al (2015) Reliability of a new method for evaluating femoral stem positioning after total hip arthroplasty based on stereo-radiographic 3D reconstruction. J Arthroplast 30:141–144
16. Humbert L, De Guise JA, Aubert A et al (2009) 3D reconstruction of the spine from bi-planar X-rays using parametric models based on transversal and longitudinal inferences. Med Eng Phys 31(6): 681–687
17. Chaibi Y, Cresson T, Aubert B et al (2012) Fast 3D reconstruction of the lower limb using a parametric model and statistical inferences and clinical measurements calculation from bi-planar X-rays. Comput Methods Biomech Biomed Engin 15(5): 457–466
18. Wu G, Siegler S, Allard P et al (2002) ISB recommendation on definitions of joint coordinate system of various joints for the reporting of human joint motion–part I: ankle, hip, and spine. Int Soc Biomech J Biomech 35:543–548
19. Grood ES, Suntay WJ (1983) A joint coordinate system for the clinical description of three-dimensional motions: application to the knee. J Biomech Eng 105:136–144
20. Yoshioka Y, Siu D, Cooke TD (1987) The anatomy and functional axes of the femur. J Bone Joint Surg Am 69:873–880
21. Sato T, Koga Y, Sobue T et al (2007) Quantitative 3-dimensional analysis of preoperative and postoperative joint lines in total knee arthroplasty: a new concept for evaluation of component alignment. J Arthroplast 22:560–568
22. Kai S, Sato T, Koga Y et al (2014) Automatic construction of an anatomical coordinate system for three-dimensional bone models of the lower extremities–pelvis, femur, and tibia. Biomechanics 47(5):1229–1233
23. Uemura K, Takao M, Otake Y et al (2017) Change in pelvic sagittal inclination from supine to standing position before hip arthroplasty. J Arthroplast 32(8):2568–2573

3D Printing in Spine Surgery

27

Hong Cai, Zhongjun Liu, Feng Wei, Miao Yu, Nanfang Xu, and Zihe Li

Abstract

In the past 5 years, the application of 3D printing technology in the field of spine surgery had obtained enormous and substantial progress. Among which, vertebral skeleton model (including lesion model) printing has been widely used in clinical application due to its relatively simple technology and low cost. It shows practical value and becomes popular as the reference of clinical education, auxiliary diagnosis, communication between doctor and patient, and the planning of surgical approaches as well as the reference of more accurate operation in surgery. On the basis of vertebral skeleton model printing, it can be used to design and make navigation template to guide internal fixation screw, which also obtains some remarkable clinical effects. However, 3D printing technology has a more profound influence on spine surgery. The part with full expectation is undoubtedly the clinical application of 3D printing microporous metal implant and personalized implant as well as the clinical application of 3D printing biological materials in the future.

H. Cai · Z. Liu (✉) · F. Wei · M. Yu · N. Xu · Z. Li
Department of Orthopedics, Peking University Third Hospital, Beijing, China
e-mail: liuzj@medmail.com.cn

Keywords

Spine surgery · 3D printing · Personalized implant · Navigation template · Developmental trend

27.1 Application of Model and Navigation Template in Spine Surgery

Model and navigation template or customized surgical auxiliary tool is a main application of 3D printing in orthopedic field, especially in serious spinal deformity, with important value in communication between doctor and patient, preoperative plan, intraoperative assistance, or medical education [1–3].

27.1.1 Model

Since 1999, D'Urso et al. began to systematically summarize the use experience of 3D printing at the earliest [4]. He took 3D printing anatomical models as intraoperative reference in the treatment of cervicothoracic or lumbar spinal deformity caused by congenital osteogenesis imperfecta. In the same year, he published its application in the cranial occipital deformity and the maxillary lesion [5].

G. Zheng et al. (eds.), *Intelligent Orthopaedics*, Advances in Experimental Medicine and Biology 1093, https://doi.org/10.1007/978-981-13-1396-7_27

There were many reports on the application of 3D printing models in spine surgery. It has the advantage to bring visual sense for surgeon through real appearance so as to increase the overall grasp of operation, and it is beneficial for the communication with patient.

Yang et al. [6], through the analysis of intraoperative and postoperative situations of Lenke 1 3D printing group and traditional operation group, found that 3D printing group had a shorter operation time (184 min vs 212 min), less perioperative blood loss (846 ml vs 1029 ml), less blood transfusion volume (827 ml vs 985 ml), less postoperative hemoglobin loss (118 g/L vs 115 g/L), lower occurrence rate of operative complications (8% vs 14.5%), and slightly higher hospitalization expenses (USD 22,797 vs USD 22,143). However, there are no differences in hospital stays, postoperative radiological outcomes, and misplacement of screws (16.9%, 120/710 vs 18.8%, 195/1036). For the scoliosis surgery with the Cobb angle of more than 50 degrees, the application of 3D printing model could significantly lower the misplacement rate of screws (9.1% vs 13.0%), by comparing with freehand screw placement. In screw placement deviation, the total deviation rate of 3D printing model group reached 16.9%, with internal wall damage of 5.21%, external wall of 8.59%, front wall of 0.99%, endplate damage of 1.13%, and intervertebral foramina damage of 0.99%, which were all lower than those of freehand screw placement.

According to our experience, the accuracy of screw placement at convex side in 3D printing group was slightly high among patients with congenital scoliosis, through comparing 298 vertebral pedicle screws assisted by 3D printing model and 344 vertebral pedicle screws imbedded with hand.

Moreover, 3D printing model is helpful for the preoperative education and communication with patients. D'Urso et al. reported that the sense of identity for operation could be increased significantly before operation for 25% of patients through 3D printing model [5]. Other authors reported that 3D printing model communication could significantly relieve anxiety-related pains [7, 8].

The advantages of computer-aided 3D printing model lie in (1) displaying the three-dimensional configuration of the vertebral body; (2) through CAD, 3Ds, MAX, and other image processing software, bony three-dimensional reconstruction model can guide into post-processing to confirm the accurate parameters of vertebral pedicle screw, including the position, angle, and depth of screw entrance point; and (3) simulating the segment and scope of orthopedic and physiological curvature of the spine to confirm whether osteotomy is needed.

However, due to the wide application of navigation system, its accuracy for screw placement cannot be replaced by 3D model system. In view of the difficulties in the scanning and reconstruction of the full spine, the scope included by general navigation system usually has three to four segments of centrum. Therefore, it cannot reach the function of integrally displaying spinal deformity. Our experience is to conduct the overall design and expectation of operation through 3D printing model before operation and use navigation equipment to assist the processing of vertebral pedicle with severe rotation deformity.

27.1.2 Template

The 3D printing template of the spine provides convenient condition of the internal fixation operation in deformity, especially the placement of vertebral pedicle screws. As is known to all, spine surgery has great demand for vertebral pedicle screw. Since it can go through the anterior, middle, and posterior column of the spine (Denis' three-column theory) so as to reach excellent correction and stability effects, vertebral pedicle screw has obvious advantage by comparing with previous fixation device. However, variation in diameter of vertebral pedicle, caused by deformity, accompanied by rotational deformity of the spine, often causes the difficulty and failure of freehand screw placement, thus to cause nerve and vascular injuries. Although the constantly updated navigation equipment can provide real-time three-dimensional image to assist surgeon to place screw, the expensive price scares off many medical institutions.

Based on image, 3D printing template can export the designed file to 3D printing equipment in fixed format so as to print individualized and accurate auxiliary screw placement tool for surgical operation, through preoperative CT scanning of folium and computer-assisted design. The template can reach the destination of guiding drilling hole and screw placement through forming specific fit with the surface of the spine.

According to purposes, 3D printing spine-assisted template for screw placement can be divided into guide position type, guide drilling type, guide screw placement type, and compound template combined by the three types. According to the guide screw placement scope of the template, it can be divided into unilateral type, bilateral type, and cross-vertebral body type. According to fitting with spinous process, the template can be divided into spinous process type and non-spinous process type. The 3D printing template-assisted screw placement is individually customized technology. Its imaging collection, design and manufacturing of the template, specific operation process, postoperative evaluation, and other links shall be treated as medical operation.

At present, the common methods of evaluating the effects of 3D printing template in spine screw placement are mainly on the basis of imaging results: (1) comparing and evaluating through radiographic measuring the distance of screw going through the bone cortex and (2) comparing the radiographic data before and after the operation. It is not difficult to find that such evaluation system is relatively backward and needs to be done in reexamination after operation and it is unable to make sure whether there is deviation in screw placement during operation. It should also be noted that the application of the template needs to conduct extensive dissection of soft tissues, which increases blood loss, operation time, and infection risk; the accurate fitting matching between the template and bone bed surface as well as stable placement is very important. In case of any deviation, all the previous efforts will be in vain. General scoliosis surgery (for instance, idiopathic scoliosis deformity with less severe rotation) can be finished through freehand screw placement with no significant difference between its result and the use of template. For high-difficulty deformity (for instance, rigid deformity with severe rotation), the advantage of the template is not higher than the results of navigational positioning.

What about the effects of spine template on different segments? At present, the studies and application of the spine are mainly study on in vitro simulated screw placement, preliminary clinical application, and control study. We will discuss them in details, respectively.

27.1.2.1 Auxiliary Screw Placement of Cervical Vertebra

Screw placement of the cervical vertebra is mainly divided into atlantoaxial and inferior cervical vertebra. The former mainly focuses on cadaver study. Hu et al. compared the preoperative and postoperative CT reconstruction three-dimensional data of atlantoaxial transarticular screw of 32 cadaveric cervical specimens and found that there is no significant statistical difference between the actual entry point in operation and ideal entry point [9]. Sugawara et al. applied 3D printing template for screw placement for 12 patients with atlantoaxial instability, with no screw breaking through cortical bone [10]. Compared with preoperative planning, the deviation was (0.70 ± 0.42) mm. Goffin et al. applied the Magerl technique (posterior atlantoaxial joint screw placement) to conduct screw placement and found that the template was much more stable when connecting both of the lamina and spinous process than connecting the lamina only [11]. This point is verified in cadaver and actual operation and is similar to the experience of other doctors. In conclusion, 3D printing template technology lacks clinical control studies with large sample in the operation of atlantoaxial screw placement. With respect to inferior cervical vertebra, Kaneyama et al. obtained successful screw placement in all cervical vertebra cross-spinous process embedded in unilateral template vertebral pedicle screw placement in cadaver study [12].

Anterior cervical vertebra-assisted screw placement: Since the anterior cervical intraoperative soft tissue peeling area is small and has much shield, it is difficult to find stable bone surface. Therefore, although there were relevant reports, for instance, Fu et al. attempted to apply 3D printing template to conduct anterior cervical pedicle screw placement on cadaveric study [13]. Its application prospect is still worrying.

In conclusion, cervical vertebra 3D printing template-assisted screw placement is still in the stage of cadaver study, with less clinical experience. This may be caused by the relatively high requirements of cervical vertebra template for entry point of vertebral pedicle, commonly unsteady placement of template, and interference of surrounding soft tissues, which make the template unable to confront the shearing force during operation and easy to break away from the preset position.

27.1.2.2 Thoracic Vertebra-Assisted Screw Placement

Thoracic vertebra pedicle screw placement is the main application demand of 3D printing template-assisted screw placement. At present, the accuracy of vertebral pedicle screw placement is mainly judged according to the criteria proposed by Rampersaud. Completely locating in vertebral pedicle shall be deemed as Level A (excellent), breaking through the vertebral pedicle cortex without exceeding 2 mm shall be deemed as Level B (good), breaking through the vertebral pedicle cortex by 2–4 mm shall be deemed as Level C (moderate), and breaking through the vertebral pedicle cortex by 4 mm shall be deemed as Level D (poor). Due to the variation of anatomical structure and effects of surrounding soft tissues, it is difficult to judge the entry point of screw placement. Ma et al. compared the freehand screw placement and the template; the rate of breaking through vertebral pedicle in the template group was 16/224, breaking through vertebral pedicle cortex by less than 2 mm, with the accuracy being higher than that of the group with hand (84/224, 58 screws broke through $\leq$2 mm, 16 screws broke through $\leq$4 mm and > 2 mm, and 10 screws broke through >4 mm) [14]. Sugawara et al. placed 58 screws in the thoracic vertebra with the help of compound unilateral template and achieved good effects without breaking through the bone cortex [15].

27.1.2.3 Lumbosacral Vertebrae-Assisted Screw Placement

Although there is difficulty in placement of screws into the anatomical structure of the lumbar vertebra and other vertebral pedicle, screw placement with template can still shorten the time and increase accuracy. However, Merc et al. also found that the offset of screw placement with template was caused by the slight relative motion between adjacent vertebral bodies in operation [16]. This might also be relevant to the greater range of motion of the lumbar vertebra.

27.1.2.4 Spinal Deformity

Due to developmental deformity of vertebral pedicle, accompanied by vertebral rotation, freehand screw placement faces relatively great difficulty in operation. The template-assisted deformity screw placement is free from the effects of rotation and morphological deformity generally. However, there is still some certain deviation in actual situation. Lu et al. reported vertebral pedicle screw placement with template in scoliosis, and the occurrence rate of vertebral pedicle cutting was 11/168, <2 mm [17]. The cutting rate reported by Putzier et al. reached 96.1% (totaled 76 screws), less than 2 mm [18]. The reason was that scoliosis deformity made it difficult to form effective attachment and fit between the template and the bone bed surface.

Enough stability between the template and the bone is the key point to decide whether this technology can be used or not. Compared with unilateral template, the template embedded with bilateral vertebral plates has obvious advantages due to its good stability. However, Kaneyama et al. used the method of applying unilateral template attached with spinous process to make unilateral template have the high specificity and stability similar to those of bilateral templates, without affecting screw placement [12]. It can be seen that spinous process plays an important role in the design of the template.

With respect to whether multi-vertebrae can use template technology, scholars widely believe at present that except instrumented vertebra (for instance, congenital hemivertebra) which can use cross-vertebral template, the rest situations shall avoid the application of cross-vertebral template. The reason is that extensive muscle exposure causes the occurrence of deviation in the placement of the template.

At present, conventional material of drilling guide template has been developed from acrylonitrile-butadiene-styrol copolymer to acrylic resin and laser-sintering polyamide. Through the process of sterile disinfection, there is no infection reported.

The advantages of 3D printing template-assisted screw placement lie in that (1) individual design, which can increase the accuracy rate of screw placement and reduce vascular and nerve injury; (2) simplified operation, which provides platform for the cultivation of young doctors; (3) reducing radiation during operation and lowering radiant quantity; and (4) reducing costs, with no need of other auxiliary equipment. Some scholars considered that its advantages have exceeded those of fluoro-navigation-assisted screw placement system, but the author thought that this argument still needed to be tested by time.

With respect to the design characteristics of template, Azimifar proposed using the articular process joint of adjacent vertebral body as support point to establish the installation mechanism of the template [19]. The advantage of doing this is avoiding the dependence on spinous process and extensive exposure of transverse process. It is the result of giving consideration to stability, reducing damage of local soft tissues, and increasing visibility. The accuracy rate of screw placement with operation can reach 94% (103/110, taking deviation of the screw placement rail of less than 1 mm to be standard accuracy rate). However, the design of this template is difficult for the fixation and application of long segments.

Putzier et al. [18] designed similar 3D printing template covering bilateral articular process, spinous process, and adjacent articular process to conduct screw placement for spinal deformity, and they evaluated the accuracy of vertebral pedicle screw placement according to Mirza principle [20] (Level 0, no cortical bone; Level 1, cortical process is cut by 2 mm or less; Level 2, cortical process is less than or equal to 4 mm; Level 3, cortical bone is cut by more than 4 mm). Fifty-six thoracic vertebra vertebral pedicle screws and 20 lumbar vertebra vertebral pedicle screws were included. Their clinical results showed that 84% of the screws reached Level 0 and 96.1% of the screws reached Level 0–1. All lumbar vertebra screws reached Level 0. A total of 14 thoracic vertebra screws were implanted into the centrum through in-out-in technology, and 6 of them were level 0. The 2-screw with poor position inclined to the lateral side. There was no case of nerve injury. The two vertebral pedicle screws of T11 inclined to the head side, without injuries of the cortical bone.

27.2 3D Printing Artificial Vertebral Body in Single-Level Cervical Corpectomy

The implantation of fusion cages made of titanium has been the standard of care in the treatment of cervical spondylotic myelopathy (CSM) by cervical corpectomy. CSM is the most common cause of spinal cord dysfunction in individuals older than 55 years and occurs in 10–15% of all patients with cervical spondylosis. Patients typically present with sensorimotor dysfunction in the extremities and disturbances in sphincter function. Patients with moderate to severe symptoms are unlikely to experience regression of myelopathy without surgical interventions. Anterior cervical corpectomy and fusion (ACCF) is an important technique primarily indicated when anterior discectomy alone would not provide sufficient decompression.

Autologous bone grafting is the gold standard for post-corpectomy reconstruction of the anterior spinal column, and the iliac crest is the most common harvesting site; however, complications including infection, hematoma formation, fracture, pain, and morbidity have been reported.

Titanium mesh cage (TMC) is a widely used alternative to autografts in restoring anterior column height. While donor site comorbidities are avoided, mismatch between the Young's modulus of the implant and the host bone can lead to a stress-shielding effect that eventually causes subsidence of the implant, which is frequently observed in the early postoperative period and associated with its own set of adverse outcomes such as neck pain, neurologic deterioration, and instrumentation failure. Contributing factors include gender, age, bone mineral density, type of implant, techniques for endplate preparation, and resection of the posterior longitudinal ligament. Successful reconstruction of the vertebral body using implant following ACCF is crucial for restoration of the stability and alignment of the cervical spine and providing structural support until definitive fusion. Different materials and various designs have been investigated for anterior reconstruction of the spinal column, such as titanium mesh cage, which may lead to endplate fracture and/or implant collapse, and the dense stress shielding caused by metallic materials may cause failure of osseous fusion to occur.

The use of 3D printing technology, such as electron beam melting (EBM), is an additive manufacturing technique that relies on metal powder to produce porous metal implants with a particular shape and pore structure. In animal studies, Yang et al. previously introduced a 3D printing artificial vertebral body (AVB) and found that its mechanical properties were comparable to those of cancellous bone and could therefore potentially be used to minimize the stress-shielding effect [21]. Additionally, the porous ultrastructure of the AVB could be advantageous for osteo-induction.

In a recent prospective randomized trial, we investigated the in vivo safety and efficacy of an AVB in comparison to a TMC used in patients undergoing ACCF for CSM. The AVB (Aikang, China) was fabricated following protocols previously established [20], in which melted titanium alloy powder (Ti6Al4V, particle size 45–100 μm) was used to fabricate a AVB in a layer-by-layer fashion using the EBM S12 system (Arcam AB, Sweden), according to computer-aided design (CAD) models with customization for the specific anatomical features of each patient. The rough surface formed by the melted metal particles could be observed. This morphology is advantageous for cell adhesion and proliferation, which were necessary steps for bone in-growth. Studies have previously confirmed the biocompatibility of Ti6Al4V. However, relevant clinical studies in humans have not been reported.

The primary hypothesis in this trial was non-inferiority regarding the safety and efficacy of the investigational group against the control group, and the design was approved by the institutional review board. Patients were recruited with informed consent regarding the aims and protocols of the study and allocated into either group according to a computerized randomization scheme. All patients received standard-of-care preoperative assessment, and a decision and plan for surgery were made by senior spine surgeons blinded to patient allocation results. Radiographic evaluation consisted of anterior-posterior (AP) and lateral X-rays and magnetic resonance imaging (MRI) for enhanced soft tissue contrast.

Patients were followed with radiographic evaluation 6 months postoperatively to assess for implant subsidence, cervical sagittal alignment, and fusion status. Subsidence was defined as a loss of any height of the fusion segments on follow-up lateral radiographs compared with the immediate postoperative radiographs. The height was measured at the center on the anterior edge of adjacent endplates. Severe subsidence was defined as a loss of height $\geq$ 3 mm. Cervical sagittal alignment was evaluated as the Cobb angles between C2 and C7. Criteria for fusion included mature bony trabecular bridge between the implant and the adjacent vertebrae, absence of peri-implant radiolucency, and less than 4° of Cobb angle variation of the adjacent endplates on dynamic lateral radiographs. In cases where dynamic radiographs were insufficient to determine fusion status, computed tomography (CT) was performed to provide a more definitive evaluation. The JOA scale, the JOA recovery rate, the VAS scale, the SF-36, and the Odom's criteria were used as the primary measures for clinical outcomes and were available for all patients both before the surgery and at the last follow-up.

Gaps between the AVB and fusion segments were indistinct at 6 months postoperatively, and motion on the flexion/extension radiographs was less than 4°. This indicated that the bone grew into the porous structure of the AVB. When such bone growth into the implant occurred, the stability of the cervical spine was enhanced. Causes of implant subsidence included factors such as increased patient age, decreased bone density, the sharp contact edge of the titanium mesh cage, and intervertebral over-distraction. Mohammad et al. showed that high mismatch angles is an important risk factor that leads to increased cage subsidence, and the authors hypothesized that adding wedges to the ends of the AVB would potentially avoid subsidence [22]. For conventional implants, endplate angles that match different patients are difficult to design. In our study, an AVB with a 4° endplate angle and porous secondary structure was shown to effectively prevent subsidence compared to a conventional titanium mesh cage, and the benefit was seen throughout the follow-up period. This observation suggests that our new type of AVB fabricated by EBM provided greater stability than the traditional titanium mesh cage. However, in addition to the AVB design, cage subsidence is also related to differences between individual patients, such as differences in bone density. To avoid subsidence, several measures have been proposed, including appropriate removal of the endplate, additional posterior internal fixation, and avoiding excessive distraction. Our study is a preliminary attempt to individualize AVB fabrication with 3D printing. Further research in this field is necessary.

The JOA score and cervical curvature are frequently used to evaluate surgical effects. In our study, there were no significant differences between the two groups in these two indexes. At the final follow-up, the JOA and VAS scores had improved significantly in both groups. Similar results were also observed in another study [23]. We speculated that the reason for these improvements was that they primarily depend on decompression and intervertebral distraction rather than implant type. Furthermore, there were individual differences between patients, and subjectivity existed when patients describe symptoms; thus, these two indexes should not be used to definitely compare different types of implants.

The findings of the present study demonstrated the safety and efficacy of an AVB fabricated by EBM for ACCF. No fracture or displacement of the implants was seen during the follow-up period, and the device was shown to prevent subsidence relative to a traditional titanium mesh cage. This work was a preliminary examination of an AVB fabricated by EBM for use in clinical applications.

27.3 3D Printing Personalized Artificial Vertebral Body

The application of 3D printing personalized artificial vertebral body in the reconstruction of spinal structure stability is the new breakthrough point of 3D printing in the internal fixation technology of the spine. Unlike the temporary tools with the function of auxiliary support, such as 3D printing model, vertebral pedicle screw positioning template, and osteotomy-assisted template, 3D printing spinal internal fixation material can permanently remain in the human body, for which there are higher requirements in biomechanics, biological safety, and biocompatibility. 3D printing titanium alloy material can be used for the development of cervical and lumbar interbody fusion cage and cage. The test results provided early foundation for the technical implementation plan and safety verification of 3D printing personalized artificial vertebral body. This section will simply introduce the 3D printing personalized artificial vertebral body, occurred in the past 2 years, used for the reconstruction of spinal structure stability after vertebrae resection.

The first case of the clinical application of 3D printing personalized artificial vertebral body reported in literature was published by us in *Spine* in January 2016 [24]. In this case, the 12-year-old patient visited a doctor due to tumor in the upper cervical vertebra. It was found through examination and evaluation that the tumor was

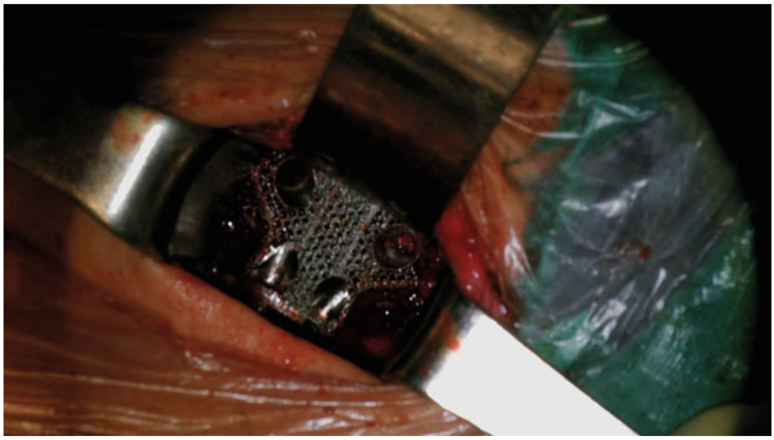

Fig. 27.1 Intraoperative view of the 3D-printed artificial vertebral body in place during the anterior procedure

at the level of axis and belonged to primary malignant bone tumor (Ewing sarcoma), without distant metastasis. Due to tumor compression, the spinal cord injury of patient developed rapidly and needed operation to reduce pressure; since the tumor was primary without distant metastasis and the patient was young, it was probably to prolong life in case radical tumor resection could be conducted. However, the anatomical structure of C2 was special, and radical tumor resection had higher requirements for postoperative reconstruction of spinal structure stability due to extensive resection range. Therefore, vertebral reconstruction of conventional international implant applied for this site was the technical difficulty all the time, with many problems, such as failure of internal fixation caused by unsatisfactory stability and bone graft fusion effects, non-healing wounds on posterior pharyngeal wall caused by the high incisura in front of internal fixation, and the demand of long time, assisted by halo-vest [25]. Liu et al. [24] designed new 3D printing personalized artificial vertebral body (Fig. 27.1) with the following characteristics: the near end applied winged structure to connect lateral mass of atlas and the far end had the slope contacted with the treated C3. Such design based on the anatomical features of patient could maximize the contact area between personalized artificial vertebral body and adjacent centrum so as to provide stability at the greatest extent. The channels of lateral mass of atlas in centrum and C3 centrum screw were the design of "zero profile," namely, the tail end of the screw after being screwed fully was at the same level with the leading edge of personalized artificial vertebral body, thus to lower the occurrence rate of non-healing wounds on posterior pharyngeal wall (Figs. 27.2a and 27.2b). Meanwhile, the microstructural parameters of 3D printing personalized artificial vertebral body applied the results of preliminary experiment [26] to improve osteoinductivity and avoid the necessity of removing the ilium and the occurrence of corresponding complications through the designs of optimized bore diameter and pore density of pore metal structure. Since the structure of 3D printing personalized artificial vertebral body could provide better biomechanical stability, patient only needed the protection of skull-neck-thorax brace after operation, instead of wearing halo-vest brace, which reduced the pains of patient and nursing difficulty. Patient accepted radiotherapy and chemotherapy after operation as well as regular follow-up. In the follow-up at 1 year after operation, the position of 3D printing personalized artificial vertebral body was good. CT of the cervical vertebra showed that the bone grew into the head and tail ends of artificial vertebral body. MR of the cervical vertebra showed that there is no manifestation of tumor relapse in the area of upper cervical vertebra. However, general PET-CT examination showed lung metastasis. Although the patient finally died of tumor metastasis due to the high malignant degree of tumor, the implant dominated by 3D printing personalized artificial vertebral

Fig. 27.2a Coronal CT reconstruction of the 3D-printed artificial vertebral body at the 3-month follow-up visit

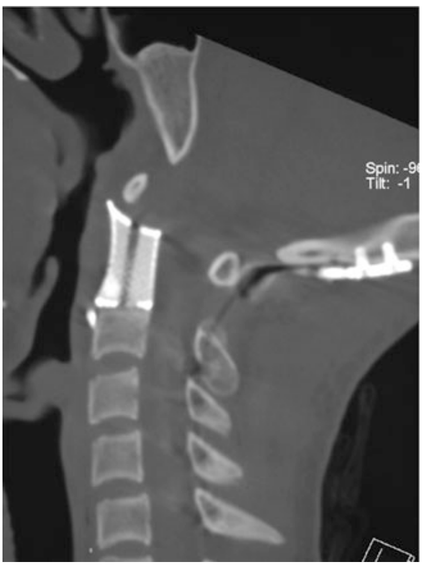

Fig. 27.2b Sagittal CT reconstruction of the 3D-printed artificial vertebral body at the 3-month follow-up visit

body was firm all the time, and no tumor relapse was found in the operation.

On the basis of this work, our team further conducted the prospective study on applying 3D printing personalized artificial vertebral body to recover the reconstruction of spinal structure stability after spondylectomy for primary tumor of axis, from April 2015 to March 2016. Based on the results of CT scanning of the cervical vertebra, 3D printing personalized artificial vertebral body was manufactured with titanium alloy powder in the method of accumulation layer by layer by applying electron beam melting (EBM). The technical parameters of microscopic pore metal structure of 3D printing personalized artificial vertebral body took the results of previous studies as reference [24, 26]. Macroscopic design took the experience of the first case [24] for reference and conducted certain improvement. Among the five patients (one case of male and four cases of female) included in the study, the average age was 30 years old (with the scope of 17–47 years old). CT-guided lesion puncture biopsy and pathological diagnosis were conducted for the five cases before operation to specify the nature of tumor. The pathological diagnosis was as follows: two cases of malignant tumor (one case of chromaffin tumor and one case of epithelioid angiosarcoma) and three cases of benign tumor (all of them were giant-cell tumor of the bone). According to the imaging examination and pathological results of patient before operation, the oncological stage of the three cases of giant-cell tumor of the bone was Enneking stage 3 and that of the other two patients was Enneking stage IIB. After perfecting preoperative examination to eliminate systemic metastases and evaluating operative tolerance, the surgical protocol of anterior and posterior radical tumor resection, "posterior fixation in Stage I and anterior tumor resection and the reconstruction of 3D printing artificial vertebral body in Stage II," was formulated for patients. Unlike in the first case, in which the patient could wear skull-neck-thorax brace to go to ground activity 1 week after operation, changed to wear Philadelphia neck collar 1 month after operation, and stopped wearing neck collar 3 months after operation, the latter patient could wear Philadelphia neck collar to go to ground activity on the day after operation and stopped wearing neck collar after 2 weeks. The five cases of patients had no severe complications in perioperative period and obtained follow-up till now. Although all patients accepted bone implantation, the CT reexamination at 3 months after operation showed that the bone had grown into 3D printing artificial vertebral body, and the CT re-examination at 6 months after operation showed that 3D printing artificial vertebral body had partially or fully fused with upper and lower centrums. By the last follow-up, all the five patients had no displacement of implant or local relapse of tumor. Based on the experience of the first two cases of patients in this series, from the 3rd case, the number of fixed segments was reduced and atlanto-occipital joint was retained, which further increased the living quality of patients. The detailed clinical data of patients in this study had been summarized and submitted for publication.

Compared with conventional implant, 3D printing personalized artificial vertebral body had been improved greatly in the reconstruction of spinal structure stability after axial tumor resection with special anatomical structure. In the prospective study of the reconstruction of spinal structure stability, conducted by Liu et al. since May 2016, by applying 3D printing artificial vertebral body after spondylectomy of several continuous sections which was conducted for patients with primary spinal tumor, five of the patients had accepted the treatment. Among the five patients (four cases of male and one case of female), with the average of 44 years old (ranging from 25 years old to 59 years old), three patients were diagnosed with chordoma, one patient was diagnosed with isolated fibrosarcoma, and one patient was diagnosed with giant-cell tumor of the bone. One patient accepted vertebral column resection for several continuous segments of the cervical vertebra and reconstruction of spinal structure stability with 3D printing artificial vertebral body. One patient accepted vertebral column resection for several continuous segments of the thoracic vertebra and reconstruction of spinal structure stability with 3D printing artificial vertebral body. The rest three patients accepted vertebral column resection for several continuous segments of the thoracolumbar vertebra and reconstruction of spinal structure stability with 3D printing artificial vertebral body. The most segments involved the reconstruction of 3D printing artificial vertebral body for the thoracolumbar segments with five centrums (T10-L2) and the length of 19 cm as well as the reconstruction of 3D printing artificial vertebral body for the cervical vertebra with four centrums (C2–C5). The application of 3D printing personalized artificial vertebral body in the reconstruction of multi-segment vertebrae resection might reduce the risk of implant displacement and sedimentation and the failure of internal fixation easily occurred in case of too long conventional titanium mesh cage and avoid the extra trauma and complications caused by the implantation of long-segment bone. Meanwhile, the 3D printing personalized artificial vertebral body was designed with the attachment of the structure of "vertebral pedicle" and connected with rear internal fixation system with screw, which could further strengthen the stability of implant and made it possible for the early mobilization of patients. The detailed clinical data of patients in this study are summarized in follow-up summary.

Since the clinical report on the application of the first case of 3D printing personalized artificial vertebral body in spine surgery [24], some other scholars reported their cases in the recent 2 years. In March and July 2017, Kim et al. and Wei et al. published the cases of conduct reconstruction by applying 3D printing technology to make prosthesis after semi-sacrectomy [27] and total sacrectomy [28]. Mobbs et al. published two case reports in April 2017 [29]. In the first case, the patient with upper cervical vertebra (C1–C2) chordoma accepted tumor resection and applied 3D printing personalized artificial vertebral body to conduct vertebral reconstruction. In the second case, the patient accepted corrective osteotomy due to complex congenital spinal deformity and also applied 3D printing personalized artificial vertebral body to conduct the stability reconstruction for the front structure of the spine. This hinted us that the application of 3D printing personalized artificial vertebral body in spine surgery is not only limited to vertebral reconstruction after tumor resection but also applicable to the stability reconstruction for bone defect caused by osteotomy operation in spine corrective operation. In September 2017, Choy et al. reported the application of 3D printing personalized artificial vertebral body in spinal reconstruction after primary tumor resection of 3D printing personalized artificial thoracic vertebra [30]. Li et al. published a case of reconstruction by applying 3D printing personalized artificial vertebral body after continuous multi-segment vertebral resection for cervical vertebra tumor [31]. In this case, the patient was diagnosed with thyroid metastasis. Although it was controversial to apply large-scale vertebral resection in the treatment of spinal tumor, this case was similar to one case of our patients with chordoma. They both hinted that the application of 3D printing personalized artificial vertebral body in the reconstruction after cervical vertebra tumor resection involved several continuous segments of dentate was a feasible technical plan.

27.4 Progress and Future Trend of the Application of 3D Printing in Spine Surgery

In recent years, the 3D printing microporous metal implant used in spine surgery mainly includes interbody fusion cage and artificial vertebral body. Although the total clinical cases have not formed large scale due to the restrictions of various factors, including the restrictions of regulations and administrative management, the treatment value of exploratory surgery cases has been revealed preliminarily and has indicated optimistic outlook. Taking artificial vertebral body, for example, the results of clinical trial of the standard cervical vertebra artificial vertebral body conducted in the Department of Orthopedics of Peking University Third Hospital from 2012 to 2014 proved that the 3D printing titanium alloy microporous artificial vertebral body obviously lowered the occurrence rate of implant collapse under the premise of safety and effectiveness, by comparing with titanium mesh cage widely used in clinical practice for many years. Up to now, the longest clinical follow-up time of the clinical application case of standard 3D printing spinal implant has exceeded 5 years, and it can still show reliable safety and satisfactory clinical curative effects. Individually customized artificial vertebral body plays an unprecedented important role and exceeds conventional implant in application as the support body of spinal structure after the resection of tumor or other lesions in the operation of cervical vertebra, thoracic vertebra, lumbar vertebra, or sacral vertebrae. The longest follow-up time of the application case of such implant has also reached 3 years. Since the cases of applying individually customized 3D printing implant are relatively scattered in various places, it is difficult to apply the investigation data with statistical significance to conduct accurate evaluation. However, the reported clinical results showed that the overall safety coefficient was relatively high, most curative effects were significant, and most cases belonged to the situation of being difficult to conduct the reconstruction of spinal stability structure with previous conventional technology after surgical resection of lesion. In other words, most of the clinical application of these individually customized 3D printing implants had innovative and challenging significance and better solved the difficult problems that were not solved satisfactorily with conventional technologies.

At the time of conducting exploratory clinical application of 3D printing microporous metal implant, the basic studies based on microporous metal implant material have been conducted step by step and have obtained more and more encouraging results. Both in vitro test and animal test used have more profound understanding of the characteristics and application value of microporous metal. The obtained results of clinical observation and relevant basic studies prove or reveal the following important facts of 3D printing microporous metal implant: (1) The biocompatibility and the function in the reconstruction of spinal mechanical structure of such implant are not inferior to or even superior to those of the implant manufactured with the same material and conventional technology. (2) The design in shape, size, and structure as well as customizability makes such implant better adapt to the demand of spine surgery, especially the operation for some special anatomic sites. (3) After implanting, its metal microporous can attract the growth of adjacent bone cells/tissues to realize the effective fusion with the host bone, thus to integrate into one. (4) If suitable processing is conducted for the surface of microporous metal of such implant, including acid etching and micro-arc oxidation [32], the osteointegration efficiency can become higher. (5) It has the potential to be ideal carrier. When it carries a drug or substance, it can play corresponding function through the slow release of these drugs or substances.

The above five manifestations or signs of 3D printing implant will trigger people's rich reverie and create many possibilities in the application in the field of spine surgery in the future. Summarizing the results of current clinical and basic studies on 3D printing microporous metal implant as well as the development of 3D printing technology, it is believed that the following development trends will appear in the application of 3D printing implant in spine surgery in the next few years:

1. The clinical application of 3D printing titanium alloy microporous structure interbody fusion cage and artificial vertebral body increases gradually. As one of optional prosthesis type, 3D printing microporous interbody fusion cage may take a place, but it is difficult to be the mainstream. The reason is that it seems to have no obvious advantage, by comparing with the current PEEK interbody fusion cage. Many years of clinical practice shows that PEEK interbody fusion cage has reached a higher fusion rate by using together with autologous/allogeneic bone or artificial bone. In contrast, it is difficult for microporous metal interbody fusion cage to reach a higher fusion rate, but the interference of metal material on imaging examination images is much larger than that of non-PEEK material, which shows its disadvantage. However, unlike microporous metal interbody fusion cage, 3D printing microporous artificial vertebral body is booming, and it has many advantages by comparing with conventional titanium mesh cage widely used in the past 20–30 years. (1) Both ends of prosthesis can be designed to be more attached with the anatomic form of the endplate of adjacent centrum, with increased contact area, thus to effectively prevent collapse. (2) Metal microporous can attract adjacent vertebral body bone to grow into it, even to realize satisfactory bone fusion without autologous/allogeneic bone. It is believed that its clinical application will become more popular or will replace titanium mesh cage widely used at present. (3) The design of the device on the main body that can be fixed with adjacent centrum directly (for instance, directly connecting implant with adjacent centrum with screw), by applying the properties of the metal material of microporous artificial vertebral body, may save the titanium plate-screw system with the function of auxiliary fixation, thus to simplify surgical procedures and realize the "zero profile" effect after the implantation of artificial vertebral body.
2. The clinical application of individually customized spinal implant will be promoted gradually. Due to the specificity of the spine in anatomic form and structure, the reconstruction of stable structure often needs to be done with the implant with corresponding form and structure in the surgical treatment of some lesions, for example, resection of atlantoaxial and sacral tumor or the correction of spinal deformity. Since it is difficult for conventional technology to manufacture the required product with irregular shape, 3D printing technology, with the advantage of designing and manufacturing any shape and structure, becomes popular. In the clinical practice in recent years, the successful implementation of artificial axis, artificial sacral vertebrae, multi-segment artificial cervical vertebra, or thoracolumbar vertebra replacement obtains satisfactory curative effects in the cases that are considered to be difficult to be treated with operation. The fact shows the important value of individually customized spinal implant. As the case in the previous section, it simulated the shape and structure of C2 and realized the demand of patient in early going to ground activity by only wearing neck collar after operation. Most of titanium mesh cage implants,

widely used after tumor resection of dentate, could only play the simple support function between anterior arch of atlas and inferior cervical vertebra, with very weak function of resistance to deflection and rotation. After operation, stronger external fixation device (for instance, halo-vest) was needed after operation, with the potential risk of loosening, collapse, displacement, and other complications. Now, we need 1–2 weeks to make the patient-specific implants, and it's free for the patient before it has been approved by CFDA.

3. 3D printing microporous metal implant turns into the repair material for bone defect. For any bone defect caused by any cause, the repair method is to wait for the early connection of bone tissues and the creeping substitution and reconstruction of bone cells in late stage after applying autologous bone, allogeneic bone, or artificial bone to filling the defect area. The final ending is the repair of bone tissue for the defect area. However, the clinical application of 3D printing microporous metal implant in recent years looks different from conventional idea, namely, metal material acts as the filler/substitute of bone defect. For the defect area with several centimeters, even a dozen centimeters after spinal multi-segment tumor resection, the activity functions of patients were well recovered after being repaired and fixed by applying microporous artificial vertebral body as support. Meanwhile, the signs of bone fusion between the implant and adjacent centrum could be observed. Relevant animal test proved that the metal microporous of implant could attract adjacent bone to grow into it and form effective fusion. Although observation is needed for the depth of bone cells growing into microporous metal implant and whether it can run through the implant with several centimeters, the results of cases with more than 18 months of follow-up show that the fusion between implant and host bone meets the demand of patients for daily living functions. It seems to believe that, for implant with larger span, the treatment goal shall be achieved if the both ends fuse with adjacent bones and it is unnecessary to consider whether there is penetrating growth of bone tissues in the middle area.
4. Titanium alloy microporous implant can become artificial prosthesis with higher bone fusion efficiency through surface technology processing. The results of relevant animal test studies showed that partial aluminum and vanadium on the surface of titanium alloy microporous implant after acid etching were free, and the growth amount of bone cells at 4 weeks after being implanted into the cervical vertebra of sheep was obviously more than that of untreated implant; while for titanium alloy microporous implant after micro-arc oxidation [32], the growth amount of bone cells at 4 weeks after being implanted into the cervical vertebra of sheep exceeded that of the acid etching group, and the phenomenon of vascular ingrowth could be seen. These results may hint that the bone fusion effects of titanium alloy microporous implant will be further improved in the future, thus to discover the improved 3D printing titanium alloy artificial prosthesis products for clinical application.
5. Development and application of other 3D printing implants. In addition to the commonly used titanium alloy in clinical application, many types of metals, such as tantalum and magnesium, may become the materials for additive manufacturing ("3D printing"). Relevant animal tests, even clinical exploration, have been conducted. However, for the clinical application in the field of spine surgery, the application value of metal implant mainly depends on its biocompatibility, integration with the bone in the implantation area (such as attachment of shape and structure, connective fixation, and fusion), biodynamical strength, and the similarity between elastic modulus and human bones. Moreover, the accessibility and costs of materials may also have certain effects on the clinical application of implant. The comparison of the characteristics of titanium alloy, tantalum, and magnesium shows that the comprehensive features of titanium alloy are more suitable to be used as the implant of bone

system. Whether tantalum and magnesium can replace titanium alloy to become the metal material of 3D printing spinal implant depends on whether tantalum and magnesium, as implant material, have the special features exceeding those of titanium alloy.

6. The 3D printing of biological materials may play an important role in the repair of soft tissue defect around the bone. In recent years, 3D printing technology of biological materials has deepening studies and process. Although there is a long way to the expectant 3D printing of human organs, 3D printing of some cells and relatively simple tissue and structure has become the reality expected to enter into clinical application. As is known to all, bone tissues, including spinal lesions, always accompany with the defect of surrounding soft tissues. When the abovementioned 3D printing metal implant successfully repairs bone defect caused by various injuries and disease, if the surrounding defected soft tissues can be repaired through 3D printing technology, it will undoubtedly bring major revolution in the treatment of spinal diseases. Throughout the development trend of 3D printing technology at present, the chance of such revolution may be coming gradually.
7. 3D printing microporous structure is taken as carrier to develop the implant with treatment function. In addition of having the mechanical functions of reconstructing bone stability structure, including filling, supporting, and fixation, 3D printing titanium alloy prosthesis can be used by taking the microporous room as important functional carrier. The loading of such drugs or active substances can certainly be used to develop various functional carriers so as to make 3D printing microporous implant become artificial prosthesis endowed with special mission, also known as "4D printing" implant.

In conclusion, it is urgent to formulate relevant standards for additive manufacturing ("3D printing") metal implant. The application of 3D printing metal implant in orthopedics, including the field of spine surgery, has become overwhelming, and its clinical value and development prospect are getting better and better. However, additive manufacturing ("3D printing") belongs to a new technology after all. Although titanium alloy has been used in clinical practice as the main orthopedic implant for many years, whether its mechanical strength and performance after being produced with new technology can remain consistent basically and whether some physicochemical indexes have significant changes, namely, that it is still safe and reliable in clinical application, naturally attract query or attention. Therefore, a series of targeted evaluation standards will be explored deeply and formed gradually. Moreover, "individually customized" will become one of the significant characteristics of 3D printing implant, and the studies and argument will be needed for the triggered ethical issues related to the safety and rationality of implant as well as the registration and supervision of individually customized medical products in different countries or regions. In conclusion, with the constant depth of studies, the application of 3D printing will be expanded in the field of spine surgery, even the whole orthopedic or medical field, and its value will be shown continuously.

References

1. Kuklo TR, Lenke LG, O'brien MF et al (2005) Accuracy and efficacy of thoracic pedicle screws in curves more than 90 degrees. Spine 30:222–226
2. Samdani AF, Ranade A, Sciubba DM et al (2010) Accuracy of free-hand placement of thoracic pedicle screws in adolescent idiopathic scoliosis: how much of a difference does surgeon experience make? Eur Spine J 19:91–95
3. Hicks JM, Singla A, Shen FH et al (2010) Complications of pedicle screw fixation in scoliosis surgery: a systematic review. Spine 35:465–470
4. D'urso PS, Askin G, Earwaker JS et al (1999) Spinal biomodeling. Spine 24:1247–1251
5. D'urso PS, Barker TM, Earwaker WJ et al (1999) Stereolithographic biomodelling in craniomaxillofacial surgery: a prospective trial. J Craniomaxillofac Surg 27:30–37
6. Yang M, Li C, Li Y et al (2015) Application of 3D rapid prototyping technology in posterior corrective surgery for Lenke 1 adolescent idiopathic scoliosis patients. Medicine 94:1–8

7. Madrazo I, Zamorano C, Magallon E et al (2009) Stereolithography in spine pathology: a 2-case report. Surg Neurol 72:272–275 discussion 275
8. Guarino J, Tennyson S, Mccain G et al (2007) Rapid prototyping technology for surgeries of the pediatric spine and pelvis: benefits analysis. J Pediatr Orthop 27:955–960
9. Hu Y, Yuan ZS, Kepler CK et al (2014) Deviation analysis of atlantoaxial pedicle screws assisted by a drill template. Orthopedics 37:e420–e427
10. Sugawara T, Higashiyama N, Kaneyama S et al (2017) Accurate and simple screw insertion procedure with patient-specific screw guide templates for posterior C1-C2 fixation. Spine 42:E340–E346
11. Goffin J, Van Brussel K, Martens et al (2001) Three-dimensional computed tomography-based, personalized drill guide for posterior cervical stabilization at C1-C2. Spine 26:1343–1347
12. Kaneyama S, Sugawara T, Sumi M (2015) Safe and accurate midcervical pedicle screw insertion procedure with the patient-specific screw guide template system. Spine 40:E341–E348
13. Fu M, Lin L, Kong X et al (2013) Construction and accuracy assessment of patient-specific biocompatible drill template for cervical anterior transpedicular screw (ATPS) insertion: an in vitro study. PLoS One 8:e53580. https://doi.org/10.1371/journal.pone.0053580
14. Ma T, Xu YQ, Cheng YB et al (2012) A novel computer-assisted drill guide template for thoracic pedicle screw placement: a cadaveric study. Arch Orthop Trauma Surg 132:65–72
15. Sugawara T, Higashiyama N, Kaneyama S et al (2013) Multistep pedicle screw insertion procedure with patient-specific lamina fit-and-lock templates for the thoracic spine: clinical article. J Neurosurg Spine 19:185–190
16. Merc M, Drstvensek I, Vogrin M et al (2013) A multi-level rapid prototyping drill guide template reduces the perforation risk of pedicle screw placement in the lumbar and sacral spine. Arch Orthop Trauma Surg 133:893–899
17. Lu S, Zhang YZ, Wang Z et al (2012) Accuracy and efficacy of thoracic pedicle screws in scoliosis with patient-specific drill template. Med Biol Eng Comput 50:751–758
18. Putzier M, Strube P, Cecchinato R et al (2017) A new navigational tool for pedicle screw placement in patients with severe scoliosis: a pilot study to prove feasibility, accuracy, and identify operative challenges. Clin Spine Surg 30: E430–E439
19. Azimifar F, Hassani K, Saveh AH et al (2017) A medium invasiveness multi-level patient's specific template for pedicle screw placement in the scoliosis surgery. Biomed Eng Online 16:130
20. Mirza SK, Wiggins GC, Kuntz CT et al (2003) Accuracy of thoracic vertebral body screw placement using standard fluoroscopy, fluoroscopic image guidance, and computed tomographic image guidance: a cadaver study. Spine 28:402–413
21. Yang J, Cai H, Lv J et al (2014) In vivo study of a self-stabilizing artificial vertebral body fabricated by electron beam melting. Spine 39:E486–E492
22. Mohammad-Shahi MH, Nikolaou VS, Giannitsios D et al (2013) The effect of angular mismatch between vertebral endplate and vertebral body replacement endplate on implant subsidence. J Spinal Disord Tech 26:268–273
23. Fengbin Y, Jinhao M, Xinyuan L et al (2013) Evaluation of a new type of titanium mesh cage versus the traditional titanium mesh cage for single-level, anterior cervical corpectomy and fusion. Eur Spine J 22:2891–2896
24. Xu N, Wei F, Liu X et al (2016) Reconstruction of the upper cervical spine using a personalized 3D-printed vertebral body in an adolescent with Ewing sarcoma. Spine 41:E50–E54
25. Wei F, Liu Z, Liu X et al (2015) An approach to primary tumors of the upper cervical spine with Spondylectomy using a combined approach: our experience with 19 cases. Spine Res Soc 22:2891–2896
26. Lv J, Xiu P, Tan J et al (2015) Enhanced angiogenesis and osteogenesis in critical bone defects by the controlled release of BMP-2 and VEGF: implantation of electron beam melting-fabricated porous Ti6Al4V scaffolds incorporating growth factor-doped fibrin glue. Biomad Mater 10(3):035013. https://doi.org/10.1088/1748-6041/10/3/035013
27. Kim D, Lim JY, Shim KW et al (2017) Sacral reconstruction with a 3D-printed implant after Hemisacrectomy in a patient with sacral osteosarcoma: 1-year follow-up result. Yonsei Med J 58: 453–457
28. Wei R, Guo W, Ji T et al (2017) One-step reconstruction with a 3D-printed, custom-made prosthesis after total en bloc sacrectomy: a technical note. Eur Spine J 26:1902–1909
29. Mobbs RJ, Coughlan M, Thompson R et al (2017) The utility of 3D printing for surgical planning and patient-specific implant design for complex spinal pathologies: case report. J Neurosurg Spine 26:513–518
30. Choy WJ, Mobbs RJ, Wilcox B et al (2017) Reconstruction of thoracic spine using a personalized 3D-printed vertebral body in adolescent with T9 primary bone tumor. World Neurosurg, 105:1032 e1013–1032 e1017
31. Li X, Wang Y, Zhao Y et al (2017) Multilevel 3D printing implant for reconstructing cervical spine with metastatic papillary thyroid carcinoma. Spine 42:E1326–E1330
32. Xiu P, Jia Z, Lv J et al (2016) Tailored surface treatment of 3D printed porous Ti6Al4V by microarc oxidation for enhanced Osseointegration via optimized bone in-growth patterns and interlocked bone/implant Interface. ACS Appl Mater Interfaces 8:17964–17975